University of Strathclyde
Department of Electronic and Electrical Engineering

Microactuators and their application in Micro-Opto-Electro-Mechanical Systems (MOEMS)

By

Lijie Li

A thesis presented in fulfilment of the requirements for the degree of

Doctor of Philosophy

April 2004

Declaration

Acknowledgements

I would like to first thank my supervisor, Professor Deepak Uttamchandani, whose guidance, support, patience, valuable ideas, and friendship has allowed me to finish this work. He was always more than happy to help me, the best supervisor anybody can have. He also offered me a RA position all through my Ph.D studies. Without his support, I would not be able to finish this thesis. So Thanks a lot, Deepak.

I would also like to thank my friends: Gordon and Justyna, who provided help on device measurement. I would also like to thank other members in the Microsystems Group for their technical cooperation and friendship.

I would also thank Prof. B. Culshaw, Dr. W. Johnstone, and Dr. G. Stewart for their encouragement. Thanks also to the other members of the Optoelectronics Group. I would like to thank Mrs. Carole Binnie and Mrs. Aileen Mitchell on their very kind help throughout.

Finally and most of all I would like to thank my lovely wife, Xiaoping Wang, and my lovely daughter, Lucy Li for their love and great support.

Abstract

Microactuators are active elements for microelectromechanical systems (MEMS), and are used to provide force to move the MEMS device in the way required. Therefore, their force characteristics, displacement capabilities and velocity ranges are of importance, and require to be investigated. Scratch drive actuators, thermal actuators, and comb drive actuators have separately been characterized, improved, and modified in this thesis.

Asymmetric thermal actuators are current driven actuators that can generate relatively high force and can be operated bi-directionally. We have designed a novel structure that has a higher displacement than traditional asymmetric actuators. The increment of maximum displacement is about 20 % above the displacement of the ordinary asymmetric thermal actuators. Detailed electro – thermal heat dissipation and expansion – deflection mechanical analyses has been performed to advance the idea. Device prototypes have been designed and the fabricated devices were tested; the experimental results show a good match to the theoretical analysis.

Scratch drive actuators (SDAs) have been modelled and characterized both on travel and force performances. Long linear travel SDAs have been designed and the fabricated devices characterized by using a high-speed camera. Detailed motion has been recorded. A theory for flexing of SDA plates has been developed. Voltage - step size relation has been obtained by theoretical analysis. Theoretical and experimental results have then been compared. Force characteristics of single and multi-plate SDAs driven by different voltages have been measured by means of micro box springs. The SDA typical step size has been measured to be 7 nm at 60 V and 100 Hz driving condition. Typically, a 4 stage SDA driven with 200 Volts produces a force of 850 μN.

Comb drive actuators are commonly used in resonators, which need high Q factors. However in some applications, such as optical choppers, they require low Q factors so that they can be operated over a large frequency range. We have designed a comb drive actuator with spring that can be operated from a few Hz up to 5 kHz. The static and dynamic testing and theoretical analysis have been undertaken in this thesis.

A variable optical attenuator (VOA) has been designed, and fabricated by surface micromachining using PolyMUMPs (Polysilicon Multi-User MEMS Processes) foundry process. The principle is simply interrupting the light beam by a vertical microshutter. An array of SDAs have been used to drive the microshutters. Microhinges are employed to build the vertical microshutter. Stress-induced beams are used to self-assemble the microshutter. Optical simulation of the VOA has been performed using Rayleigh-Sommerfield diffraction theory. Devices have also been tested with single mode optical fibres. Testing results show a dynamic range of 34.2 dB. The VOA structure was driven at a speed of 1.6 μm/s at 150 volts and 100 Hz driving condition.

An optical chopper has been realized by a pair of comb drive actuators driving two shutters. Two shutters are employed to double the response time. The device has been designed and fabricated using SOIMUMPs (Silicon On Insulator Multi-User MEMS Processes) foundry process. Completely design, simulation and testing of the chopper has been undertaken. The attenuation range of chopper has been measured to be from – 1.4 dB to – 29 dB. The response time of the chopper has been measured to be 90 μs.

Contents

Chapter 1

Introduction

1.1 Brief historical background

Microelectromechanical systems (MEMS) is a term about a technology for making small devices and systems that are (a) a substitute for larger devices or (b) perform actions that have no equivalence in larger devices. MEMS can be found in systems ranging across automotive, medical, electrical, electronics and communication applications. Its techniques and devices have the potential to affect our lives and the way we live. First introduction of this technology should be owed to Richard P. Feynman who delivered a very famous talk: *There's Plenty of Room at The Bottom* [1] in 1959. His exploration gave opportunities and challenges for manipulating and controlling devices on a small scale. That is the time when the Integrated Circuit (IC) technology was not too advanced, so there were many technological unknowns and limitations for making physically small structures. He considered the application of increasing storage by minimizing the material required to represent element of information. He said: *An entire encyclopedia could be written on the head of a pin.* Less than a decade later, in 1967 Nathanson invented the resonant gate transistor, which probably was the first batch-fabricated MEMS device [2]. In this device, a suspended cantilever beam coated with gold modulated the electrical performance of the transistor. In 1982, another remarkable paper was published: it reviewed single crystal silicon as a mechanical material, and was written by Kurt Peterson [3]. A few years later in 1986, Howe and Muller at the University of California, Berkeley developed a new technology that used polysilicon as a mechanical material; this technology is called surface micromachining [4], and is widely used to fabricate multi-layer MEMS devices. An impressive example of a commercial MEMS device that has been fabricated using surface micromachining is the AD-XL50 microaccelerometer produced by Analog Devices Inc. [5]. Researchers developed valuable electrostatic controlled micromotors using surface micromachining in 1989 [6]. The 1992 paper *'Microfabricated hinges'* gave an opportunity to build out of

plane 3-D structures [7]. In 1992, MCNC started the Multi-User MEMS Process (MUMPS). It is now a commercial MEMS foundry, which now provides a polysilicon surface micromachining process (PolyMUMPs), a SOI micromachining process (SOIMUMPs) and a metal micromachining process (MetalMUMPs). It dramatically increases the speed of MEMS prototype development. Following surface micromachining, Deep RIE technique was developed, and it offer great opportunity to micromachine thick single crystal silicon structures [8].

1.2 Motivation:

There has been a rapid development of microelectromechanical systems (MEMS) for optical communications, such as variable optical attenuators [9], [10], [11], [12], optical switches [13], [14], [15], and optical scanners [16], [17], [18]. All these MEMS optical devices need high performance actuators to realize their functions. Microactuators fabricated by MEMS are operated by electrical signals, and include scratch drive actuators (SDAs) [19], comb drive actuators [20] and electro-thermal actuators [21]. Although these actuators are well developed, there is also increasing need to precisely characterize them and improve their performances. Integrating microactuators with micro-optical elements such as shutters and mirrors is also important to optimize.

For asymmetric electro-thermal actuators, the deflection is limited by thermal effect. Normally, a "traditional" surface micromachined asymmetric thermal actuator will stop bending at around 10 μm, further increasing input power will lead to damaging the structure [21]. It is essential to develop a technique to compensate this drawback. In this thesis, a novel implementation of the asymmetric thermal actuator meets this requirement. This approach introduces a brand new concept: 'electro-heating beam shape factor'. With this concept, the displacement range of the electro-thermal actuators is extended.

For scratch drive actuators, the force generated has previously been measured using buckling beams [19]. In this thesis, a more precise way is used to measure the force

generated by SDAs and also the SDA force under different applied voltages is evaluated by this method.

Much research has been conducted on MEMS variable optical attenuators. Table 1-1 lists the technology and performance of recent micromachined variable optical attenuators.

Table 1-1. MEMS variable optical attenuators

	Attenuator 1 [9]	Attenuator 2 [10]	Attenuator 3 [11]	Attenuator 4 [12]
Technology	Surface micromachining	Silicon-on-insulator	Polysilicon surface micromachining	Polysilicon surface micromachining
Performance	25 dB range, 3 μs response time	50 dB range, 5 ms response time	50 dB range, 100 μs response time	45 dB range, 37 ms response time.

In this thesis, a self-assembled 3D MEMS VOA driven by scratch drive actuators was designed and tested. The device was designed and fabricated using Polysilicon multi-layer surface micromachining. The shutter in the device was assembled by means of stress-induced bending beams. The advantage of the SDA driven VOA is precisely controllable attenuation due to the precise step size of the SDA. The step size of SDA is examined both experimentally and theoretically. The dynamic attenuation range was measured to be 35 dB, and one-step distance of SDA was estimated to be 16 nm.

Miniaturised optical choppers fabricated by various micromachining technologies and in different material systems have been reported in earlier literature [22-25]. In [22] a micromachined chopper based on a moving diffractive element was reported for infra-red measurements. The device was fabricated on LPCVD silicon nitride deposited on a sacrificial LPCVD oxide deposited on a silicon substrate. In [23] an electrostatic actuator was used to drive a single polysilicon shutter integrated with a silicon phodetector. Polysilicon surface micromachining is used in the fabrication process. In [24] the micromachined chopper reported was fabricated in quartz and the device was piezoelectrically driven. The quartz chopper of [24] with dimensions

of 6mm x 7mm is substantially larger than the compact device developed during our research. In [25] the chopper was also fabricated using polysilicon micromachining, but with the inclusion of a back-side etched hole through which the light to be chopped is transmitted.

The chopper described in this thesis has been fabricated in BSOI (bonded silicon-on-insulator) which is mechanically superior to polysilicon. The single crystal silicon has larger value of Young's Modulus than polysilicon, and also the layer of the BSOI can be thicker than deposited polysilicon layer. The design is symmetric about its centre. Each half of the chopper consists of a blade attached to a suspension and electrostatically driven by a comb microactuator. The two comb drives are electrically connected in parallel. The two blades form a slit that can periodically be closed, resulting in the chopping action if an a.c. voltage is applied. The advantage of comb drive optical chopper is its high response speed. The comb drive actuator along with proper suspension was simulated both in a lumped model and FEM model. Experiments using a high-speed camera verified the theoretical mechanical model. An optical model was built for double shutter optical chopper using diffractive theory. The overall dimensions of the chopper, including the microactuators and micromechanical suspension, are 1200 μm x 1200 μm making it very compact. Experimentally, the device was driven from 0-34 volts d.c. to measure its static characteristics. For dynamic characterisation, the device was operated from 0-28 volts a.c. and its fundamental resonant frequency was measured to be 3 kHz.

1.3. Outline of this thesis:

The rest of the thesis has been written as follows:

A brief review of microactuators is presented in Chapter 2. Actuators driven by different principles such as electrostatic, magnetic, electro-thermal and so on are described in general. Applications of those actuators are listed.

The content in Chapter 3 mainly focuses on our designing and modelling of the electro-thermal actuators. Three types of thermal actuators were theoretically investigated both in heat conduction domain and mechanical domain; conduction effects were considered only in these analyses for the reason of simplification. The emphasis of this chapter is introducing a concept 'ohmic heating shape factor'. A novel asymmetric electro-thermal actuator was designed using this technique. Detailed temperature distribution analysis (including substrate effect during the heat dissipation) was performed together with mechanical analysis. Devices designed using this technique have been fabricated by PolyMUMPs. The performance of those devices was characterized, and are shown to match the theoretical result very well.

In Chapter 4, the designing modeling, design and evaluation of scratch drive actuators is presented. Motion characteristics of SDA (including short track and long track) was investigated, the step size of the SDA was obtained experimentally. The travel speed variation due to the different surface contact was analyzed by surface profiler – Veeco system. Also the step size of SDA was theoretically solved by constructing a static model of the SDA. The force characteristics of SDA were investigated. Microsprings attached to the SDAs have the function of measuring the force generated by SDAs. Nonlinearity of the microsprings have been analyzed by FEM software – ANSYS. Forces of 250 ± 36 μN for one plate SDA up to 850 ± 36 μN for 4 plate SDAs have been measured for 200 volts driving voltage.

In Chapter 5, the design of a variable optical attenuator driven by SDAs is presented. In the mechanical design section, the microhinge is described and design sequence is presented step-by-step using L-Edit software. The microhinges connect the SDA array to a microshutter. Stress-induced bimorph beams have been used to assemble the microshutter. The theoretical model of stress-induce beams has been built using classic mechanical theory. Also the temperature variation of the stress-induced beam has also been investigated both in theory and experiment. The optical model was built using Rayleigh-Sommerfield diffractive theory due to the 'near field' distance in the system. Experiments have also been done on the optical performance of the variable optical attenuator.

Chapter 6 is about an optical chopper driven by a comb drive actuator. The novelty of this device is the double shutter mechanism. It doubled the response time of the attenuator. The detailed analysis of the structure as well as its optical properties have been conducted. Devices were fabricated by the SOIMUMPs Process. Experimental results are also presented in this chapter.

In chapter 7 the main conclusions are made for the entire thesis.

All the devices of this thesis have been fabricated by MEMSCAP Multi-User MEMS Process (MUMPs), which is briefly reviewed in Appendix A.

1.4 Main achievements reported in this thesis

The following are the main achievements of the research:

1. We optimized the traditional asymmetric thermal actuator, which has enabled an increase of the maximum bending displacement 20 % more than that of traditional asymmetric thermal actuators. Theoretical derivation and experimental testing are described.

2. The scratch drive actuator's force has been characterized using microsprings. Forces of 250 ± 36 μN for one plate SDA up to 850 ± 36 μN for 4 plate SDAs have been estimated for 200 volts driving voltage. Within the uncertainty quantified above, there is a near linear relationship between the number of SDA plates and the force generated.

3. Integrated microhinges and stress-induced bimorph beams are introduced and used to self-assemble vertical micro-shutters. The theoretical analysis and experimental results show this method having the potential to realize complex 3-D structures.

4. Scratch drive actuators and comb drive have been successfully utilized to build micro-optical systems – variable optical attenuator (VOA) and optical chopper. The advantage of SDA driving VOA is that the device can be controlled in a very precise way, because the step size of SDA is very small (around 16 nm in measurement). The advantage of the optical chopper driven by comb drive actuators is that it has fast response speed (around 90 μs) with a high operation bandwidth.

Chapter 2

Review of Microactuators

2.1 Introduction

Actuators are energy converters, which usually convert electric energy into mechanical energy. Microactuators are key devices allowing MEMS to perform physical functions. Many types of microactuators have been successfully implemented. Here, some types of microactautors are briefly reviewed and application examples are listed.

2.2 Electrostatic actuators

Electrostatic actuators utilize coulombic attraction between two bodies to induce displacement or to exert force [26]. The electrostatic force can be calculated from the stored energy (U_e) in the electrostatic field of the device. In general, this energy is given by $U_e = \frac{1}{2}CV^2$, where C is the capacitance of the device, and the force is given by the gradient of U_e:

$$F = -\nabla U_e, \qquad (2.1)$$

in component form, the above equation can be written as:

$$F_x = -\frac{\partial U_e}{\partial x}, \quad F_y = -\frac{\partial U_e}{\partial y}, \text{ and } F_z = -\frac{\partial U_e}{\partial z} \qquad (2.2)$$

Many electrostatic actuators configurations have been reported in the literature [27], [28], [29]. In this section, we list the principle of some electrostatic actuators.

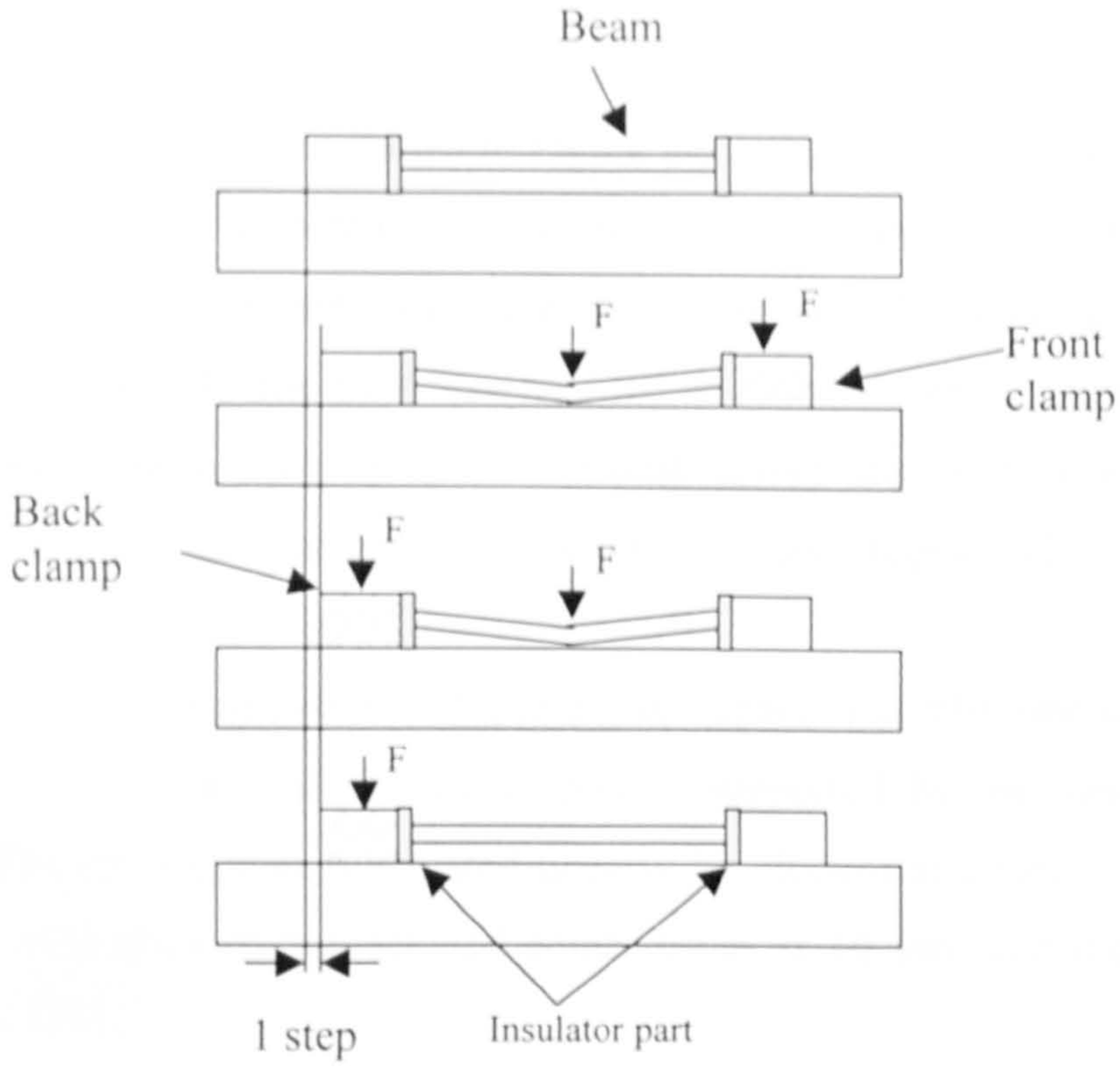

Fig. 2-1. Principle of operation. First the front clamp is activated and the actuator plate is deflected downward. This causes contraction of the actuator and back clamp is pulled forward. Next the back clamp is activated, the front clamp and the actuator plate are released. The plate stretches and the front clamp is pushed forward.

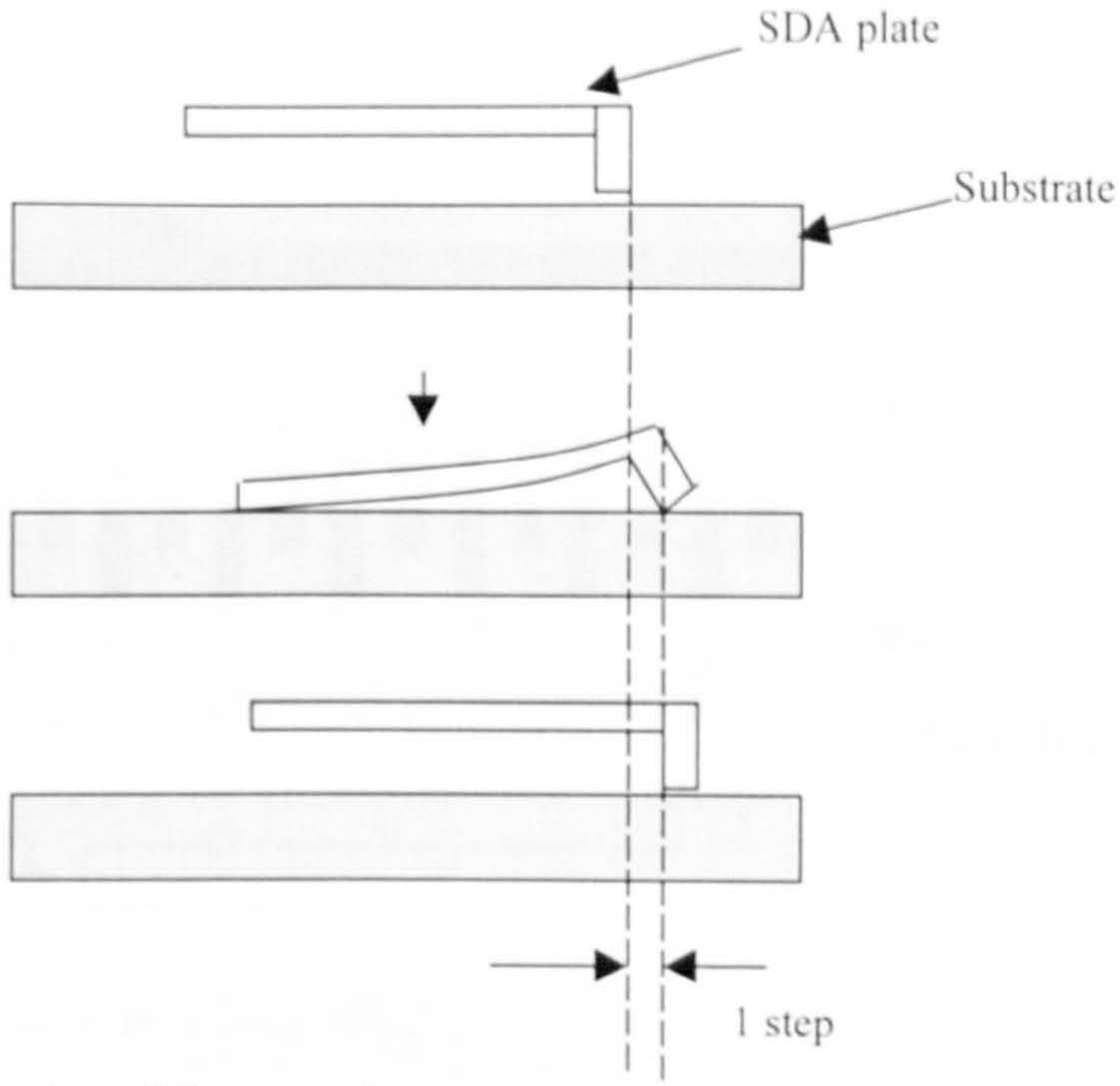

Fig. 2-2. Principle of operation. When a voltage is applied across the capacitor-like structure formed by the plate and substrate, the plate experiences an electrostatic force that pulls it down towards the substrate. The warping of the plate causes the bushing to tilt, thereby sliding forwards the edge in contact with the substrate. When the voltage is removed, the plate and bushing return to their horizontal position, but translated forward a small distance.

The working principle of an electrostatic stepper motor is shown in Figure 2-1 [29], scratch drive actuator (SDA) is shown in Figure 2-2 [19], and comb drive actuator is shown in Figure 2-3. Scratch drive actuator normally has large output force (~ 100 μN at 120 V single plate), and long travel displacement [19]. Analysis of SDA is undertaken in Chapter 4. The SDA can be used to assemble micro components or actuate the micro parts, such as mirrors. Comb drives are used in a variety of applications. They are incorporated in optical switches and choppers [25], [16].

The comb drive consists of two sets of interdigital capacitor combs, one side comb is fixed; another side comb called moving part is supported by mechanical elastic beams [30]. The moving part is actuated linearly by electrostatic force. The typical displacement of surface-micromachined comb drives is 10 μm, and the generated force is 10 μN [31].

Comb drives are also used in micro accelerometers and gyroscopes. Figure 2-3 shows the schematic figure of a comb drive actuator. Analysis of comb-drive actuator is undertaken in Chapter 6.

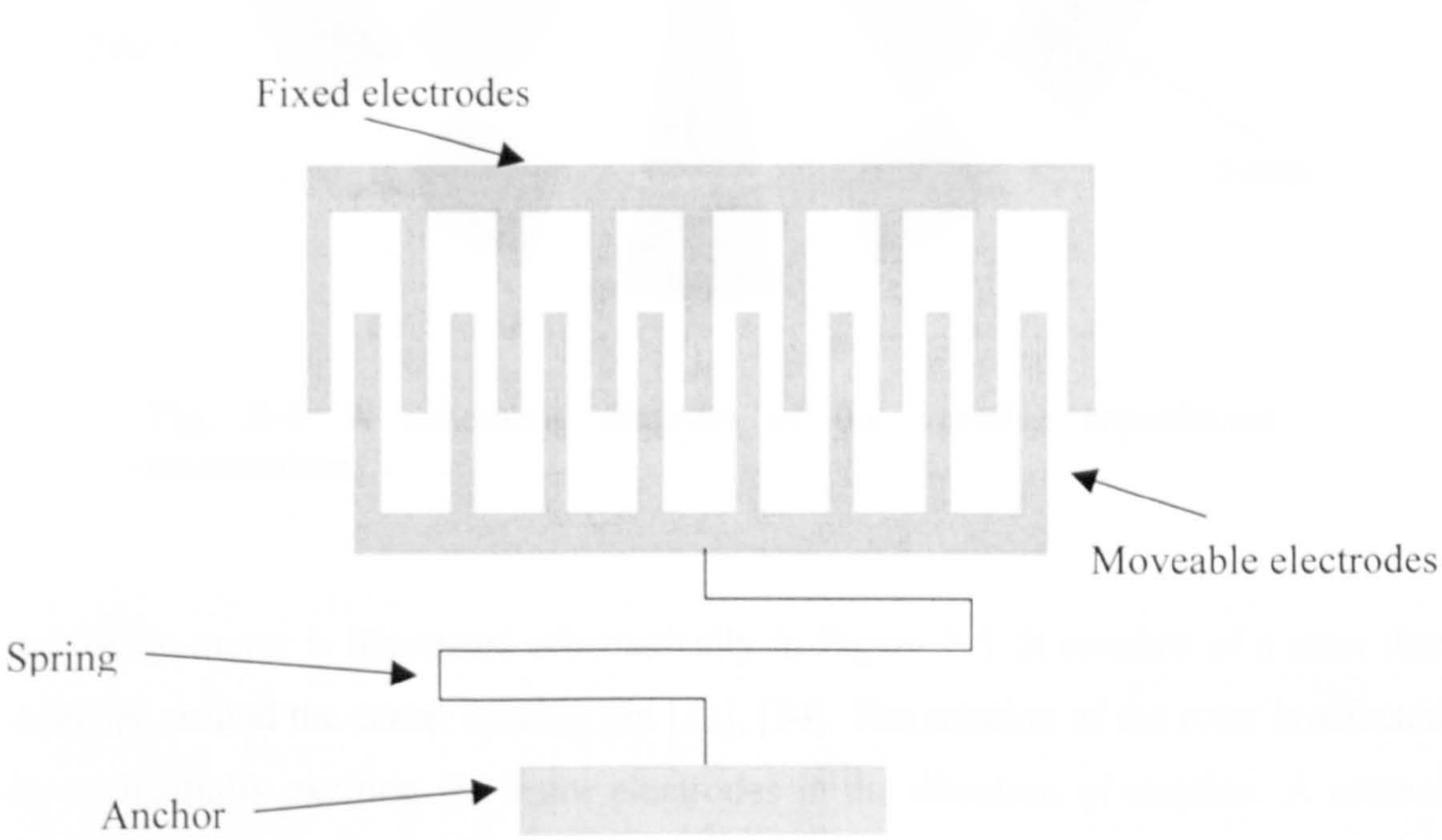

Fig. 2-3. Schematic figure of a comb drive actuator.

A variable-capacitance micromotor (VCM) is shown in Figure 2-4. It consists of a rotor with poles that form a capacitor with the stator poles situated on the stator loop [6], [32]. It is operated by applying different phase signals to the stator. Rotational speed was on the order of 500 rpm which was reported in reference [6]. Later improvement by Mehregany et al [32] enabled rotational speeds of up to 15000 rpm and continuous operation for more than a week, where the driven voltage is 80 V.

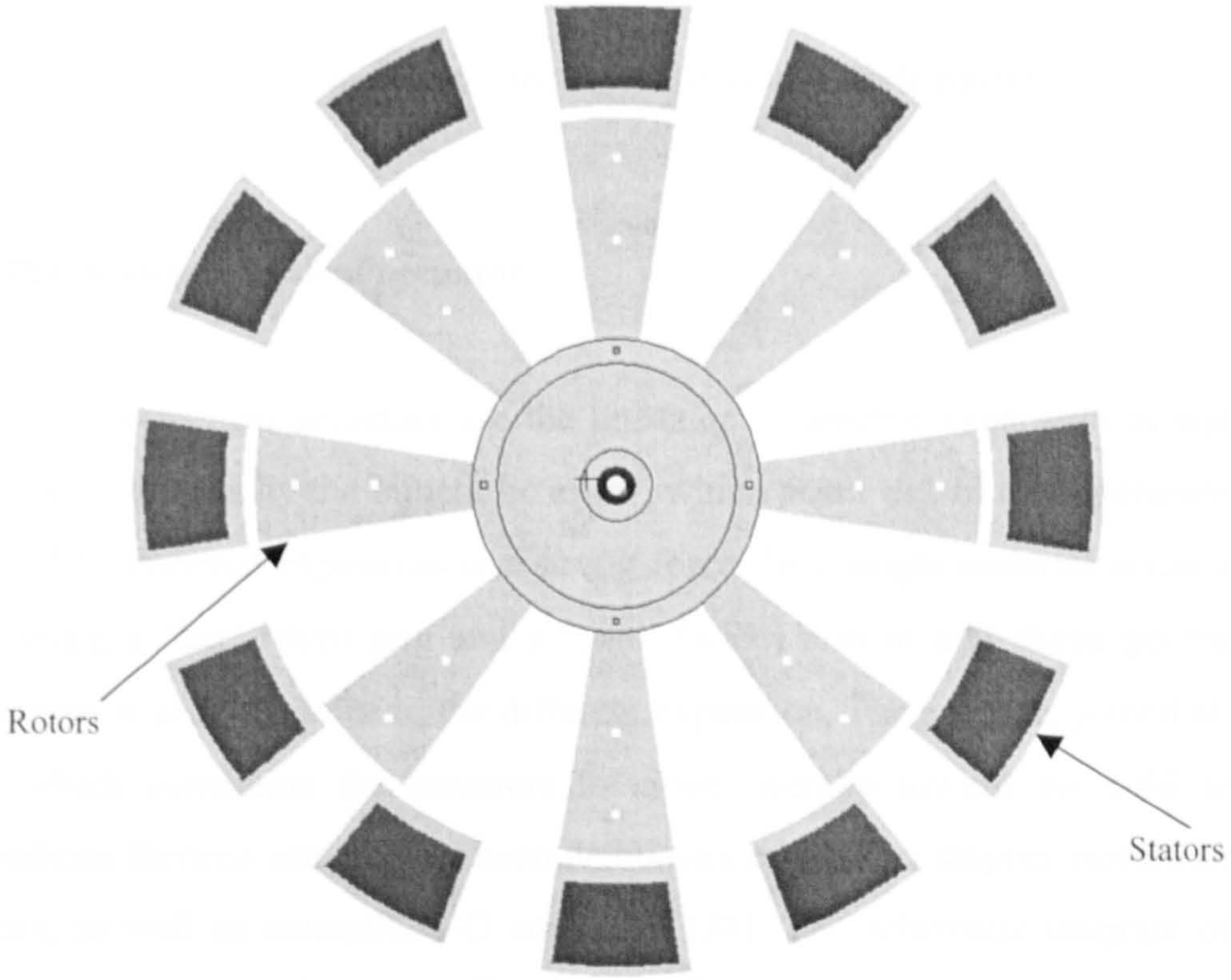

Fig. 2-4. A schematic diagram of the variable capacitance micromotor.

A wobble motor is illustrated schematically in Figure 2-5. It consists of a rotor that wobbles around the center bearing pin [33], [34]. The rotation of the rotor is affected by sequentially exciting the stator electrodes in the direction of rotation. A normal force develops between the excited stator electrode and the electrically grounded rotor pulling the rotor close to the excited electrode. As the electrical excitation travels around the stator loop, the rotor rolls and rotates. Wobble Motors have been operated successfully at driving voltages as low as 6 V at speeds up to 150 rpm. [35]

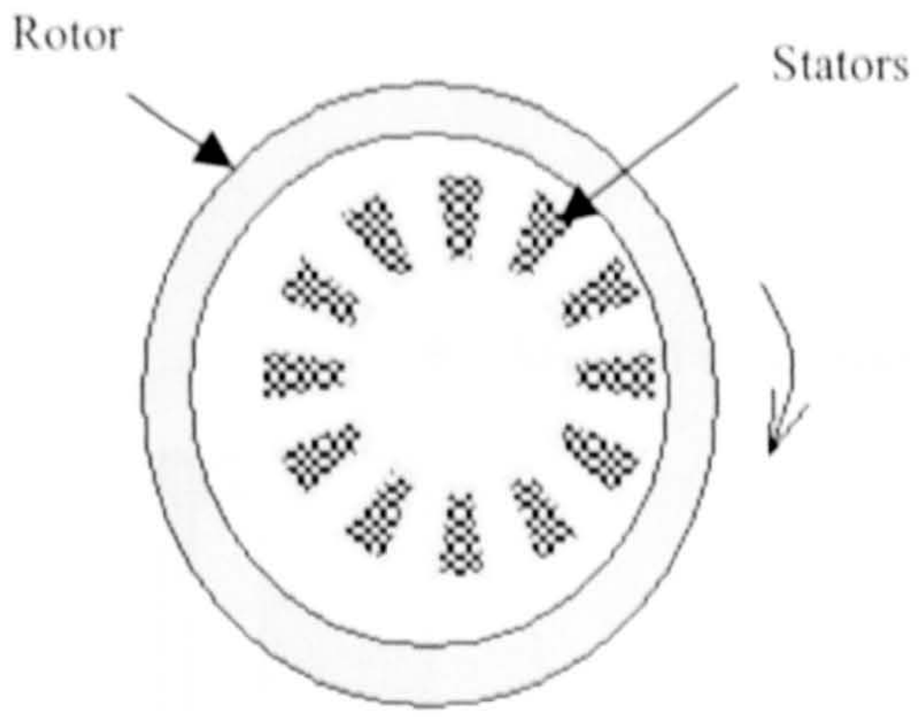

Fig. 2-5. A micro electrostatic wobble motor.

2.3 Thermal-mechanical actuator

Thermal-mechanical actuators use the linear or volumetric expansion as well as the shape deformation by the bimetallic effect, which occur due to a temperature change [36], [37]. Thermal expansion is a strong force. In a single material actuator, when combining a 'hot' (thin) arm and a 'cold' (wide) arm in a U-shape geometry, the deflection is generated due to the different expansion. The arms are joined at the free end, which constrains the actuators to move laterally toward the cold arm. The polysilicon thermal actuator has been demonstrated to drive stepper motors and linear motors, as well as assemble 3-D structures [38]. The schematic diagram of such a thermal actuator is shown in Figure 2-6. The typical output force of a surface micromachined shape bimorph thermal actuator is 10 μN at 5 μm displacement, the length of hot arm is 240 μm, and cold arm length is 200μm.

Another type of thermal actuator called the 'V' shaped thermal actuator shown in Figure 2-7 [39]. The 'V' shape thermal actuator consists of two thin hot beams at a small angle respect to each other. This is a toggle mechanism that provides large motion amplification, proportional to $1/\theta$ for small angles. When a current passes through the structure, the ohmic heating and thermal expansion of the ribs causes linear motion of the middle shuttle. This type of actuator can be used to actuate rf

switch or micro optical components [40]. Electro-thermal actuators are analyzed in Chapter 3.

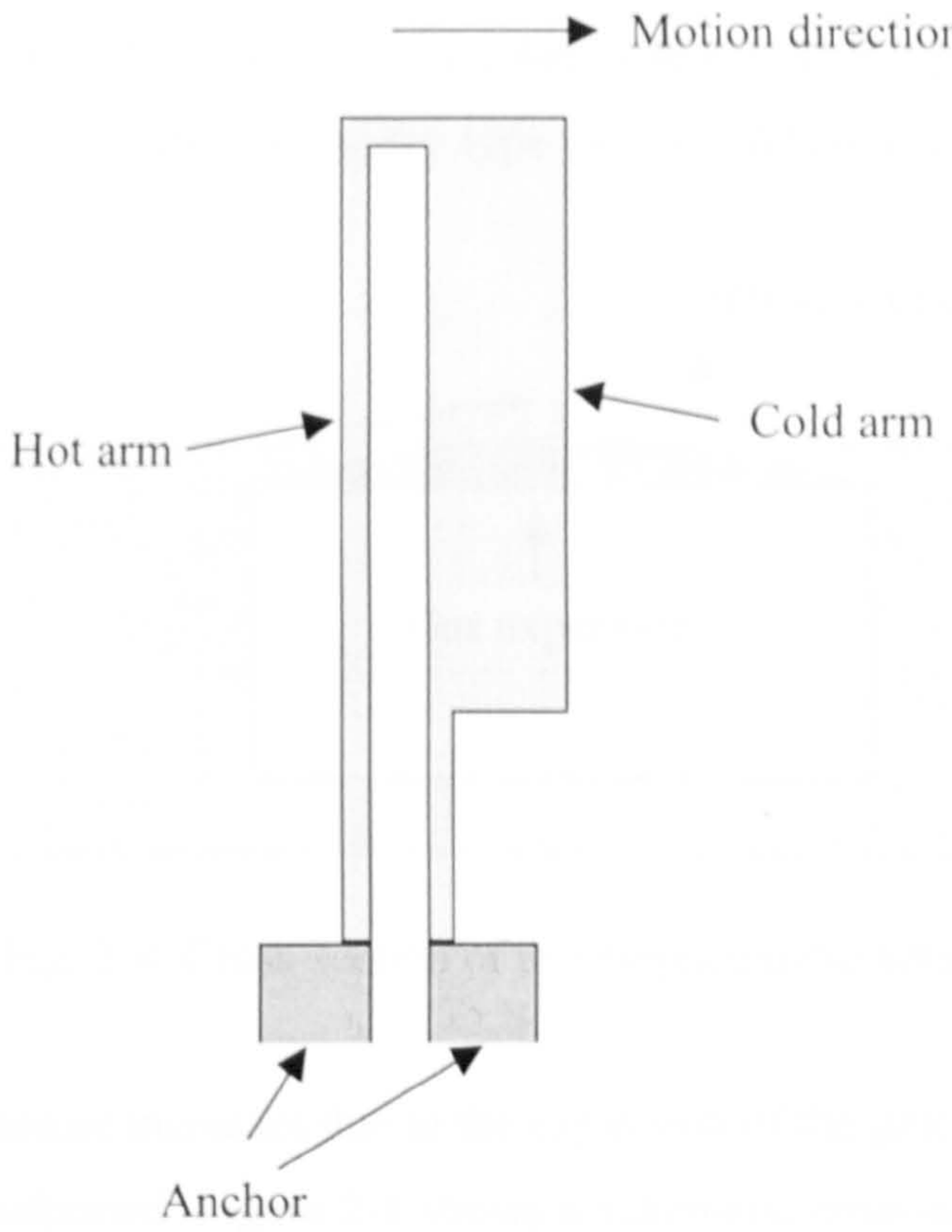

Fig. 2-6. A schematic figure of the 'hot arm'-'cold arm' thermal mechanical actautor.

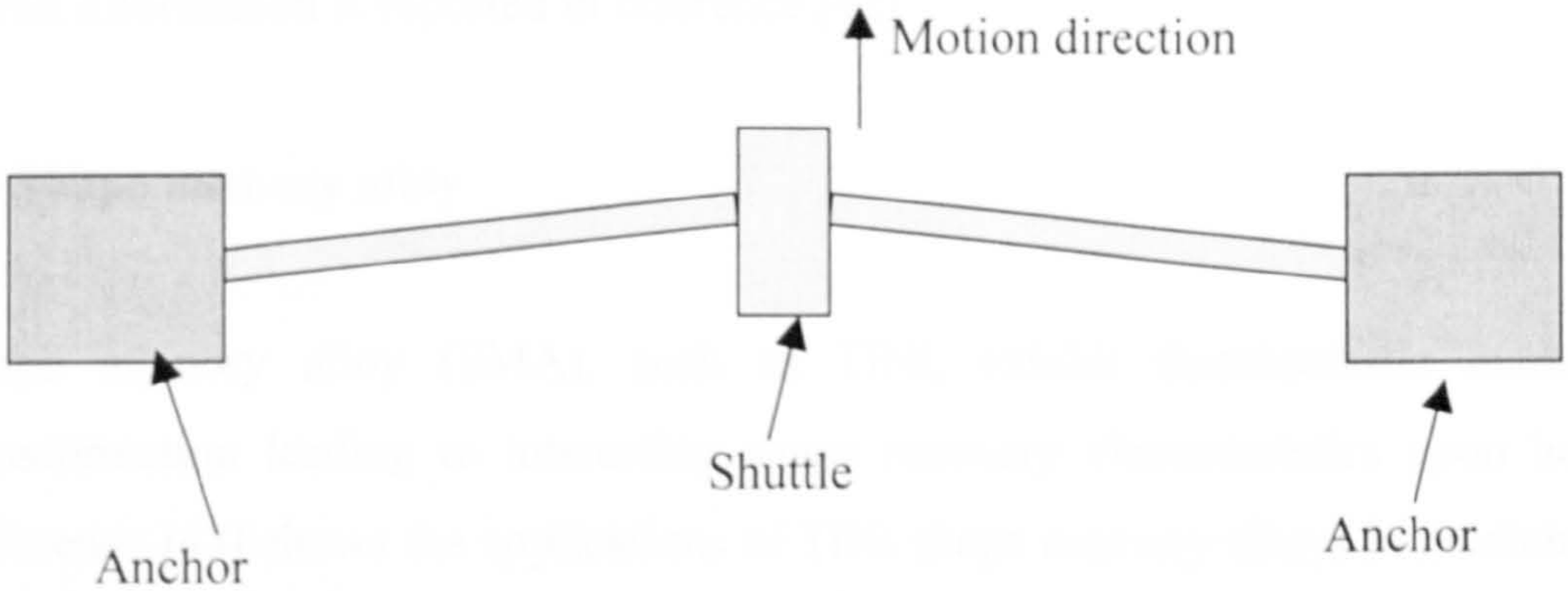

Fig. 2-7. A schematic figure of the 'V' shape thermal mechanical actautor.

2.4 Thermopneumatic actuator

Thermopneumatic actuator is based on the gas expansion. When simple gases are heated they expand according to the well known ideal law: $PV = nRT$, where P is the gas pressure, V is the volume, T is the absolute temperature, R is the gas constant (0.0821 liter atm/mole K) and n is the number of moles. This type of actuator usually has a chamber which contains some type of gas. When temperature of the gas

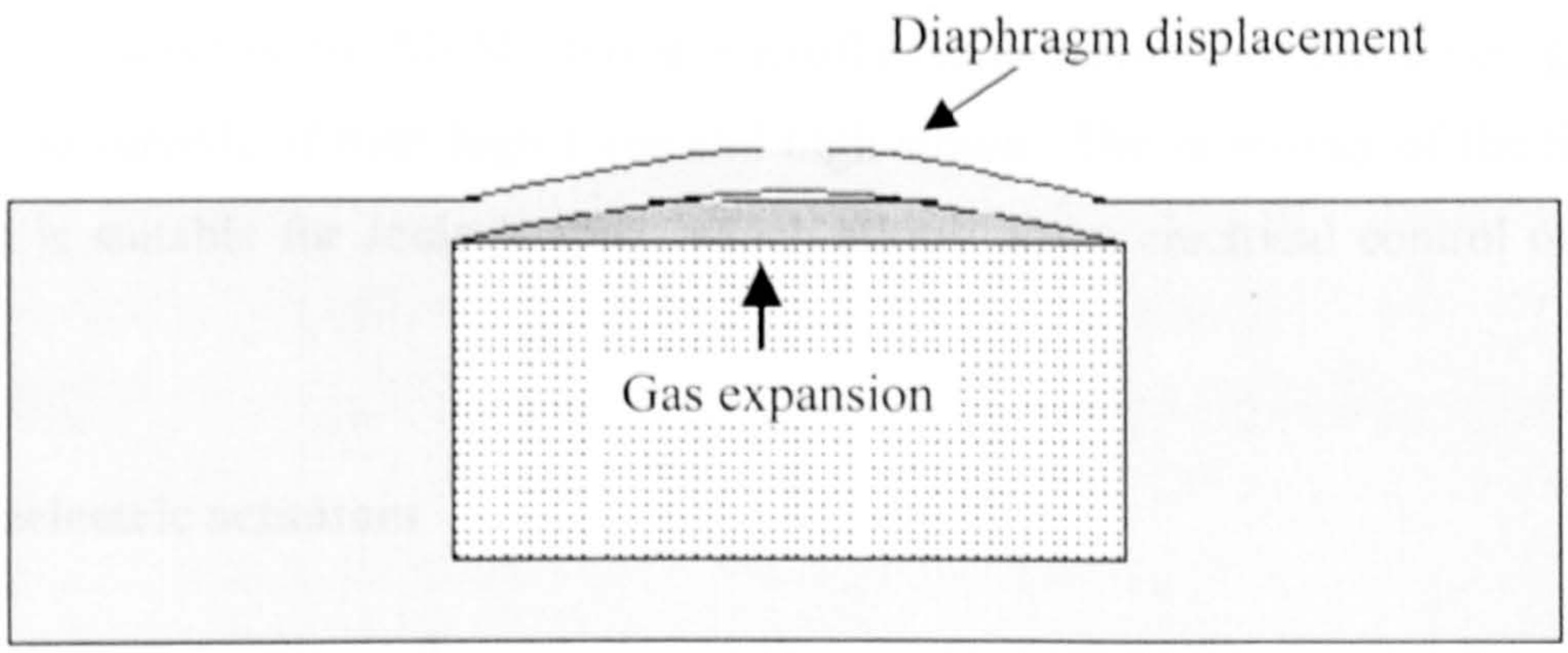

Fig. 2-8. Cross-section of thermopneumatic actuator.

increases, the pressure increases due to the expansion of the gas; then the thin wall of the chamber is deformed. Figure 2-8 shows a schematic cross-section of an actuator using gas expansion. A thermopneumatic actuated micropump is reported in [41]. Up-to-date micropump actuated by a thermopneumatic consists of a corrugated diaphragm, where the maximum deflection point in the diaphragm can reach 100 μm. Detail information is reported in reference [42].

2.5 Shape memory alloy

Shape memory alloy (SMA), such as TiNi, exhibit thermoelastic martensitic transformation leading to interesting shape recovery characteristics upon heating. Reference [43] shows the applications of TiNi shape memory alloys in medicine and other fields. Thin film shape memory alloys (SMAs) have the potential to become a primary actuating mechanism for mechanical devices with dimensions in the micron-to-millimeter range requiring large forces over long displacements. The work output per volume of thin film SMA microactuators exceeds that of other microactuation

mechanisms such as electrostatic, magnetic, thermal bimorph, piezoelectric, and thermopneumatic, and it is possible to achieve cycling frequencies on the order of 100 Hz due to the rapid heat transfer rates associated with thin film devices [44].

A gripper formed by SU-8 thick photoresist and shape memory alloy film has been reported [45]. Here the shape memory alloy film was the actuation mechanism. The shape-memory effect (SME) in sputter-deposited thin-film SMA titanium nickel (TiNi) as an actuator for MEMS-based microfluidic devices, has been investigated [46] as it is capable of both high force and high strains. The resistivity of the SMA thin film is suitable for Joule heating, which allows direct electrical control of the actuator.

2.6 Piezoelectric actuators

Piezoelectric materials produce charge on their surface when they are mechanically deformed, and conversely, they become deformed when they are subjected to an electric field [47]. Piezoelectric materials can be divided into single crystals, ceramics, and polymers. Examples of the single crystal piezoelectric materials are lithium sulfate, rochelle salt, quartz, tormaline, and $LiNbO_3$. General ceramic piezoelectrics are Lead zirconate titanate (PZT), barium titanate, and ZnO. Polyvinylidene fluoride is an example of a piezoelectric polymer. Piezoelectric materials are usually of two kinds: materials with build-in net electric dipole moment and materials that need poling to become piezoelectric.

In piezoelectric materials, the strain-stress relationship is modified by the presence of the applied electric field. Thus, one can write [48]:

$$S = sT + dE \qquad (2.3)$$

where S is the strain, T is the stress, s is a coefficient connecting S and T, and d is the coupling coefficient between the electric field (E) and the strain. S, T, and E are vectors, and s and d are tensors. Some typical piezoelectric transducer displacement

modes are shown in Figure 2-9 (a) and 2-9 (b). It is reported that maximum pressure of 2 kPa was measured in a piezoelectric actuated micromachined pump [49].

Fig. 2-9 (a), Thickness expansion (TE) mode of piezoelectric devices.

Fig. 2-9 (b), Thickness shear (TS) mode of piezoelectric devices.

Piezoelectric actuator has been used in an optical scanner [50], which is used in a variety of optical systems, including laser radar, optical communication systems, object indentification and sizing (by triangulation), distance measurements and holographic data storage. A PZT unimorph cantilever actuator, fabricated on a sacrificial polysilicon layer and released using a xenon difluoride dry etch, was used to realize a micromachined electrical switch [51]. A piezoelectrically driven hydraulic amplification microvalve for use in compact high-performance hydraulic pumping systems was described in [52].

2.7 Magnetic microactuator

Magnetic actuators are used in everyday applications in the form of relays, electromotors and automatic valves. Magnetic actuation methods offer the repulsive forces in addition to attractive forces. This is in contrast to electrostatic method which offer only attractive forces.

Most magnetic actuators that are reported use attractive forces that can be generated between a ferromagnetic material and a current-carrying coil (an electromagnet), as shown in Figure 2-10 [53]. There is another type of actuation that uses a permanent magnetic instead of the magnetizable part. In these devices, the actuators can generate both attractive and repulsive forces [54].

The net force (F_y) in the direction of y, experienced by the magnetic material is:

$$F_y = -\frac{\partial W_M}{\partial y}, \qquad (2.4)$$

where, W_M is the potential energy of the a magnetic material, with total magnetization M_T (= MV, where V is the volume, M is magnetization, the magnetization M of a dielectric is defined by M= N μ, where N is the number of magnetic dipoles per unit volume and μ is magnetic dipole moment per dipole.). In an external field, B,

$$W_M = -M_T \cdot B, \qquad (2.5)$$

The equation (2.4) can be used to calculate the force that can be generated in the configuration shown in Figure 2-10.

Magnetic forces has been reported to assemble a micro miror [59]. In another paper [56], magnetic force have been applied to realize a optical scanner.

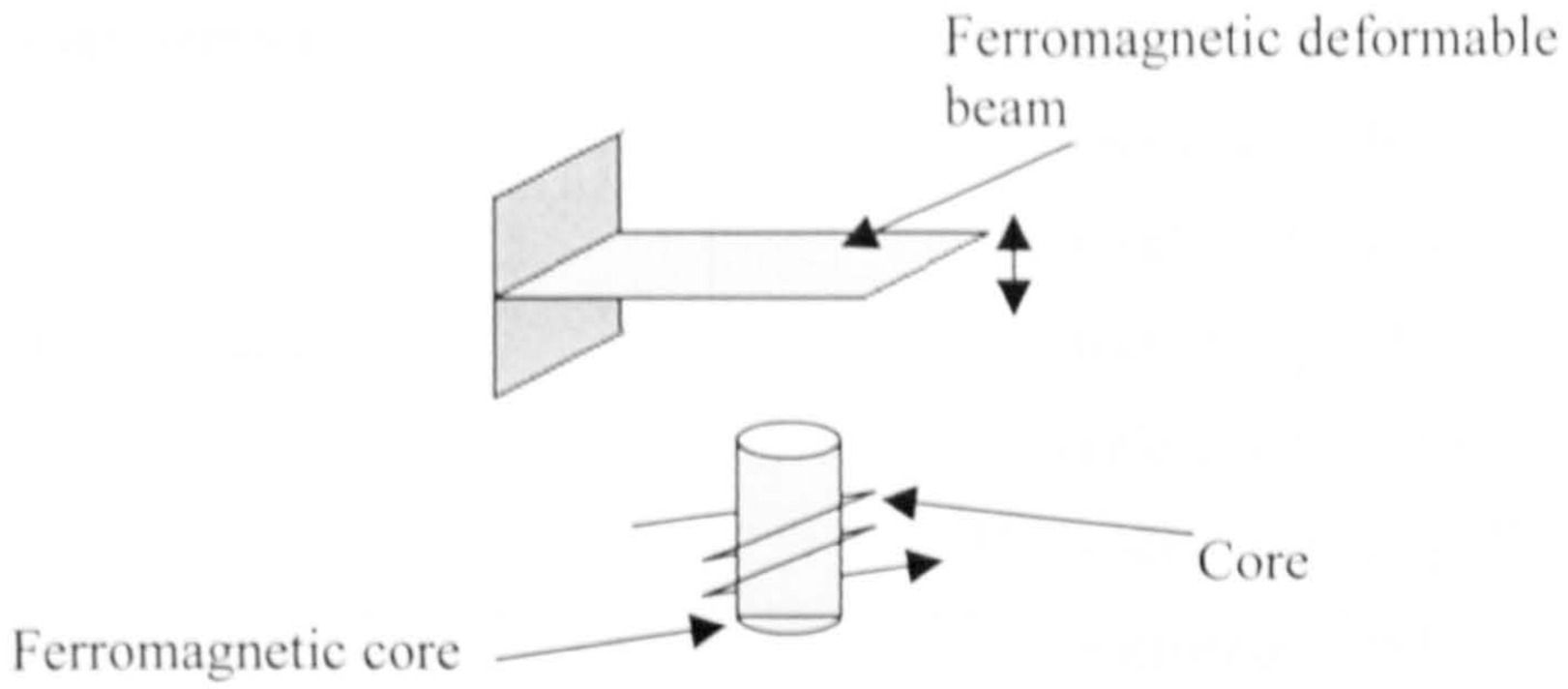

Fig. 2-10. An magnetically driven cantilever.

2.8 Applications of microactuators

Table 2-1 lists MEMS devices together with their actuation principle, which have been succesfully realized.

Table 2-1. Applications for actuators reviewed above.

actuation principle	**typical MEMS devices**
electrostatic	micromotor (shutter) [57] accelerometer and gyroscope [58, 55] microshutter [60] micromirror [61, 62] microscanner [63] fibre switch [64] microrelay [65, 66, 67]
thermomechanic	microvalve [68] fibre-switch [69] micromirror [70]
thermopneumatic	micropump [41, 42]

phase conversion	microvalve [71] inkjet printhead [72]
shape memory	microvalve [73] micropump [46] optical switch [74]
piezoelectric	micropump [75] accelerometer [76] HDD servo system [77]
electromagnetic	microrelay [78] microgyroscope [79] mircoscanner [56] micropump, micro-valve [80, 81]

Chapter 3

Optimization of Micro-Electro-Thermal Actuator

3.1 Introduction to thermal actuators

Thermal microactuators are widely used components in active MEMS devices, and are capable of generating large force (e.g. single asymmetric thermal actuators, the output force is typically 10 μN, the force can be increased by using actuator array), and have bi-directional operation. Thermal actuators rely on thermal expansion due to temperature increases. Different means have been applied to raise the temperature of the structures. These are divided into actively heated and passively heated structures. For actively heated structures, an electrical current is passed through the actuator, and Joule heating occurs (here, named electro-thermal-actuator). For passively heated structures, the actuator is heated by a heater around it, under it, beside it, or on top of it. In this chapter, the electro-thermal-actuators are focused upon.

In electro-thermal-actuator (ETA), various geometries have been utilized to obtain lateral or vertical motion. The basic structure is a straight buckling beam fixed at its two ends [82]. When the beam expands, it can buckle upward or downward thereby exerting a force. The second approach is the asymmetrical thermal actuator [37], which comprises beams of two different widths connected at one end and made from the same material. Different expansions of these two beams due to different electrical resistances of these two beams causes lateral deflection when same current is applied. 'U' shape thermal actuators have been realized to actuate an optical switch [69]. Thermal actuators constructed from two different thermal expansion materials (bimorph) have also been reported to achieve in-plane and out-of-plane movement [83]. Thermal actuators consisting of beams having the same cross-sections, but different lengths connected together at one end is another type of electro-thermal

actuator [84]. Another type of thermal actuator is called the thermal-mechanical in-plane microactuator (TIM) [39], also called 'V' shaped thermal actuator. The basic V-shaped thermal actuator design consists of a moveable shuttle connected to electrical contact pads on the substrate by slender thermal expansion legs and current flows through the legs and the shuttle. The high current density in the legs causes heating and thermal expansion. If the thickness/width ratio is larger than 1, it will deliver the lateral motion, if this ratio smaller than 1, it will buckle up. Figure 3-1 shows the schematic layout of the above thermal microactuators.

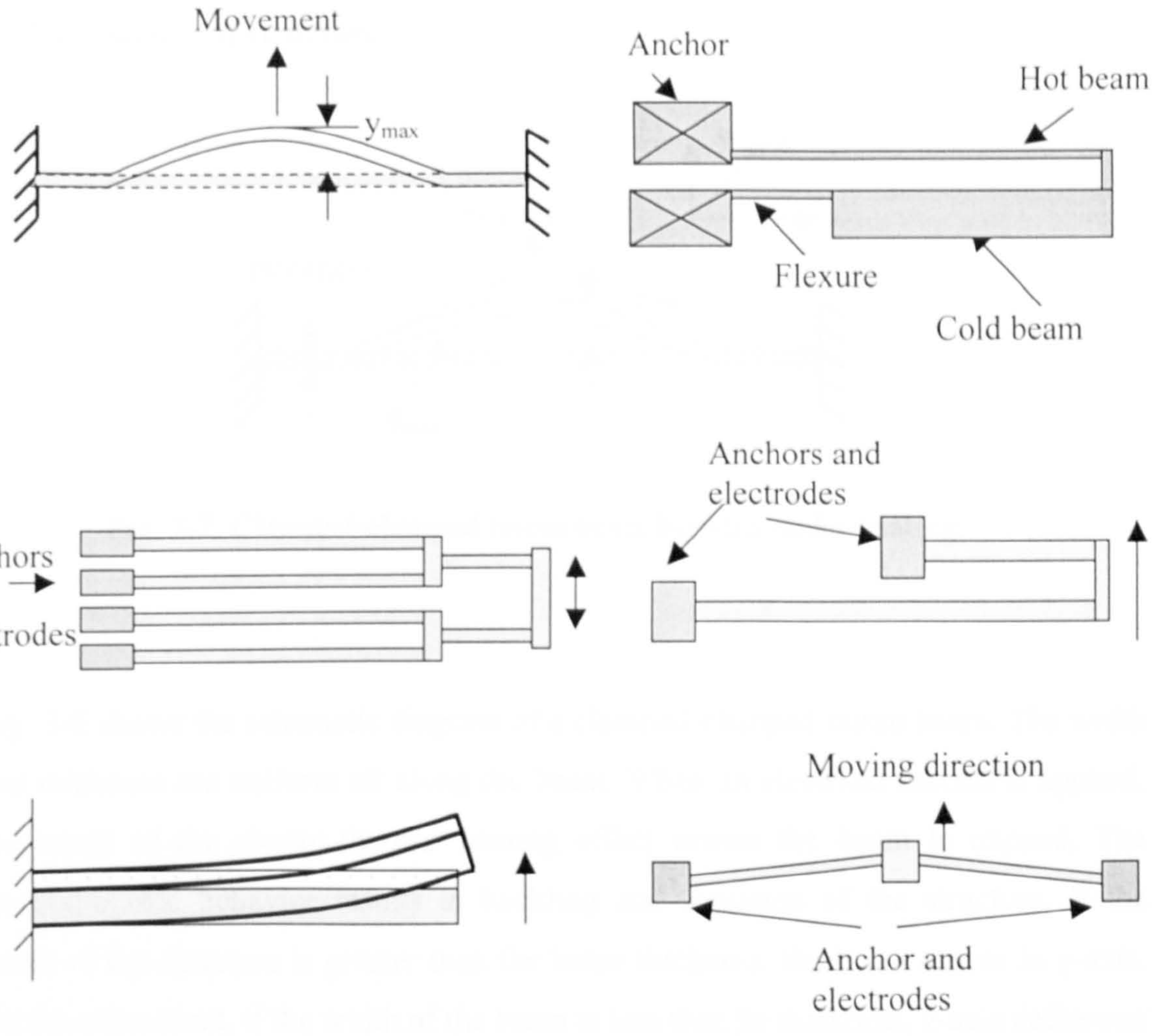

Fig. 3-1. Schematic of six types of electro-thermal actuators.

In this thesis, three types of electro-thermal actuators have been numerically analyzed. Here, only thermal conduction is considered for simplification in analysis, and still allows important conclusions to be made. The idea for adjusting the temperature profile of the asymmetric electro-thermal-actuator was introduced as 'world first'. The modified asymmetric electrothermal actuator has been designed and fabricated using PolyMUMPs to verify the idea. Experiments performed show that the modified asymmetric thermal actuator has more deflection and operating displacement range than the traditional actuator.

3.2 Straight beam thermal actuator

3.2.1 Geometry of structure

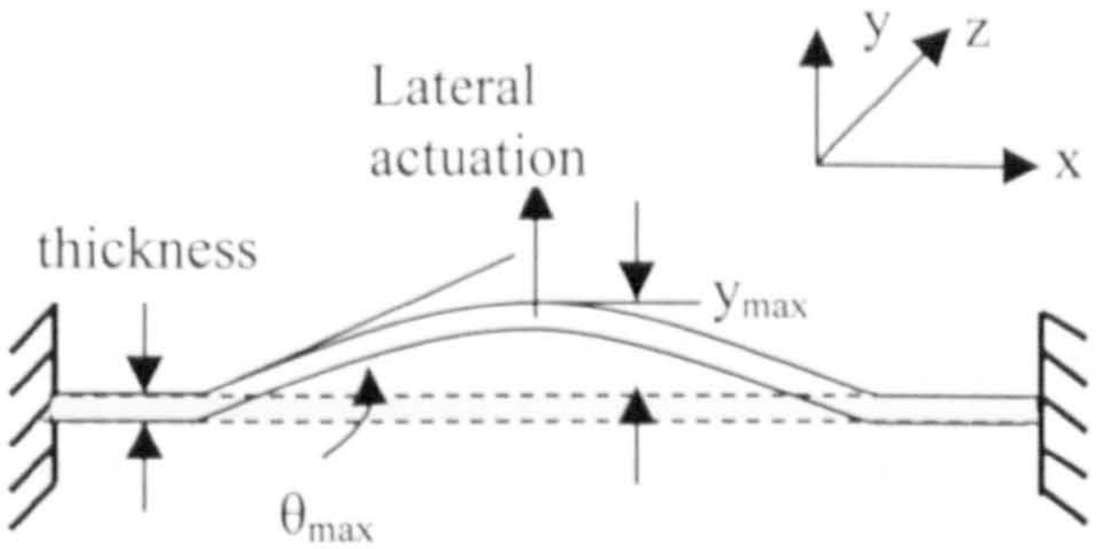

Fig. 3-2. Clamped-clamped micro beam buckles under heating.

Fig. 3-2 shows the schematic diagram of a clamped-clamped micro beam. The width and thickness are uniform all along the beam. When an electrical current is applied, the result of the electro-thermal heating effect causes the beam to expand. The thermal-elastic behavior results in buckling and actuation of the structure. If the width of the structure is greater than the beam thickness, the beam moves in y-axis. On the other hand, if the width of the beam is less than its thickness, z-axis deflection is expected. The whole mechanism consists of two parts: the electro-thermal reaction due to the joule heating, and the thermal elastic reaction due to thermal expansion.

3.2.2. Temperature distribution analysis

There are three mechanisms of heat flow: conduction, convection and radiation. Conduction transfers energy from hot to cold regions of a substance by atomic and molecular interaction. Convection is the heat transfer between the air (a fluid) and the solid interface when there is a temperature difference. Radiation is the energy emitted from a body due to its temperature [85]. According to the finite element analysis [86], heat dissipation through radiation to ambient can be neglected in comparison with heat losses through conduction in the types of micro-thermal devices analyzed here.

First of all, Joule heating of section dx (shown in Fig. 3-3) in the beam resulting from voltage V_i is

$$Q_{Ji} = \frac{V_i^2}{A_i R_i L_i} \cdot A_i dx, \qquad (3.1)$$

where, Q_{Ji} stands for the heat generated by the element dx of beam i (here, i = 1, because only 1 segment in this type of actuator). V_i stands for voltage applied on the beam, A_i is the area of the cross-section of the beam i, R_i is the resistance of the beam i, $R_i = \rho L_i/A_i$, where ρ is the resistivity of polysilicon (2.32×10^{-3} Ω-cm) and L_i is the length of the beam i.

Only heat conduction is considered in this analysis. From reference [87], we assume the beam material possessing thermal conductivity, k_p, independent of direction. Then the one-dimensional form of Fourier's law of conduction is:

$$-k_p A_i \frac{\partial T}{\partial x} = Q_{Ji}, \qquad (3.2)$$

Substituting equation (3.1) into equation (3.2), we can obtain the thermal transfer equation of the electro-thermal actuator

$$-k_p A_i \frac{\partial T}{\partial x} = \frac{V_i^2}{A_i R_i L_i} \cdot A_i dx \,, \quad (3.3)$$

re-organizing equation (3.3),

$$\frac{\partial^2 T}{\partial x^2} = -\frac{V_i^2}{R_i L_i k_p A_i} \,, \quad (3.4)$$

Assuming purely conductive heat transfer, the temperature along the thermal actuator satisfies the equation (3.4). It is Assumed that the material properties keep constant though the temperature range. The dimensions of the buckling beam are shown in Fig. 3-3.

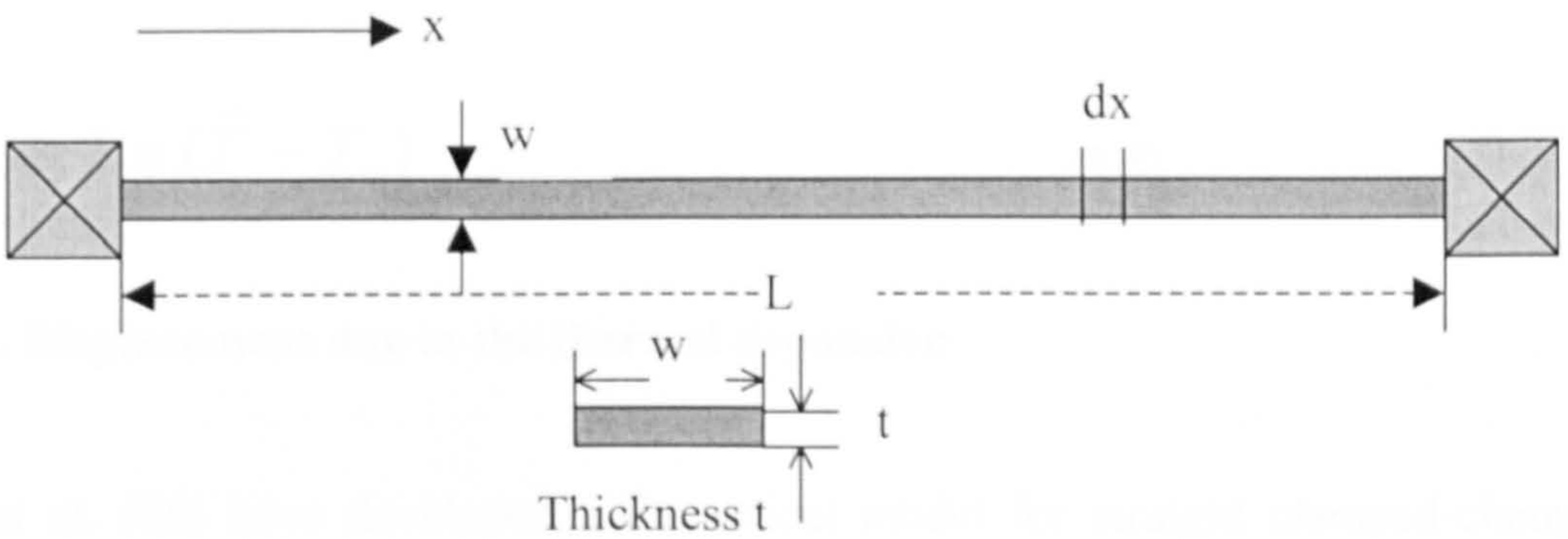

Fig. 3-3. A fixed-fixed beam.

Solving equation (3.4), we get

$$T_i(x) = -\frac{1}{2} K_i x^2 + C_1 x + C_2 \quad \text{.....(3.5)}$$

here, $K_i = \frac{V_i^2}{R_i L_i k_p A_i}$, C_1 and C_2 are arbitrary constants.

The boundary conditions of equation (3.5) are

$$T(0) = C_2 = T_0 \quad ; \tag{3.6}$$

$$T(L) = -\frac{1}{2} K_i L_i^2 + C_1 L_i + C_2 = T_0 \tag{3.7}$$

Taking, T_0, the temperature of the environment to be 20 deg. C and solving equation (3.6) and equation (3.7), we can get the C_1 and C_2 values. Then substituting C_1, C_2 to the equation (3.5), and letting k_p = 50 W/m.K for polysilicon, t = 2 μm, w = 2 μm (and assuming there is no substrate under the beam, and ignoring the heat radiation to the air), three different lengths (200 μm, 300 μm, 400 μm) beams have been analyzed. We find that when the same input power 4.1 mW is applied to these buckling beams, the temperature profiles obtained, are shown in Fig. 3-4. The expansion of this clamped-clamped beam is defined using the formula

$$\Delta L = L\,\alpha(\overline{T} - T_0) \tag{3.8}$$

3.2.3. Displacement due to the thermal expansion

Lin et al. [88] have developed a theoretical model for straight clamped-clamped micro beams under electrothermal buckling conditions. The maximum deflection at the center of the beam is a function of temperature (average temperature).

$$y_{\max} = 4\beta\sqrt{\frac{I}{[\alpha\overline{T} - \varepsilon]A}} \tag{3.9}$$

where A and I represent the cross-sectional area and moment of inertia of the beam. $\overline{T}$ is the average temperature and ε the minimum strain for the beam buckling. α is thermal expansion coefficient. β is a function of maxmum deflection angle, θ_{max}, which occurs at one-fourth of the beam length as shown in Fig. 3-2.

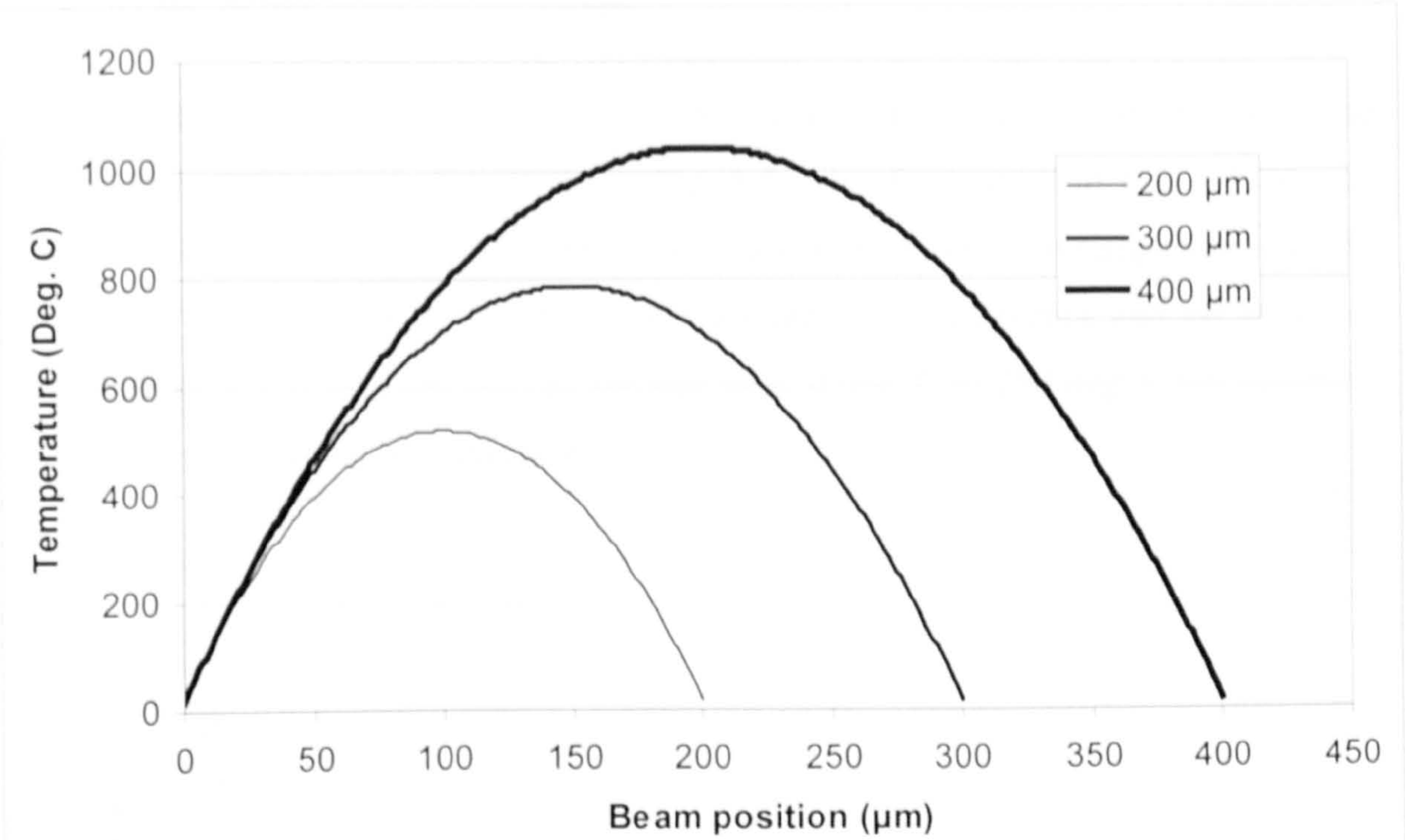

Fig. 3-4, Temperature profiles of three buckling beams for constant input power = 4.1 mW, and other parameters defined in the text.

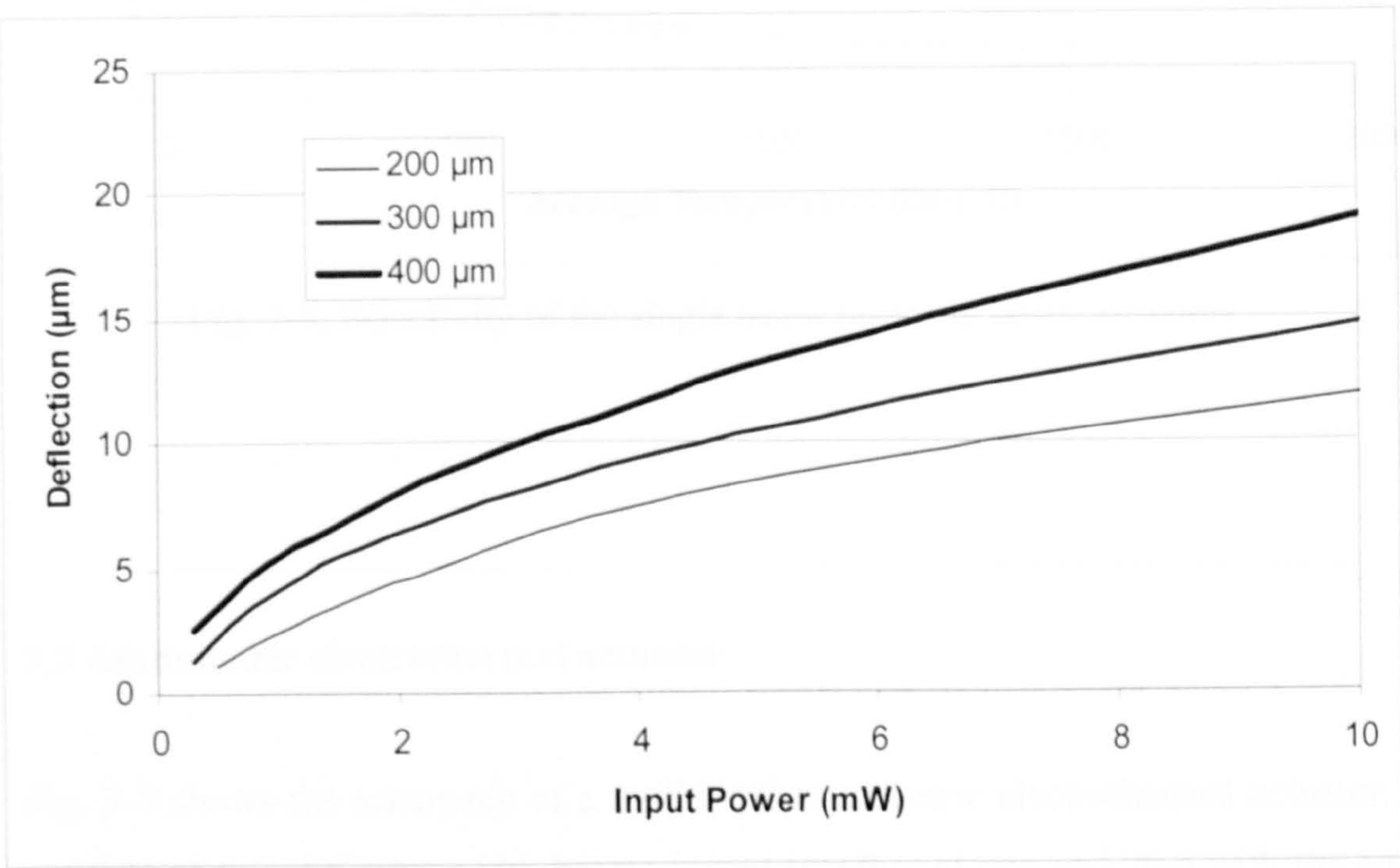

Fig. 3-5, Deflection vs. input power, with parameters described in the text.

$$\beta = \sin \frac{\theta_{\max}}{2} \qquad (3.10)$$

Taking the data used in section 3.2.2, the relationship between input power and maximum deflection is than shown in Fig. 3-5. Also from result of Fig. 3-5, we can obtain the sensitivity (*dy/dW*) of these three actuators at different temperature points, which is shown in Fig. 3-6. Where, *dy* is displacements difference and *dW* is power difference. From Fig. 3-6, we can see that from 0 *deg. C* to 250 *deg. C* the actuators are very sensitive to the temperature.

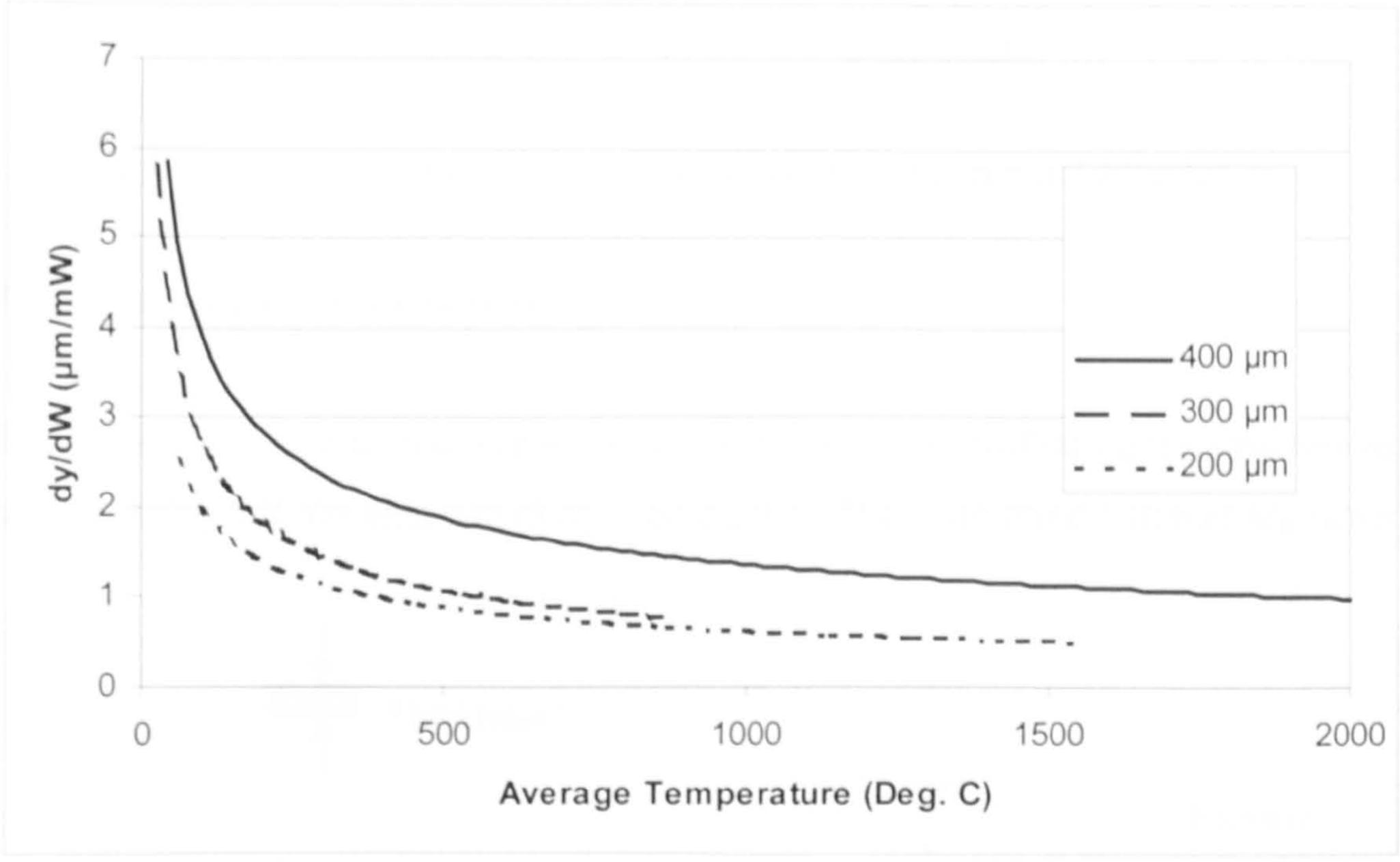

Fig. 3-6, Sensitivity of the single beam buckling beam actuators.

3.3 Asymmetric electrothermal actuator

Fig. 3-7 shows the schematic of a traditional asymmetric electrothermal actuator. It consists of two different width beams joined together at one end, and with the ends anchored to the substrate. All the beams are made of same material which possesses the same electrical and mechanical properties. Because the beams have different

widths, the corresponding electrical resistances are different. When a current is applied into the two beams, different amount of heat will be generated due to the different resistances.

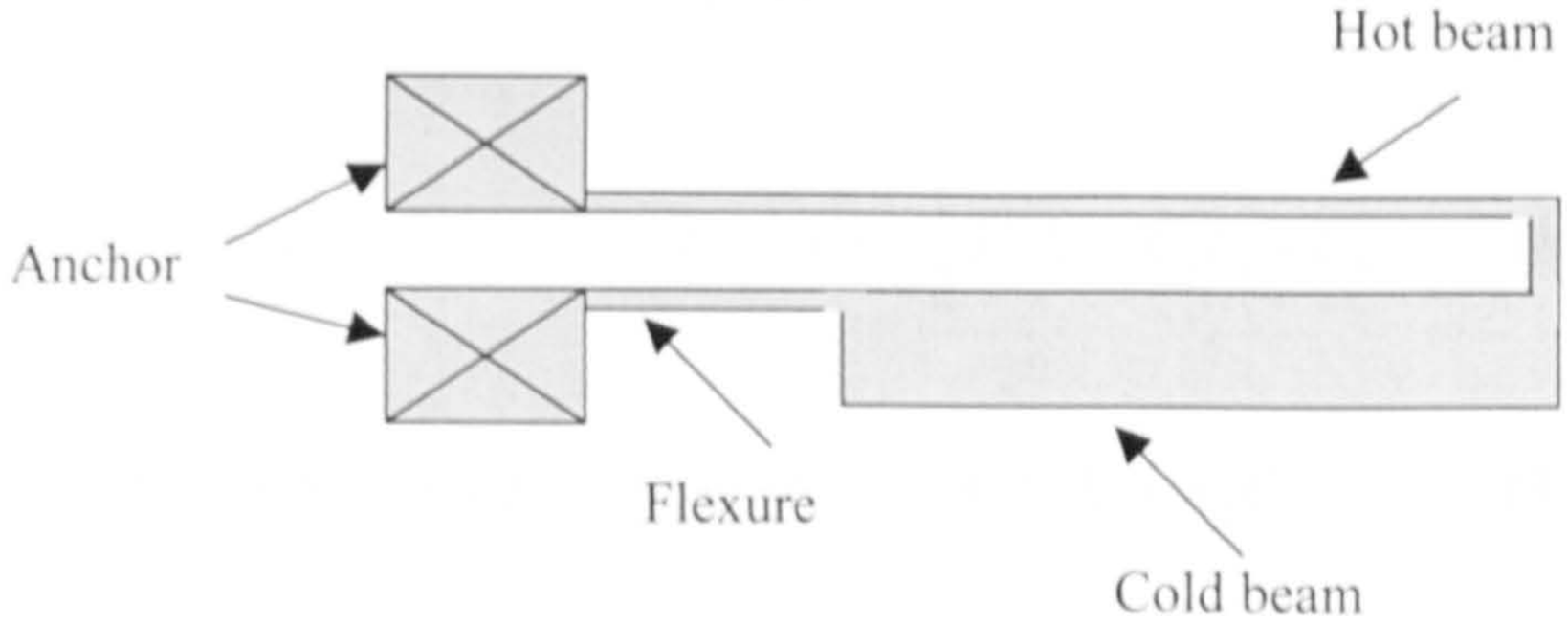

Fig. 3-7. Schematic picture of traditional asymmetric thermal actuator.

3.3.1 Temperature distribution

Again, only heat conduction is considered in this analysis. Unfolding the structure as shown in Fig. 3-8, the equation (3.4) is used again. There are three different segments

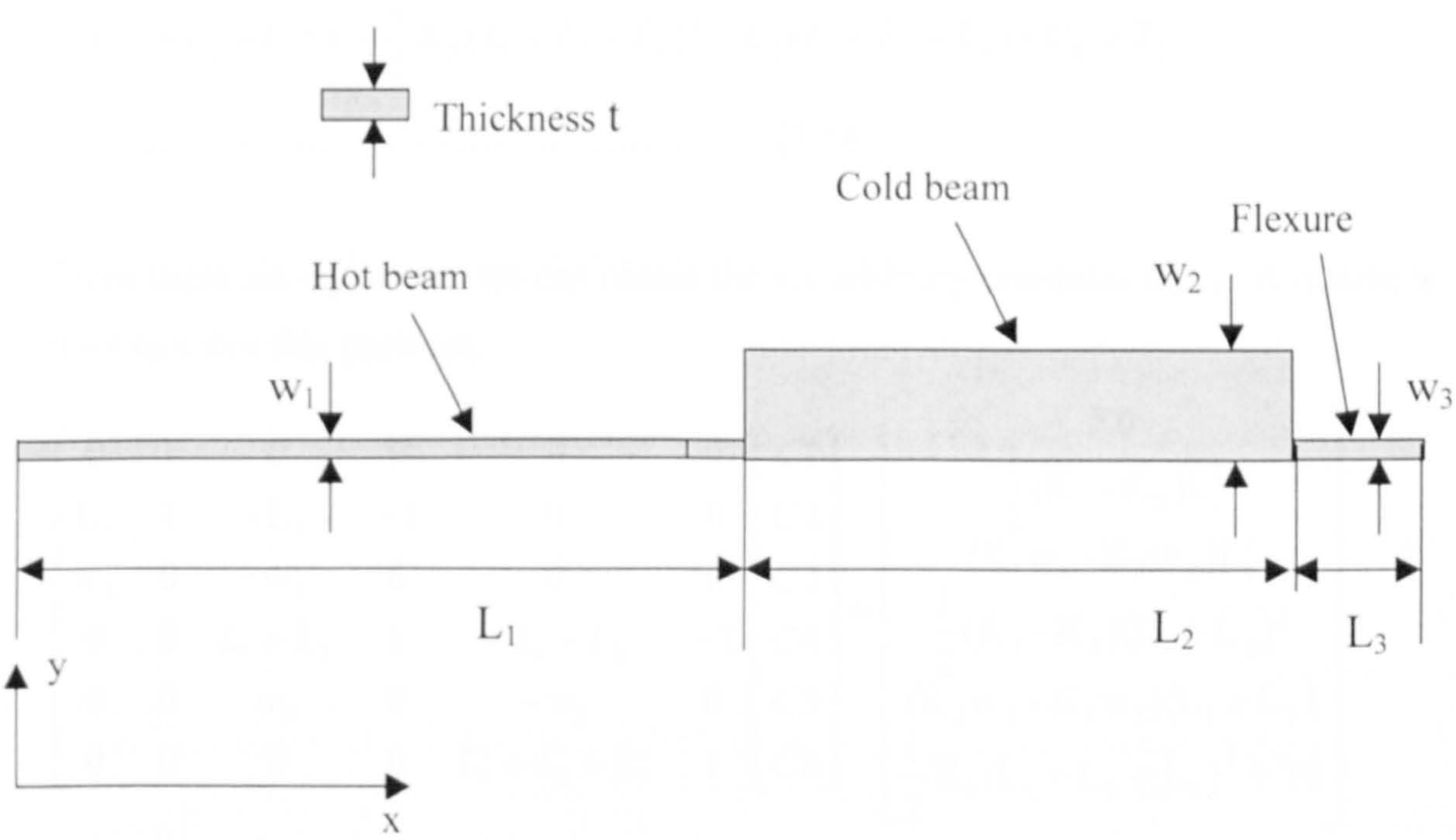

Fig. 3-8. Unfolded thermal actuator.

in this actuator, so we need boundary conditions to obtain the arbitrary constants C_i. The boundary conditions for equation (3.5) are:

$$T_1(0) = C_2 = T_0 \qquad (3.11)$$

$$T_1(L_1) = -\frac{1}{2}K_1L_1^2 + C_1L_1 + C_2 = T_2(L_1) = -\frac{1}{2}K_2L_1^2 + C_3L_1 + C_4 \qquad (3.12)$$

$$w_1T_1'(L_1) = -w_1K_1L_1 + w_1C_1 = w_2T_2'(L_1) = -w_2K_2L_1 + w_2C_3 \qquad (3.13)$$

$$T_2(L_1+L_2) = -\frac{1}{2}K_2(L_1+L_2)^2 + C_3(L_1+L_2) + C_4 = T_3(L_1+L_2) = -\frac{1}{2}K_3(L_1+L_2)^2 + C_5(L_1+L_2) + C_6$$

.....(3.14)

$$w_2T_2'(L_1+L_2) = -w_2K_2(L_1+L_2) + w_2C_3 = w_3T_3'(L_1+L_2) = -w_3K_3(L_1+L_2) + w_3C_5$$

.....(3.15)

$$T_3(L_1+L_2+L_3) = -\frac{1}{2}K_3(L_1+L_2+L_3)^2 + C_5(L_1+L_2+L_3) + C_6 = T_0,$$

.....(3.16)

From these six equations, we can obtain the six arbitrary constants C_{1-6}. A matrix is built to solve this problem.

$$\begin{bmatrix} 0 & 1 & 0 & 0 & 0 & 0 \\ L_1 & 1 & -L_1 & -1 & 0 & 0 \\ w_1 & 0 & -w_2 & 0 & 0 & 0 \\ 0 & 0 & L_1+L_2 & 1 & -L_1-L_2 & -1 \\ 0 & 0 & w_2 & 0 & -w_3 & 0 \\ 0 & 0 & 0 & 0 & L_1+L_2+L_3 & 1 \end{bmatrix} \begin{bmatrix} C1 \\ C2 \\ C3 \\ C4 \\ C5 \\ C6 \end{bmatrix} = \begin{bmatrix} T0 \\ \frac{1}{2}(K_1 - K_2)L_1^2 \\ (K_1w_1 - K_2w_2)L_1 \\ \frac{1}{2}(K_2 - K_3)(L_1+L_2)^2 \\ (K_2w_2 - K_3w_3)(L_1+L_2) \\ \frac{1}{2}K_3(L_1+L_2+L_3)^2 + T0 \end{bmatrix}$$

.....(3.17)

From matrix (3.17), we can obtain the constants C_i, then transfer these constants to equation (3.5). In order to obtain numerical results, the geometrical parameters and other properties of the material used to calculate are given: w_1, w_2, and w_3 are 2 μm, 20 μm, and 2 μm separately. Again three different length actuators are analyzed, L_1, L_2, and L_3 are 240 μm, 200 μm, 40 μm; 300 μm, 250 μm, 50 μm; and 360 μm, 300 μm, 60 μm separately. The thickness of all the beams is the same, t = 2 um. (we assume no substrate under the beam, and ignore the heat radiation to the air).

Thermal expansion coefficient is assumed same as the value we used in section 3.2 for polysilicon. In Fig. 3-9, temperature profiles are solved when 3.6 mW power is applied into all the three different length actuators.

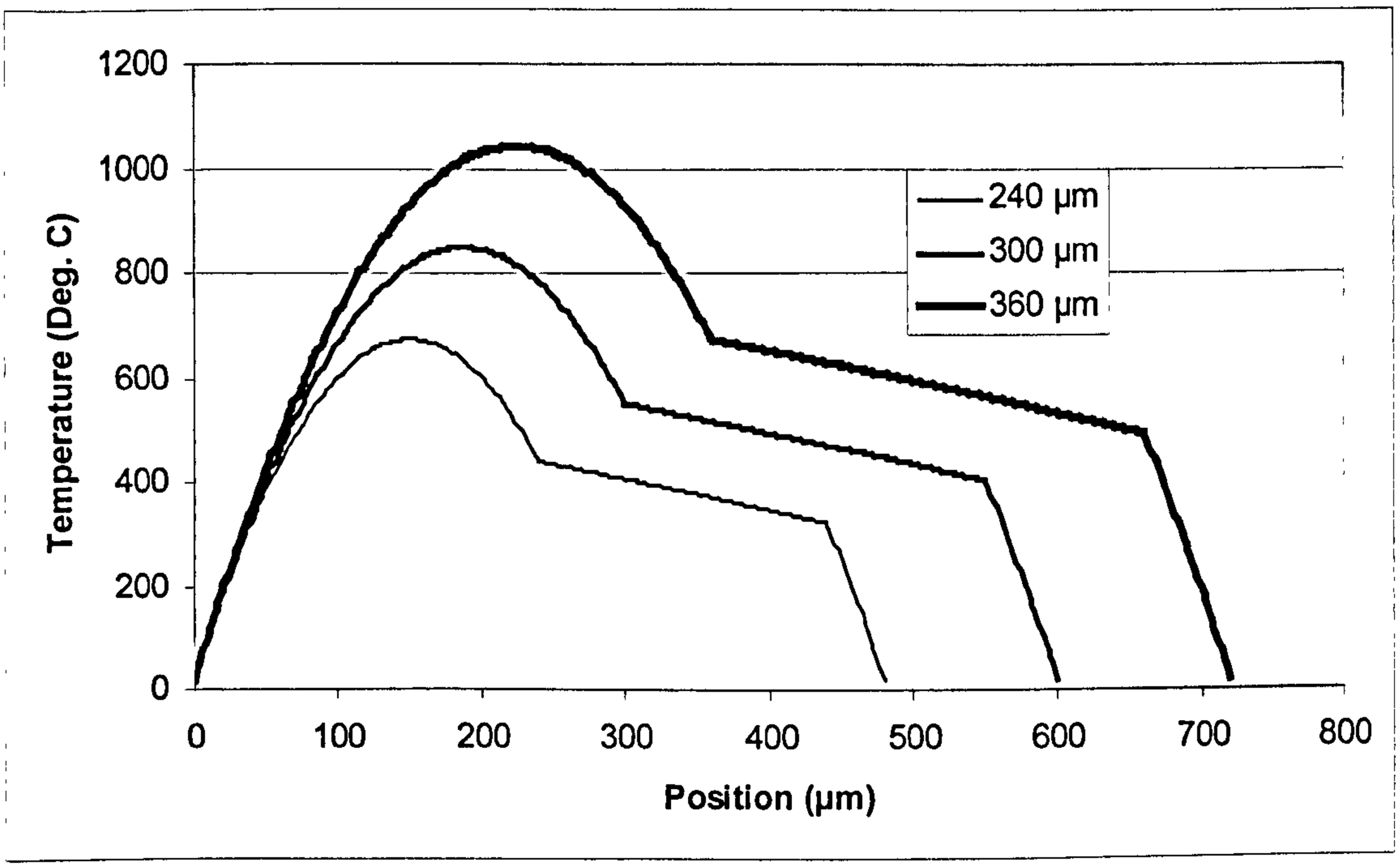

Fig. 3-9, Temperature distribution of three asymmetric electrothermal actuators. Input power = 3.6 mW, with parameters given in the text.

3.3.2 Deflection analysis

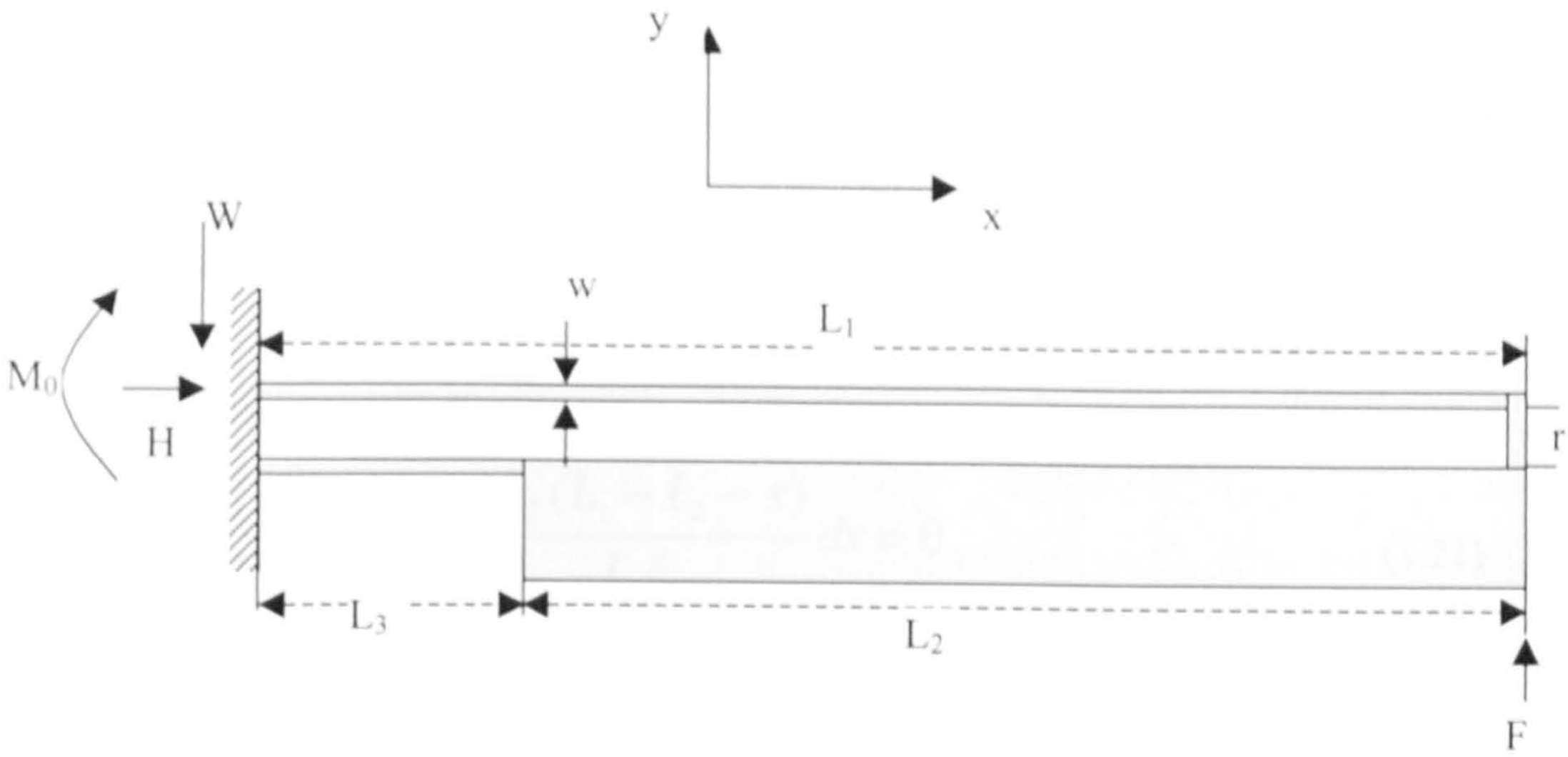

Fig. 3-10. Schematic figure of traditional asymmetric thermal actuator.

In reference [89], Castigliano's method (energy method) was utilized to obtain the function of the deflection '*dy*' related to the length of the hot beam 'L_1', external force 'F', and average net temperature of the actuator. In Fig. 3-10, W is the vertical force reaction generated by the thermal expansion at the anchor point of the hot beam, H is the horizontal reaction force, M_0 is the reaction moment. Assuming an external force is applied at the free tip of the hot beam the moments in the hot and flexure components are

$$M_h = Wx + M_0, \qquad (3.18)$$

$$M_f = -W(L_1 - L_2 - x) + M_0 + Hr - F(L_2 + x), \qquad (3.19)$$

Furthermore, in order to get three unknowns H (horizontal force), W (vertical force), and M_0 (rotation moment), three formulae can be written from the fact that horizontal displacement, vertical deflection, and rotation at the anchor of the hot beam are all zero.

First, the horizontal displacement contributions:

$$\int_0^{L_1} \frac{H}{A_1 E} dx + \int_0^{L_3} \frac{H}{A_3 E} dx + \int_0^{L_3} \frac{M_f(r)}{I_3 E} dx - \alpha \Delta T_{net} L_1 = 0, \qquad (3.20)$$

In equation (3.20), the first term stands for the expansion of the hot beam, second term represents the expansion of the flexure, third term represents the bending of the flexure beam due to the horizontal force H, and fourth term represents the net thermal expansion of the hot beam.

Second, the vertical displacement contributions:

$$\int_0^{L_1} \frac{M_h(x)}{I_1 E} dx + \int_0^{L_3} \frac{M_f(L_1 - L_2 - x)}{I_3 E} dx = 0, \qquad (3.21)$$

In equation (3.21), first term stands for the hot beam vertical displacement, second term stands for the vertical displacement of the flexure.

Third equation, rotation contributions:

$$\int_0^{L_1} \frac{M_h(1)}{I_1 E} dx + \int_0^{L_3} \frac{M_f(1)}{I_3 E} dx = 0, \qquad (3.22)$$

the first term stands for the rotation of the hot beam, the second term stands for the rotation of the flexure.

In the above equations, I_1 and I_3 represent the moment of inertia of hot beam and flexure, E is the Young's modulus of the material we used (polysilicon), A_1 and A_3 are the cross-section areas of hot beam and flexure beam.

Using these three equations, we can get the three unknowns H, W, and M_0 respectively. Mathematic software must be used due to the complexity of the equations.

The tip displacement can be obtained using following equation

$$dy = -\int_0^{L_3} \frac{M_f (L_2 + x)}{I_3 E} dx \,, \qquad (3.23)$$

Taking three terms H, W, and M_0 into the equation (3.23), letting $I_1 = I_3 = I$, $A_1 = A_3 = A$, $a = L_3 / L_1$, $L_2 = (1\text{-}a)\, L_1$. Simplifying the result, the displacement of the thermal actuator is therefore

$$dy = \frac{((a^4 - a^2 + 2a) ArEI)\alpha \Delta T_{net} L^2 - ((4a^5 + 8a^4 - 8a^3 + 12a)I + a^4 Ar^2) FL^3}{2EI(5a^4 I + a^4 r^2 A - 2a^3 I + 5aI + r^2 aA + I + a^5 I - 2a^2 I)}$$

.....(3.24)

$$dy_{noload} = \frac{((a^4 - a^2 + 2a) ArEI)\alpha \Delta T_{net} L^2}{2EI(5a^4 I + a^4 r^2 A - 2a^3 I + 5aI + r^2 aA + I + a^5 I - 2a^2 I)}$$

..... (3.25)

In equation (3.25), the external force is 0, so this is called 'dy_{noload}'.

Using equation (3.25) and section 3.3.1, taking data from section 3.3.1, we can obtain the relationship between input current and tip displacement. The result is shown in Fig. 3-11. Taking all the dimension and physical parameters from section 3.3.1.

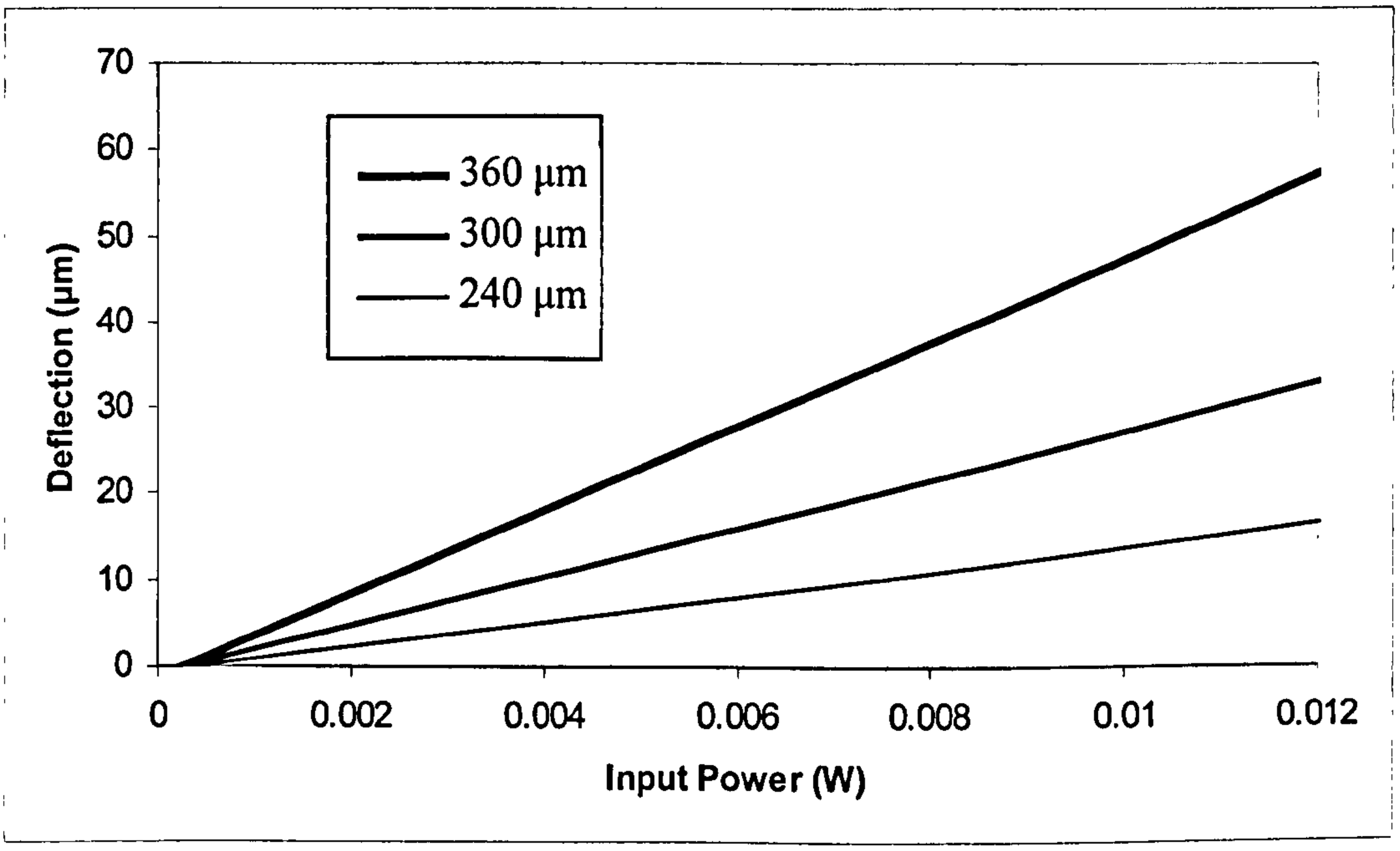

Fig. 3-11. Input power vs. no load displacement, with parameters described in the text.

The sensitivity of this type of actuator has also been solved, which is shown in Fig. 3-12.

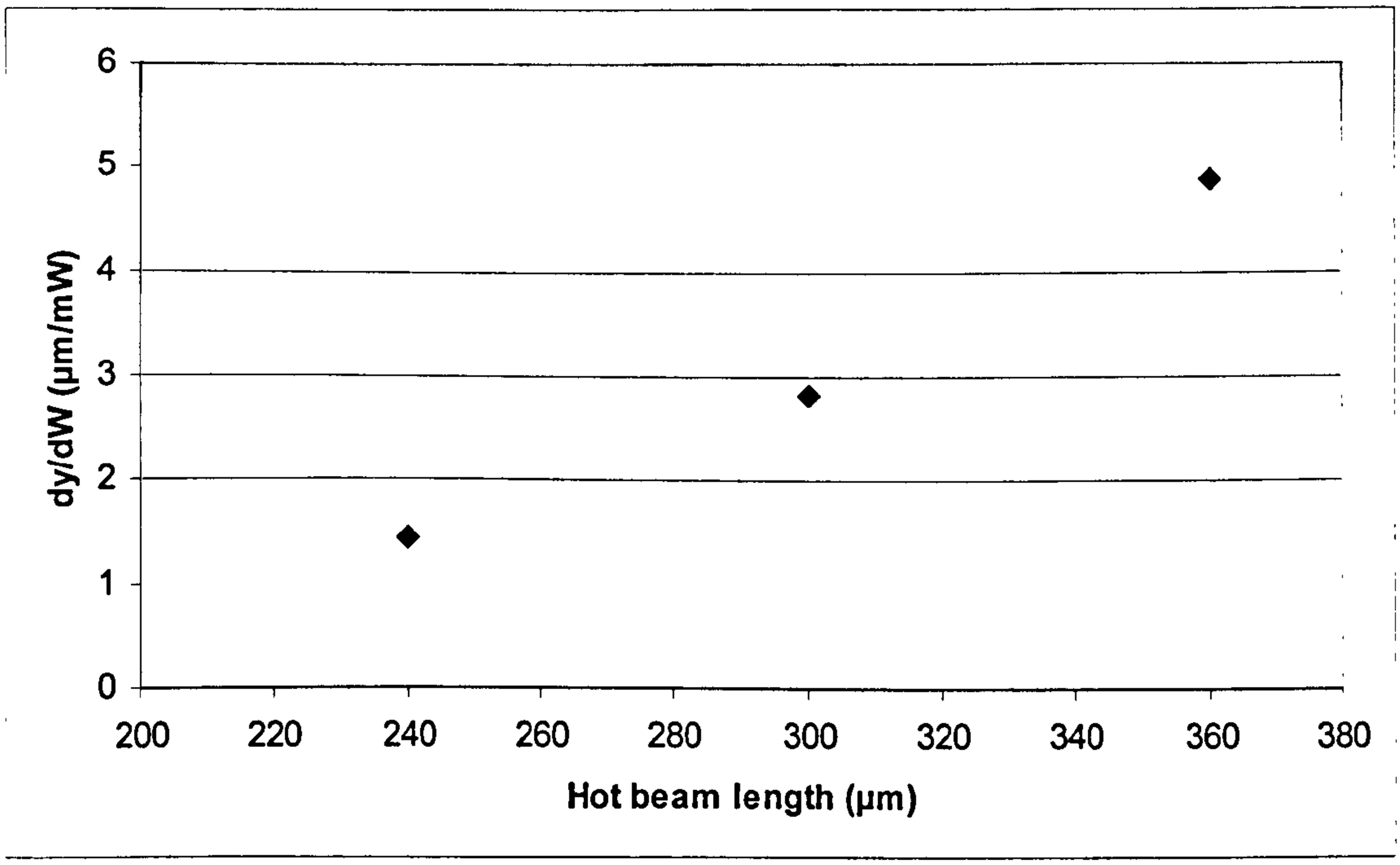

Fig. 3-12, Sensitivity of the traditional asymmetric electrothermal actuators (no load).

3.4 'V' shaped thermal actuator

The micro 'V' shaped electro-thermal actuator (bent beam thermal actuator) was introduced by Long Que et al [39]. The schematic is shown in Fig. 3-13. It consists of two same length, same width, same thickness beams connected at one end and anchored at the other end. These two beams form a 'V' shape. When applying current through these two beams, thermal expansion occurs in both beams, and lateral displacement is generated. This type of actuator has been used to drive a variable optical attenuator [90], and a radio frequency relay [40]. Here, temperature analysis of the actuator is conducted considering only heat conduction. Deflection analysis has also been performed.

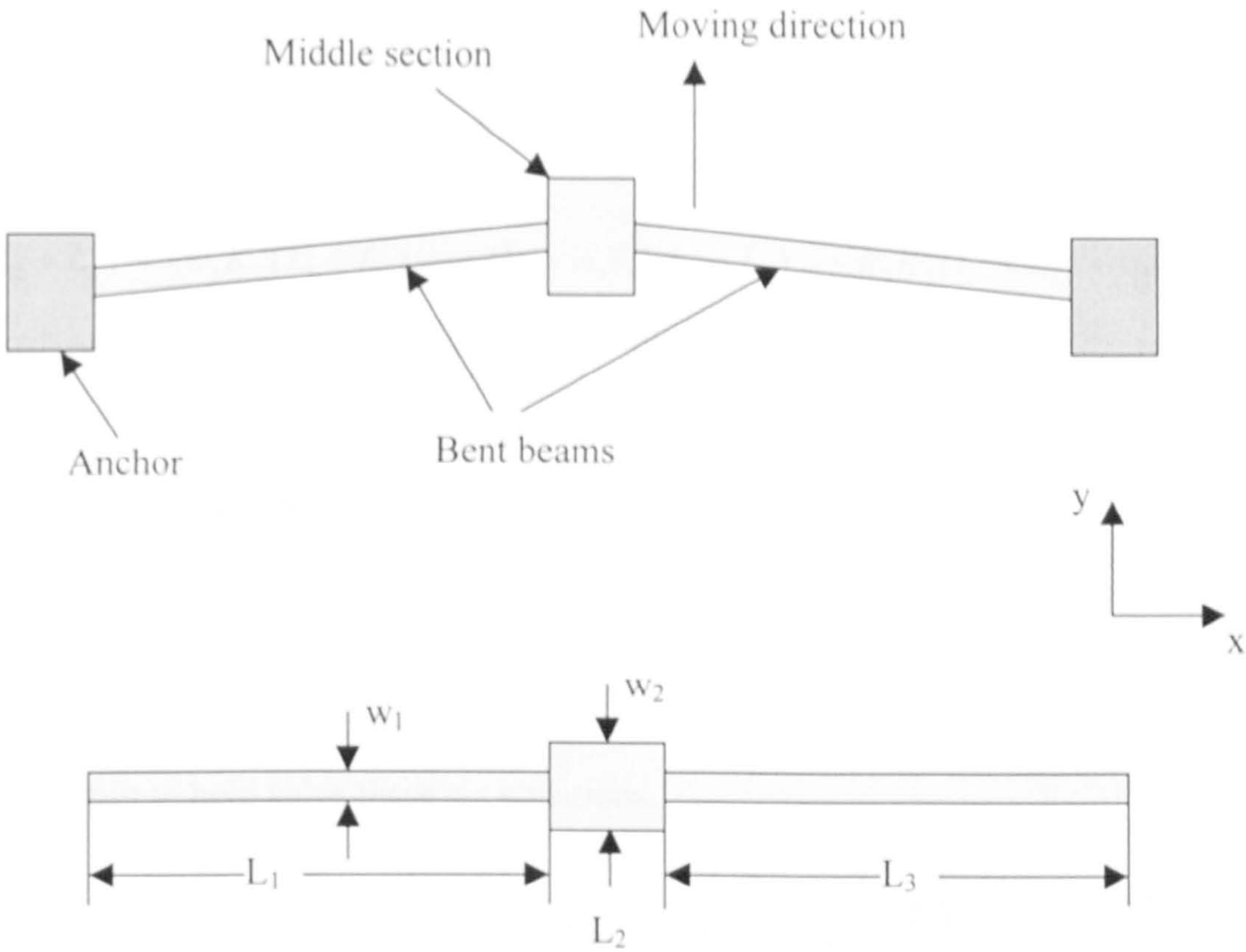

Fig. 3-13. Schematic picture of the bent beam thermal actuator.

3.4.1 Temperature analysis

Equation (3.5) is again used for obtaining the temperature distribution of this type of actuator. There are three segments in this type of actuator, so 6 unknown constants ($C_{1\text{-}6}$) are required to be worked out. Again applying the boundary conditions to the formula (3.5), so we can obtain 6 equations as follows

$$T_1(0) = C_2 = T_0 \tag{3.26}$$

$$T_1(L_1) = -\frac{1}{2}K_1 L_1^2 + C_1 L_1 + C_2 = T_2(L_1) = -\frac{1}{2}K_2 L_1^2 + C_3 L_1 + C_4 \tag{3.27}$$

$$w_1 T_1'(L_1) = -w_1 K_1 L_1 + w_1 C_1 = w_2 T_2'(L_1) = -w_2 K_2 L_1 + w_2 C_3 \tag{3.28}$$

$$T_2(L_1+L_2)=-\frac{1}{2}K_2(L_1+L_2)^2+C_3(L_1+L_2)+C_4=T_3(L_1+L_2)=-\frac{1}{2}K_3(L_1+L_2)^2+C_5(L_1+L_2)+C_6$$

.....(3.29)

$$w_2T_2'(L_1+L_2)=-w_2K_2(L_1+L_2)+w_2C_3=w_3T_3'(L_1+L_2)=-w_3K_3(L_1+L_2)+w_3C_5$$

.....(3.30)

$$T_3(L_1+L_2+L_3)=-\frac{1}{2}K_3(L_1+L_2+L_3)^2+C_5(L_1+L_2+L_3)+C_6=T_0,$$

(3.31)

A matrix is built to help solve these six equations.

$$\begin{bmatrix} 0 & 1 & 0 & 0 & 0 & 0 \\ L_1 & 1 & -L_1 & -1 & 0 & 0 \\ w_1 & 0 & -w_2 & 0 & 0 & 0 \\ 0 & 0 & L_1+L_2 & 1 & -L_1-L_2 & -1 \\ 0 & 0 & w_2 & 0 & -w_3 & 0 \\ 0 & 0 & 0 & 0 & L_1+L_2+L_3 & 1 \end{bmatrix} \begin{bmatrix} C1 \\ C2 \\ C3 \\ C4 \\ C5 \\ C6 \end{bmatrix} = \begin{bmatrix} T0 \\ \frac{1}{2}(K_1-K_2)L_1^2 \\ (K_1w_1-K_2w_2)L_1 \\ \frac{1}{2}(K_2-K_3)(L_1+L_2)^2 \\ (K_2w_2-K_3w_3)(L_1+L_2) \\ \frac{1}{2}K_3(L_1+L_2+L_3)^2+T0 \end{bmatrix}$$

..... (3.32)

Again in order to obtain the numerical solution, the geometrical parameters of the actuator are given as follows: $w_1 = w_3 = 3$ μm, $L_2 = 40$ μm, $w_2 = 40$ μm; again three sets of L_1 (L_3), 100 μm, 150 μm, 200 μm are investigated; the thickness of all the beams is the same, $t = 2$ um. (Assuming no substrate under the beam, and ignoring the heat radiation to the air). Other properties (e.g thermal expansion coefficient, resistivity) are same as the values we used in the last sections.

The simulated temperature distributions are shown in Fig. 3-14. Here, 6.1 *mW* is applied to the actuator.

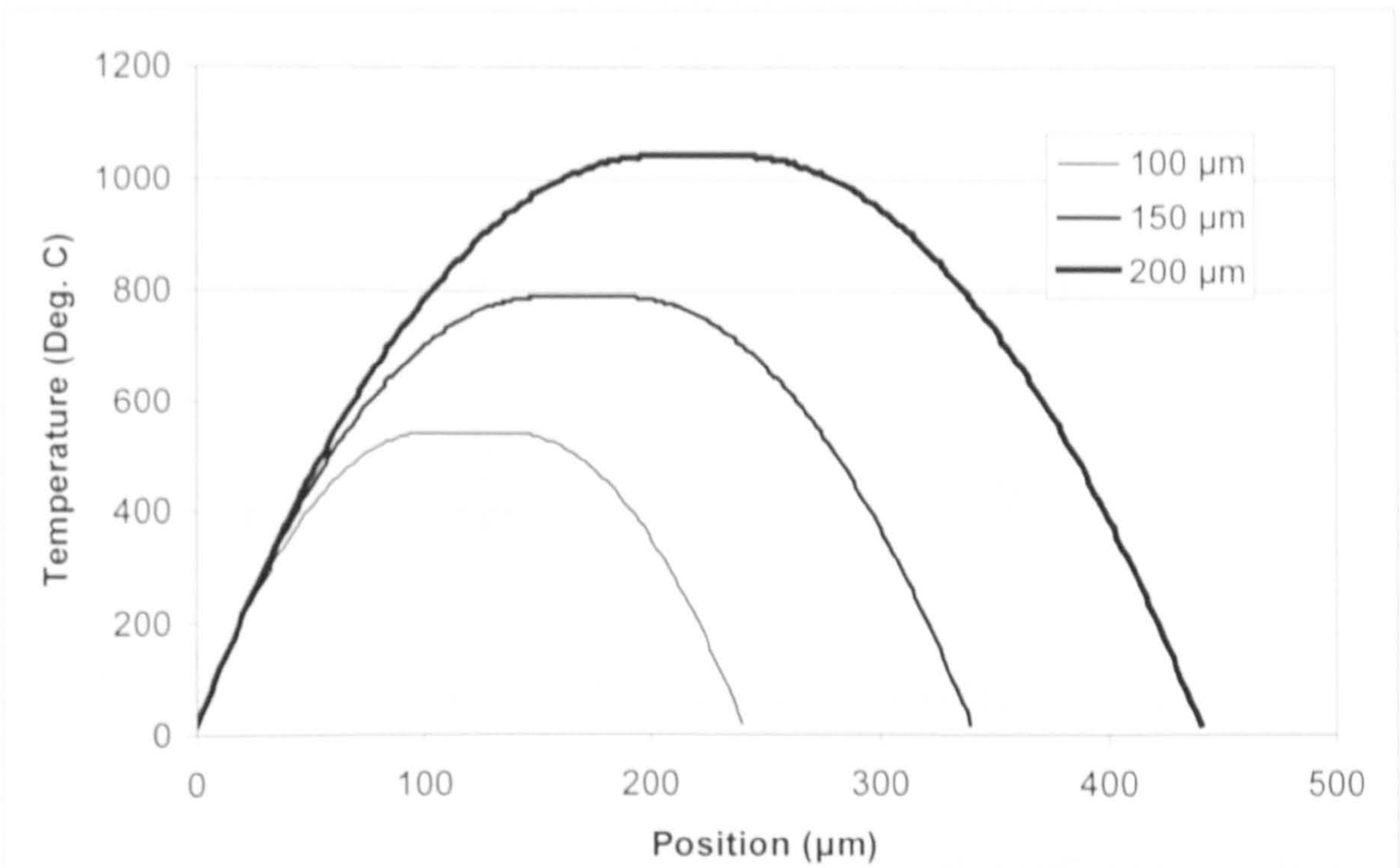

Fig. 3-14, Temperature distribution of three 'V' shaped electrothermal actuators. Input power = 6.1 mW, with parameters given in the text.

3.4.2 Mechanical analysis

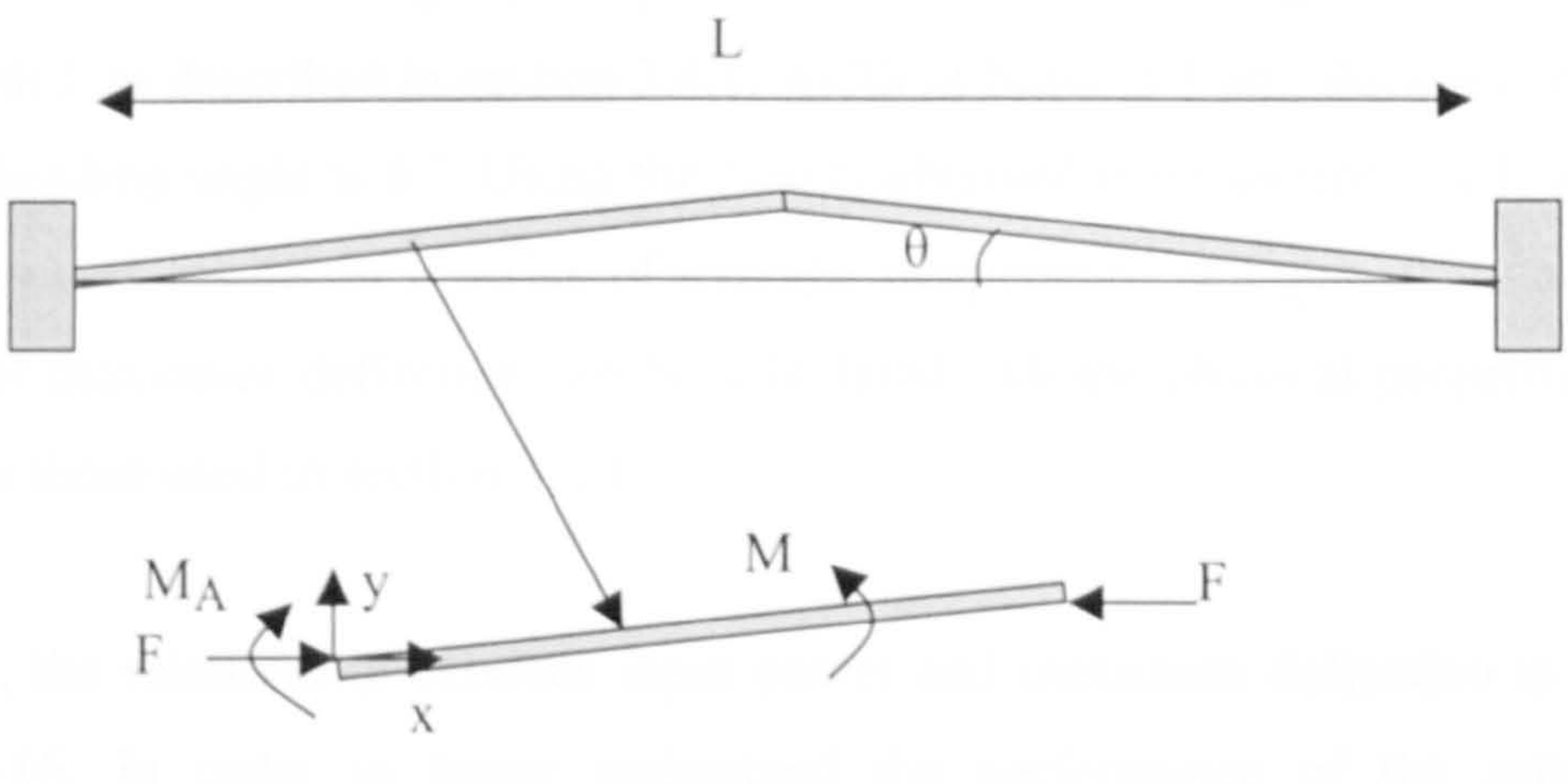

Fig. 3-15. Analytical model of a 'V' shape thermal actuator.

From reference [39], an analytical method is employed to solve the maximum displacement of this type of actuator (shown in Fig. 3-15). The maximum displacement, d_{max}, can be calculated from the beam bending equation with a correction term for the beam compression:

$$d_{\max} = 2\frac{\tan\theta}{k}\tan\frac{kL}{4} - \frac{L}{2}\tan\theta, \qquad (3.33)$$

$$\bar{T} = \frac{1}{\alpha L}(\Delta L' + \frac{FL}{Ewt}), \quad k = \sqrt{\frac{F}{EI}}, \qquad (3.34)$$

$$L' = \frac{(\tan\theta)^2}{4k}[2G + kL + kLG^2 + \sin kL - 2G\cos kL - G^2\sin kL], \qquad (3.35)$$

where, $G = tan(kL/4)$; E is Young's modulus; α is expansion coefficient; t is beam thickness; w is beam width; I is moment of inertia of the beam; L is length defined in Fig. 3-15; θ is bending angle defined in Fig. 3-15; F is reaction force along the x-axis at the anchors shown in Fig. 3-15; $\bar{T}$ is average temperature of the beam; $\Delta L'$ is change in L' due to F.

From last section, the length L is equal to sum of $L_1 + L_3$, taking three different value of length L as described in section 3.4.1; width of beam is 3 um; thickness of beam is 2 um; bending angle is 6 °. Using the results obtained from section 3.4.1, a series of input powers results in a series of average temperature changes, then, a series of value of maximum deflection can be calculated. All the physical properties are the same as those used in section 3.4.1.

Finally, the relationship between input power and maximum deflection is shown in Fig. 3-16. In order to better understand the performance of the actuator, the sensitivity dy/dW has been worked out, which is shown in Fig. 3-17.

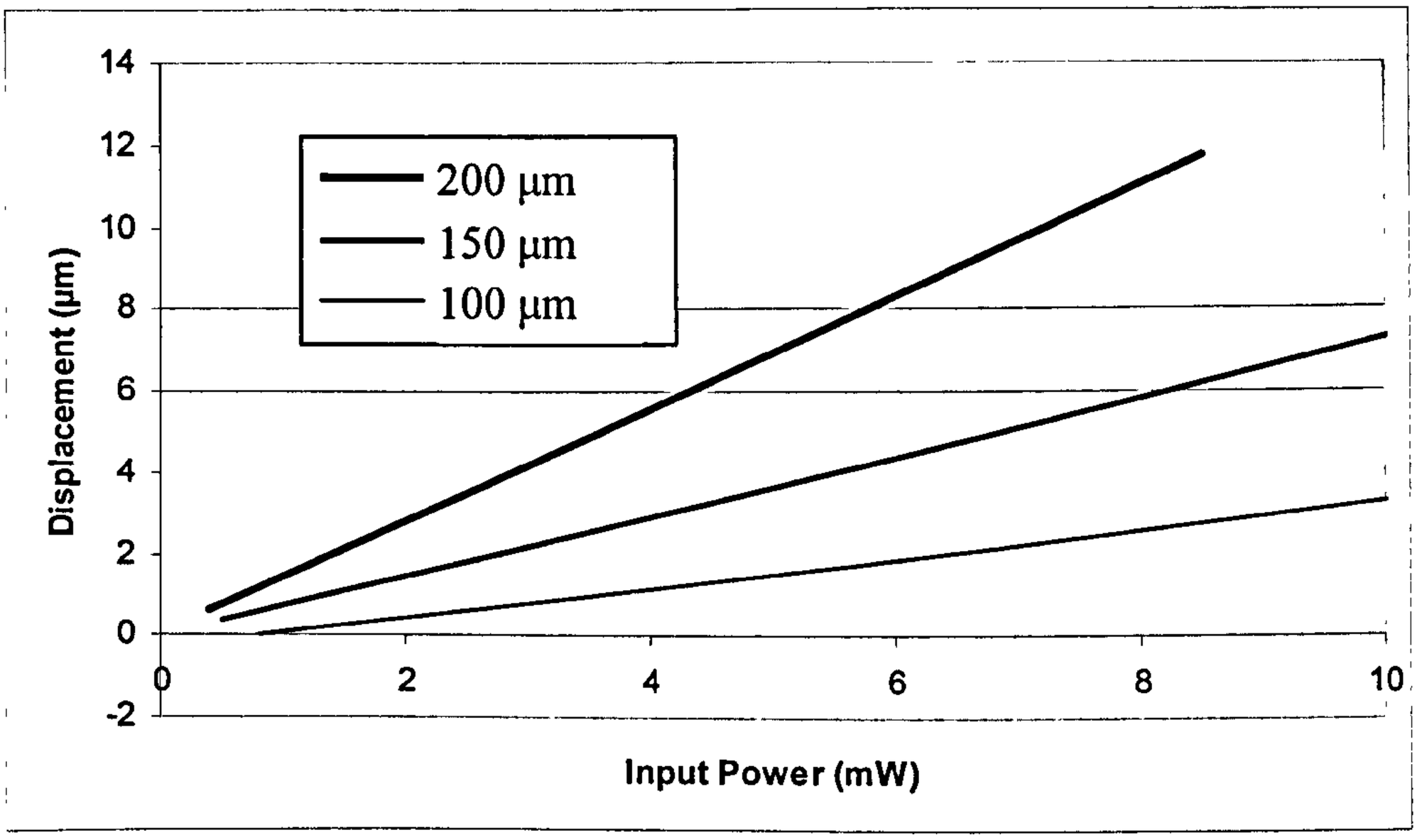

Fig. 3-16, Deflection vs. input power, with parameters described in the text.

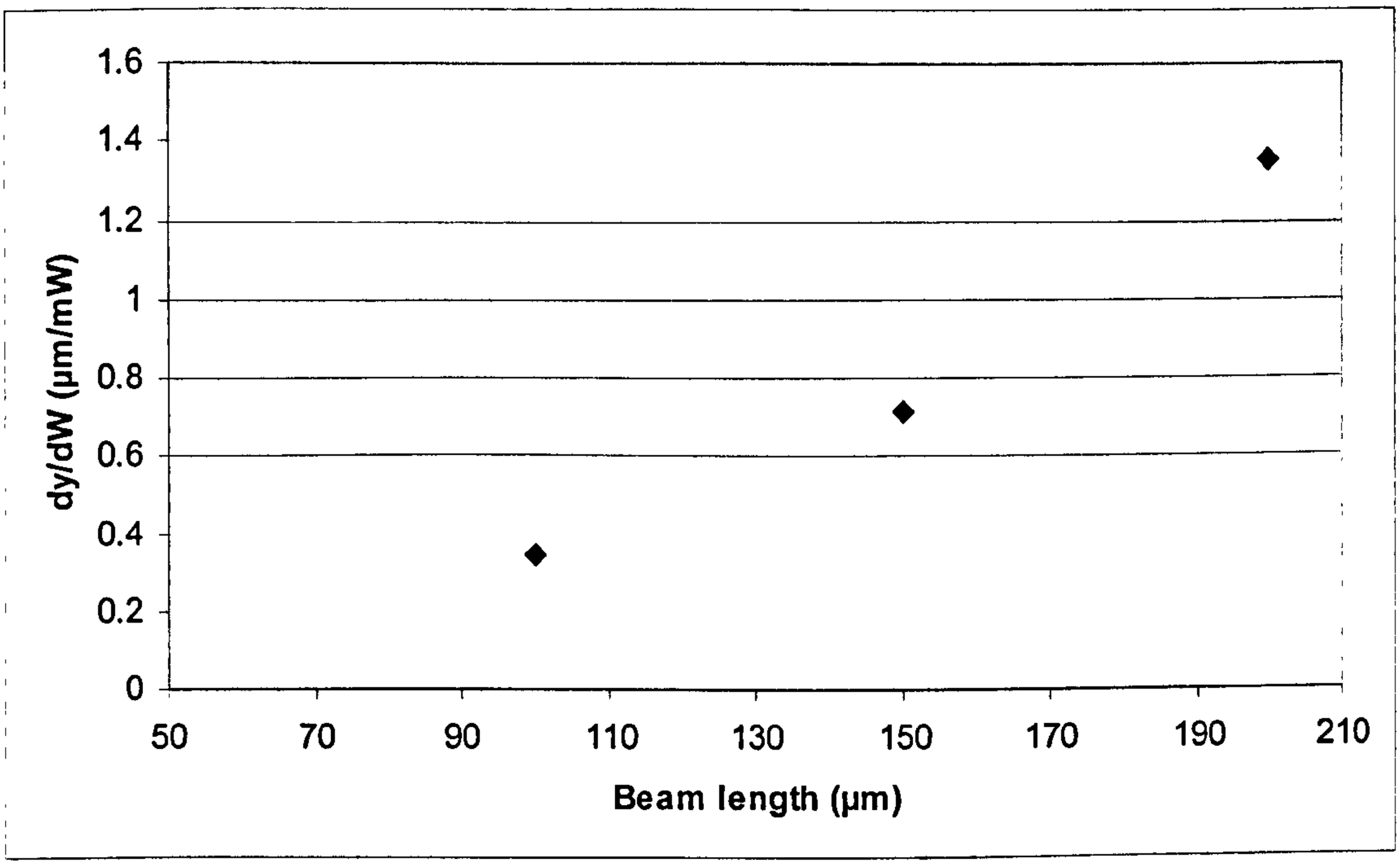

Fig. 3-17, Sensitivity of the 'V' shaped electrothermal actuators.

3.5 Optimization of asymmetric electrothermal actuator

The asymmetric-beam thermal actuator is a well-known thermal actuator, which consists of two connected beams made from the same material, but having different widths and therefore cross-sections. The schematic diagram of such an actuator is shown in Fig. 3-18. In Fig. 3-18, L_1 is the length of the hot beam, L_2 is the length of the cold beam, w_1 is the width of the hot beam, w_2 is the width of the cold beam. The length of the flexure is L_1 - L_2, the width of the flexure is the same as the width of the hot beam. The operation of this actuator is well known. Briefly, electrical current is passed through the actuator from one anchor to the other. The electrical resistance of the narrower beam is higher than that of the wider beam. Accordingly, the heat generated in the beam of smaller cross-section (the "hot" beam) is much higher than that of the wider beam (the "cold" beam). This results in the temperature of the hot beam being much higher than the cold beam. Since the cold and hot beams are made of the same material, the temperature difference generated causes the hot beam to expand more than the cold beam. The beams are connected to each other at one end,

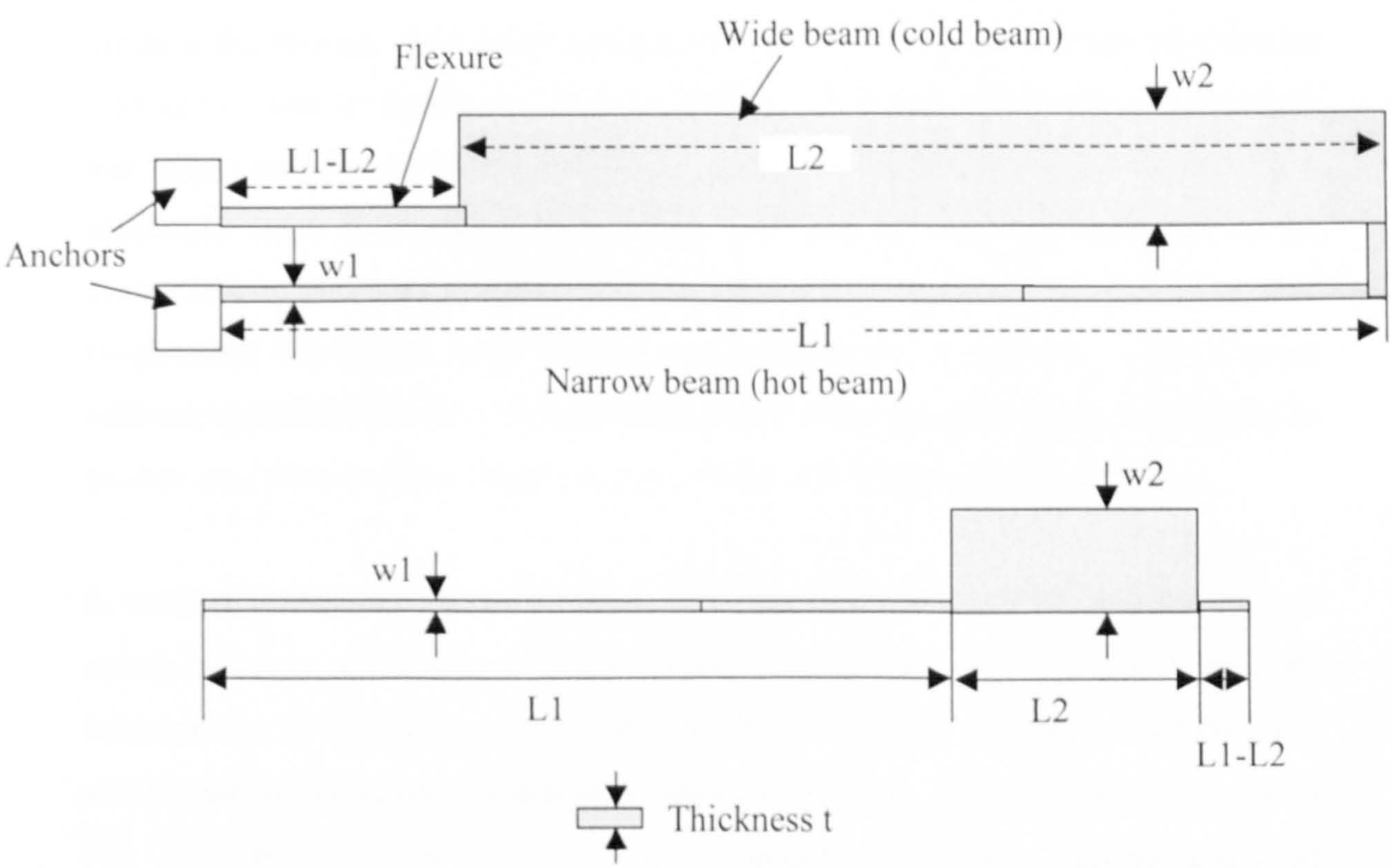

Fig. 3-18. Schematic figure of the traditional asymmetric thermal actuator. The lower diagram is an unfolded thermal actuator.

so this differential expansion will cause the actuators to bend laterally. Surface micromachining and SOI micromachining are commonly used to fabricate such thermal actuators.

This type of thermal actuator has been well analyzed both experimentally [37], [38] and theoretically [89], [91]. In this type of actuator, the cold beam does not have the main role for actuation; it is the hot beam which is of greater importance and acts as the 'active' part of the actuator. Generally the higher the temperature of the hot beam, the greater its expansion and the larger will be the deflection of the actuator. The temperature referred to above is the average temperature along the hot beam. Normally, this type of actuator is designed with the hot beam having a uniform width. The temperature profile of the actuator with a constant width hot beam has been obtained by solving the heat flow equations as described in [89], [91]. The result shows that the temperature profile along the hot beam has a single peak value, which appears at the middle of the beam. If the actuator is fabricated in polysilicon, the peak value of the temperature should be kept below 1000 °C to avoid thermal failure. In order to avoid permanent damage, the actuator is driven with a current which ensures that the peak temperature of the hot beam is below that required to produce the damage. The direct consequence of this is a lower average temperature leading to a smaller deflection. It is intuitive that if a beam of constant cross-section, and hence constant electrical resistance, generates a temperature profile having a maximum value at its center, then locally lowering the electrical resistance in the center zone of the beam to reduce Joule heating in that region will modify the overall temperature distribution such that the peak temperature is reduced. Thus, a more uniform spatial distribution of temperature with higher average value is produced in the hot arm, without there being hot spots which could lead to thermal failure.

In order to manipulate the temperature of the hot beam to avoid thermal damage yet obtain a large deflection, a novel design is introduced to prevent high peak temperature. In this design, the width of the hot beam is no longer uniform. The middle part of the beam is made wider than its two ends. The schematic is shown in Fig. 3-19. In Fig. 3-19, L_1, L_2, L_3 are the lengths of the first, second, and third sections of the hot beam separately. L_4 is the length of the cold beam. w_1 is the width

of the first and third section of the hot beam, w_2 is the width of the second section of the hot beam, w_3 is the width of the cold beam. The length of the flexure is $L_1 + L_2 + L_3 - L_4$, and the width of flexure is the same as that of the first section of the hot beam. With this particular shape of beam, the temperature profile of the hot beam is changed, and it will be shown that it no longer has the peak temperature at a single central point. Instead, a more uniform temperature profile is achieved. With this design, the new actuator can deflect more in comparison to the traditional design made in the same material. A temperature analysis and experimental results are presented in the following sections. The effect of dimensions on the temperature distribution of the hot beam is analysed in the next section, showing that an optimized temperature distribution can be obtained. The values of electrical, mechanical and thermal constants used in all the analysis undertaken are for polysilicon, since this was the material used to fabricate the test actuators which were experimentally evaluated.

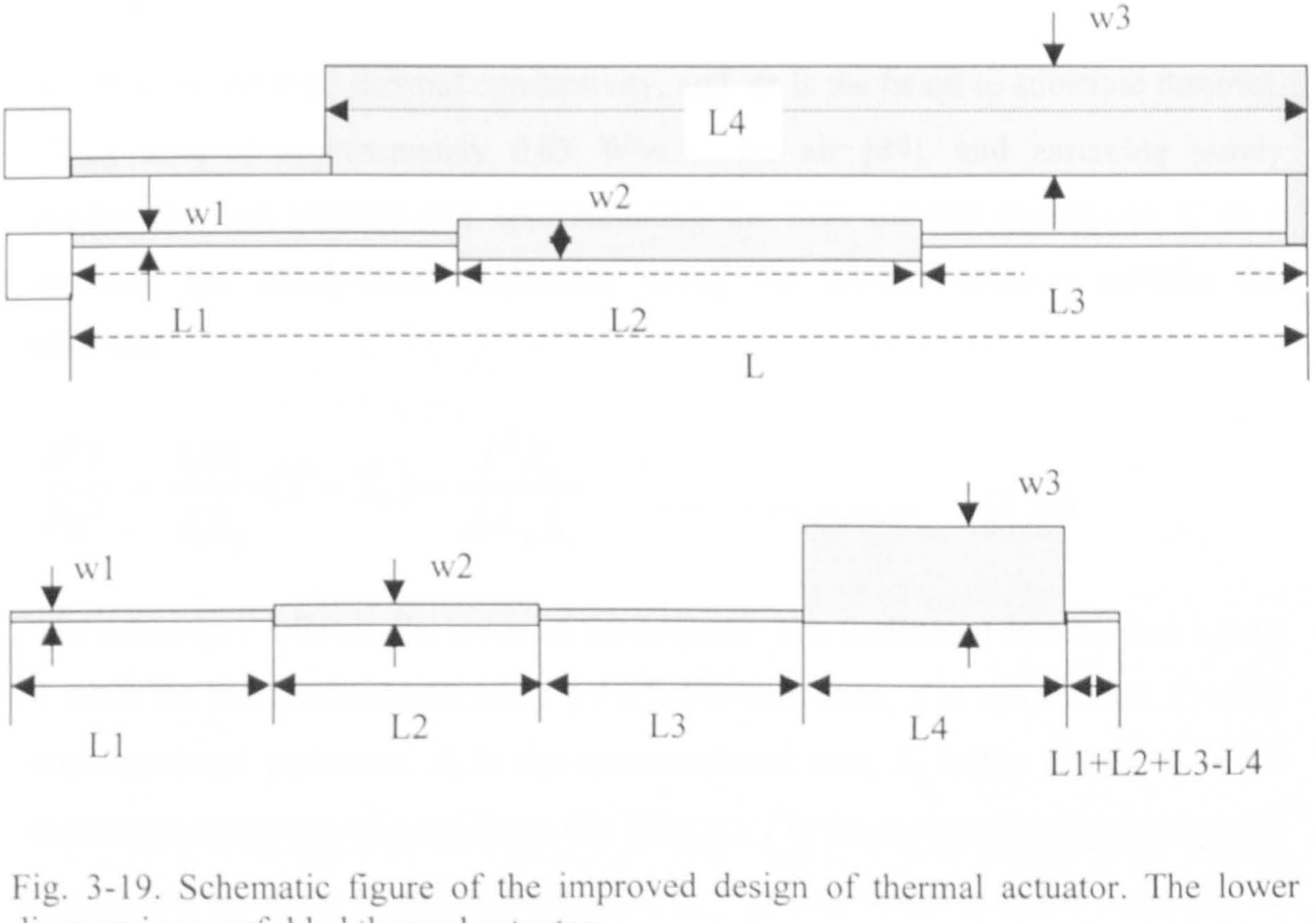

Fig. 3-19. Schematic figure of the improved design of thermal actuator. The lower diagram is an unfolded thermal actuator.

3.5.1. Temperature Analysis

3.5.1.1 Dimensionless temperature parameter

There are three mechanisms of heat flow in the thermal actuator: conduction, convection and radiation. According to reference [89], the natural convection is determined by the Rayleigh number *Ra*. $Ra = g\beta/(v\alpha_T)(T-T\infty)S^3$, where g is the acceleration due to gravity, β is the coefficient of thermal expansion of air, v is the kinematic viscosity of air and α_T is the thermal diffusivity of air. T is the heating element's temperature, and $T\infty$ is the ambient temperature and S is a characteristic dimension, here S is the width of hot beam. In the macroworld, *Ra* is typically large: 10^5 to 10^9 and convection is therefore important. For a hot beam 2 μm in width at 800 K, Ra = 2.7 x 10^{-8}: diffusion dominates and the microscale heat transfer takes place by conduction, as opposed to convection. The conduction heat transfer coefficient U can be approximated by:

$$U = \frac{k_f}{\Delta z}$$

where k_f is the fluid thermal conductivity, and Δz is the beam to substrate distance. Using a k_f of approximately 0.03 W/m.K, for air [89], and assuming purely conductive heat transfer and approximating the heat transfer coefficient U as a constant, the steady-state temperature along the thermal actuator satisfies the equation:

$$\frac{\partial^2 T}{\partial x^2} = \frac{UP_i}{A_i k_p}(T - T_0) - \frac{I^2 R_i}{A_i k_p L_i} \quad \text{.....(3.36)}$$

The subscript i refers to the zones of the actuator. The traditional actuator has $1 \leq i \leq 3$ while the modified actuator has $1 \leq i \leq 5$. For each zone, T is temperature, P_i is the cross-sectional perimeter, A_i is the cross-sectional area, L_i is the length, k_p is the thermal conductivity of polysilicon (50 W/m.K), I is the current flowing through the device and R_i is the electrical resistance. $R_i = \rho L_i/A_i$, where ρ is the resistivity of polysilicon (2.32×10^{-3} Ω-cm) used in our fabricated devices [90]. The first term on the right side of equation (3.36) is the heat transfer from the surface of the thermal

actuator to the air, and the second term is the heat generation due to the electric current. Equation (3.36) is solved using the method described in section 3.2 and 3.3. The peak temperature of the actuator can be obtained by finding the maximum from the numerical solution set. The average temperature can be obtained from the area under the temperature versus distance curve

$$\overline{T} = \frac{\sum \int T(x)_i dx}{\sum L_i} \quad \text{.....(3.37)}$$

A dimensionless temperature parameter *Tr* is introduced, and is defined as the ratio:

$$Tr = \frac{Peak\ \ Temperature\ \ of\ \ the\ \ hot\ \ beam}{Net\ \ average\ \ temperature} \quad \text{.....(3.38)}$$

The values of peak and average temperature are obtained from the solutions of Equations (3.36) and (3.37). The closer the value of *Tr* is to 1, the more uniform will be the spatial temperature distribution along the hot arm of the actuator.

3.5.1.2. Effect of dimensions on Tr

The analysis involves only the hot beam of the actuator. There are six independent variables (see Fig. 3-19), namely: L, L_1, L_2, w_1, w_2 and t that define the overall geometry of the hot arm of the actuator. For simplification the width of the cold beam is kept constant (22 μm). The width of the flexure is kept constant (2 μm), and the ratio of the length of flexure to L is kept constant (17 %) following reference 8. The parameter t not shown in Fig. 3-19 is the thickness of the actuator. In this thesis, all the devices fabricated have a thickness of 2 μm (determined by the fabrication process), and so this thickness value has also been used in the analysis, and will remain constant.

In order to investigate the impact of the remaining five dimensions on the thermal distribution, the following procedure was followed:

Step 1). Value of driving current to actuator is selected. Values of dimensions L and w_1 of the hot beam are selected.

Step 2). The value of Tr is calculated for different values of L_1, L_2 (and L_3 by default since $L = L_1 + L_2 + L_3$) and different values of w_2, and a data-set for Tr is thereby generated. Here, L_1 and L_2 are varied from 0 to L, $L_1 + L_2 \leq L$.

Step 3). For each value of w_2 analysed in Step 2, the variation of Tr can be plotted as a function of L_1 and L_2. This is illustrated in Figs. 3-20 and 3-21 which are just two representative plots showing how Tr varies with different dimensions. The values of L, w_1 and w_2 are given in each of these Figures.

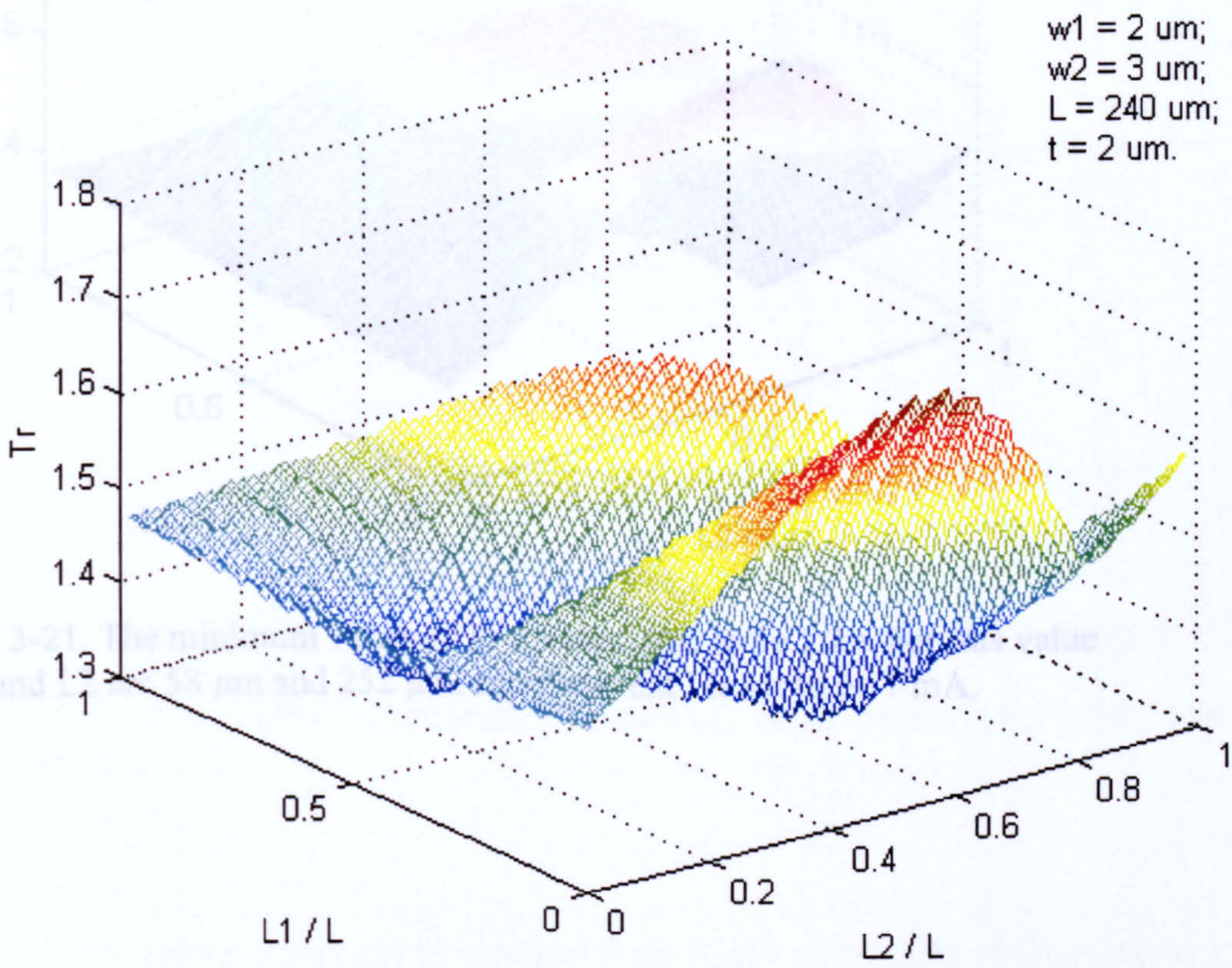

Fig. 3-20. The minimum value of Tr is calculated to be 1.33. For this value, L1 and L2 are 55 μm and 134 μm. Input current I is set to be 7 mA.

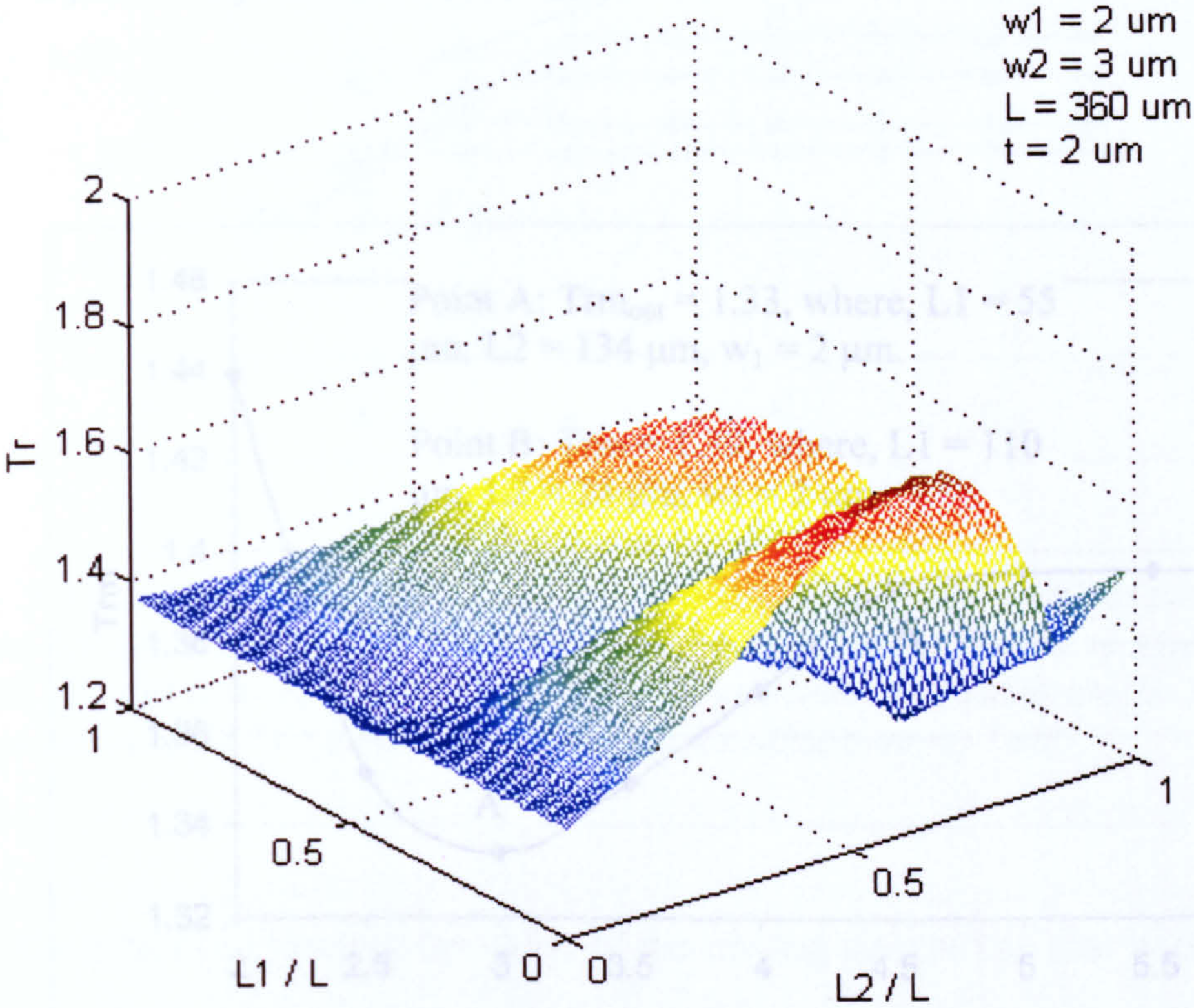

Fig. 3-21. The minimum value of Tr is calculated to be 1.29. For this value L1 and L2 are 58 μm and 252 μm. Input current I is set to be 7 mA.

Step 4). From each data-set of *Tr* a minimum value, designated as *Trm*, can be found. Each *Trm* is produced by a specific value of L_1, L_2 and w_2. These values of *Trm* have been plotted against the width w_2 in Fig. 3-22. It can be seen that in the set of *Trm* there will be a minimum value, and this is designated as Trm_{opt}. Trm_{opt} will therefore have associated values of w_2, L_1 and L_2 thereby giving the optimised dimensions of the hot beam. In Fig. 3-22, Trm_{opt} is at point A. It should be noted in Fig. 3-22 that w_2 = 2 μm corresponds to a traditional actuator.

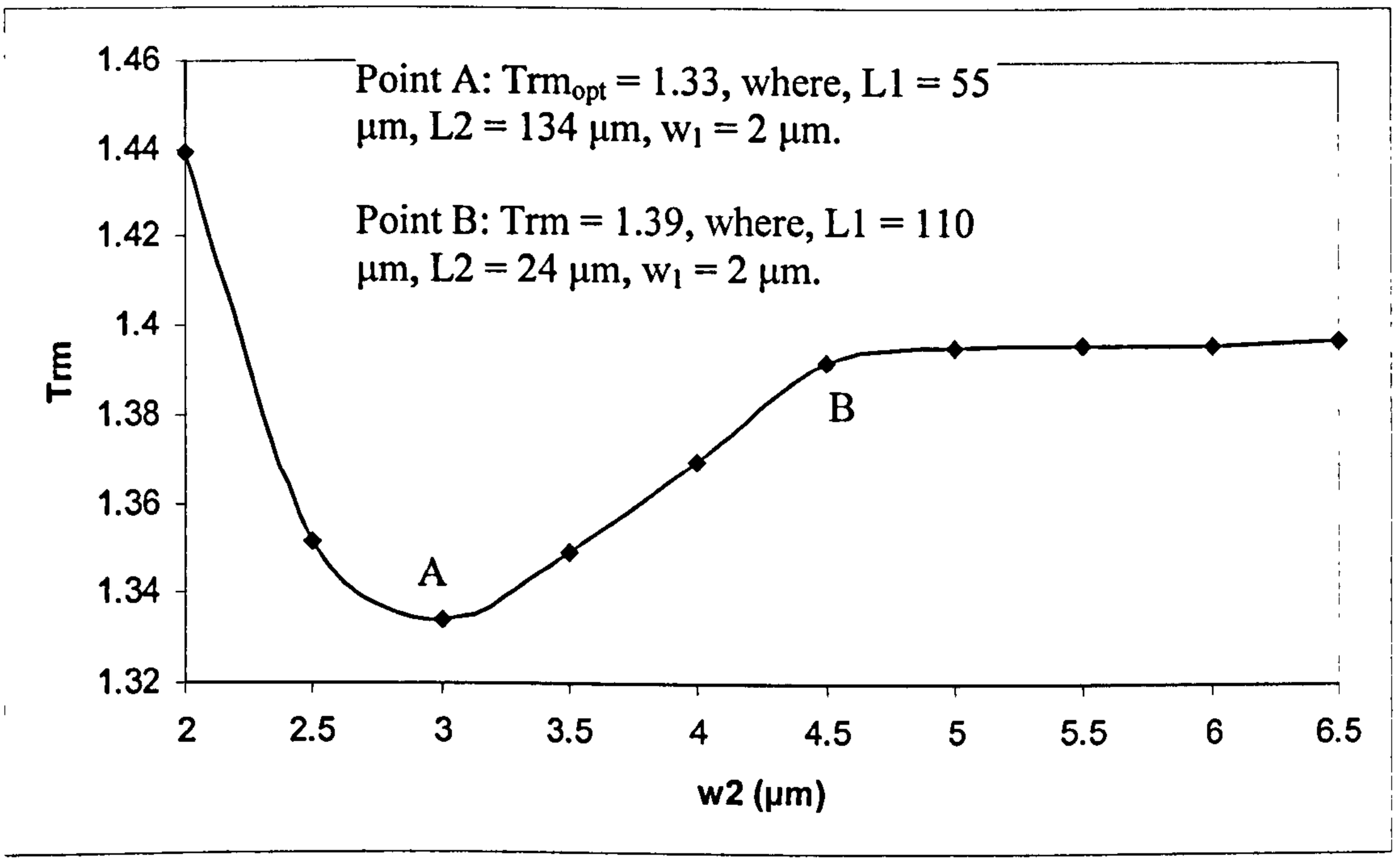

Fig. 3-22. The relationship between Trm and w2. Input current is set to be 7 mA, L = 240 μm.

Step 5). The entire process can be repeated from Step 1 using different starting values of *L* and w_1. Fig. 3-23 shows the results of analysing six values of *L* ranging from 180 μm to 480 μm. The value w_1 is the same for all these plots, and is 2 μm.

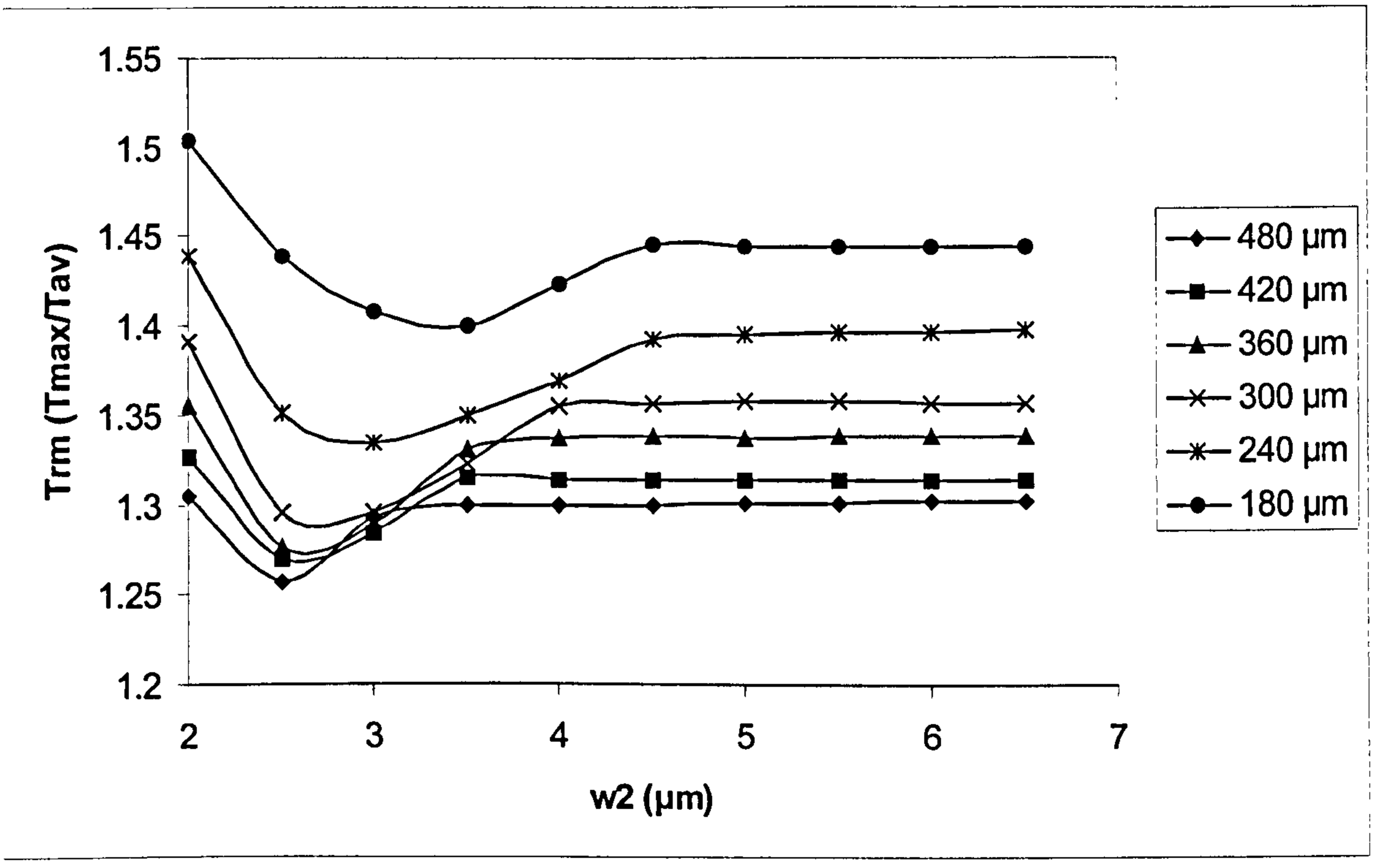

Fig. 3-23 shows the modeling under the following conditions: width of flexure and two ends of the hot beam 2 μm; thickness 2 μm; ratio of length of the flexure to whole length is 17 %; width of cold arm 22 μm; air gap between structure and substrate is 2 μm; ambient air temperature is 20 ° C; input current is same for all actuators, 7 mA.

The effect of changing the value of the driving current has also been investigated. For a fixed value of L and w_1 (240 μm and 2 μm respectively), the minimum value of *Trm* (i.e. Trm_{opt}) was obtained for three different values of actuation currents. Whilst the values of Trm_{opt} are found to be numerically different, the hot beam dimensions at which Trm_{opt} occurred were found to be the same, irrespective of the driving current. This is illustrated in Fig. 3-24. From Fig. 3-24, we can see the important result that the optimised dimensions L_1, L_2 and w_2 are independent of the input current.

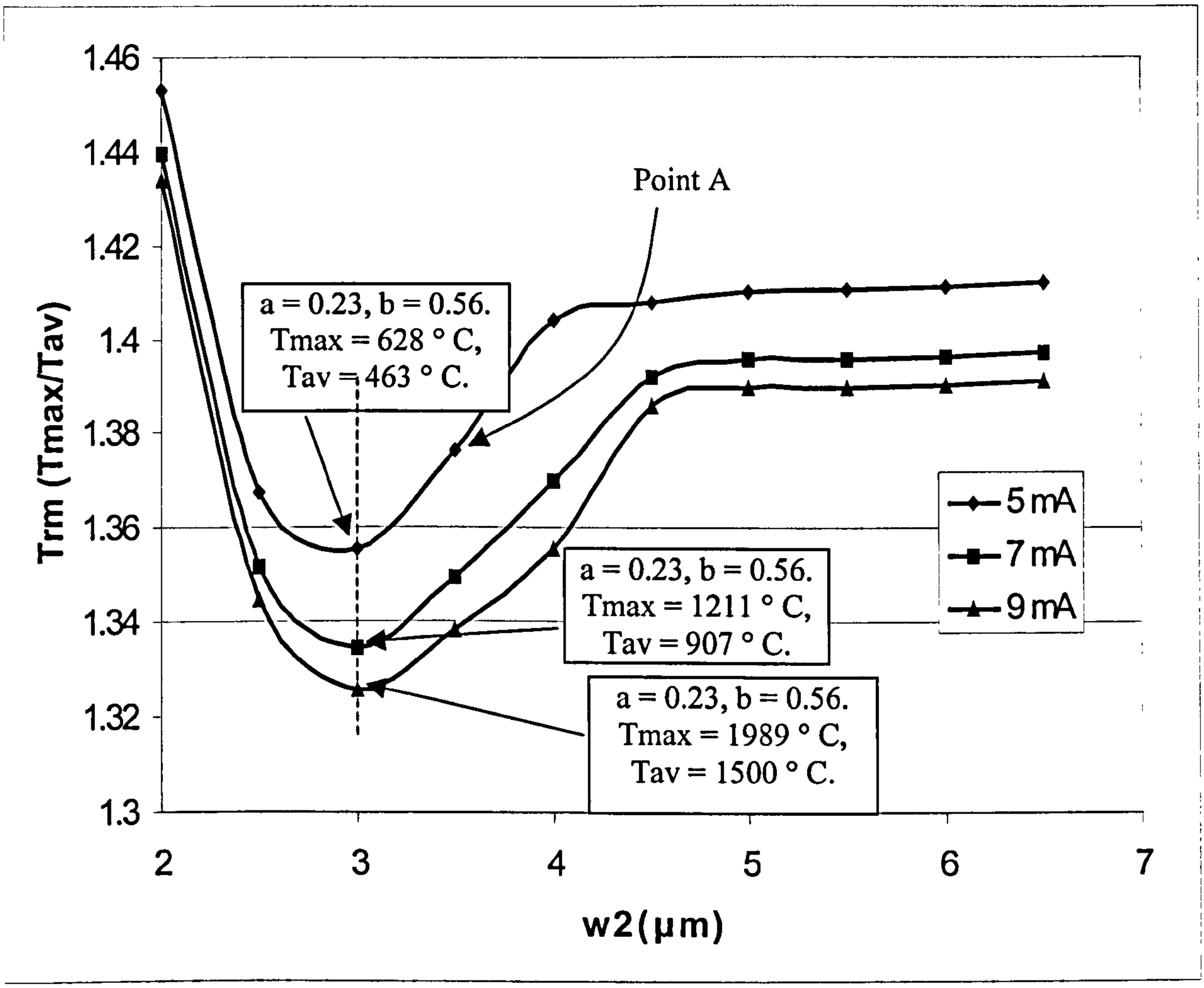

Fig. 3-24 shows the modeling under the following conditions: width of flexure and two ends of the hot beam 2 μm; thickness 2 μm; ratio of length of the flexure to whole length is 17 %; width of cold arm 22 μm; air gap between structure and substrate is 2 μm; ambient air temperature is 20 ° C; total length L is 240 μm, a = L1 / L, b = L2 / L.

3.5.1.3 Temperature distribution

The one-dimensional temperature distribution along the actuator is obtained for both the novel and traditional designs. For the analysis, the devices structures have a thickness of 2 μm as stated earlier. The following dimensions were selected for the traditional design of asymmetric thermal actuator (see Fig. 3-18): w_1 = 2 μm, L_1 = 240 μm; L_2 = 200 μm; width of cold beam is 22 μm; length of flexure beam is

therefore 40 μm. An overall length of 240 μm was selected for the unloaded traditional actuator because this is the longest length at the given cross-section for which the internal force in the hot beam is less than the critical buckling load [89]. In the same reference [89], the flexure length for maximum displacement of an unloaded actuator is calculated to be around 17% of the overall length. This flexure length, 40 μm, has therefore also been selected in this analysis. In the novel design, the hot beam is divided into three sections L_1, L_2 and L_3 and there are two widths to be considered, w_1 and w_2. A total hot beam length of 240 μm is selected, so that the overall length of the novel actuator is the same as the length of the traditional actuator. For the same reason, w_1 is chosen to be 2 μm. The cold beam of the novel structure has the same dimensions as the cold beam of the traditional structure. The parameters w_2, L_1, L_2 and L_3 are selected as follows: Referring to Fig. 3-24, a value of 3.5 μm for w_2 is chosen on the graph relating to the 240 μm length actuator. This is shown as point A on the graph. Although 3.5 μm is not the optimised value of w_2 for a 240 μm length and 2 μm wide hot arm (i. e. w_1), it is still nevertheless a minimum value of the dimensionless parameter *Trm*. The actual optimised value of w_2 is 3 μm but it was decided that for convenience of fabrication, a slightly larger value of w_2 would be helpful in achieving a clear change in width. As explained in last sections, the point A represents values of L_1 and L_2 (and by default L_3) which are then chosen. Fig. 3-25 shows the calculated temperature profile of the actuators of length when w_2 = 3.5 μm. It also shows the traditional actuator temperature distribution (w_2 = 2 μm). Additionally, the temperature profile for arbitrary selected L_1 and L_2 is also shown for comparison. Input current is 5 mA. Table 1 shows the comparison of the absolute calculated temperature value shown in Fig. 3-25. Fig. 3-26 shows how the temperature distribution varied with electric current, for both traditional design and novel design. (Trm = 1.38 at 4 mA and Trm = 1.37 at 5 mA).

Detail program written in Matlab can be found in Appendix G.

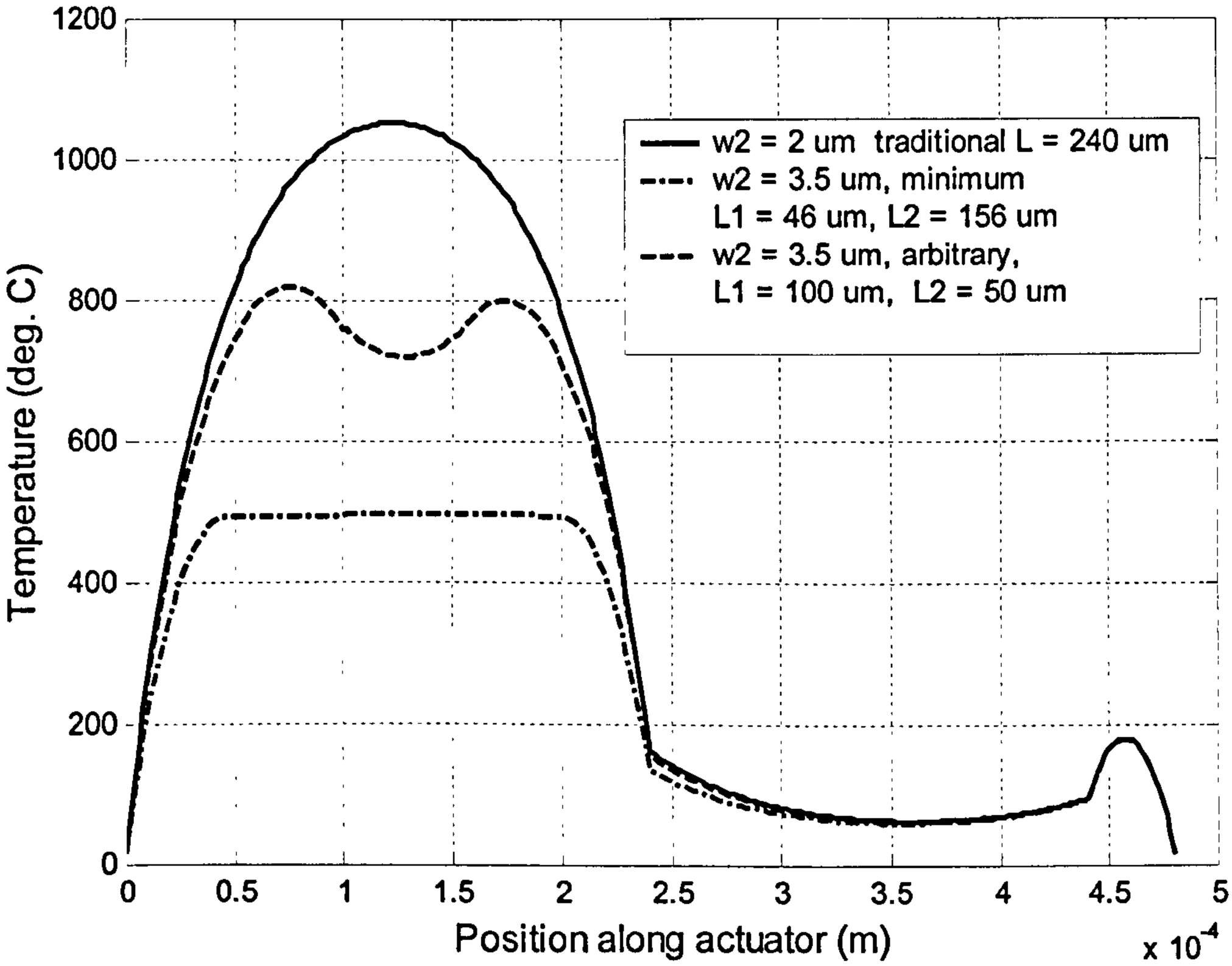

Fig. 3-25. The different temperature profiles representing different structure of actuators are shown in this figure. $w_1 = 2\ \mu m$ and the input current is 5 mA.

Table 1. Comparison of temperature values in different structures (input current = 5 mA).

	Peak temperature (deg. C) of hot arm	Net average temperature (deg. C)	Peak temp / average temp (Trm)
Traditional	1052	724	1.45
$w_2 = 3.5\ \mu m$ (minimised)	494	359	1.37
$w_2 = 3.5\ \mu m$ (arbitrarily selected L1 and L2)	821	580	1.42

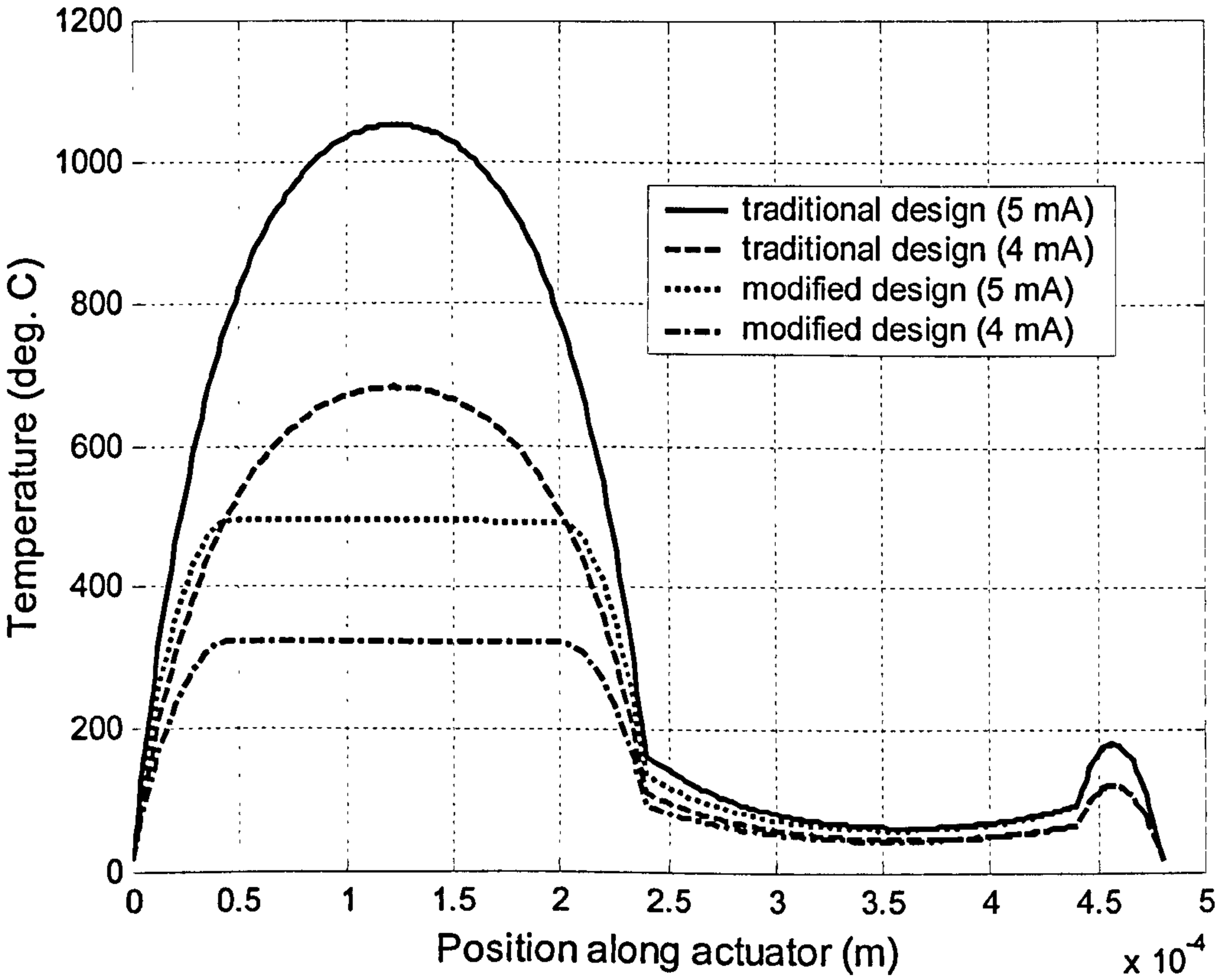

Fig. 3-26. Temperature distribution of the traditional and modified thermal actuator. Traditional: $L_1 = 240\ \mu m$, $w_1 = 2\ \mu m$. Modified: $L_1 = 46\ \mu m$, $L_2 = 156\ \mu m$, $w_2 = 3.5\ \mu m$

Table 2. Theoretical results of traditional and novel actuator

	Peak temperature (deg. C) of hot arm	Net average temperature (deg. C)	Peak temp / average temp (Trm)
Traditional structure (4 mA)	681	461	1.48
Novel structure (4 mA)	324	234	1.38
Traditional structure (5 mA)	1052	724	1.45
Novel structure (5 mA)	494	359	1.37

From this Table, it can be seen that the peak temperature/average temperature ratio of novel structure is lower than that of traditional structure. The trend indicated in Table 2 that has been calculated for the device of Fig. 3-26 is that the traditional structure has a higher deflection than the novel structure so long as it is operated below thermal failure. This observation is based on using the unconstrained expansion of the hot beam as an indicator for deflection. However, as the drive current increases, the traditional design will reach its limit because of thermal failure while the novel design will continue to deflect. The overall outcome expected is that the maximum deflection produced from the novel structure will exceed the maximum deflection from the traditional structure.

3.5.2 Mechanical Analysis

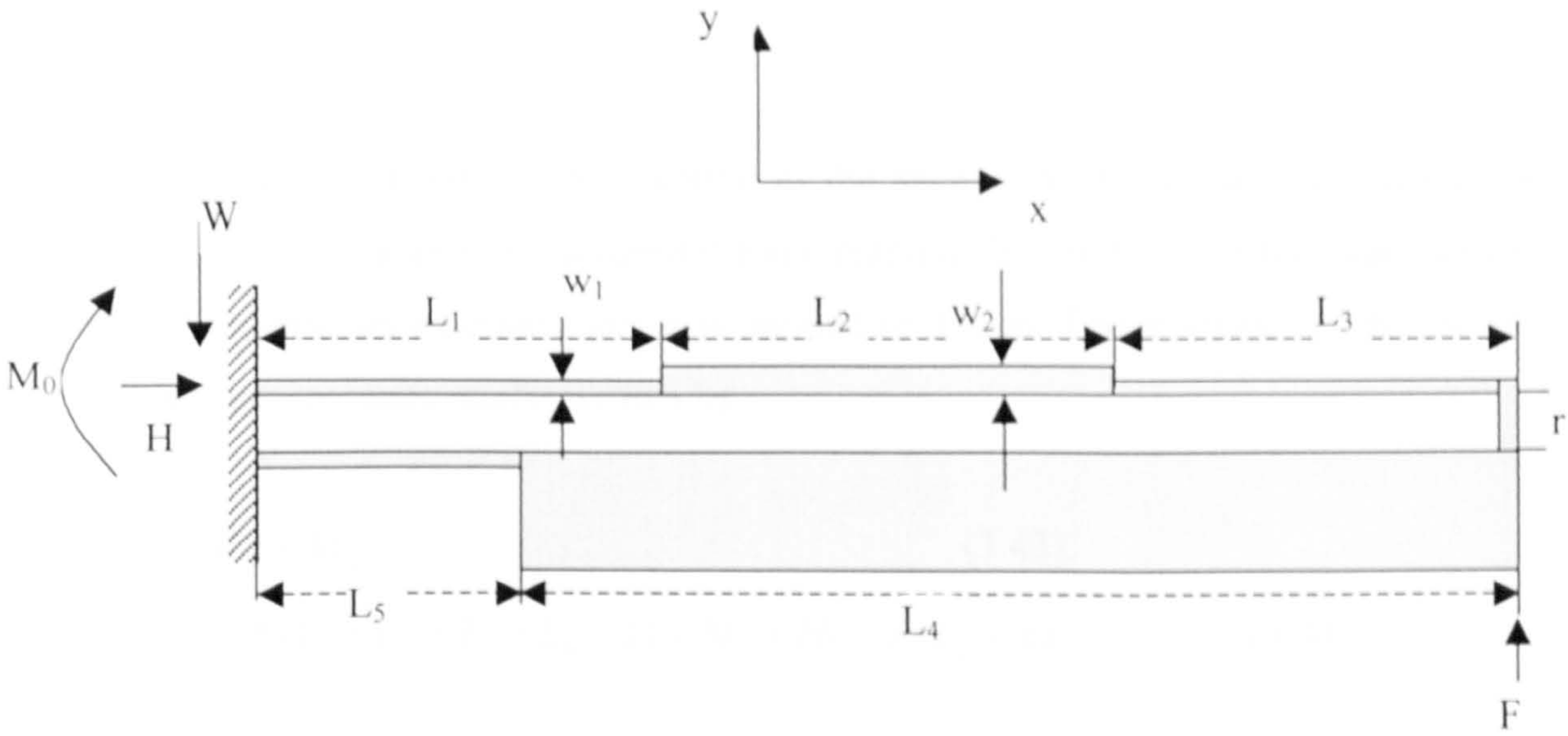

Fig. 3-27. Model for mechanical analysis.

Following the approach of reference [89], the novel asymmetric thermal actuator has five components, which are L_1, L_2, L_3, L_4, and L_5. L_1, L_2, and L_3 are hot beams, which have different widths. L_4 is the cold beam, and L_5 is the flexure beam. Let the joint beam between the hot and cold be r. The ratio of the flexure length to hot beam length is a, so

$$a = \frac{L_5}{L_1 + L_2 + L_3}. \qquad (3.39)$$

Assuming the ratio of the first section length of the hot beam to the whole hot beam is b, so

$$b = \frac{L_1}{L_1 + L_2 + L_3}, \qquad (3.40)$$

and the ratio of the second length of the hot beam to the full hot beam is c, so

$$c = \frac{L_2}{L_1 + L_2 + L_3}. \qquad (3.41)$$

So the equations for L_4 and L_5 are

$$L_4 = (1-a)(L_1 + L_2 + L_3) \qquad L_5 = a(L_1 + L_2 + L_3) \qquad (3.42)$$

The x axis is defined by unfolding the actuator and defining each beam separately: $0<x_1<L_1+L_2+L_3$, $0<x_2<L_4$, $0<x_3<L_5$. The energy method can be used to obtain the deflection.

From mechanical theory, the reaction in the anchor can be divided to three parts: vertical force reaction W, horizontal force reaction H, and rotation reaction moment M_0. Assuming an external force F is applied to the tip. The moments in the hot and flexure components can be written by

$$M_h = Wx + M_0 \tag{3.43}$$

$$M_f = -W(L_1 + L_2 + L_3 - L_4 - x) + M_0 + Hr - F(L_2 + x) \tag{3.44}$$

The Castigliano's theorem shows that the derivative of the strain energy with respect to the load is equal to the deflection corresponding to the load. The strain energy stored in a beam in terms of the applied moments M is

$$U = \int \frac{M^2}{2EI} dx \tag{3.45}$$

here, M is the moment, E is the Young's Modulus, I is the moment of inertia. According to Castigliano's theorem, the deflection of the beam can be expressed

$$\delta_i = \frac{\partial}{\partial P_i} \int \frac{M^2 dx}{2EI} \tag{3.46}$$

In the thermal actuator system, three orientations of the deflection have been considered, which are horizontal, vertical and rotation. Since there is no horizontal or vertical deflection or rotation in at the hot beam anchor, three equations can be written as:

$$\int_0^{L_1}\frac{H}{A_1E}dx+\int_{L_1}^{L_1+L_2}\frac{H}{A_2E}dx+\int_{L_1+L_2}^{L_1+L_2+L_3}\frac{H}{A_1E}dx+\int_0^{L_5}\frac{H}{A_1E}dx+\frac{\partial(\int_0^{L_5}\frac{M_f(r)}{I_5E}dx)}{\partial H}$$
$$=\alpha\Delta T(L_1+L_2+L_3)$$

.....(3.47)

$$\frac{\partial\left(\int_0^{L_1}\frac{M_h^2}{2EI_1}dx+\int_{L_1}^{L_1+L_2}\frac{M_h^2}{2EI_2}dx+\int_{L_1+L_2}^{L_1+L_2+L_3}\frac{M_h^2}{2EI_3}dx\right)}{\partial W}$$
$$+\frac{\partial\left(\int_0^{L_5}\frac{M_f^2}{2EI_5}dx\right)}{\partial W}=0$$

.....(3.48)

$$\frac{\partial\int_0^{L_1}\frac{M_h^2}{2EI_1}dx}{\partial M_0}+\frac{\partial\int_{L_1}^{L_1+L_2}\frac{M_h^2}{2EI_2}dx}{\partial M_0}+\frac{\partial\int_{L_1+L_2}^{L_1+L_2+L_3}\frac{M_h^2}{2EI_3}dx}{\partial M_0}+\frac{\partial\int_0^{L_5}\frac{M_f^2}{2EI_5}dx}{\partial M_0}=0$$

.....(3.49)

E is the Young's modulus for polysilicon (169 GPa); A_i and I_i are cross-section areas and moments of inertias, respectively. Equation (3.47) calculates the horizontal deflection contributions. Equation (3.48) calculates the vertical deflection contributions. Equation (3.49) calculates the rotation contributions.

These three equations are solved to get the W, H, and M_0. These values are substituted into Eq. (3.44) to obtain M_f. The deflection dy is

$$dy = \int_0^{L_5} \frac{M_f (\partial M_f / \partial F)}{I_5 E} dx, \qquad (3.50)$$

In the Section 3.5.1, the optimized dimensions of the hot beam has been investigated. The optimal lengths of L_1, L_2, and L_3 are 46 um, 114 um, and 40 um respectively. Assume the full hot beam length is L. So the ratios b and c are designed to be 0.23 and 0.57. Therefore, $L_1 = 0.23\ L$, $L_2 = 0.57\ L$, $L_3 = (1\text{-}0.23\text{-}0.57)$ and $L = 0.2\ L$. Also according the optimization of section 3.5.1, $I_1 = I_3 = I_5$.

Fig. 3-28. shows the theoretical result of deflections of both novel and traditional asymmetric thermal actuators.

Note: When peak temperature exceeds around 525 deg. C (around half annealing temperature of polysillicon), the plastic deformation occurs, so the deflection of the actuator becomes very complicated; and we *cannot* apply this method to calculate the deflection. Here, it is assumed that both novel and traditional thermal actuators stop bending at this condition. In fact, experimental results show that this assumption is correct (shown in Section 3.5.3).

Note: In the field of MEMS, the larger deflection of actuator is required. This modification to the traditional thermal actuator is in terms of obtaining maximum deflection, not in terms of sensitivity (ie deflection/power).

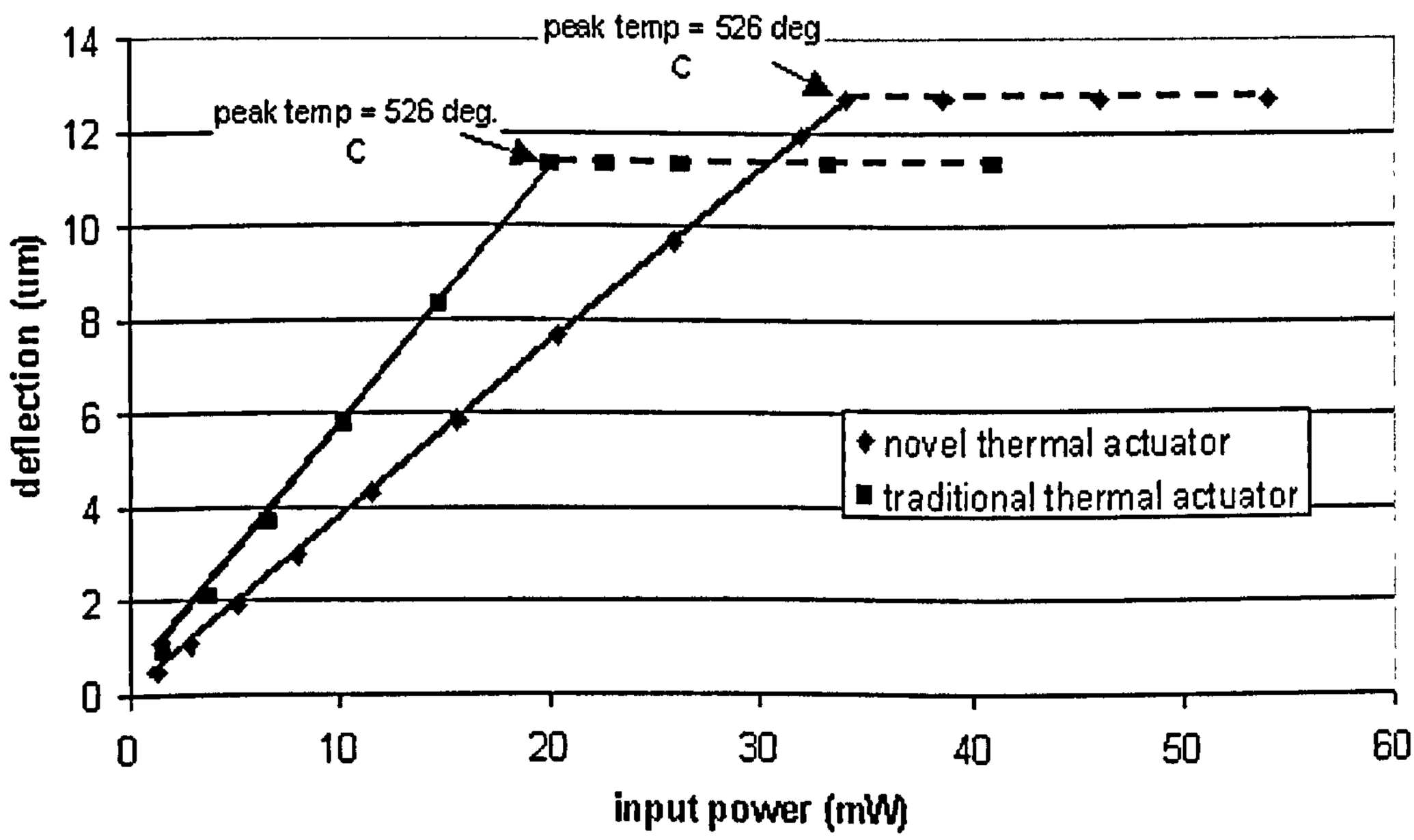

Fig. 3-28. Theoretical result of deflection related to the input power.

3.5.3 Experimental results

The devices analyzed above have been designed, and fabricated using the PolyMUMPs foundry process (PolyMUMPs Run 52). Layouts are shown in Appendix D. Both hot and cold beams are defined in *Poly1* layer. The traditional thermal actuator and novel thermal actuator were designed for the purpose of comparison, as shown in Fig. 3-29 (a) and 3-29 (b).

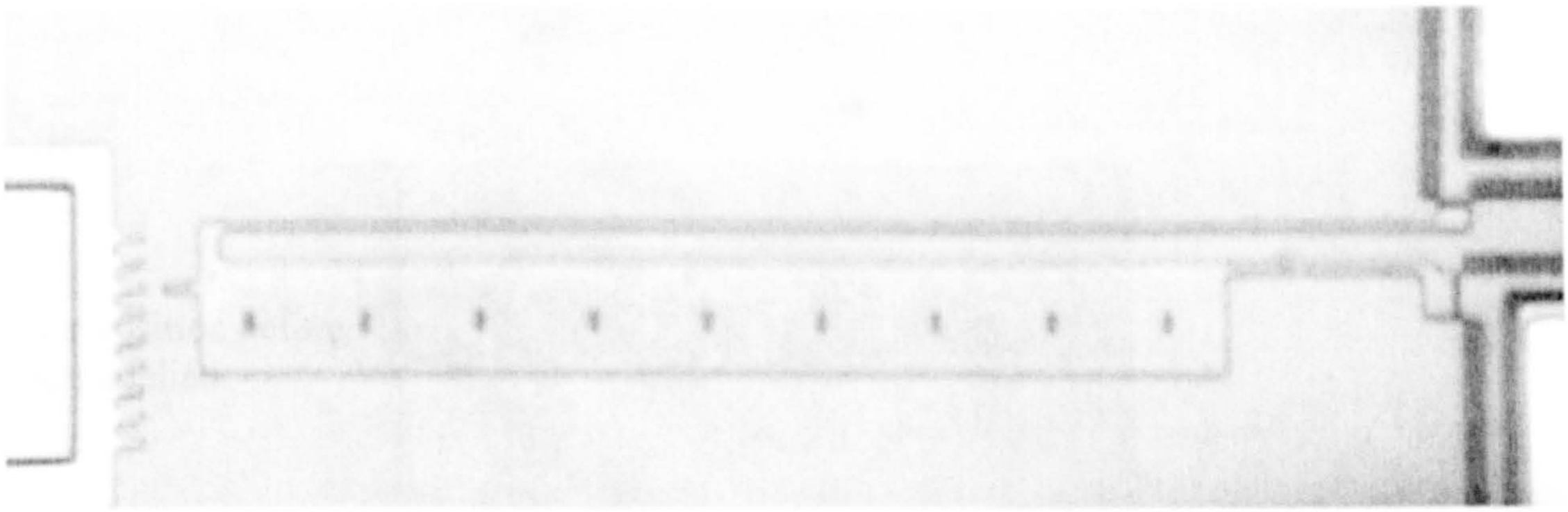

Fig. 3-29 (a). Microphotograph of traditional two-beam asymmetric thermal actuator.

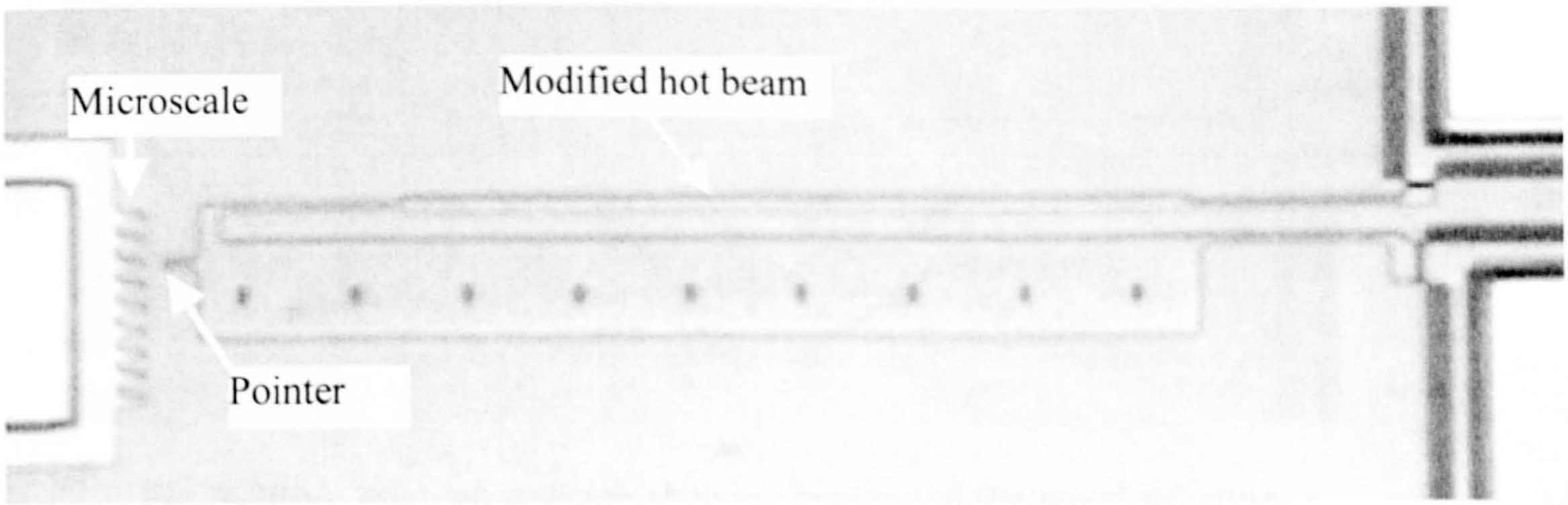

Fig. 3-29 (b). Microphotograph of novel design of asymmetric thermal actuator.

DC currents from 0 mA to 5.5 mA have been applied to both structures separately. Micro scales with 5 μm graduations and a pointer at the end of the devices are used to measure the deflections. At low current up to 4 mA, the traditional design does indeed produce a greater deflection than the new design. Fig 3-30(a) and 3-30(b) show the photographs of the deflected actuators at 5 mA; Fig 3-30(a) is the modified structure, Fig 3-30(b) is the traditional structure. Note the thermal induced distortion of the hot arm in Fig 3-30(b) which has reached maximum deflection.

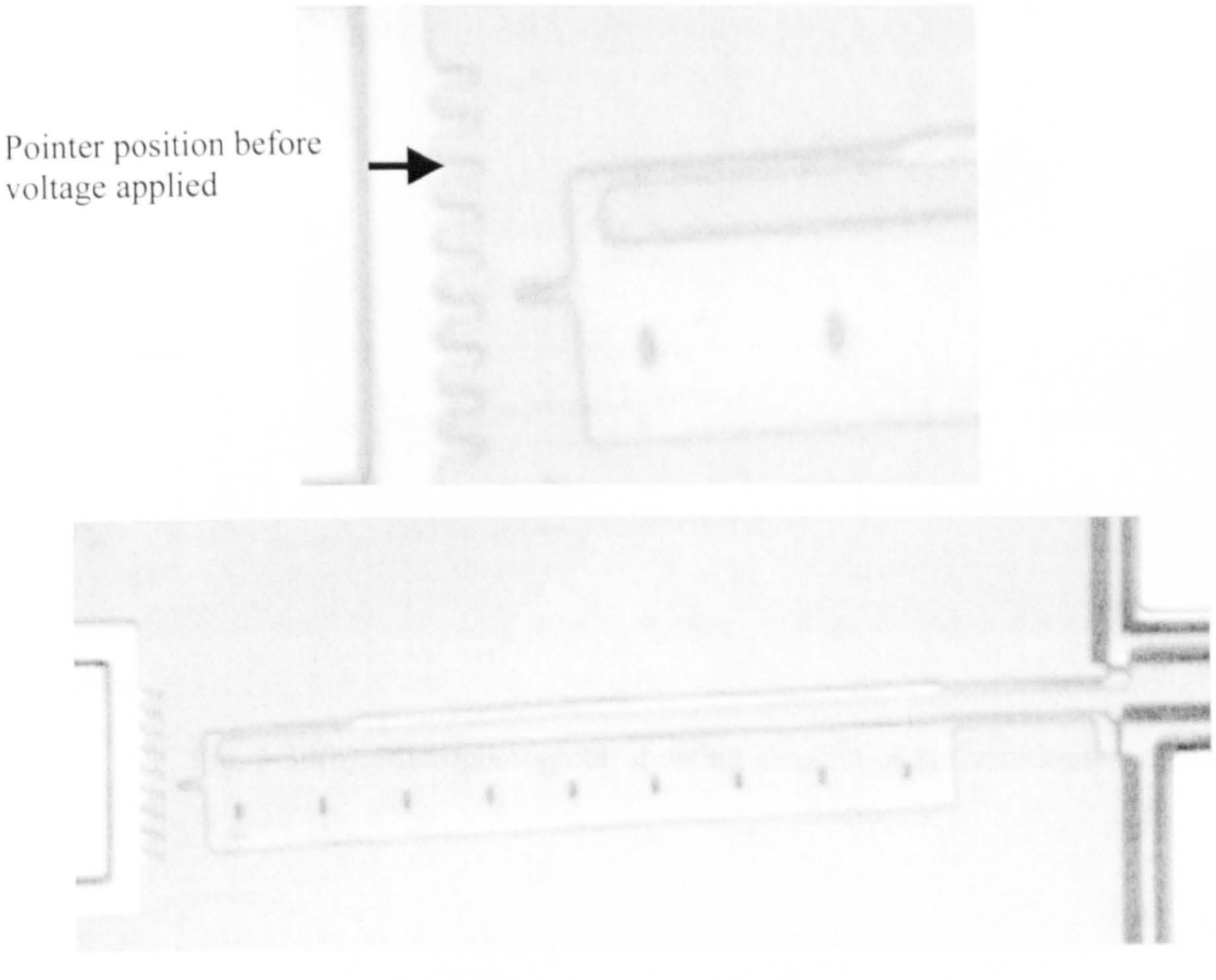

Fig. 3-30(a). Microphotograph showing bending of the novel structure.

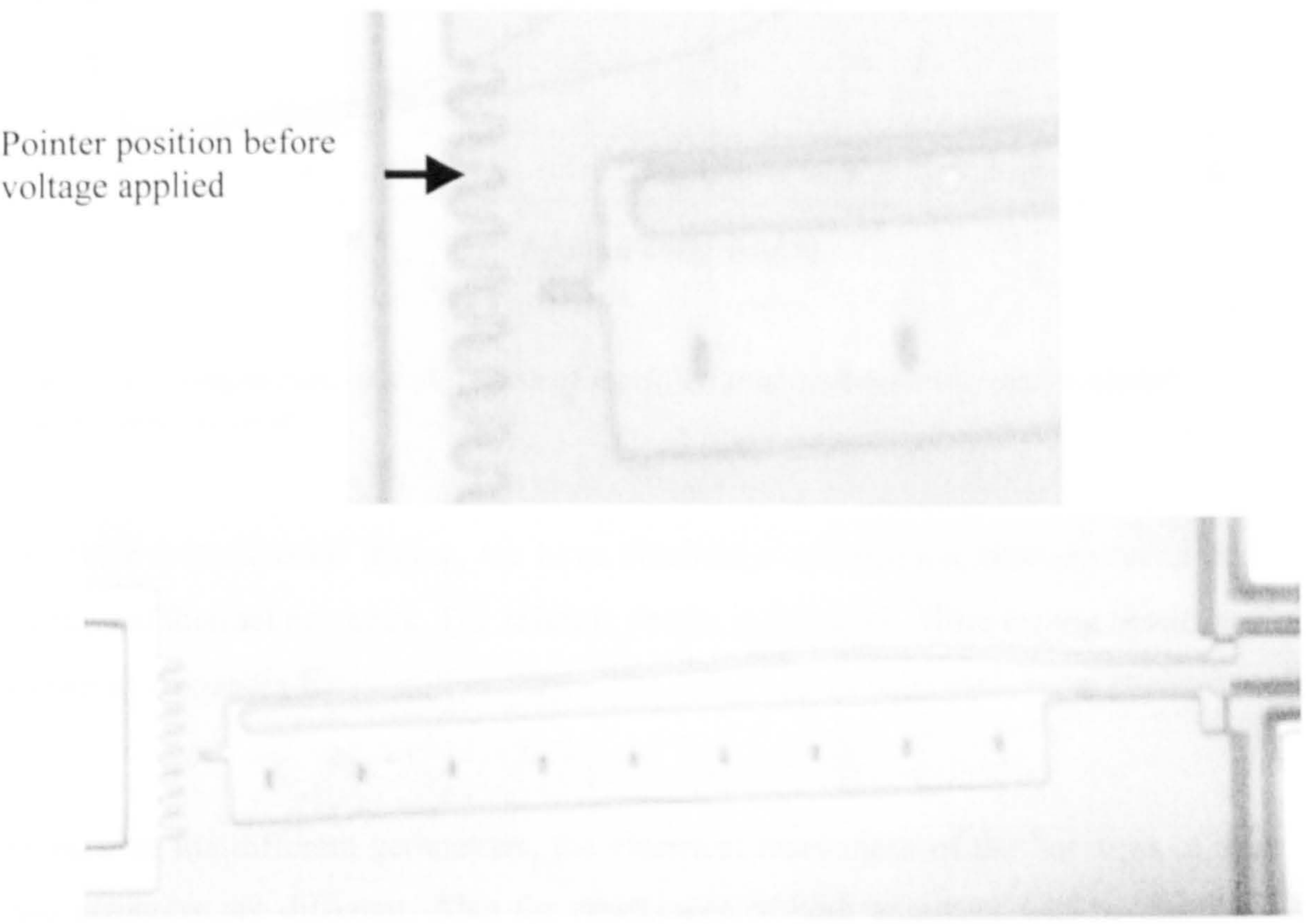

Fig. 3-30(b). Microphotograph showing bending of the traditional structure.

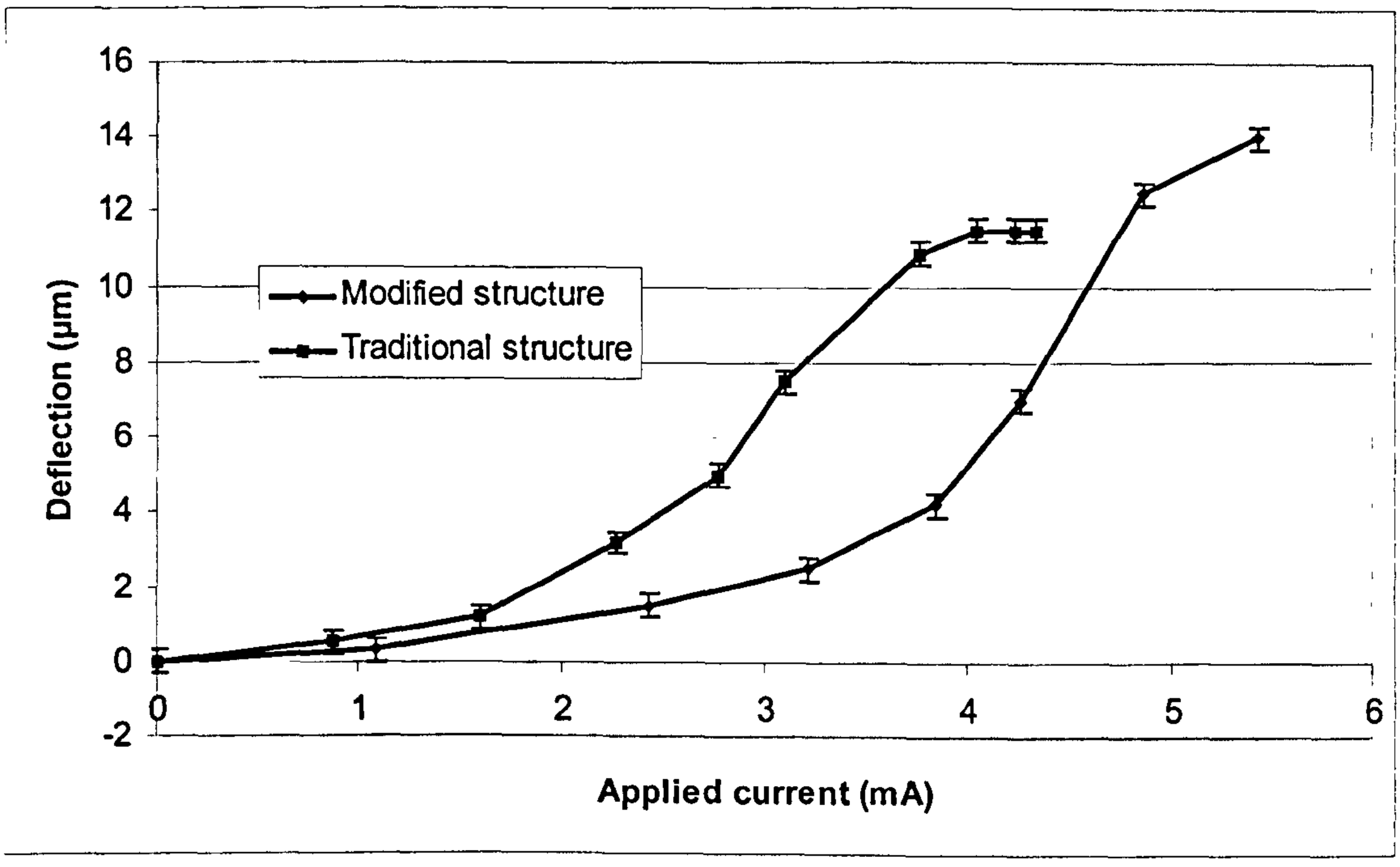

Fig. 3-31. Comparison of deflections of modified and ordinary thermal actuator under same currents.

From the experimental testing, we have obtained a comparison between novel and traditional thermal actuators. The result is shown in Fig 3-31. More testing results are shown in Appendix E.

In view of the different geometries, the electrical resistances of the hot arms of the two actuators are different. Also the resistances of both actuators will be changed while increasing the temperature. Experiments were conducted for the purpose of obtaining the relationship between deflection and input power by measuring the current and voltage in the circuit. Fig 3-32 shows the relationship between the deflection and input power of both structures. The error bars shown in Figures 3-31 and 3-32 depend on the image magnification and detector resolution which determine how accurately the spring displacement is measured. Displacements measured using our imaging equipment (microscope-coupled camera) have an uncertainty of ±0.3 μm. Error bars of this magnitude are shown in Figures 3-31 and 3-32. In Fig. 3-33, the comparison between experiment and theory has been made, the experimental result shown in the graph is close to the theoretical calculation.

From the result, we can see that when higher power is applied to the traditional structure, the deflection reaches saturation.

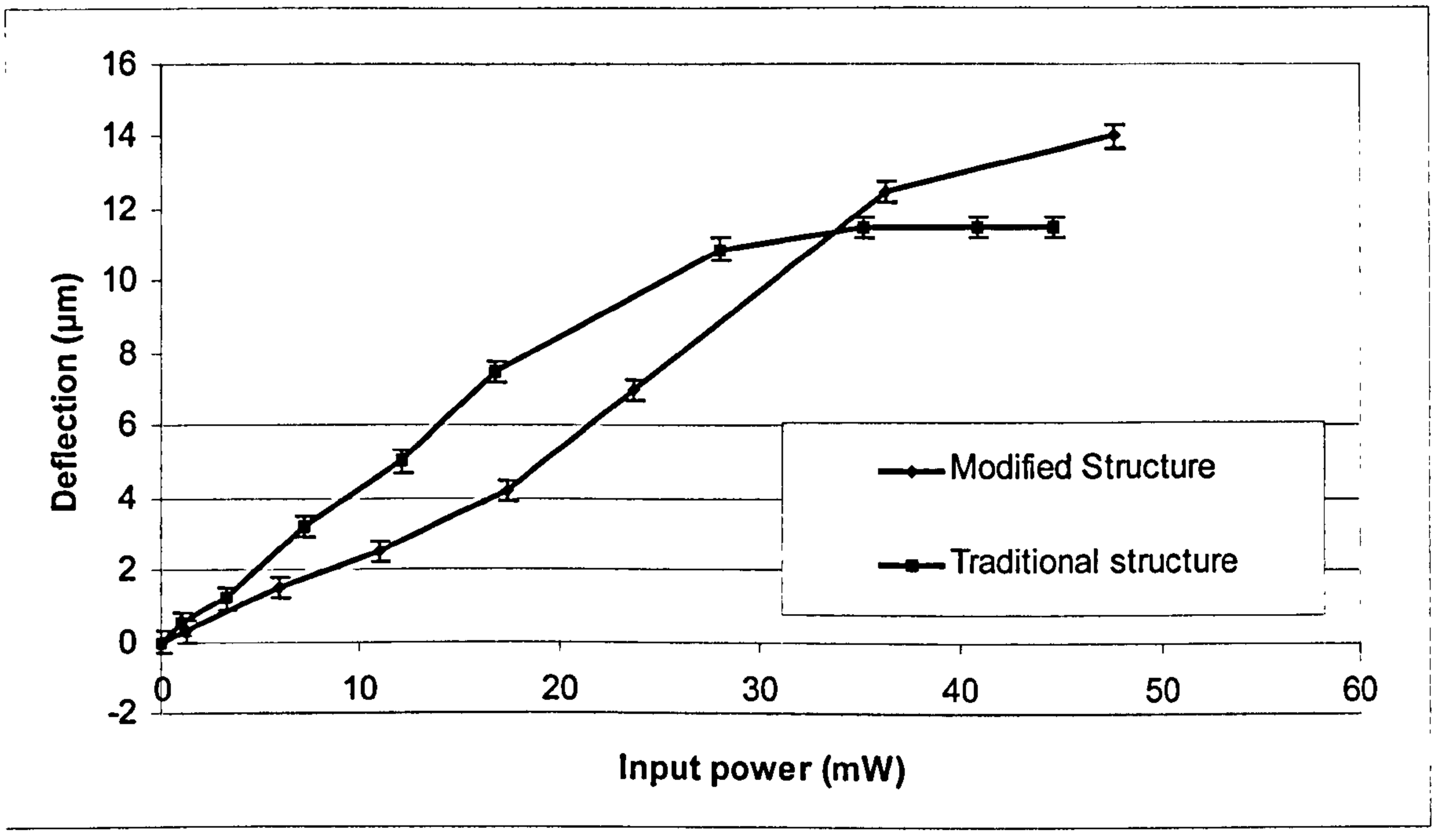

Fig. 3-32. The relationship between input power and deflection of both structures.

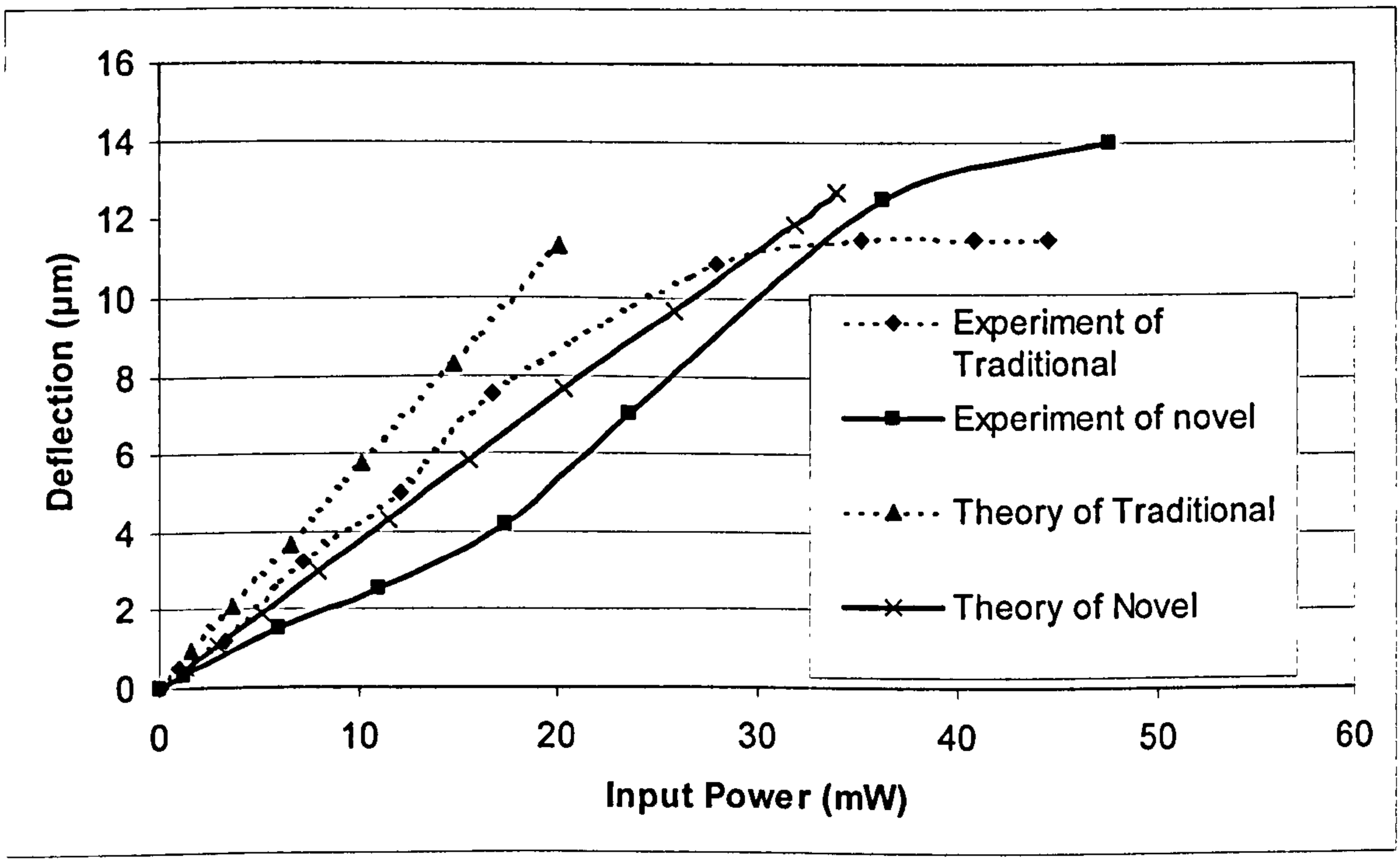

Fig. 3-33, Comparison between experiment and theory.

3.6 Conclusion

In this chapter, three types of electro-thermal actuators have been theoretically analyzed for both thermal and mechanical behaviour. Heat transfer analysis was performed using simple conduction theory.

An innovative design of the asymmetric thermal microactuator with a non-uniform hot beam has been presented. The design yields higher deflection of the actuator. Both theoretical analysis and experimental testing have been undertaken to verify the idea. The results show that the novel structure has a "better" temperature profile than the traditional one in terms of immunity to the thermal damage. In practice the novel structure has been shown to deflect more at high power without being damaged. The comparison of theoretical and experimental results is shown in Fig. 3-33. The theoretical results are valid until the calculated peak temperature reaches 526 deg. C in both novel and traditional structures. In the effective range, the theoretical deflections are always higher than the experimental deflections, that is because the assumption of pure conduction (conduction through polysilicon and conduction through air gap) was taken, the calculated temperatures are higher than the experimental temperatures.

Chapter 4

Study of Scratch Drive Actuator

4.1 Introduction

The SDA is an important element for many types of silicon-based micro-electro-mechanical systems (MEMS). Many other microactuators have been proposed and studied in order to realize moveable structures. Those that are commonly used in silicon MEMS technology are: comb drive actuators [30], operated by the electrostatic force between a pair of interdigitated moveable and fixed combs; linear microvibromotors [92], which uses impact actuation to obtain large motion from small-displacement resonant structures such as comb drive actuators; stepper motors [93], which can achieve large force and large displacement; micro-engines [94], fabricated by Sandia National Laboratory, operated by orthogonal pistons connected to a crank shaft, in a similar way to an internal combustion engine; and electro-thermal actuators [36] that provide a large force, but a very small deflection. The SDA possesses several features that makes it well-suited to creating motion in MEMS and particularly micro-opto-electro-mechanical systems (MOEMS): it produces linear motion directly (c.f. comb-drives and microvibromotors), has a potentially large range of travel (over several hundred microns) with relatively high force and with very fine control of position and step size (of order 10 nm, which is important for optical applications) [19], and can operate over a wide range of speeds. It has been used, for example in driving optical devices [95], and 3-D self-assembling [96].

The SDA described here is fabricated by surface micromachining, a process in which structural layers and sacrificial layers are sequentially deposited and etched on a silicon substrate. During the different fabrication runs it is possible that the deposition and etching might vary slightly from wafer to wafer. Consequently, it is important to compare the properties of devices, which are made to a common design

but fabricated on different wafers or different parts of the same wafer. Such a comparison is one of the purposes of this chapter. Linear SDA test structures have been designed for our experimental study because many SDA applications, e.g. micro-positioning or micro-assembly, are based on a linear configuration. The SDAs for this study were fabricated by PolyMUMPs [90]. Two- and three-stage linear SDAs were fabricated and tested using a high-speed camera. Measurements have been conducted to obtain the velocity and step size for different SDAs under a range of driving voltages and frequencies. Long linear motion SDAs have also been fabricated and tested to investigate their characteristics during travel.

The MEMS designer requires models of the SDA in order to incorporate these devices into their microsystem applications. A further objective of this chapter is to develop models for the SDA in its working state, building upon previous work reported in the literature. A suspended SDA plate actuated by electrostatic force is analyzed. A mathematical model is established based on electrostatic coupled mechanical theory. Two SDA modes have been analysed namely the "non-contact" mode and the "contact" mode. The non-contact mode allows the designer to establish the threshold voltage after which the actuator plate snaps down. For the contact mode, the relationship between applied voltage and contact distance is first obtained. Subsequently, the geometrical model of a bending plate is established to determine the relationship between contact distance and step size. These two results can then be combined to obtain the value of actuator step size versus applied voltage. Finally, coupled-field electro-mechanical simulation has been performed using the commercially available software tool - IntelliSuite. The dimensions of the scratch drive actuator used for the analysis match the dimensions of the experimental SDAs that have been fabricated by PolyMUMPs. All the SDA material properties are obtained from data provided by the manufacturers of our actuators. On the experimental front, a Veeco NT1000 surface profiling tool has been used to measure the bending of the SDA plate. The results obtained from modeling, simulation and experimentation are compared.

Different devices have different actuation requirement and the forces that they need to operate are also different. The calculation of a microactuator's force is therefore very important. Certain microactuators use microsprings to pull them back to the original position by the restoration force of the spring, because these actuators are single direction actuators. An example of this is the scratch drive actuator [19]. Microsprings can be used to measure the force of microactuators by measuring the displacement of the spring, providing the spring constant is known. Therefore, it is important to develop the model for such a spring. In terms of modeling of these springs the spring constant can be controlled by adjusting the dimensions and geometry of the springs. Here, two types of springs have been investigated, namely the zig-zag spring and the box spring. Several 'Z' shape micromechanical beams connected to each other form the planar zig-zag. Box springs have several planar rectangular frames joined by small bars. These two types of springs are analyzed assuming the spring has been fabricated by a polysilicon surface micromachining process. All the material properties of the polysilicon used in this analysis apply to the PolyMUMPs process [90].

4.2 Principle of operation

The SDA consists of three parts: plate, bushing, and substrate electrode, as shown conceptually in Fig. 4-1. The principle of operation has previously been described elsewhere [97]. When a voltage is applied across the capacitor-like structure formed by the plate and substrate, the plate experiences an electrostatic force that pulls it down towards the substrate. The warping of the plate causes the bushing to tilt, thereby sliding forwards the edge in contact with the substrate. When the voltage is removed, the plate and bushing return to their horizontal position, but translated forward a small distance. By driving the device with a periodic voltage the SDA can

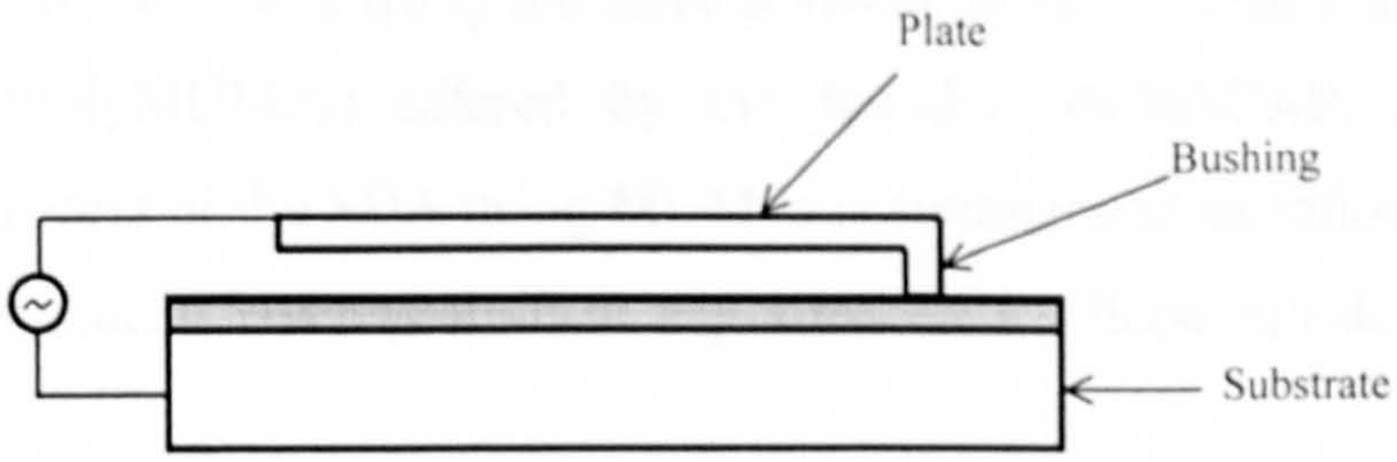

Fig. 4-1: Schematic of single-plate SDA.

advance across the substrate at a velocity and step size determined by the frequency and amplitude of the driving signal.

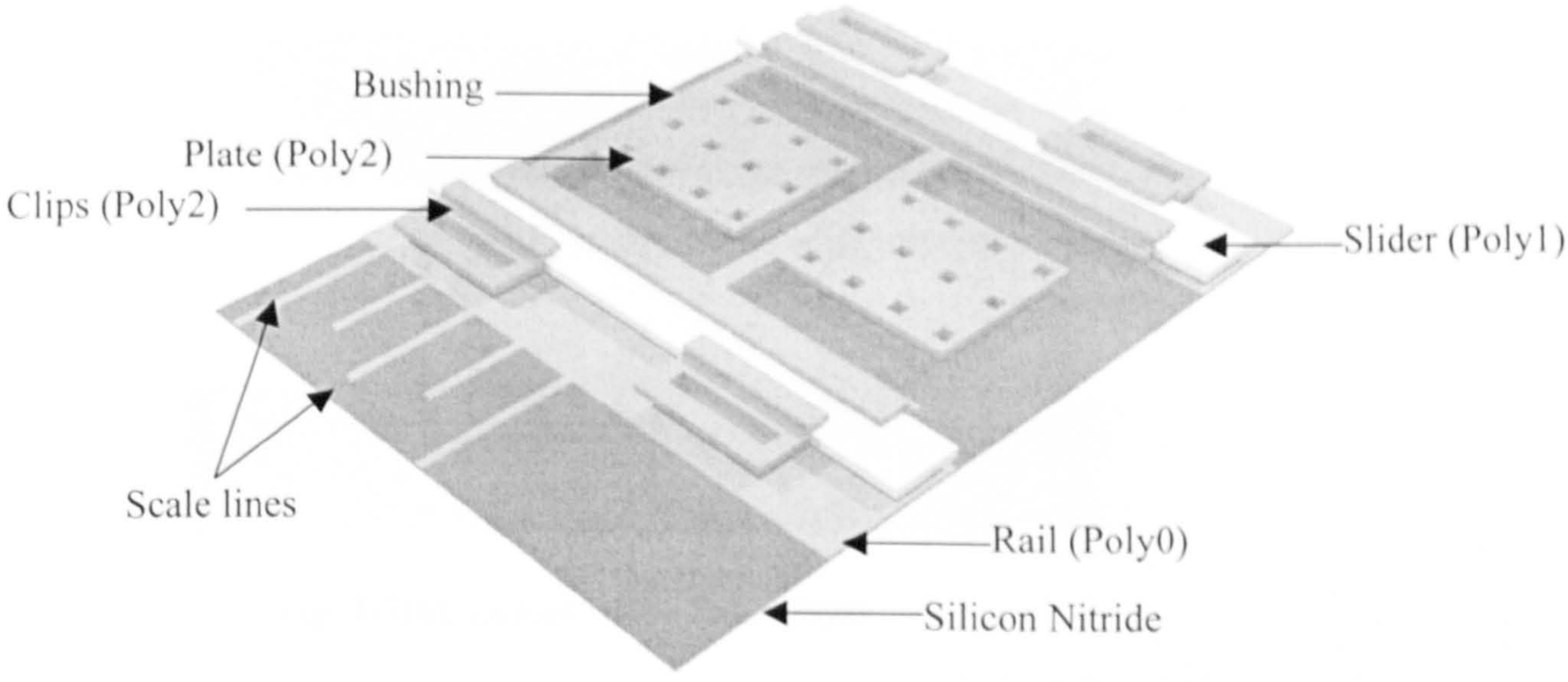

Fig. 4-2: 3-D SDA model generated from layout.

4.3 Design and Fabrication

The 3-D model of our SDA design is shown in Fig. 4-2. In addition to the three parts of the SDA shown in Fig. 4-1, there is a rail and a slider either side of the SDA that guides the device, and also provide an electrical connection to the plates, and clips loosely restrain the device on the surface of the substrate.

The SDAs were fabricated using the three polysilicon layer surface-micromachining technology (PolyMUMPs) offered by the foundry MEMSCAP, Inc. [90] The fabrication process of the SDA using MUMPs is summarized as follows. First, a 0.5 μm-thick polysilicon layer (Poly0) is deposited on a silicon nitride-coated silicon

substrate. This layer, Poly0, is used for electrical connection (rail). Fig. 4-3 (a) shows the Poly0 layout.

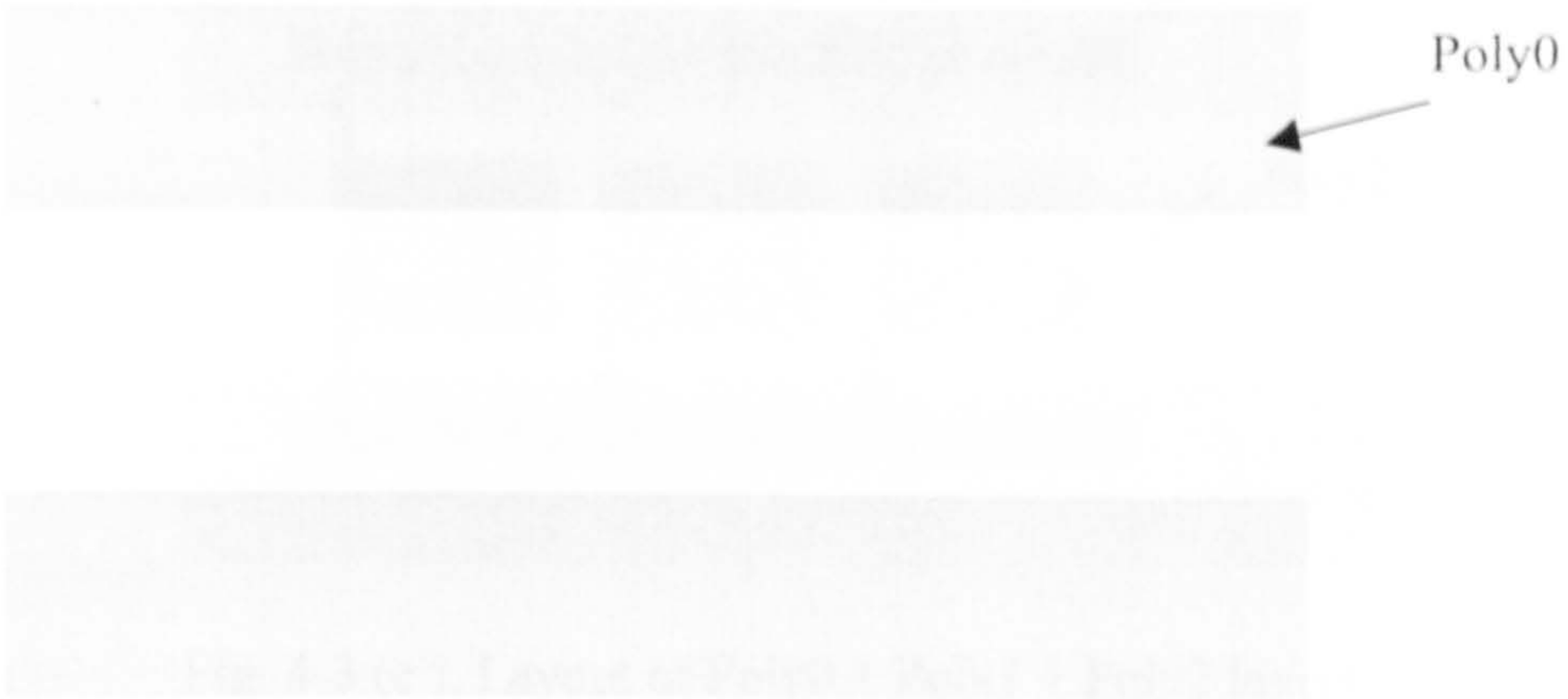

Fig. 4-3(a), Layout of the Poly0 layer.

After the deposition of a sacrificial phosphosilicate glass (Ox1), the first structural polysilicon layer (Poly1) is deposited. The sliders of the SDA are defined in the Poly1 layer. Fig. 4-3(b) shows the layout of the Poly0 + Poly1 layers.

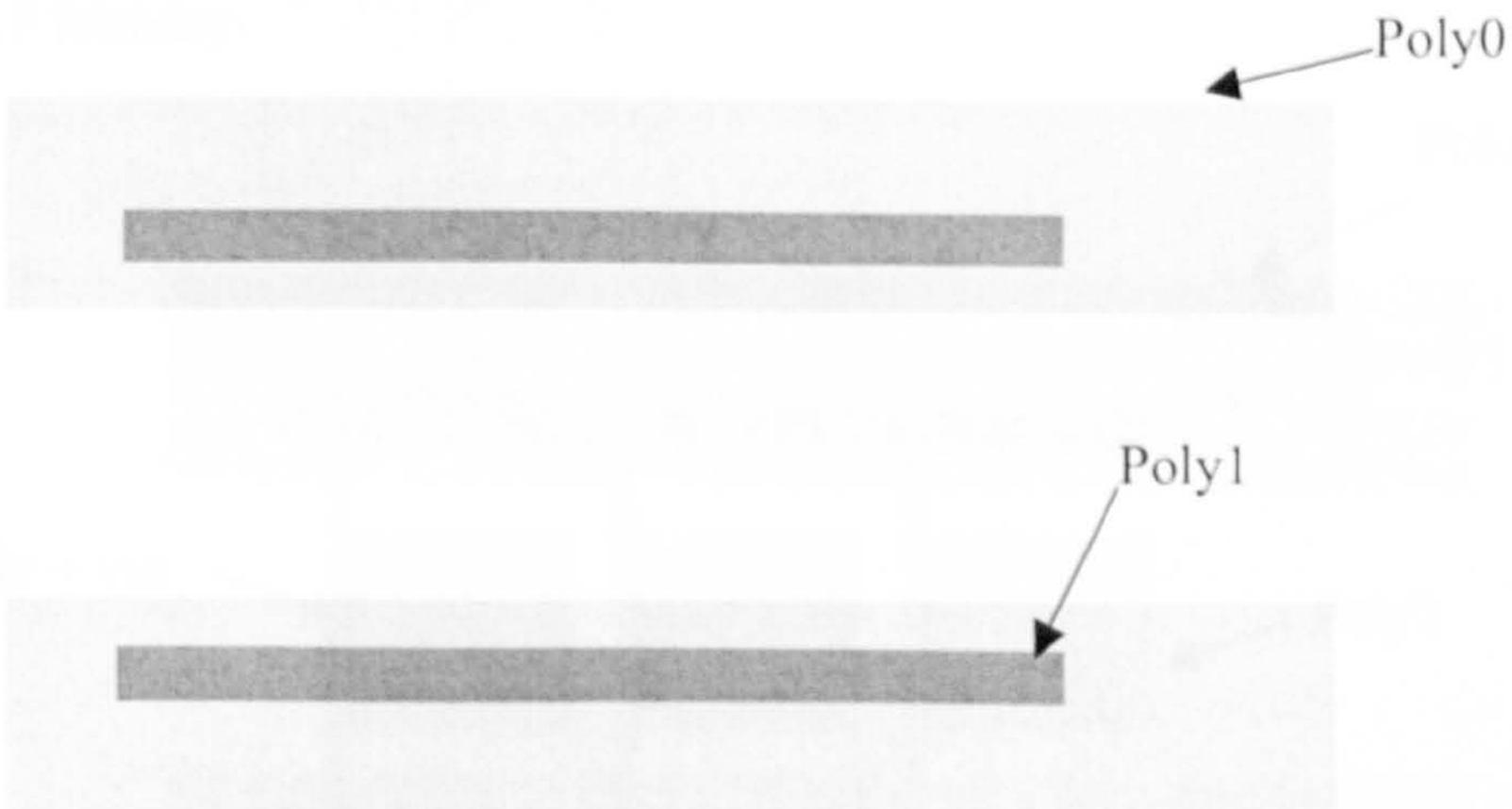

Fig. 4-3(b), Layout of the Poly0 + Poly1 layer.

The second phosphosilicate glass layer (Ox2) is then deposited, and following this step, the second structural polysilicon layer (Poly2) is deposited. The SDA plate is defined in the Poly2 layer. Fig. 4-3 (c) shows the layout of Poly0 + Poly1 + Poly2 layers.

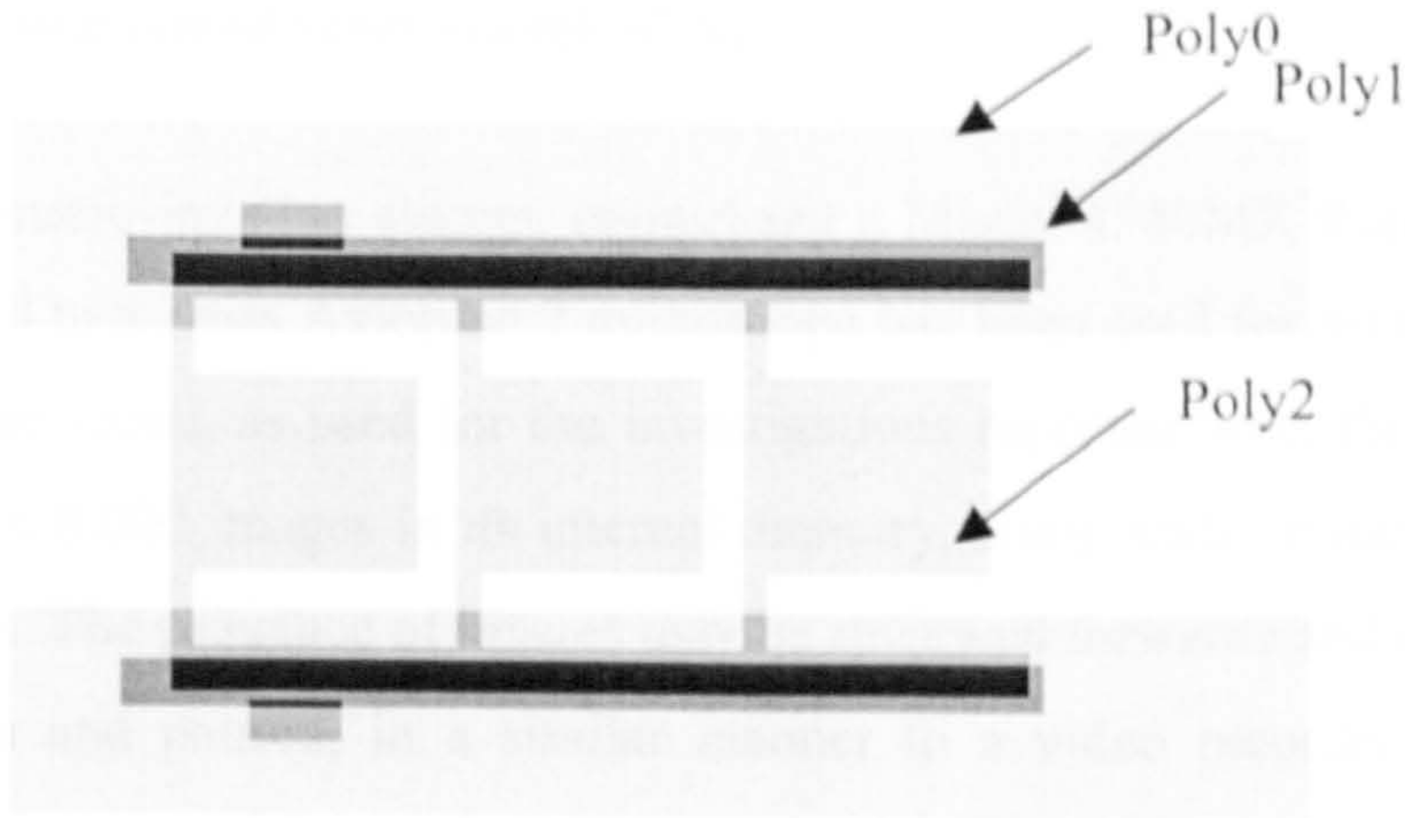

Fig. 4-3 (c), Layout of Poly0 + Poly1 + Poly2 layers.

The bushing is fabricated in the "dimple plus via" mask layer, which is shown in Fig. 4-3 (d). As a consequence of using the standard PolyMUMPs process both the bushing and the plate are approximately 1.5 μm thick. Post-fabrication HF release and supercritical CO_2 drying (to minimize stiction) were carried out by the MEMSCAP foundry.

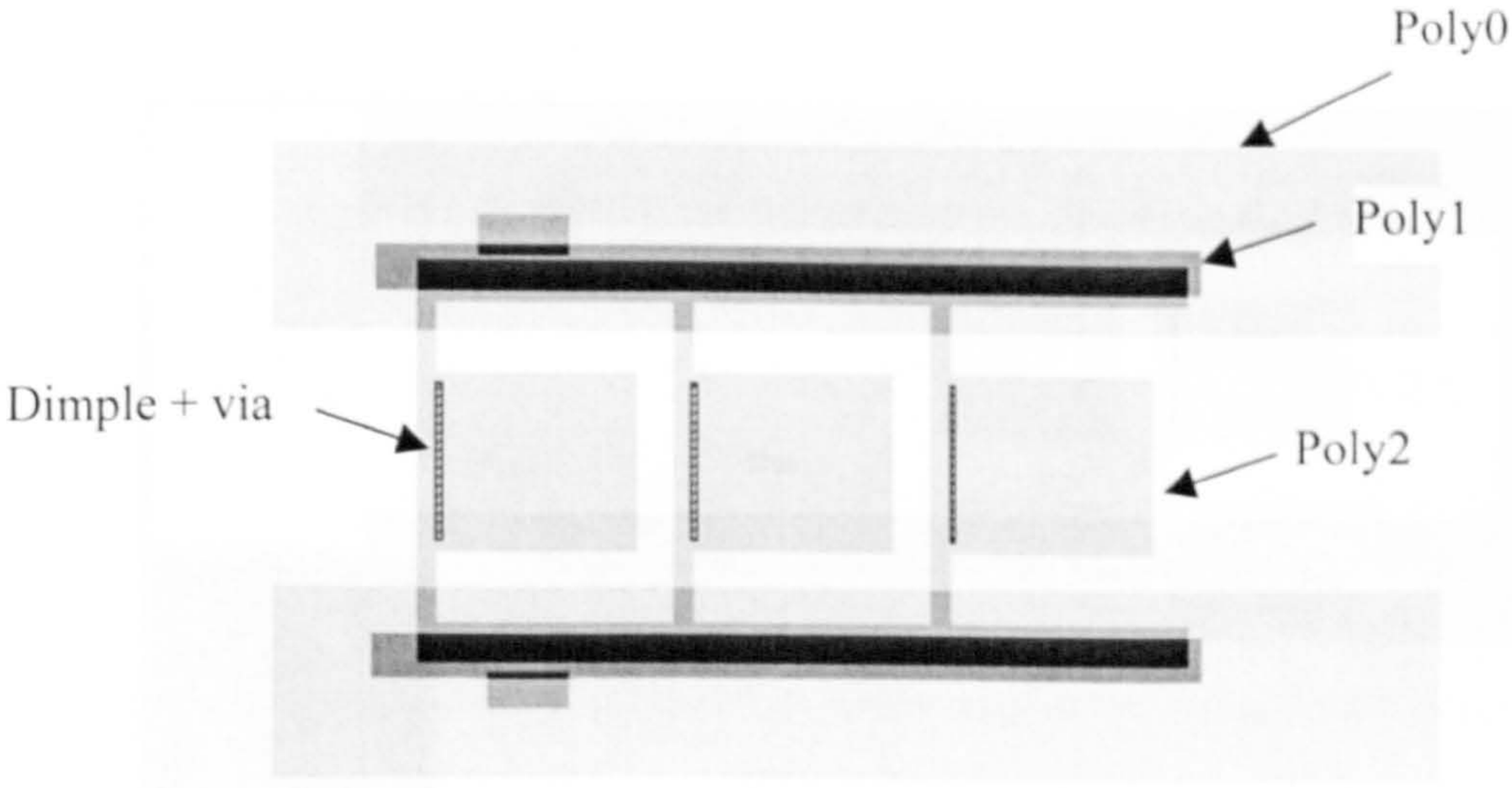

Fig. 4-3 (d), final device layout.

4.4 Motion analysis through short and long travel;

4.4.1. Motion analysis of short-travel SDAs

A high-speed micro-imaging system, comprising a Model 4540MX Roper Scientific camera coupled to a Zeiss Axioplan 2 microscope has been used for motion analysis. In its full-frame mode, as used for the investigations reported here, the camera can store more than 8,000 images in its internal memory, along with timing information for each frame. The sequence of images may be reviewed forwards and backwards at various speeds and paused, in a similar manner to a video recorder. An initial impression of features of the motion can be gained before the images are transferred to a computer for analysis in a software package, such as Adobe PhotoShop, to obtain measurements of displacement of the SDA. The displacement and time information is then applied to determine the velocity of the SDA.

Short-travel actuators with two mechanically and electrically connected SDAs (2-stage SDAs) were fabricated in the PolyMUMPs-40 batch. The layout as submitted to the foundry is shown in Fig. 4-4 and a photomicrograph of the device is shown in Fig. 4-5. The maximum possible travel length is 60 μm, as indicated in Fig. 4-5.

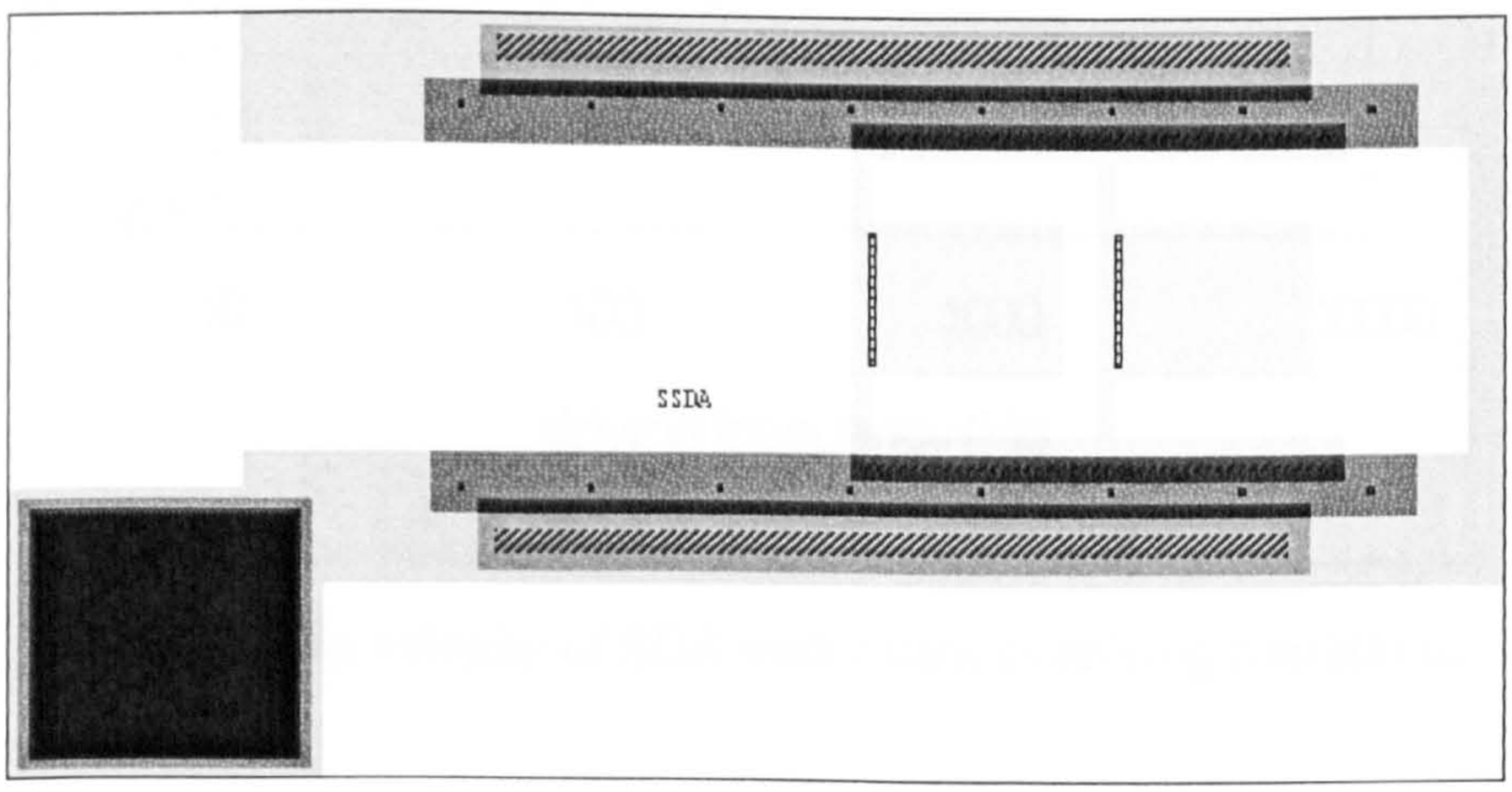

Fig. 4-4: Layout of short-travel SDA.

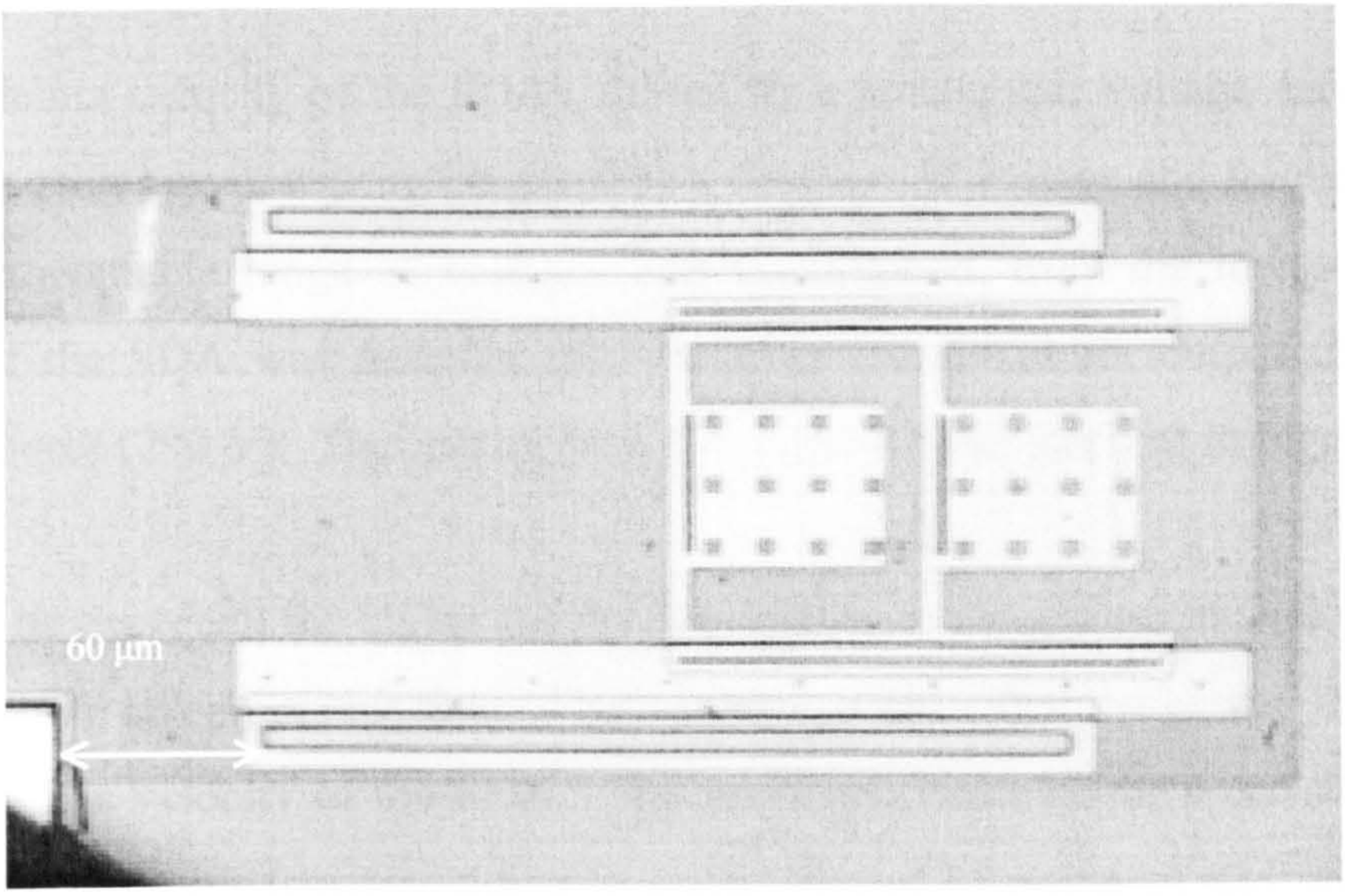

Fig. 4-5: Microphotograph of short-travel SDA.

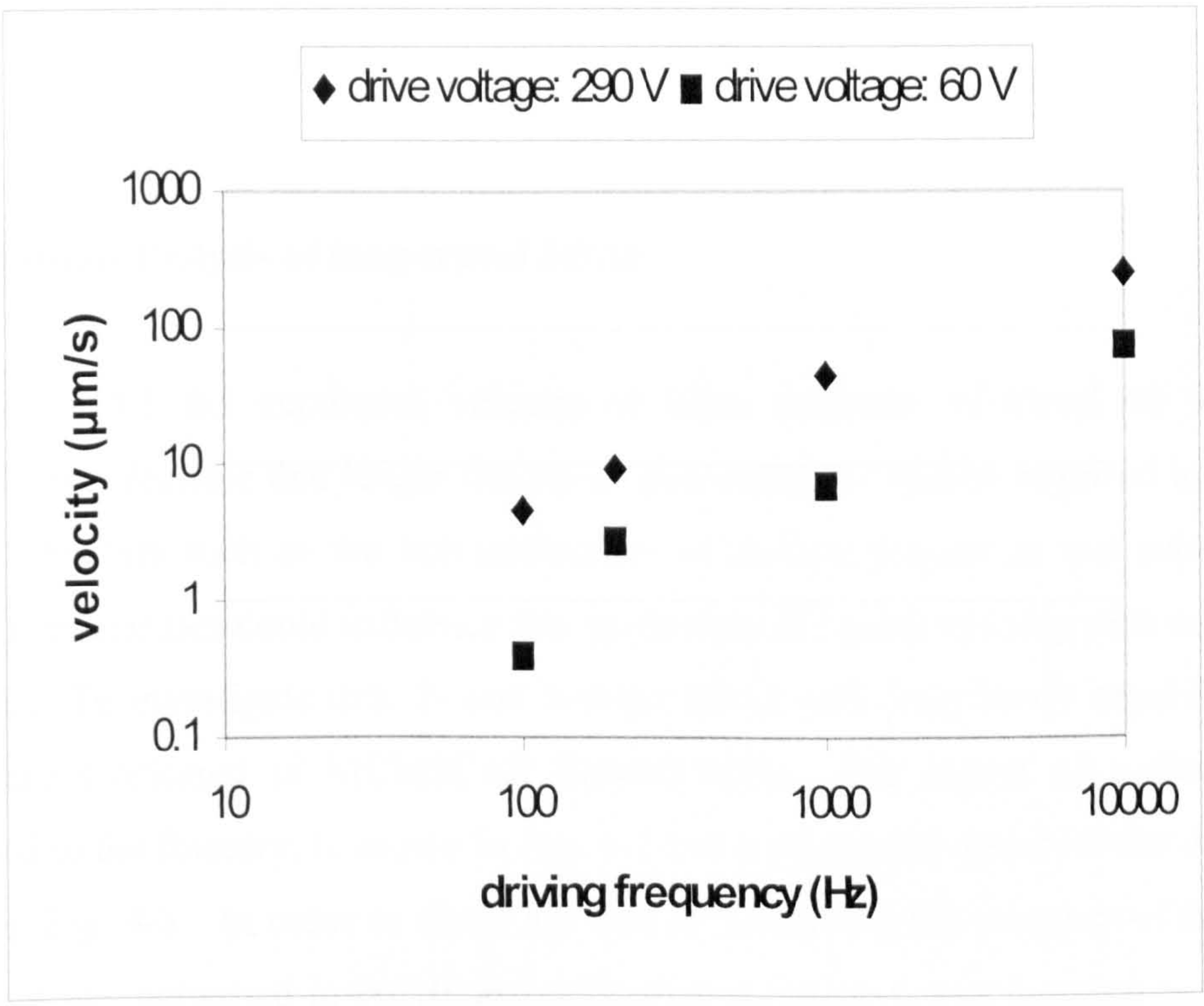

Fig. 4-6: Maximum velocity of SDA under various driving conditions.

The maximum velocity of the SDAs, driven by a rectangular voltage waveform, of 50% duty cycle wave, was investigated as a function of voltage and frequency. The maximum available range of voltages was investigated, from the lowest at which motion of the SDA was detected (60 V) up to the maximum output of the high voltage source (290 V). The results from 8 devices are summarized in Fig. 4-6.

As might be expected, the higher the driving frequency the greater the velocity, since more steps are taken per unit time. The results also show that the greater the voltage, the greater the velocity of the SDA. The maximum velocity for a drive voltage of 290 V was 250 μm/s (corresponding to a step size of 25 nm/step) and for 60 V, 70 μm/s (corresponding to a step size of 7 nm/step). A higher driving voltage leads to greater flexing of the plate, pushing the corner of bush further forward resulting in a greater step size. This has directly been observed by placing an SDA for analysis under a Veeco NT1000 surface profiling tool. This will be discussed later in this chapter.

4.4.2. Motion analysis of long-travel SDAs

In Section 4.4.1 the maximum velocity of SDA actuators of travel 60 μm was reported. It is feasible that longer travels of microactuator will be required in certain MEMS. Factors such as the non-uniformity of surface properties and sub-micron surface irregularities could influence the uniformity of speed and step size over long distances. To investigate this, 2- and 3-stage SDAs with long travel capability (~1 mm) were fabricated in MEMSCAP PolyMUMPs. The layout of a device, as submitted to the foundry, is shown in Fig. 4-7 and a photomicrograph of the device is shown in Fig. 4-8. In order to make the task of measuring the progress of the SDA easier, a scale, patterned in Poly0 and calibrated in microns, was incorporated in the design alongside the rails.

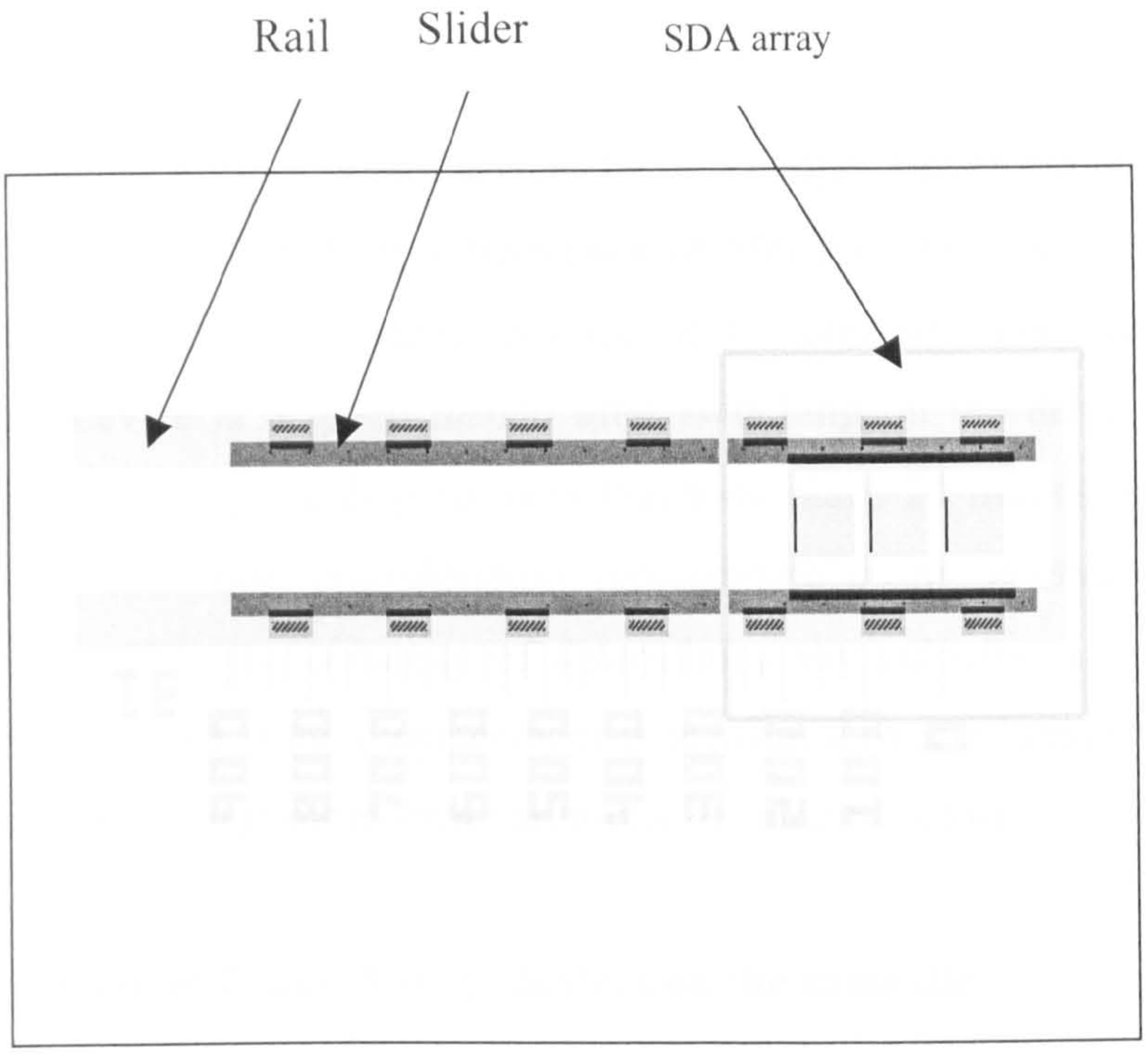

Fig. 4-7: Layout of long-travel SDA.

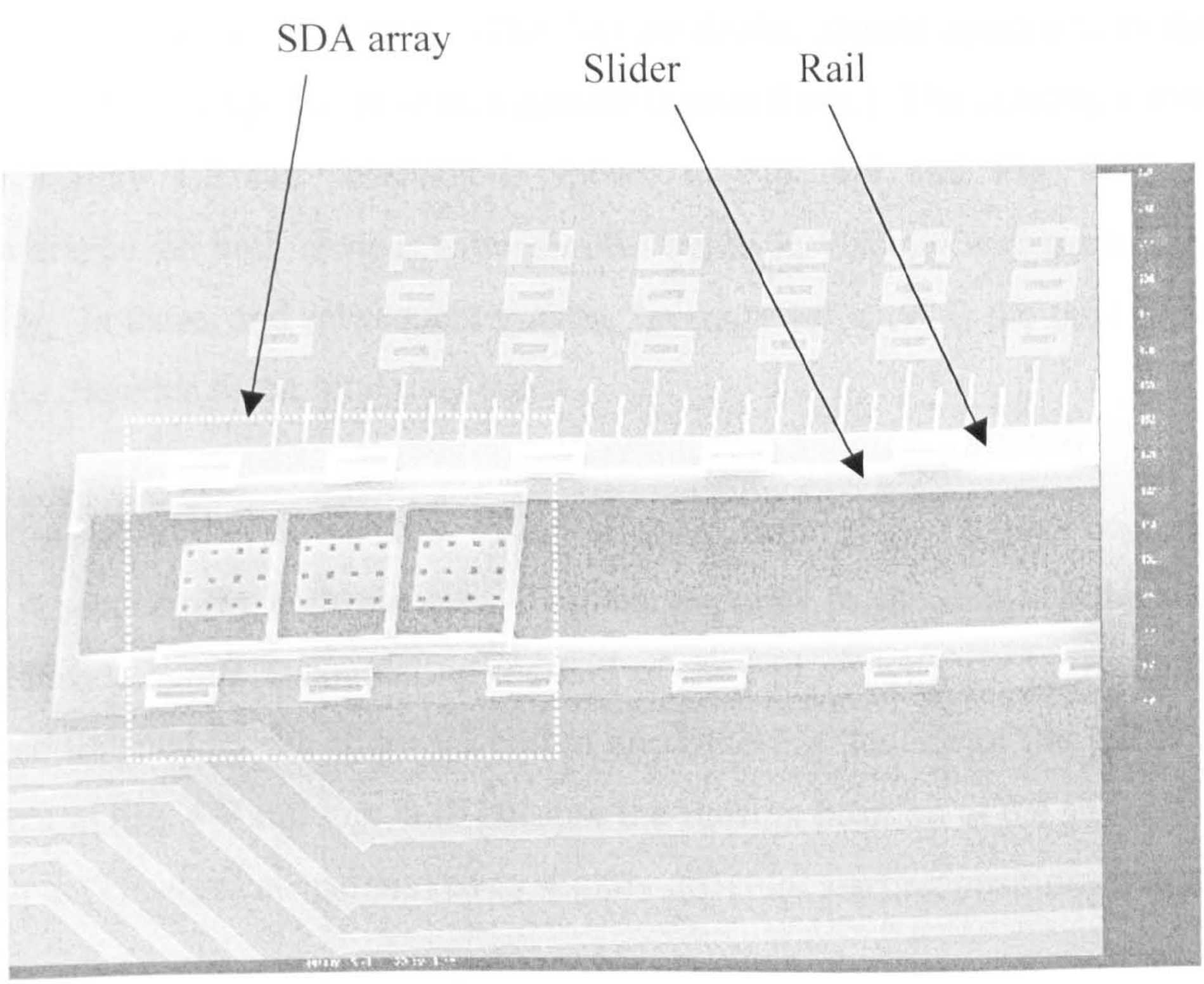

Fig. 4-8: Microphotograph of long-travel SDA.

All the long-travel devices were driven by a voltage waveform as previously described of magnitude 120 V at a frequency of 500 Hz. Images of the actuators were captured at a rate of 125 frames per second for analysis. The "instantaneous" velocity of the device at a given instant after switching on the drive voltage was determined by measuring the displacement that took place 20 frames before and 20 frames after the time under consideration, representing a time interval of 0.32 sec. There is a trade-off in the accuracy of determining the velocity: a more accurate figure can be calculated if the displacement is measured over a longer time interval but then information about short-term variations in velocity is lost.

4.4.2.1 Comparison of 2- and 3-stage devices on the same die

Single examples of a 2-stage and a 3-stage SDA located on the same chip were tested in the manner described above. (The 3-stage device should operate with the same velocity as the 2-stage but provide a greater motive force.) The velocity measured at approximately 1.5 sec. intervals is shown in Fig. 4-9 and Fig. 4-10. Initial measurements on both devices show similar trends in velocity and similar values of velocity. In these, and subsequent graphs, "average velocity" is the ratio of the total distance travelled to the total time taken.

It was observed that a reduction of initial speed from 37 to 22 μm/s occurred after about 4 seconds for both devices. This corresponds to the distance the tip of the slider travels before encountering the end of the rail on which it is traveling. The distance traveled by the slider tip before encountering the end of the rail is slightly different in Fig. 4-9 and Fig. 4-10 because the starting position of the sliders were not the same. (The devices had moved to slightly different starting positions in transit.)

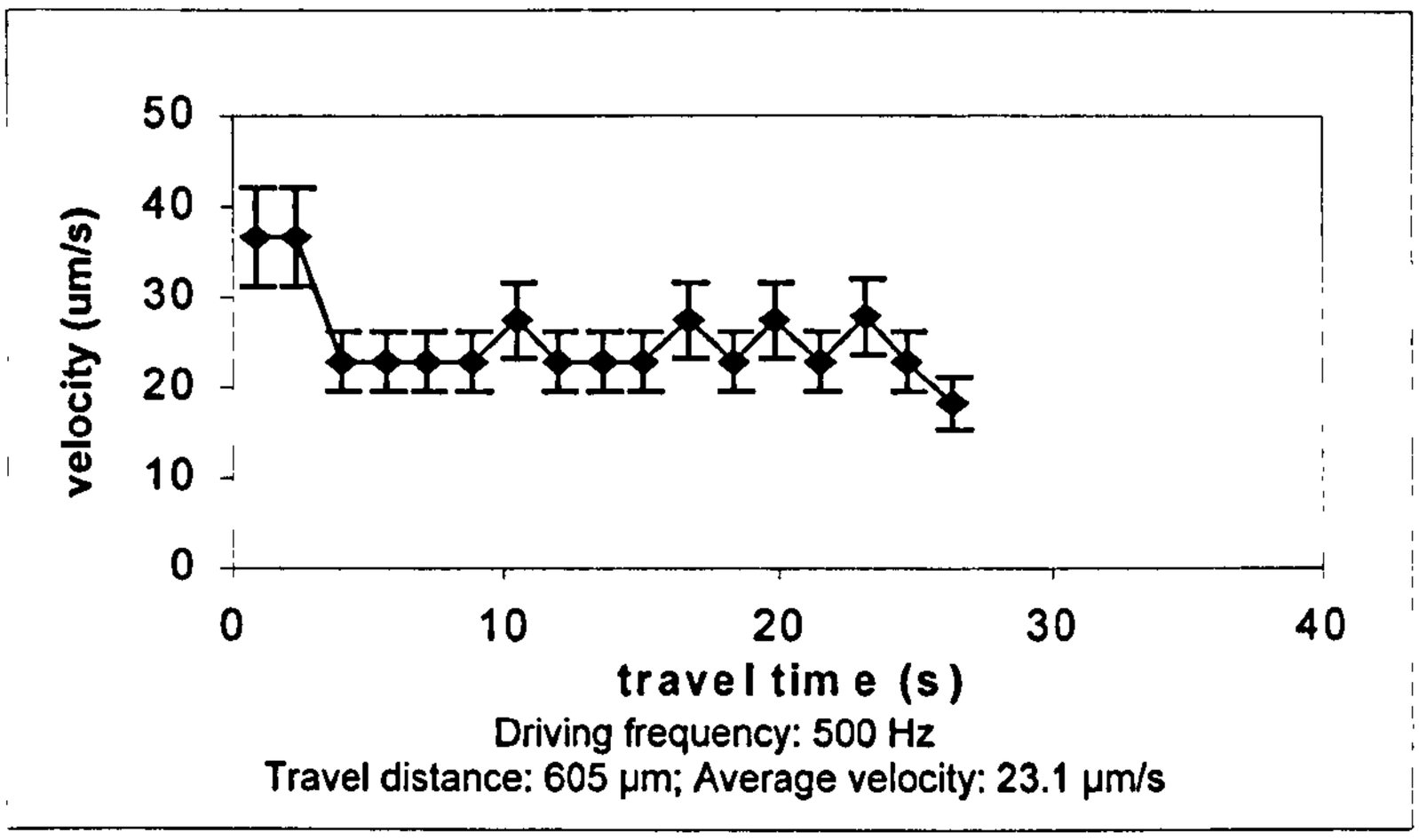

Fig. 4-9: Velocity of slider as a function of time for a 2-stage SDA.

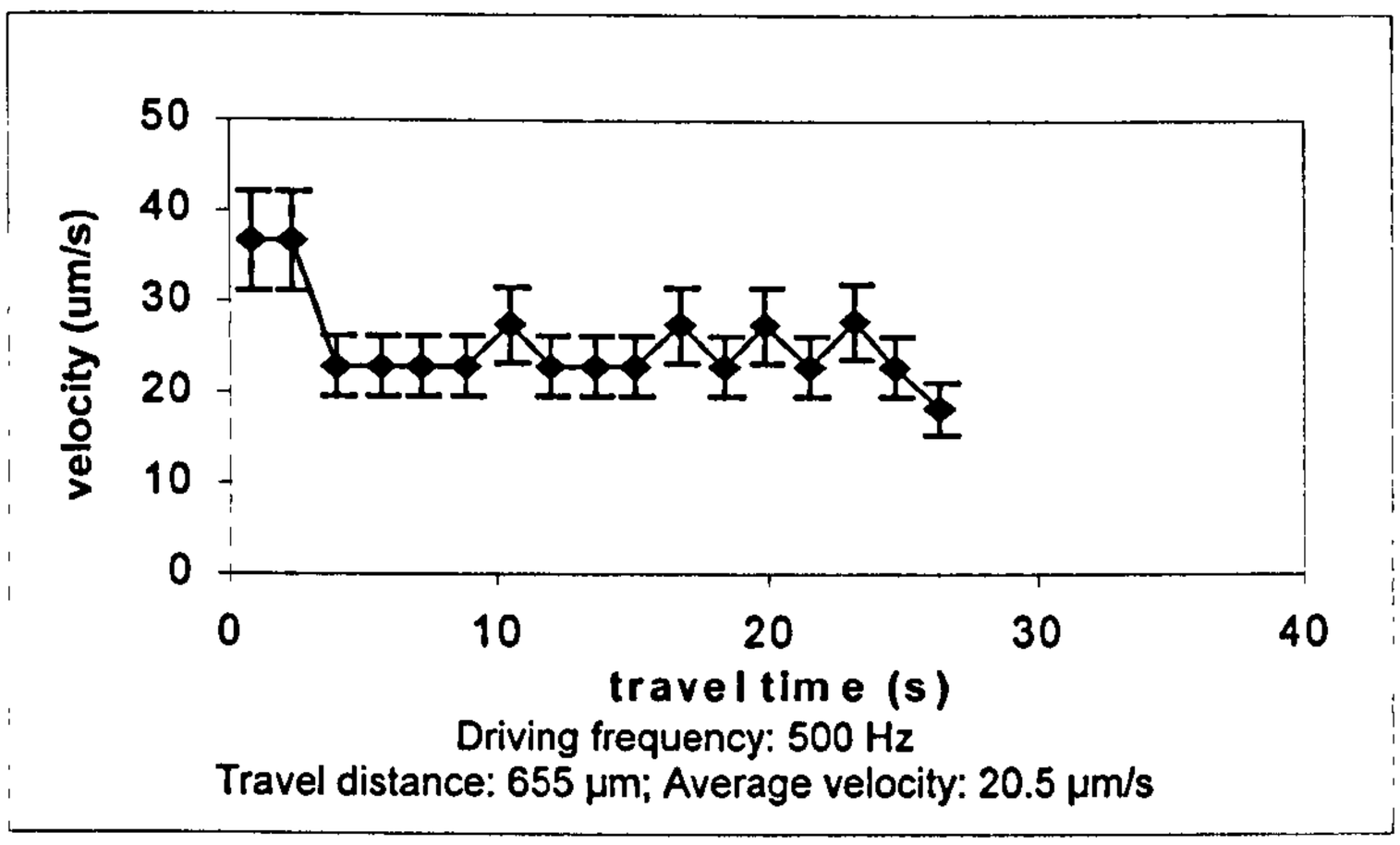

Fig. 4-10: Velocity of slider as a function of time for a 3-stage SDA. 2-stage SDA in Fig. 4-9 and 3-stage SDA in Fig. 4-10 are in same die.

In SDAs, the "engine" is connected to the "sliders" by torsion bars. There are two regimes of motion experienced by the sliders, and this is differentiated by the surface over which the tip of the slider is traveling. In the higher velocity regime shown in Fig. 4-9 and Fig. 4-10, the full length of the slider moves on a polysilicon surface (Poly0 rail). Detailed surface profiling of the tip of the rail using the Veeco NT1000 tool shows that on application of voltage to the SDA, the tip bends upwards, away from the similarly charged rail. This is obvious from Fig. 4-11 which show the height of the slider tip above the reference nitride surface before and after voltage application. After applying voltage, the SDA plate is attracted down to the substrate, therefore the torsion of the connector introduces the sliders tip bending up. The tip

presents a lower resistance and the overall velocity is therefore "high". Fig. 4-11 (b) and Fig. 4-11(d) show measurements of the tip.

In the low velocity regime, the polysilicon slider tip is traveling along the nitride surface having slid off the end of the rail. The tip is oppositely charged to the silicon substrate producing a high attractive force between the two. This is shown in the

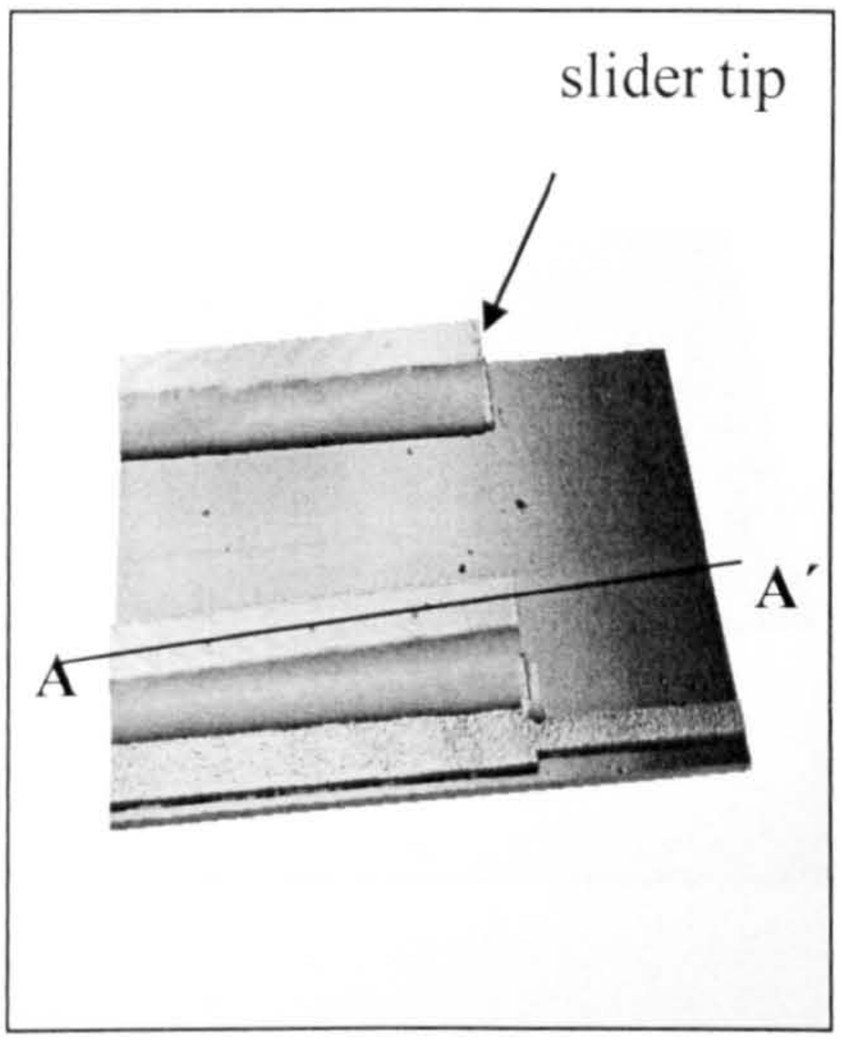

Fig. 4-11 (a)

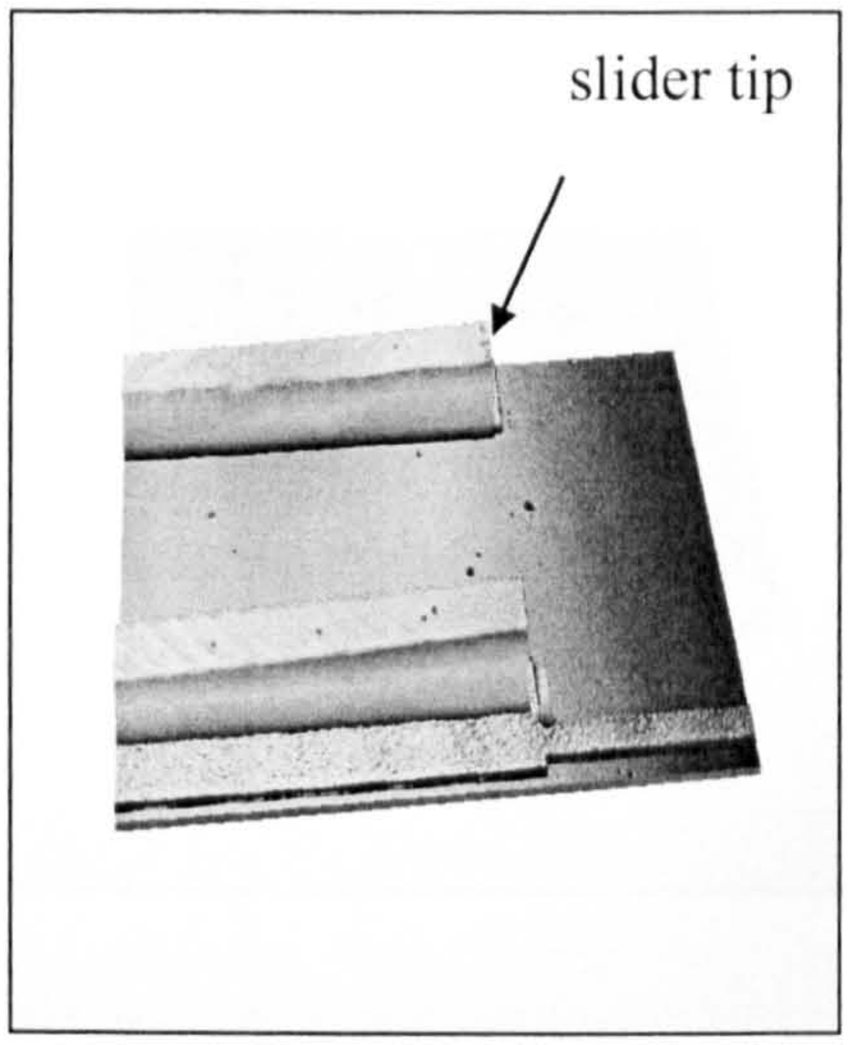

Fig. 4-11 (c)

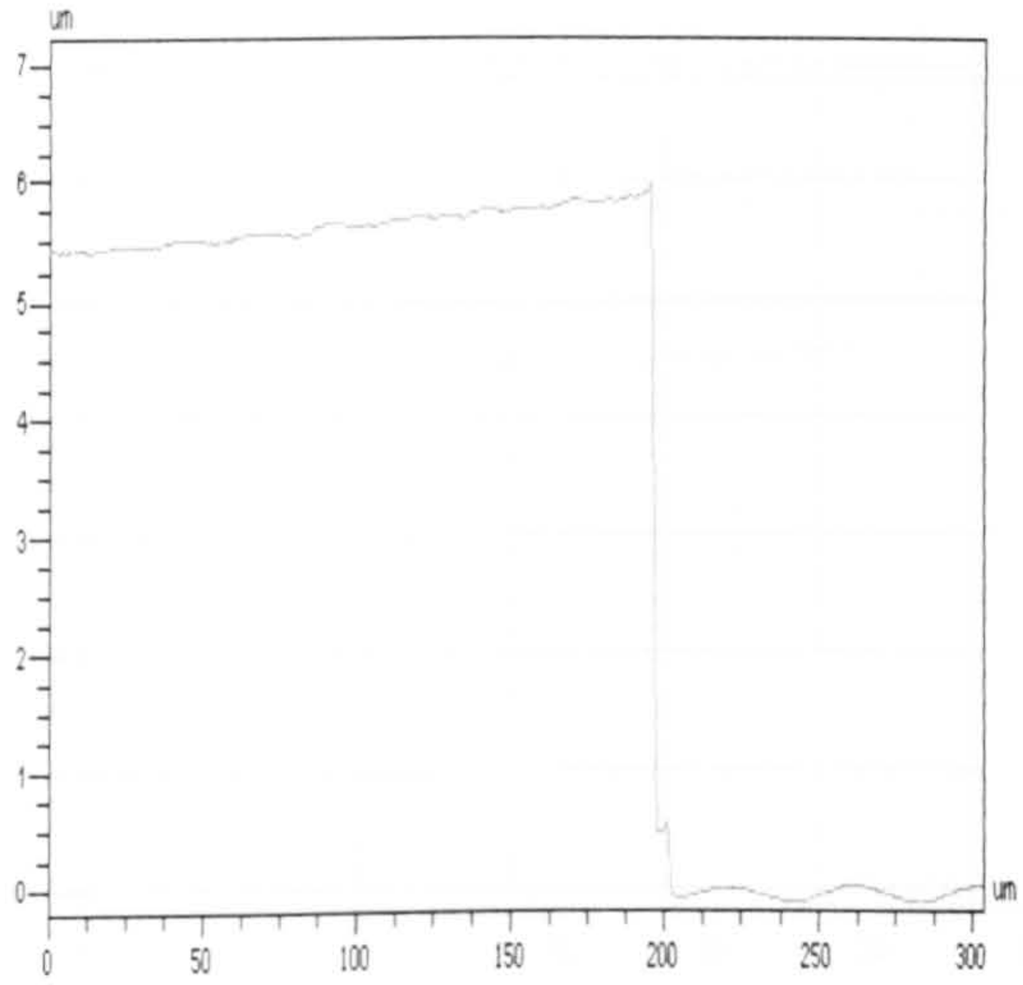

Fig. 4-11 (b)

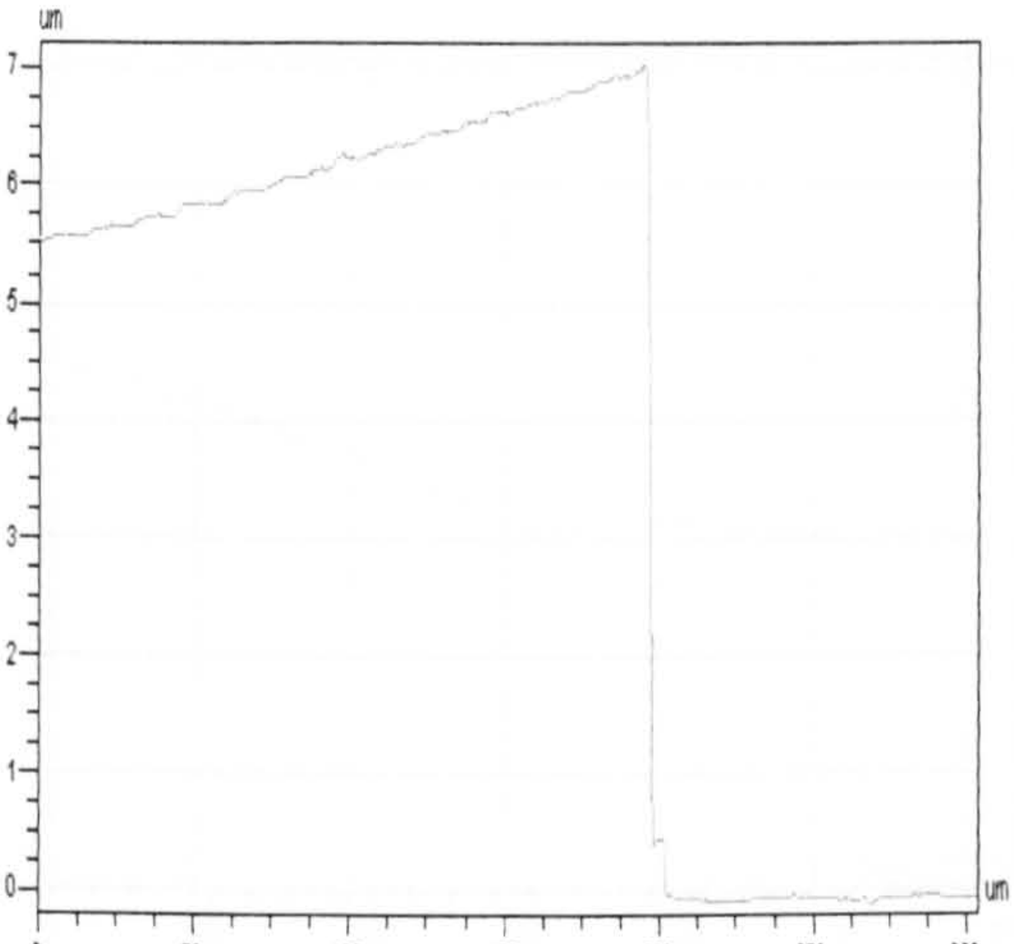

Fig. 4-11 (d)

Fig. 4-11: Slider on rail. Surface profile (a) and cross-section along AA′(b) for unpowered device; surface profile (c) and cross-section (d) for device with 140 V applied.

surface profiles of Fig. 4-12 which show the tip overhanging the end of the slider. In Fig. 4-12 (a) and Fig. 4-12 (b) the voltage is 0 and in Fig. 4-12 (c) and Fig. 4-12 (d) the voltage is 140 V. The tip is clearly seen to bend towards the substrate thereby making contact with the nitride surface. The result of this is an increase in resistance due to friction, and a decrease in velocity.

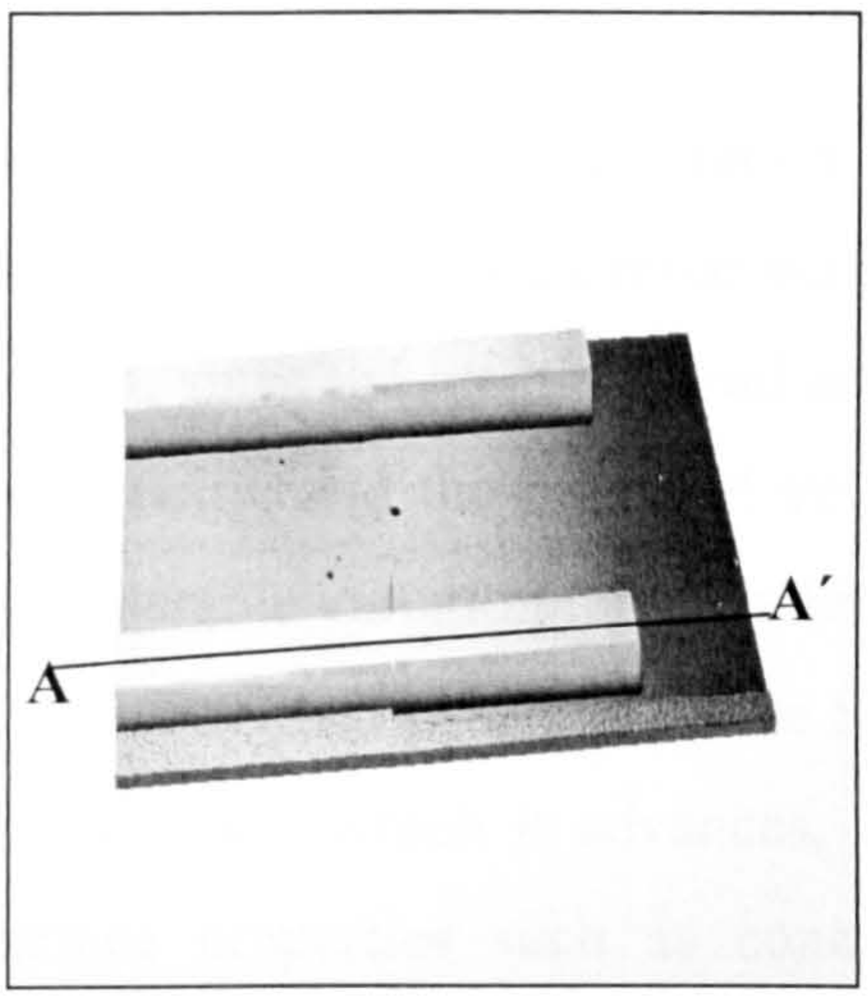

Fig. 4-12 (a)

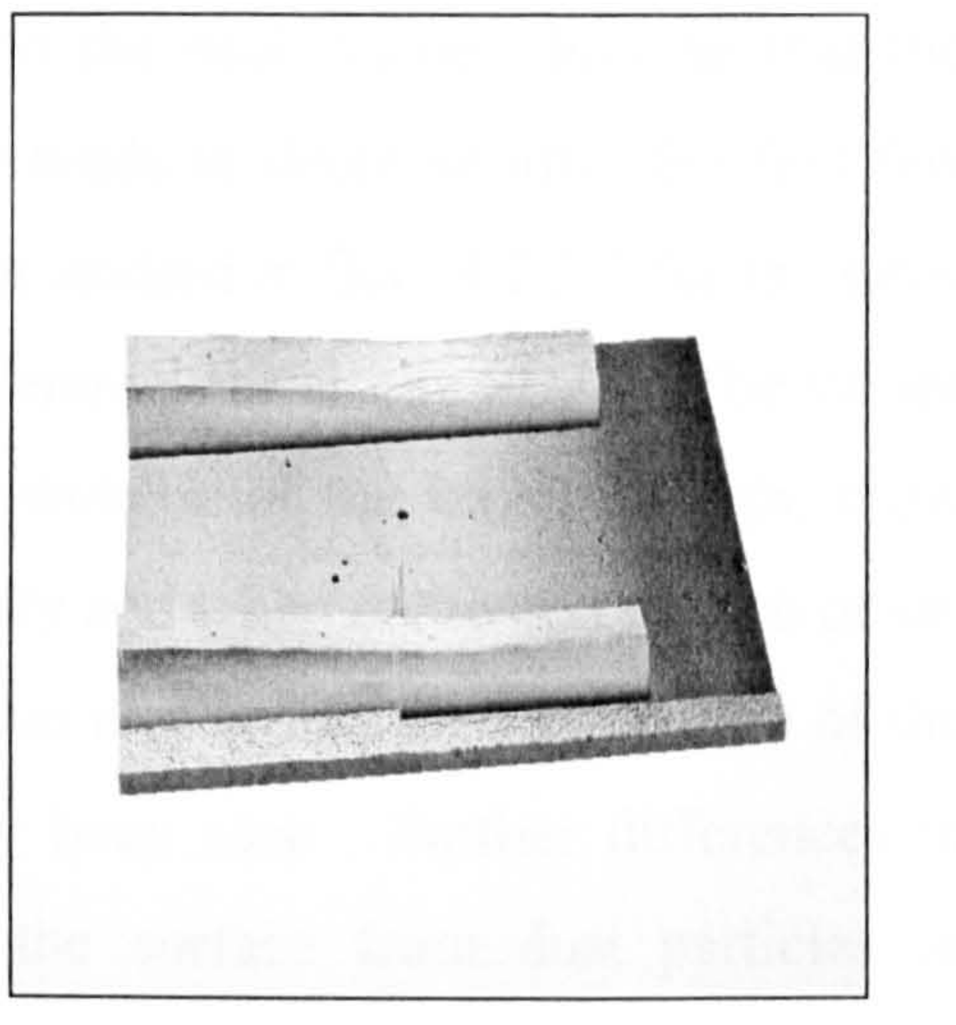

Fig. 4-12 (c)

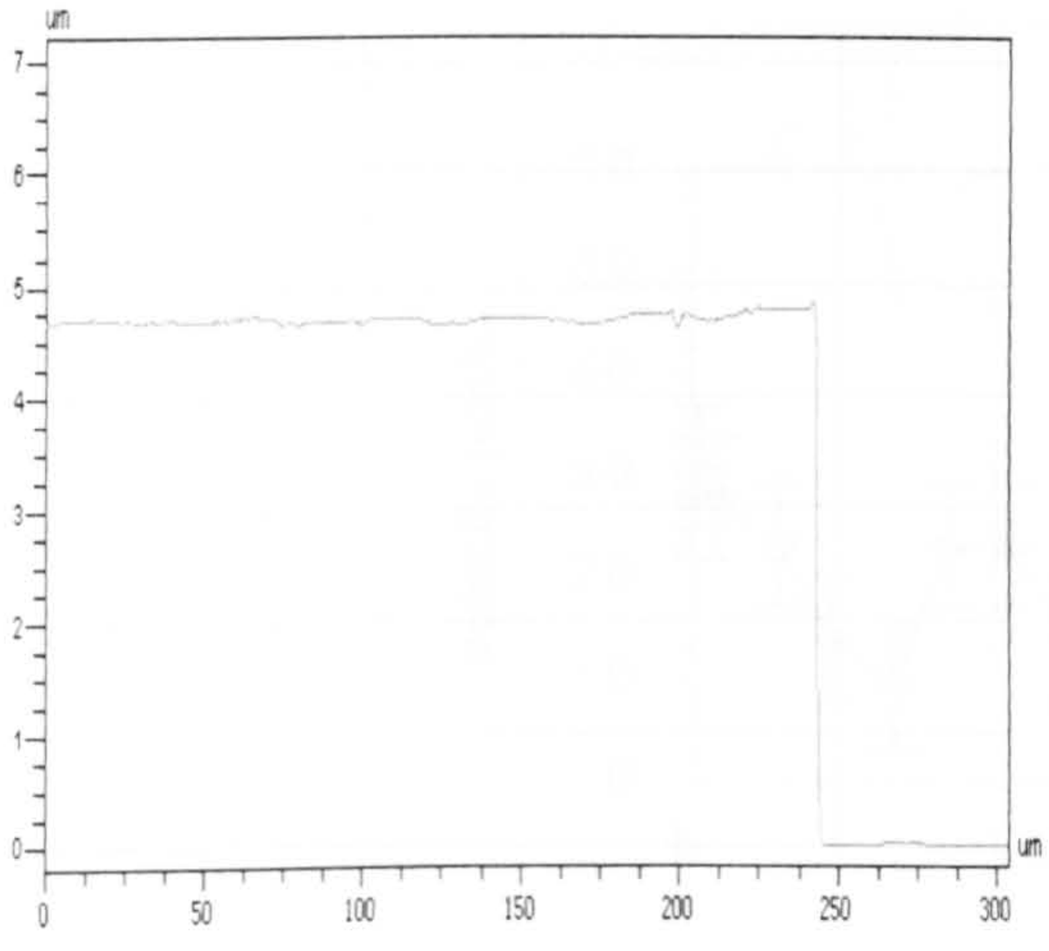

Fig. 4-12 (b)

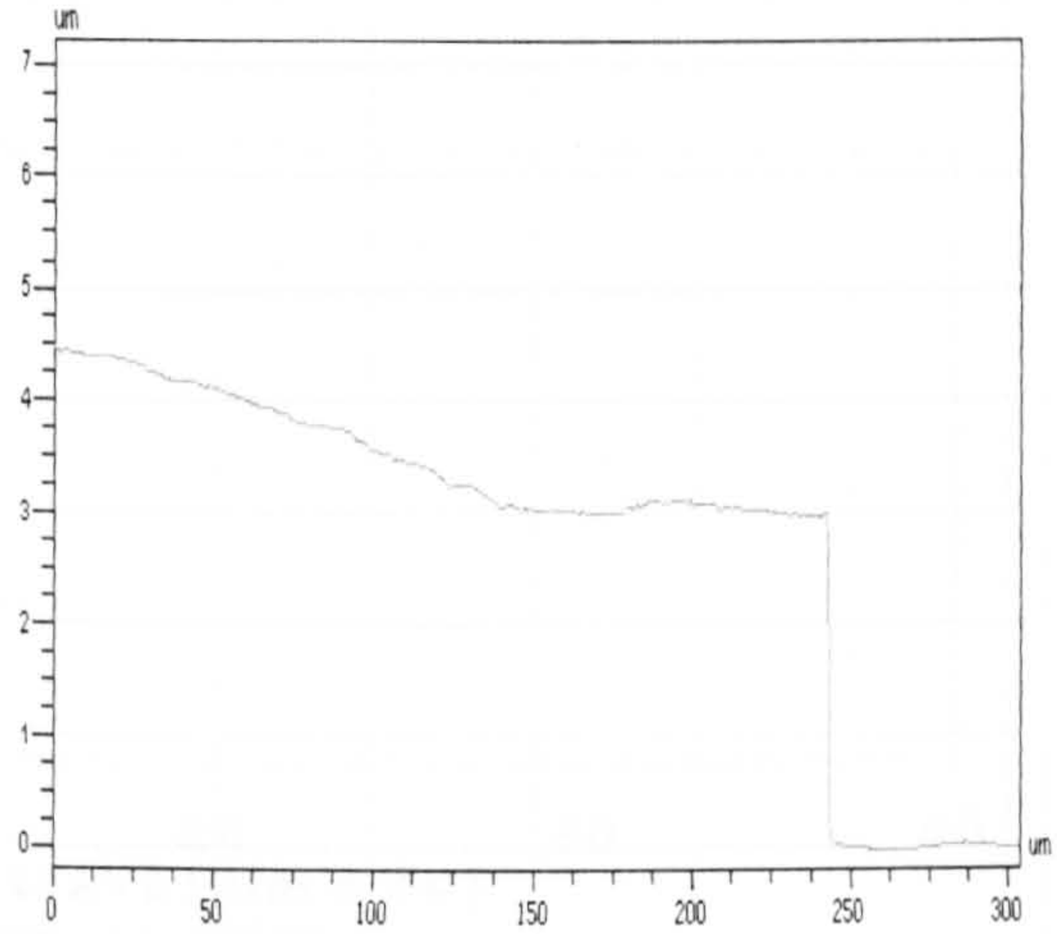

Fig. 4-12 (d)

Fig. 4-12: Slider beyond end of rail. Surface profile (a) and cross-section along AA´(b) for unpowered device; surface profile (c) and cross-section (d) for device with 140 V applied.

4.4.2.2 Comparison of 2-stage devices from different dies.

The instantaneous velocity of 4 different 2-stage SDAs, each from a different die fabricated in the same PolyMUMPs batch was measured as described in section 4.2.2.1 and the results are shown in Figs. 4-13 - 4-16. The first data point in each graph represents the velocity at time ~0.125 sec (i.e. after only ~60 pulses supplied to the SDA) when the velocity is already close to the peak value, showing that the devices exhibit high acceleration. The velocity tends to decrease after the first few seconds of travel, in a similar way to the devices studied in Sec. 4.2.2.1 for the same reason, since the lengths of rail and slider are identical for all the SDAs. The values of velocity, and the trends of velocity in later sections of the travel, though, show considerable variation for each device individually and when compared to each other. The operational principle of the SDAs means that it is sensitive to the nature of the surface over which it advances, as has already been seen. Further differences in surface properties such as contamination of the surface from dust particles or remnants of processing are among the several factors that could lead to the differences in performance of the SDAs shown in the figures.

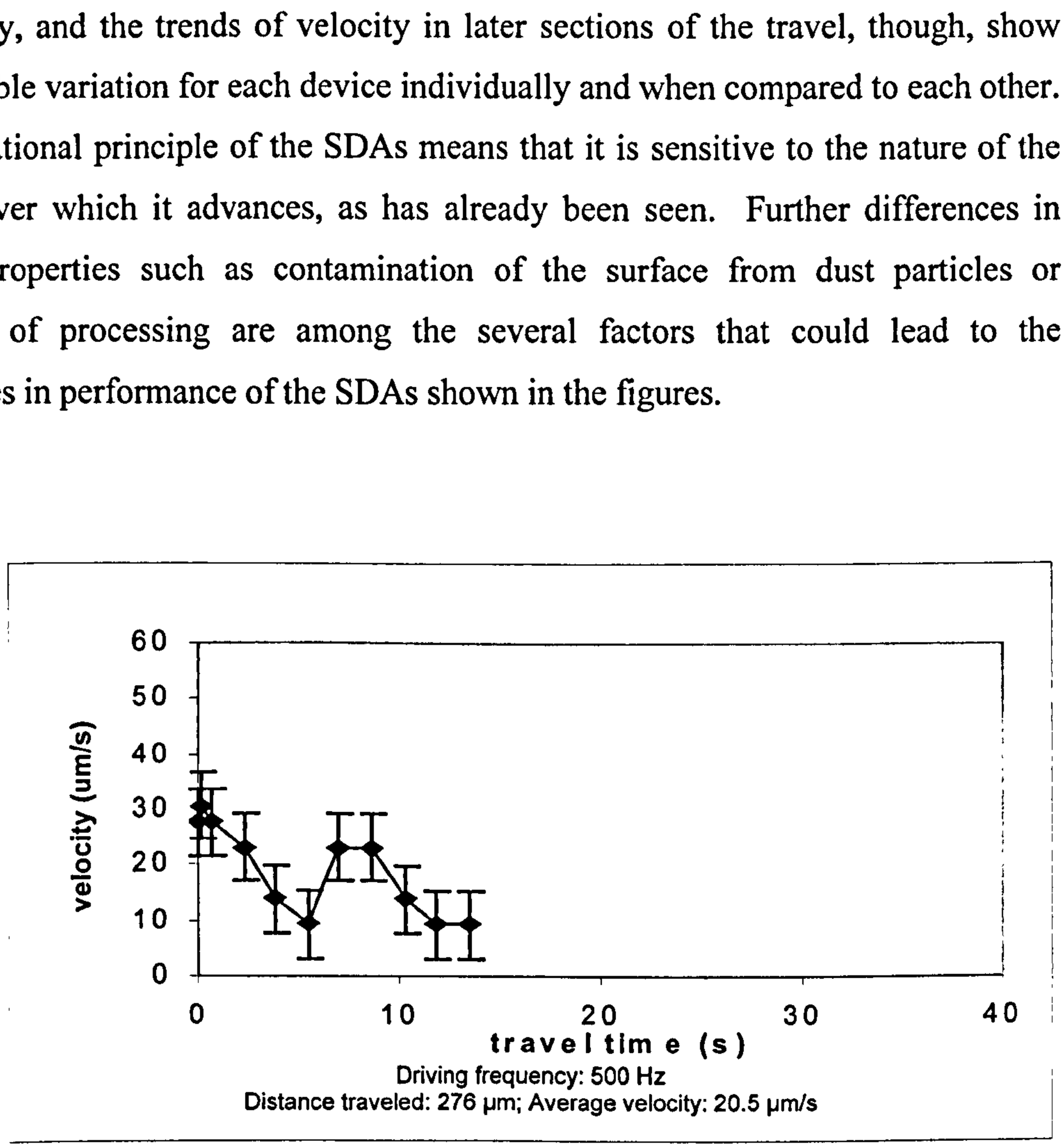

Fig. 4-13: Velocity as a function of time for a 2-stage SDA (die 1).

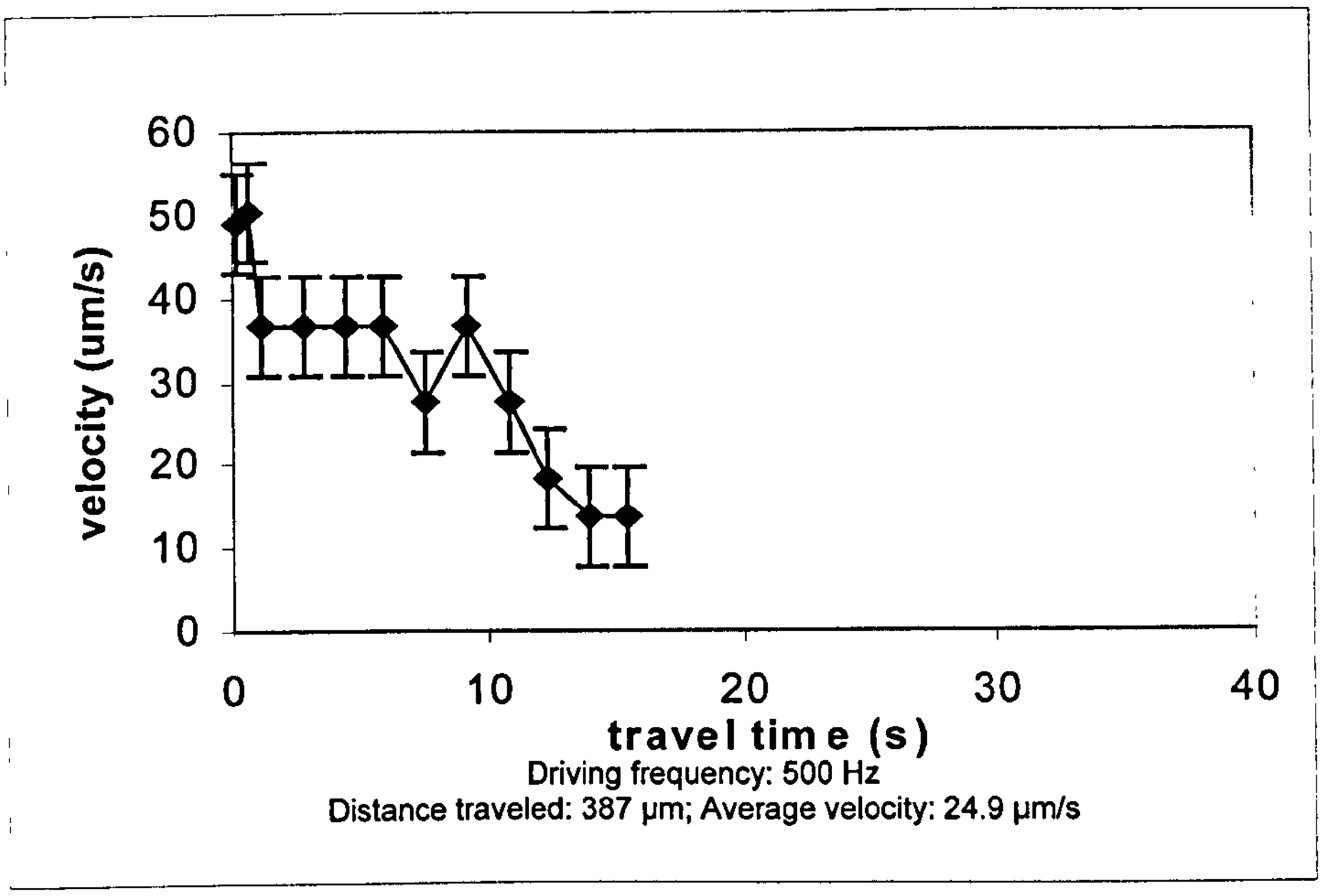

Fig. 4-14: Velocity as a function of time for a 2-stage SDA (die 2).

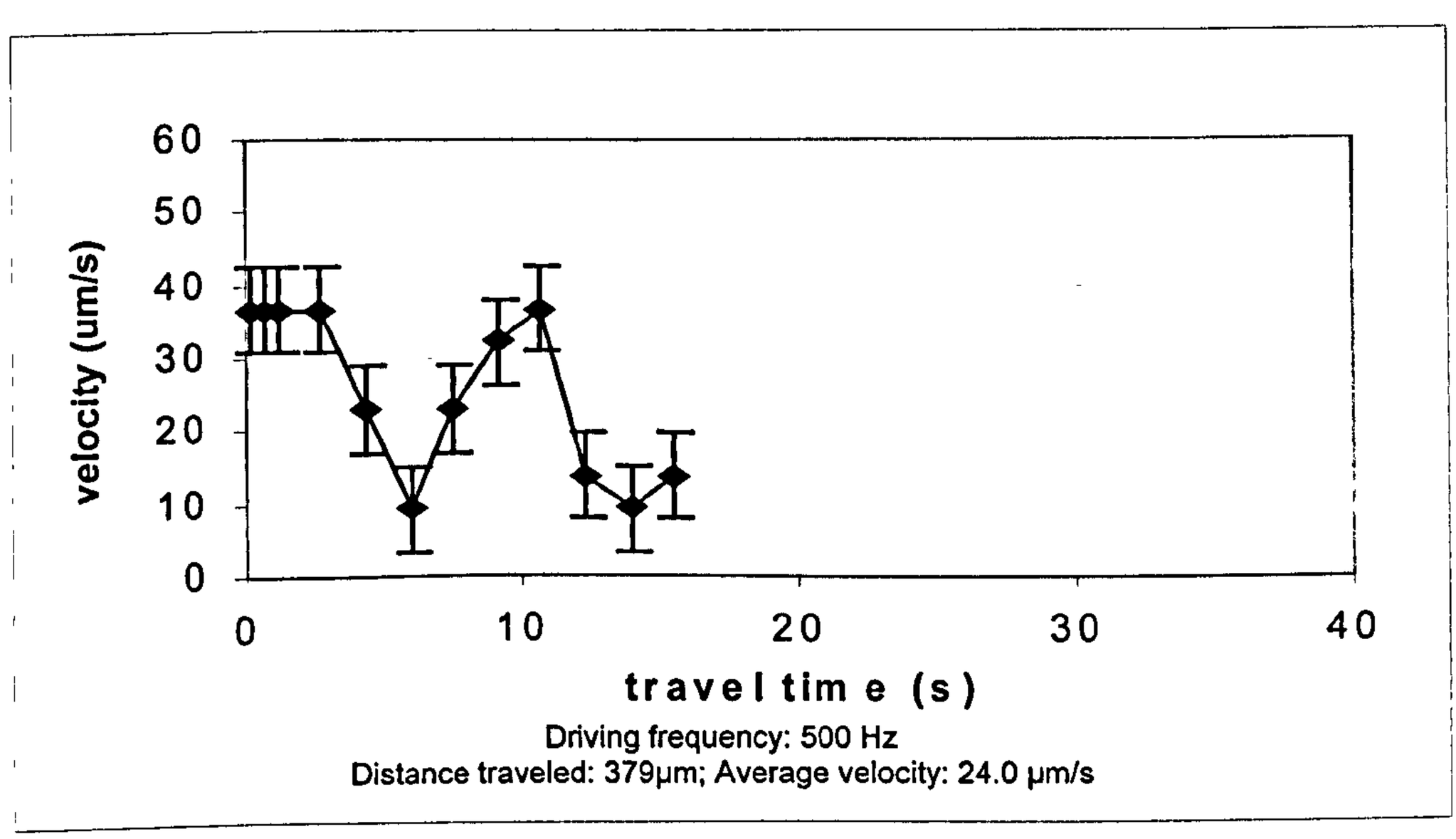

Fig. 4-15: Velocity as a function of time for a 2-stage SDA (die 3).

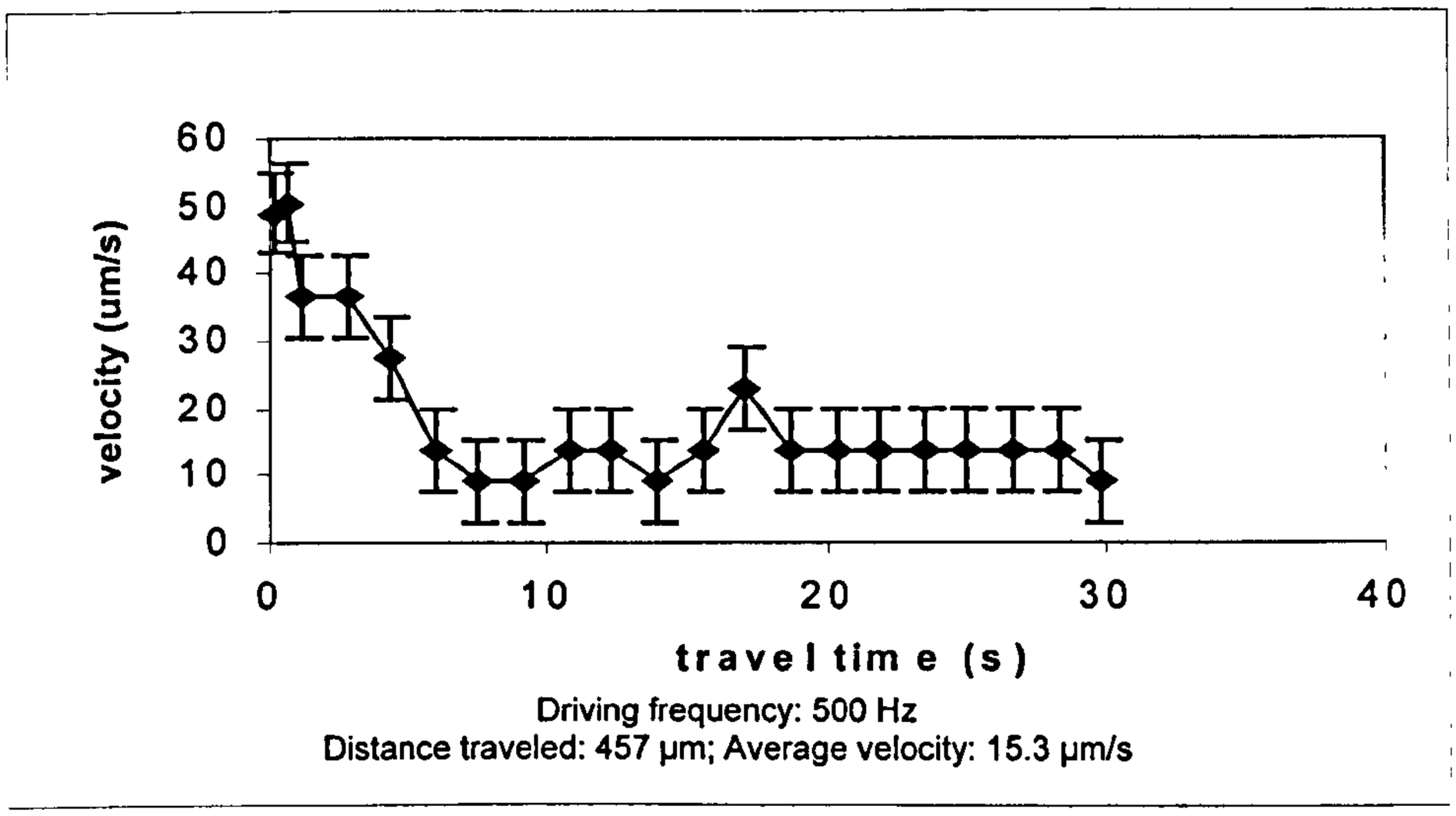

Fig. 4-16: Velocity as a function of time for a 2-stage SDA (die 4).

4.5 Analysis of the plate bending;

The physical behaviour of the SDA plate as the applied voltage increases is as follows: in response to the application of the voltage signal, the SDA plate is initially attracted down towards the substrate. When the voltage exceeds the threshold voltage (defined later in this chapter), the tip of the SDA plate will make contact with the substrate. When a higher voltage is applied, the plate will be flattened starting from the free end due to the large electrostatic force. The flattening increases as more voltage is applied, resulting in a longer "contact length" from the tip end. The contact length depends on the voltage, and will also determine the step size according to the geometrical model of the actuator. Therefore, there are two modes occurring during its motion – one is the non-contact mode when the actuator plate has not yet contacted the substrate, while the second is the contact mode. These modes are generated in sequence during every step of the actuator; furthermore the contact mode will determine the step size. The applied voltage affects the velocity of the

SDA when the driving frequency is fixed. The SDA is driven by a square wave signal in our work. (It can be also driven by a sine wave).

4.5.1 Mathematical model of SDA

The SDA consists of three parts: suspended plate, bush, and substrate electrode. The principle of operation has been described in section 4.2.

4.5.1.1 Mode 1- non contact mode

Fig. 4-17 shows a profile of a simplified scratch drive actuator. In Fig. 4-17(a), no voltage is applied to the suspended plate, and it is flat with a constant separation from the bottom surface.

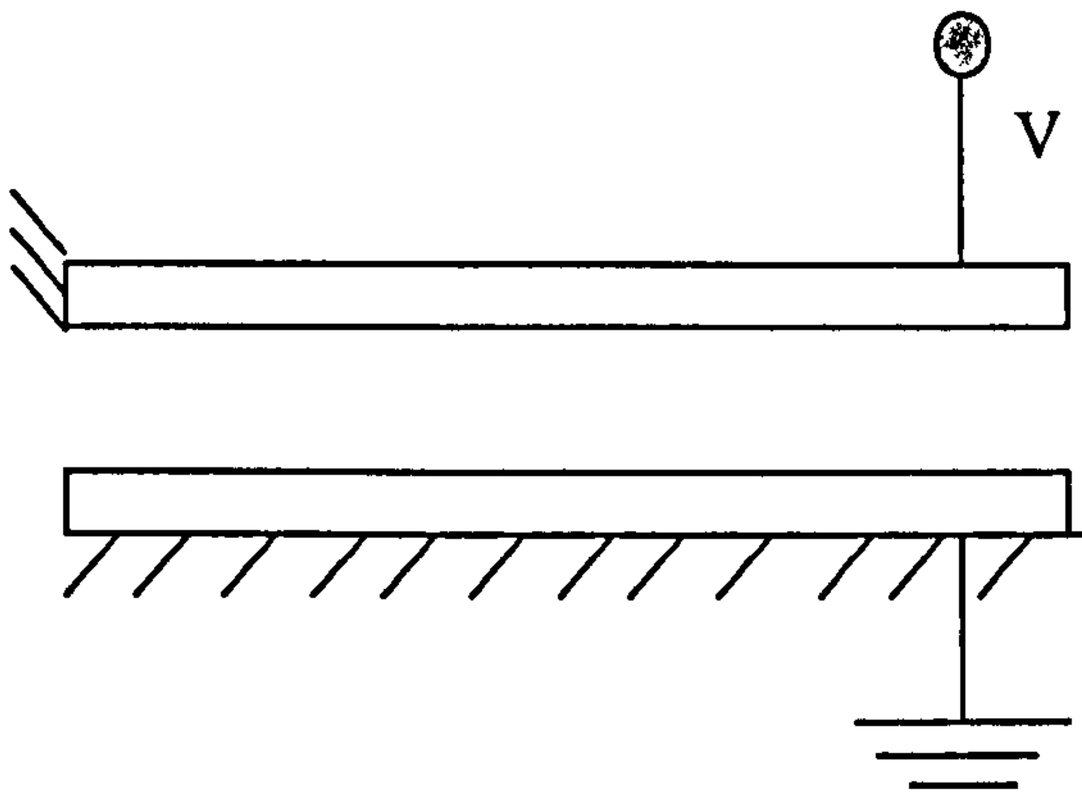

Fig. 4-17 (a)

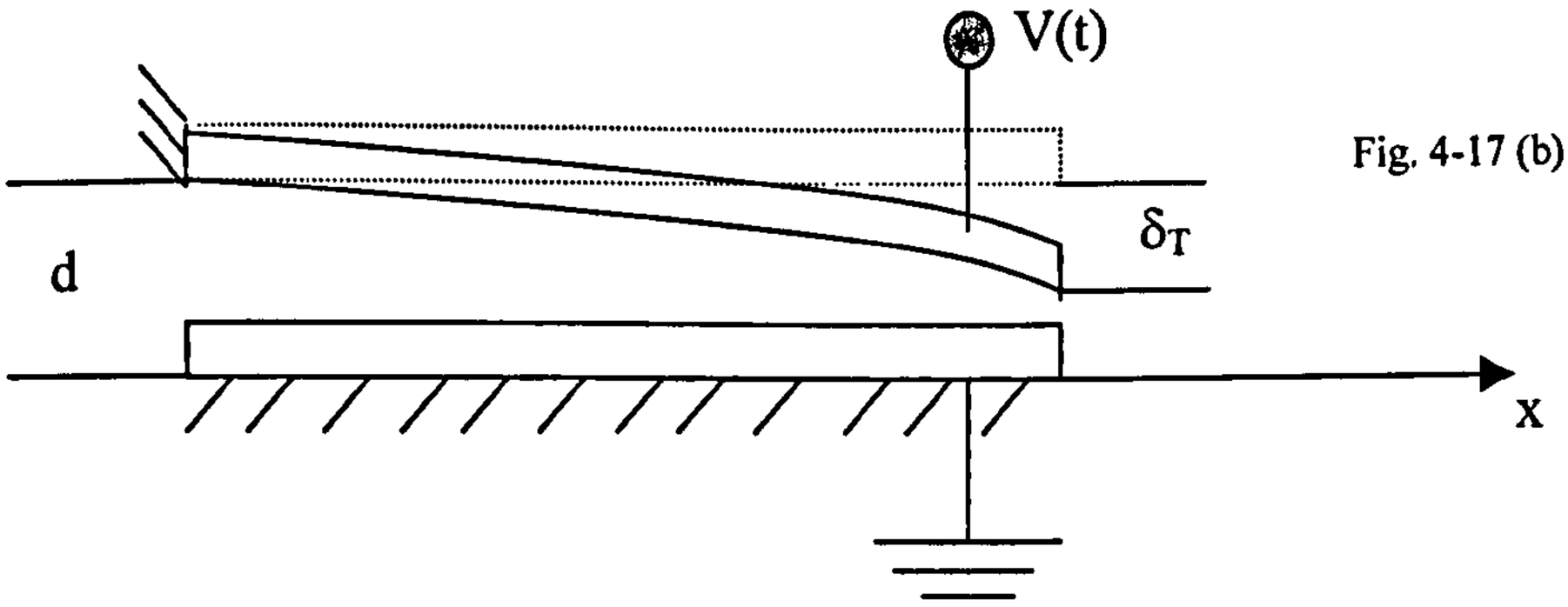

Fig. 4-17 (b)

Fig. 4-17: Profile of non-contact mode of the SDA.

From this figure, it is clear that the structure forms a parallel-plate capacitor. When a voltage is applied, charge will be stored in this capacitor and generates an electrostatic force. Because one end of the top plate is fixed, the electrostatic force will pull the free end down towards the substrate, as shown in Fig. 4-17(b).

The force on the plates of a parallel plate capacitor is given by:

$$F = \frac{\varepsilon A V^2}{2d^2} \quad , \tag{4.1}$$

where ε is the permittivity of the free space, A is the area of the plate, V is the applied voltage, d is the initial gap between the two plates. In the case of the SDA only one end of the upper plate is fixed, so single fixed end beam theory is applied for the analysis.

The deflection of the plate due to an applied force is a function of the dimensions and material properties of the plate. Assuming that the Young's modulus is E and the moment of inertia is I and the plate length is L, the deflection δ_T of the tip of the plate is given by [98]:

$$\delta_T = \left[\frac{x^2}{6EI}\right](3L - x)F(x) \tag{4.2}$$

where F (x) is the electrostatic force at distance x along the plate which can be expressed by [99]:

$$F(x) = \frac{bk\varepsilon}{2}\left(\frac{V}{d - \delta(x)}\right)^2 dx \quad . \tag{4.3}$$

In formula (4.3), δ(x) is the deflection at the point x, k is the effective dielectric constant of the air layer and nitride layer below the SDA plate. The square law curvature can be used to determine the relationship between the deflection of the tip δ_T and any point of the plate [99].

$$\delta(x) = (\frac{x}{L})^2 \delta_T \qquad (4.4)$$

In the case analysed here, the forces are distributed, so the deflection of the tip is derived by integrating the formula (4.2) from x=0 to x=L yielding:

$$\delta_T = \int_0^L \frac{3L - x}{6EI} x^2 F(x) dx \qquad (4.5)$$

Substituting formula (4.3) in formula (4.5) defines the function of deflection at the tip of the plate.

$$\delta_T = b \int_0^L \frac{3L - x}{6EI} x^2 \left[\frac{k\varepsilon}{2} (\frac{V}{d - (\frac{x}{L})^2 \delta_T})^2 \right] dx \qquad (4.6)$$

Letting $\Delta = \frac{\delta_T}{d}$, integrating and solving for the voltage as a function of deflection of the tip, gives:

$$V = \sqrt{\frac{12 EId^3 \Delta^3}{bk\varepsilon L^4} \left[\frac{\Delta}{1+\Delta} - \frac{3\sqrt{\Delta}}{2} \tanh^{-1}(\sqrt{\Delta}) - \frac{1}{2} \ln(1-\Delta) \right]^{-1}}$$

.....(4.7)

In the design of our devices, the SDA plate length L is 75 μm, the plate width b is 65 μm, and the thickness of the plate is 1.5 μm. The initial gap d between the plate and

substrate consists of two parts: first is the thickness of the air gap d_1 (=1.5 μm), and the second is the thickness of the silicon nitride d_2, which is 0.6 μm, hence $d = d_1 + d_2$ is 2.1 μm. All the layer thicknesses are determined by the MUMPs fabrication process. The material properties of polysilicon are also supplied from the commercial foundry. The dielectric constant of air k_{air} is 1, and the dielectric constant of nitride $k_{nitride}$ is 5.7. Dielectric constant of 0.6 μm nitride layer can be taken the value of the dielectric constant of 0.1 μm air layer. So here d = 1.5 μm +0.1 μm = 1.6 μm. E is the Young's Modulus of polysilicon, which is 1.69×10^{11} N/m^2. The permittivity of air ε is 8.85×10^{-12} F/m. I is the moment of inertia of the plate, which is $\frac{1}{12}bt^3 = 1.828 \times 10^{-23}$ m^4. The plot of Equation 4.7 for the parameters above is shown in Fig. 4-18.

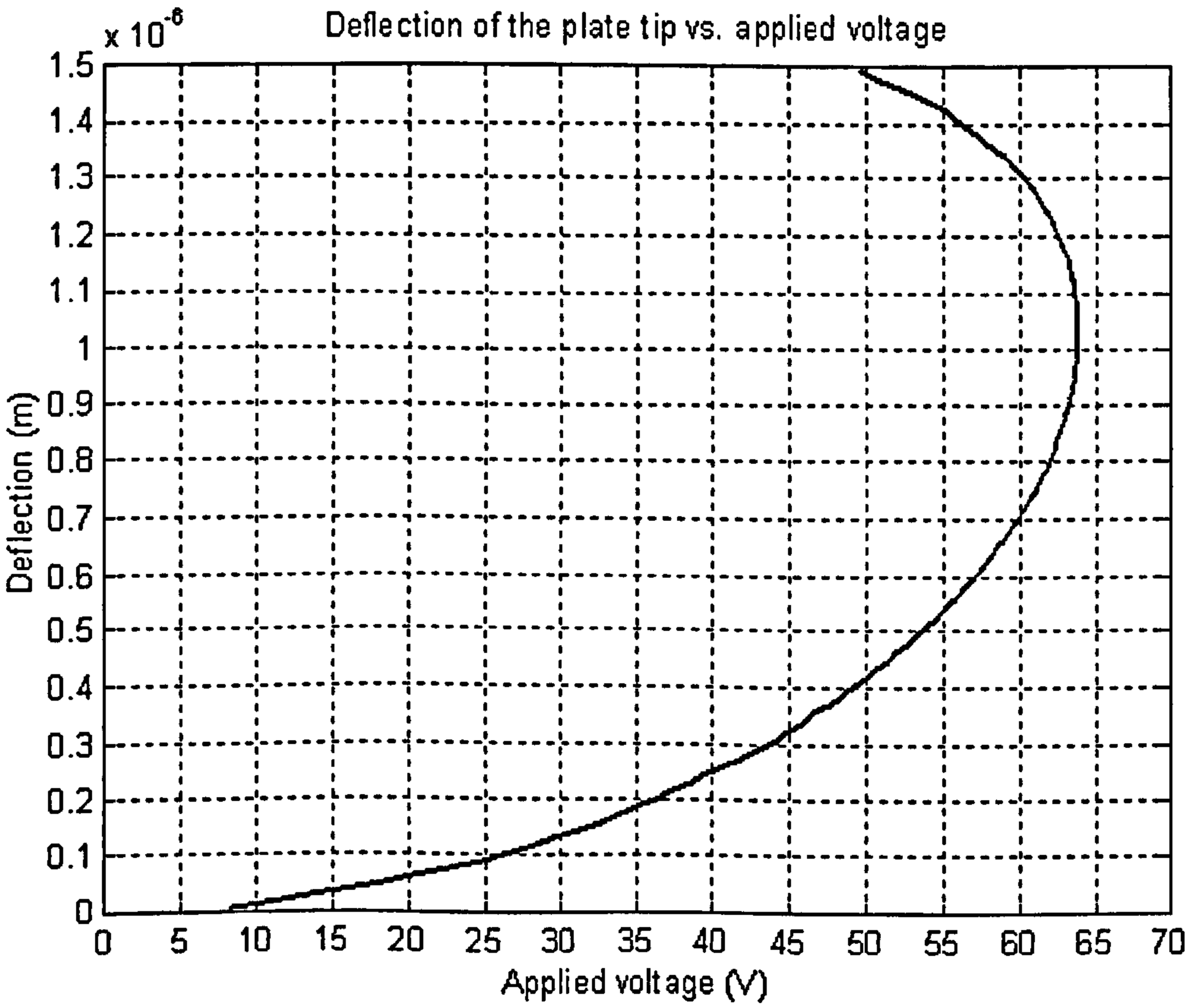

Fig. 4-18: Deflection of SDA plate tip vs. applied voltage for non-contact mode.

Fig. 4-18 shows a hysteretic behavior of the plate since equation 4.7 has two solutions over a certain range of voltage. As the applied voltage is increased from a low value, the tip deflection monotonically increases until a value of around 63 V, which is the threshold voltage for stability. Beyond this threshold voltage, the electrostatic forces become increasingly concentrated on the free end of the plate rather than being distributed along the length of the plate, given rise to the second solution of the equation 4.7. In the physical domain, the plate becomes unstable beyond the threshold voltage and undergoes spontaneous deflection over the remaining distance to the substrate [101]

4.5.1.2. Mode 2- contact mode

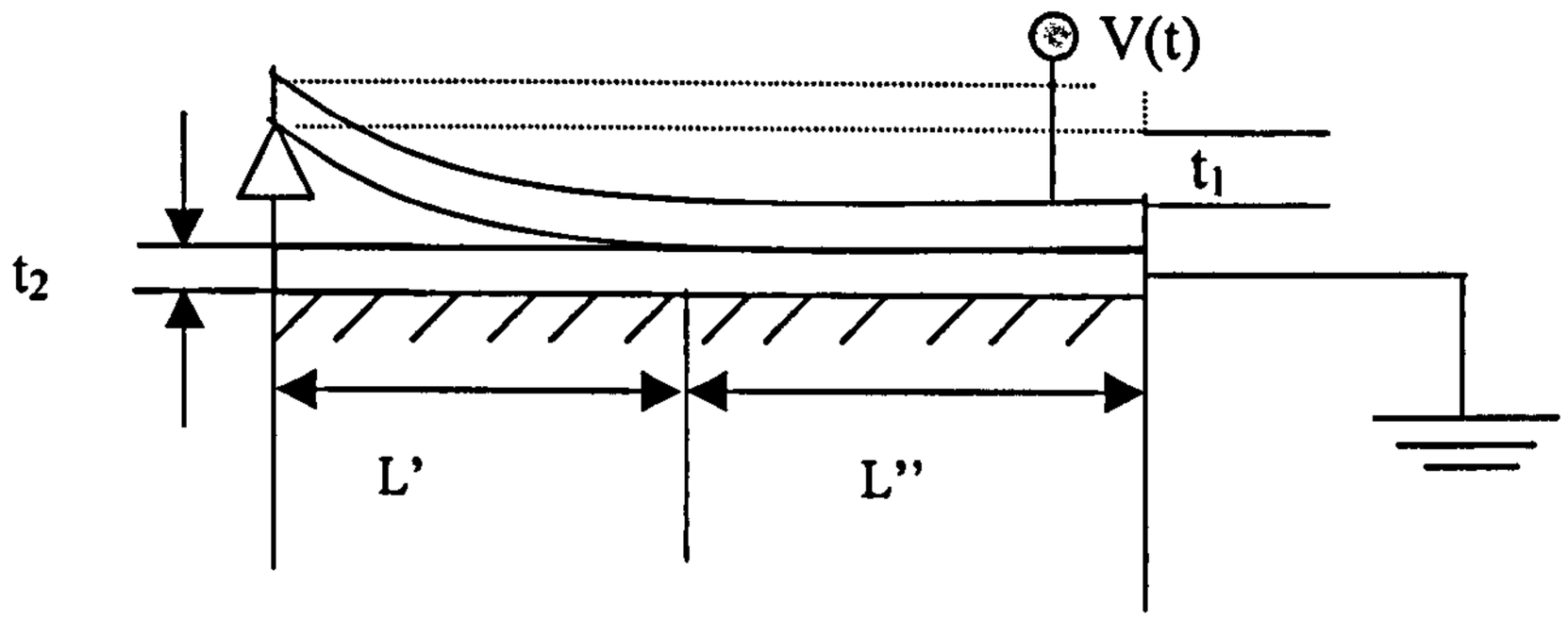

Fig. 4-19: Geometry of contact mode of the SDA plate when higher than threshold voltage is applied.

When the voltage exceeds the threshold value, the plate of the SDA will snap down, and the free end of the plate will make contact against the substrate. The geometry of the plate will thus be changed, as Fig. 4-19 shows. In Fig. 4-19, t_1 is the thickness of air gap, t_2 is the thickness of the silicon nitride, which are 1.5 μm and 0.6 μm. L'' is the contact length of the SDA plate. L' is the non-contact length of SDA plate.

A previous paper has investigated the contact mode of the SDA plate [100]. In the work, the relationship between applied voltage and contact length is calculated by the calculation step used in reference [100].

Based on the geometry of the contact mode the slope at the bushing at the point of contact, t_1/L (here, L is the length of the beam), can be substituted into a standard formula for simply supported beams.

$$\frac{t_1}{L} = \frac{1}{6LEI}\int_0^L F(x)(L-x)[L^2-(L-x)^2]dx, \qquad (4.8)$$

The electrostatic force for the contact mode is expressed as

$$F(x) = \frac{\varepsilon K_1}{2}\left[\frac{V}{t_2 + (\frac{x}{L})^2 t_1}\right]^2, \qquad (4.9)$$

substituting equation (4.9) into equation (4.8), integrating and solving equation (4.8), we can obtain equation (4.10), which determines the relationship between voltage and non-contact length L'.

$$V = \sqrt{\frac{24\ t_1^2\ EI}{\varepsilon\kappa_1 L'^4\ b}\left(\frac{2}{t_2} + \frac{1}{t_1}\ln\left(\frac{t_1 + t_2}{t_2}\right) - \frac{3}{\sqrt{t_1 t_2}}\tan^{-1}\frac{t_1}{\sqrt{t_1 t_2}}\right)^{-1}}$$

.....(4.10)

From equation (4.10), we can obtain L'' as a function of voltage:

$$L'' = L - \left(\frac{24\ t_1^2\ EI}{V^2\varepsilon k_1 b}\left(\frac{2}{t_2} + \frac{1}{t_1}\ln\left(\frac{t_1 + t_2}{t_2}\right) - \frac{3}{\sqrt{t_1 t_2}}\tan^{-1}\frac{t_1}{\sqrt{t_1 t_2}}\right)^{-1}\right)^{\frac{1}{4}}$$

.....(4.11)

From equation (4.11), we can obtain the contact length of SDA plate as a series of voltages are applied. The result is shown in Fig. 4-20. Here, the effective dielectric k_l for the nitride and air layers is different from k used in equation (4.7), because the geometry of the plate has been changed. The value of k_l is larger than k. A value of 2.7 is estimated, also following reference [100].

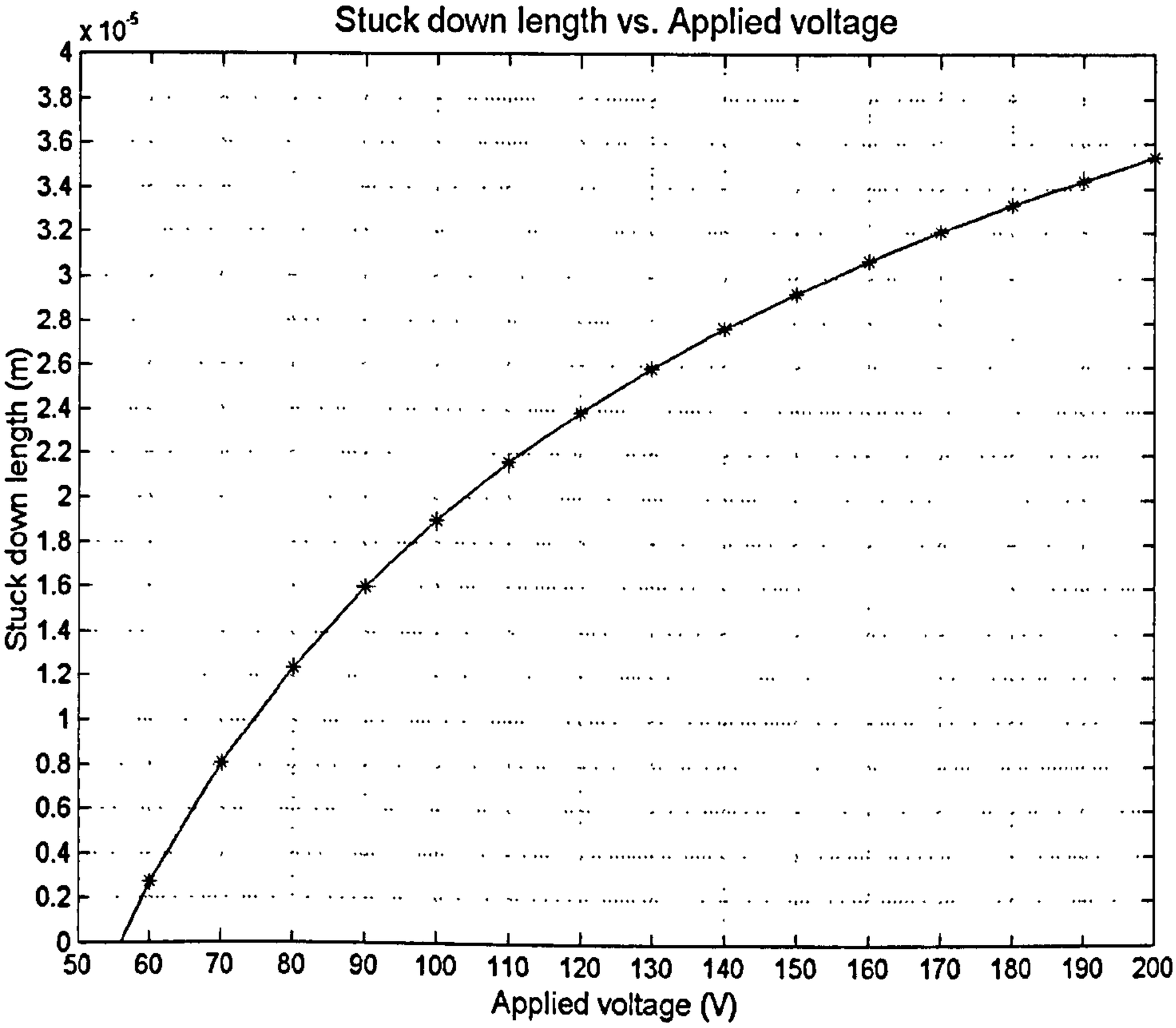

Fig. 4-20: The relationship between stuck down length and applied voltage.

4.5.1.3. Geometrical model of SDA in contact mode

In order to obtain the relationship between the SDA step size and the applied voltage, an analytical geometrical model has been built [102]. It is assumed that the angle between the bushing and plate remains constant as 90 degrees during the SDA

motion, as illustrated in Fig. 4-21. In Fig. 4-21, h is the bushing height, t is the thickness of the SDA plate, l is the contact length between SDA plate and substrate, l_1 is the rest of the plate that is non-contact, and L is the whole plate length. The calculation of the step size related to the contact length can be done with the

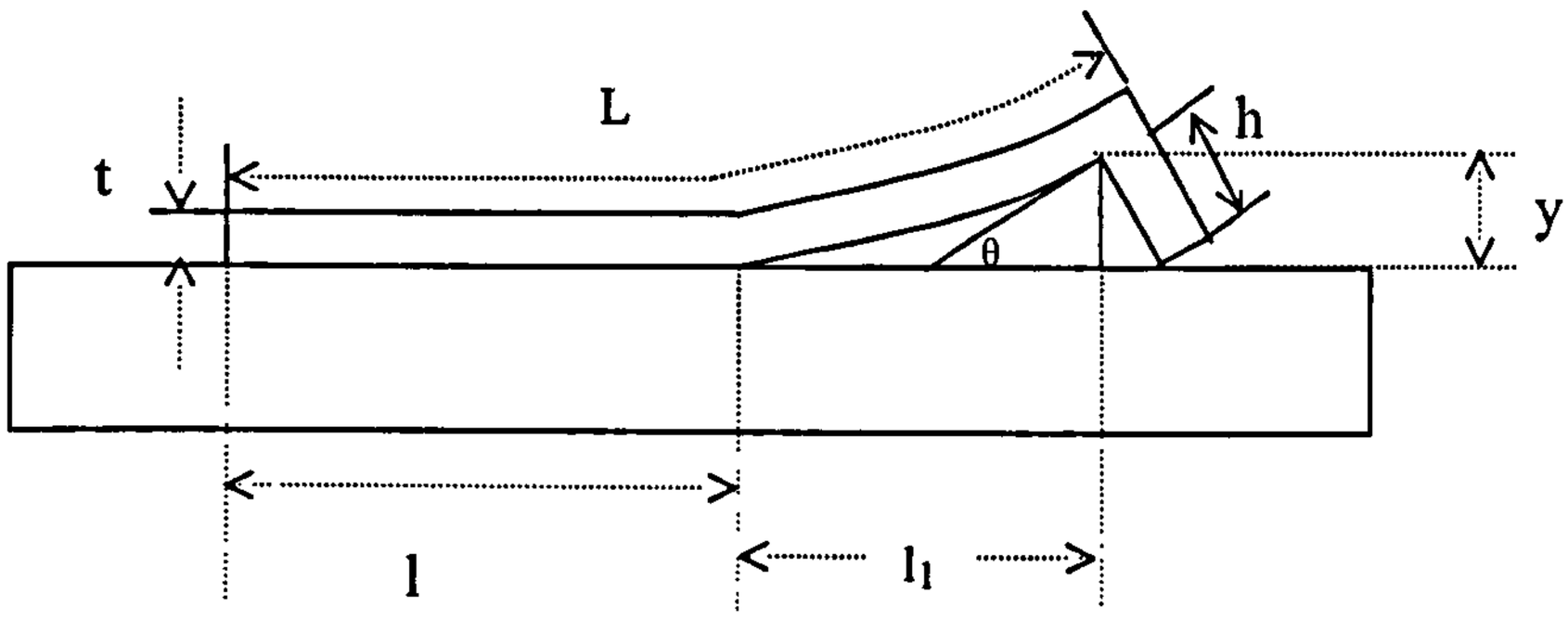

Fig. 4-21: Geometrical model of the SDA motion

following equations [102]:

$$y = h\cos\theta \tag{4.12}$$

$$\tan\ \theta\ = \frac{3\ y}{2\ l_1}\ \text{[98]} \tag{4.13}$$

$$(L - l)^2 = l_1^{\ 2} + y^2 \tag{4.14}$$

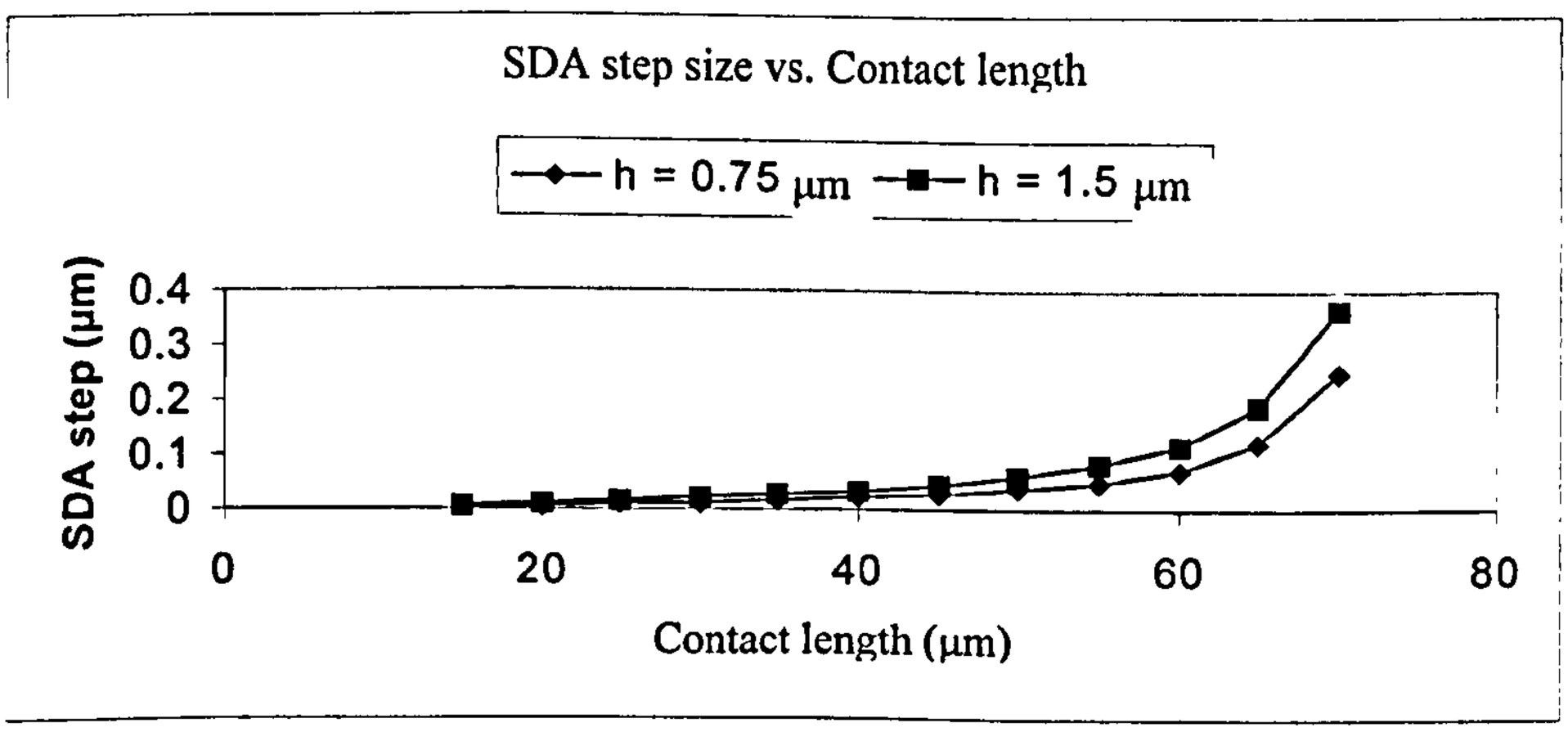

Fig. 4-22: Calculated result of the SDA step size versus distortion displacement.

The total lateral length of the SDA plate $L_t = l + l_1 + h$ *sinθ, so the step distance ΔL_t can be calculated using equations (4.12 – 4.14) above. The step size ΔL_t was calculated for an SDA plate of our design, measuring 75 μm in length and the results are shown in Fig. 4-22.

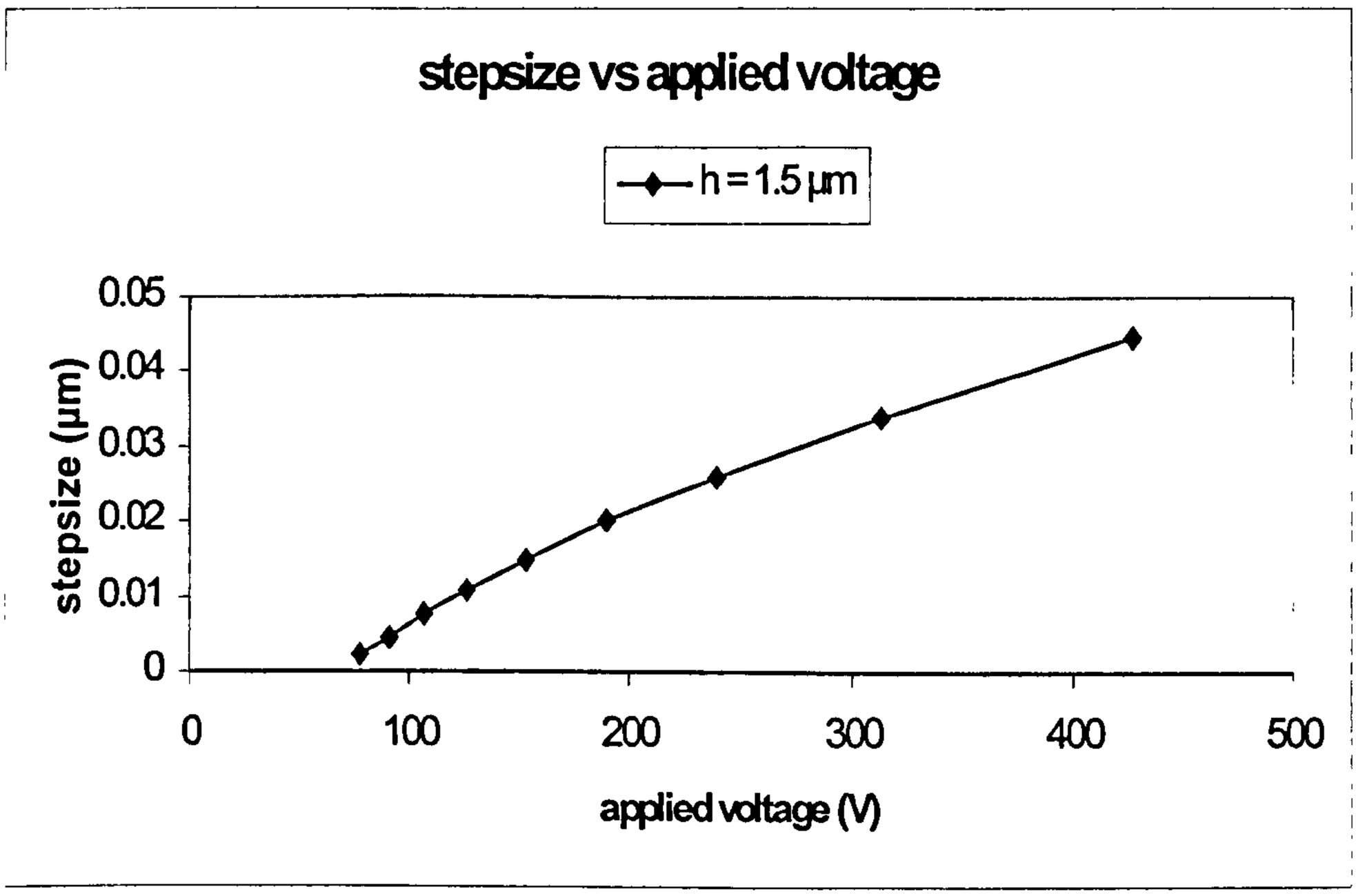

Fig. 4-23: The relationship between SDA step size and applied voltage.

From section 4.3.1.2 and 4.3.1.3, we can deduce the relationship between SDA step size and applied voltage. The plot is shown in Fig. 4-23. The SDAs have been fabricated by the PolyMUMPs process. Through laboratory testing of these SDA devices, our measurements have yielded typical step sizes varying from 7 nm at a driving voltage of 60 V to 23 nm at 290 V. These are very close to the results shown in Fig. 4-23. The discrepancy between the measured and theoretical results is put down to the fact that our analysis ignores surface friction effects between the bushing of the SDA and the substrate surface. Slippage can occur as the SDA crawls along

the surface, and it is beyond the scope of this thesis to deduce the effect of surface friction and slippage on the microactuator.

4.5.2. Simulation of SDA using IntelliSuite

IntelliSuite enables modeling of SDAs by coupled-filed analysis [103]. In our SDA, the plate length is 75 μm, and width is 65 μm. The thickness of the plate is 1.5 μm, and air gap is 2 μm. The plate is made in the second polysilicon layer (POLY2) of the PolyMUMPs fabrication process . The bushing depth is 1.5 μm. To analyse the model, a series of voltages is applied between the plate and substrate. The simulation results output from IntelliSuite are attached in the Appendix B of this thesis. In these figures, the shapes of the SDA plates bended by electrostatic voltages are shown in colormap. Fig. 4-24 shows the profile of an SDA plate that has been bent down by the application of different voltages. The data of Fig. 4-24 is obtained from IntelliSuite simulation. Table 4-1 shows the comparison between the IntelliSuite simulation and our theoretical result. It is clear that there is good agreement between the two approaches.

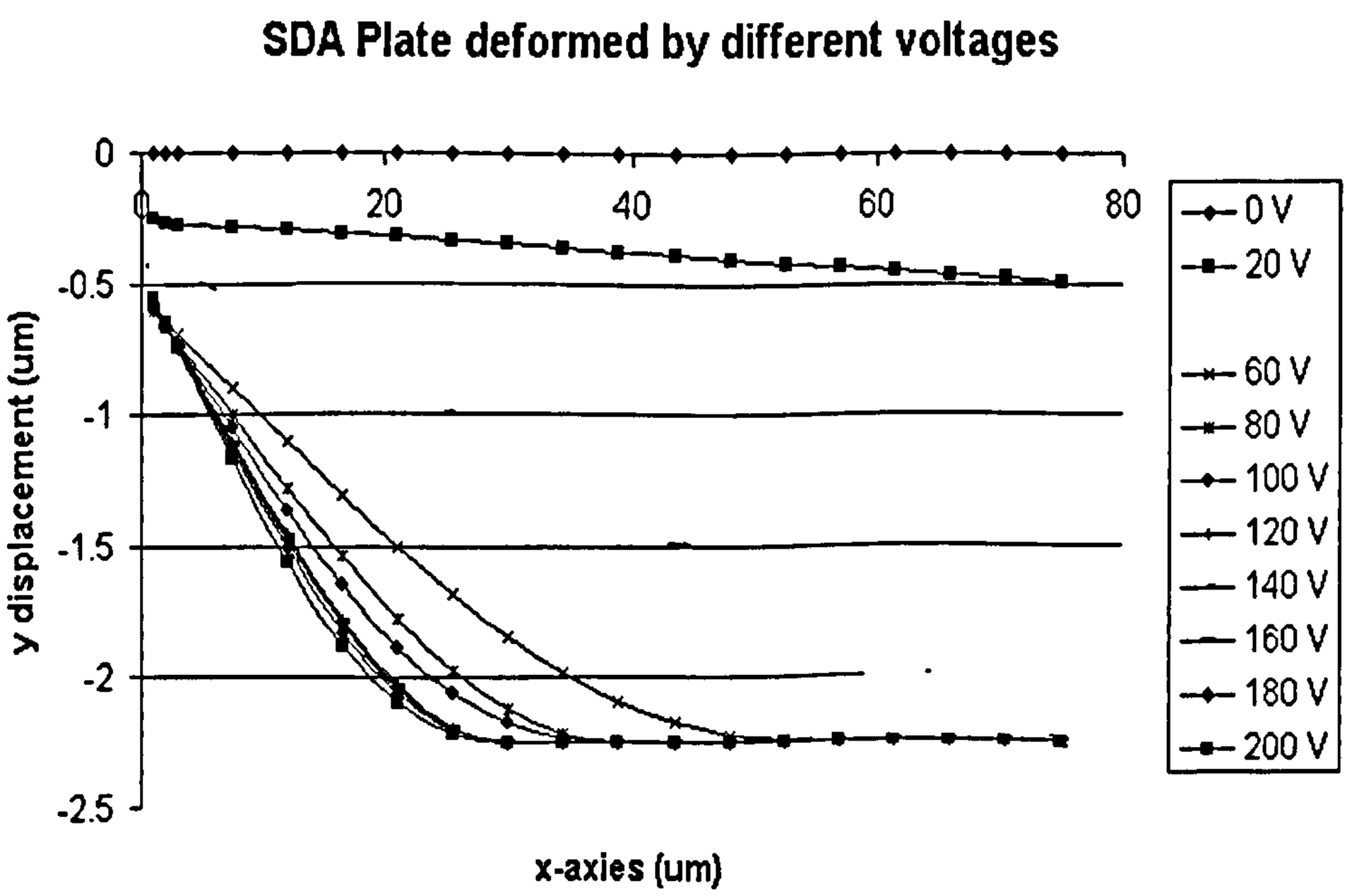

Fig. 4-24: SDA plate deformed by different electrostatic forces.
Result from IntelliSuite simulation.

Applied voltage (V)	Contact length (μm)	
	Simulation result	Theoretical calculation
60	3.5	2.8
100	21.2	19.1
140	28.8	27.9
200	34.1	33.3

Table 4-1: Results from FEM and theoretical calculation.

4.6 Experimental results of SDA plate bending

In addition to the theoretical analysis and simulation, we have conducted experiments on the SDA microactuators using a non-contact surface profiling tool based on broadband optical interferometery (Veeco NT1000 surface profiling tool). Figs. 4-25 (a) – (d) are three-dimensional renderings showing the actual flexing of our SDA plates when different DC voltages are applied.

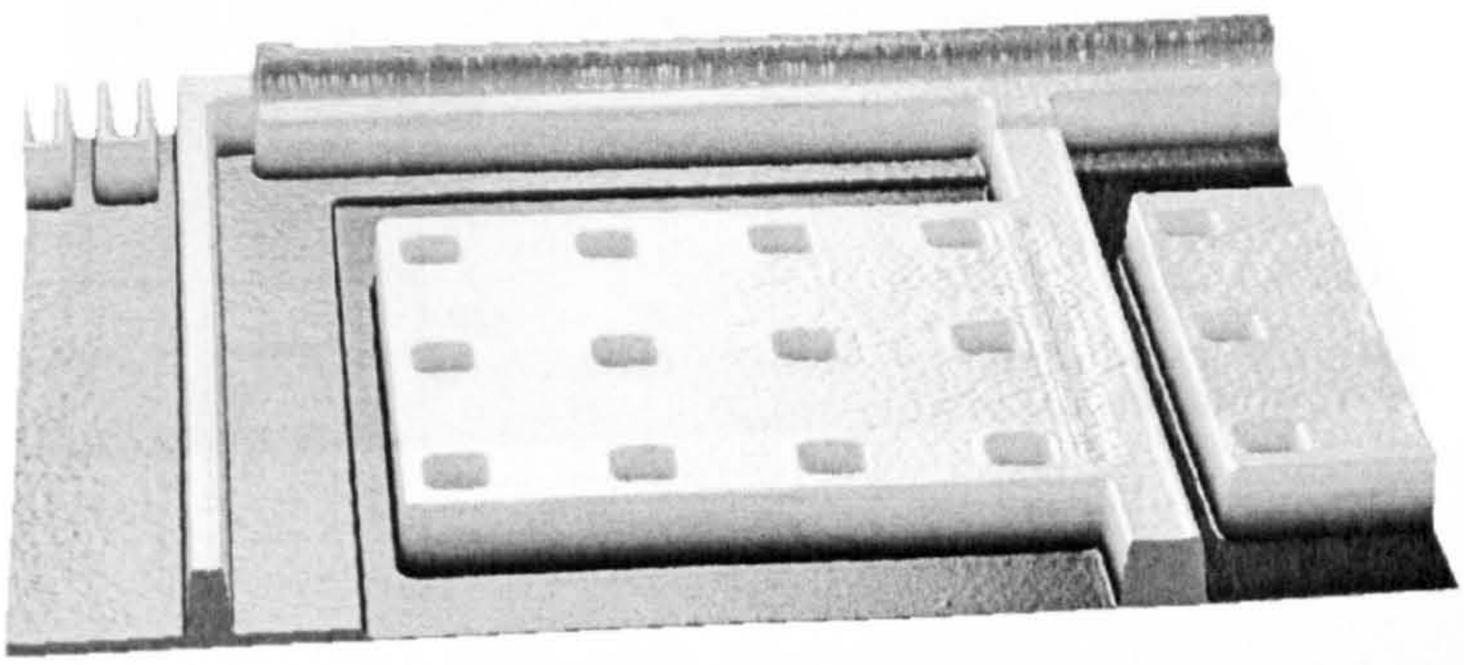

Fig. 4-25 (a): SDA plate imaged by optical surface profiler, driven by 0 V.

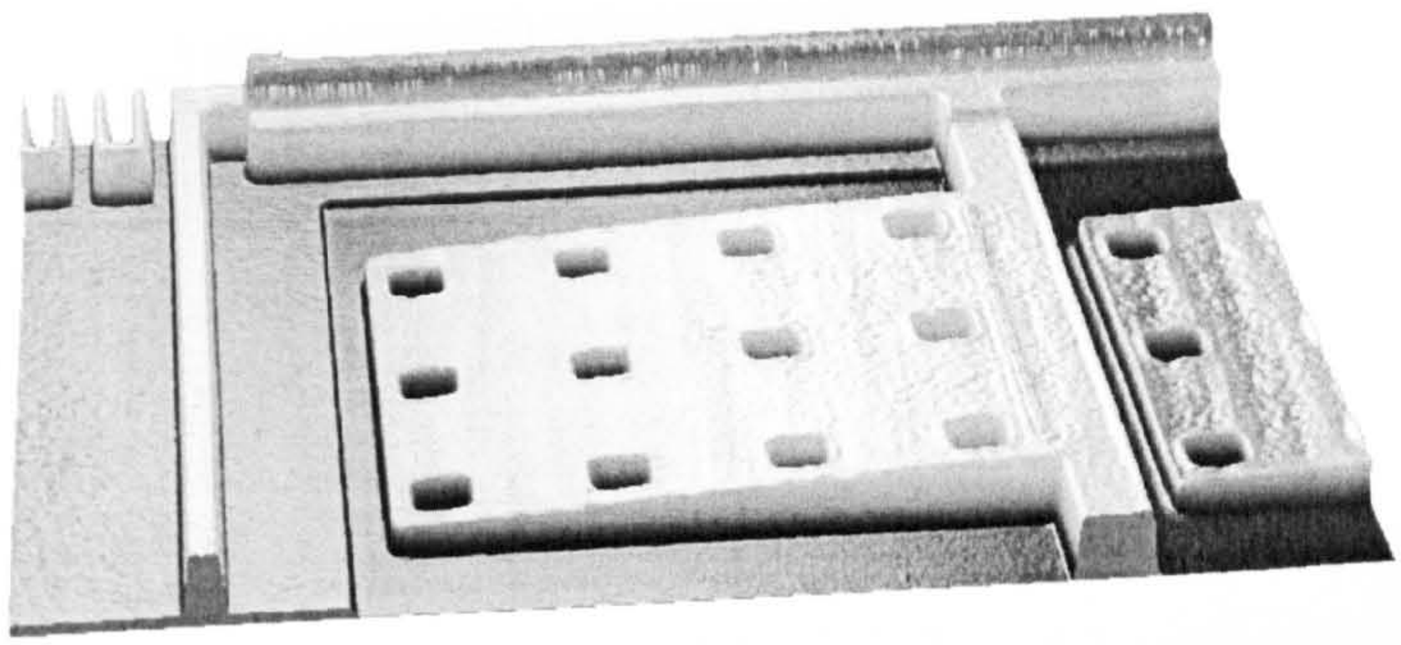

Fig. 4-25 (b): SDA plate imaged by optical surface profiler, driven by 60 V.

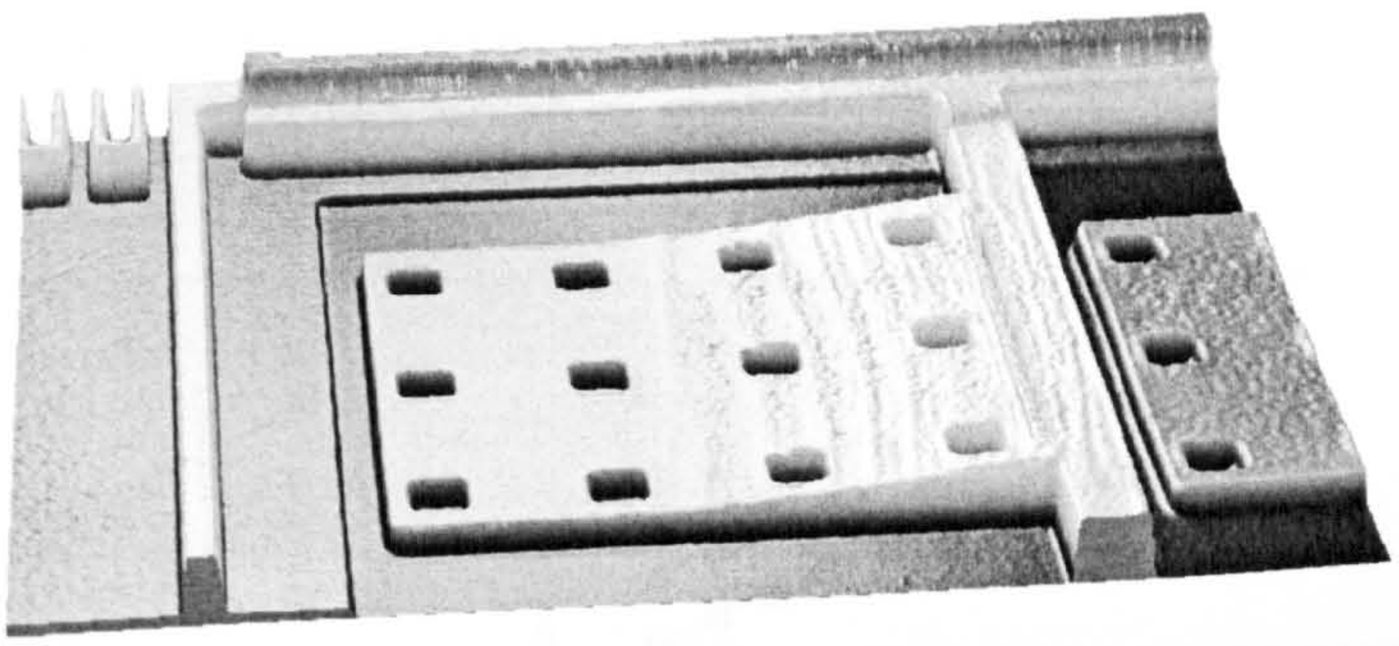

Fig. 4-25 (c): SDA plate imaged by optical surface profiler, driven by 120 V.

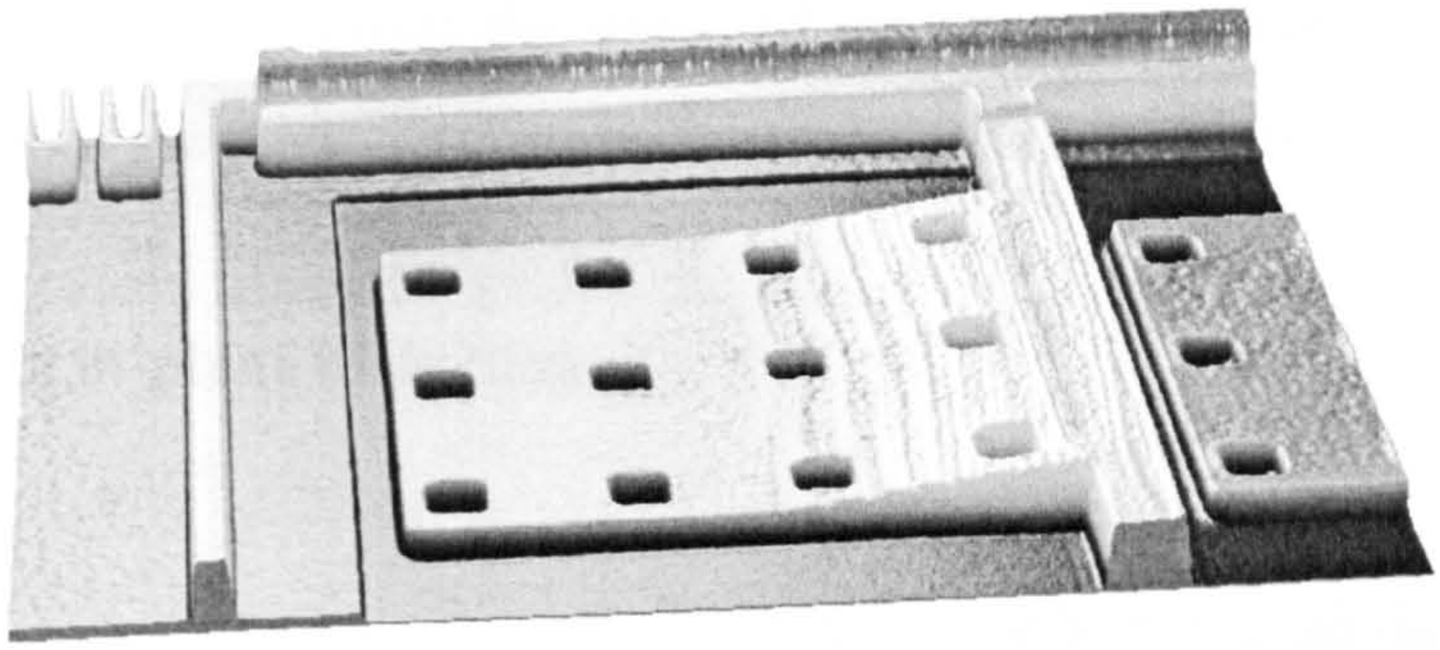

Fig. 4-25 (d): SDA plate imaged by optical surface profiler, driven by 200 V.

The equipment can also display a cross-section showing the profile of the bent plate, from which measurements of contact length can be made. Using these data, a result comparing the theoretical and experimental findings is shown in Fig. 4-26. From Fig. 4-26, the theoretical results are seen to be in close agreement to the experimental results, under the assumptions made earlier.

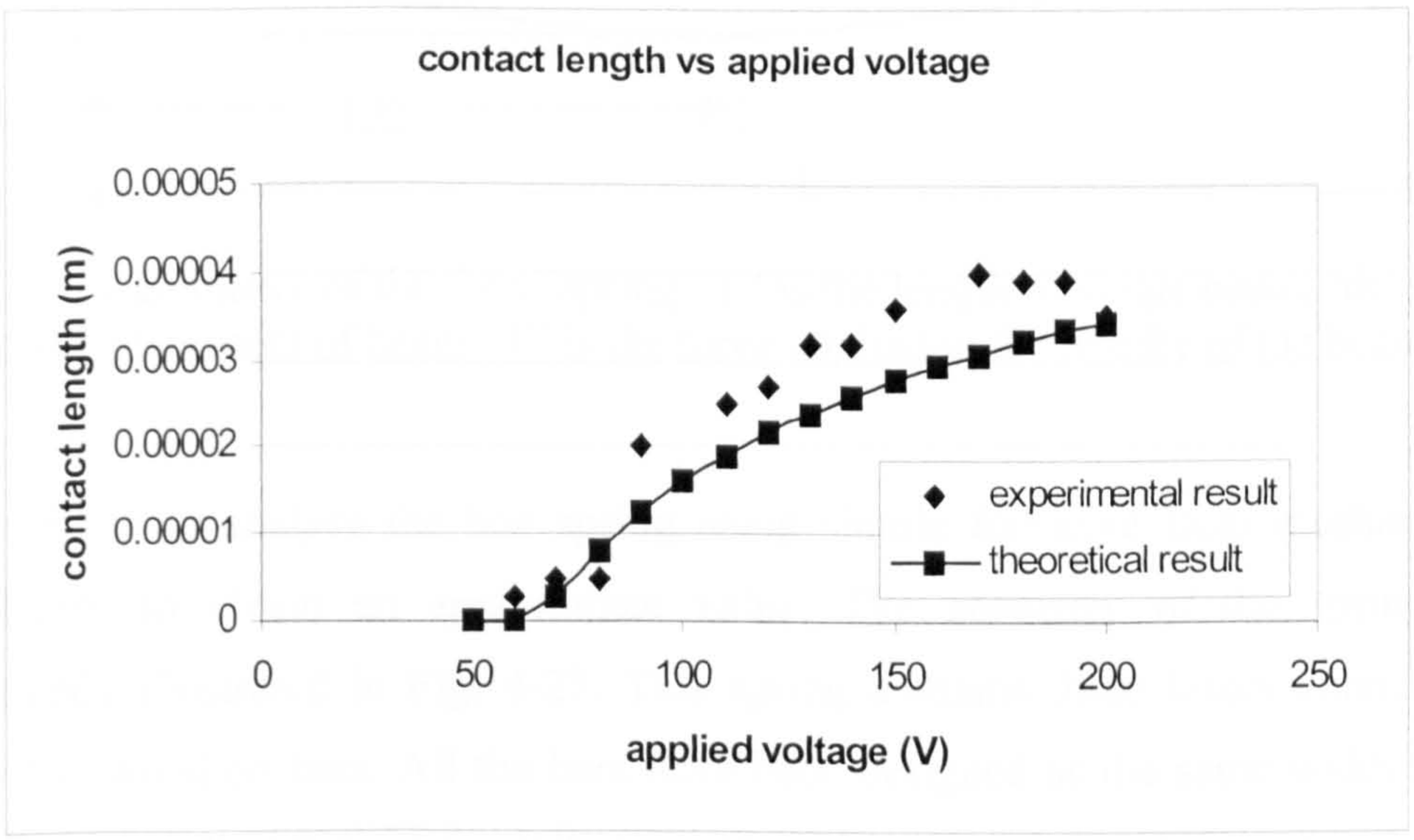

Fig. 4-26: The relationship between contact length and applied voltage.

4.7 Microspring analysis

The analysis of microspring is performed to calculate the spring constant using both formula and FEM method. From the value of the spring constant, we are able to calculate the force of the microactuator by measuring its extension.

4.7.1 'Box' spring in-plane distortion

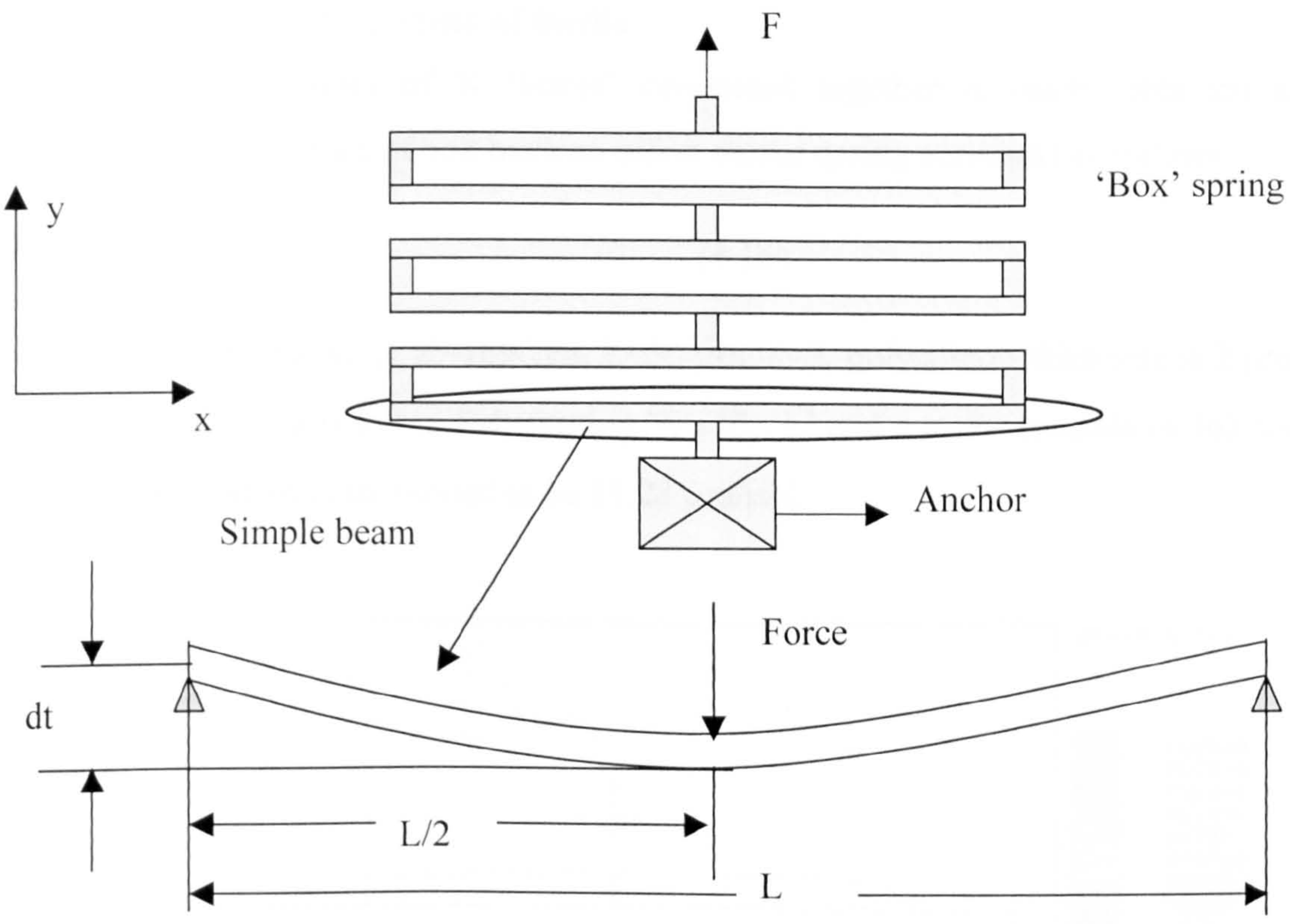

Fig. 4-27. The geometry of the 'box' spring. 'L' is the length of single beam, 'dt' is the maximum displacement of beam. 'F' is the force applied to the middle of the beam.

We first begin to analyse the box spring using simple formulae from mechanical beam theory to obtain an approximate value. The geometry of the spring is schematically illustrated in Fig. 4-27. This spring contains three boxes connected together by two short bars. All the bars have been designed as the same width. We call each box a cell. All the three cells are of the same structure and we only need to analyse one of these cells. From the Figure, one cell contains four mechanical beams,

two short beams and two long beams. The force is applied in the y direction and we assume that the two short beams cannot stretch in the y direction. Selecting one of two long beams, centre loaded clamped beam theory can be used to calculate the displacement in this case. The centre displacement of the clamped-clamped beam under centre loading is [98]:

$$dt = \frac{FL^3}{192EI} \tag{4.15}$$

Where, 'dt' is the displacement at centre position in the y-axis, 'F' is the force applied to the centre of the beam, 'L' is the length of the beam, 'E' is the Young's Modulus, and 'I' is the moment of inertia.

So the spring constant of N 'boxes' connected together is easily obtained as (assuming the short bars of box have no effect on the spring constant) as follows:

$$k = \frac{96EI}{nL^3} \tag{4.16}$$

We assume the following: E=169GPa, L=50 μm, n=3, polysilicon thickness is 2 μm, width of polysilicon is 2 μm. Substituting 'E', 'I', 'L' and n to the formula (4.16), the box spring constant is calculated to be 51.28 μm/μN.

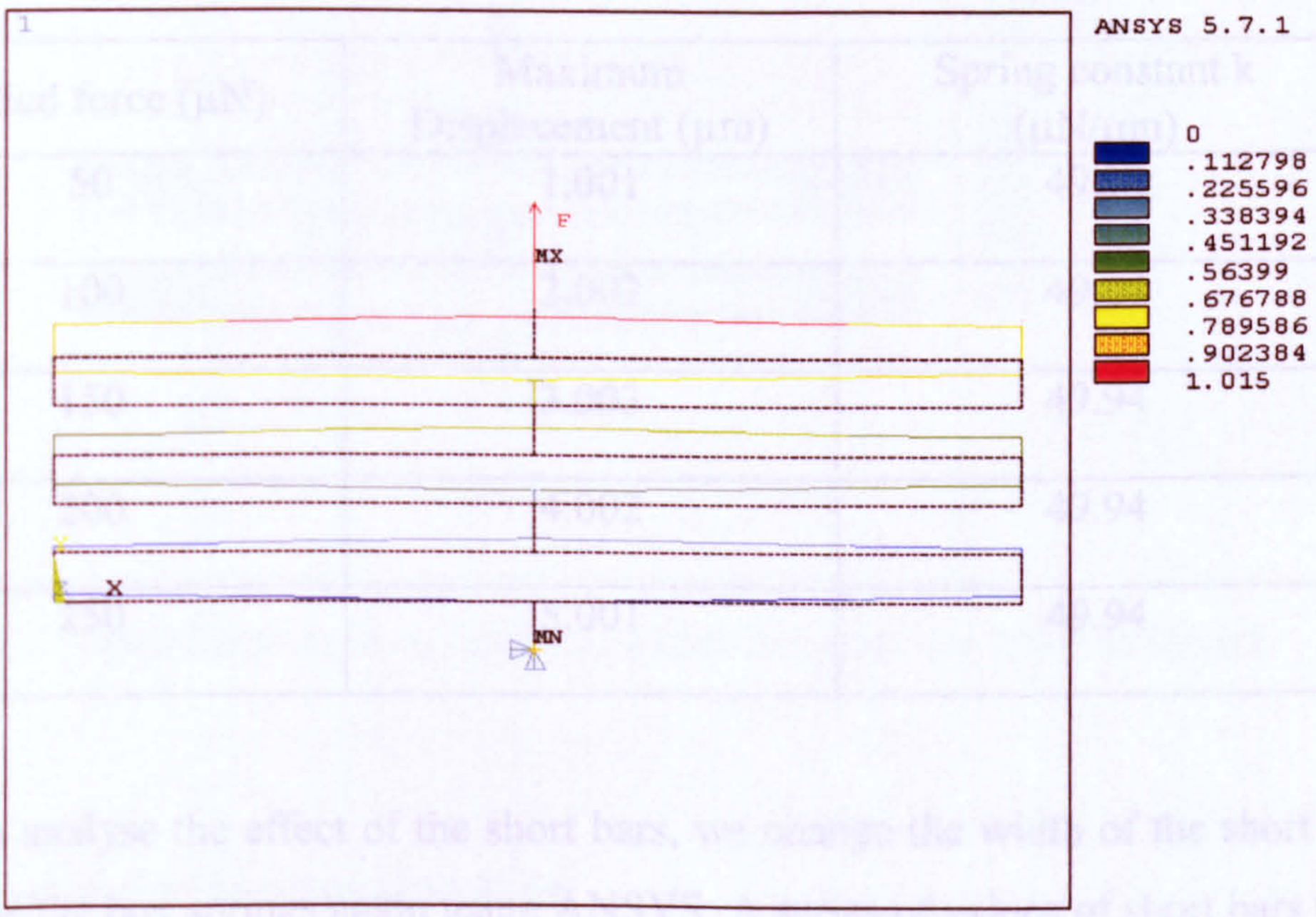

Fig. 4-28. Result from ANSYS software, the numbers in the right of the figure represent the nodes displacement in y direction. The unit is micron.

Next we build a beam model of the spring using ANSYS finite-element package (version 5.7.1). The model of the spring structure is described here. We consider a spring made from polysilicon. All the polysilicon bars have the same width and depth. The dimension of the spring is as follows: the length of the polysilicon box is 50 um, the width of the polysilicon box is 2 um and the thickness of the polysilicon layer is 2 um. The thickness is the same value as normally obtained from the PolyMUMPs process. In this model, the Young's Modulus of polysilicon is 169 GPa, again as obtained from the PolyMUMPs process. One end of the spring is fixed and a force is applied to the other end of spring at its centre. The ANSYS static analysis can directly calculate the displacement of the centre corresponding to an applied force, then the formula $k = \frac{F}{x}$ is used to calculate the spring constant k. The spring constant k of this spring is shown in table 4-2 where a series of forces are separately applied to the box spring. One of the results of the spring distortion under a force is shown in Fig. 4-28. From Table 4-2, we can see that the theoretical approximations and ANSYS results are close in value.

TABLE 4-2. Results of 'box' spring constant k using ANSYS static analysis

Applied force (μN)	Maximum Displacement (μm)	Spring constant k (μN/μm)
50	1.001	49.94
100	2.002	49.94
150	3.003	49.94
200	4.002	49.94
250	5.001	49.94

In order to analyse the effect of the short bars, we change the width of the short bar and analyse the box springs again using ANSYS. A series of values of short bars that were analysed is shown in Table 4-3. One of ANSYS results is shown in Fig. 4-29.

TABLE 4-3. Results of different wide of bars

Short bar width (μm)	Maximum Displacement (μm) (force is 50 μN)	Spring constant k (μN/μm)
2	1.015	49.26
3	0.971662	51.46
4	0.954371	52.39
5	0.951012	52.58
10	0.950474	52.61
20	0.950477	52.61

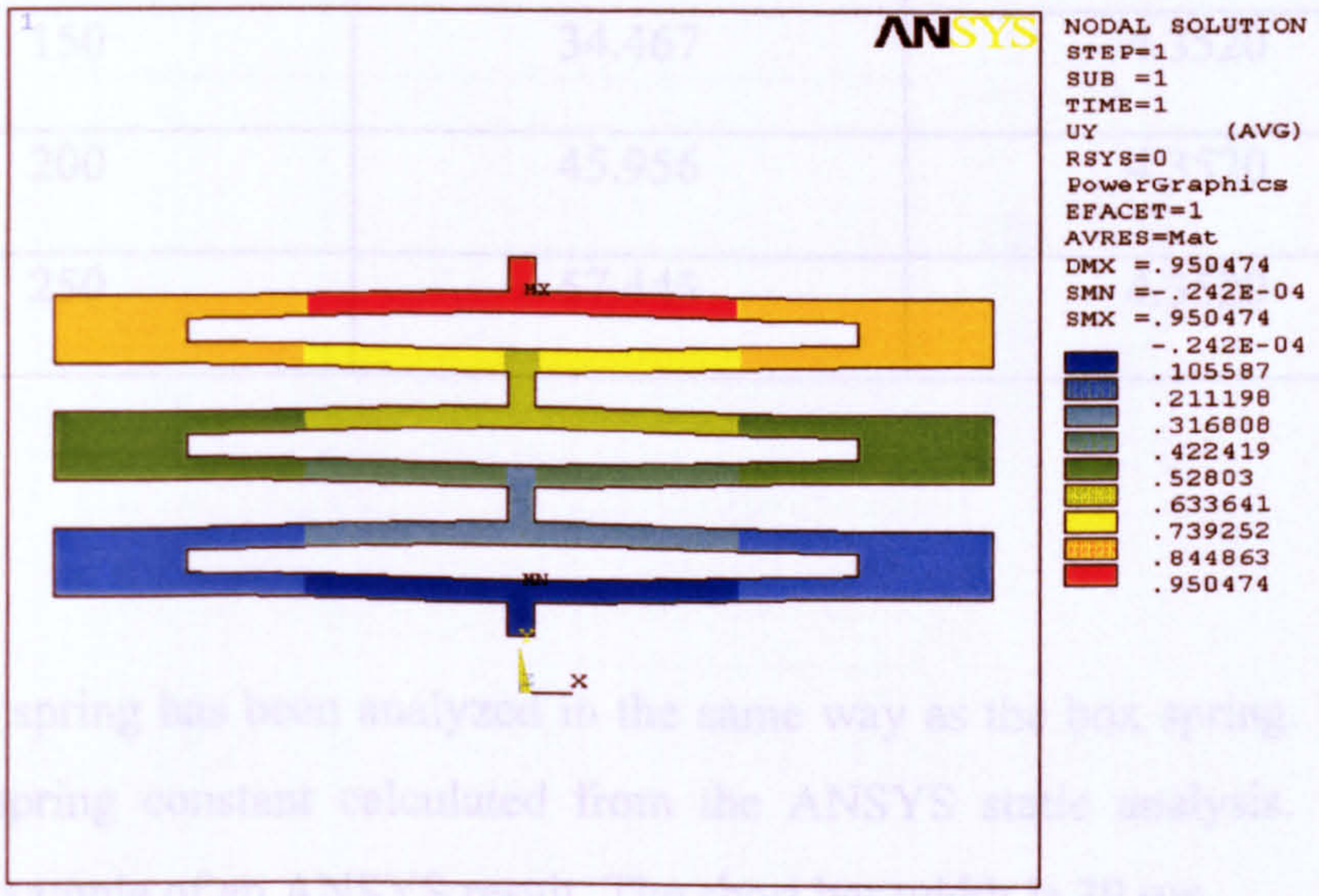

Fig. 4-29. One of results from ANSYS, where the short bar width is 10 μm.

4.7.2 'zig-zag' spring in-plane distortion

Another spring that has been analysed is called 'zig-zag' spring. This type of spring contains a numbers of bars connected in a 'zig-zag' path. A beam model has been constructed for analysing in ANSYS software. In this model, one end of this spring is fixed and at the other end a series of forces are applied and a series of displacement results are obtained as shown in Table 4-4. The spring constant k is calculated as before. The force direction is along the y-axis as shown in Fig. 4-30. It is noticed that together with the extension in the y-direction, there is a small distortion of the structure in the x-direction. The unbalance of the spring appears in Fig. 4-31. The reason is the short bar between two long bars also bends when the force is applied.

TABLE 4-4. Results of 'zig-zag' spring constant k using ANSYS static analysis

Applied force (μN)	Maximum Displacement (μm)	Spring constant k (μN/μm)
50	11.489	4.3520
100	22.978	4.3520
150	34.467	4.3520
200	45.956	4.3520
250	57.445	4.3520

The zig-zag spring has been analyzed in the same way as the box spring. Table 4-5 shows the spring constant calculated from the ANSYS static analysis. Fig. 4-32 shows one example of an ANSYS result. The short bar width is 20 μm.

Fig. 4-30. ANSYS analysis of 'zig-zag' spring, the force F_y=50μN. The result shows the y-axis displacement. The numbers (μm) on the left of the figure represented the displacement value.

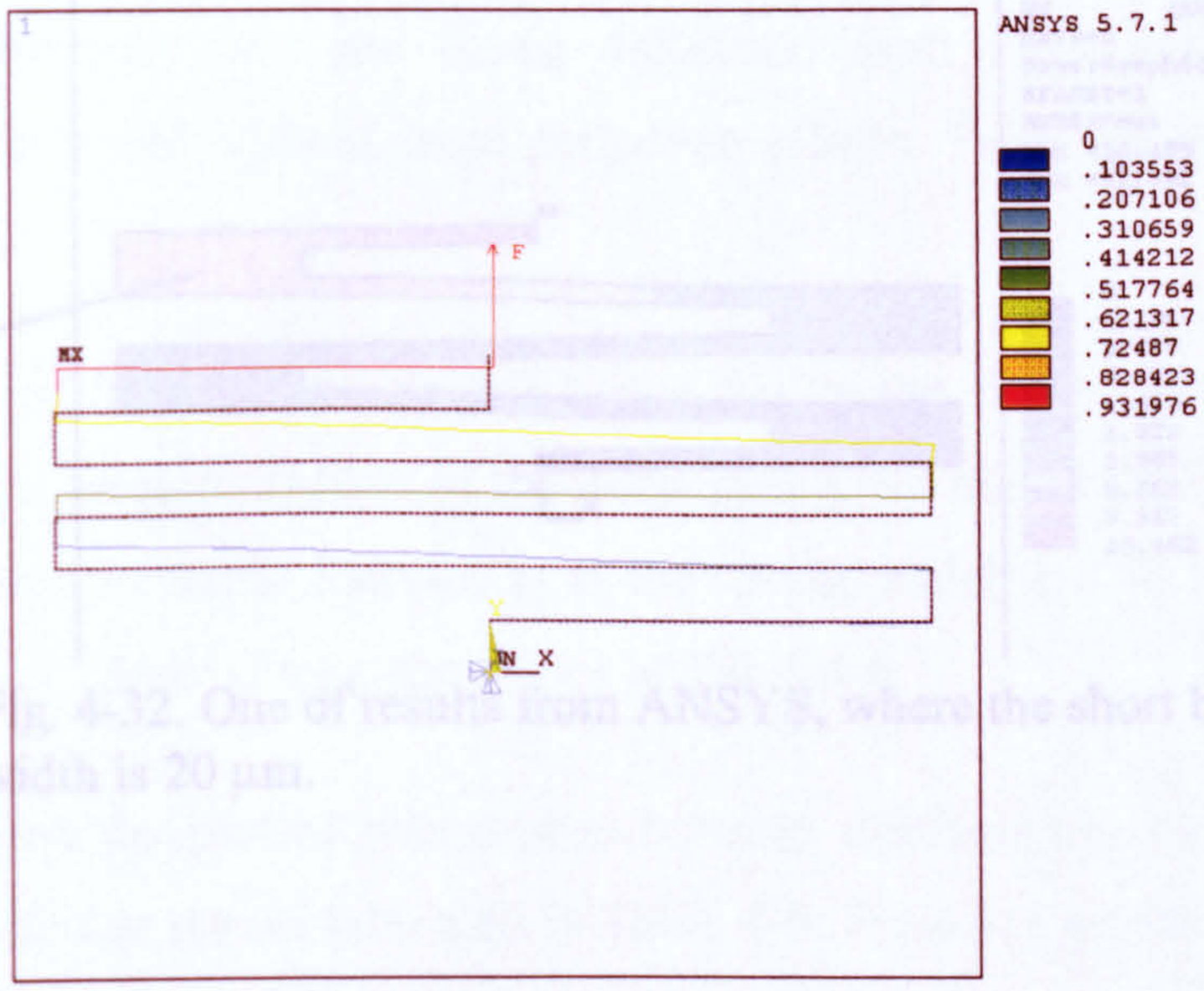

Fig. 4-31. ANSYS analysis of 'zig-zag' spring, the force F_y=50μN. The result shows the x-axis displacement. The numbers (μm) on the left of the figure represented the displacement value.

TABLE 4-5. Results of different width of bars for zig-zag spring

Short bar width (um)	Maximum Displacement (μm) (force is 50 uN)	Spring constant k (μN/μm)
5 um	10.504	4.76
10 um	10.482	4.77
20 um	10.482	4.77

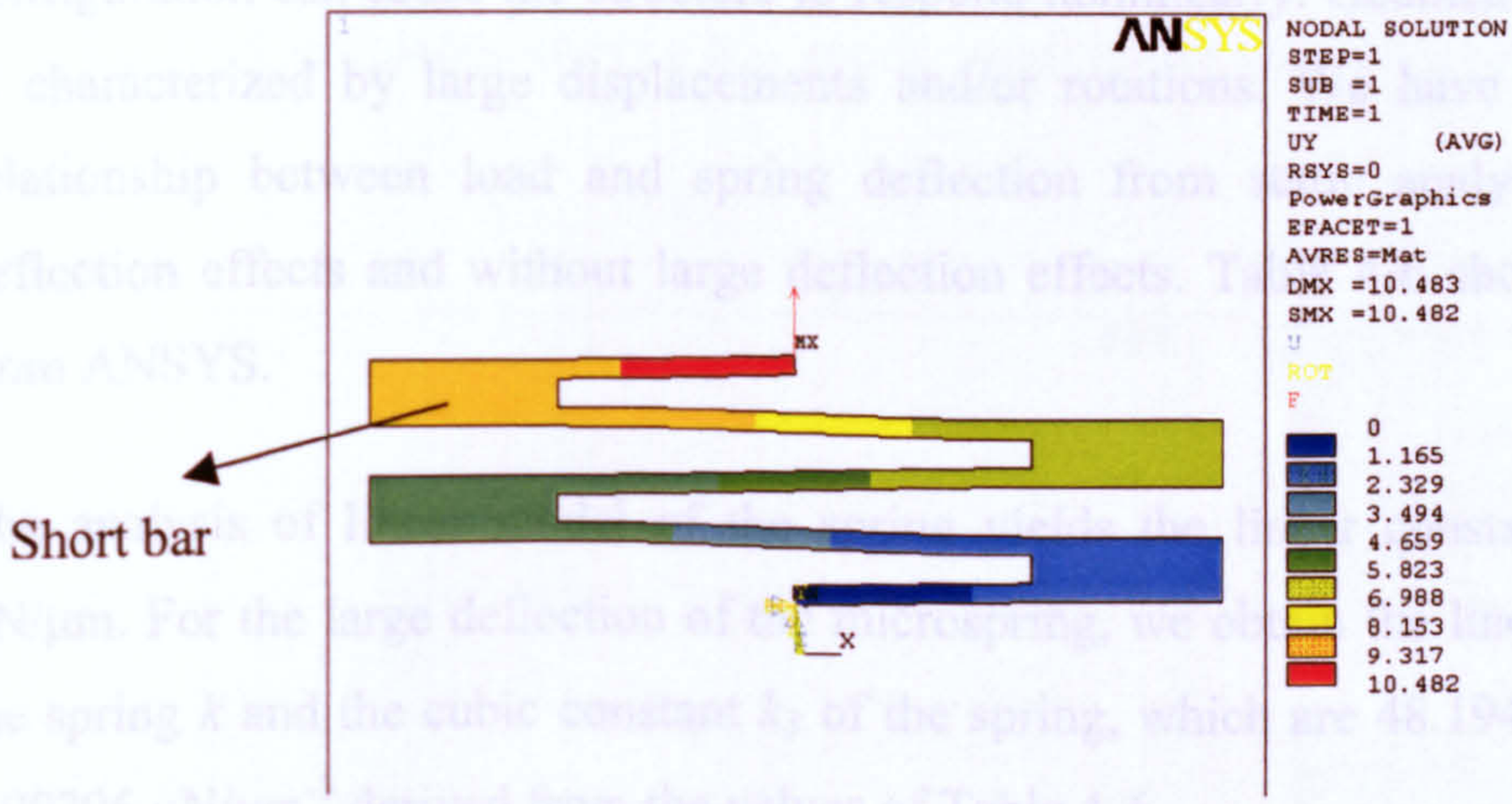

Fig. 4-32. One of results from ANSYS, where the short bar width is 20 μm.

4.7.3 Nonlinear analysis of the box spring

Two types of microsprings have been analysed by FEM using ANSYS. Box spring has been selected to measure the force of SDA. Nonlinearity has to be considered.

Here, FEM large deformation analysis has been performed for obtaining the deflection under large loading.

In the large deflection case of elastic beams, the Duffing equation [104] can explain the relationship between the load and spring distortion. When taking account of large deflections, the elastic restoring force can be simply modeled as the sum of a linear term and a cubic term of x, x being the displacement of the spring. The spring restoring force F is,

$$F = - kx - k_3 x^3 \quad \text{.....(4.17)}$$

where k and k_3 are the linear and cubic elastic constants of the spring.

The FEM simulations were performed in order to obtain the linear spring constant k and cubic spring constant k_3. These simulations were performed with the ANSYS large deformation option. In the large deformations option, its changing geometric configuration can cause the structure to respond nonlinearly. Geometric nonlinearity is characterized by large displacements and/or rotations. We have compared the relationship between load and spring deflection from static analysis with large deflection effects and without large deflection effects. Table 4-6 shows the results from ANSYS.

The analysis of linear model of the spring yields the linear constant k as 49.94 μN/μm. For the large deflection of the microspring, we obtain the linear constant of the spring k and the cubic constant k_3 of the spring, which are 48.1948 μN/μm, and 0.00296 $\mu N/\mu m^{-3}$ derived from the values of Table 4-6.

Fig. 4-33 shows the plotted relationship between displacement and load using the linear and nonlinear results tabulated in Table 4-6. From the results, we can see that when the applied load is below 1000 μN, the nonlinear effect is not significant in this box-spring. Fig. 4-34 shows one of the results from ANSYS nonlinear simulation of the box spring.

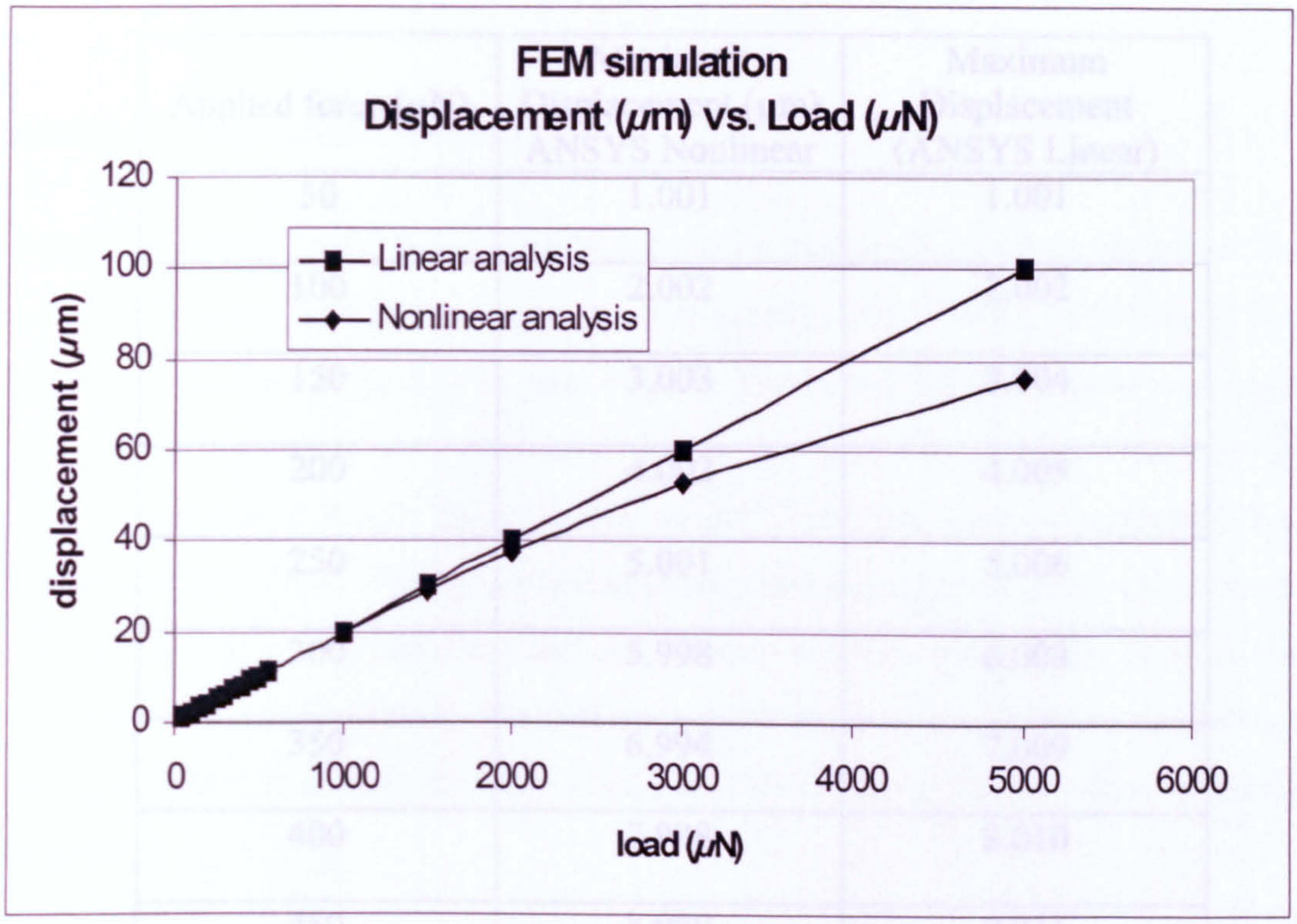

Fig. 4-33: FEM simulation about a box spring using Linear and Nonlinear analysis.

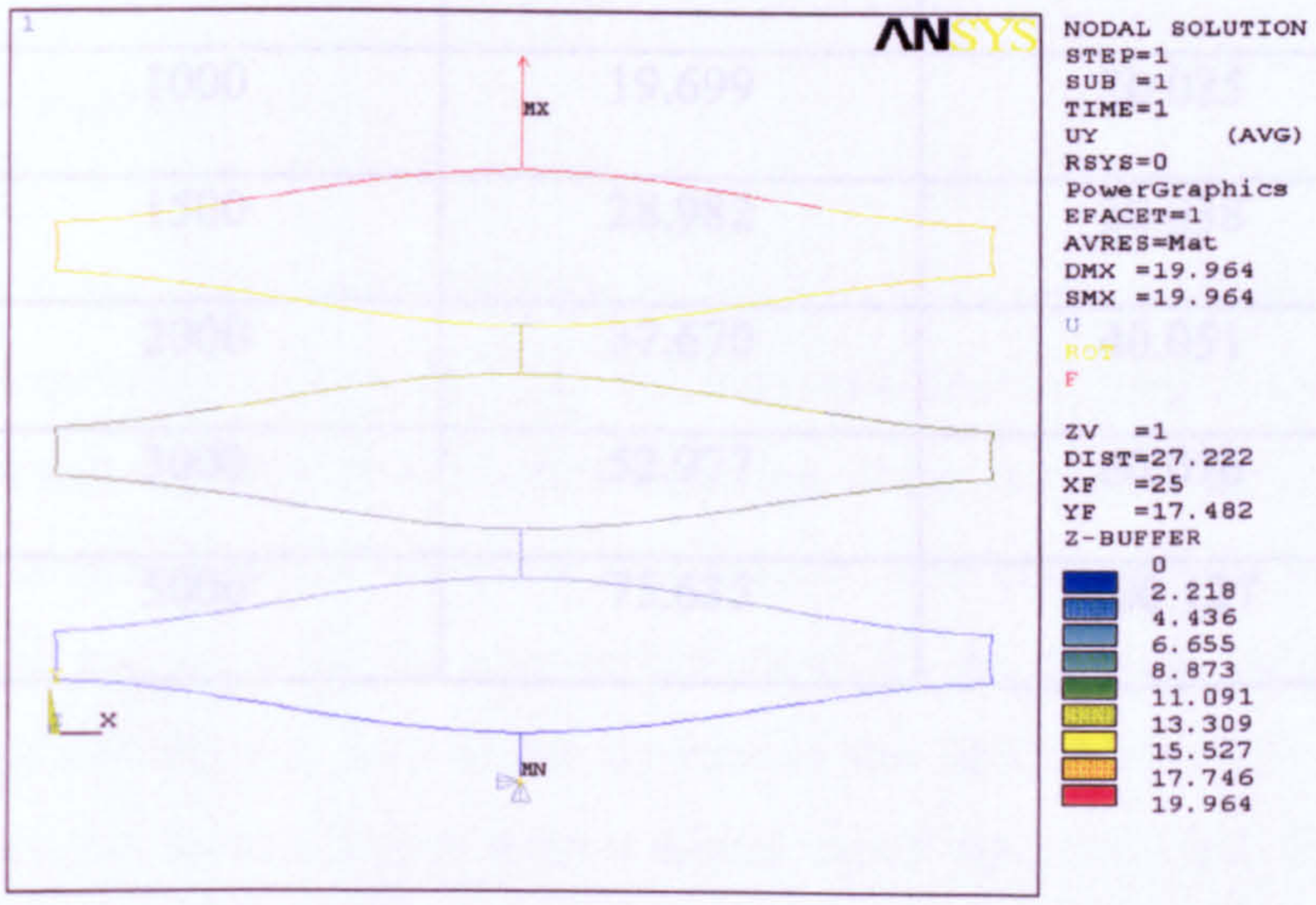

Fig. 4-34: Picture of nonlinear analysis of micro polysilicon box spring using FEM packaging ANSYS.

Applied force (μN)	Maximum Displacement (μm) ANSYS Nonlinear	Maximum Displacement (ANSYS Linear)
50	1.001	1.001
100	2.002	2.002
150	3.003	3.004
200	4.002	4.005
250	5.001	5.006
300	5.998	6.008
350	6.994	7.009
400	7.998	8.010
450	8.980	9.011
500	9.970	10.013
550	10.958	11.014
1000	19.699	20.025
1500	28.982	30.038
2000	37.670	40.051
3000	52.977	60.076
5000	75.635	100.127

TABLE 4-6. Load and deflection relation with nonlinear analysis and linear analysis.

4.8 Force measurement of SDA

Forces generated by SDAs have previously been measured [19] by a technique using a buckling beam. The SDA is connected to a beam that buckles out of the plane of the silicon surface as the SDA exerts a force. The buckled beam acts as a spring and its vertical displacement is measured. In another publication, the optimized SDA plate length for a single SDA versus output force has been investigated by R. Linderman et al [105]. We have experimentally investigated the relationship between applied voltage and output force and relationship between the number of SDA plates and output force with the same type of spring. We have concentrated on modeling the spring constant accurately in order to obtain precise results, as described in previous section.

In terms of modelling of these springs the spring constant can be controlled by adjusting the dimensions and geometry of the springs. The box-spring has been used in our work.

4.8.1 Experiment set up

The set up of the experiment is shown in Fig. 4-35. Devices were put onto the x-y moveable stage of the microscope. On top of the microscope, there is a digital camera mounted, which can capture the detailed motion of the devices. The camera has the ports to be connected to the computer and monitor. The frame rate of the camera can be controlled and set to be the appropriate value for the testing. Two probes were employed to connect the pads of the devices to the BNC wires. The signal that is used to drive the devices comes from a digital signal generator, and then was input into the amplifier. After amplification, the signal plus DC bias was applied to the devices. The output signal was monitored by the oscilloscope.

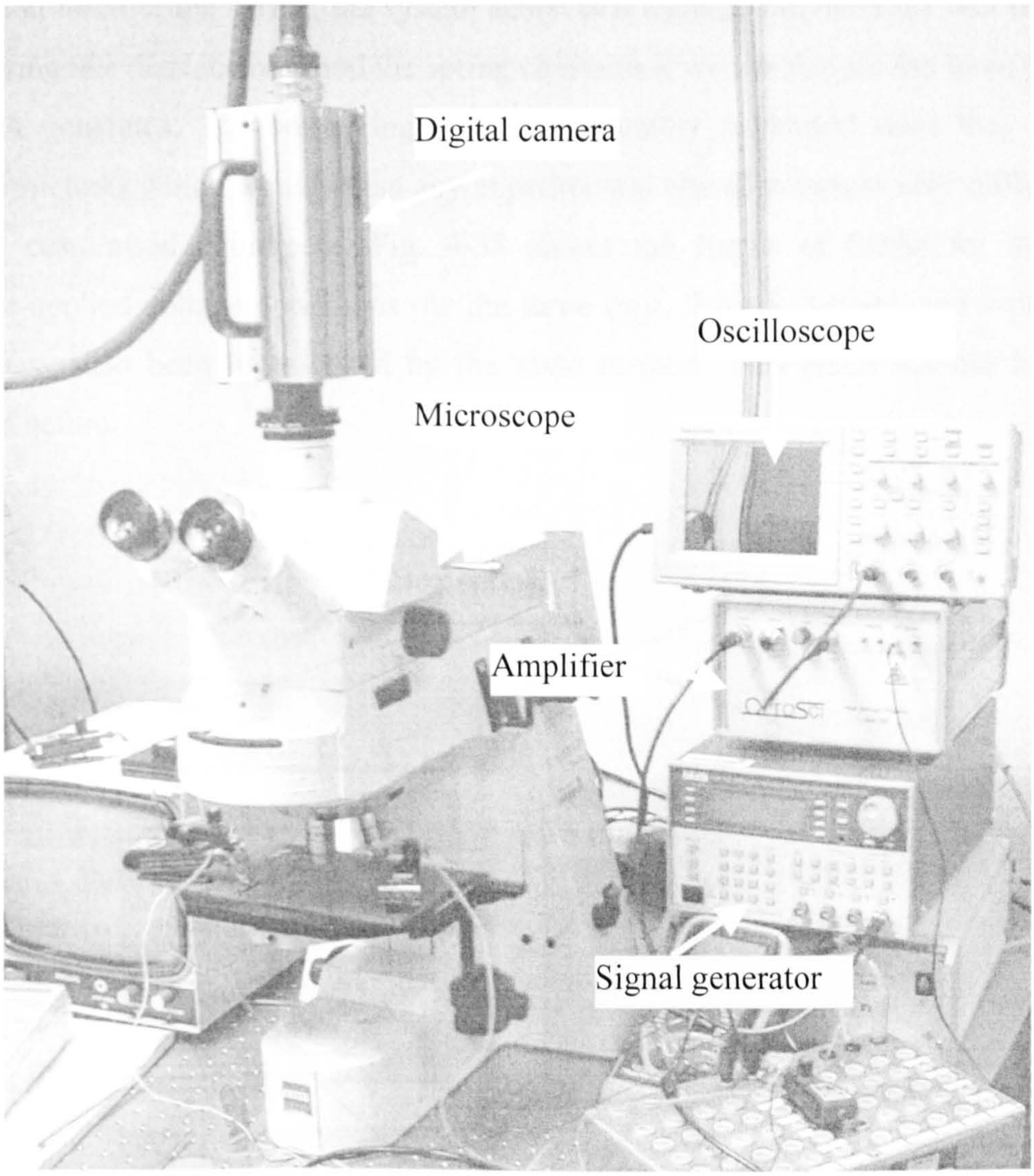

Fig. 4-35. Experimental set up for testing the SDA.

4.8.2 Experimental results of SDA force

For our experiments, four different designs of spring-loaded SDAs have been fabricated in PolyMUMPs run 44. They have from 1 to 4 plates with two box-springs as shown in Fig. 4-36. In this picture, the small comb is the scale for measuring the displacement of the SDA. Different peak voltages from 100-200V have been applied

to the SDA. The driving frequency is constant and has a value of 100Hz. When voltage is applied to the electrode, the SDA moves forward and stretches the spring. The stretch can be measured from the scale. Once the force of the SDA equals the restoration force of the spring, the system achieves a balance and the SDA will stop. Thus, using this displacement and the spring constants k we can deduce the force that the SDA generates. The box-springs are not separately calibrated since they are planar structures which would make any experimental characterization very difficult without customised equipment. Fig. 4-38 shows the forces of SDAs for three different applied voltage conditions. At the same time, 2-plate, 3-plate, and 4-plate SDAs have also been investigated by the same method. This result has not been reported before.

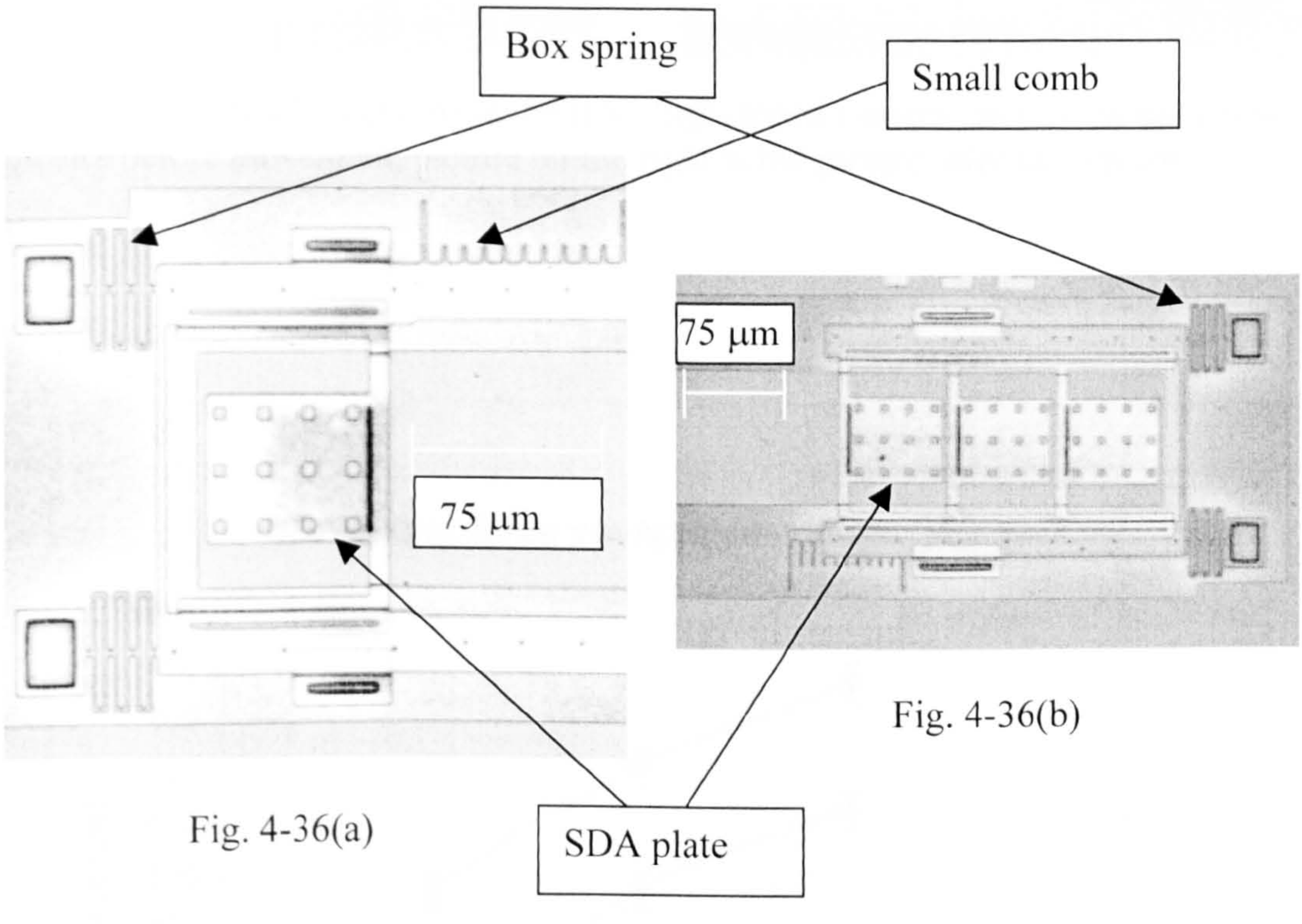

Fig. 4-36(a)

Fig. 4-36(b)

Fig. 4-36: Photographs of scratch drive actuator with box-spring. Fig. 10(a) is one-plate SDA and Fig. 10(b) is three-plate SDA.

We designed a set of the comb finger scales attached to the moving part and fixed part in order to clearly see the distance that the devices traveled. In Fig. 4-37, the

picture on the left is the picture before the actuator has moved, and on the right is the picture after the actuator has moved.

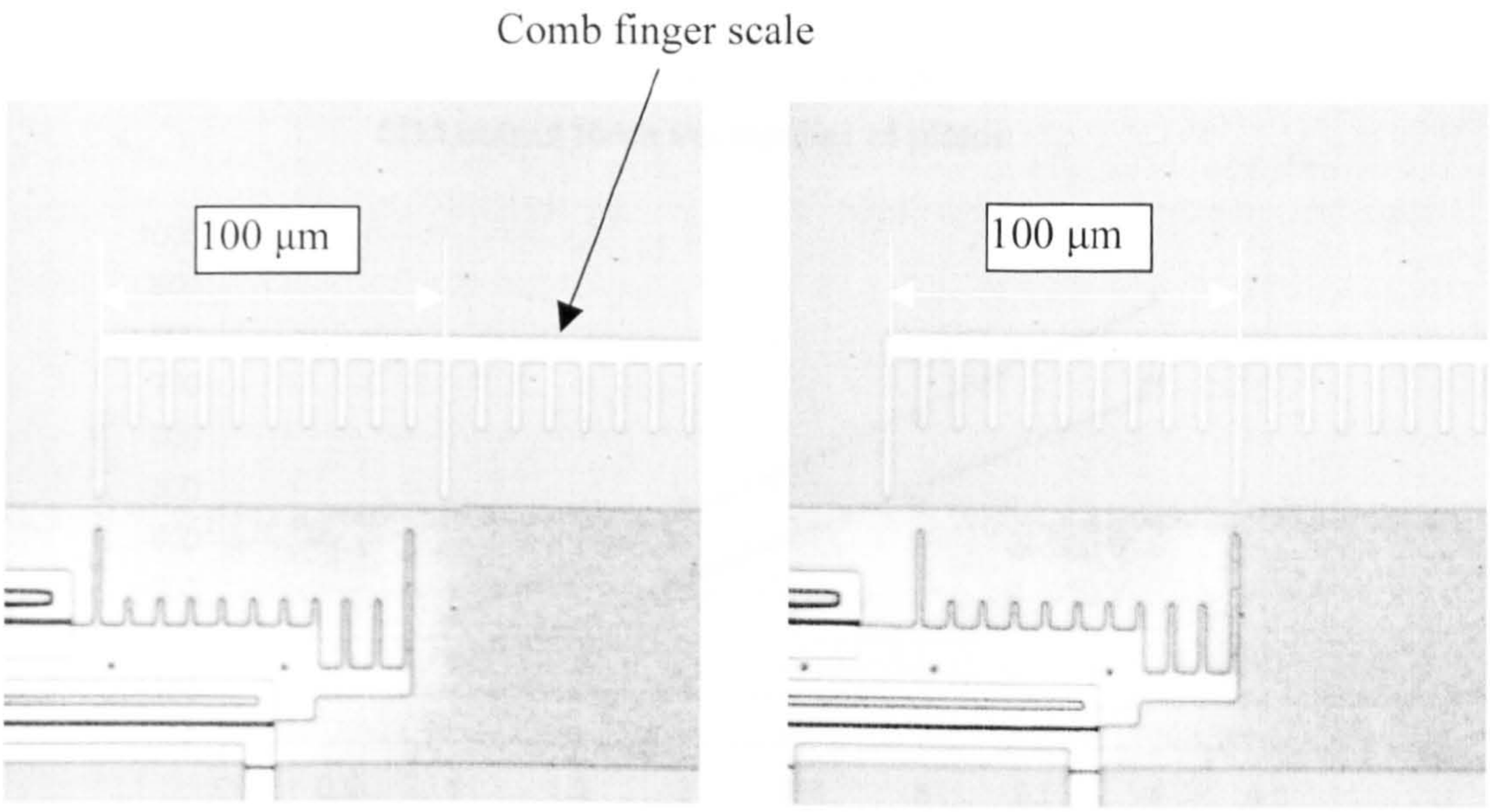

Fig. 4-37: Micro photographs taken from high-speed camera, picture on the left is picture before movement, picture on the right is the picture after movement.

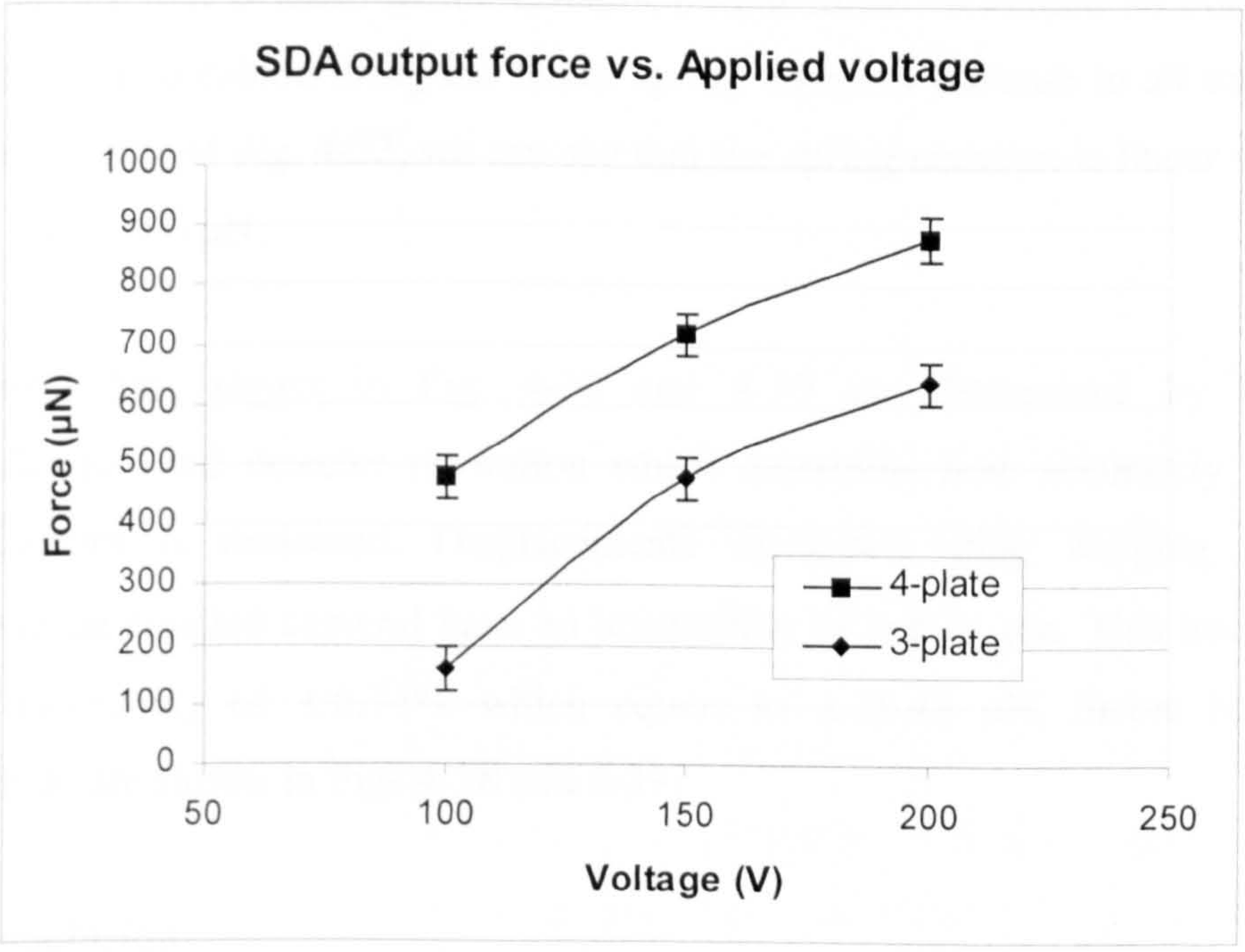

Fig. 4-38: The experimental result showing output force versus voltage applied to the device.

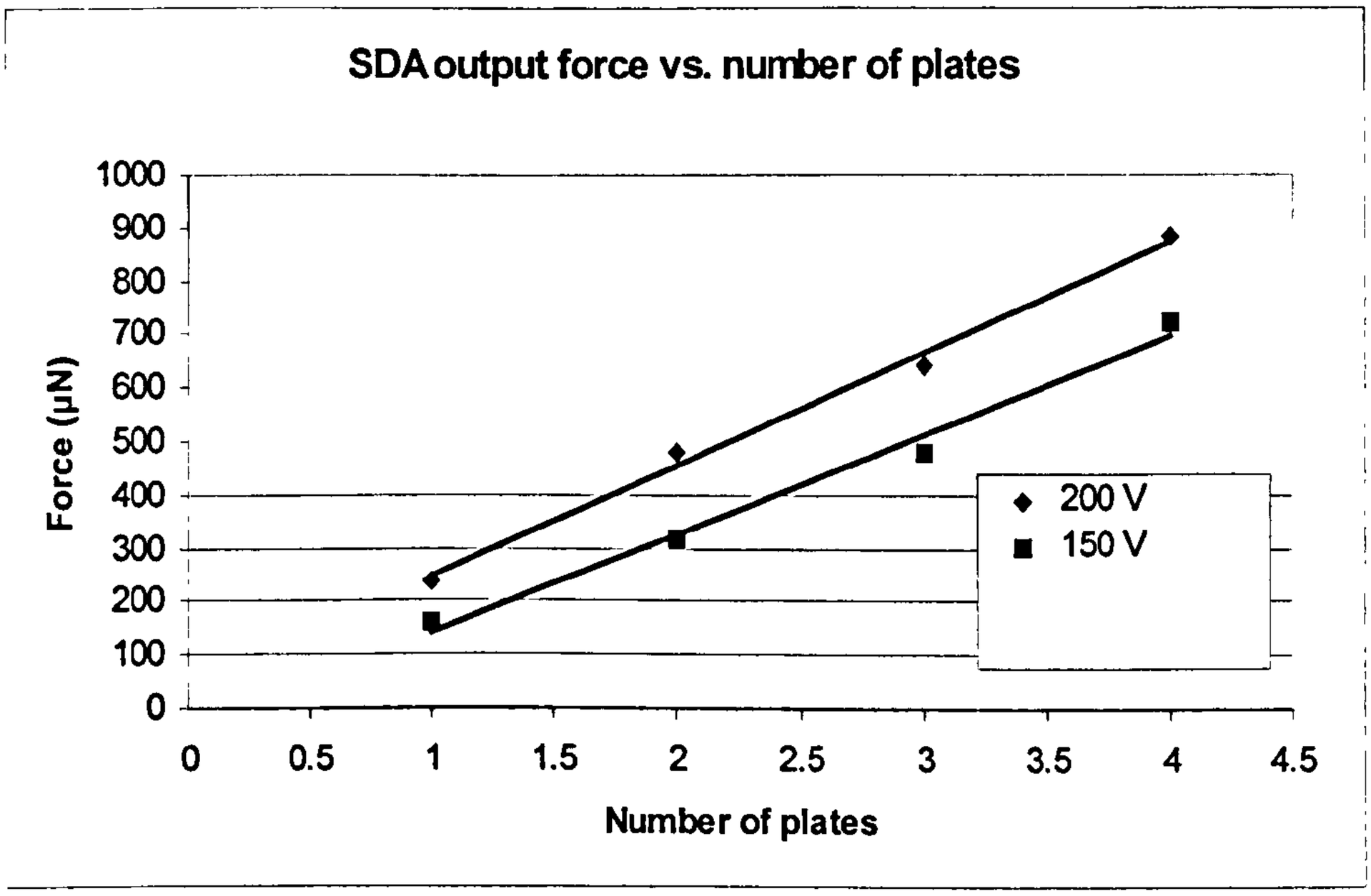

Fig. 4-39: The relationship between actuator output force versus plate number of plates.

The nonlinear equation of the spring has been used to calculate the restoration force of the spring that is taken as the actuator output force. It should be noted that the same result is obtained using the linear spring equation because in all experiments, From the result of Fig. 4-33, we can see that the spring constant is linear when force is less than 1000 μN.

The error bars shows in Fig. 4-38 and 4-39 are determined by the image magnification and detector resolution which determine how accurately the spring displacement is measured. Displacements measured using imaging equipment (microscope coupled camera) have an uncertainty of ± 0.74 μm. This translates to a force uncertainty of ± 0.74*k which equals to ± 36.48 μN. Errors bars of this magnitude are shown in Figs 4-38 and 4-39.

4.9 Conclusion

SDAs are versatile microactuators with the potential for enabling precise positioning of microcomponents on a substrate. They are often integrated with micro-optic elements where precise positioning is important. Some devices prototypes driven by SDA array have been designed and shown in Appendix C. An empirical comparison of the motion of SDAs formed on different substrates by a foundry process - PolyMUMPs – has been conducted, and the findings of this investigation have been presented. For this study, long-travel linear SDAs (travel of around 1000μm) have been designed so that there is ample scope to observe their motion characteristics. Our findings show variation in the motion of SDAs formed on different dies, but to the same design. The velocity profile of long-travel SDAs has been explained in terms of changes in friction. These observations have been supported by surface analysis of the SDA sliders before and after voltage application. All measurements have been undertaken under similar laboratory conditions. We therefore attribute the variations to small differences in the surface characteristics of the deposited and etched layers and variations during post-processing release and storage. Whereas slight process variations of this kind are not significant in microelectronics, they can be more significant in MEMS where the behavior of a micro-electro-mechanical device, such as the scratch drive actuator, is determined by surface friction which can be made to vary by small differences in the properties of the layers of material from which the MEMS is fabricated. From the experimental conducted in this chapter, we would make the SDA with much longer rails in the future designs.

The SDA modes during its working state have also been analysed in this chapter. Depending on the value of the voltages applied, two modes are identified, namely non-contact and contact modes. The contact mode is very important for obtaining the relationship between applied voltage and step size. The theoretical expressions have been applied to our SDAs of fixed dimensions, although it is easy to expand this model to an SDA of any dimension. Experiments on our SDAs have been carefully performed using a Veeco NT1000 Surface Profiling Tool. The theoretical results have been compared to experimental measurements, with good agreement being obtained between the two. Separately, IntelliSuite software has been used to simulate

the flexing of the SDA plate with DC voltage. Once again, the result from the simulation compare very well with the experimental findings.

In this chapter, the SDA forces have also been estimated. Micro box-springs have been analysed by FEM using ANSYS. The ANSYS results of the spring constant compare very closely with the simple beam theory results of the spring constant. As far as we are aware, no work has been reported on using the FEM of a box-spring as a means of accurate estimation of SDA forces. Scratch drive actuators with box-springs and different number of plates have been fabricated using the PolyMUMPs process. These SDAs have been experimentally analysed to determine their force generation. Forces of 250 ± 36 μN for one plate SDA up to 850 ± 36 μN for 4 plate SDAs have been estimated for 200 volts driving voltage. Within the uncertainty quantified above, there is a near linear relationship between the number of SDA plates and the force generated.

Chapter 5

Variable Optical Attenuator Driven by SDA

5.1 Introduction:

A variable optical attenuator (VOA) can be used to manage and control the power levels (power equalisation) in optical fibre networks. Manually controlled variable attenuators can be included on optoelectronic circuit packs and factory adjusted to match the particular network specifications. Electrically controlled variable attenuators enable remote compensation for dynamic changes in the network. Micromachined variable optical attenuators are mainly electrically controllable. MEMS technology has been used by several research groups as a way of devising a VOA [12], [106], [10], [11]. The general MEMS approach relies on introducing a moveable shutter between two facing optical waveguides (usually single mode optical fibres) and using various forms of micro/nanoactuation to control the shutter position. The shutter controls the transmission of light between the fibres depending on its position. A schematic diagram of the MEMS VOA is shown in Fig. 5-1.

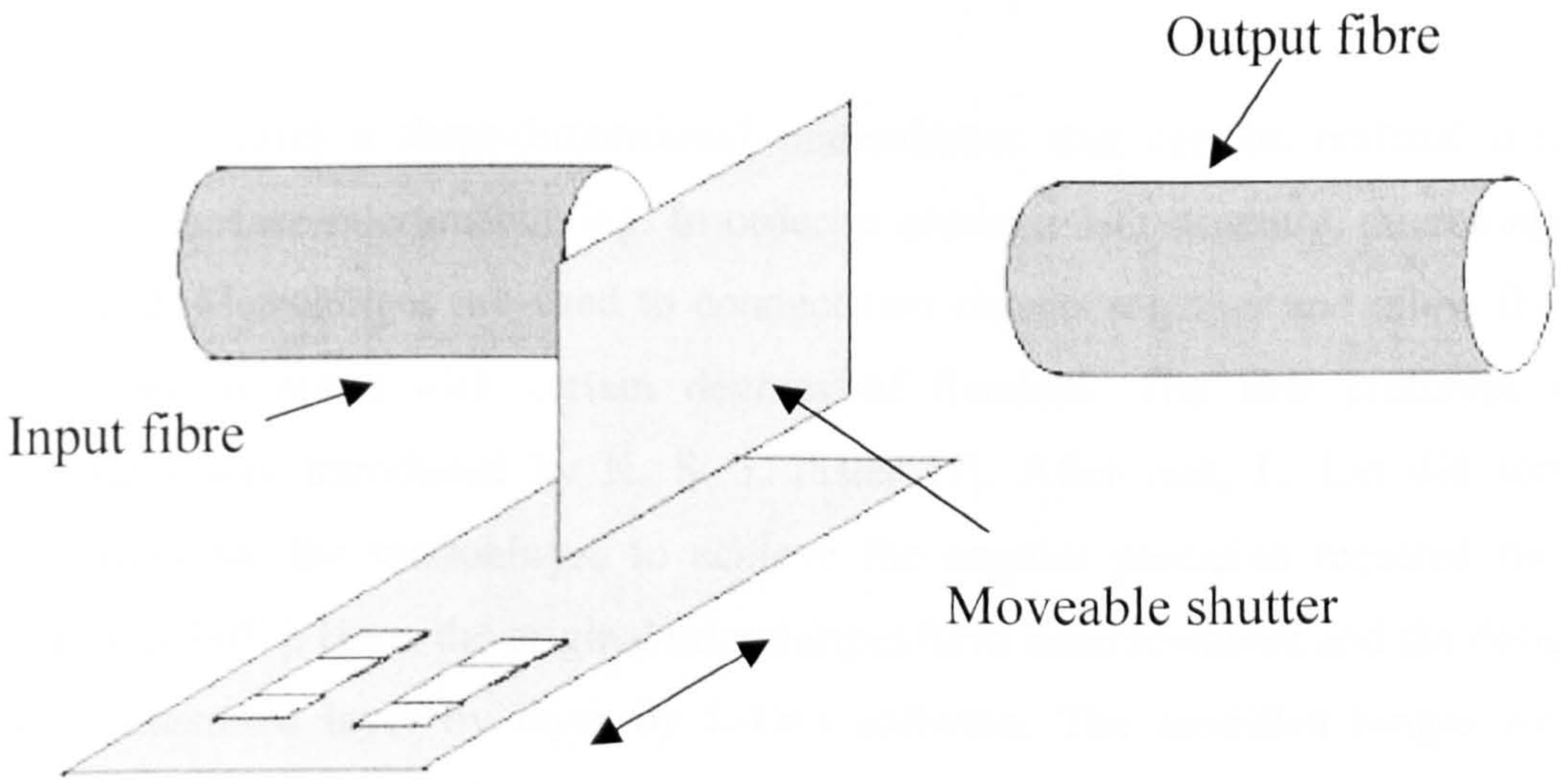

Fig. 5-1. Schematic diagram of MEMS VOA.

In Chapter 4, the characteristics of the scratch drive actuator (SDA) have been investigated in detail. In this chapter, we have used such SDA arrays integrated with a microshutter to realize the function of a variable optical attenuator. The advantage of this type of VOA is that the position of the microshutter can be precisely controlled by nano-stepping scratch drive actuators. Such a variable optical attenuator has been designed and analyzed both for its mechanical and optical characteristics. PolyMUMPs process of MEMSCAP foundry has been used to build the prototype of the VOA. In the VOA device, the key components are actuators and moveable shutters. The actuator used is the scratch drive actuator that was treated in Chapter 4. Therefore, in this chapter we put our emphasis into the moveable microshutter design and optical design. The microshutter consists of microhinges and a vertical shutter. Microhinges are reviewed and designed in Section 5.2. Vertical shutter has been realized using integrated self-assembly technique, discussed in Section 5.3 and 5.4. Optical model was built using diffractive theory and the attenuation function was calculated by compiling a program using Matlab software. This is described in Section 5.4. Finally, the fabricated VOA has been characterized by putting the microshutter between two face-to-face single mode optical fibres, as described in Section 5.5.

5.2 Microhinge design for VOA

The VOA requires a three-dimensional microshutter that can be realized using polysilicon surface micromachining. In order to obtain a 3-D structure, microhinges are utilized. Microhinges are used to connect two objects together and allow these two objects to move with certain degrees of freedom. The first prototype of microhinges was introduced by K. S. J. Pister [7]. After that, L. Lin did some modification for the microhinges to achieve the angular precision required for a micromirror [107]. Here, the original microhinges have been reviewed and the design flow is illustrated layer by layer by L-Edit software. The modified hinges were employed to construct the shutter.

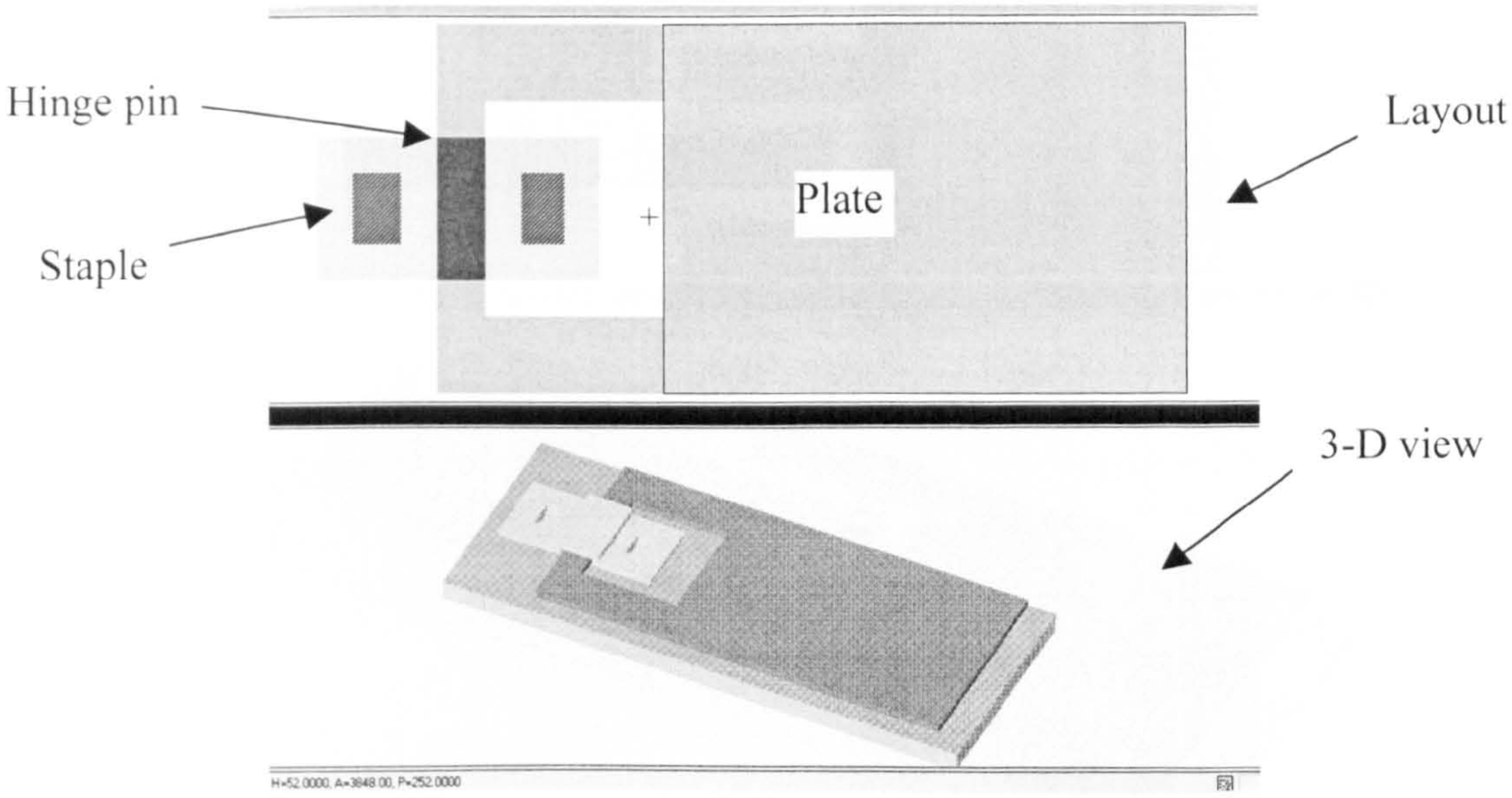

Fig. 5-2. Simple microhinge layout together with 3-D view.

Fig. 5-2 shows a simple microhinge layout together with 3-D view.

Conventional MEMS microhinge consists of a hinge pin, staple and plate. Using PolyMUMPs, the plate is formed by Poly1 layer, staple is formed by Poly2 layer, and hinge pin part is formed by Poly1. This type of hinge has no movement in the x-, y-axis, and can only be used for moving the plate out of the plane, so it is called a 'substrate' hinge. Furthermore, a 'scissor' hinge can be used to connect two plates together. The design flow is described as follows. Fig. 5-3 (a) – (c) show the design sequence of a 'scissor' hinge by PolyMUMPs.

Step1. Patterning the Poly1 layer, as the Fig. 5-3 (a) shown.

Step 2. Etching the oxide 2 layer and forming the 'via' between poly1 and poly2.

Step 3. Patterning the poly2 layer for the connection.

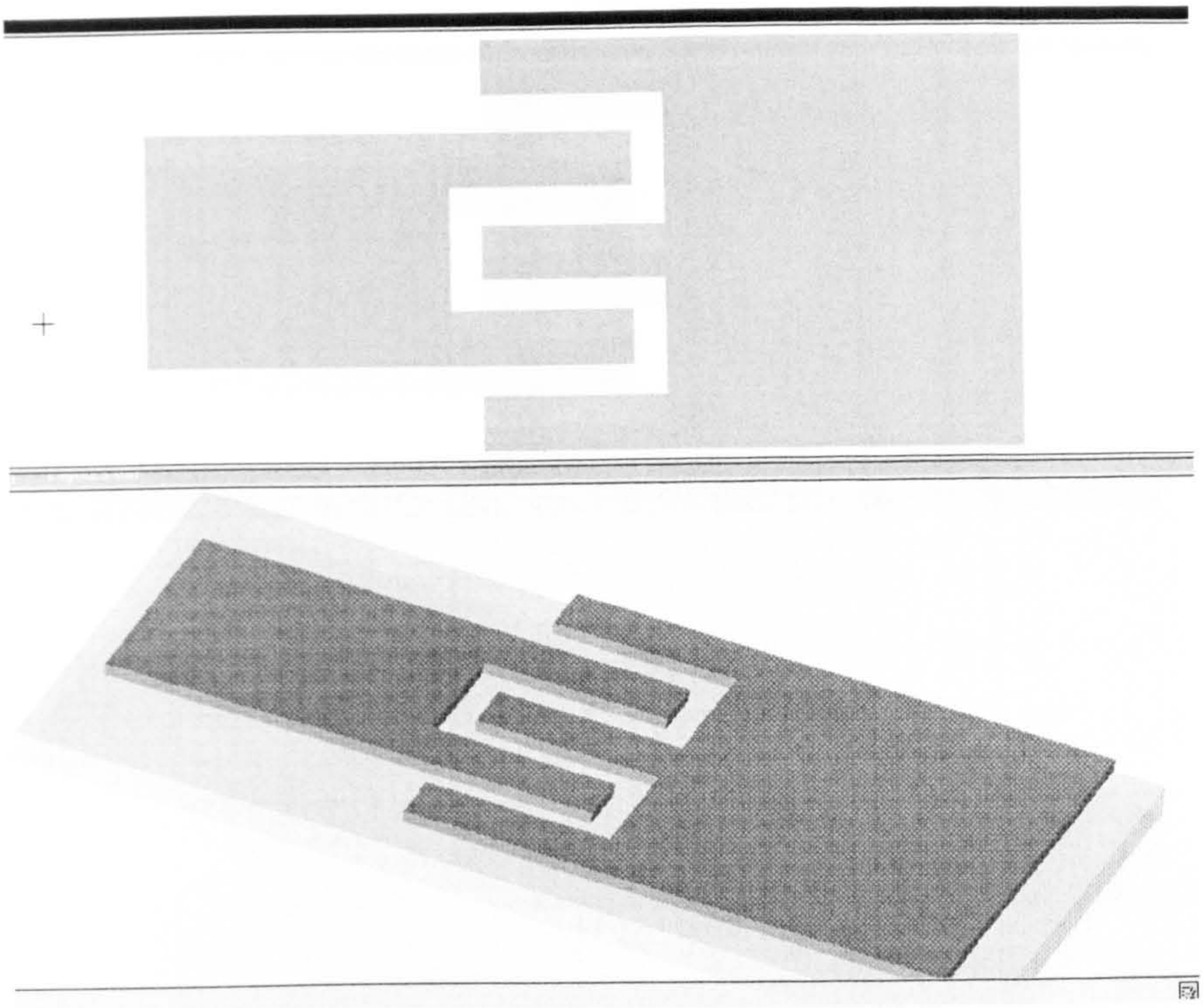

Fig. 5-3 (a). Layout and 3-D view of step1.

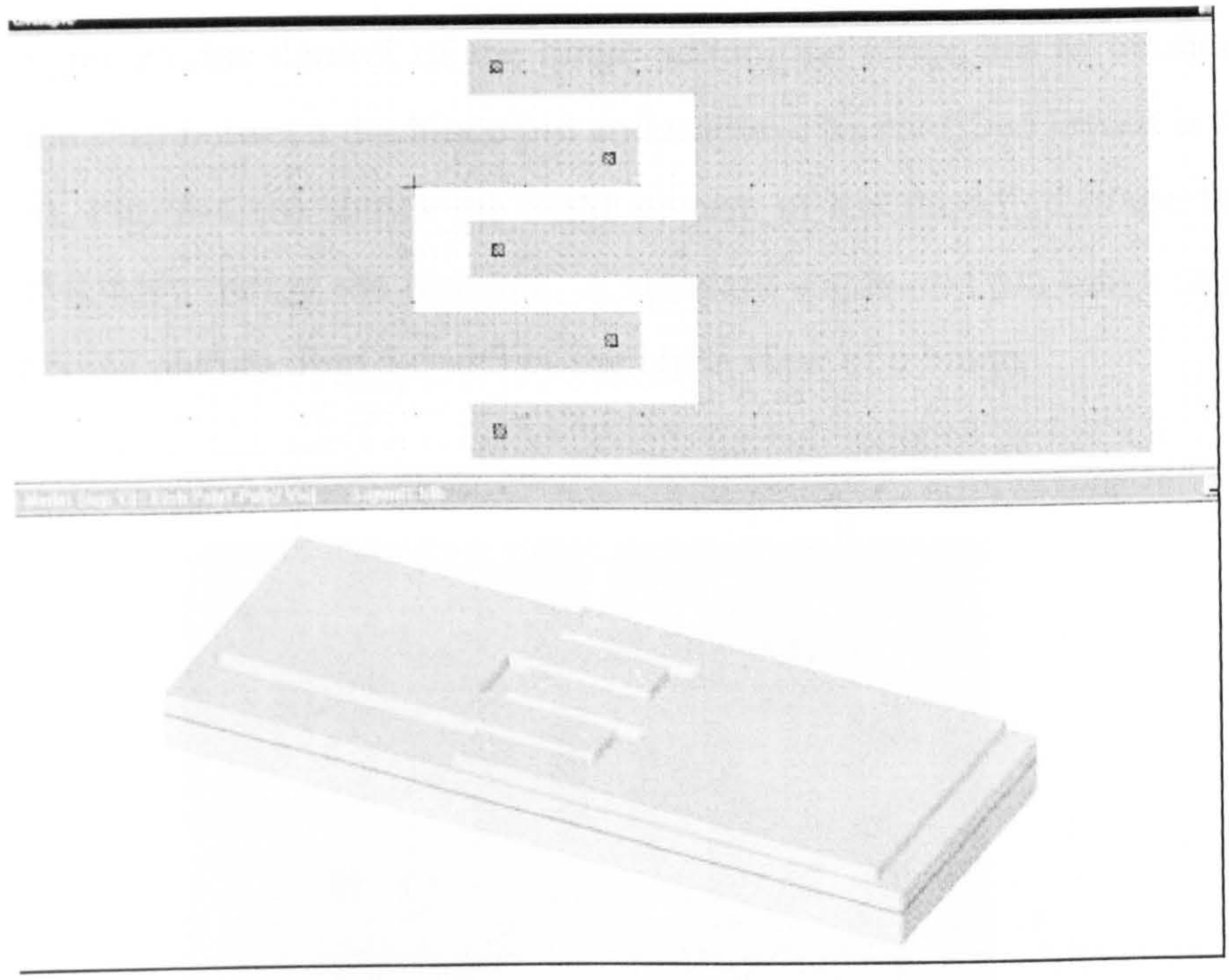

Fig. 5-3 (b). Layout and 3-D view of step2.

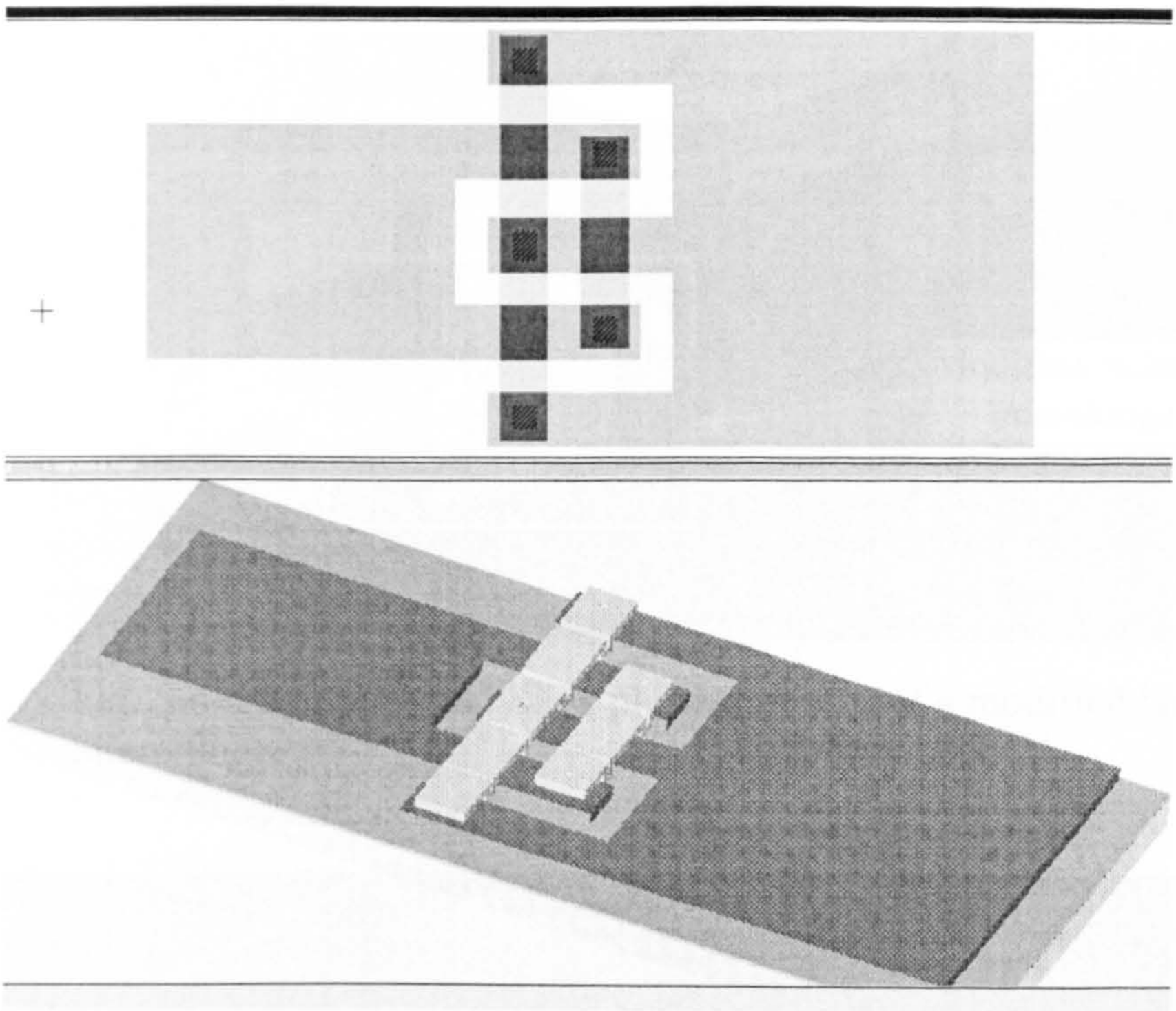

Fig. 5-3 (c). Layout and 3-D view of step3.

In order to get precise control of the hinge action, the hinge has to be modified to minimize the shift between the hinge pin and staple. The modified layout is shown in Fig. 5-4 (a). Fig. 5-4 (b) shows the SEM picture of the modified hinge fabricated using PolyMUMPs during the research. A standard staple and pin hinge can also be seen in the SEM picture. Fig. 5-5 shows the close view of a hinge.

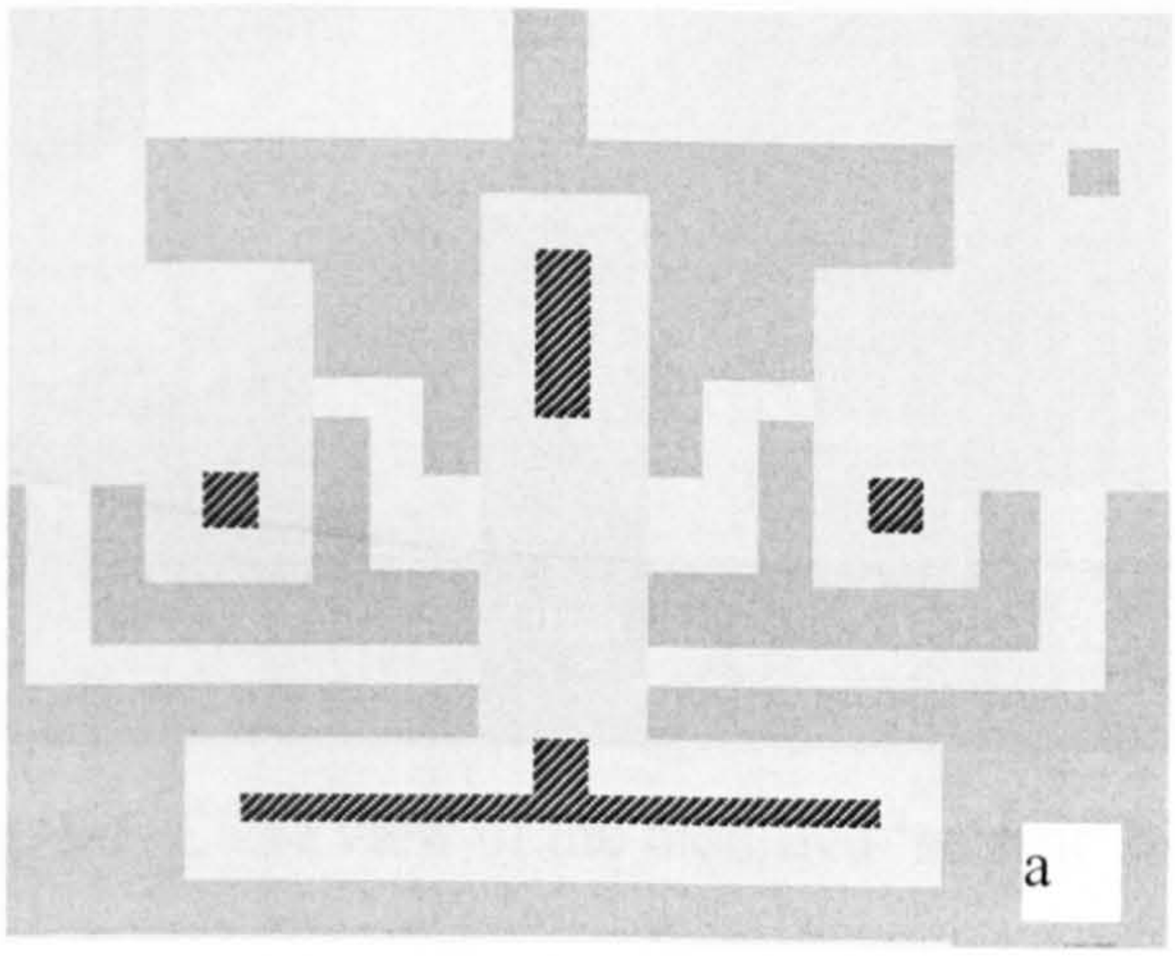

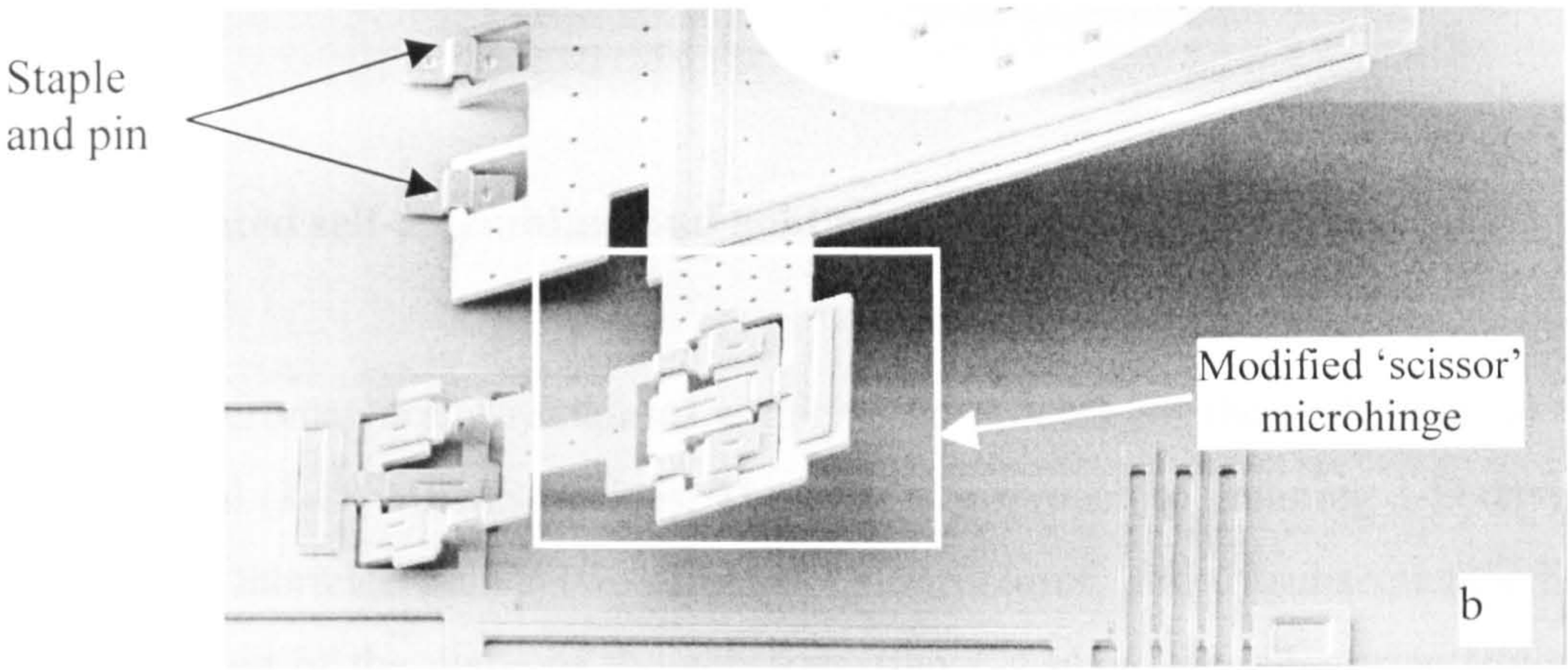

Fig. 5-4. Layout (a) and SEM photograph (b) of a modified 'scissor' microhinge.

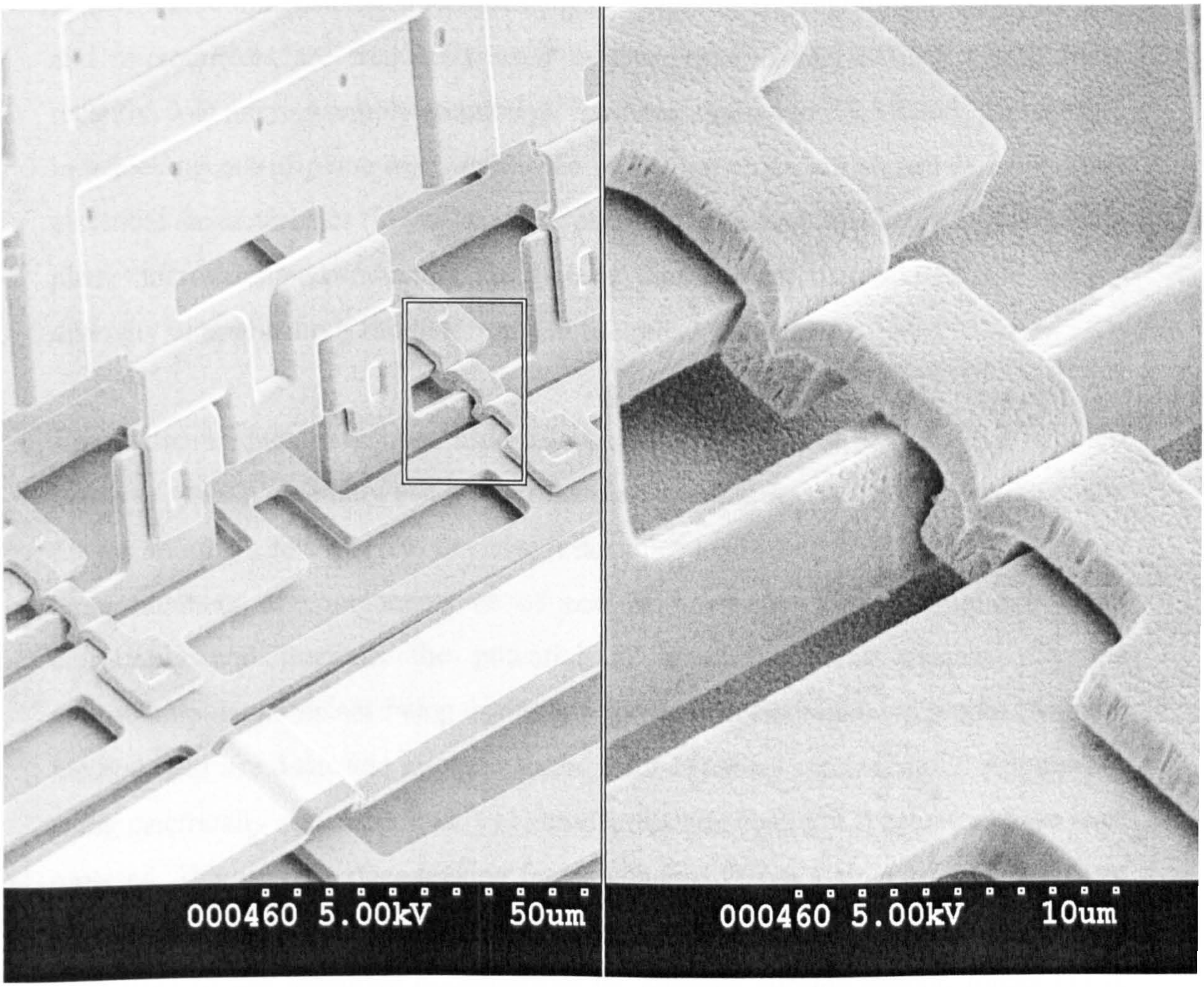

Fig. 5-5. Close view of the modified 'scissor' hinge.

5.3 Integrated self-assembling and holding technique

Surface micromachining remains a widely used process for the realization of three-dimensional (3-D) MEMS devices. The general approach to attaining 3-D devices is to initially fabricate planar two-dimensional structures, and to subsequently lift the structures out of the plane of the substrate (the x-y plane) thereby orientating them parallel to the z-direction. Considerable research effort has been expended in developing approaches to assembling such 3-D MEMS; some of these are described below. Three-dimensional microstructures, including micrograting, microshutters, and micromirrors are frequently used in free-space optical MEMS [108]. More recently, 3-D microassembly technology has been applied to RF MEMS, for example in achieving out-of-plane micromachined inductors which are shown to have better electrical characteristics (lower loss, less parasitic capacitance) when compared to in-plane micromachined inductors [109]. It is thus evident that 3-D MEMS have a diversity of applications ranging from RF to optical frequencies.

Various techniques have been used to assemble such 3-D structures. The simplest involves manual assembly using micromanipulators [110]. Whilst this may be useful for assembling a few discrete devices, it does not lend itself to efficient assembly of large numbers of components or of complex systems. The technique is time-consuming and there is the potential of structures being damaged by the micromanipulators or not being accessible to the micromanipulator probes. Another method is to use dedicated microactuators for 3-D lifting and assembly. Approaches using electrically active thermal [111] or electrostatic [19], [112] actuators have been reported. The use of surface tension forces generated from a range of materials is an alternative technique for 3-D self-assembly. Meltable pads of thick photoresist have been used to self-assemble micromirrors by utilizing surface tension forces [113]. Molten Pb/Sn solder spheres [114] and thermally shrunk polyimide joints [115] are other materials that have also been used for 3-D assembly. Magnetic forces [59]

including plastic deformation magnetic assembly [116] have also been used to assemble microstructures, and this requires the incorporation of a magnetic material on the sections of the structures requiring assembly. Direct electrostatic forces have also been applied to lift microstructures [117] and potential differences of between 35-40 volts have been shown to be sufficient to produce lifting forces for hinged micromirrors.

In the approach described in this Section, a stress-induced curved bimorph cantilever is utilized to self-assemble a moveable optical microshutter which has been fabricated by polysilicon surface micromachining. When a bimorph cantilever is formed from two different films having different values of internal stress, the cantilever will bend to a concave or convex shape depending on the values and type of stress (i.e. whether tensile or compressive). Polysilicon and metal are materials often used in surface micromachining technology and can be used for forming such self-bending beams because of the different internal stresses present in these materials. Such bent bimorphs have several interesting applications. In micro-optics they have been used in the realization of curled cantilever optical switches [118]. They have also been used for elevating flat micromirrors parallel to the plane of the silicon substrate in order to obtain a higher angular deflection from the micromirrors [119]. In RF applications, they have been used to form out-of-plane inductors [120]. This chapter describes how this principle of a curved bimorph cantilever induced by differential stress has been used to realize self-assembling and holding of moveable optical microshutters. The theoretical deflection of the bimorph is derived and compared with experimental measurements. Measurements of the angular elevation of a batch of self-assembled microshutters have been made, and these are presented. Thermal measurements on the bimorph beams have also been made, and these are compared with theoretical results. Finally, optical measurements on a fibre optic variable optical attenuator (VOA) incorporating the self-assembled microshutters are presented.

5.3.1 Self-assembly architecture

A metal/polysilicon bimorph cantilever is applied for the self-assembly of the microshutter in a MEMS fibre optic variable optical attenuator. A moveable microshutter is placed between two unlensed single mode optical fibres whose end-faces are separated by a distance of 60 μm. Optical power coupled from one fibre to the other is controlled by allowing the shutter to partially block the passage of light between the two fibres. The shutter is connected by microhinges to a transport plate that is moved by nanostepping microactuators commonly called scratch drive actuators (SDAs). This MEMS device has been fabricated to our design by the PolyMUMPs process. This is a polysilicon surface micromachining process. The shutter which controls the exchange of light between the two optical fibres is initially formed flat, and lies on top of the transport plate to which it is connected by microhinges as shown in Fig. 5-6. The transport plate is formed in the Poly 1 layer whilst the shutter is formed in the Poly 2 and Metal layers of the process. The requirement is to raise and hold the shutter in position so that a 3-D microsystem is realized without any post-processing of the foundry fabricated dies. Avoiding such post-processing to the standard foundry processes is advantageous to those researchers having limited in-house fabrication capability.

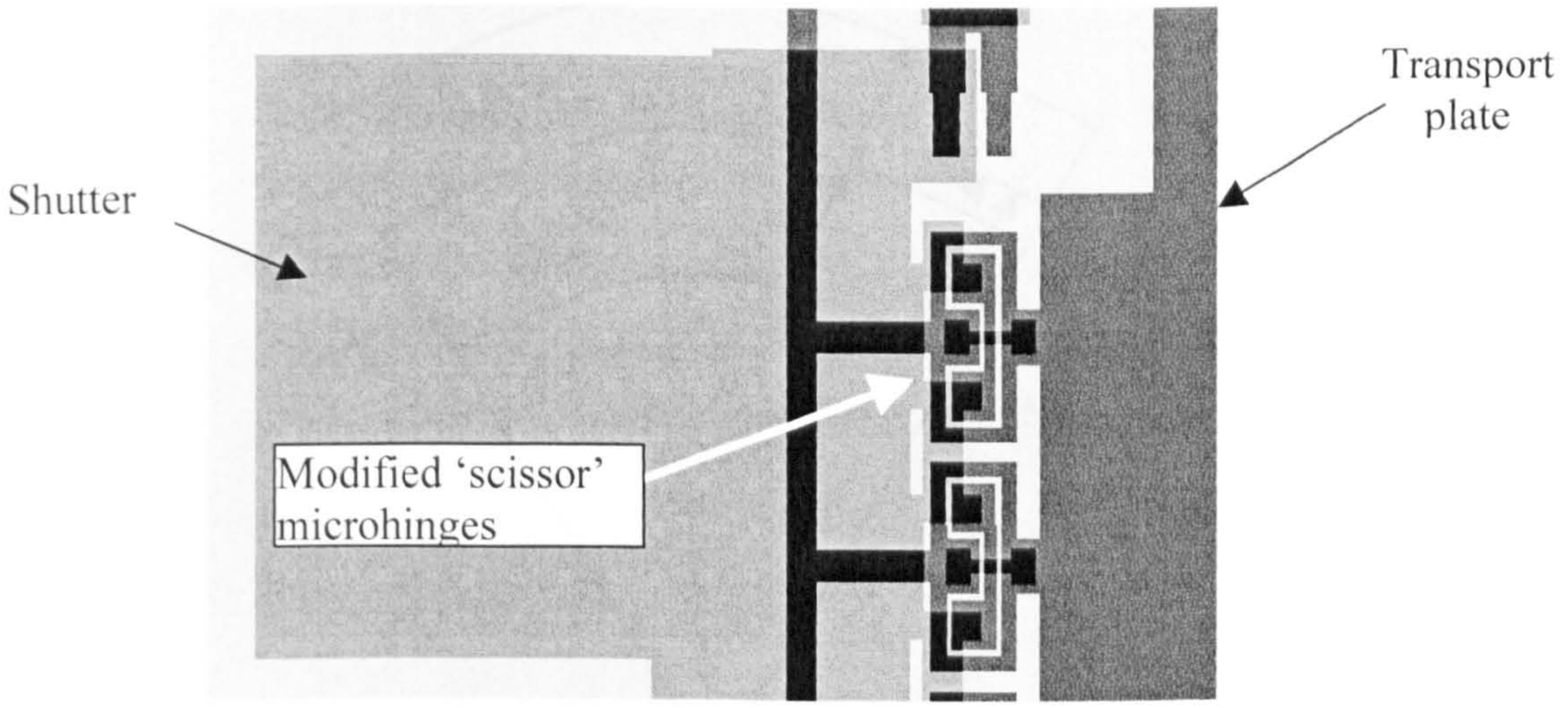

Fig. 5-6. Layout shows the microshutter mounted on the transport plate, microhinge shown is modified.

5.3.2 Design parameters

In this section, we calculate the tip displacement of a bimorph cantilever and then illustrate how this structure has been integrated into the VOA design to achieve self-assembly of the shutter.

Fig. 5-7 shows the dimensions of a bimorph beam, which is composed of polysilicon and a metal (gold) layer on the top. Differential stress in the two layers generates a curvature of the beam and the radius of curvature is denoted as ρ.

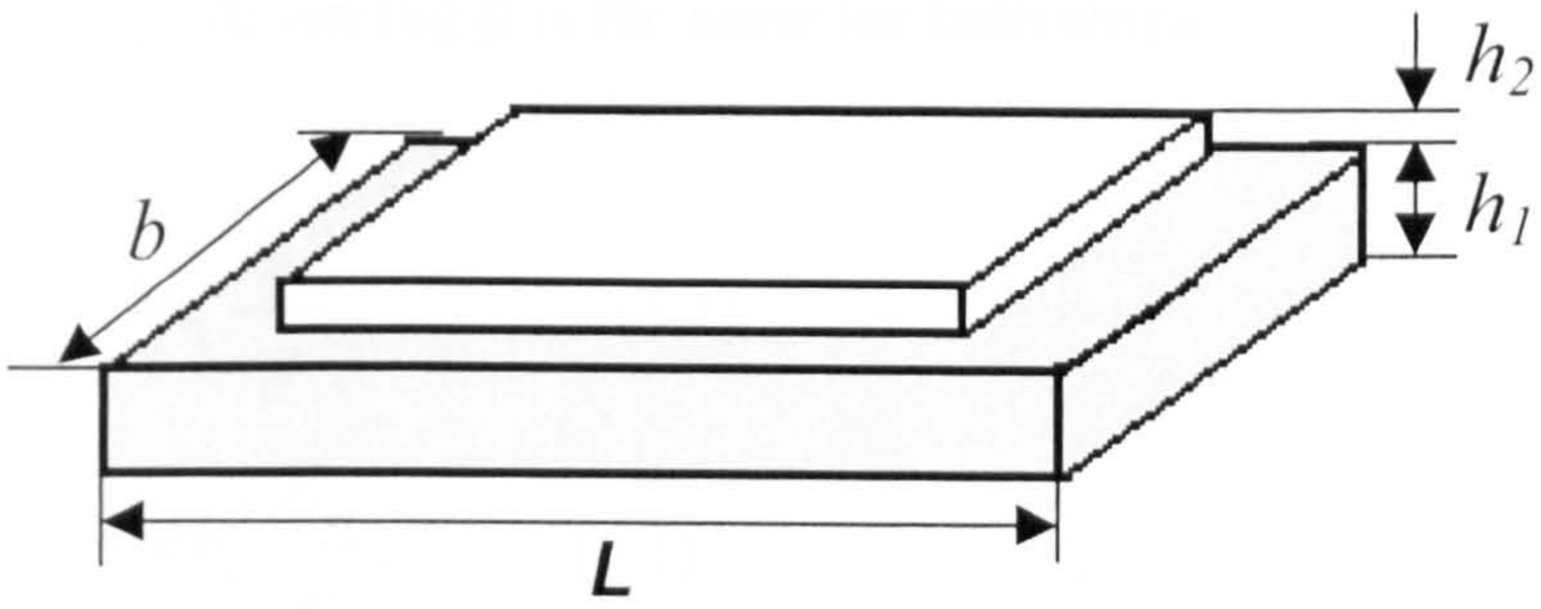

Fig. 5-7: Dimensions of bi-layer beam

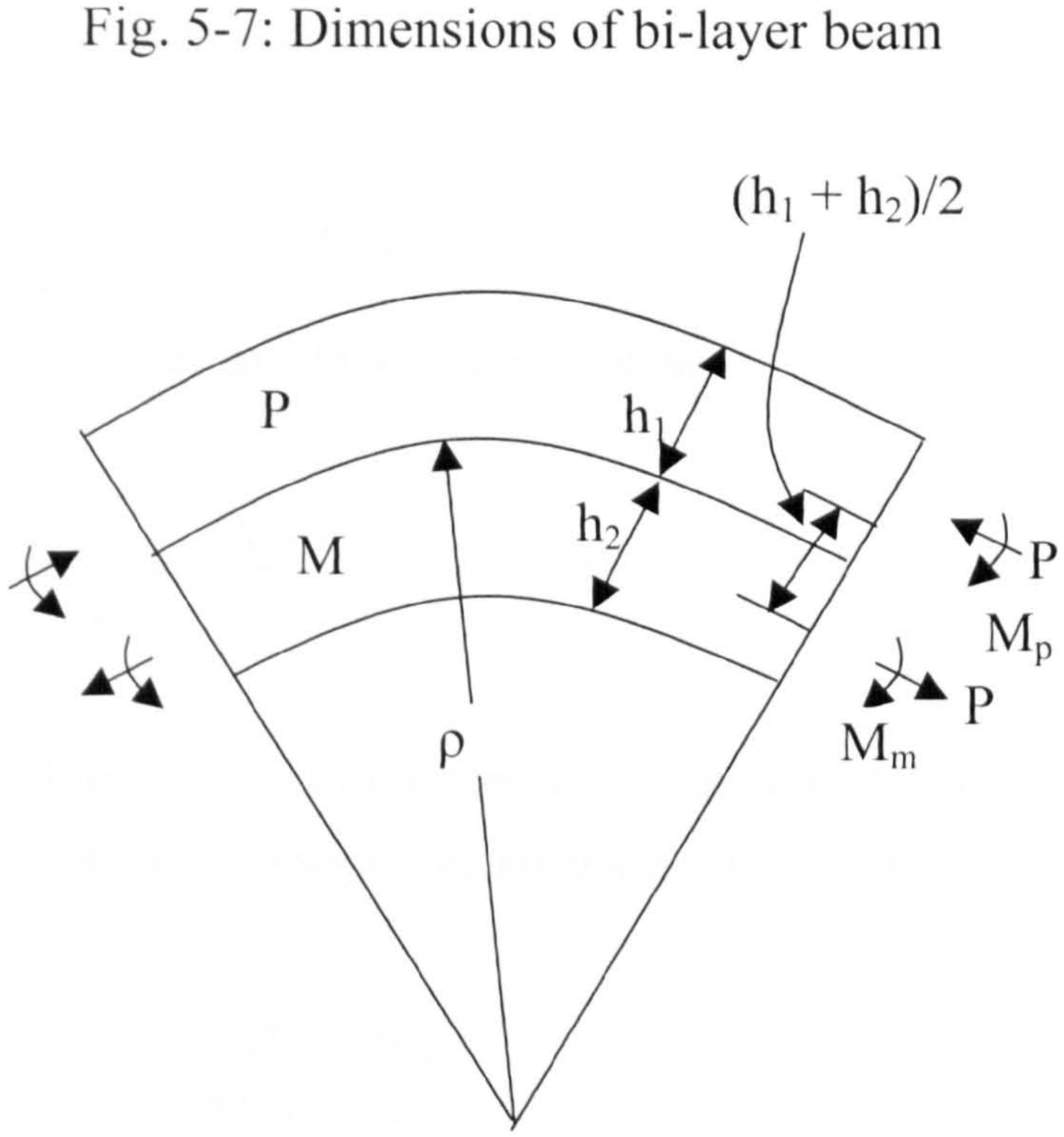

Fig. 5-8. parameters of the bi-layer strip.

From reference [121], the expression for the radius of curvature due to the different initial stress can be deduced. The problem can be described as bi-layer strip consisting of polysilicon and metal. Assuming that initial stress of polysilicon is σ_p, thickness is h_1, Young's modulus is E_p. The initial stress of metal is σ_m, thickness is h_2, Young's modulus is E_m. (shown in Fig. 5-8)

The interaction between the two strips produces a force at the common surface tending to compress the metal and extend the polysilicon. If the internal force is P, it gives rise to a 'direct' load P at the center of each section, together with a bending moment in each strip. Assuming ρ is the same for both strips

$$M_p = \frac{E_p}{\rho} I_p = \frac{1}{12} b h_1^3 \frac{E_p}{\rho}, \qquad (5.1)$$

$$M_m = \frac{E_m}{\rho} I_m = \frac{1}{12} b h_2^3 \frac{E_m}{\rho}, \qquad (5.2)$$

For equilibrium of the cross-secion,

$$M_m + M_p = P \frac{h_1 + h_2}{2}, \qquad (5.3)$$

From equations (5.1), (5.2), and (5.3), we can obtain

$$\frac{1}{12} b h_2^3 \frac{E_m}{\rho} + \frac{1}{12} b h_1^3 \frac{E_p}{\rho} = P \frac{h_1 + h_2}{2}, \qquad (5.4)$$

The difference in linear strains at the central axis of each strip is $(h_1 + h_2)/2\rho$, and allowing for load and initial stress, the compatibility equation is

$$\frac{h_1 + h_2}{2\rho} = -\frac{P}{b h_1 E_p} + \frac{\sigma_p}{E_p} - \frac{P}{b h_2 E_m} + \frac{\sigma_m}{E_m}, \qquad (5.5)$$

Re-arranging the equations (5.4) and (5.5), the radius of the curvature is

$$\rho = -\frac{1}{6}\frac{4E_pE_mh_1^3h_2 + 6E_pE_mh_1^2h_2^2 + 4E_pE_mh_1h_2^3 + E_m^2h_2^4 + E_p^2h_1^4}{h_1h_2(h_1+h_2)(\sigma_pE_m + \sigma_mE_p)}$$

.....(5.6)

σ_p is the residual stress of polysilicon, the value for the residual stress in the polysilicon is 10.31 MPa (compressive) [90], which is from PolyMUMPs Run Data; and σ_m is the residual stress of the gold layer, the residual stress value for the gold film is 33.17 MPa (tensile) [90]. E_p is the Young's modulus of polysilicon, which is taken to be 169GPa while E_m is the Young's modulus of gold, which is taken to be 70GPa. In accordance with the PolyMUMPs process, the thickness of polysilicon h_1 equals to 1.508 μm, and the thickness of gold layer h_2 equals to 0.513 μm.

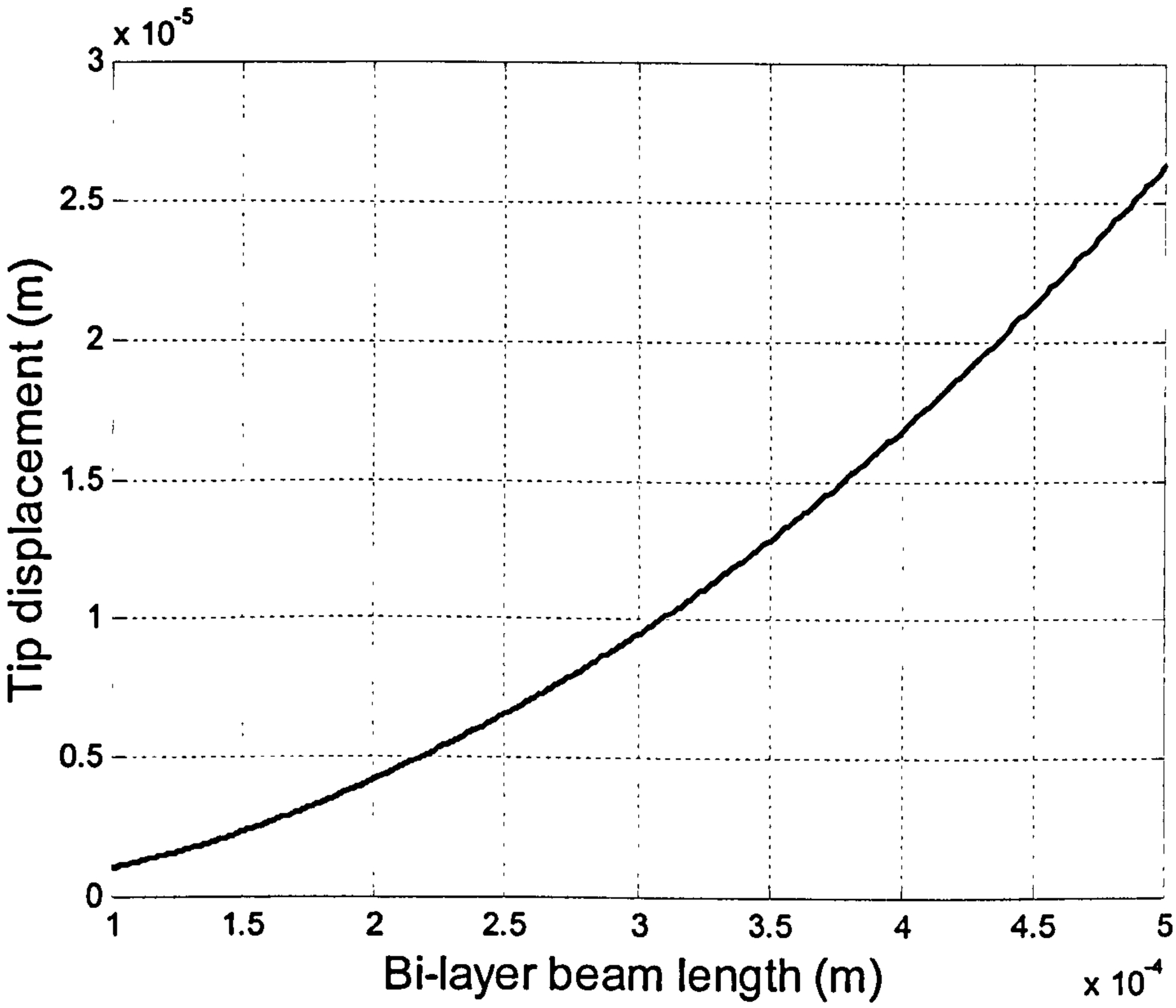

Fig. 5-9. Calculated result showing the relationship between bimorph beam length and tip displacement.

The displacement, δ, of the tip is:

$$\delta = \rho(1-\cos(\frac{L}{\rho})) \quad \text{.....(5.7)}$$

where L is the beam length. The relationship between tip displacement and beam length was calculated using equations (5.6) and (5.7) and is shown in Fig. 5-9.

In our design, a 400 μm bimorph beam was designed in order to get enough tip height to assemble and hold the shutter.

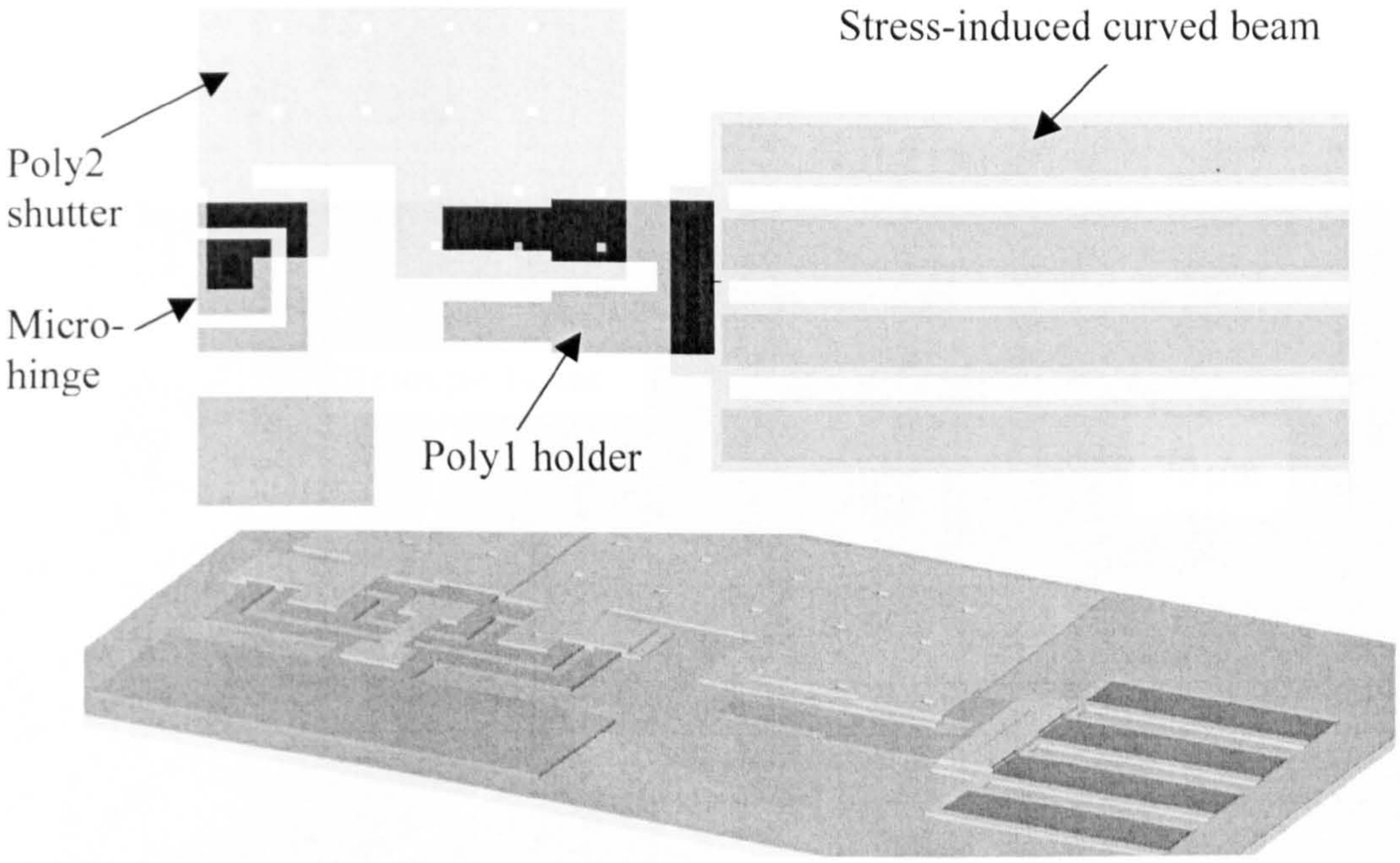

Fig. 5-10: Layout and 3-D picture of assembling part of self-assembling method.

5.4 Experimental demonstration

The layout of the self-assembled shutter of the MEMS VOA is shown in Fig. 5-10. In this layout diagram, the holder is made by Poly1 that is partially underneath the

Poly2 shutter before release by HF etching and supercritical CO_2 drying. This holder is connected to a stress-induced curved beam which is formed by Poly2 coated with gold. After releasing, the bimorph beam is bent upward due to the large difference of residual stress between polysilicon and metal. The holder will rise and make the shutter lift up immediately also holding it in position. The microhinge is designed to link the shutter to the translation stage, and therefore the shutter is self-assembled and permanently upright on the translation stage. 3-D self assembly has therefore been achieved very simply, without further post-processing. Fig. 5-11 (a) and (b) are two electron micrographs, in which the shutter is shown standing on the translation plate and held by the bimorph beam.

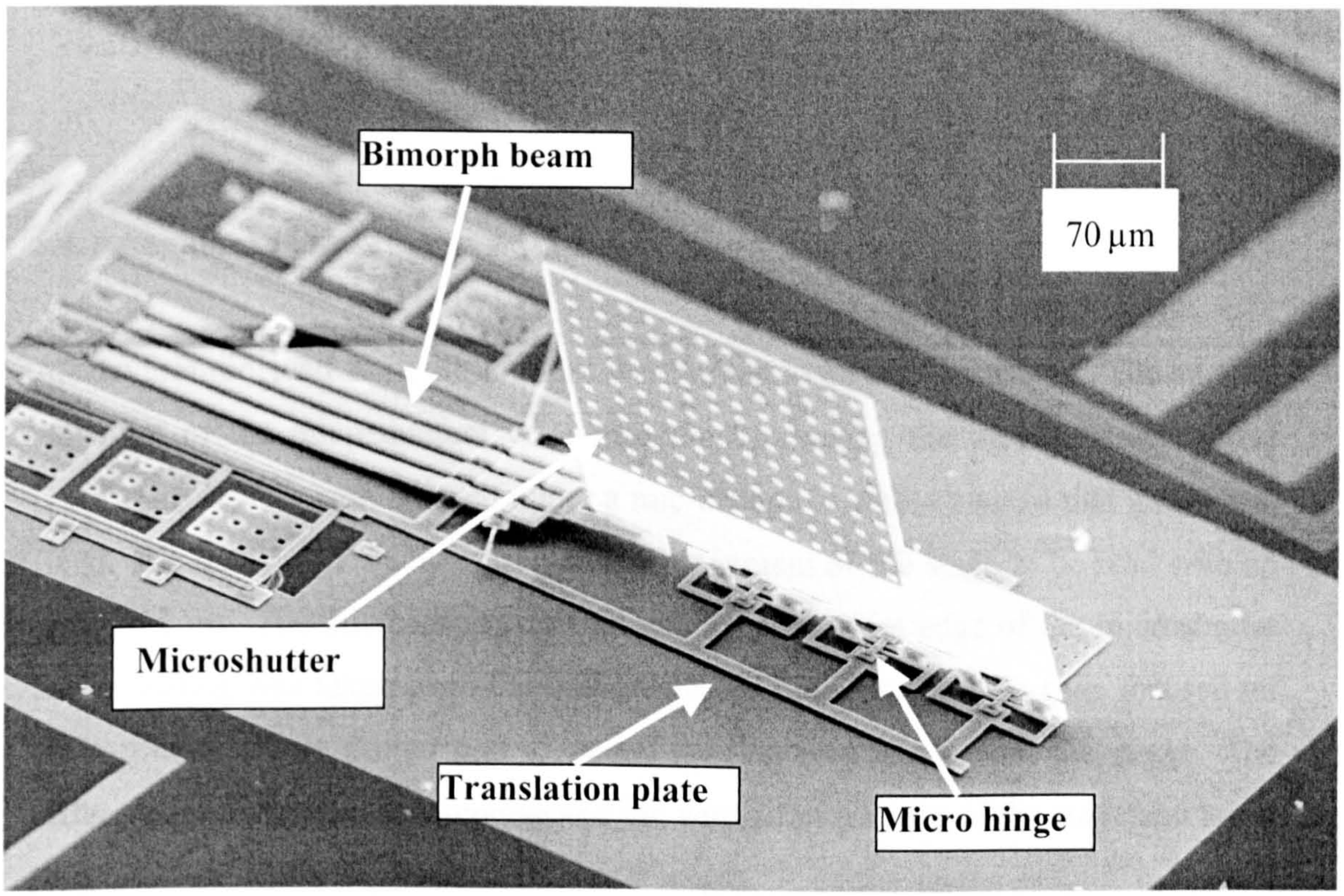

Fig. 5-11 (a): Electron micrograph of VOA showing self-assembled microshutter.

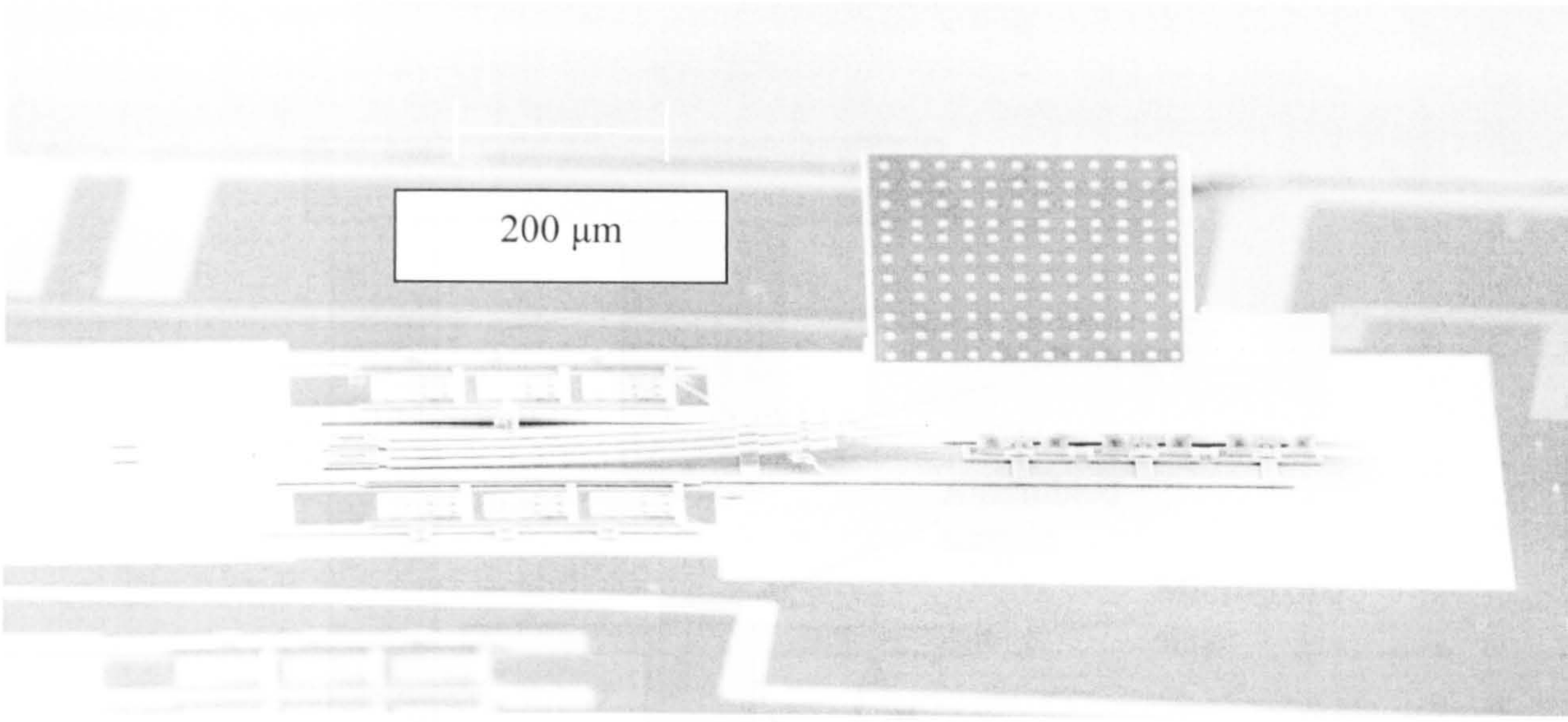

Fig. 5-11 (b): Electron micrograph of VOA showing self-assembled microshutter.

5.4.1 Angular measurement

All devices received from the foundry were noted to be self-assembled. The angular elevation of the microshutters were measured following the process described in [116]. The devices were viewed under a microscope to whose stage a dial gauge was fixed. The dial gauge enabled the vertical movement of the stage to be read with an error of 2 μm. The microscope was focused on the bottom edge of the microshutter and a reading was taken from the dial gauge. The microscope was then focused on the top edge of the shutter and a second reading was taken from the gauge. The difference in these readings represented the vertical movement of the stage and is the height "y" shown in Fig. 5-12. The actual length "l" of the shutter is known *a priori* and so the elevation angle "θ" is calculated using trigonometry. Altogether, a batch of 16 devices was measured. Fig. 5-13 shows the range of angular elevations obtained from the measurements.

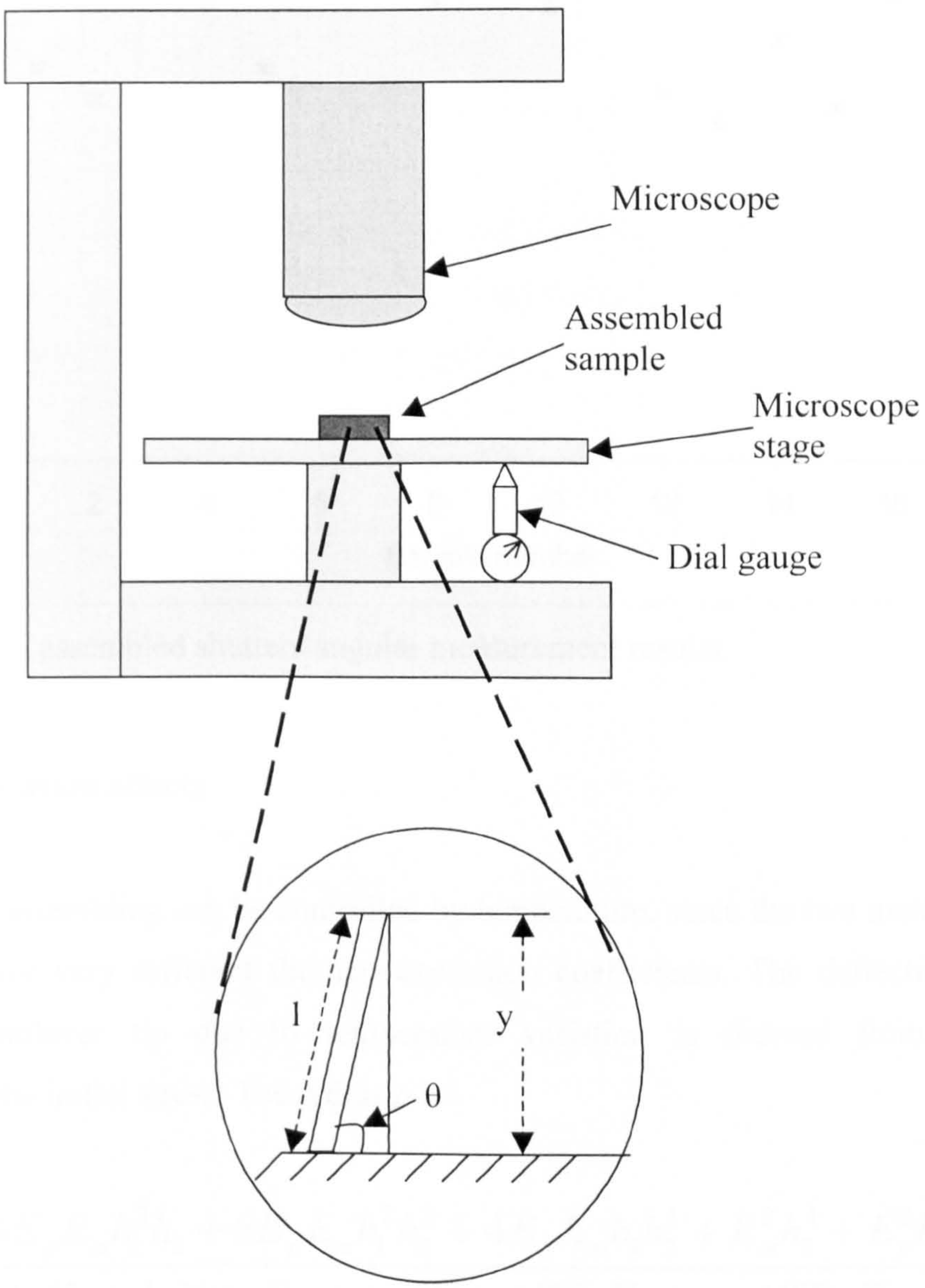

Fig . 5-12. Experiment setup for measuring the angle of the assembled shutter.

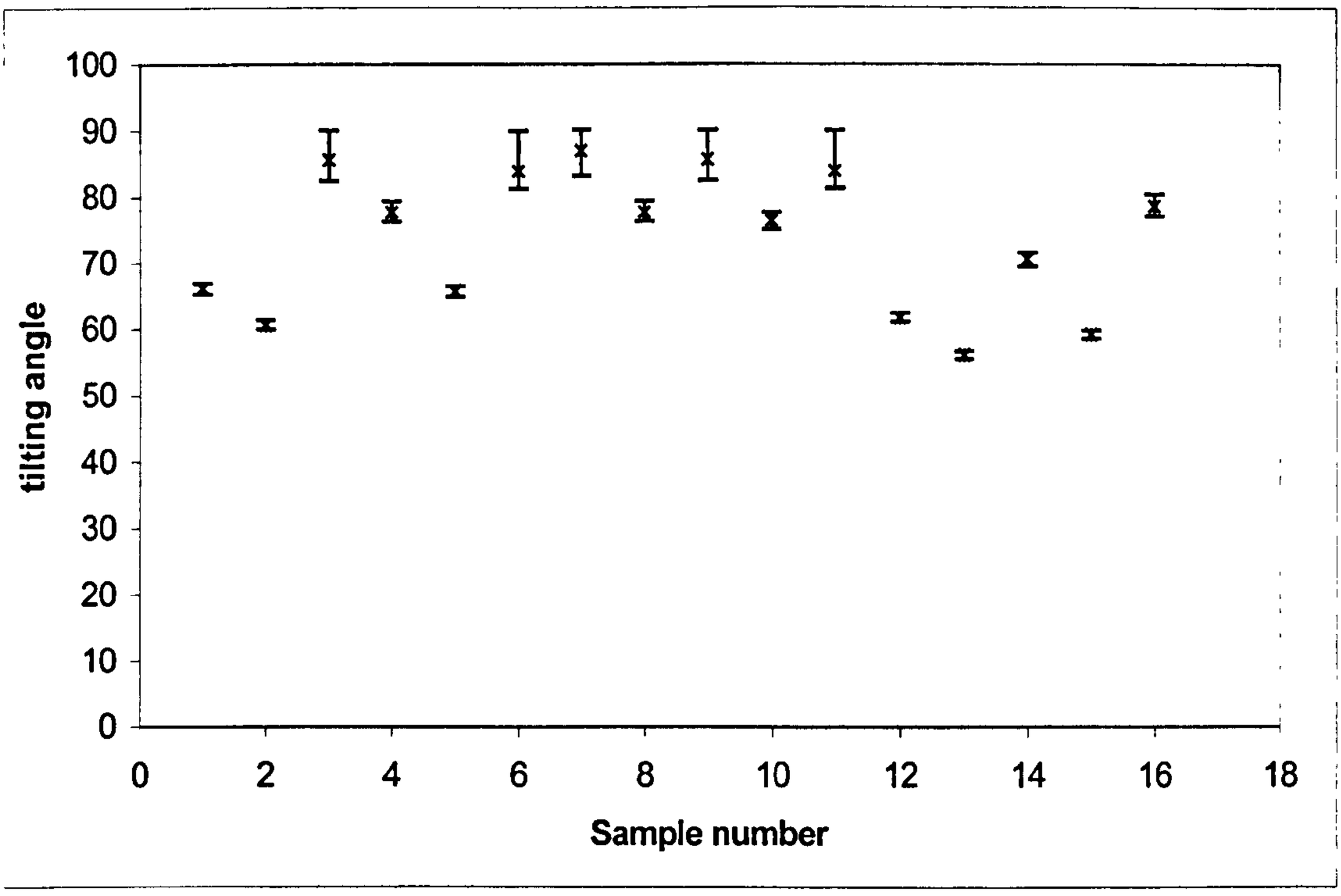

Fig. 5-13. assembled shutters angular measurement results.

5.4.2 Temperature effects

This type of assembling can be controlled by temperature, since the two materials of the beam have very different thermal expansion coefficients. The deflection of a bimorph cantilever tip due to temperature variation is derived from [121], considering the initial stress. The radius ρ is:

$$\rho = -\frac{1}{6}\frac{4E_pE_mh_1^3h_2 + 6E_pE_mh_1^2h_2^2 + 4E_pE_mh_1h_2^3 + E_m^2h_2^4 + E_p^2h_1^4}{h_1h_2(h_1+h_2)(\sigma_pE_m + \sigma_mE_p + \Delta TE_pE_m\alpha_p - \Delta TE_pE_m\alpha_m)}$$

.....(5.8)

where, E_p and E_m are Young's modulus; h_1 and h_2 are thickness; α_p and α_m are the thermal expansion coefficients of the low expansion material (polysilicon) and high expansion material (metal) respectively. In our bimorphs, the values of thermal expansion coefficients are 2.5 x 10^{-6} K^{-1}, and 23 x 10^{-6} K^{-1} for polysilicon and gold, and all other parameters are as for the beam in last section. From equation (5.8), assuming the bi-layer beam is 400 μm, the relationship between temperature

variation ΔT and tip displacement is shown in Fig. 5-14. A positive value indicates that the tip is moving up away from the substrate. From the fig. 5-14, the tip of the beam bends upward (initially around 17 um) when the temperature change is 0 K, i.e. at room temperature is 20 Celsius. It is assumed that the constants are not changed with the temperature for small temperature excursions. When increasing the temperature by small value, the beam bends down rapidly due to the large thermal expansion coefficients of polysilicon and metal. The tip motion is very sensitive to the temperature changing. The advantage is that the bi-layer beam can be controlled by temperature to the required position. The disadvantage of this assembly method is the unstability due to the environment temperature.

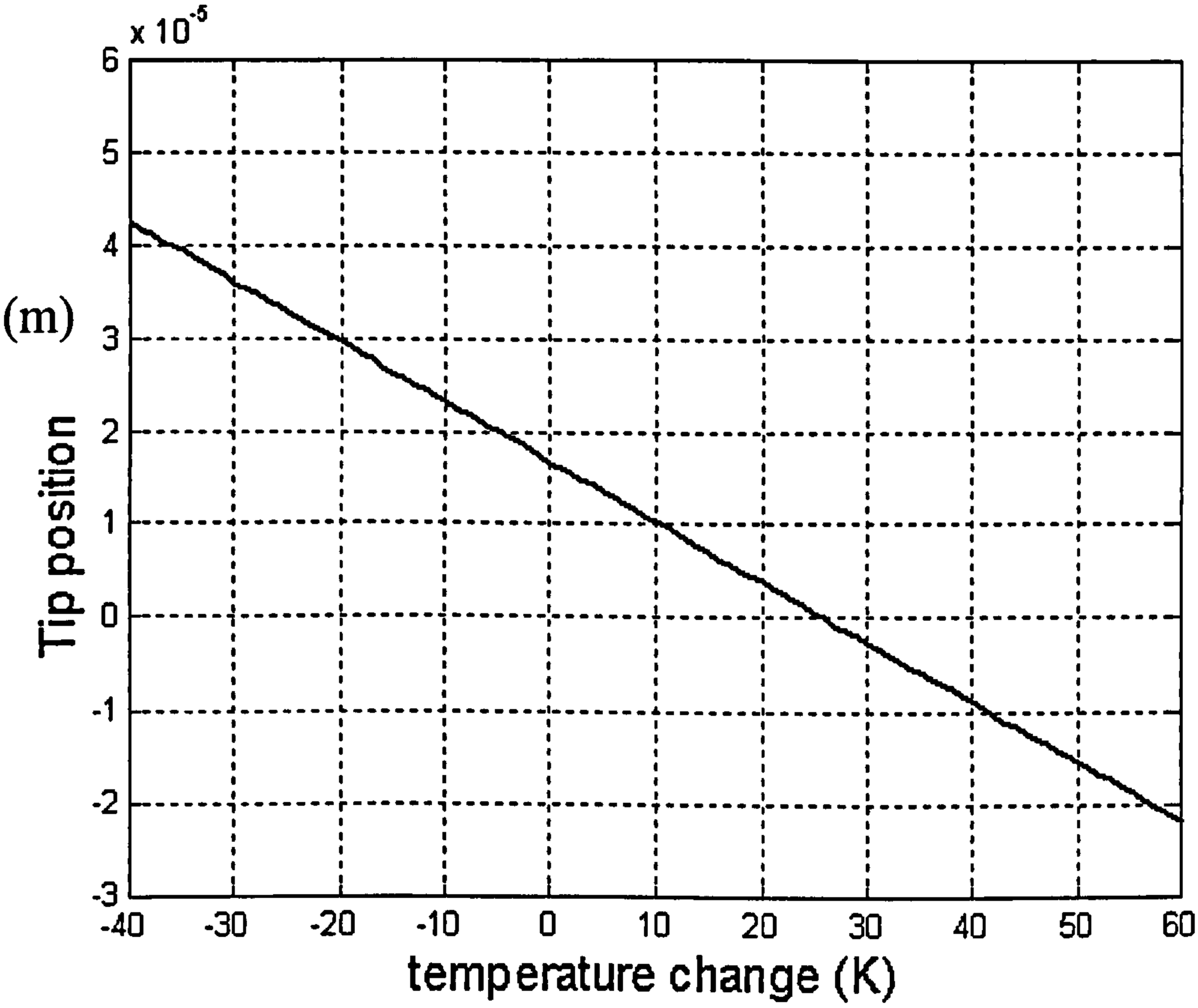

Fig. 5-14. Relationship between temperature changing and tip displacement, assuming the initial bending caused by initial stresses of polysilicon and metal. Assume room temperature is 20 Celsius.

An experiment to verify the theory described above has been performed using the following procedure. The VOA device is placed on a Peltier element whose

temperature can be raised or lowered by applying a DC voltage. A series temperature values have been set, the room temperature was measured to be 20 Celsius. The device and Peltier element were placed on the surface of a Veeco NT 1000 Profiling tool. The profiling tool can precisely measure the height change of the beam. The experimental results are shown in Fig. 5-15. The reaction of the bimorph beam to the temperature change is shown in Appendix F.

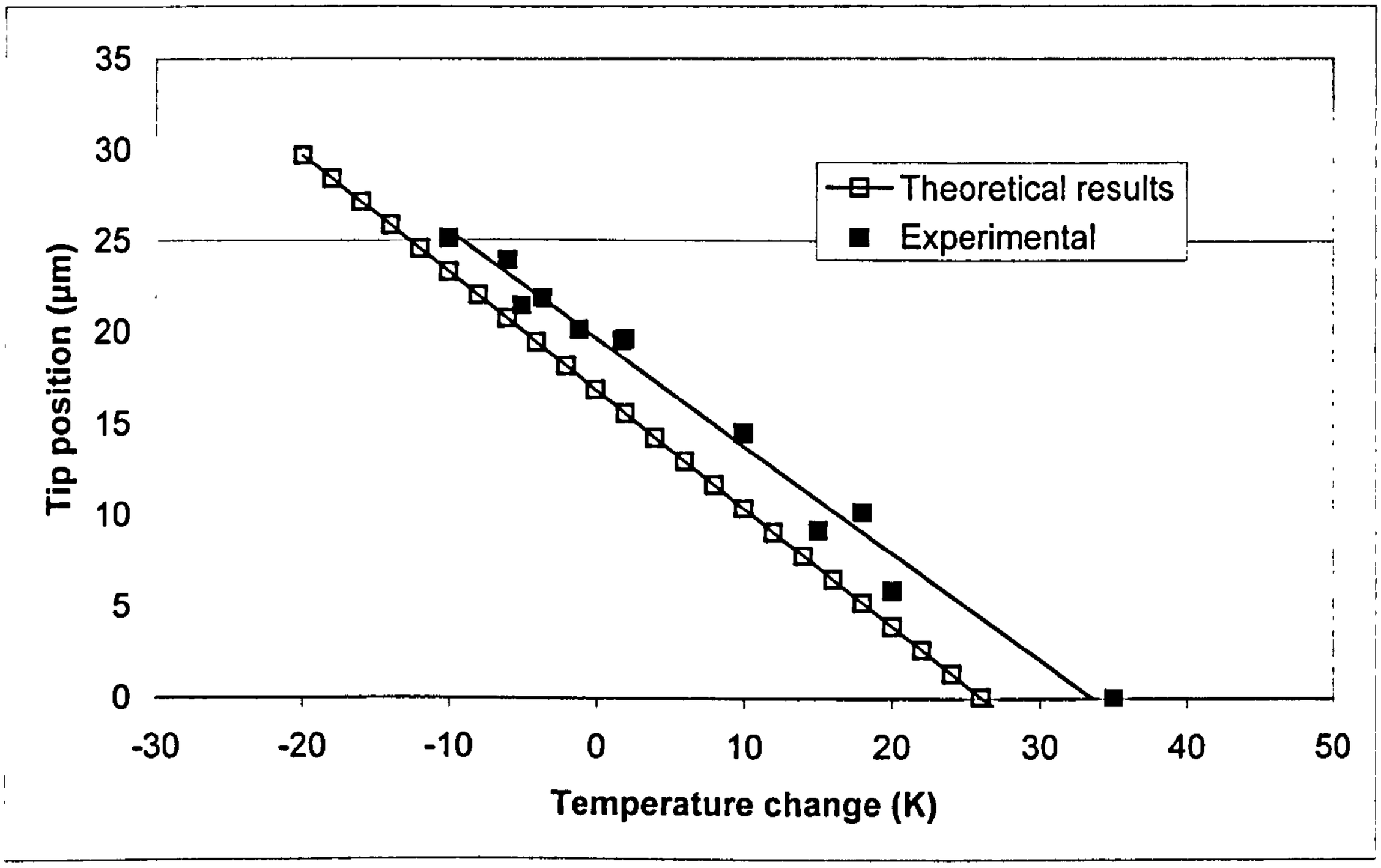

Fig. 5-15. Relationship between tip position and temperature change for a 400μm length bimorph.

5.5 Optical design:

The schematic diagram of the VOA is shown in Fig. 5-16. A shutter is located between two single mode optical fibres, and can be driven to move into the light beam to block the light energy partially (like a knife edge). First of all, the light comes out from input fibre propagated as a Gaussian distribution. Then the shutter blocks part of the light at distance z_1 from the tip of the input fibre. Then it is

diffracted to the output fibre's facet and coupled into the output. These following steps are described as:

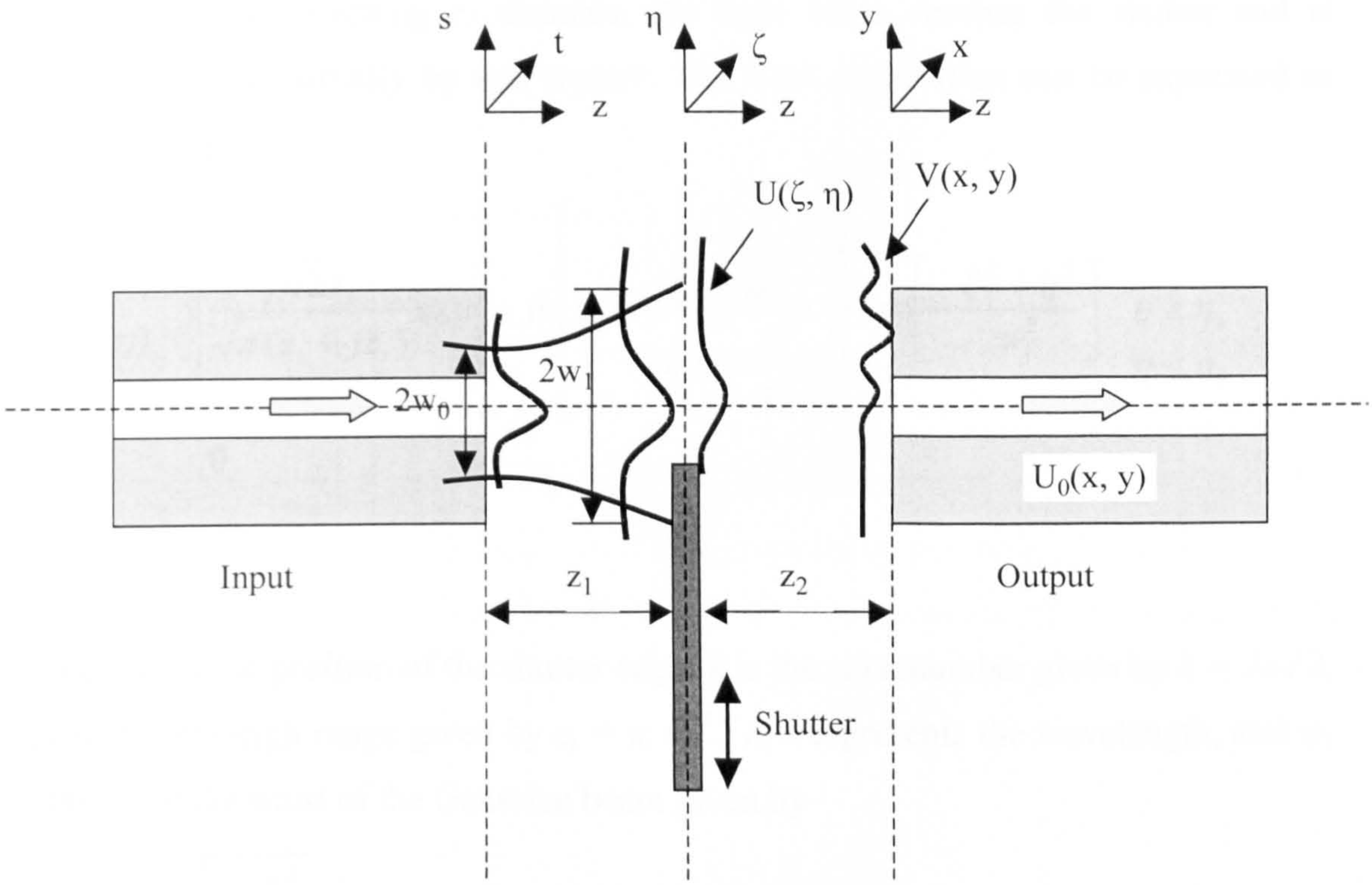

Fig. 5-16. Attenuator system in the optical modeling.

1. The light beam in the input fibre end has an amplitude $U_0(t,s)$ given by

$$U_0(t,s) = \sqrt{\frac{2}{\pi w_0^2}} \exp\left(-\frac{t^2 + s^2}{w_0^2} \right), \qquad (5.9)$$

where w_0 is the waist radius of the Gaussian beam. The term $\sqrt{\frac{2}{\pi w_0^2}}$ is used to normalize the energy to 1.

2. After transmitting z_1 distance, the light beam reaches the shutter and is blocked partially by this shutter. The field distribution can be expressed as [122]

$$U(\xi,\eta)=\begin{cases}\dfrac{j\sqrt{2}z_r}{\sqrt{\pi}(z_1+jz_r)}\exp\left\{-jk\left[z_1+\dfrac{\xi^2+\eta^2}{2z_1(1+\dfrac{z_r^2}{z_1^2})}\right]\right\}\exp\left[-\dfrac{\xi^2+\eta^2}{w_1^2}\right] & \eta\geq\eta_0\\ 0 & \eta<\eta_0\end{cases},$$

(5.10)

where η_0 is the position of the shutter edge, k is the wavenumber given by $k = 2\pi / \lambda$, z_r is the Rayleigh range given by $z_r = \pi\, w_0^2 / \lambda$, λ represents the wavelength, and w_1 stands for the waist of the Gaussian beam given by

$$w_1 = w_0\sqrt{1+\frac{z_1^2}{z_r^2}}, \qquad (5.11)$$

3. The light beam is then diffracted to the output facet. The field distribution $V(x,y)$ can be expressed by using Rayleigh-Sommerfield diffraction formula [123]

$$V(x,y)=\frac{z_2}{j\lambda}\iint_{\Sigma}U(\xi,\eta)\frac{\exp(jkr_{01})}{r_{01}^2}d\xi d\eta, \qquad (5.12)$$

where z_2 is the distance between the shutter and output facet. r_{01} is the distance between point (ζ, η) in shutter plane and point (x,y) in the output plane, which given by

$$r_{01} = \sqrt{(x-\xi)^2 + (y-\eta)^2 + z_2^2}\ , \qquad (5.13)$$

The output power is calculated by correlating the output field with the fundamental mode of the output fibre, as follows [128]:

$$\varsigma = \left| \iint_{\infty} V(x,y) \cdot U_0^*(\xi,\eta) dx dy \right|^2 , \qquad (5.14)$$

therefore, the attenuation L is obtained as

$$L = -10 \log \varsigma , \qquad (5.15)$$

Other parameters are λ = 1.55 um, w_0 = 5.1 um, z_1 = 30 um, z_2 = 30 um.

The output field is compared to the field on the shutter plane showing in Fig. 5-17, Fig. 5-18, and Fig. 5-19. Equation 5.15 is used to calculate the actual optical power coupling to the output fibre, and thus, the transfer function of the attenuator is obtained in Fig. 5-20.

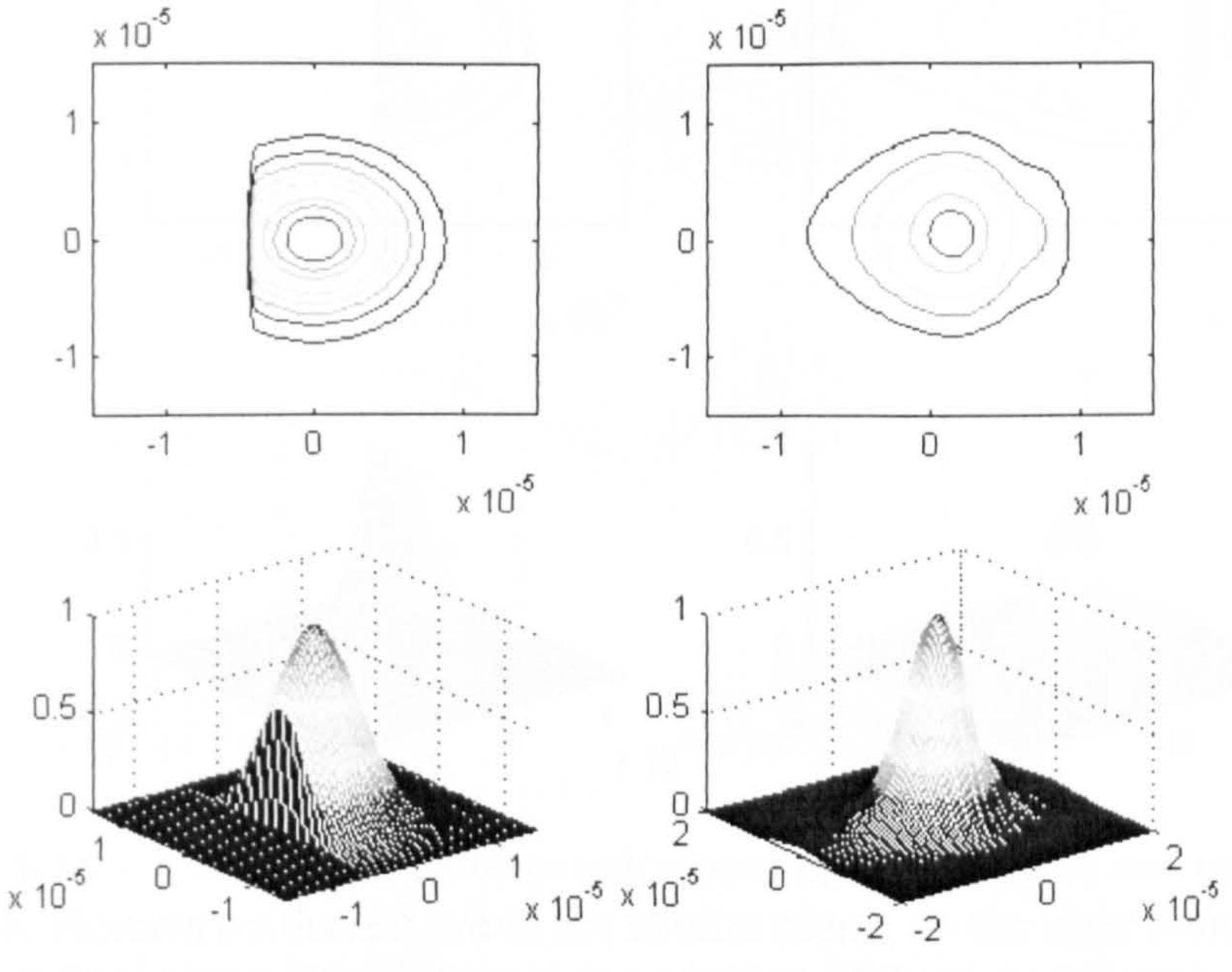

Fig. 5-17 – 1, Diffracted patterns calculated in shutter plane and output fibre plane. Pictures on the left are in the shutter plane, on the right hand are in the output fibre plane. The shutter in the position of – 4 μm (η = - 4 μm).

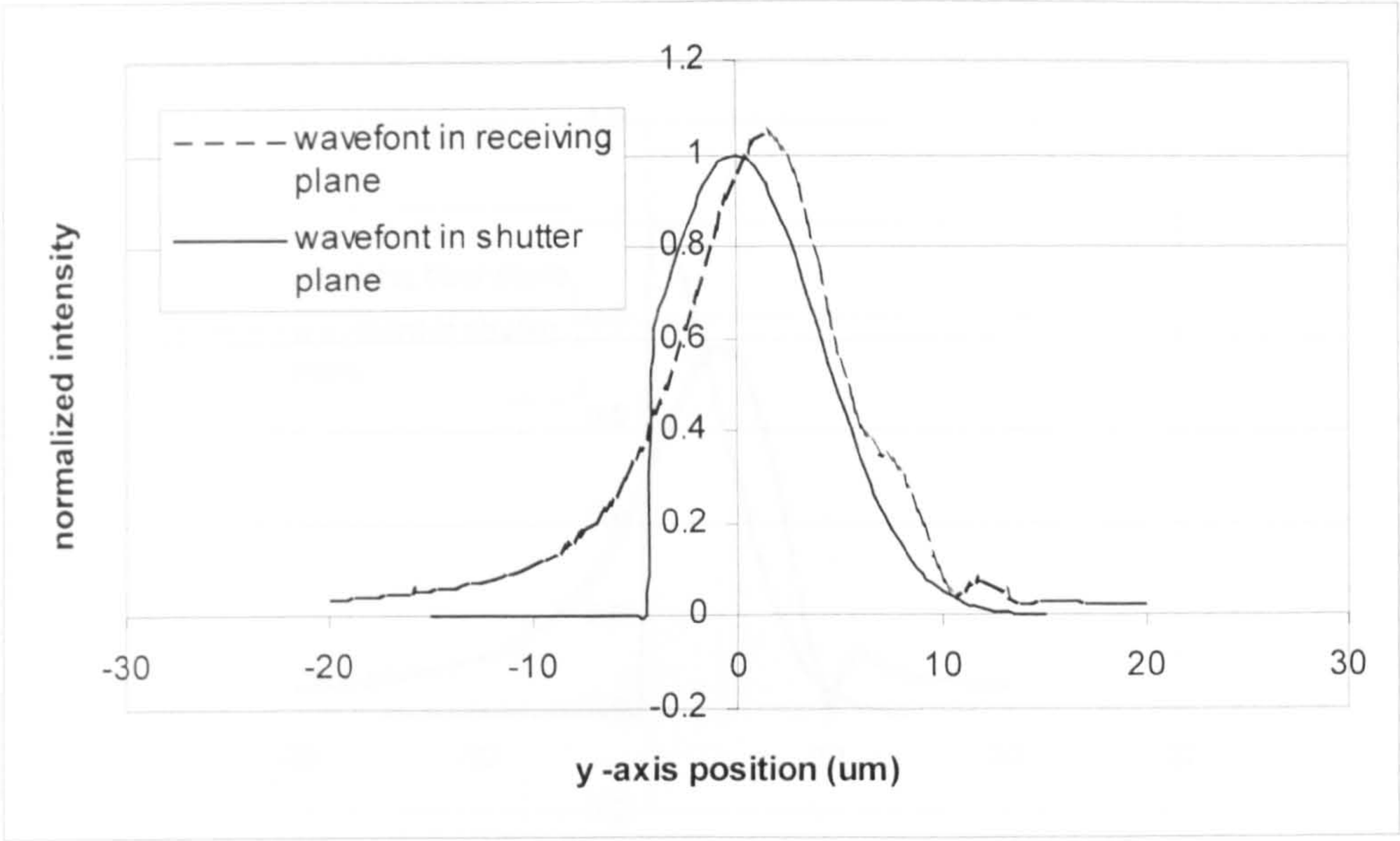

Fig. 5-17 – 2, 2-D optical output field compared to the field on the shutter plane. The shutter in the position of – 4 μm.

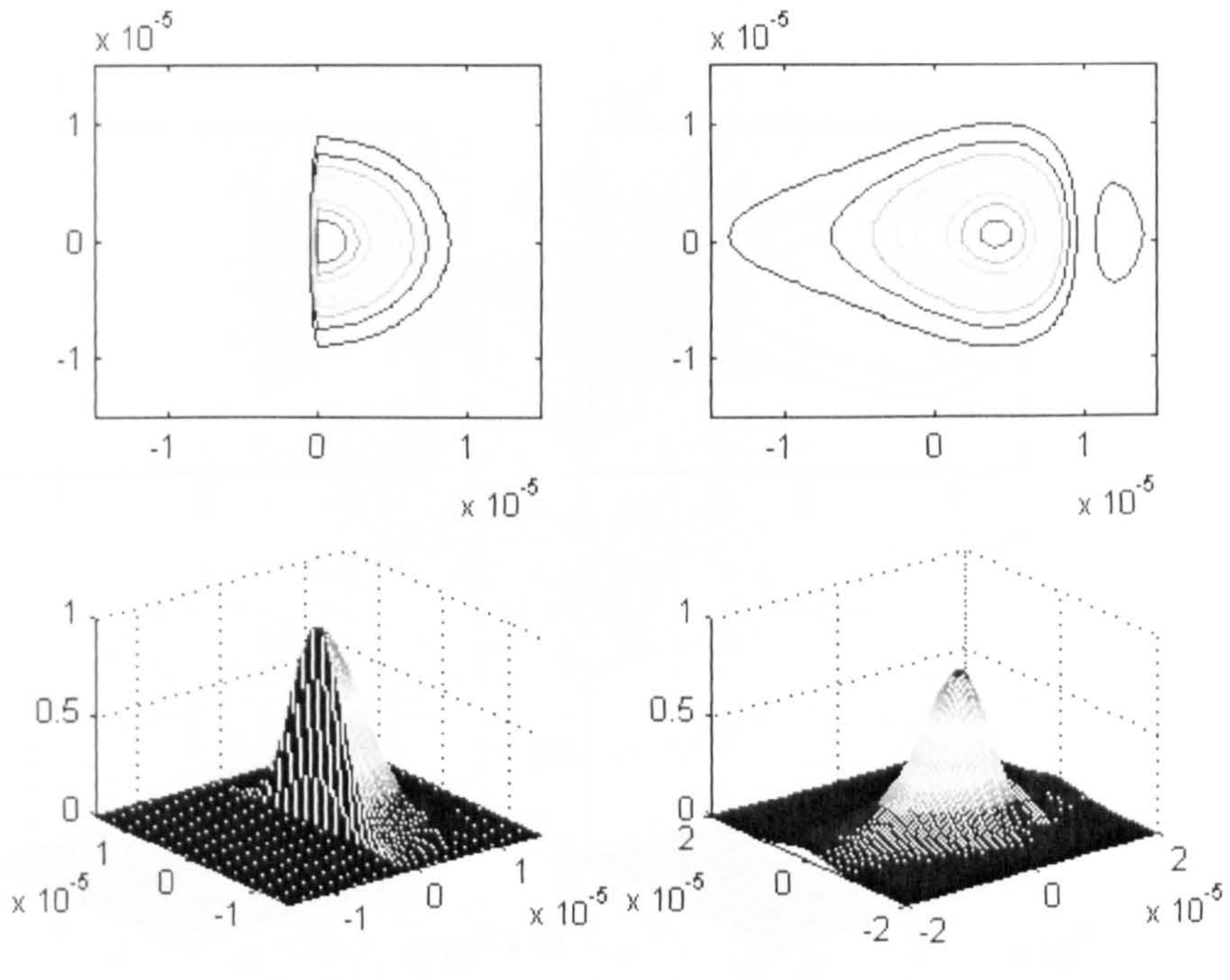

Fig. 5-18 – 1, Diffracted patterns calculated in shutter plane and output fibre plane. Pictures on the left are in the shutter plane, on the right hand are in the output fibre plane. The shutter in the position of 0 μm (η = 0 μm).

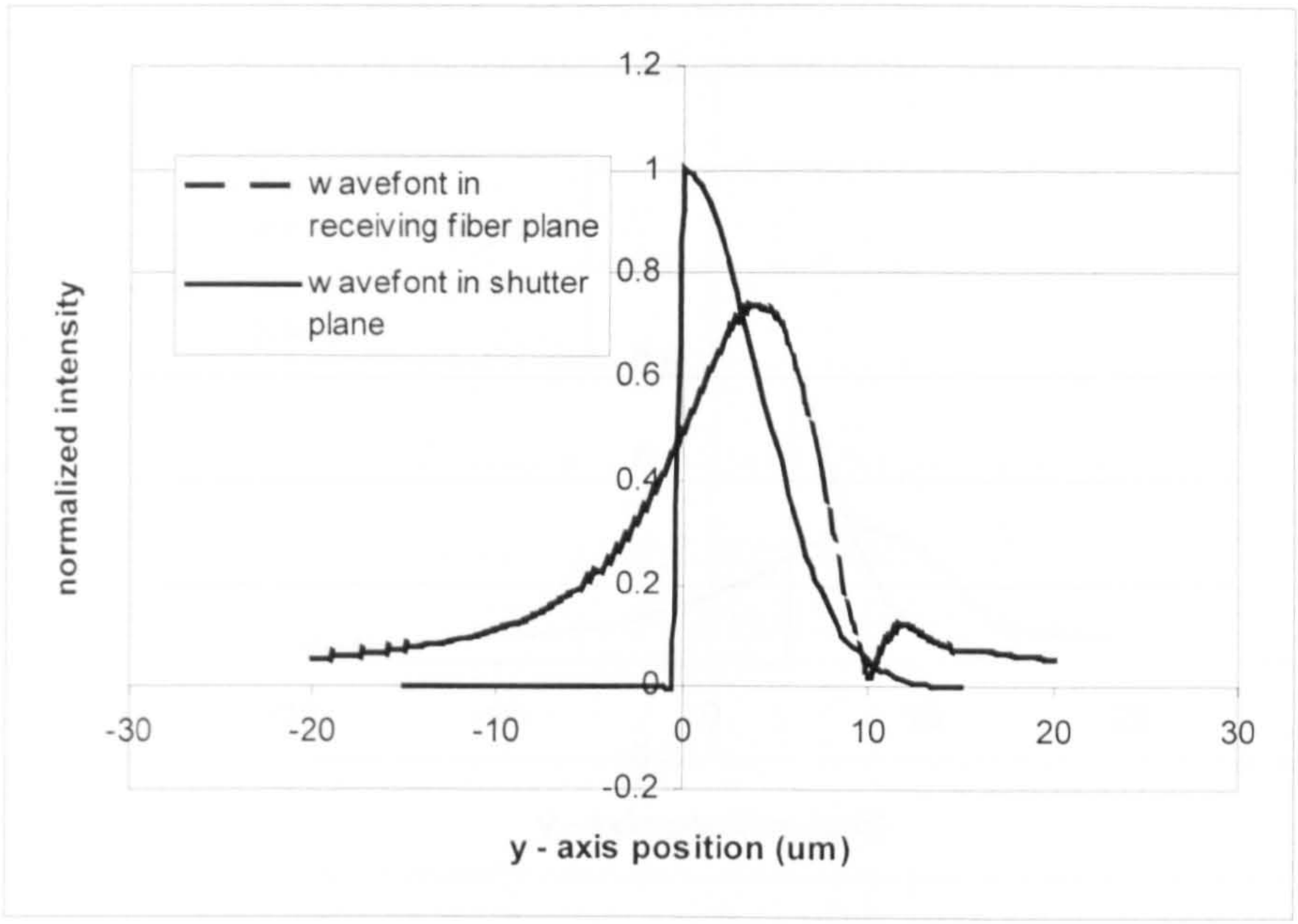

Fig. 5-18 – 2, 2-D optical output field compared to the field on the shutter plane. The shutter in the position of 0 μm.

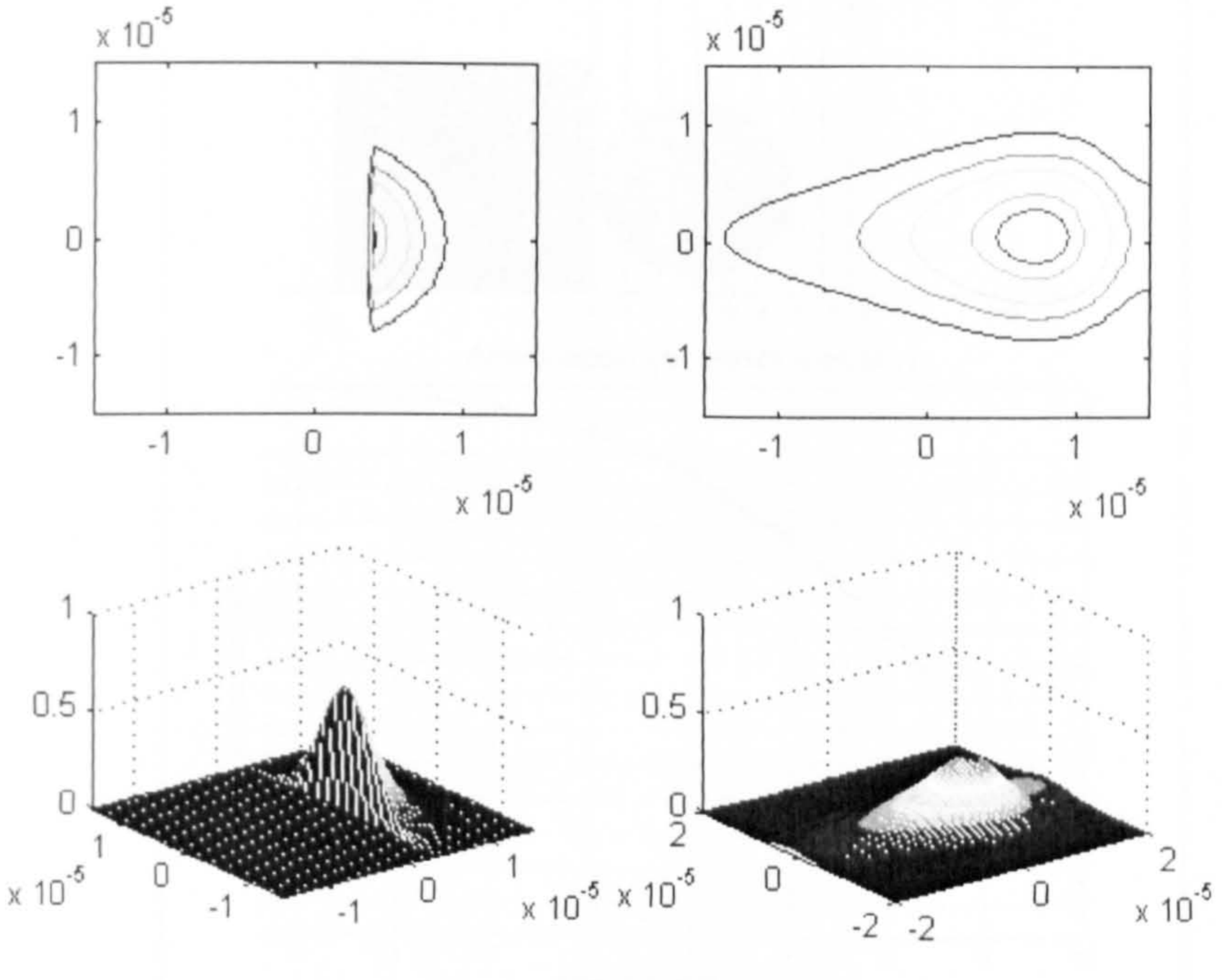

Fig. 5-19 – 1, Diffracted patterns calculated in shutter plane and output fibre plane. Pictures on the left are in the shutter plane, on the right hand are in the output fibre plane. The shutter in the position of 4 μm (η = 4 μm).

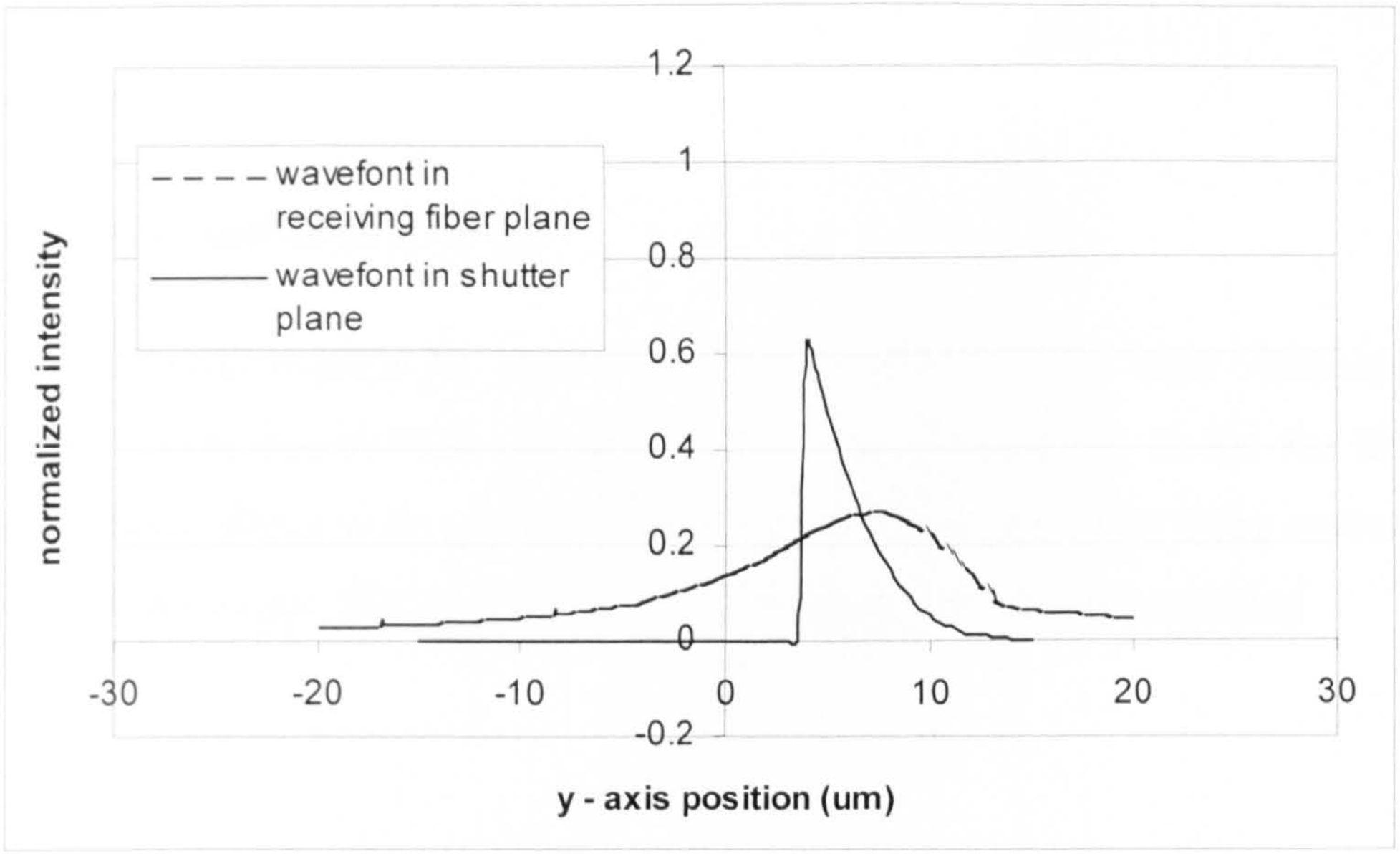

Fig. 5-19 – 2, 2-D optical output field compared to the field on the shutter plane. The shutter in the position of 4 μm.

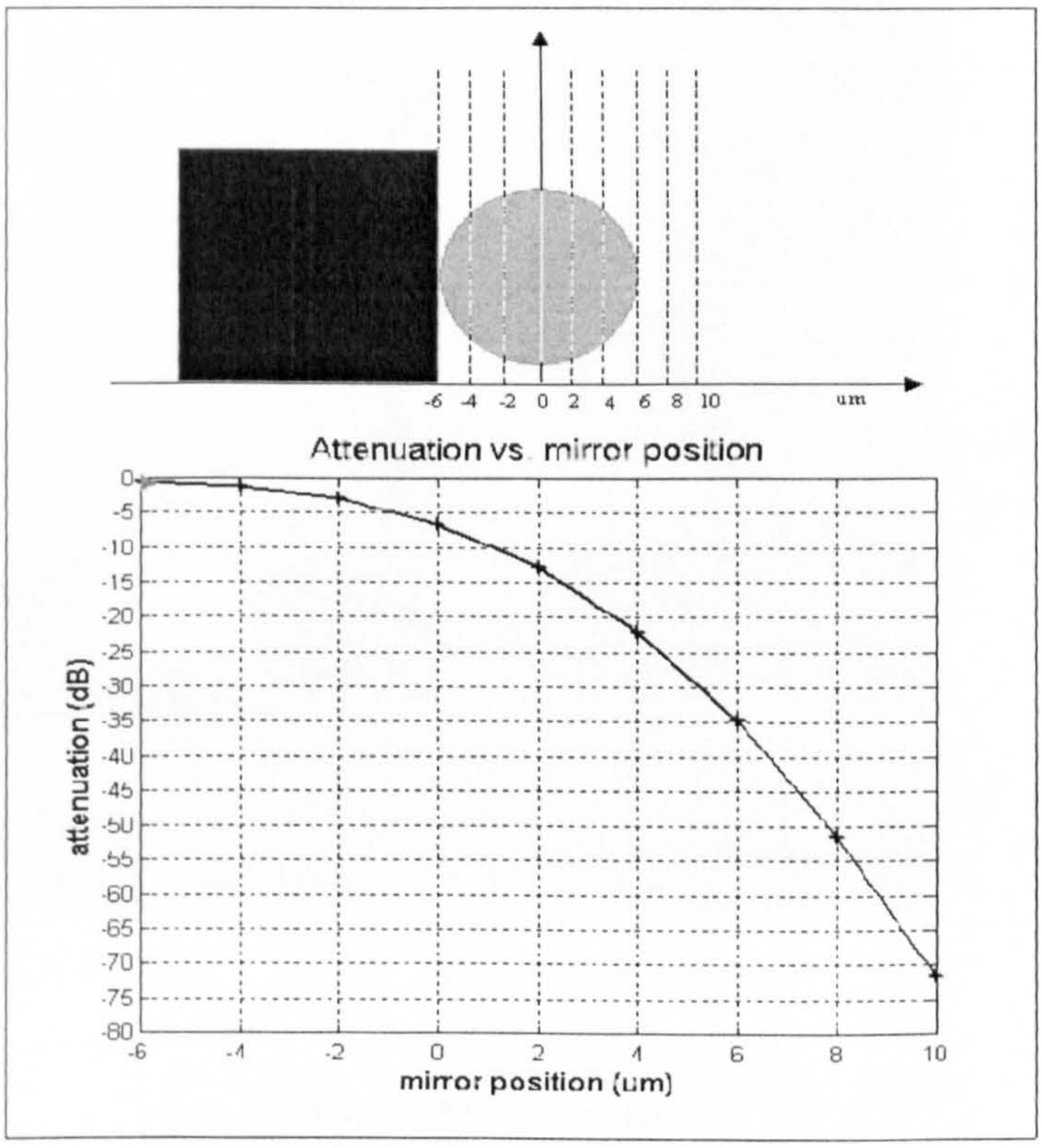

Fig. 5-20. Transfer function of the attenuator calculated using above method.

5.6 Experiment

5.6.1 Equipment and devices setup

During experimental evaluation, the silicon chips with the VOA were electrically connected to a customized PCB and placed under the microscope to aid the fibre alignment. Optical fibres were precisely positioned close to the VOA using ordinary optical translation stages. Fig. 5-21 shows the two fibres with the microshutter.

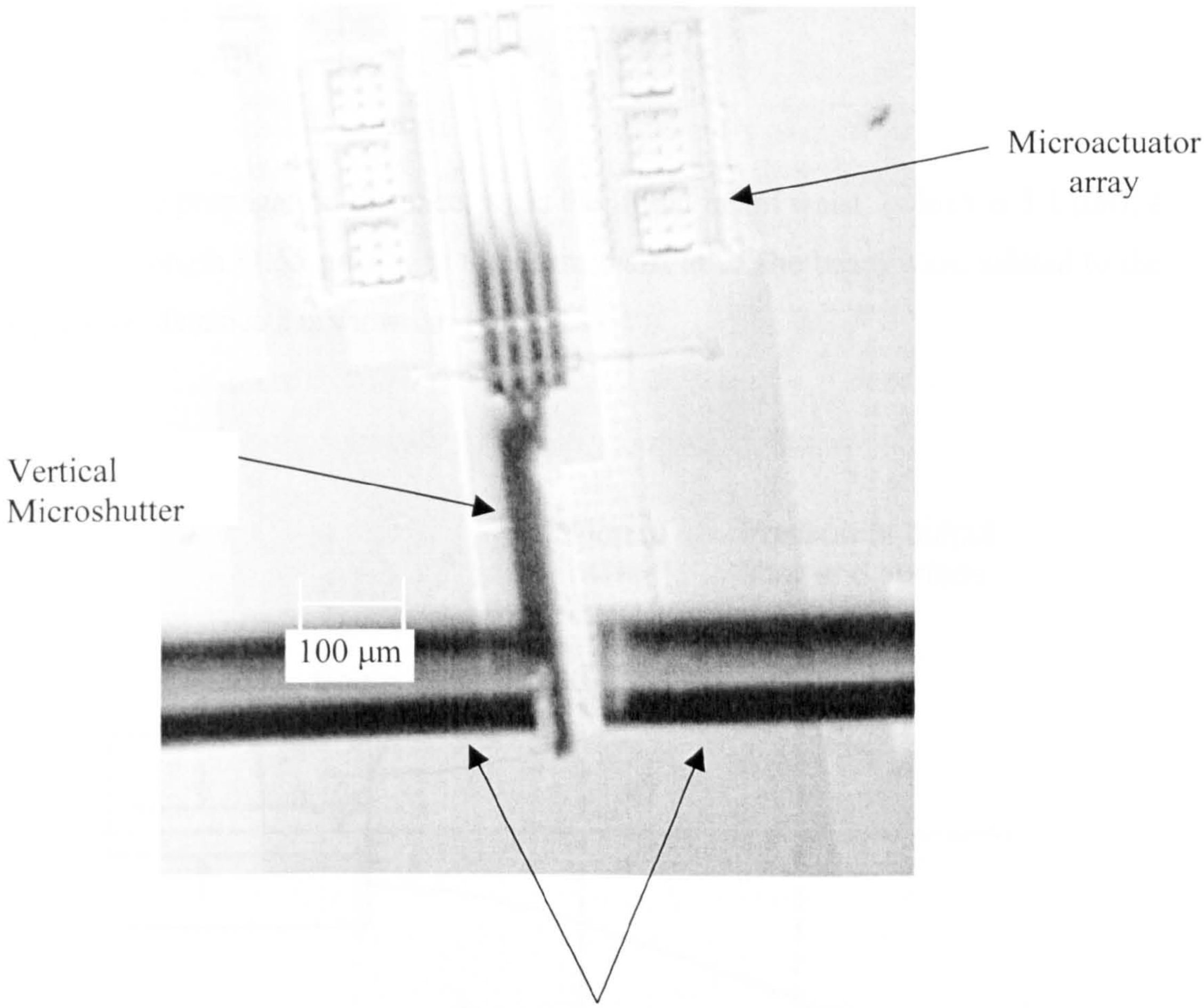

Fig. 5-21. Experiment arrangement of the VOA testing.

5.6.2 Static testing

The attenuation characteristic of the VOA was tested at 150 V rectangular voltage waveform of 50% duty-cycle. To measure precisely the attenuation characteristic during one cycle the device was driven at 100 Hz. First of all, the beam waist in the shutter plane should be calculated, because the displacement to be achieved by the SDA depends on the beam size at the surface of the shutter. (The Gaussian beam will diverge when it comes out from an optical fibre shown in Fig. 5-22). For a standard SMF, the waist of the beam emerging from the fibre is given as

$$w = w_0\left[1+\left(\frac{\lambda z}{\pi w_0^2}\right)^2\right]^{1/2}. \qquad (5.16)$$

Here, z is the propagation distance, w_0 is the initial beam waist, (which is 5.1 μm); λ is the wavelength (1.55 μm); w is the beam waist at z. The beam waist related to the propagation distance z is shown in Fig. 5-23.

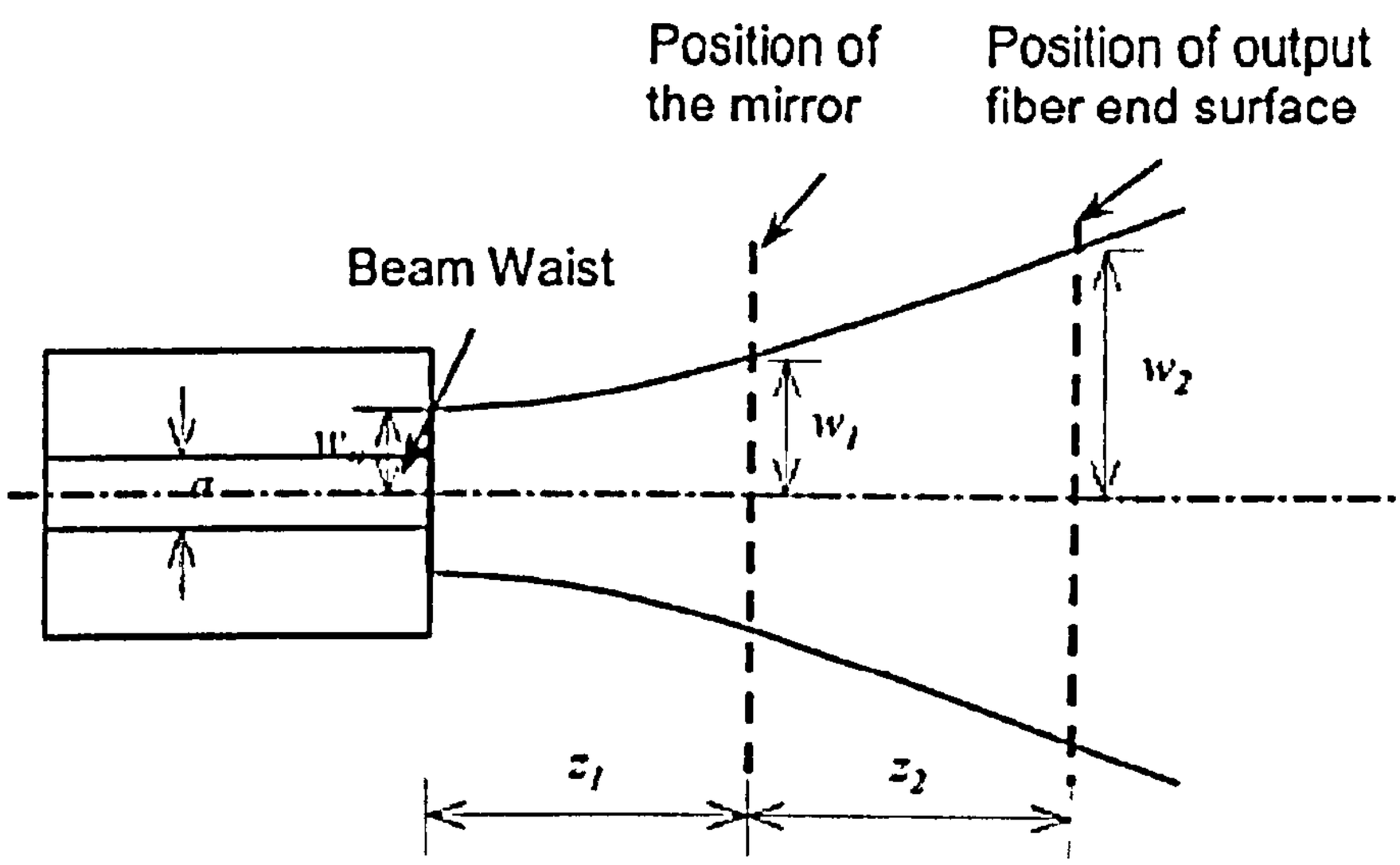

Fig. 5-22. Divergence of the Gaussian beam.

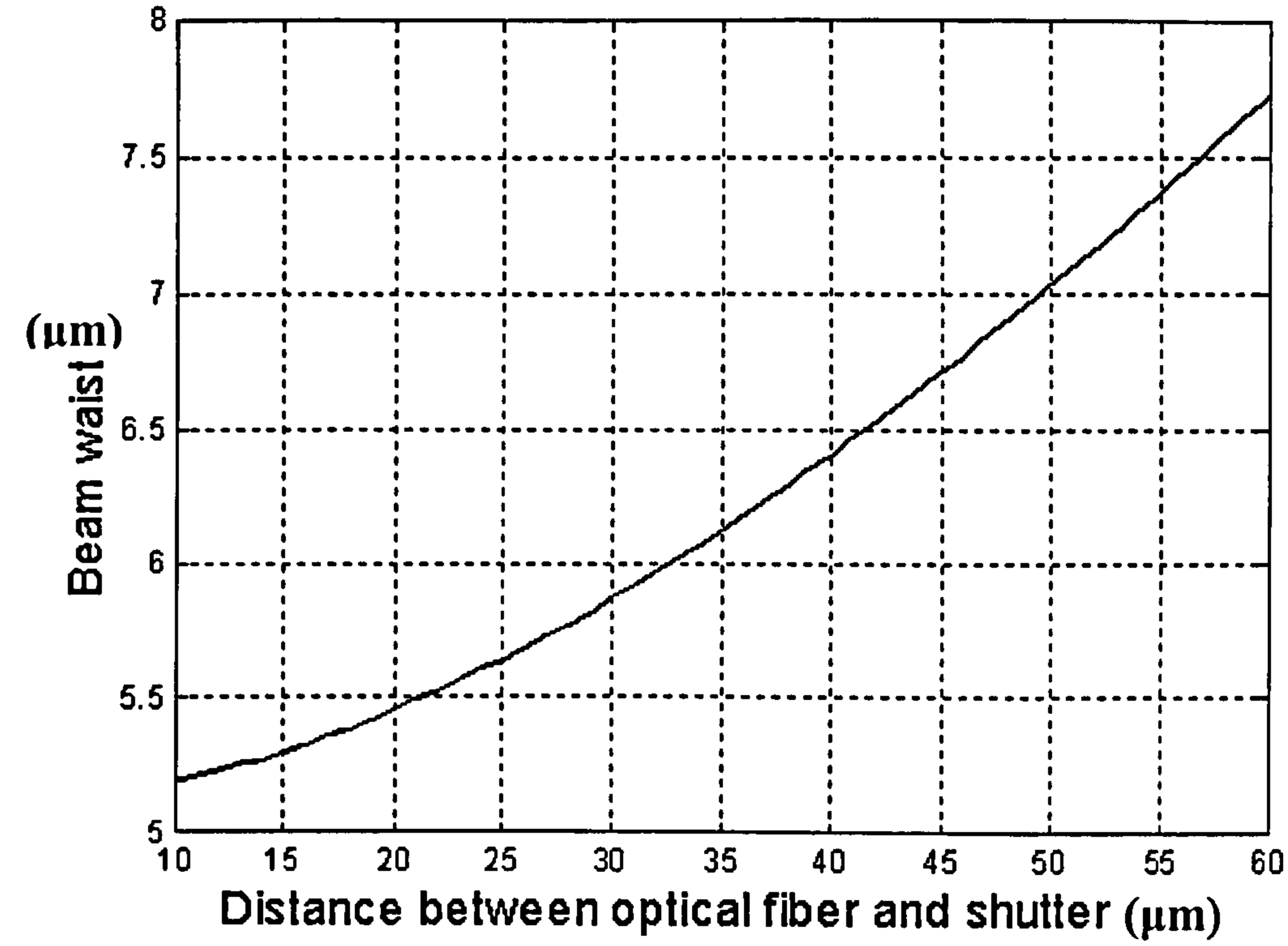

Fig. 5-23. Beam waist vs. distance.

From above calculation, the beam waist is around 5.8 μm at the 30 μm from the input fibre. So the SDAs are required to move at least 11.6 μm. Fig. 5-24 shows the testing result of the relationship between moving time and attenuation.

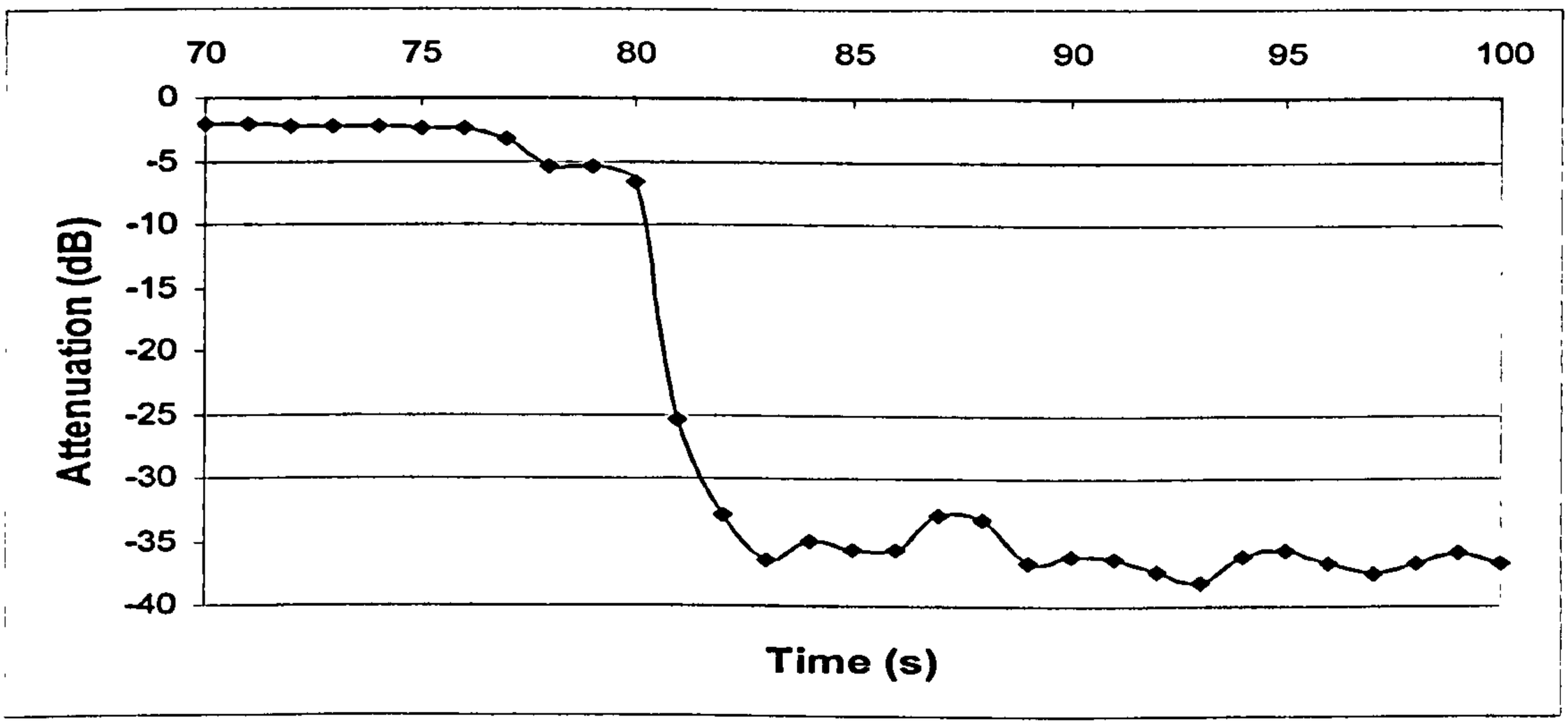

Fig. 5-24. Moving time vs. attenuation.

From Fig. 5-24, it took the actuator arrays 7 seconds from beginning shutting light to completely closing the light beam. So the speed of the actuator is calculated to be 2 x 5.8 / 7 = 1.6 μm/s. Also the step size of the SDA is deduced to be 16 nm because the driving frequency is 100 Hz. The insertion loss for ideally aligned fibres separated by 60 μm is 1.15 dB (assuming the angular and laterally misalignments are 0). Experimentally, the fibre to fibre coupling was measured - 2.3 dB (here, input power was recorded 500 μW, and output power was recorded 290 μW). The maximum attenuation is measured to be – 36.5 dB. The experimental results of attenuator has been compared with theoretical result from Fig. 5-20, which is shown in Fig. 5-25.

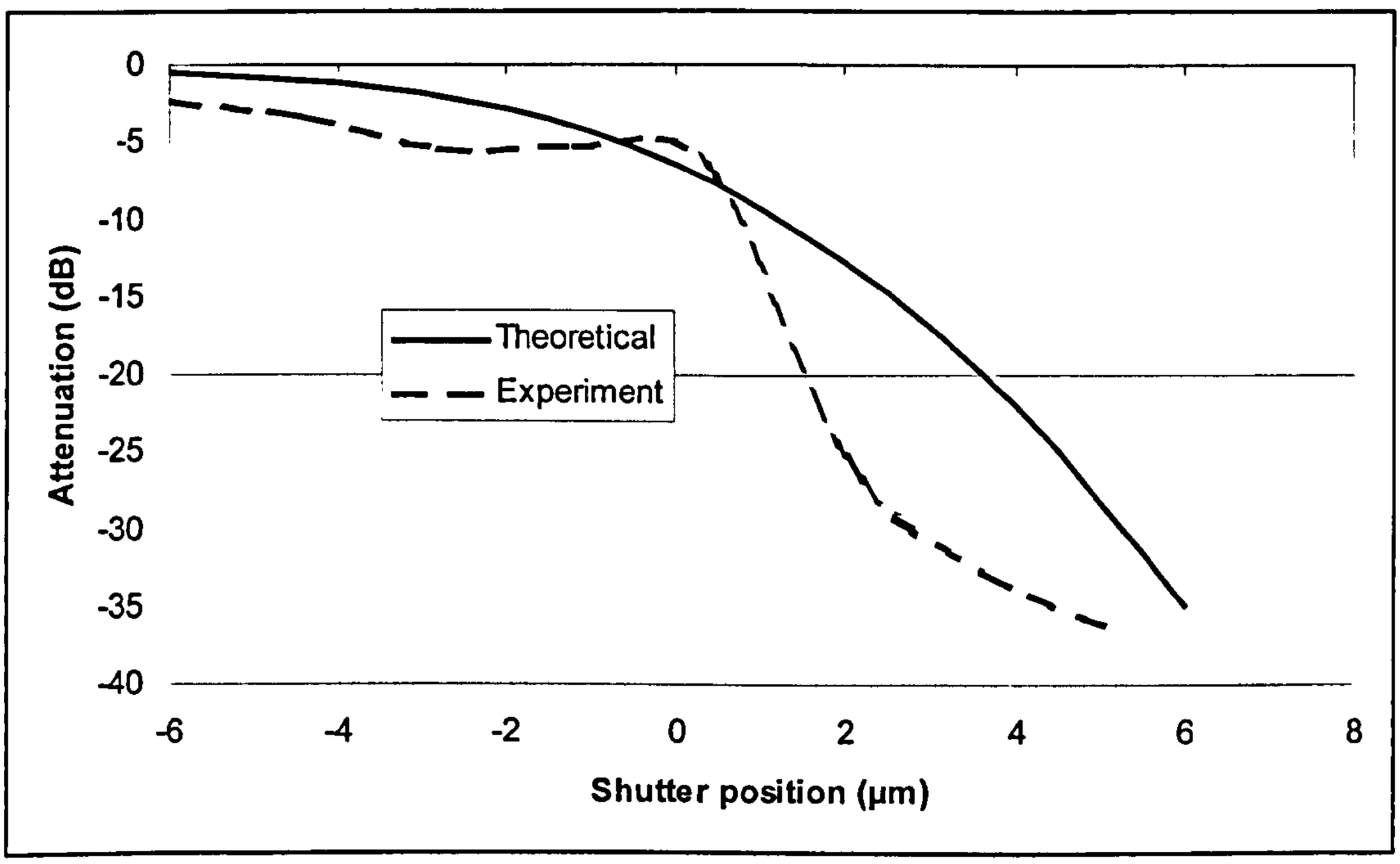

Fig. 5-25, Comparison of theoretical and experimental results.

Through the experiments, the moving of the transport stage causes the wobbling of the microshutter, which induces the error between theoretical and experimental results.

5.6.3 Repeatability testing

The repeatability of the device was measured at 100 Hz. The measured insertion loss of the aligned fibres was typically – 2.3 dB. The attenuation speed depends on the driving frequency of the SDAs. The VOA was driven at 100 Hz and once the transmission dropped to its lowest value the driving voltage was switched off. This allowed the restoring force of the spring to pull the device back to its original position re-establishing the full light coupling between the fibres. This action was repeated up to 100 times. During that time it was always possible to move the device backward and forward to achieve the on-off action of the VOA. The result is shown in Fig. 5-26. Decay in the Fig. 5-26 is caused by the continuous knocking between transport plate and the fibres, then disalignments happened.

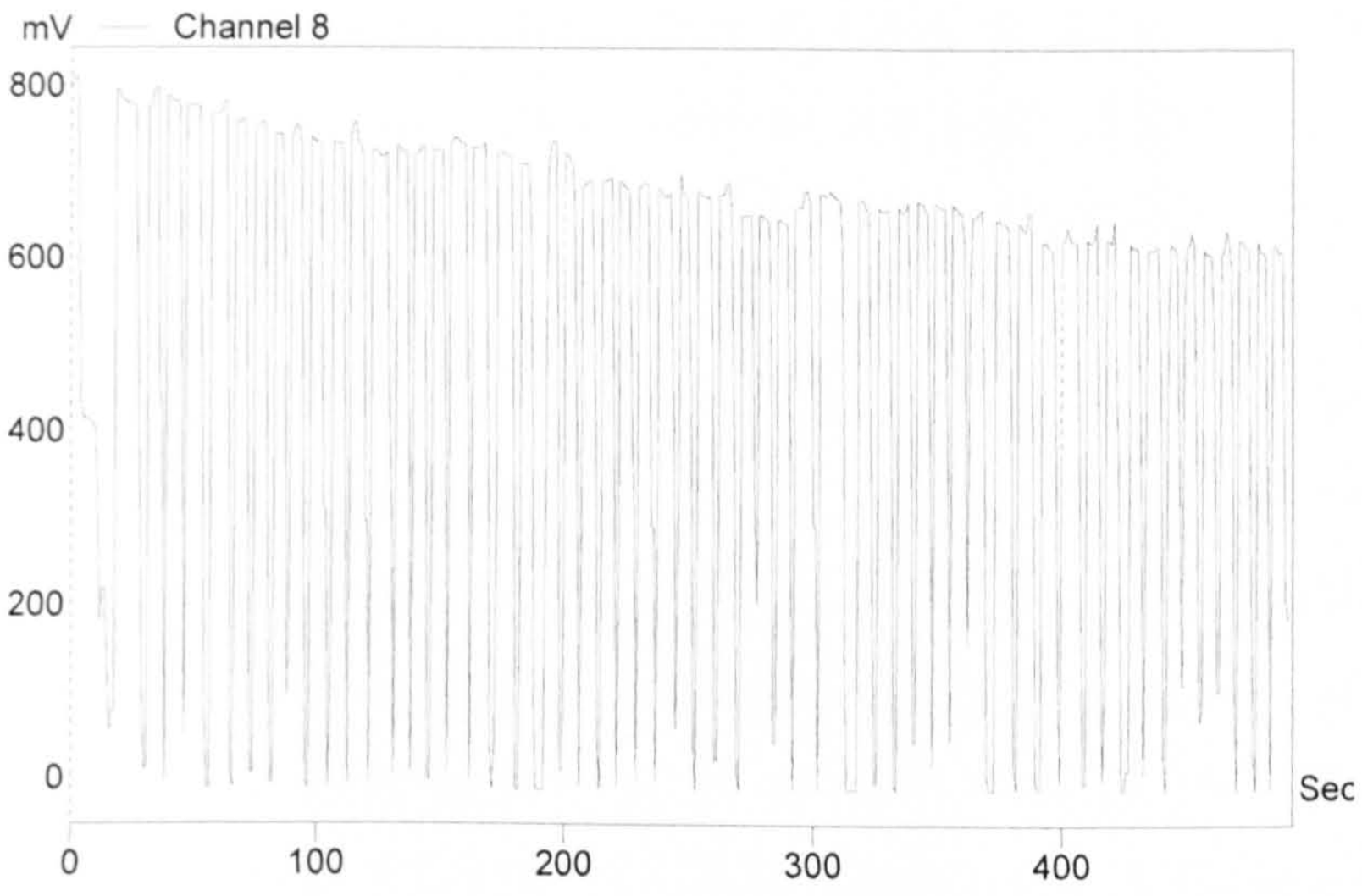

Fig. 5-26. Repeatable testing of VOA. The x- axis is time, the unit is second. The y- axis is the recorded data of the output power, scaled by mV.

5.7 Conclusion

A variable optical attenuator powered by scratch drive actuator has been designed, analyzed, and characterized. Microhinges are employed to construct a 3-D moveable microshutter. The principle of 3-D self-assembly using stress-induced beams has

been applied to assemble this shutter. The major advantage of the self-bending beam is that it immediately assembles the 3-D structure automatically after the HF releasing process. There is no extra step or process to be implemented because the assembled beams are integrated into the structure design. The stress-induced beams can also be controlled by changing the temperature, because the two layers of the bimorph have a large difference of thermal expansion coefficients. Such self-assembly techniques may have many application in areas such as micromirrors and microoptical switches, and other 3-D MEMS applications. An optical model has been built using diffractive theory, and attenuation function was obtained. Measurements of the optical attenuator show that the attenuation can be precisely controlled because the SDA has precise step size (measured 16 nm). The measured insertion loss is – 2.3 dB in open state, and – 36.5 dB in off state.

Chapter 6

Design and Evaluation of a MEMS Optical Chopper

6.1. Introduction

Optical choppers are mainly used in precise optical measurements for both free-space and guided-wave optics particularly where the influence of stray light is perceived to be a problem. Light from the optical source that is used for the measurements is "chopped", that is the light signal is modulated in intensity so that the received light signal is converted into an alternating current at a photoreceiver. The received a.c. photocurrent which is directly proportional to the light intensity is fed into a synchronous detector, such as a lock-in-amplifier, so that its amplitude can be measured with greater accuracy without the error induced by d.c. drift in the electronics or stray light from the environment. Conventional optical choppers are usually in the form of a motor-driven wheel with regularly spaced apertures through which the light to be "chopped" will pass. They are thus large in size and are hence not suitable for optical microsystems. Miniaturised optical choppers fabricated by various micromachining technologies and in different material systems have been reported in earlier literature [22-25]. In [22] a micromachined chopper based on a moving diffractive element was reported for infra-red measurements. The device was fabricated on LPCVD silicon nitride deposited on a sacrificial LPCVD oxide deposited on a silicon substrate. In [23] an electrostatic actuator was used to drive a single polysilicon shutter integrated with a silicon photodetector. Polysilicon surface micromachining is used in the fabrication process. In [24] the micromachined chopper reported was fabricated in quartz and the device was piezoelectrically driven. The quartz chopper of [24] with dimensions of 6mm x 7mm is substantially larger than the compact device reported here. In [25] the chopper was also fabricated using polysilicon micromachining, but with the inclusion of a back-side etched hole through which the light to be chopped is transmitted.

The chopper reported here has been fabricated in BSOI (bonded silicon-on-insulator) which is mechanically and electrically superior to polysilicon. The design is symmetric about its centre. Each half of the chopper consists of a blade attached to a suspension and electrostatically driven by a comb microactuator. The two comb drives are electrically connected in parallel. The two blades form a slit that can periodically be closed, resulting in the chopping action if an a.c. voltage is applied. Alternatively, application of a d.c. voltage will simply result in an optical slit whose width can be controlled by the magnitude of the voltage. The microfabrication process includes back-side etching of an aperture through the wafer, thereby making it convenient to align and accommodate optical fibres with respect to the chopper. The entire structure is shown schematically in Figure 6-1. The overall dimensions of the chopper, including the microactuators and micromechanical suspension, are 1200 μm x 1200 μm making it very compact.

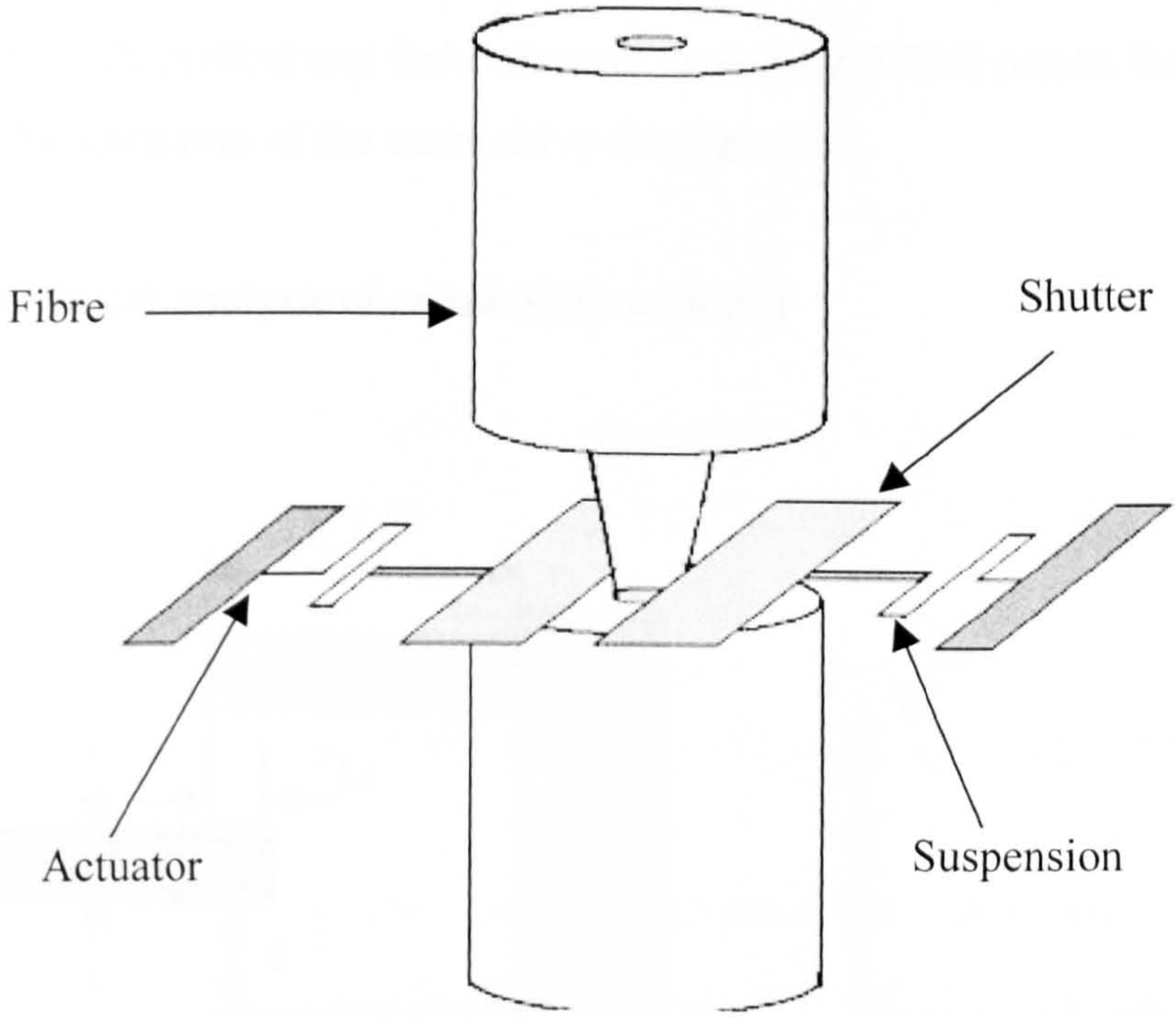

Fig. 6-1. Schematic diagram of the fibre optical chopper.

The comb-actuator driven chopper, designed for use in conjunction with fibre optics, has been fabricated in silicon-on-insulator material which has been back-etched to create an optical path through the thickness of the substrate. General electro-mechanical design considerations, including factors to minimise the side instability of the comb drive, are described in this Chapter. Finite element modelling (FEM) of the chopper has been backed up by simple theoretical results, and the results from the theoretical work verify the findings from the FEM. Optical modelling of the chopper has also been undertaken. Experimentally, the device was driven from 0-34 volts d.c. to measure its static characteristics. For dynamic characterisation, the device was operated from 0-28 volts a.c. and its fundamental resonant frequency was measured to be 3 kHz. The shutters come in contact at greater than 28 volts, which influence the dynamic performance of device. Experimental evaluation of the device characteristics are shown to closely match the theoretical predictions.

6.2. Mechanical design considerations

In this section, theoretical and finite element modelling (FEM) results for static and dynamic characteristics of the comb drive are presented.

6.2.1. Theoretical analysis of comb drive actuator

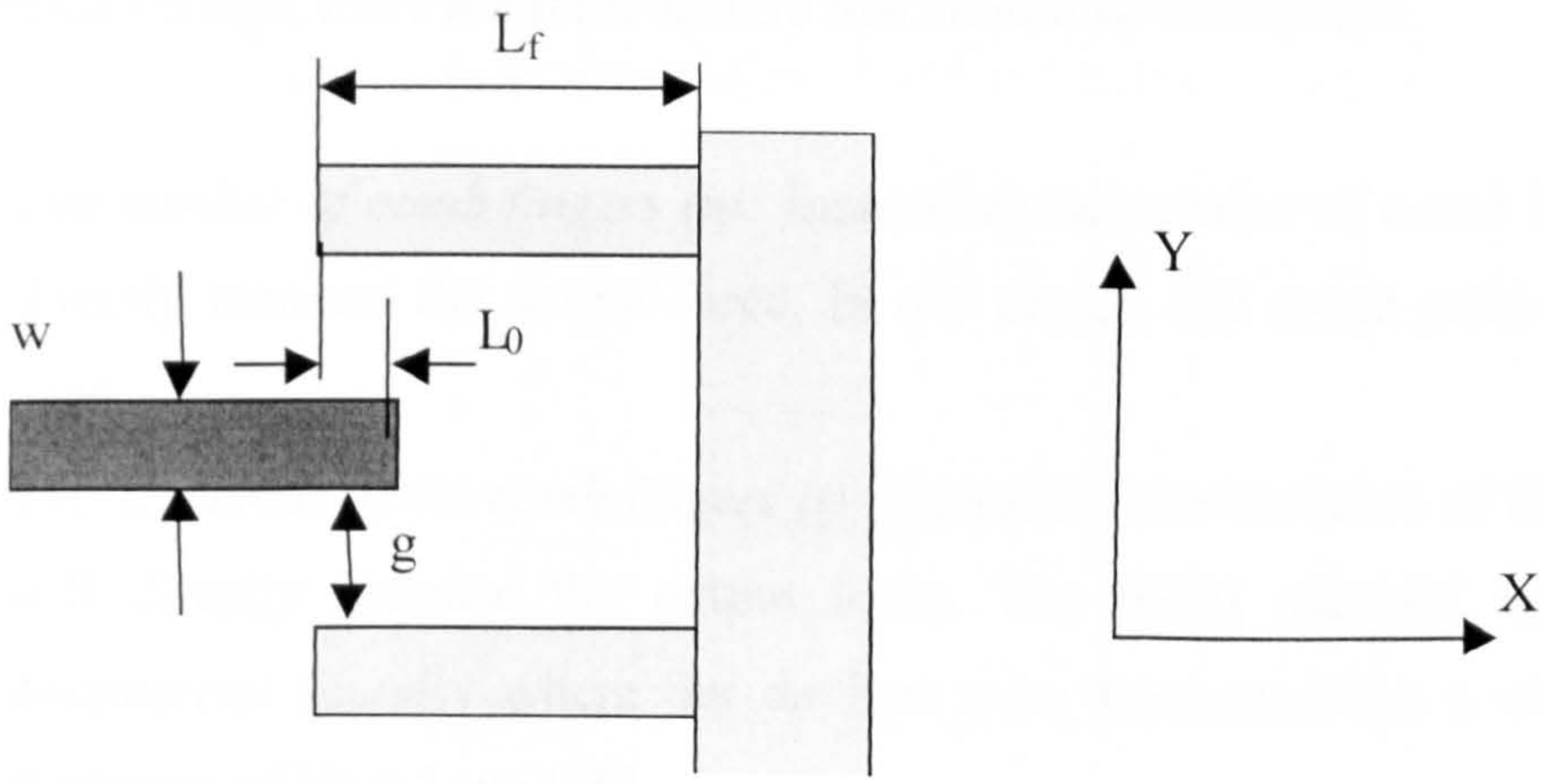

Fig. 6-2. Single comb drive cell.

A comb drive microactuator consists of two interdigitated finger structures (combs) with one comb fixed and the other connected to a compliant suspension. Application of a voltage difference between the combs results in the deflection of the moveable comb by electrostatic forces. An engaged pair of fingers, defined as one cell of a comb actuator, is shown in Figure 6-2.

To simplify modelling, the electrostatic field between the fixed and moveable fingers is approximated by a one-dimensional parallel-plate model. In the analysis, three-dimensional effects like fringing fields, comb-finger end effects and the ground-plane levitation effect are neglected. The capacitance between the fixed and moveable comb fingers can be expressed as:

$$C = \frac{2n\varepsilon_0 t(x + L_0)}{g} \quad \text{.....} \quad (6.1)$$

where n is the number of fingers, ε_0 is the dielectric constant of air which is 8.85 x 10^{-12} F/m, t is the thickness of the comb fingers, L_0 is the initial comb finger overlap, x is the comb finger displacement and g is the gap spacing between the fingers. The lateral electrostatic force in the x- direction is equal to the derivative of the electrostatic energy with respect to x:

$$F_x = \frac{1}{2}\frac{\partial C}{\partial x}V^2 = \frac{n\varepsilon_0 t}{g}V^2 \quad \text{.....} \quad (6.2)$$

According to Equation (6.2), in order to obtain a large force while keeping a relative low applied voltage, there are three factors that should be considered.

1. *The number of comb fingers (n):* Increasing the number of comb fingers will directly increase the output force. In our design 102 comb pairs have been used.
2. *The thickness of the comb fingers (t):* Increasing the thickness of the structure will directly increase the output force. The BSOI material used by the commercial foundry where our devices were fabricated has a silicon layer thickness of 10 ± 1 μm [90].

3. *The gap between the comb fingers (g):* Decreasing the gap spacing will result in larger driving force, but at the same time increasing the side instability. Analysis of side instability is described in the next section. Based on this analysis the gap spacing in our design was selected to be 2.5 μm.

6.2.1.1 Side instability and the stable travel range:

The phenomenon of side sticking has been taken into consideration in our design. A series of theoretical calculations introduce the concept of side sticking [124]. Figure 6-3 shows a typical comb-drive actuator with two pairs of folded spring suspensions. When a driving voltage, V, is applied between the moveable and fixed fingers, an electrostatic force F_x along the x-direction is generated. Additionally there is an electrostatic force along the y-axis pulling the moveable and fixed fingers together. The net electrostatic force in the y direction, F_y, generated by both sides of the moveable fingers, instead of pulling the moveable finger structure back to the original position, will push it further off equilibrium. The maximum stable displacement d_{max} [124] can be expressed as:

$$d\max = \frac{1}{2}\sqrt{L_0^2 + 2\frac{K_y}{K_x}g^2} - \frac{L_0}{2} \qquad \text{.....} \qquad (6.3)$$

where K_x and K_y are the spring constants in the x- and y- directions and all other symbols are as previously defined. From Equation 6.3, it can be seen that increasing the comb gap g will increase the stable travel distance, but at the cost of increasing the electrostatic voltage required to produce the force F_x (see Equation 6.2).

In the folded spring suspension, the x-direction and y-direction spring constants are [125]:

$$K_x = \frac{2Etw^3}{L_s^3} \qquad \text{.....} \qquad (6.4)$$

$$K_y = \frac{2Etw}{L_s} \qquad \text{.....} \qquad (6.5)$$

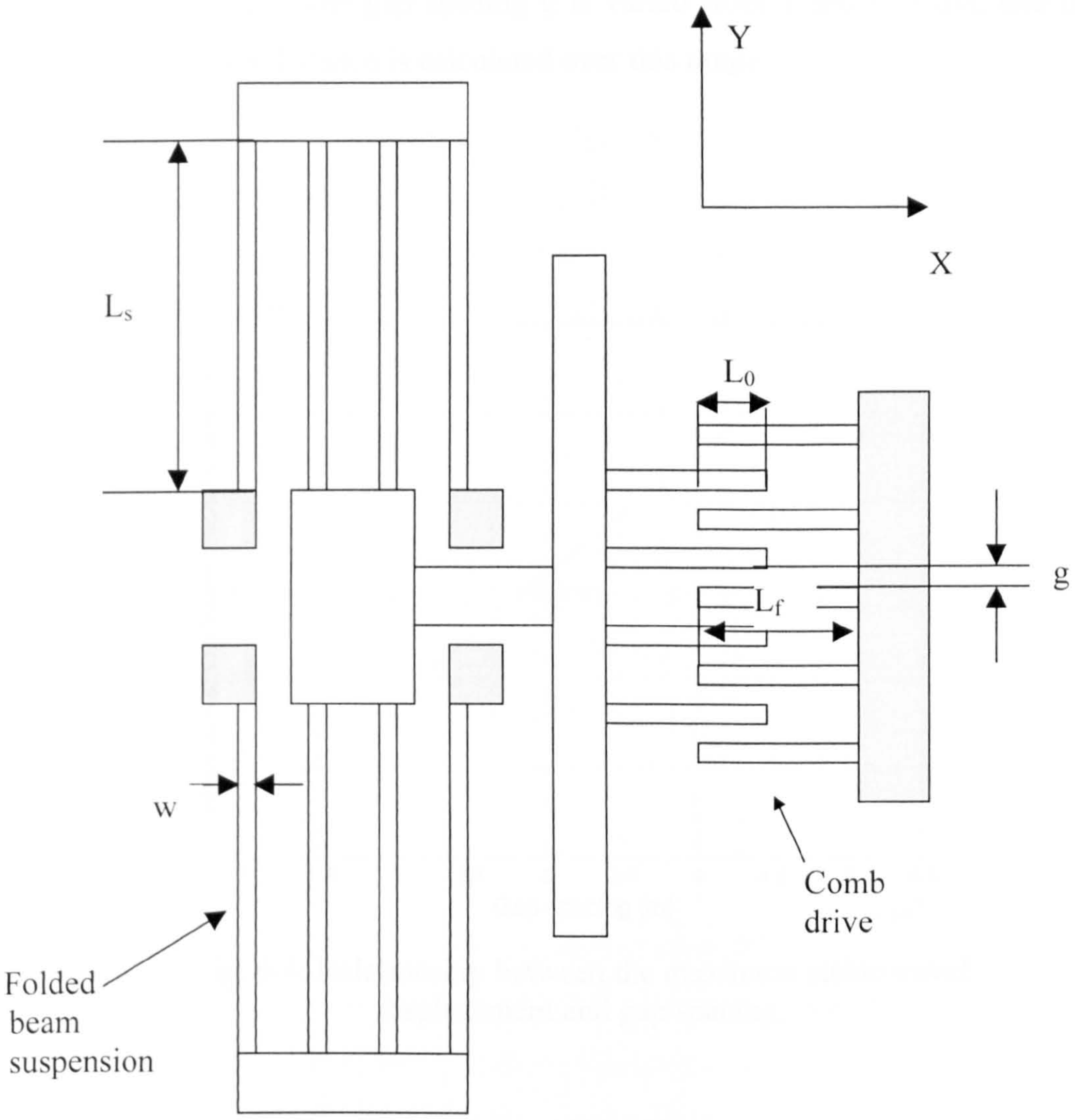

Fig. 6-3. Single comb drive with folded beam suspension.

where t is the thickness of the beam, w is the width of the beam, and L_s is the length of the suspension beam of the folded spring. Substituting Equations (6.4) and (6.5) into Equation (6.3), the maximum displacement obtained is given by the expression:

$$d\max = \frac{1}{2}\sqrt{L_0^2 + \frac{2L_s^2}{w^2}g^2} - \frac{L_0}{2} \qquad \ldots\ldots\ldots\ldots \qquad (6.6)$$

Figure 6-4 shows the result calculated from Equation (6.6) where L_0 = 3 μm, L_s = 590 μm and w = 3 μm. The gap spacing g is varied from 1 μm to 5 μm, and the maximum stable travel distance is calculated over this range.

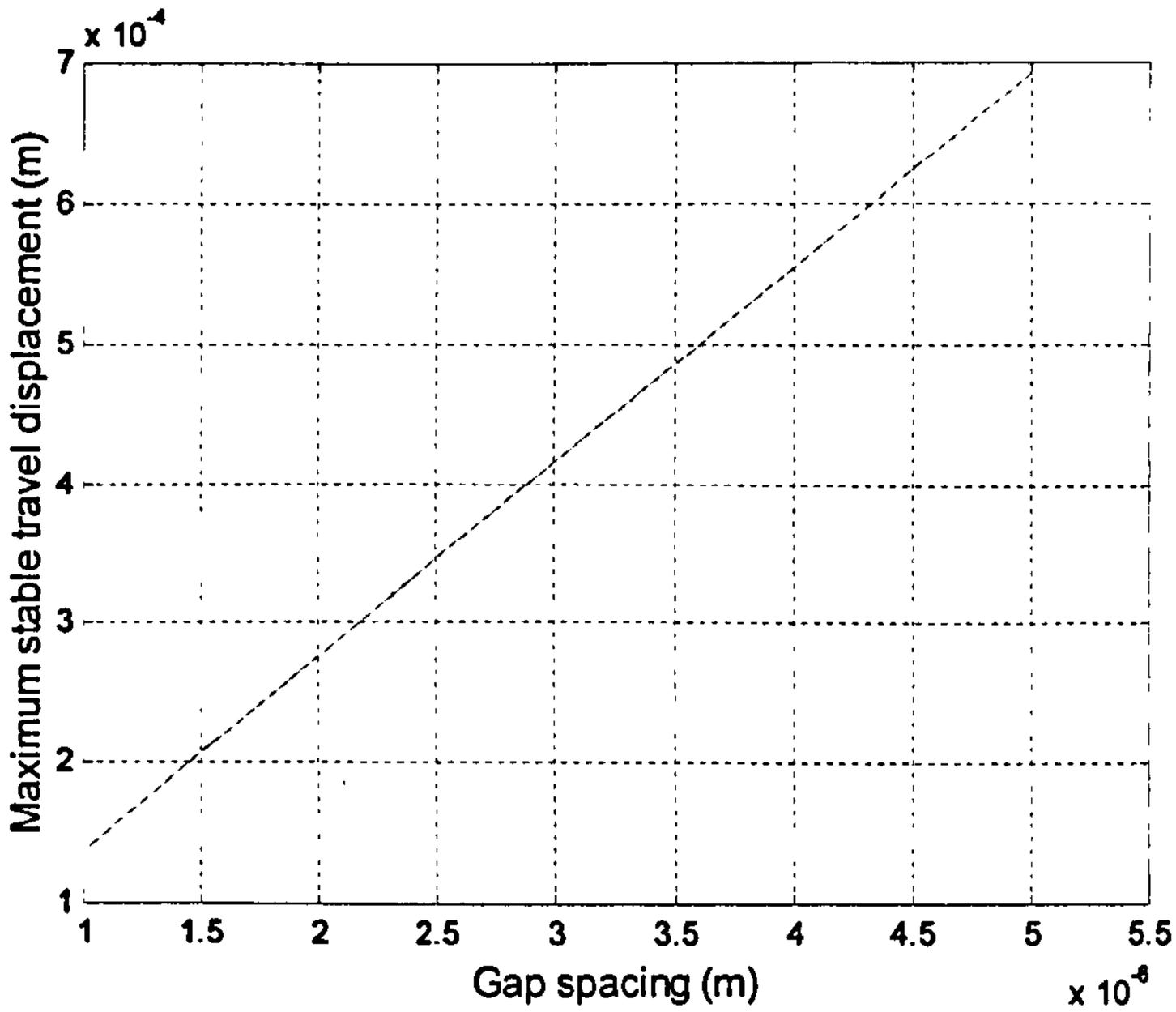

Fig. 6-4. Relationship between the maximum stable travel displacement and gap spacing.

In our design of the comb drive, the gap spacing is set to be 2.5 μm. The maximum stable displacement is around 350 μm. This value is much larger than the length of each comb finger in our device design (L_f = 40 μm) making our comb actuator inherently stable.

6.2.1.2 Resonant frequency

An expression for the fundamental frequency of a folded spring structure has been derived in [30] as :

$$f = \frac{1}{2\pi}\sqrt{\frac{K_x}{M_{plate} + 0.3714 M_{beam}}} \qquad \text{.....} \qquad (6.7)$$

where K_x is the lateral spring constant, M_{plate} is the plate mass, M_{beam} is the supporting beam mass. For our device design, the plate mass (M_{plate}) is calculated to be 7.93 x 10^{-10} kg and M_{beam} is calculated to be 3.33 x 10^{-10} kg. For these values, the spring constant K_x is calculated to be 0.50 μN/μm and the fundamental frequency is calculated to be 3.72 kHz.

6.2.2 FEM analysis

In this section we present the results of FEM of the mechanical elements of the optical chopper, comparing the values obtained from FEM with those obtained from the theoretical expressions of the previous section.

6.2.2.1 FEM : Static analysis

Using ANSYS software, we obtained the spring constant K_x for the structure as follows: a finite element model of the chopper was constructed and static loading applied to this model. For each value of load applied, the deflection in the x direction was obtained using the software. A plot of the load vs. deflection data for the structure yields the spring constant which was calculated to be 0.51 μN/μm. This value is in good agreement with that calculated in section 6.2.1.2. The relationship between applied voltage and displacement of the moveable fingers is likewise obtained through the FEM simulation using ANSYS software. During modelling it is assumed that the travel of the finger is in the constant electrostatic force range. Figure 6-5 shows the results from the analysis.

6.2.2.2 FEM : Dynamic analysis

Modal analysis helps to determine the vibration characteristics (natural frequencies and mode shapes) of a mechanical structure or component, showing the movement of

different parts of the structure under dynamic loading conditions, such as due to the lateral force generated by the electrostatic actuators. The natural frequencies and mode shapes are important parameters in the design of a structure for dynamic loading conditions. Modal analysis of the chopper was performed using ANSYS. Figure 6-6 shows the mode shape of the chopper at its fundamental frequency, while Table 6-1 shows the natural frequencies of the chopper for its different vibration modes.

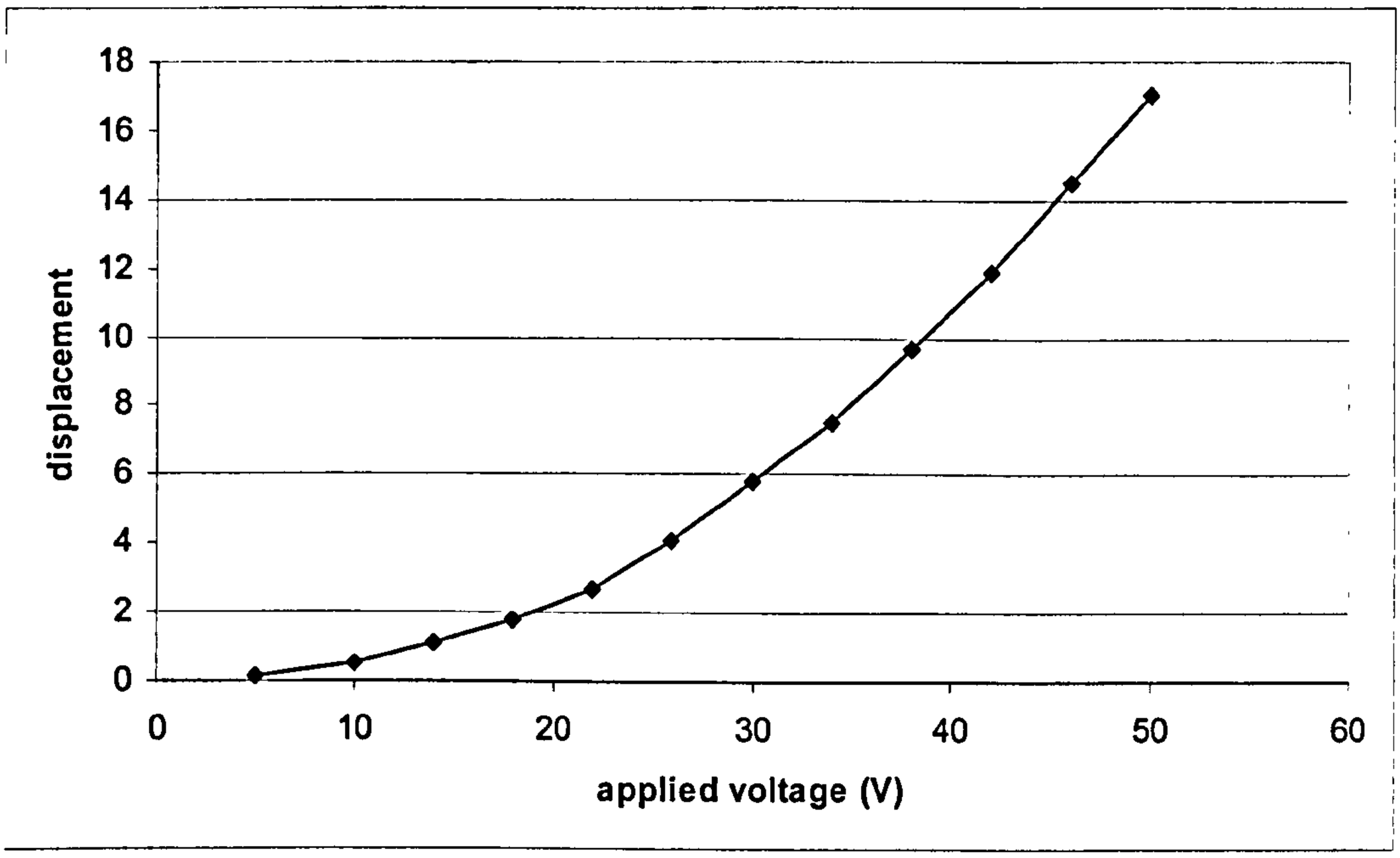

Fig. 6-5. FEM simulation result of relationship between displacement (μm) and applied voltage (V).

Table 6-1. Frequencies in different resonant modes.

Modes	Frequency (Hz)
1	3350
2	10765
3	10810
4	11395
5	12222

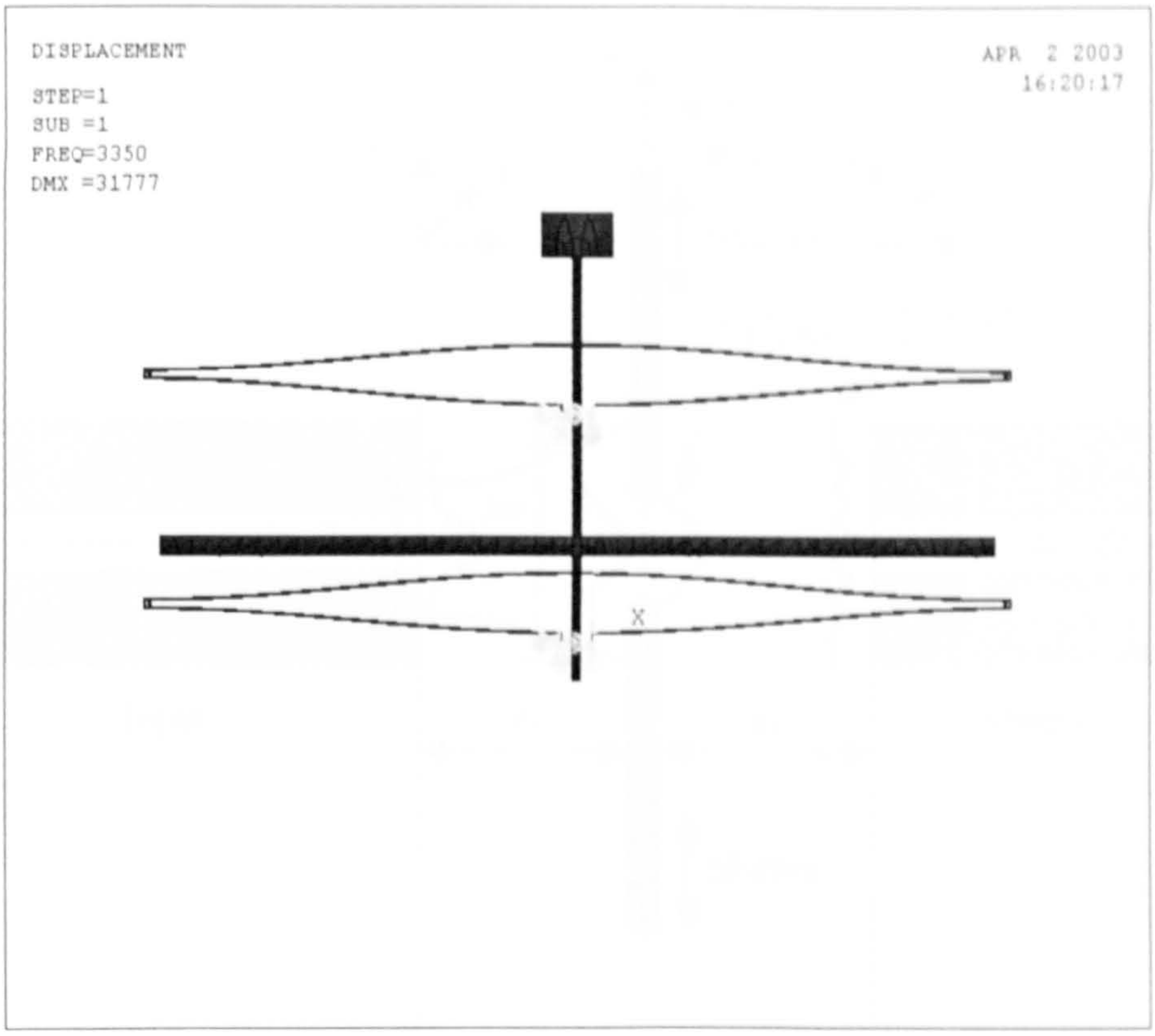

Fig. 6-6. The mode shape of the chopper structure in fundamental frequency.

6.3 Optical design considerations

The optical system consists of the following arrangement: two identical single mode fibres are aligned face to face with a separation of around 70μm. This separation was chosen to minimise the risk of physical damage to the microdevice by a possible collision with the optical fibre ends during experimentation. The input fibre carries infrared light of 1550 nm wavelength, which is emitted from the fibre end-face towards the output fibre, which collects the light. The chopper is located in the gap between the two fibres. When the shutters of the chopper begin to close the light received at the output fibre will be attenuated. The attenuation is modelled using the notation and parameters shown in Figure 6-7.

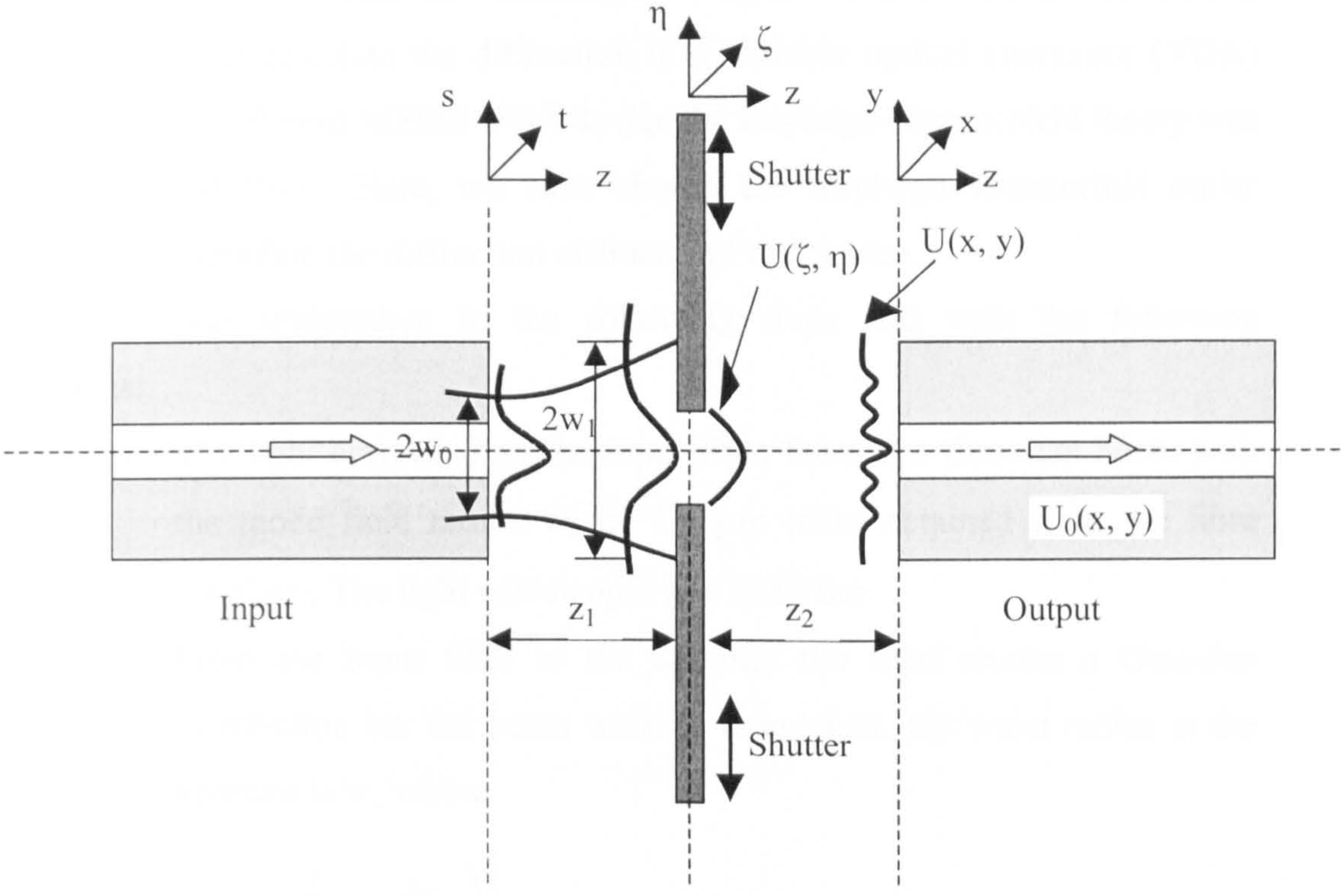

Fig. 6-7. Shutter system in the optical modelling.

Several theoretical approaches involving diffraction theory [126] can be used to analyse the attenuation of light travelling through the aperture formed by the chopper blades. In reference [127], a detailed explanation for the choice of the most appropriate of the diffraction theories has been given. Here, we briefly introduce what diffraction formula can be used in our case. In scalar theory, there are four diffraction methods, namely Fraunhofer, Fresnel, Fresnel-Kirchoff and the Rayleigh-Sommerfeld method. The Fraunhofer technique is valid when the light striking the aperture plane can be assumed to be a plane wave, which is in the "far-field", where the light has propagated to a distance far from the aperture, and the diffraction pattern is the same as that at infinity. These conditions are not present in our arrangement, so this theory cannot be used. The Fresnel technique is valid in both the far and near field, where the "near field" is defined as the region where the diffraction pattern differs from that observed at an infinite distance. The Fresnel-Kirchoff and Rayleigh-

Sommerfeld scalar formulations are similar, and only limited by the propagation distance being "greater" than the wavelength of light. Fresnel-Kirchoff diffractive theory was used to calculate the diffraction in a variable optical attenuator (VOA) device [11]. In a different MEMS VOA device the Rayleigh-Sommerfeld theory was successfully used [61]. Here, we have chosen the Rayleigh-Sommerfeld scalar formulations to simulate the diffraction character of our device.

The analysis was undertaken in the following steps and with the following assumptions:

a. The light emitted from the input fibre facet is a Gaussian beam with the mode field radius w_0 of 5.1 μm (data obtained from the fibre supplier). The light wavelength λ is 1550 nm.

b. From the input fibre to the aperture the light retains a Gaussian distribution but the beam waist is broadened: the waist radius at the aperture is w_1 where

$$w_1 = w_0\left(1+\frac{\lambda z_1}{\pi w_0}\right)^{\frac{1}{2}} \qquad \text{.....} \qquad (6.8)$$

and z_1 is the distance from input fibre facet to the centre position of the aperture and is 35 μm.

c. The light is partially blocked by the blades forming the aperture. The unblocked light diffracts to the output fibre facet. Here the Rayleigh-Sommerfield formula is used [123], which has the form as:

$$U(x,y,z) = \frac{z_2}{j\lambda}\iint_{\Sigma} U(\xi,\eta,0)\frac{\exp(jkr)}{r^2}\partial\xi\partial\eta$$

.....(6.9)

where, k is $2\pi/\lambda$, r is the distance from the point (ξ, η) in the aperture plane to the point (x, y) in output fibre plane, Σ represents the area of

the aperture, and z_2 is the distance that the light propagates from the centre position of the aperture plane to the output fibre plane and is 35 μm in our device. U is the complex optical wave function. Figures 6-8, 6-9 and 6-10 are typical results of calculations using the Rayleigh-Sommerfield diffraction theory. From those images, we can see that the light in the aperture plane is cut by the symmetric shutter blades and changed to a narrow slit, and diffracted to the output fibre facet plane.

d. After completing the calculations of step c, we obtain the intensity distribution at the output fibre facet plane. The proportion of light coupled from the output facet plane into the output fibre is represented as T and is determined by use of the mode-coupling method [128]. The mode coupling can be expressed as :

$$T = \left| \iint_{\infty} U(x,y) \cdot U_0^*(x,y) dxdy \right|^2, \qquad (6.10)$$

where, U_0 (x, y) is the fundamental mode distribution of the output fibre. The simulated attenuation result due to the position change of the chopper blades is shown in Figure 6-11. Also in Figure 6-11 the attenuation of the double chopper blades is compared to that obtained if just a single blade had been used. It is clear that in a double blade arrangement, a much smaller deflection from the comb-actuator is required for each blade than for the single blade arrangement. This means that a lower operating voltage would be required for the double blade arrangement because of the smaller deflection needed.

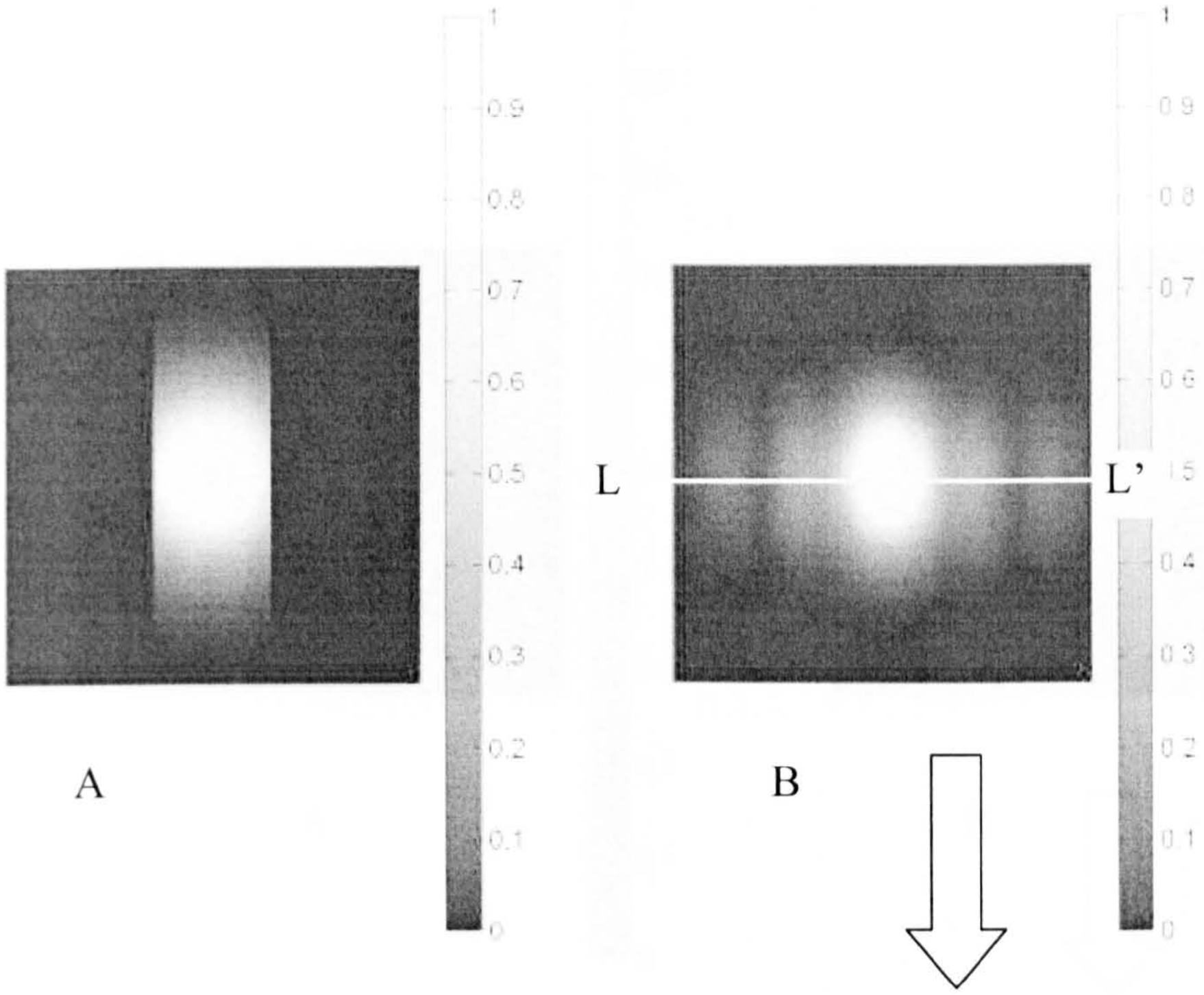

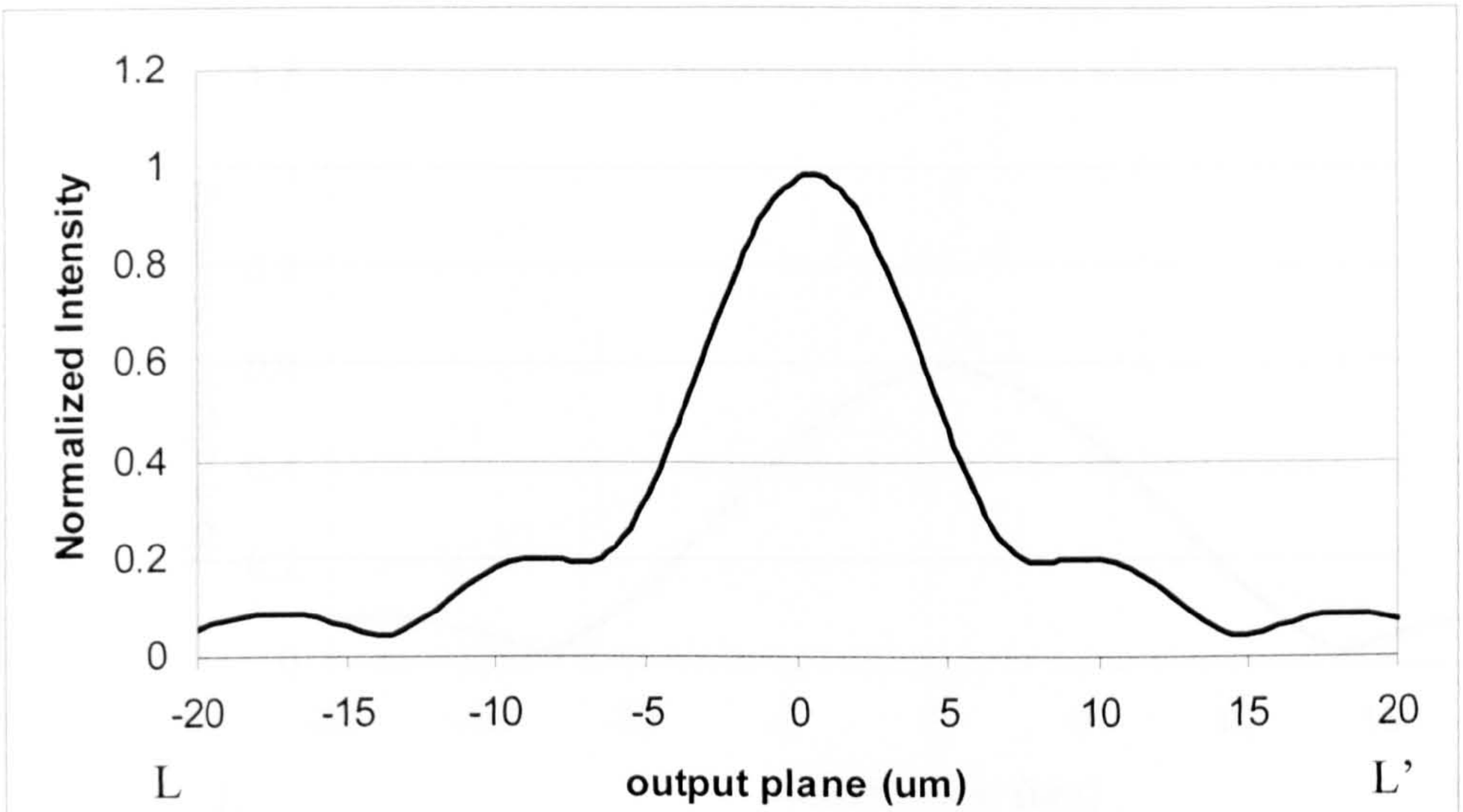

C

Fig. 6-8. A is the light intensity in shutter plane, and B is light intensity in receiving fibre plane. In picture A, the frame dimension is from –15 um to 15 um. In picture B, the frame dimension is from – 20 um to 20 um. The color bar stands for the normalized intensity value. Two shutters are in the position of ±4um from the center. Fig C is the cross section view of Fig B.

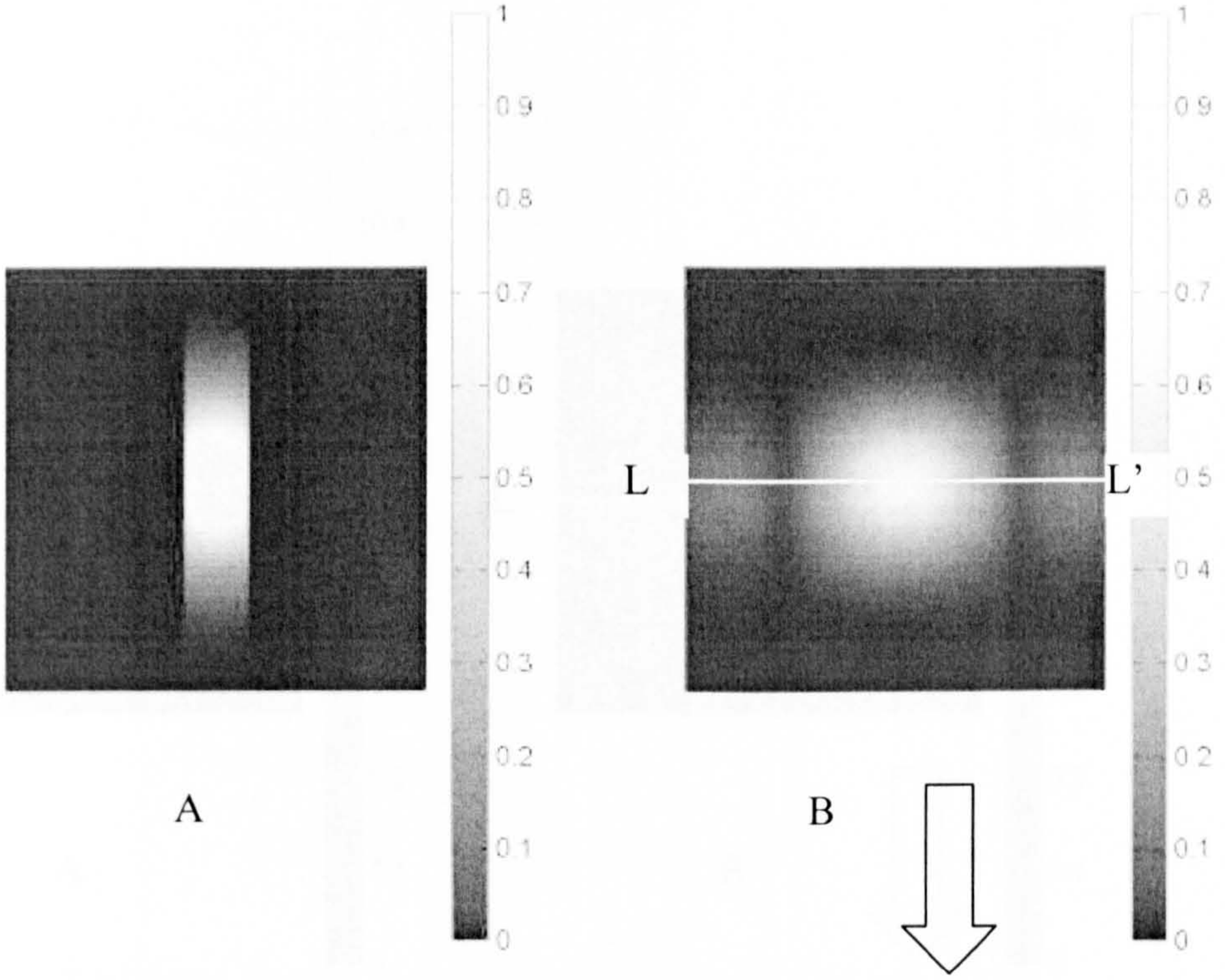

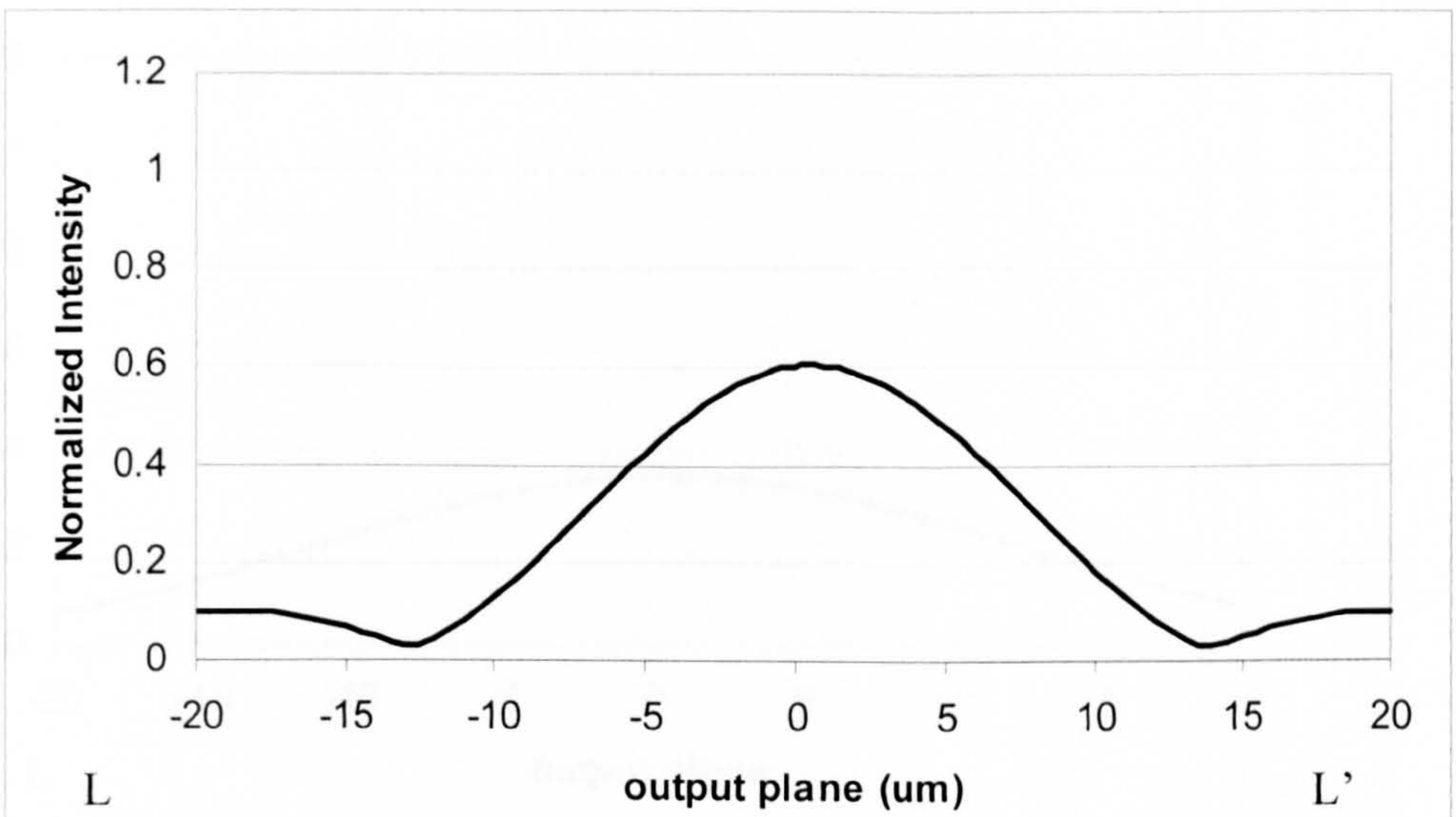

C

Fig. 6-9. A is the light intensity in shutter plane, and B is light intensity in receiving fibre plane. In picture A, the frame dimension is from –15 um to 15 um. In picture B, the frame dimension is from – 20 um to 20 um. The color bar stands for the normalized intensity value. Two shutters are in the position of ±2um from the center. Fig C is the cross section view of Fig B.

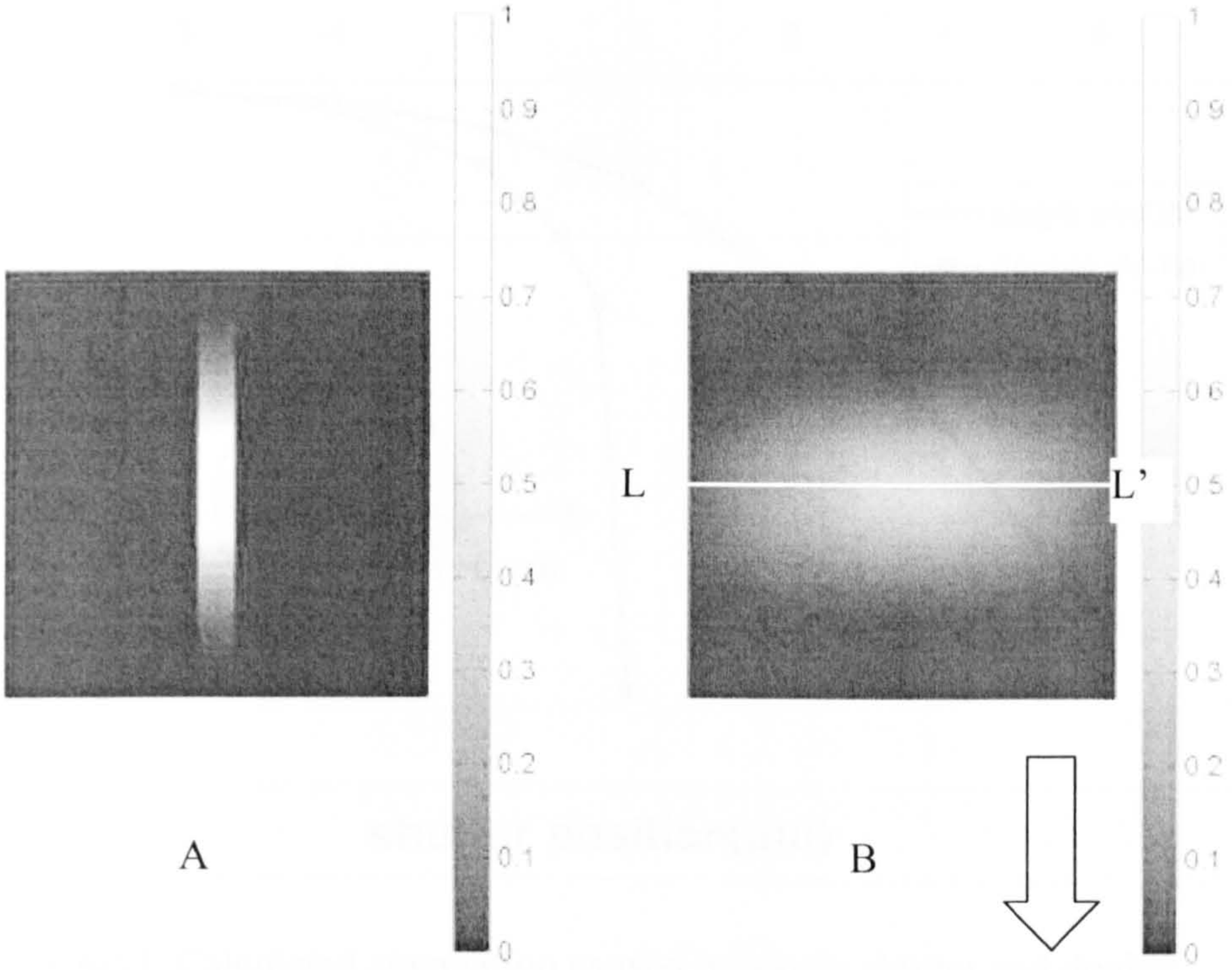

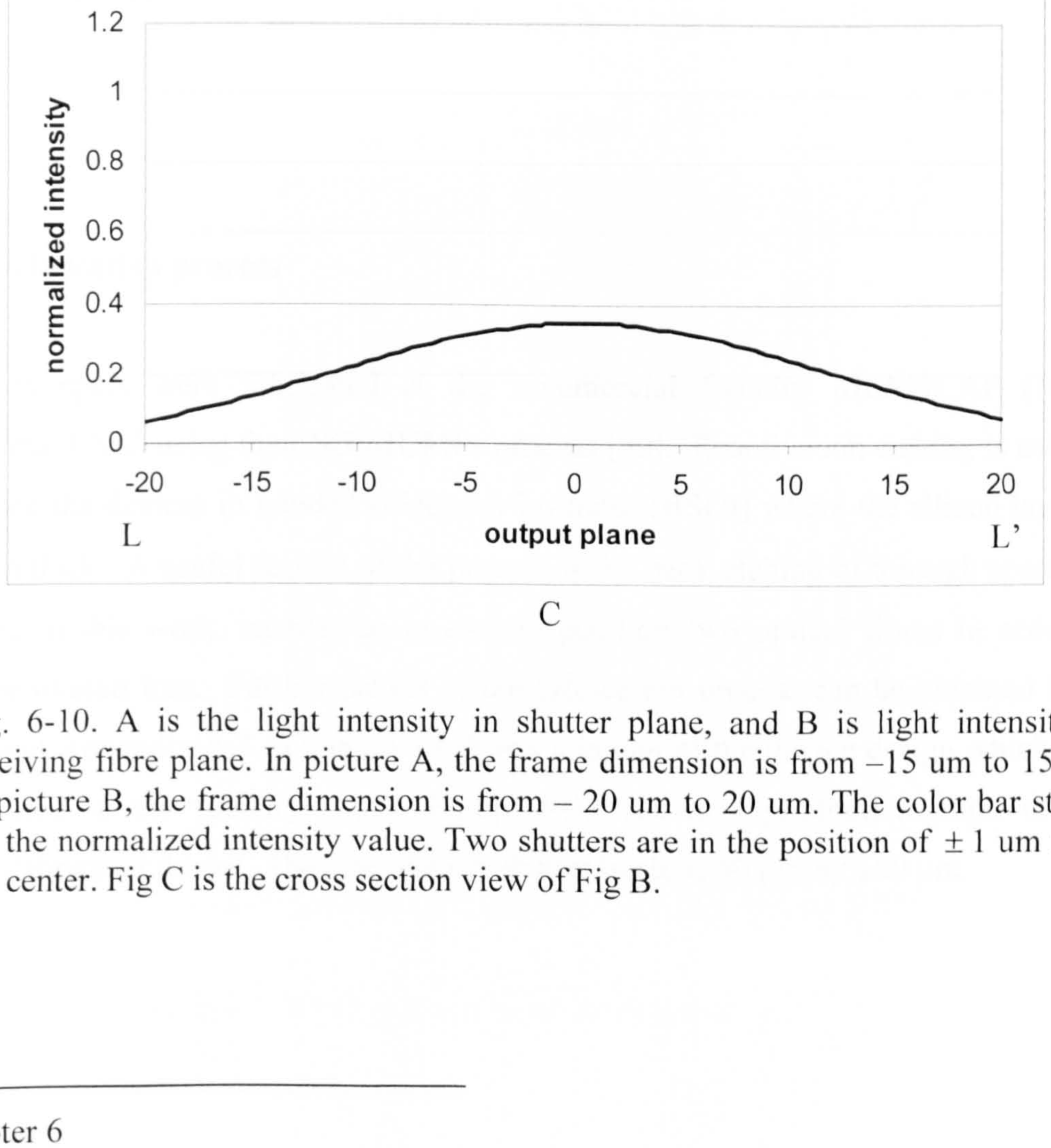

C

Fig. 6-10. A is the light intensity in shutter plane, and B is light intensity in receiving fibre plane. In picture A, the frame dimension is from –15 um to 15 um. In picture B, the frame dimension is from – 20 um to 20 um. The color bar stands for the normalized intensity value. Two shutters are in the position of ± 1 um from the center. Fig C is the cross section view of Fig B.

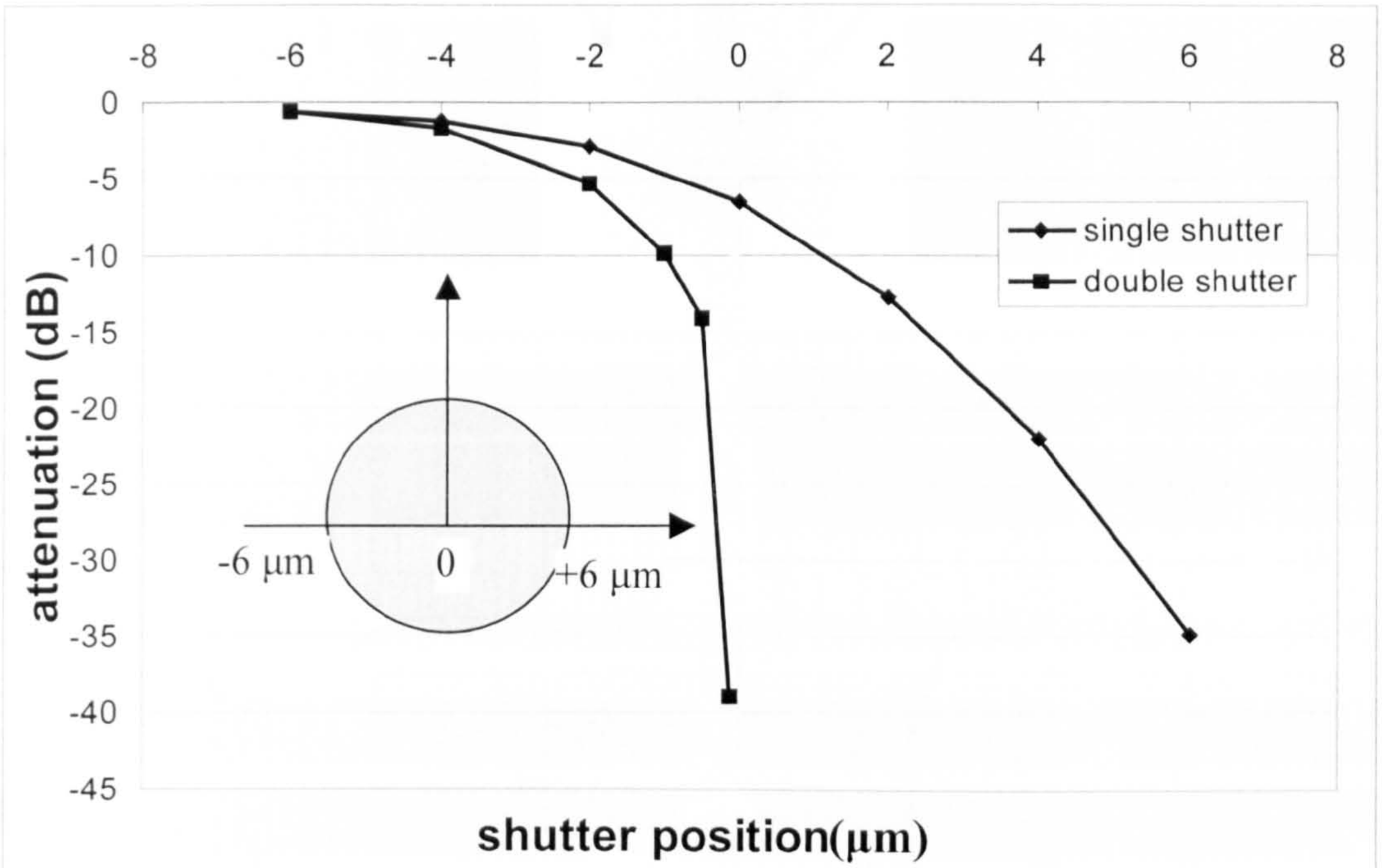

Fig. 6-11. Calculated attenuation caused by single shutter and double shutter.

6.4. Fabrication process

The choppers were fabricated at the commercial foundry MEMSCAP (North Carolina, USA) using their SOIMUMPs process [90]. Reactive ion etching is used to produce the devices in bonded silicon-on-insulator (BSOI) where the silicon layer is 10 μm thick. A useful feature of the process is the back-etching of through apertures which, in this work, enables us to closely position two optical fibres in order to reduce overall loss. Further details of the fabrication process can be obtained from [90] and Appendix A.3. Figure 6-12 shows a layout of the device design which was submitted to the foundry, while Figure 6-13 shows a photomicrograph of the microfabricated device. The size of each shutter blade is 50 μm by 100 μm.

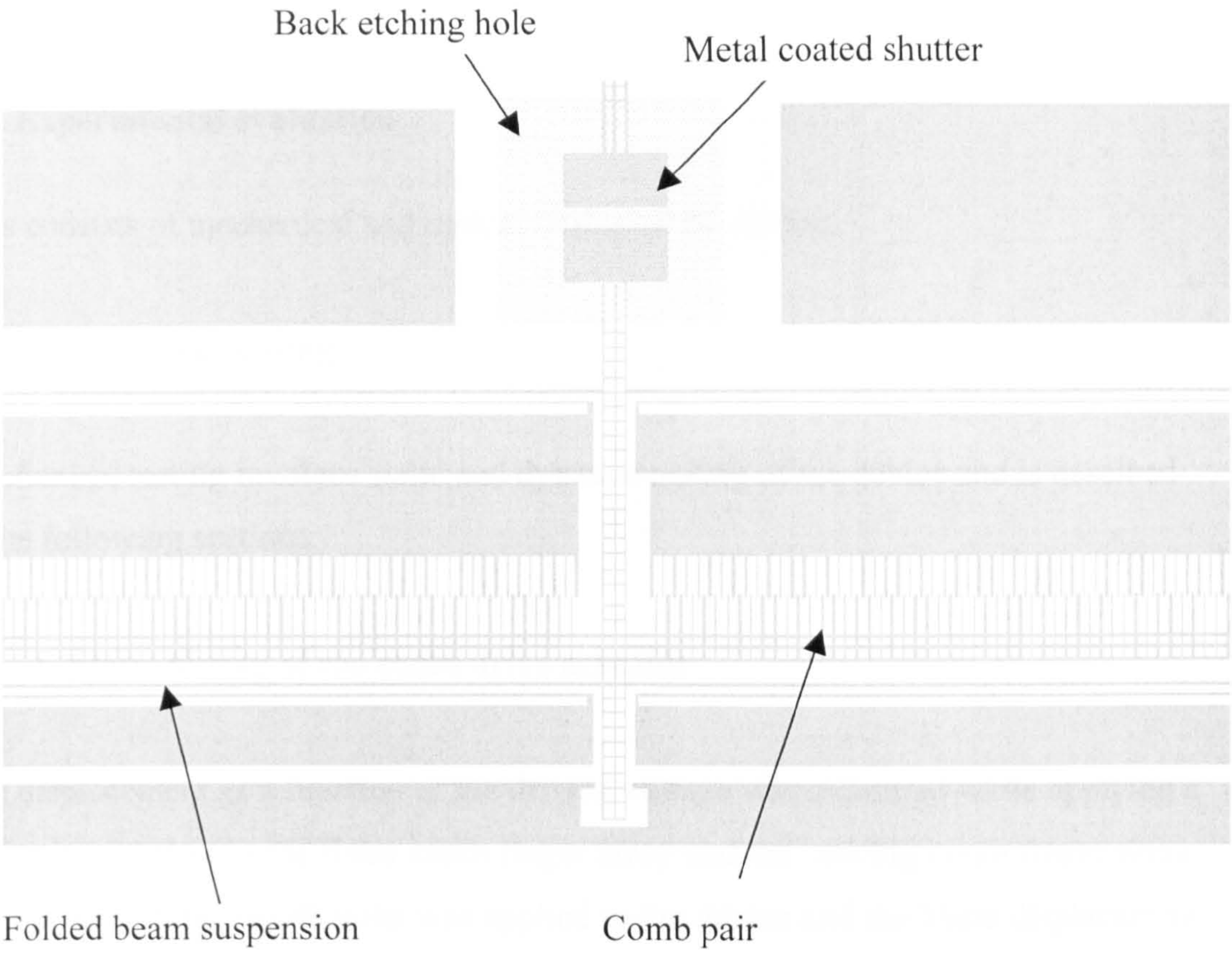

Fig. 6-12. Layout of comb drive actuator with shutters.

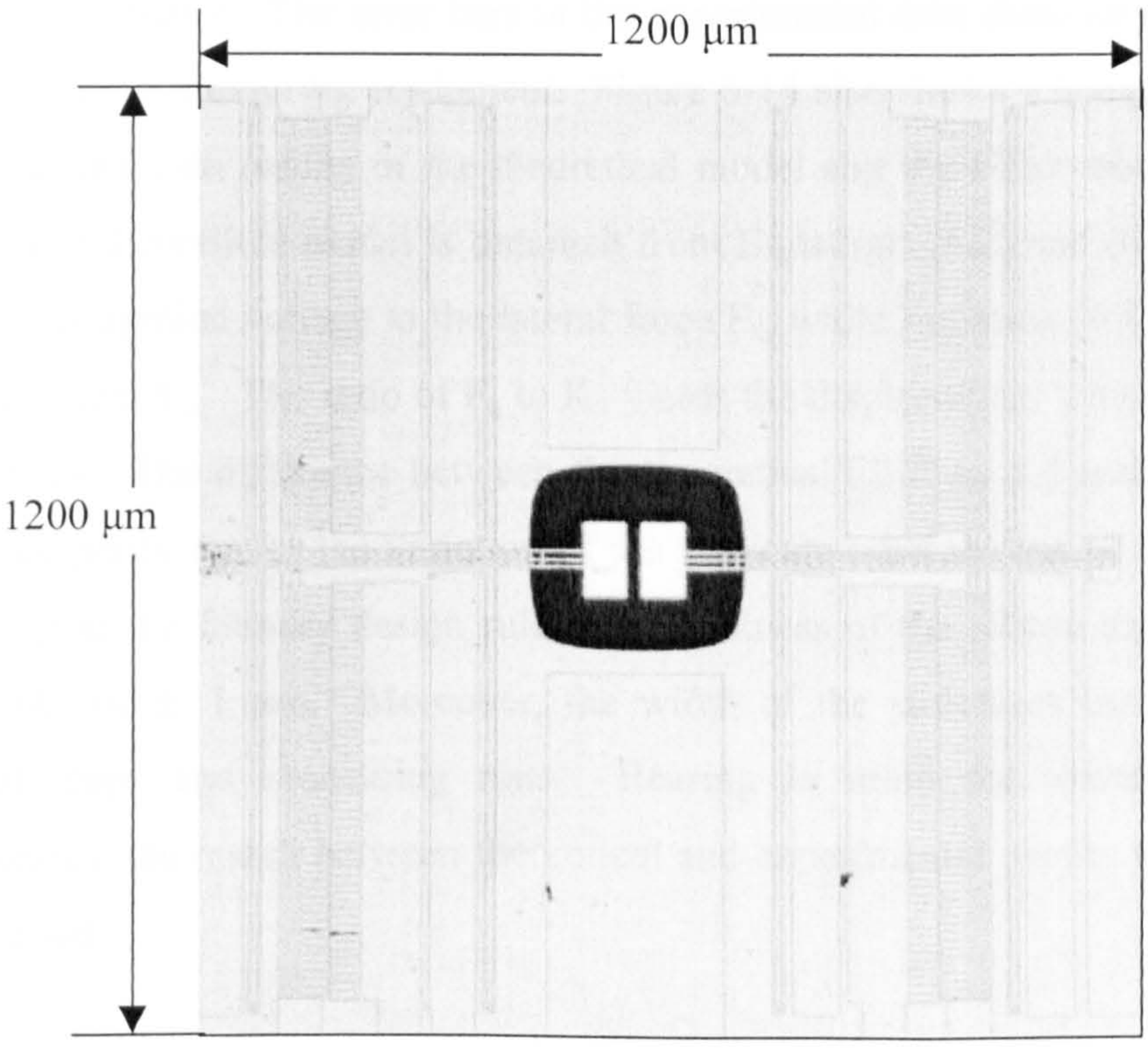

Fig. 6-13. Microphotograph of the micro-optical chopper.

6.5. Experimental evaluation

This consists of mechanical and optical testing of the device.

6.5.1. Mechanical testing

Mechanical testing involves static and dynamic testing of the device and is descibed in the following sections.

6.5.1.1. Static testing of the comb drive actuator

The displacement as a function of the driving voltage was measured while applying a d.c. voltage between the fixed comb finger array and the moving comb finger array. DC voltage from 0 to 48 volts was applied to the device and the blade displacement measured separately by observation under a high magnification microscope coupled to a high-resolution camera. Figure 6-14 shows the measured displacement of the comb drive actuator. The error bars in the experimental data show an uncertainty of ± 0.4 μm in our measuring equipment. Figure 6-14 also shows a comparision of the measured data with results of the theoretical model and the FEM model mentioned above. The theoretical model is obtained from Equations (6.2) and (6.4). Equation (6.2) relates applied voltage to the lateral force F_x, while Equation (6.4) provides the spring constant K_x. The ratio of F_x to K_x yields the displacement which is plotted in Figure 6-14. The difference between the theoretical/FEM model and experimental results are partly due to the variation of the fabricated dimensions of the structures. According to the foundry design rules, the thickness of the silicon structure has an uncertainty of $\pm$ 1 μm. Moreover, the width of the structures can be varied in different chips and processing runs. Bearing in mind the existence of these uncertainties, the match between theoretical and experimental results in Figure 6-14 is very good.

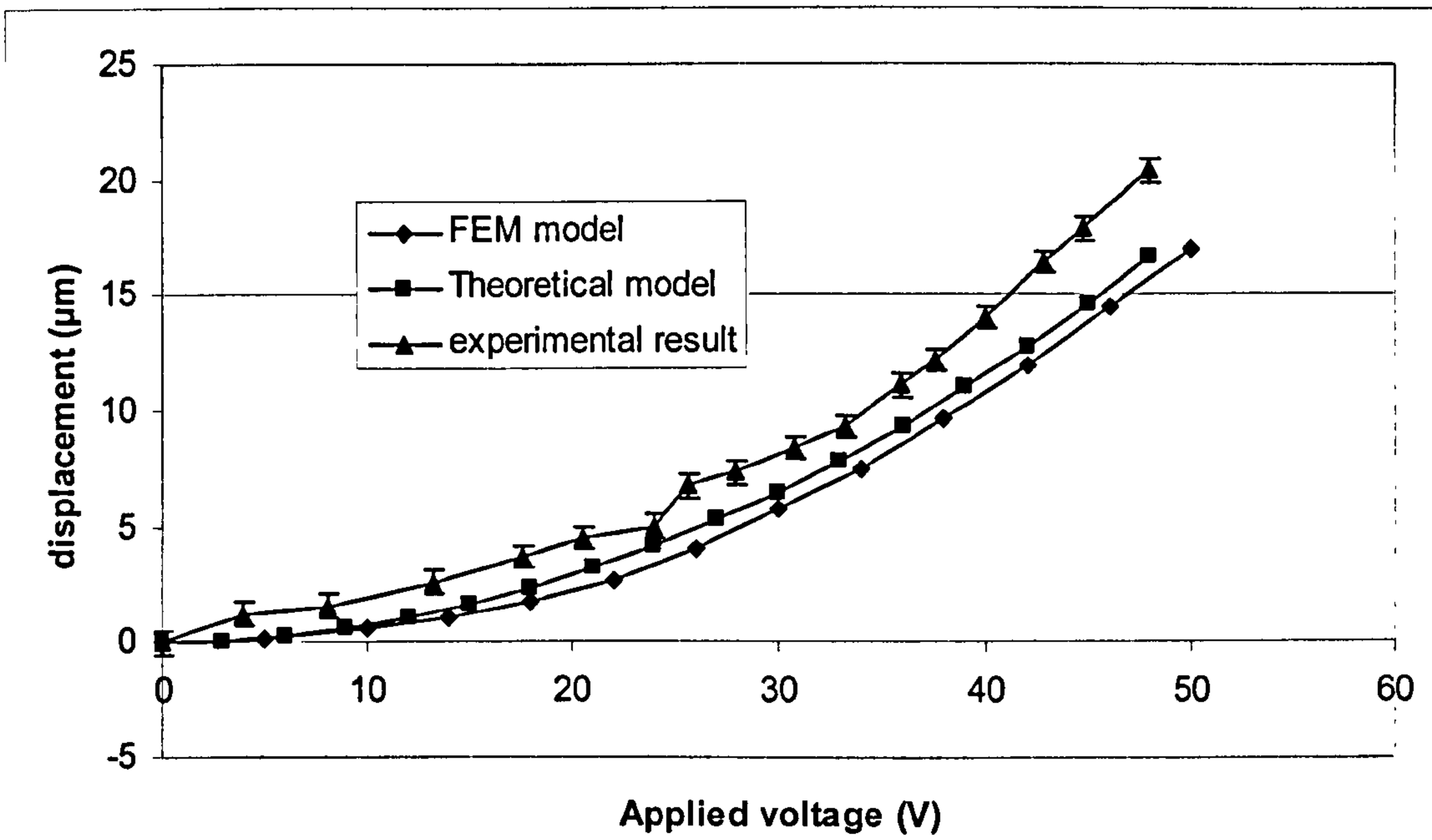

Fig. 6-14. Voltage vs. displacement (experiment and theory).

6.5.1.2. Dynamic testing using Roper Camera

The frequency response of the device was obtained using a high-speed imaging camera (Roper Model 4540MX) that is coupled to an optical microscope. The fundamental mode of the device is in the plane of the chip and consequently, microscope-coupled laser Doppler systems which are optimised to measure out-of-plane deflections cannot be used. The Roper high speed camera, which the Strathclyde Group operates, can capture up to 44,000 frames per second. In this sequence of measurements, it was set to operate at 9000 frames per second which is above the expected resonant frequency of the device. The sequence of frames captured are played back and carefully analysed to determine the amplitude of deflection for each applied frequency. The measurements obtained are plotted in Figure 6-15 from where it is evident that the fundamental resonant frequency is around 3 kHz. The difference between the FEM and theoretical results comes from

the fact that the formula used to calculate the resonating frequency (Equation 6.7) is an approximate formula whose real usefulness is to confirm the results of the analysis obtained through the FEM. Moreover, the fabricated structure will have small variations in dimensions leading to difference between the measured and simulated/calculated results. The FEM result (3.3 kHz) is close to the experimental result (3 kHz) as would be expected for a complex structure like the chopper. The Q factor in air is around 0.47. The error bars show that our imaging system has an uncertainty of ± 0.4 μm. Although no lifetime tests were conducted, the device was left running for over 10 hours at 100 Hz without failure.

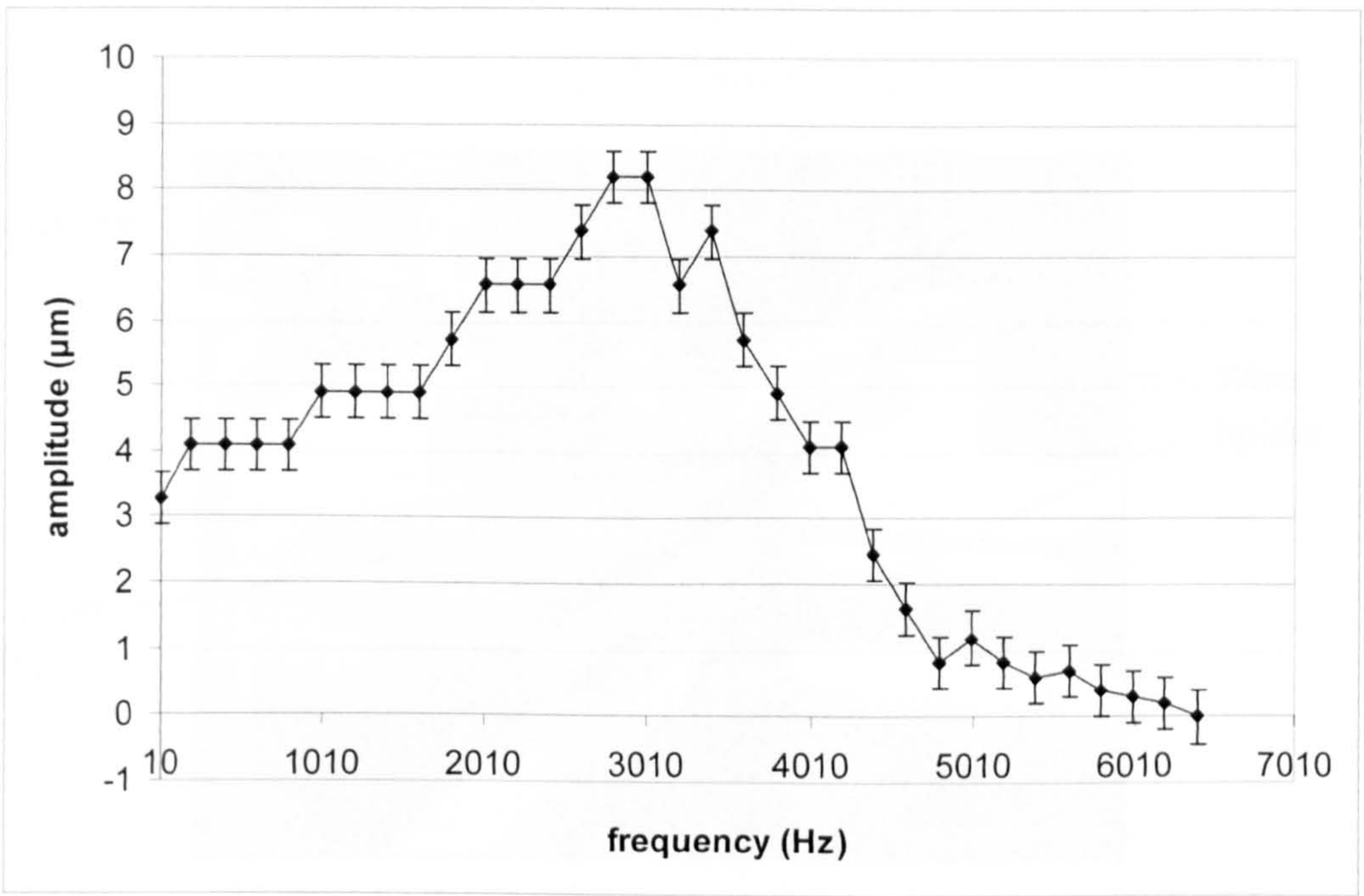

Fig. 6-15. Dynamic behaviour of the chopper.

6.5.2. Optical testing

The dies supplied were of 1 cm sides and because of the etched hole through the die, they were not mounted on conventional circuit boards. Instead, an optical test station

was set up which allowed the input and output single mode fibre to be aligned facing each other and with the chopper placed in the gap between the fibre faces. A microscope was used to assist in the alignment of the fibres, and the test station used is shown in Figure 6-16.

Single mode optical fibres transmitting light of 1550 nm wavelength and with 5.1 μm mode field diameter were used to test the performance of the chopper. The aperture formed by the blades of the chopper is initially 20 μm, that is when the voltage applied is 0 volts. When the two shutter blades driven by the comb actuators each travel 10 um the aperture is closed entirely. The driving voltage was monitored by a digital oscilloscope. The light coupled to the output fibre is detected by a photodetector and monitored by a different channel of the same oscilloscope.

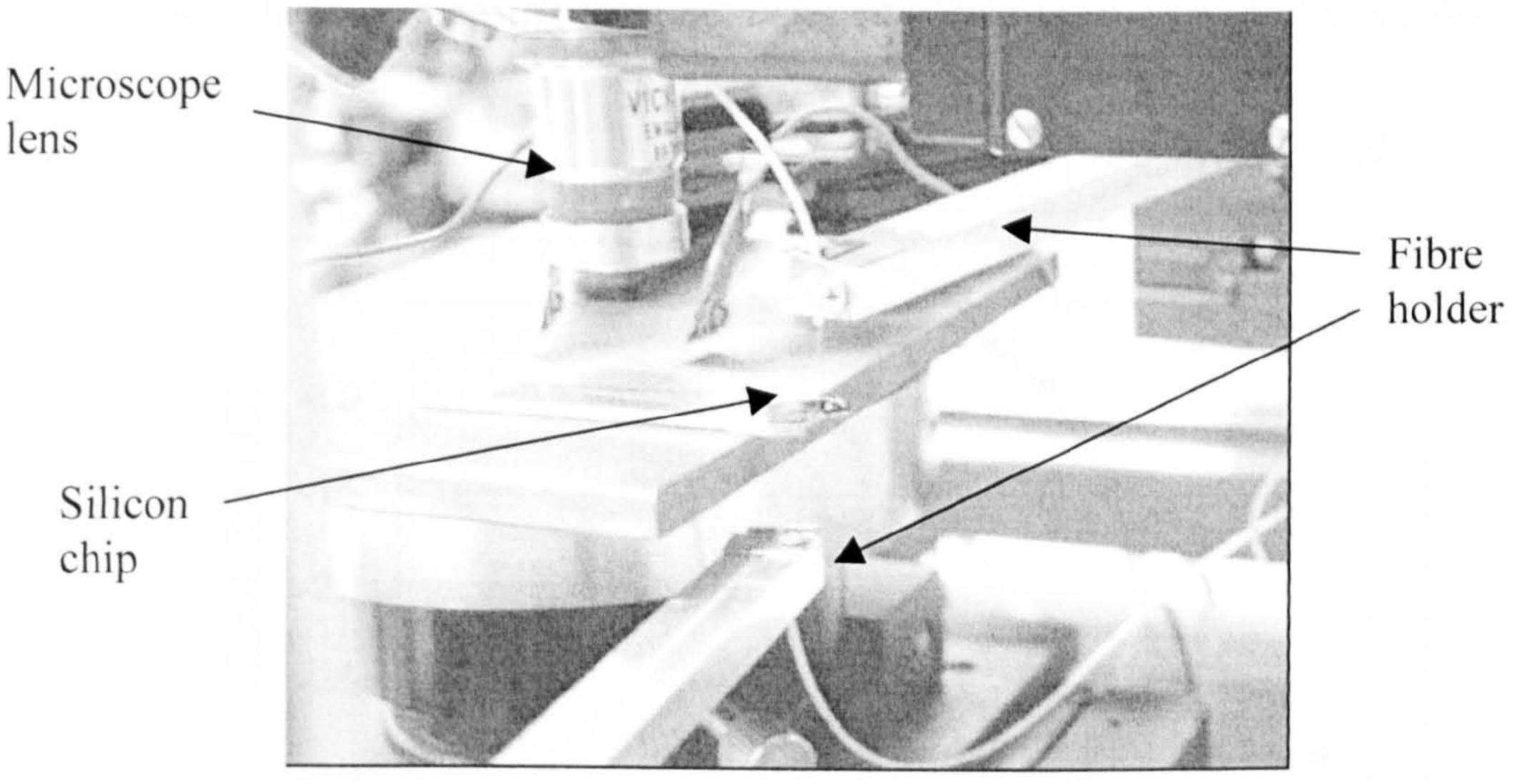

Fig. 6-16. The optical testing setup for the chopper.

6.5.2.1 Static performance:

The static optical performance is measured by applying a d.c. voltage to the device, and measuring the optical throughput at each voltage. In this mode the chopper functions as a miniaturised optical slit whose width is changed by application of d.c.

voltage. Figure 6-17 shows the results obtained. When the slit is fully closed, it would be expected that no light transmits through because although silicon is transparent at this wavelength, the blades are gold coated thus rendering the structure opaque. However, slight imperfections in the etching and squareness of the blades lead to the closed blades, though contacting, having the possibility of allowing some light through. Moreover, the deposition of gold might not be perfectly to the edge of the blade. Both these effects lead to a measured ON/OFF ratio of around 27dB. The intensity coupled from the input to the output fibre in the ON position was measured to be 72 %, corresponding -1.4 dB insertion loss. This is caused by the separation of the two fibre faces and any misalignments. Between 2V to 20V, the attenuation changes slowly because the shutters are in the edge of the light spot where the Gaussian beam distribution of the light spot has low intensity. Also from the previous testing of the comb actuator, the electrostatic voltage applied from 0 V to around 20 V produces a displacement of each blade of 5 μm with a further 5 μm to be traversed by each blade. Increasing the electrostatic voltage from 20V to 34V results

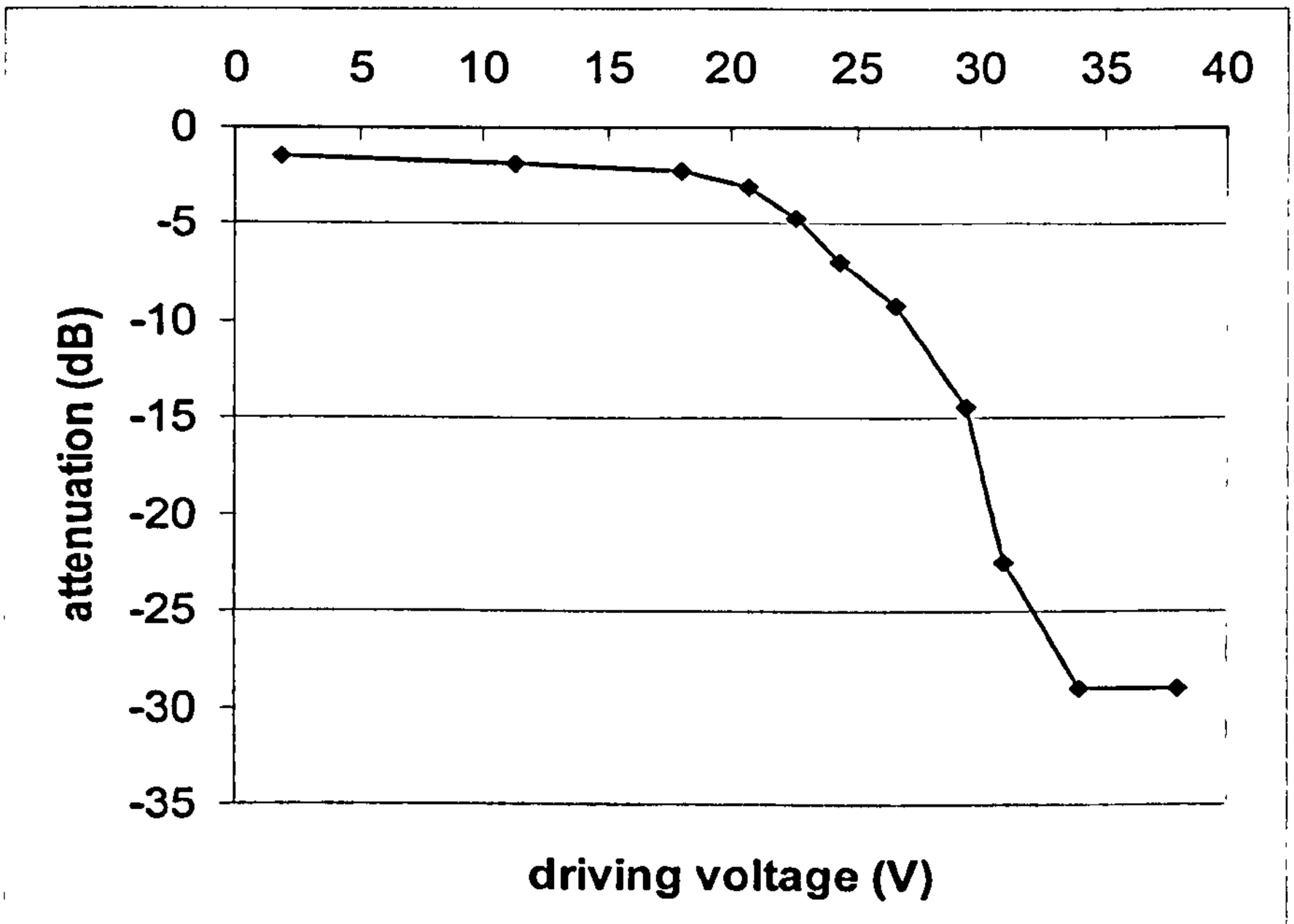

Fig. 6-17. Static performance of chopper.

in a rapid increase in attenuation as expected from this arrangement. In the OFF position, the power from the output fibre end was measured to be 0.12 %, corresponding – 29 dB attenuation. When the driving voltage is increased to around

40 V, the attenuation remains unchanged confirming that the chopper blades are fully closed. Comparison of experimental and theoretical results is shown in Fig. 5-18.

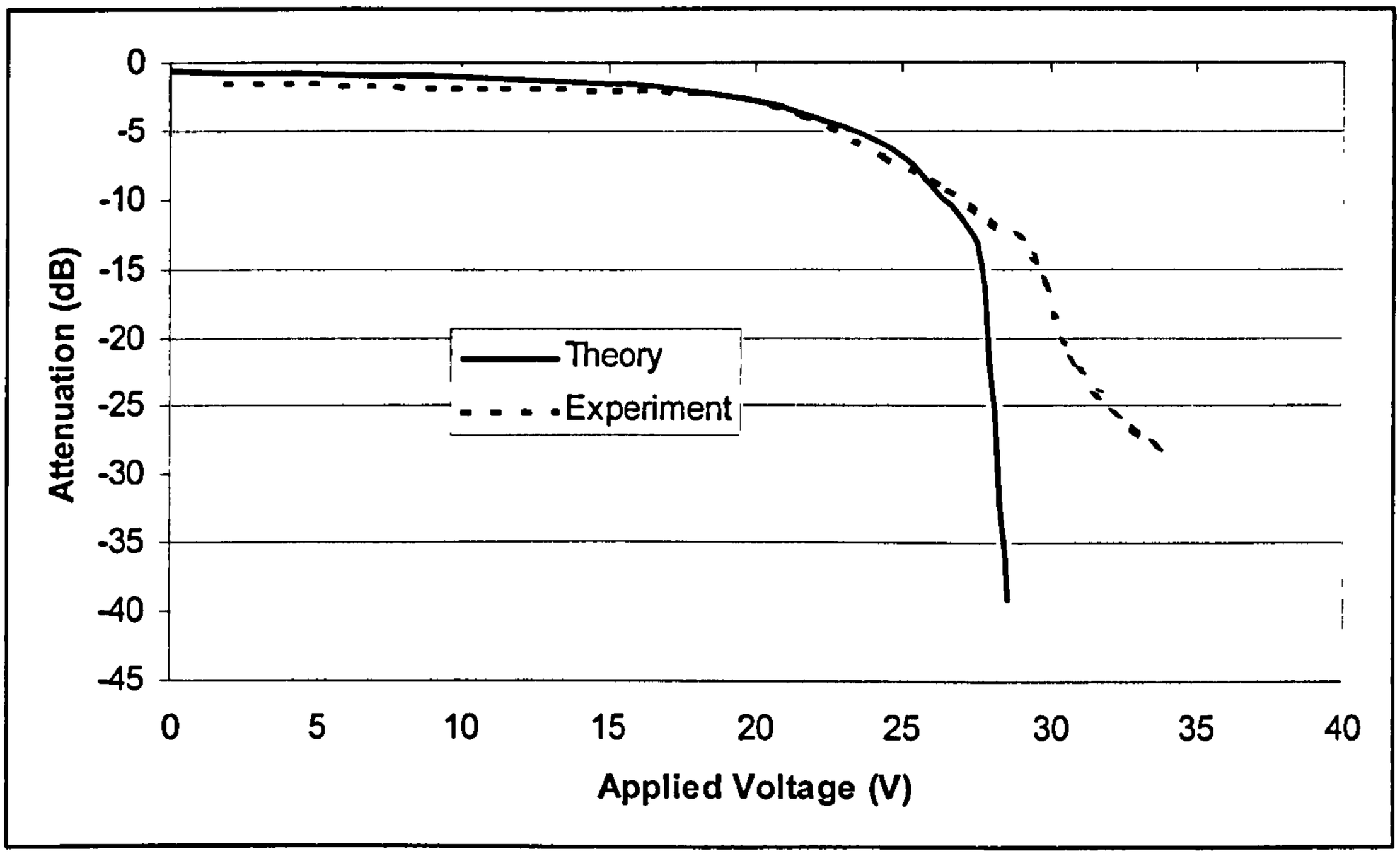

Fig. 6-18, Comparison of experimental and theoretical results.

6.5.2.2 Dynamic response:

The mechanical frequency response has been presented in section 6.5.1. Here, the dynamic response of the fibre optic chopper is obtained from optical measurements, as shown in Figure 6-19. A 0-28V square signal of 1000 Hz frequency (upper trace) was applied to the comb actuator, and the received power was detected by a photoreceiver and displayed on a digital oscilloscope (lower trace). In the rise cycle, the 0 % - 90 % rise time was measured to be 90 μs, and 100 % to 10 % fall time was also measured to be 90 μs.

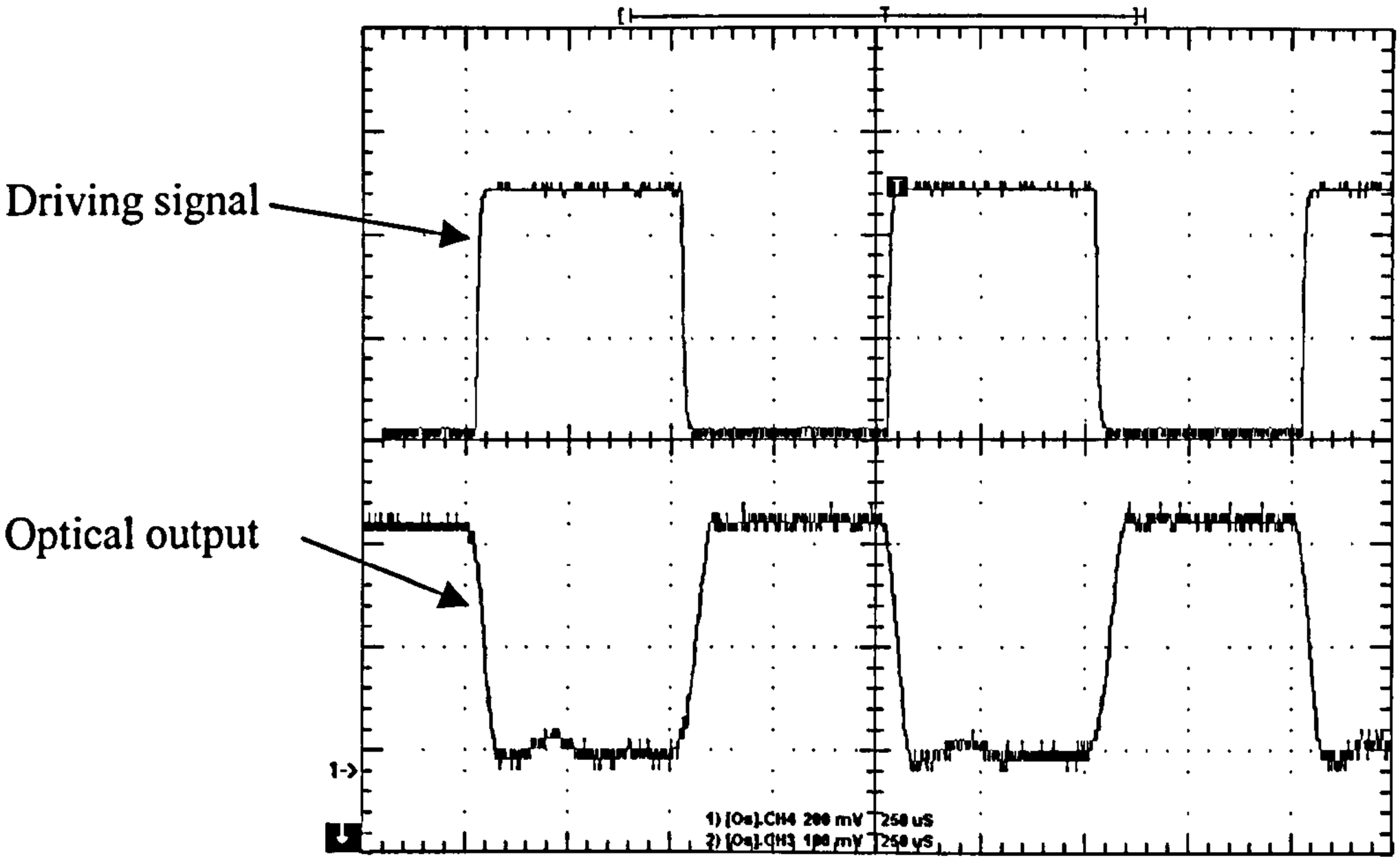

Fig. 6-19. Dynamic response of the chopper captured from the oscilloscope.

6.6. Conclusion

A novel micromechanical optical chopper for use with optical fibre has been designed using a double-bladed shutter system actuated by an integrated comb drive actuator. A detailed design analysis has been performed of the entire microsystem taking into account the effect of several important factors. For the electro-mechanical modelling of the structure, the side instability of the comb actuator has been considered in particular to ensure that this effect does not limit the performance of the chopper. In the dynamic mechanical analysis, a simplified analytical model has been used to obtain the fundamental resonant frequency of the device. Optical modelling of the shutter system has been performed using the appropriate theory suited for the microsystem regime. Through this modelling, we have shown that a double bladed shutter system has advantages over a single bladed system in terms of the attenuation rate and driving voltage. Micromachined choppers using the above results as design factors were fabricated in bonded silicon-on-insulator (BSOI) at a

commercial foundry. Electro-mechanical experiments show that the comb drive can move 10 μm under 34V d.c., and the resonant frequency of the device is around 3 kHz with Q factor of 0.47. These experimental measurements have a good fit with the theoretical analysis. Optical experiments have been performed using precisely aligned single mode fibres. It is shown from the optical measurements experiments that the attenuation of the chopper ranges from -1.4 dB to -29 dB (-1.4 dB is the insertion loss). The experiment has been compared with theoretical calculation, which is also presented. The dynamic response has also been observed through an oscilloscope showing rise and fall times of around 90 μs.

Chapter 7

Conclusions

7.1 Conclusion of this thesis

Microactuators are important elements in miniature optical systems, since they are required to drive micro-parts such as shutters, mirrors and gratings to realize various functions. Electrically controllable microactuators such as electrostatic and electrothermal actuators give us good opportunities for integration into IC devices. In this thesis, several microactautors and optical microdevices incorporating microactuators have been investigated.

We have investigated three different operating principle microactuators namely scratch drive actuator (SDA), electrothermal actuator and comb drive actuator. We found that the SDA can be designed to travel over a long distances (1 mm), and supply large force (250 ± 36 μN for one plate SDA for 200 volts driving voltage). However, it is very sensitive to the surface properties, even a small particle could lead to failure of operation of the SDA. Also the SDA needs special post-processing to achieve bi-directional motion. Thermal actuator is a bi-directional actuator, but its displacement is rather small (10 μm for a traditional asymmetric actuator). Compared to the SDA, it occupies a big area, and makes the micro-device to be large. Comb drive is a non-contacting actuator, and no friction occurs during its movement. So it is suitable for a resonant structure, because it inherently has a low damping force and relatively high Q factor. The findings on these actuators are as follows:

Three types of electro-thermal actuators (single beam buckling electrothermal, symmetric electrothermal and 'V' shaped electrothermal) have been theoretically analyzed for both thermal and mechanical characteristics. Heat transfer analysis was performed using simple conduction theory. Quantitative analysis has been performed showing detailed behaviour of three different thermal actuators. From these results, we can see that the asymmetric electrothermal actuator has linear deflection related to

input power, while deflections of single beam buckling and 'V' shaped are not linearly related to input power. An innovative design of the asymmetric thermal microactuator with a non-uniform hot beam is presented. The design yields higher deflection of the actuator. Both theoretical analysis and experimental testing have been undertaken to verify the idea. Several 240 μm hot-beam traditional asymmetric electrothermal actuators and 240 μm novel electrothermal actuators have been designed using PolyMUMPs. Comparison of novel and traditional actuators has been made both theoretically and experimentally. Experiments show the novel structure deflects more than 13 μm at high input power (~ 40 mW) without being damaged, while the traditional design stops bending at 11.7 μm at lower power (~ 34 mW).

Scratch drive actuators (SDA) have also been studied in detail. Beginning with design and fabrication, an empirical comparison of the motion of SDAs formed on different substrates by the PolyMUMPs foundry process has been conducted. Results show variation in the motion of SDAs formed on different dies, but to the same design. The average velocity of SDAs is 37 μm/s, when the slider is on the polysilicon surface, and 24 μm/s, when the slider is on the nitride surface, when the driving frequency is the same (500 Hz). We attribute the variations to small differences in the surface characteristics of the deposited and etched layers and variations during post-processing release and storage of these devices. Whereas slight process variations of this kind are not significant in microelectronics, they can be more significant in MEMS where the behavior of a micro-electro-mechanical device, such as the scratch drive actuator, is determined by surface friction which can be made to vary by small differences in the properties of the layers of material from which the MEMS is fabricated. In order to model the motion of every step, then, the static analysis of the SDA plate bending has been undertaken. Depending on the value of the voltages applied, two modes are identified, namely non-contact and contact modes. The contact mode is very important for obtaining the relationship between applied voltage and step size. The theoretical expressions have been applied to our SDAs of fixed dimensions, although it is easy to expand this model to an SDA of any dimension. Experiments on static performance of the SDAs have been carefully performed using a Veeco NT1000 Surface Profiling Tool. The theoretical

results have been compared to experimental measurements, with good agreement being obtained between the two. From the calculations, the step size of the SDA is around 10 nm at 60 V driving voltage, and from experiment, the step size of SDA is around 7 nm at 60 V driving voltage. These values compare favourably. Furthermore, the force characteristic of the SDA is of importance to know when we intend to incorporate the SDA into microsystems. Microsprings have been used to measuring the output force of the SDA. We assume the restoring force of microsprings is equal to force of the SDA. We obtained the extension of spring and spring constant, then convert it to force F by their product. Microsprings have been analysed by FEM using ANSYS. The ANSYS results of the spring constant compare very closely with the simple beam theory results of the spring constant. Scratch drive actuators with box-springs and different number of plates have been fabricated using the PolyMUMPs process. These SDAs have been experimentally analysed to determine their force generation. Forces of 250 ± 36 μN for one plate SDA up to 850 ± 36 μN for 4 plate SDAs have been estimated for 200 volts driving voltage.

Apart from the actuators, we have developed two different types of light modulating systems. One is a micro-shutter that travels across the face of an optical fibre to close the light path making a variable optical attenuator. This device has been designed and fabricated using polysilicon surface micromachining (PolyMUMPs). The shutter is hinged and assembled out of the wafer plane. Another light modulating system consists of two shutters moving oppositely towards the center of the face of an optical fibre, and closing the light path making an optical chopper. This device has been designed and fabricated using SOI process (SOIMUMPs). The shutter and actuators are in the wafer plane. Through our research, we found that the device made by SOIMUMPs is superior to the device made by PolyMUMPs, because the SOI structure is thicker than polysilicon layer, so the device made by SOI is more robust and reliable than the device made by surface micromachined polysilicon.

The PolyMUMPs variable optical attenuator mentioned above is powered by scratch drive actuators (SDA) and has been designed, analyzed, and characterized. Since SDAs have been studied in detail, the main conclusions reached are about self-

assembled shutter and optical performance of the device. Microhinges are employed to construct 3-D moveable microshutter. The principle of 3-D self-assembly using stress-induced beams has been applied to assemble this shutter. The major advantage of the self-bending beam is that it immediately assembles the 3-D structure automatically after the HF releasing process. There is no extra step or process to be implemented because the assembling beams are integrated into the structure design. The stress-induced beams can also be controlled by changing the temperature, because the two layers of the bimorph have a large difference of thermal expansion coefficients. A 400 μm bimorph beam array has been used to lift the 300 μm x 300 μm microshutter. The bending caused by initial stress has been calculated using traditional mechanical theory. Temperature dependence of the bimorph beam has also been analyzed. The size of the whole structure is 1.2 mm x 0.8 mm. An optical model has been built using diffractive theory, and the attenuation function has been obtained. Measurements of the variable optical attenuator show that the attenuation can be precisely controlled because the SDA has precise step size (measured 16 nm at 150 V driving voltage). The measured insertion loss is – 2.3 dB in open state and – 36.5 dB in off state.

The second light modulation microsystem is a micromechanical optical chopper for use with optical fibre which has been designed using a double-bladed shutter system actuated by an integrated comb drive actuator. The overall dimensions of the chopper, including the microactuators and micro-mechanical suspension are 1200 x 1200 μm making it very compact. A detailed design analysis has been performed of the entire microsystem taking into account the effect of several important factors. For the electro-mechanical modelling of the structure, the side instability of the comb actuator has been considered in particular to ensure that this effect does not limit the performance of the chopper. In the dynamic mechanical analysis, a simplified analytical model has been used to obtain the fundamental resonant frequency of the device. Optical modelling of the shutter system has been performed using the appropriate theory suited for the microsystem regime. Through this modelling, we have shown that a double bladed shutter system has advantages over a single bladed system in terms of the attenuation rate and driving voltage. Micromachined choppers

using the above results as design factors were fabricated in bonded silicon-on-insulator (BSOI) at the MEMSCAP foundry. Electro-mechanical experiments show that the comb drive can move 10 μm under 34V d.c., and the resonant frequency of the device is around 3 kHz with Q factor of 0.47. These experimental measurements have a good fit with the theoretical analysis. Optical experiments have been performed using precisely aligned single mode fibres. It is shown from the optical measurements experiments that the attenuation of the chopper ranges from -1.4 dB to -29 dB. The dynamic response has also been observed through an oscilloscope showing rise and fall times of around 90 μs.

7.2 Further work

Through the above investigations, we find that SDA is one of the best actuators, since it can offer large force and long travel range. Unfortunately it only can be driven in a single direction when fabricated using PolyMUMPs. When bi-directional SDAs are required, extra insulator layers have to be fabricated to join opposite actuators together. The MEMSCAP foundry does not carry out this extra process. Further design or post-processing is required to overcome this problem.

Thermal actuator driven stepping motor is another direction of further work, because this device can move in both directions and over long distance (theoretically).

In high temperature regime, the properties of the polysilicon will be changed; the traditional approach of increasing electric current and temperature to increase the deflection of thermal actuators cannot be used. A further investigation both from experimental and theoretical point of view needs to be done for other electrothermal designs.

In optical MEMS, quite successful prototypes such as the VOA and the Fibre Optic Chopper have been achieved in this thesis. Further work should concentrates on the integrating the driving circuit and different optical components together to achieve complete 'Optical-system-on-a-chip'.

References:

1. R. P. Feynman, "There's Plenty of Room at the Bottom," presented at the American Physical Society Meeting in Pasadena, CA, Dec 26, 1959.
2. H. C. Nathanson, W. E. Newell, R. A. Wickstrom, and J. R. Davis, Jr., "The resonant gate transistor," *IEEE Transaction on Electron Devices*, Vol. ED-14, p. 117, 1967.
3. K. E. Petersen, "Silicon as a mechanical material," *Proceeding of IEEE*, vol. 70, no. 5, May 1982, pp. 420-457.
4. R. T. Howe and R. S. Muller, "Resonant-microbridge vapor sensor," IEEE *Transactions on Electron Devices*, vol. ED-33, no. 4, April 1986, pp. 499-507.
5. Analog Devices Company, http://www.analog.com/ .
6. L. S. Fan, Y. C. Tai, and R. S. Muller, "IC-processed electrostatic micromotors," *Sensors and Actuators*, vol. A20, Nov. 1989, pp. 41-47.
7. K. S. J. Pister, M. W. Judy, S. R. Burgett, and R. S. Fearing, "Microfabricated hinges," *Sensors and Actuators*, vol. A33, no. 3, June 1992, pp. 249-256.
8. I. W. Rangelow, "Reactive ion etching for high aspect ratio silicon micromachining," *Surface & Coatings Technology*, vol. 97(1-3), pp. 140-150, 1997.
9. J. E. Ford, J. A. Walker, D. S. Greywall, and K. W. Goossen, "Micromechanical fiber-optic attenuator with 3 μs response," *J. Lightwave Technol*, 16 (9), pp. 1663-1670, 1998.
10. C. Marxer, P. Griss, and N. F. de. Rooij, "A variable optical attenuator based on silicon micromechanics," *IEEE Photon. Technol. Lett.*, 11 (2), pp. 233-235, 1999.
11. C. R. Giles, V. Aksyuk, B. Barber, R. Ruel, L. Stulz, and D. Bishop, "A variable MEMS optical switch attenuator and its use in lightwave subsystems," *IEEE J. Selected Topics in Quantum Electronics*, 5 (1), pp. 18-25, 1999.

12. X. M. Zhang , A. Q. Liu, C. Lu, et al, "MEMS variable optical attenuator using low driving voltage for DWDM systems," *Electron Lett.*, 38 (8): 382-383 APR 11 2002.
13. M. Hoffmann, P. Kopka, E. Voges, "All-silicon bistable micromechanical fiber switch based on advanced bulk micromachining," *IEEE J Sel. Top. Quan.*, 5 (1): 46-51 JAN-FEB 1999.
14. A. Q. Liu, X. M. Zhang, V. M. Murukeshan, et al., "An optical crossconnect (OXC) using drawbridge micromirrors," *Sensors and Actuators*, A-PHYS 97-8: 227-238 APR 1 2002.
15. F. Chollet, M. D. Labachelerie, H. Fujita, "Compact evanescent optical switch and attenuator with electromechanical actuation," *IEEE J Sel. Top. Quamt.*, 5 (1): 52-59 JAN-FEB 1999.
16. M. H. Kiang, O. Solgaard, K. Y. Lau, R. S. Muller, "Electrostatic combdrive-actuated micromirrors for laser-beam scanning and positioning" *J. Microelectromech. Syst.* 7, 27-37 (1998).
17. F. Pan, J. Kubby, E. Peeters, J. K. Chen, O. Vitomirov, "Design, modelling and verification of MEMS silicon torsional mirror" *Proc. SPIE* 3226, 114-124 (1997).
18. R. R. A. Syms, "Operation of a surface-tension self-assembled 3-D micro-optomechanical torsion mirror scanner" *Elect. Lett.* 35, 1157-1158 (1999).
19. T. Akiyama, D. Collard, H. Fujita, "Scratch drive actuator with mechanical links for self-assembly of three-dimensional MEMS," *J. Microelectromech. Syst.* 6 (2): 179-179 JUN 1997.
20. W. C. Tang, T. C. H. Nguyen, M. W. Judy, "Electrostatic-comb drive of lateral polysilicon resonators," *Sensors and Actuators*, vol. A 21 (1-3), pp. 328-331, 1990.
21. J. T. Butler, V. M. Bright, W. D. Cowan, "Average power control and positioning of polysilicon thermal actuators," *Sensors and Actuators*, A-PHYS 72 (1): 88-97 JAN 8 1999.
22. M. Ueda, T. Shiono, T. Ito, "High-efficiency diffractive micromachined chopper for infrared wavelength and its application to a pyroelectric infrared sensor," *Appl. Optics.*, vol. 37, no. 7, pp. 1165-1170, 1998.

23. R. Wolffenbuttel, G. Degraaf, "Noise performance and chopper frequency in integrated micromachined chopper-detectors in silicon," *IEEE T Instrum. Meas.*, vol. 44, no. 2, pp. 451-453, 1995.
24. H. Toshiyoshi, H. Fujita, T. Ueda, "A piezoelectrically operated optical chopper by quartz micromachining," *J Microelectromech. S.*, vol. 4, no. 1, pp. 3-9, 1995.
25. M. T. Ching, R. A. Brennen, R.M. White, "Microfabricated optical chopper," *Opt. Eng.*, vol. 33, no. 11, pp. 3634-3642, 1994.
26. W. S. N. Trimmer and K. J. Gabriel, "Design considerations for practical electrostatic micromotor." *Sensors and Actuators*, Vol. 11, pp. 189-206 (1987).
27. S. Kumar, D. Cho, W. Carr, "A proposal for electrically levitating micromotors." *Sensors and Actuators*, A 21-A 23, pp. 219-225. (1990).
28. N. Triole, D. Hauden, P. Blind, M. Froelicher, and L. Guadriot, "Three-dimensional silicon electrostatic linear microactuator." *Sensors and Actuators* Vol. A 48, pp. 145-150 (1995).
29. N. Tas, J. Wissink, L. Sander, T. Lammerink and M. Elwenspoek, "The shuffle motor: A high-force, high-precision linear electrostatic stepper motor." *Transducer '97*, pp. 777-780 (1997).
30. W. C. Tang, T.-C. H. Nguyen, and R. T. Howe, "Laterally driven polysilicon resonant microstructures," *Sensors and Actuators,* A vol. 20, pp. 25–32, 1989.
31. C. J. Kim, A. P. Pisano, R. S. Muller, "Polysilicon Microgripper," *Sensors and Actuators*, A 33, pp. 221-227, 1992.
32. M. Mehregany, S. F. Bart, L. S. Tavrow, J. H. Lang, S. D Senturia, and M. F. Schlecht, "A study of three microfabricated variable-capacitance motors." *Sensors and Actuators*, A 21- A 23, pp. 173-179. (1990).
33. M. Sakata, Y. Hatazawa, A. Omodaka, T. Kudoh, and H. Fujita, "An electrostatic top motor and its characteristics." *Sensors and Actuators*, A21-23, pp. 168-172. 1990.
34. S. C. Jacobson, R. H. Price, J. E. Wood, T. H. Rytting and R. Rafaelof, "A design overview of an eccentric-motion electrostatic microactuator (the wobble motor)." *Sensors and Actuators*, Vol. 20, pp. 1-16. 1989.

35. R. Legtenberg, E. Berenschot, J. Vanbaar, M. Elwenspoak, "An electrostatic lower stator axial-gap polysilicon wobble motor, part II: Fabrication and performance," *Journal of Microelectromechanical Systems*, vol. 7, pp. 87-93, 1998.
36. H. Guckel, J. Klein, T. Christenson, K. Skrobis, M. Laudon, and E. G. Lovell, "Thermalmagnetic metal flexure actuators," in *Proc. IEEE Solid state sensors and actuators workshop*, Hilton Head, SC, 1992, p. 73.
37. J. H. Comtois, V. M. Bright, and M. W. Phipps, "Thermal microactuators for surface-micromachining processes," in *Proc. SPIE*, 1995, vol. 2642, pp. 10-21.
38. J. H. Comtois and V. M. Bright, "Applications for surface-micromachined polysilicon thermal actuatorsand arrays," *Sensors and actuators* A, vol. A58, pp. 19-25, 1997.
39. L. Que, J.-S. Park, and Y. B. Gianchandani, "Bent-Beam Electrothermal Actuators – part I: Single beam and cascaded devices." *Journal of Microelectromechanical System*, Vol. 10, No. 2, June, 2001, pp. 247- 253.
40. Y. Wang, Z. H. Li, D. T. McCormick, N. C. Tien, "A micromachined RF microrelay with electrothermal actuation," *Sensors and Actuators*, A 103, pp. 231-236, 2003.
41. F.C M. Van De Pol, H. T. G. Van Lintel, M. Elwenspoek and J. H. J. Fluitman, "A thermopneumatic micropump based on micro-engineering techniques." *Sensors and Actuators* A21-A23, pp. 198-202, 1990.
42. O. C. Jeong and S. S. Yang, "Fabrication and test of a thermopneumatic micropump with a corrugated p+ diaphragm," *Sensors and Actuators* A: Physical, Volume 83, Issues 1-3, 22 May 2000, Pages 249-255.
43. T. W. Duerig, "Present and future applications of shape memory and superelastic material." *Mat. Res. Symp. Proc.* Vol. 360, pp. 497-506, 1995.
44. P. Krulevitch, A. P. Lee, P. B. Ramsey, J. C. Trevino, J. Hamilton, M. A. Northrup, "Thin film shape memory alloy microactuators," *Journal of Microelectromechanical Systems*, vol. 5, Dec 1996, pp. 270-282.

45. I. Roch, P. Bidaud, D. Collard, "Fabrication and characterization of an SU-8 gripper actuated by a shape memory alloy thin film," *J Micromech. Microeng.*, 13 (2): 330-336 MAR 2003.
46. E. Makino, T. Mitsuya and T. Shibata, "Micromachining of TiNi shape memory thin film for fabrication of micropump," *Sensors and Actuators* A: Physical, vol 79, Issue 3, 25 February 2000, Pages 251-259.
47. T. Ikeda, *Fundamentals of Piezoelectricity*. Oxford University Press, New York, pp. 213 – 226 (1984).
48. K. F. Etzold, "Ferroelectric and Piezoelectric Materials". In: *Electrical Engineering Handbook*. Edited by R. C. Dorf,, CRC Press Boca Raton, Florida, pp. 1087-1097 (1993).
49. M. Koch, N. Harris, A. G. R. Evans, N. M. White and A. Brunnschweiler, "A novel micromachined pump based on thick-film piezoelectric actuation," *Sensors and Actuators A: Physical,* Volume 70, Issues 1-2, 1 October 1998, pp. 98-103.
50. M. E. Motamedi, et. Al., "Development of micro-electro-mechanical optical scanner." *Opt. Eng.*, Vol. 36 (5), pp. 1346-1353 (1997).
51. S. J. Gross, S. Tadigadapa, T. N. Jackson, "Lead-zirconate-titanate-based piezoelectric micromachined switch," *Appl. Phys. Lett.* 83 (1): 174-176 JUL 7 2003.
52. D. C. Roberts, H. Q. Li, J. L. Steyn, "A piezoelectric microvalve for compact high-frequency, high-differential pressure hydraulic micropumping systems," *J Microelectromechanical Systems,* 12 (1): 81-92 FEB 2003.
53. W. Affane, and T. S. Birch, "A microminiature electromagnetic middle-ear implant hearing device." *Sensors and Actuators*, A 46-47, pp. 584-587. 1995.
54. J. W. Judy and R. S. Muller, "Magnetic microactuation of torsional polysilicon structures." *Sensors and actuators*, A 53, pp. 392-397. 1996.
55. H. Yang, M. Bao, H. Yin and S. Shen, "Two-dimensional excitation operation mode and phase detection scheme for vibratory gyroscope," *J. Micromech. Microeng.* 12 No 3 (May 2002) 193-197.
56. H J Cho and C H Ahn, "Magnetically-driven bi-directional optical microscanner" *J. Micromech. Microeng.* 13 No 3 (May 2003) 383-389.

57. T. Kraus, M. Baltzer, E. Obermeier, "A Micro Shutter for Applications to Optical and Thermal Detectors," *Trans. '97: 9th Int. Conf. S.-S. Sens. Act.* 1997; 67-70.

58. O. Ruiz, J. Samitier, S. Marco, J. R. Morante, C. Burrer and J. Esteve, "Electrostatically controlled multi-purpose torsional structures obtained on monocrystalline silicon," *J. Micromech. Microeng.* 6 No 1 (March 1996) 103-104.

59. Y. W. Yi and C. Liu, "Assembly of micro-optical devices using magnetic actuation", *Sensors and Actuators*, vol. A 78, pp. 205-211, 1999.

60. J. Lin, V. Schlichting, E. Obermeier, "Design and Fabrication of an Electrostatically Driven Micro-Shutter," *Trans '93: 7th Int. Conf. S.-S. Sens. Act.*, Yokohama Japan. 1993.

61. A Q Liu, X M Zhang, C Lu, F Wang, C Lu and Z S Liu, "Optical and mechanical models for a variable optical attenuator using a micromirror drawbridge," *J. Microchem. Microeng.* 13 No.3, May 2003, pp. 400 – 411.

62. W. Lang, H. Pavlioek, Th. Marx, H. Scheithauer and B. Schmidt, "Electrostatically actuated micromirror devices in silicon technology," *Sensors and Actuators* A: Physical, vol 74, Issues 1-3, 20 April 1999, Pages 216-218.

63. J-H Lee, Y-C Ko, B-S Choi, J-M Kim and D Y Jeon, "Bonding of silicon scanning mirror having vertical comb fingers," *J. Micromech. Microeng.* 12 No.5, 2002, pp. 644 – 649.

64. M. Hoffmann, D. Nusse and E. Voges, "Electrostatic parallel-plate actuators with large deflections for use in optical moving-fibre switches," *J. Micromech. Microeng.* 11 No 4 (July 2001) 323-328.

65. M-A Gretillat, F Gretillat and N F de Rooij "Micromechanical relay with electrostatic actuation and metallic contacts," *J. Micromech. Microeng.* 9 No. 3, 1999, pp. 324 – 331.

66. Z. Li, D. Zhang, T. Li, W. Wang and G. Wu, "Bulk micromachined relay with lateral contact," *J. Micromech. Microeng.* 10 No. 4, 2000, pp. 329 – 333.

67. R. Sattler, P. Voigt, H. Pradl and G. Wachutka, "Innovative design and modelling of a micromechanical relay with electrostatic actuation," *J. Micromech. Microeng.* 11 No 4 (July 2001) 428-433.
68. P. Selvaganapathy, E. T. Carlen and C. H. Mastrangelo, "Electrothermally actuated inline microfluidic valve," *Sensors and Actuators* A: Physical 18 March. 2003.
69. P. Kopka, M. Hoffmann and E. Voges, "Coupled U-shaped cantilever actuators for 1×4 and 2×2 optical fibre switches," *J. Micromech. Microeng.* 10 No 2 (June 2000) 260-264.
70. J. Buhler, J. Funk, O. Paul, H. Baltes and F. -P. Steiner, "Thermally actuated CMOS micromirrors," *Sensors and Actuators* A: Physical, vol 47, Issues 1-3, March-April 1995, Pages 572-575.
71. K. Hosokawa and R. Maeda, "A pneumatically-actuated three-way microvalve fabricated with polydimethylsiloxane using the membrane transfer technique," *J. Micromech. Microeng.* 10 No 3 (September 2000) 415-420.
72. P. Krause, E. Obermeier, W. Wehl, "A micromachined single-chip inkjet printhead," *Sensors and Actuators*. 1996; A 53: 405-9.
73. M. Kohl, K. D. Skrobanek and S. Miyazaki, "Development of stress-optimised shape memory microvalves," *Sensors and Actuators* A: Physical, vol 72, Issue 3, 16 February 1999, Pages 243-250.
74. J. A. Walker, K. W. Goossen, S. C. Arneyt, N. J. Frigo, "A Silicon Optical Modulator with 5 MHz Operation for Fibre-In-The-Loop Applications," *Transducer '95*, Sweden, pp. 285-288, 1995.
75. M C Carrozza, N Croce, B Magnani and P Dario, "A piezoelectric-driven stereolithography-fabricated micropump," *J. Micromech. Microeng.* 5 No 2 (June 1995) 177-179.
76. P. Scheeper, J. O. Gullov and L. M. Kofoed, "A piezoelectric triaxial accelerometer," *J. Micromech. Microeng.* 6 No 1 (March 1996) 131-133.
77. W. Zhu, K Yao and Z. Zhang, "Design and fabrication of a novel piezoelectric multilayer actuator by thick-film screen printing technology,"

Sensors and Actuators A: Physical, vol 86, Issue 3, 15 November 2000, Pages 149-153.

78. C. H. Ahn and M. G. Allen, "A planar micromachined spiral inductor for integrated magnetic microactuator applications," *J. Micromech. Microeng.* 3 No 2 (June 1993) 37-44.
79. A. J. Harris, J. S. Burdess, D. Wood, R. Langford, G. Williams, M. C. L. Ward and M. E. McNie, "Issues associated with the design, fabrication and testing of a crystalline silicon ring gyroscope with electromagnetic actuation and sensing," *J. Micromech. Microeng.* 8 No 4 (December 1998) 284-292.
80. S. Santra, P. Holloway and C. D. Batich, "Fabrication and testing of a magnetically actuated micropump," *Sensors and Actuators* B: Chemical, vol 87, Issue 2, 10 December 2002, Pages 358-364.
81. D. Bosch, B. Heimhofer, G. Mück, H. Seidel, U. Thumser and W. Welser, "A silicon microvalve with combined electromagnetic/electrostatic actuation," *Sensors and Actuators* A: Physical, Volumes 37-38, June-August 1993, Pages 684-692.
82. L. Lin and S. H. Lin, "Vertically driven microactuators by electrothermal buckling effects." *Sensors and Actuators*, A 71 (1998), pp.35-39.
83. H. Sehr, A. G. R. Evans, A. Brunnschweiler, G. J. Ensell and T. E. G. Niblock, "Fabrication and test of thermal vertical bimorph actuators for movement in the wafer plane", *J. Micromech. Microeng.* **11** No 4 (July 2001) pp. 306-310.
84. C. S. Pan and W. Hsu, "An electro-thermally and laterally driven polysilicon microactuator", *J. Micromech. Microeng.* **7** No 1 (March 1997), pp.7-13.
85. Y. Bayazitoglu and M. N. Ozisik, *elements of heat transfer*, McGraw Hill College Div, 1988.
86. B. Romanowicz P. Lerch, C. K. Slimane and P. Renaud, "Modelization and characterization of asymmetrical thermal micro-actuators," *J. Micromech. Microeng.*, vol. 6, pp. 134—137, 1996.
87. Frank M. White, *Heat and Mass Transfer*, Addison-Wesley Publishing Company, 1988.

88. L. Lin, and M. Chiao, "Electro, thermal and elastic characterizations of suspended micro beams." *Microelectronics Journal*, 29 (1998) pp. 269- 276.

89. R. Hickey, M. Kujath, T. Hubbard, "Heat transfer analysis and optimization of two-beam microelectromechanical thermal actuators", *J. Vac. Sci. Technol.* A 20(3), May/Jun 2002.

90. MEMSCAP, Inc. www.memscap.com.

91. Q. Huang, N. Lee, "Analysis and design of polysilicon thermal flexure actuator," *J. Micromech. Microeng.* 9 (1999) 64-70.

92. W. M.Daneman, N. C. Tien, O. Solgoard, A. P. Pisano, K. Y. Lau, and R. S. Muller, "Linear microvibromotor for positioning optical components," *J. Microelectromech. Syst.* **5**, pp. 159-165, 1996.

93. R. Yeh, E. J. J. Kruglick, and K. S. J. Pister, "Surface-micromachined components for articulated microrobots," *J. Microelectromech. Syst.* **5**, pp. 10-17, 1996.

94. E. J. Garcia and J. J. Sniegowski", "Surface micromachined microengine," *Sensors and Actuators A* **48**, pp. 203-214, 1995.

95. L. Y. Lin, E. L. Goldstein, R. W. Tkach, "Free-Space Micromachined Optical Switches with submillisecond switching time for large scale optical crossconnects", *IEEE Photon. Technol. Lett.*, vol. 10, pp. 525-527, 1998.

96. L. Fan, M. C. Wu, K. Chquette, and M. H. Crawford, "Self-assembled microactuated XYZ stages for optical scanning and alignment," in *Proc. 1997 Int. Conf. Solid-State Sensors and Actuators (TRANSDUCERS 97)*, 1997, paper 2A2.01.

97. T. Akiyama and K. Shono, "Controlled Stepwise Motion in Polysilicon Microstructures," *Journal of Microelectromechanical Systems*, Vol. 2, No. 3, September 1993, pp.106-110.

98. J. M. Gere and S. P. Timoshenko, *Mechanics of Materials*, 3rd ed. Boston, MA: PWS-Kent, 1990.

99. K. E. Petersen, "Dynamic Micromechanics on Silicon: Techniques and Devices," *IEEE Trans. Electr. Dev.*, Vol. ED-25, 1978, pp. 1242-1249.

100. R. J. Linderman, V. M. Bright, "Optimized Scratch Drive Actuator for Tethered Nanometer Positioning of Chip-Sized Components," *Proceedings of*

the 2000 Solid-State Sensor and Actuator Workshop, Hilton Head Island, SC, pp. 214-217, June 4-8, 2000.

101. H. Santos, "Introduction to Microelectromechanical (MEM) Microwave Systems," Chapter 2, pp. 29 – 33, Artech House, 2000.

102. P. Langlet, D. Collard, T. Akiyama, H. Fujita, "A quantitative analysis of scratch drive actuation for integrated X/Y motion system," *Transducers 97*, Chicago, Illinois USA, 1997, paper 3A2.01.

103. N. Finch, J. Marchettil, H. Fujita, J. Gouy, "CAD Modeling of Scratch Drive Actuation", *IntelliSense Corp.*

104. Stoker J. J., *Nonlinear Vibrations*, New York University, 1941.

105. R. Linderman, V. Bright, "Nanometer precision positioning robots using scratch drive actuators," *Sensors and Actuators* A91 (2001) 292-300.

106. H. Toshiyoshi, D. Miyauchi, H. Fujita, "Electromagnetic Torsion Mirrors for Self-Aligned Fibre-Optic Crossconnects by Silicon Micromachining", *IEEE J. Sel. Top. Quantum Electronics* **5**, pp. 10-17, 1999.

107. Lih Y. Lin, Evan L. Goldstein, and Robert W. Tkach, "Angular-precision enhancement in free-space micromachined optical switches." IEEE Phonics technology letters, Vol. 11, No. 10, Oct. 1999.

108. R. S. Muller and K. Y. Lau, "Surface-micromachined micro-optical elements and systems," *Proceedings of IEEE*, vol. 86, no. 8, pp. 1707-1720, Aug. 1998.

109. J. Zou, C. Liu, D. R. Trainor, J. Chen, J. E. Schutt-Aine and P. L. Chapman, "Development of three-dimensional inductors using plastic deformation magnetic assembly (PDMA)," *IEEE Transactions on Microwave Theory and Techniques*, vol. 51, no. 4, pp. 1065-1075, April. 2003.

110. M. C. Wu, L. Y. Lin, S. S. Lee and K.S.J. Pister, "Micromachined free-space integrated micro-optics", *Sensors and Actuators,* vol. A50, pp. 127-134, 1995.

111. J. R. Reid, V. M. Bright and J. T. Butler, "Automated assembly of flip-up micromirrors," *Sensors and Actuators*, vol. A66, pp. 292-298, 1998.

112. N. C. Tien, O. Solgaard, M. H. Kiang, M. Daneman, K. Y. Lau and R. S. Muller, "Surface micromachined mirrors for laser beam positioning," *Sensors and Actuators,* vol. A52, pp. 76-80, 1996.

113. R. R. A. Syms, C. Gormley and S. Blackstone, "Improved yield, accuracy and complexity in surface tension self-assembled MOEMS", *Sensors and Actuators,* vol. A88, pp. 273-283, 2001.

114. K. F. Harsh, V. M. Bright and Y. C. Lee, "Solder self-assembly for three-dimensional microelectromechanical systems," *Sensors and Actuators,* vol. A77, pp. 237-244, 1999.

115. T. Ebefors, E. Kalvesten and G. Stemme, "New small radius joints based on thermal shrinkage of polyimide in V-grooves for robust self-assembly 3D microstructures," *J. Micromech. Microeng.*, vol. 8, pp. 188-194, 1998.

116. J. Zou, J. Chen, C. Liu and J. E. Schutt-Aine, "Plastic deformation magnetic assembly for out-of-plane microstructures: technoogy and applications," *Journal of Microelectromechanical System*, vol. 10, no. 2, pp. 302-309, 2001.

117. R. W. Johnstone, M. Parameswaran, "Self-assembly of surface-micromachined structures using electrostatic attraction", *MOEMS and Miniaturized Systems II, Proceedings of SPIE,* vol. 4561, pp. 66-76, 2001.

118. R. T. Chen, H. Nguyen and M. C. Wu, "A high-speed low voltage stress-induced micromachined 2x2 optical switch", *IEEE Photonics Tech. Letts.*, vol. 11, no.11, pp. 1396-1398, 1999.

119. V. A. Aksyuk, F. Pardo and D. J. Bishop, "Stress-induced curvature engineering in surface-micromachined devices," *Design, Test, and Microfabrication of MEMS and MOEMS, Proceedings of SPIE,* vol. 3680, pp. 984-993, 1999.

120. V. M. Lubecke, B. Barber, E. Chan, D. Lopez, M. E. Gross and P. Gammell, "Self-assembling MEMS variable and fixed RF inductors", *IEEE Transactions on MTT,* vol. 49, no. 11, pp.2093-2098, 2001.

121. G. H. Ryder, *Strength of Material*, 3rd Edition, pp 105-106, 1970.

122. A. K. Ghatak, and K. Thyagarajan, *Optical Electronics,* Cambridge: Cambridge University Press, p142, 1989

123. J. W. Goodman, *Introduction to Fourier Optics,* 2nd edition, McGraw-Hill, p 49, 1996.

124. G. Zhou and P. Dowd, "Tilted folded-beam suspension for extending the stable travel range of the comb-drive actuator," *J Micromech. Microeng.,* vol. 13, pp. 178-183, 2003.

125. R. Legtenberg, A. W. Groeneveld and M. Elwenspoek, "Comb-drive actuators for large displacement", *J Micromech. Microeng.,* vol. 6, pp. 320-329, 1996.

126. J. C. Palais, *Fibre optic communications*, Prentice Hall, New Jersey, 1998.

127. T. P. Kurzweg, S. P. Levitan, J. A. Martinez, P. J. Marchand, D. M. Chiarulli, "Diffractive Optical Propagation Techniques for a Mixed-Signal CAD Tool", *Optics in Computing (OC2000),* Quebec City, CA, June 18--23, 2000.

128. H. Kogelnik, "Coupling and conversion coefficients for optical modes," in *Proc. Symp. Quasi-Optics*, New York, pp. 333-347, Jun. 1964

Appendix A: Multi-User MEMS Process (MUMPs)

A.1 Reasons for using foundry processes

Microfabrication of MEMS is mainly based on IC process, therefore it needs a lot of facilities such as furnace, mask aligners, plasma etching systems, and metalization equipment and so on. These facilities are costly and require to be situated inside clean rooms. Commercial foundry based fabrication of MEMS enables research groups and small companies without their own in-house microfabrication facilities to participate in exploiting the advantage of MEMS technology without having to incur the very significant costs of installing and maintaining their own facilities to the high standards required to obtain reliable and repeatable processes. The use of commercial foundries for MEMS fabrication follows the well established approach in the domain of microelectronics manufacture where microelectronic systems are designed in one part of the world and fabricated wherever an appropriate foundry is available that offers the required processes at competitive costs. Invariably this trend will emerge in the field of commercial MEMS, and foundries will be selected on the basis of the fabrication processes that they offer. MEMS foundries can provide quick response for the reason that the processes are well-organized and mature.

In using multi-user foundry services, such as the well-known MUMPS family of processes, MEMS designers have to be both innovative and ingenious with their designs because the foundry's design rules are fixed for all users alike.

We have submitted our designs to the foundries as appropriate, and the fabricated microsystems have been returned to us for experimental evaluation/testing. In our research, we have used Polysilicon surface micromachining process – PolyMUMPs and Silicon On Insulator process – SOIMUMPs (MUMPs – Mutli User MEMS Process). Both processes are undertaken the in USA and belong to MEMSCAP Inc [1].

A.2 Introduction to PolyMUMPs

PolyMUMPs is a polysilicon surface micromachining process. It uses polysilicon as structural material and SiO_2 as the sacrificial layer. Three polysilicon layers, two sacrificial oxide layers, one metal layer and one silicon nitride layer are available. The process defines all the layer thicknesses and their functions. All MEMS designers have to follow these definitions and design rules. These definitions and design rules make it possible for many different designs to be put together in one single fabrication process. Also, the standardization of the fabrication process reduces the fabrication cost and lets more and more designers submit their designs. Table A-1 shows the main definitions of layers in PolyMUMPs process and a brief introduction of each layer's function [1].

Table A-1, MUMPs process layers and their properties.

Material Layer	Nominal Thickness	Lithography level name	Function
Silicon Nitride	0.6 μm		Insulator
Poly0	0.5 μm	Poly0 and hole0	Conductive layer
First Oxide	2.0 μm	Dimple	Reduce friction
First Oxide	2.0 μm	Anchor 1	Fix poly1
Poly 1	2.0 μm	Poly 1 and hole 1	Structural layer
Second Oxide	0.75 μm	Poly 1-poly 2-via	Connection with poly 1 and poly 2
Second Oxide	0.75 μm	Anchor 2	Fix poly 2
Poly 2	1.5 μm	Poly 2 and hole 2	Second structural layer
Metal	0.5 μm	Metal and metal hole	Conductive layer, bonding pad, mirror surface etc.

The PolyMUMPs process begins with 100 mm n-type silicon wafers. In order to prevent or reduce charge feed through to the substrate from electrostatic devices on the surface, these wafers are first heavily doped with phosphorus. Next, a 600 nm low-stress silicon nitride is deposited on the wafers, which normally is used as insulator. After that a 500 nm polysilicon film (Poly0) is deposited. This is followed directly by the patterning through photolithography, a process that includes coating of wafers with photoresists, exposure of photoresist with the appropriate mask and developing exposed photoresists to create the desired etch mask for subsequent pattern transfer into the underlying layer. After patterning the photoresist, the Poly 0 layer is then etched in a special system.

A 2.0 μm phosphosilicate glass (PSG) layer (first sacrificial layer – Ox1) is deposited and annealed. This layer can be used to free the first polysilicon layer after final releasing step. The sacrificial layer can be patterned and etched with mask such as Dimple and Anchor 1. After that, the first structural layer – poly 1 is deposited at a thickness of 2.0 μm. The poly 1 is then patterned using a mask to form the first structural layer. After Poly 1 is etched, a second oxide layer is deposited and annealed. The second oxide layer can be patterned and etched using two masks: Poly 1_Poly 2_Via and Anchor 2, with different objectives. The Poly 1_Poly 2_Via level offers the mechanical and electrical connection between Poly 1 and Poly 2 layers. The Anchor 2 level is used to anchor the poly 2 layer directly down to the poly 0 or silicon nitride layer.

After etching the Oxide 2, another polysilicon layer is deposited with the thickness of 1.5 μm. Poly 2 layer is patterned by mask Poly 2 to form the structure. A 0.5 μm metal layer is final deposited layer in the PolyMUMPs process. It provides bonding, probing, electrical routing, and highly reflective mirrors. The metal layer is then patterned and etched using the mask called Metal. Finally, the wafer is released in HF solvent. The releasing process is as follows: First, immersing the wafer into the acetone for 3 minutes, and then into De-ionized (DI) water for 30 seconds. These two steps can strip photoresist off. After that, chips are put in the 49 % HF solvent for 1.5 – 2 minutes to etch the oxide away. This is followed by several minutes in DI water

and then alcohol for 2 minutes to reduce friction followed by at least 10 minutes in an oven at 1100 C. Figure A-1 shows the process flow. Figure 3-2 shows the example device fabricated using PolyMUMPs.

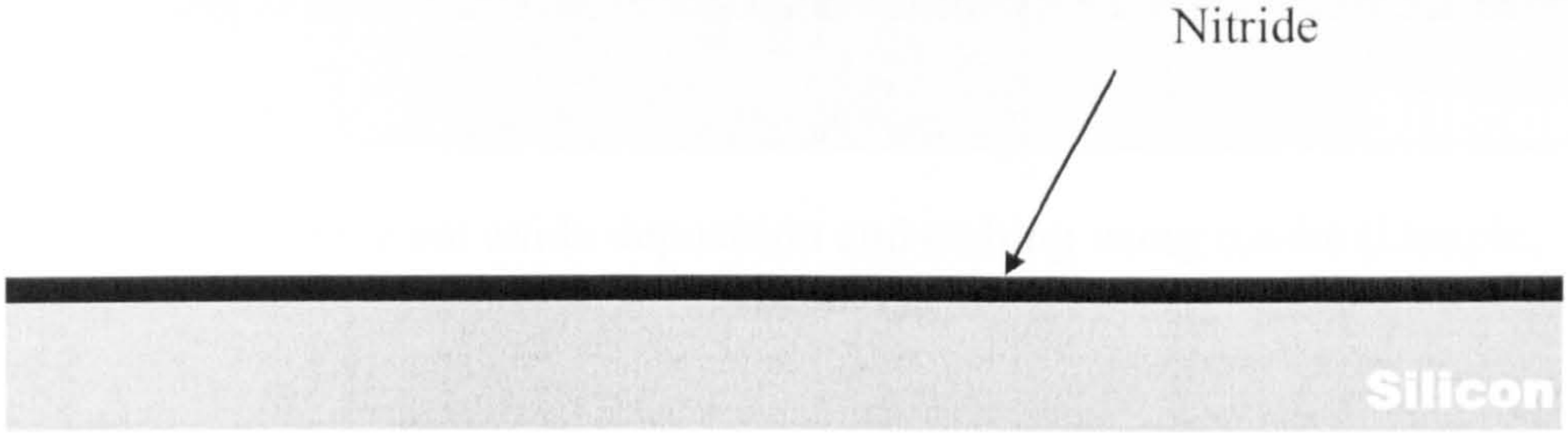

Fig. A-1 (a). Add nitride.

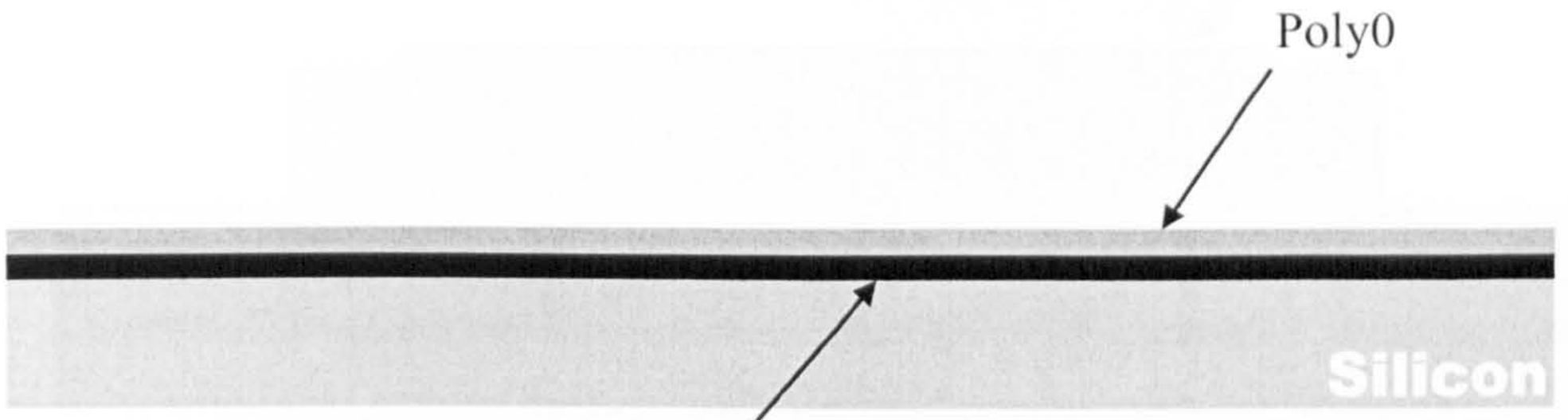

Fig. A-1 (b). Add Poly0.

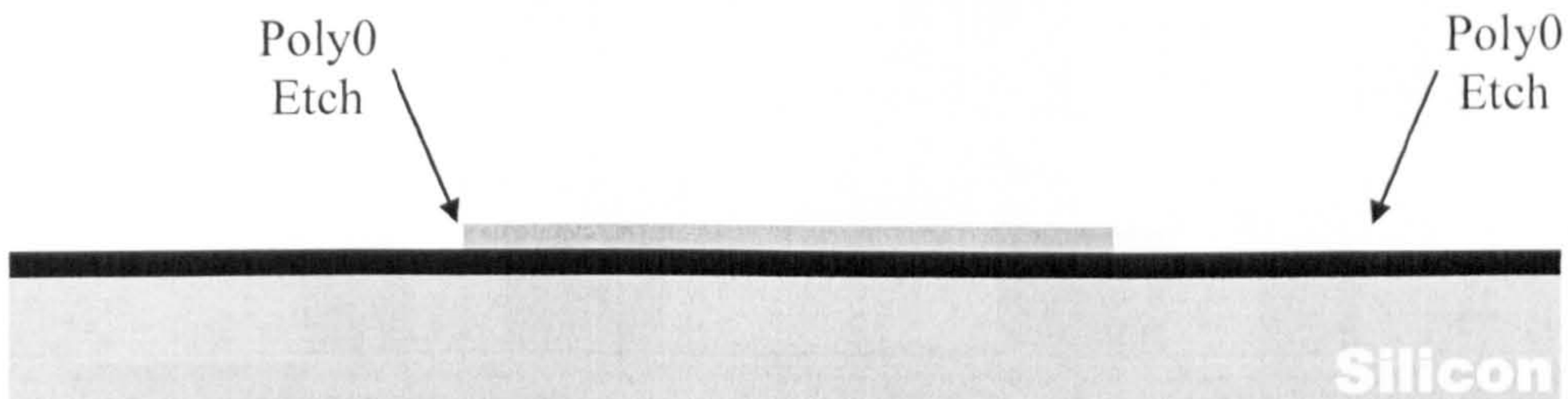

Fig. A-1 (c). Patterning through 1st level mask (Poly0) using Photolithography, Removal of Unwanted Poly0 using Reactive Ion Etching.

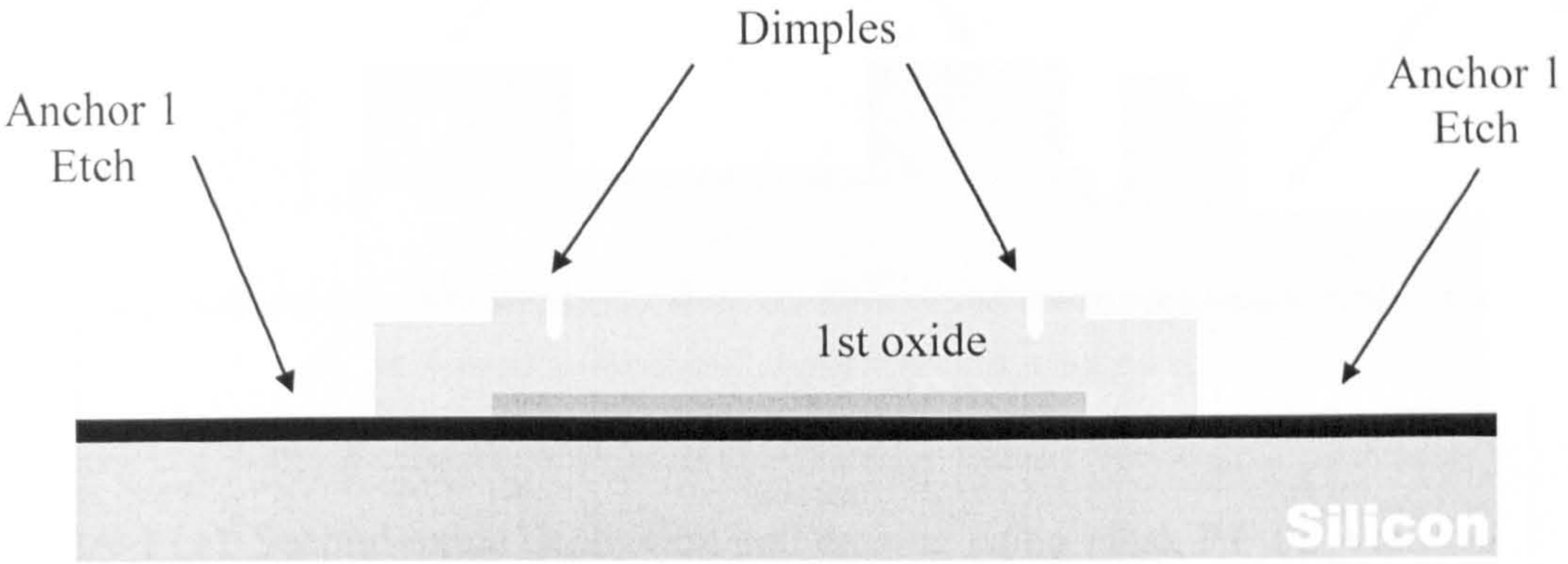

Fig. A-1 (d). First oxide deposition and etching using masks (Dimple, Anchor1).

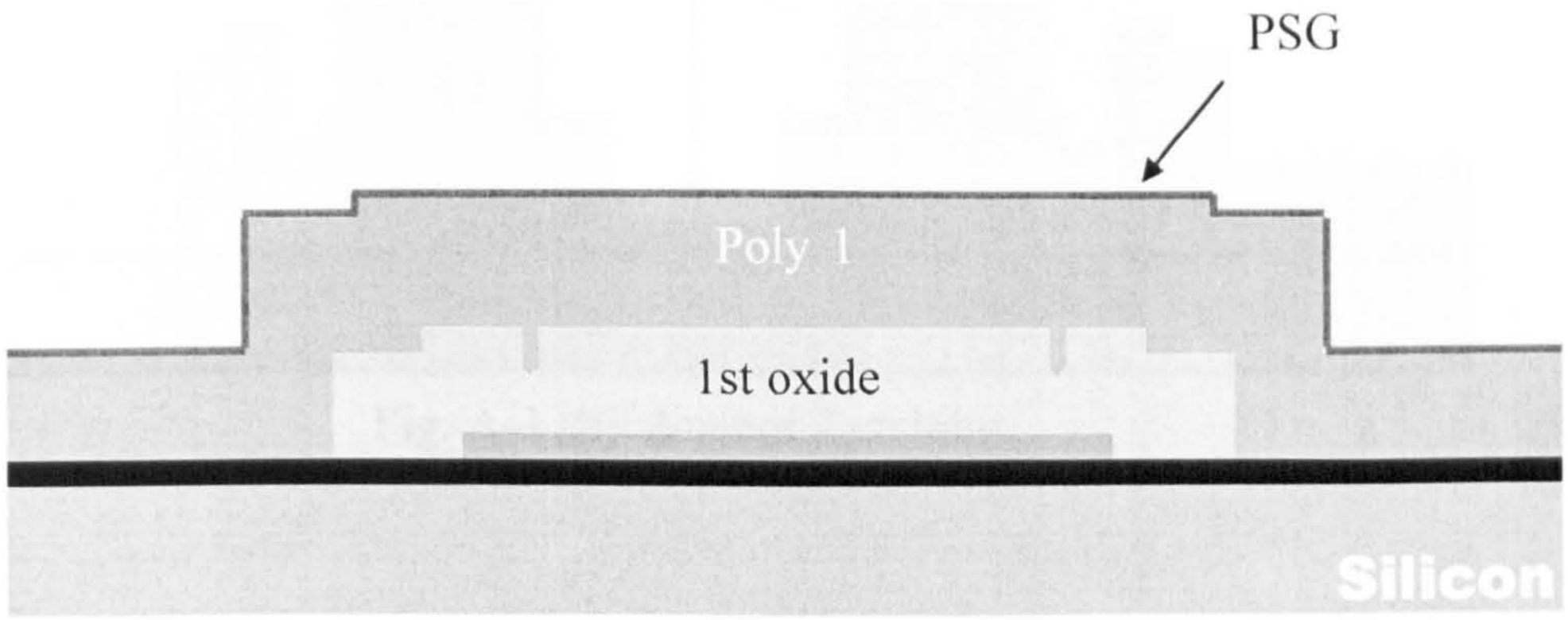

Fig. A-1 (e). Polysilicon (Poly1) deposition, following by oxide deposition and annealing.

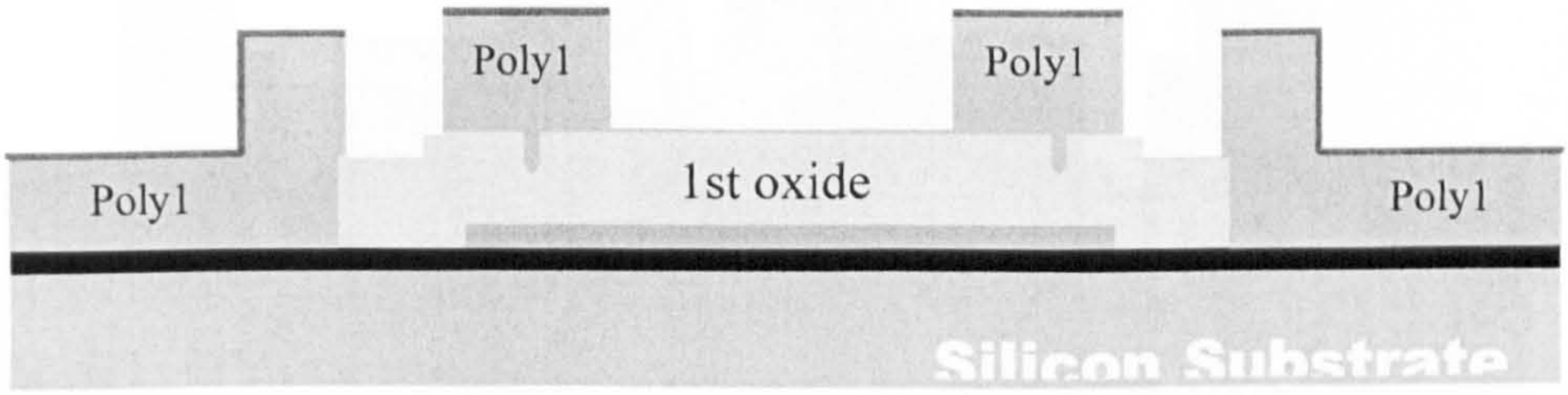

Fig. A-1 (f). Patterning through mask (Poly1) using Photolithography and Deep RIE.

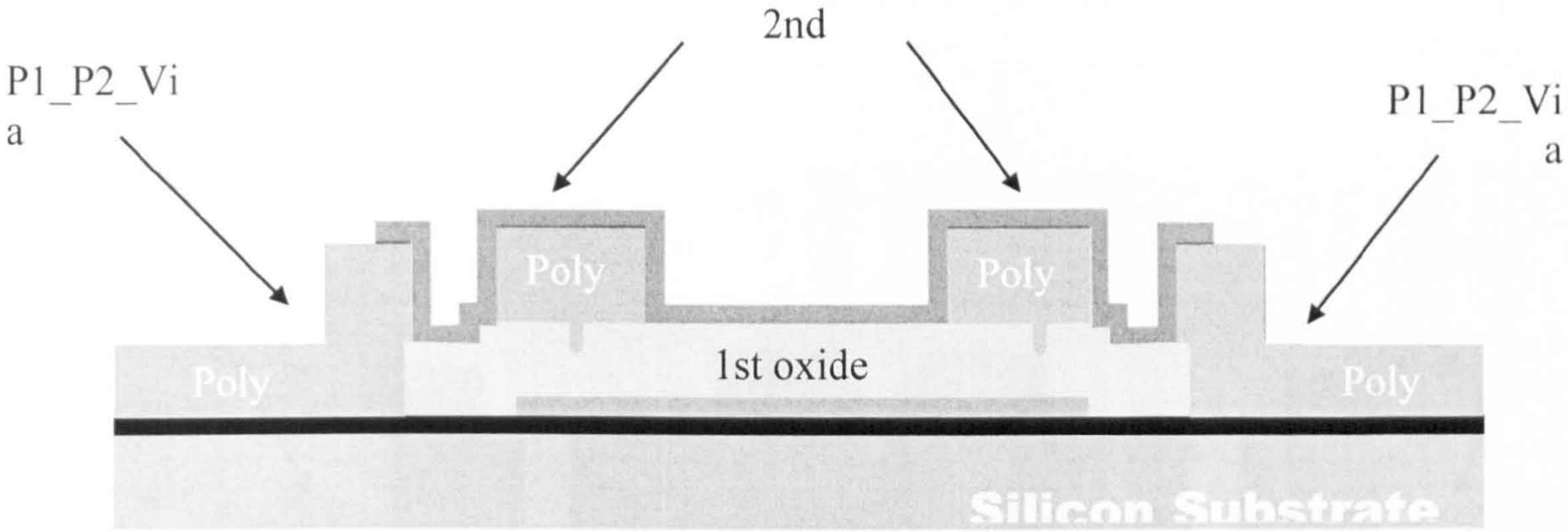

Fig. A-1 (g). Second oxide deposition and etching using mask P1_P2_via.

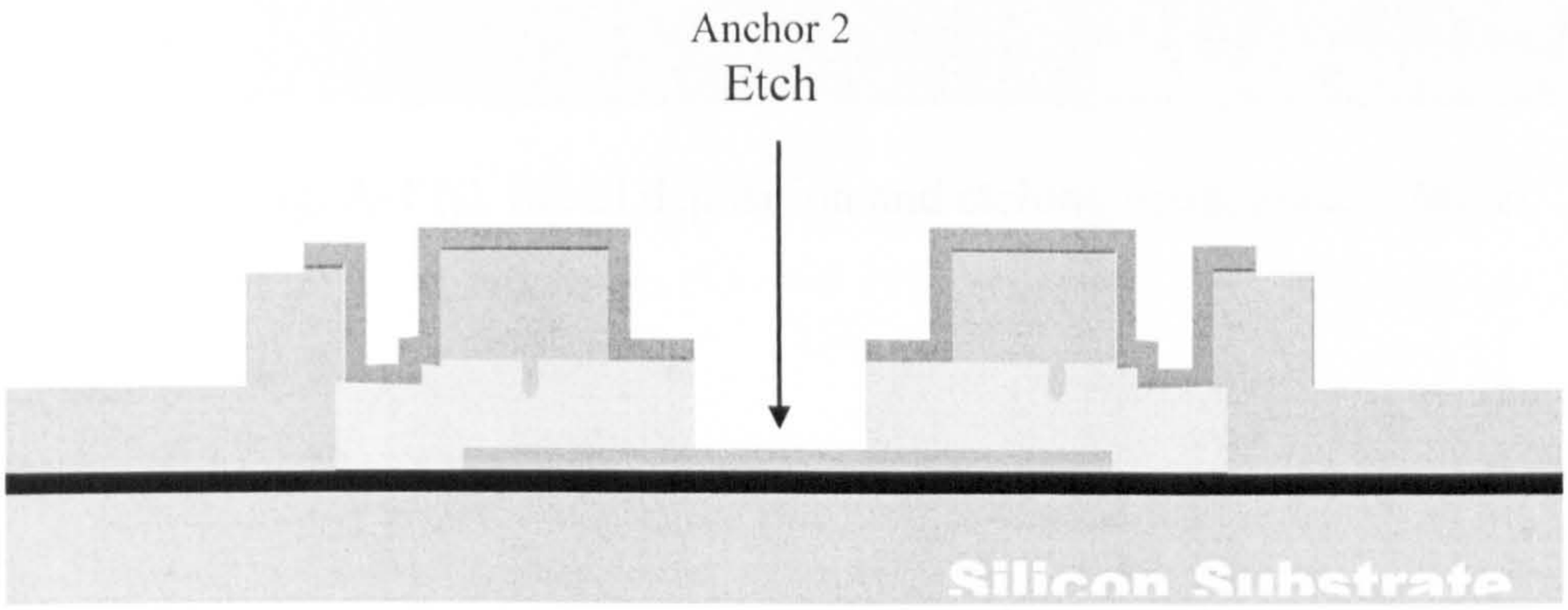

Fig. A-1 (h). Anchor 2 etching.

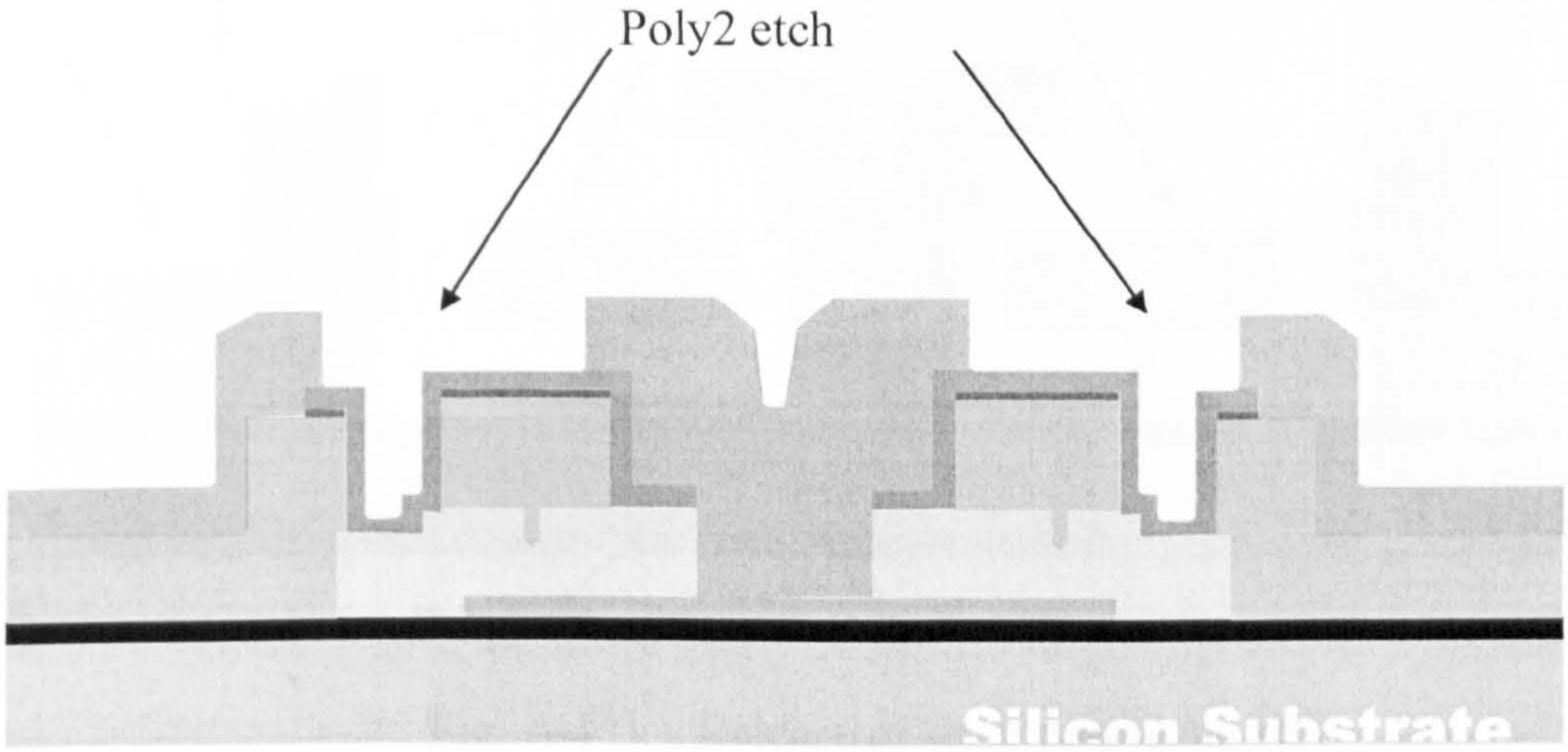

Fig. A-1 (i). Poly2 deposition and etching using mask – Poly2.

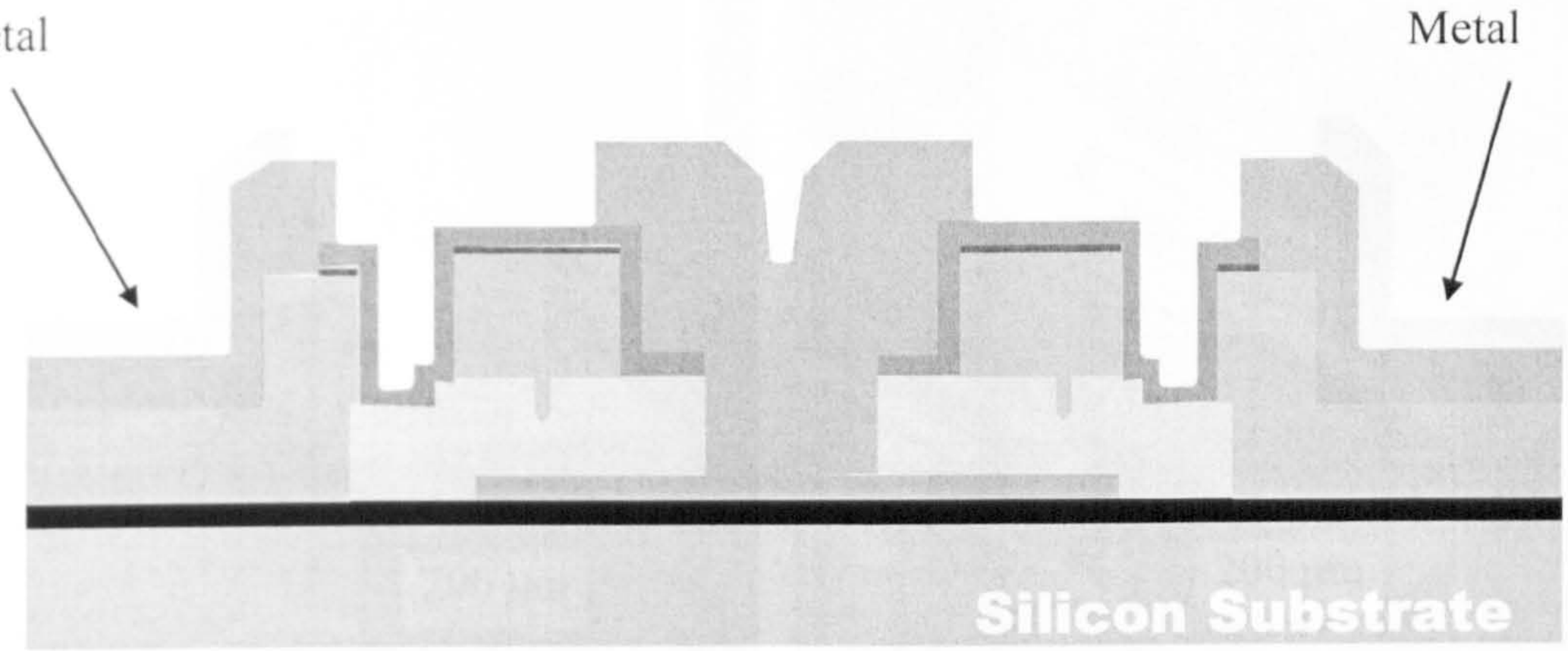

Fig. A-1 (j). Metal deposition and etching using mask – Metal.

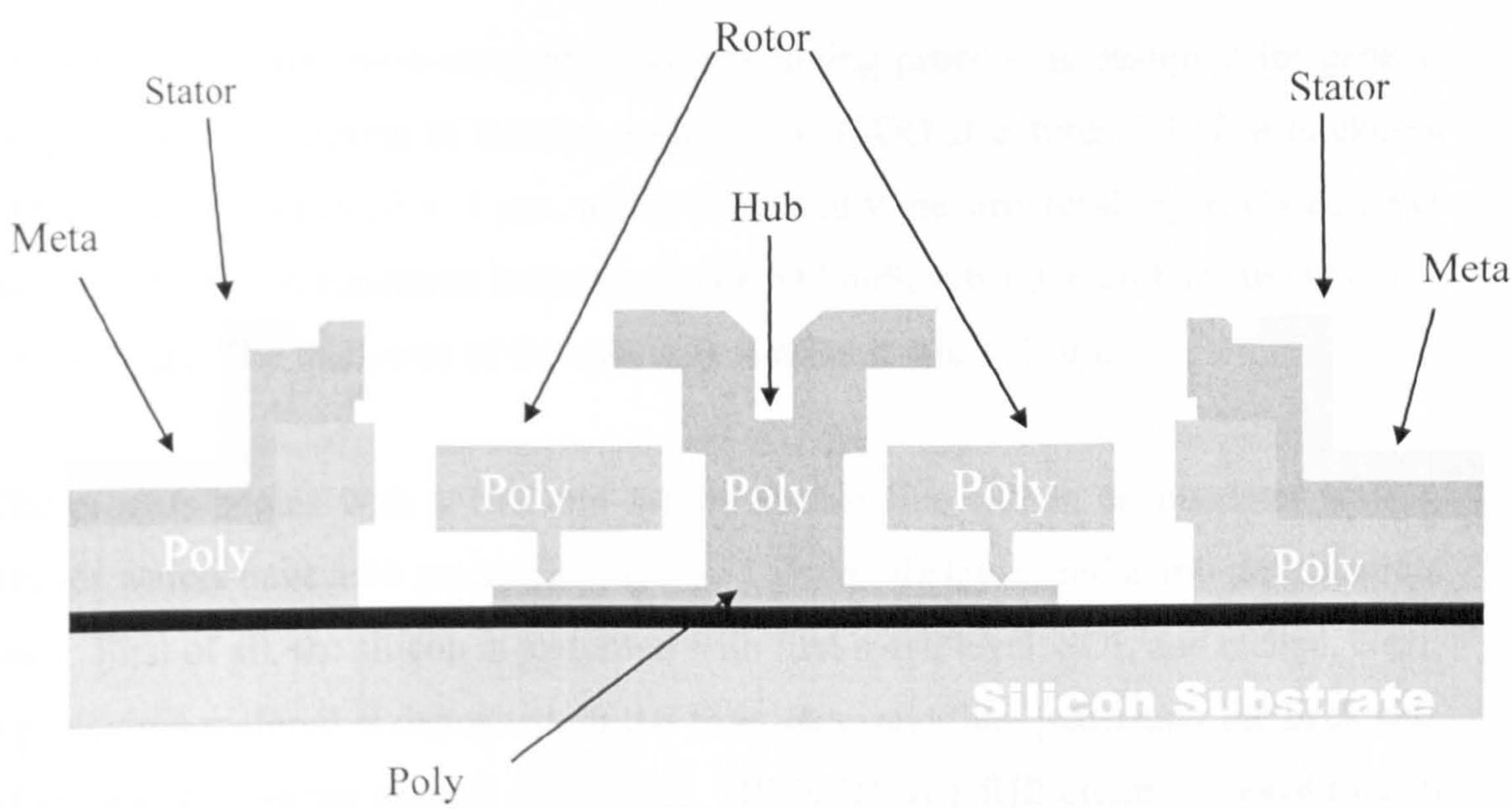

Fig. A-1 (k). Release of structures using HF.
Finished device: motor

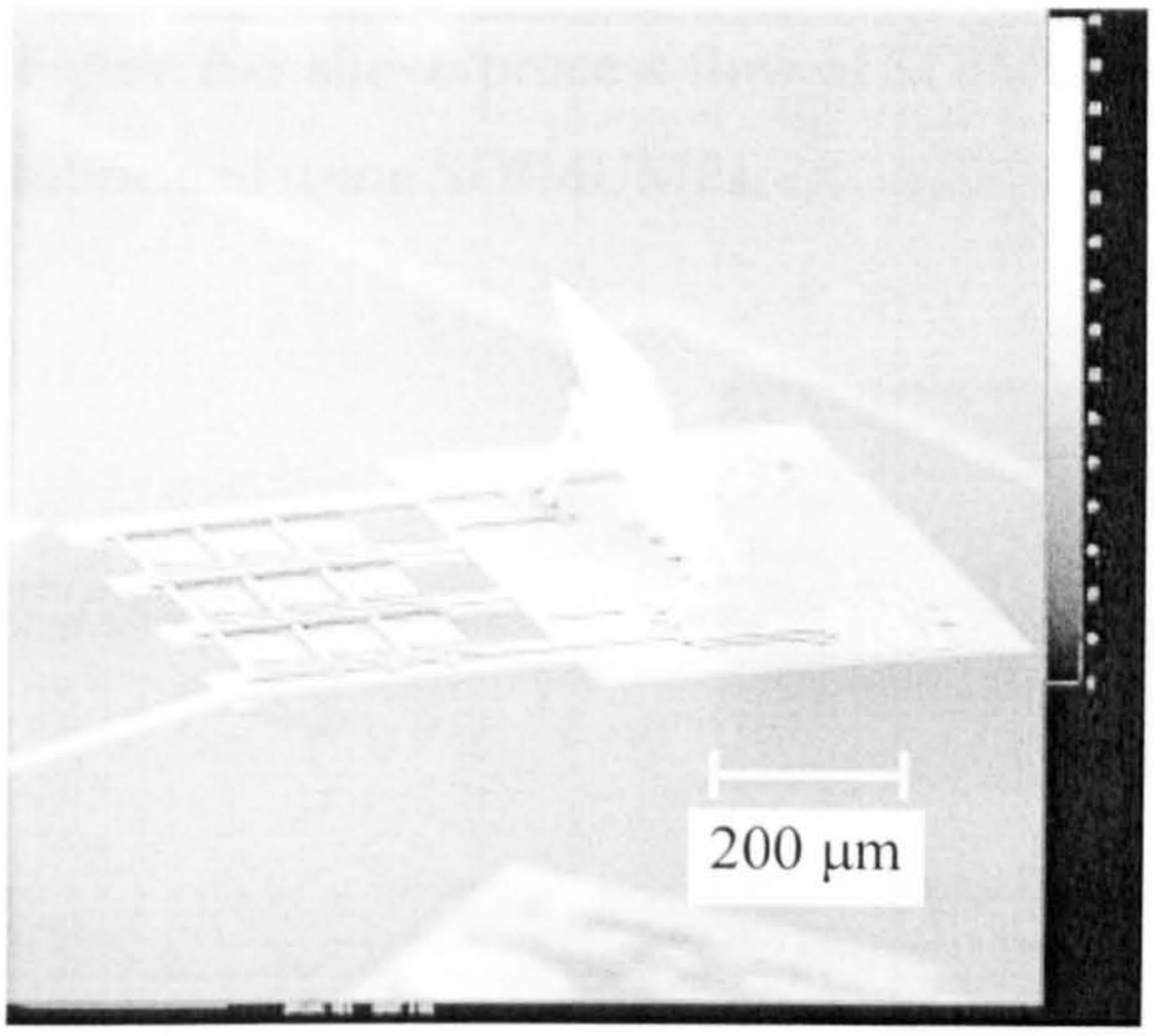

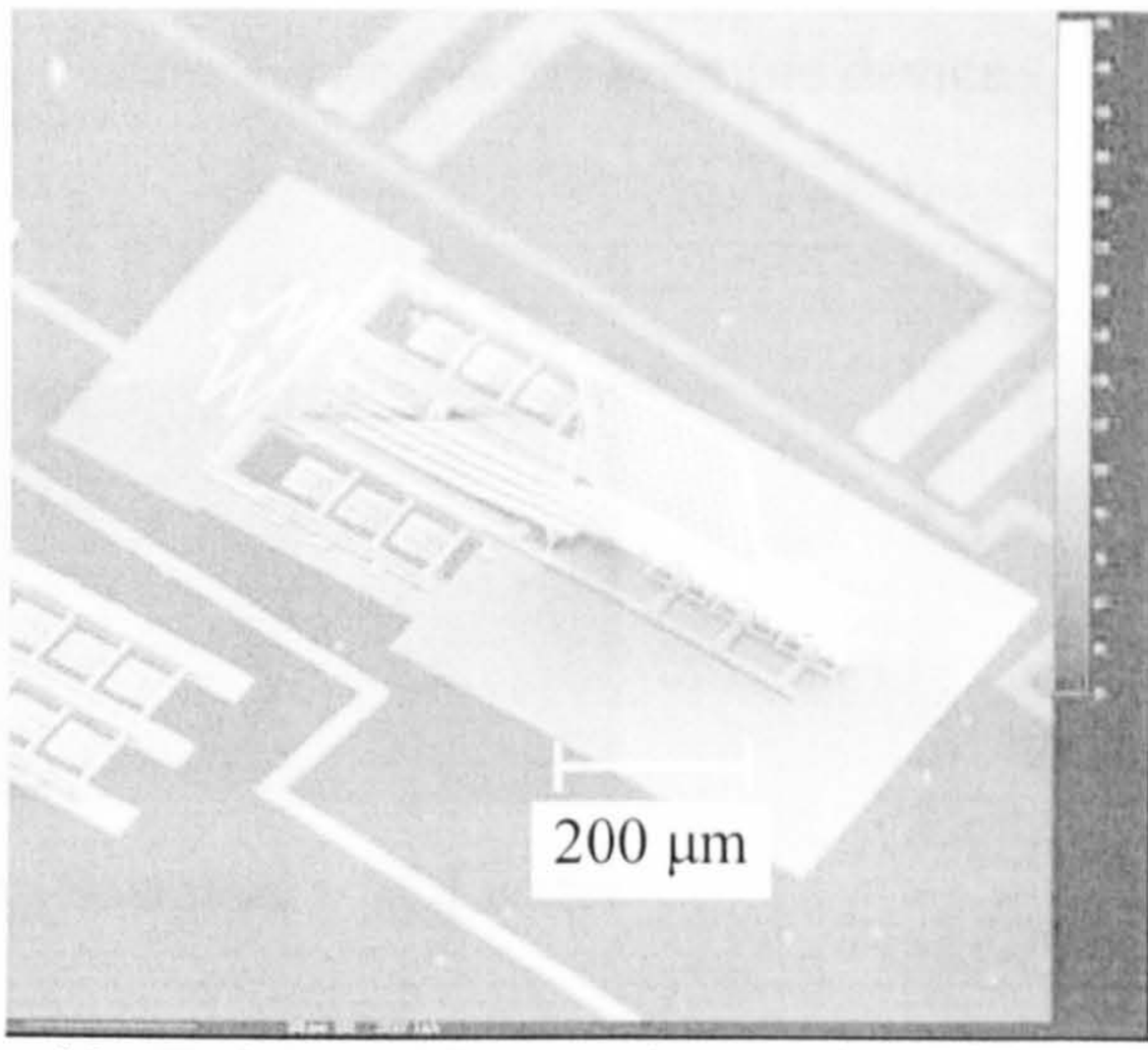

Fig. A-2. Examples of Strathclyde devices fabricated by PolyMUMPs. Device on the left is a SDA erected micromirror, device on the right is a self-assembled microshutter driven by SDA.

A.3 Introduction to SOIMUMPs

SOIMUMPs, a silicon-on-insulator micromachining process, is designed for general purpose micromachining of Silicon-on-Insulator (SOI) structures [1]. The thickness of the silicon layer is 10 ± 1 μm, which is normally the structural layer. Oxide layer has the function of insulation between silicon and bulk substrate, and has thickness of 1 ± 0.05 μm. The thickness of the substrate is around 400 ± 5 μm.

The process begins with a 100 mm n-type double-side silicon on insulator wafers. Theses wafers have a 10 μm silicon layer, a 1 μm oxide layer, and a 400 μm substrate layer. First of all, the silicon is patterned with first mask level, SOI, and etched. Next, a protection material is deposited on the front face, and then patterning the back side of the wafer using the second mask level, TRENCH. A DRIE etching is used to etch these features completely through the substrate layer. The HF releasing process is followed and silicon structures on top of the trench hole are completely released. Finally, the metal layer, consisting of 50 nm Cr+ and 600 nm Au, is deposited and

patterned using shadow masking technique. The wafers are then diced using a scribe and break method.

Figure A-3 shows process flow of SOIMUMPs. Figure 3-4 shows the example device fabricated using SOIMUMPs.

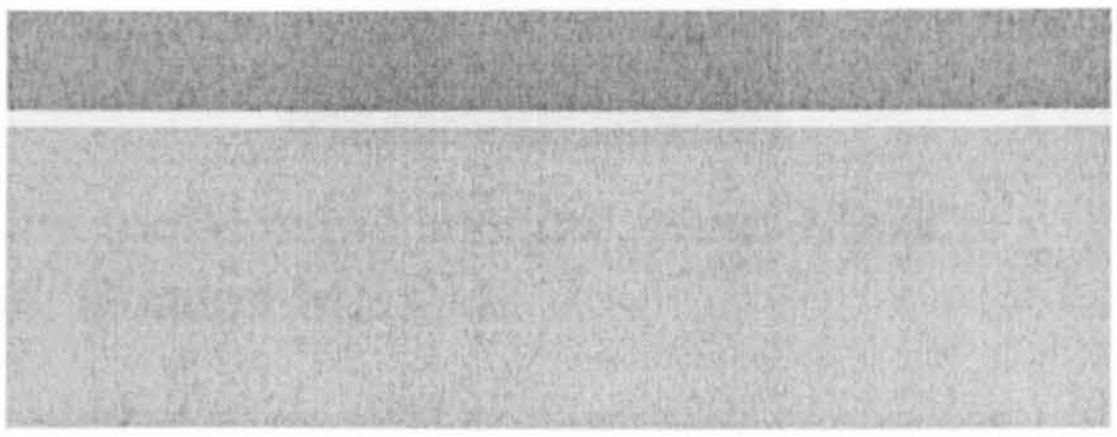

Fig. 3-3 (a). Starting Substrate – SOI wafer

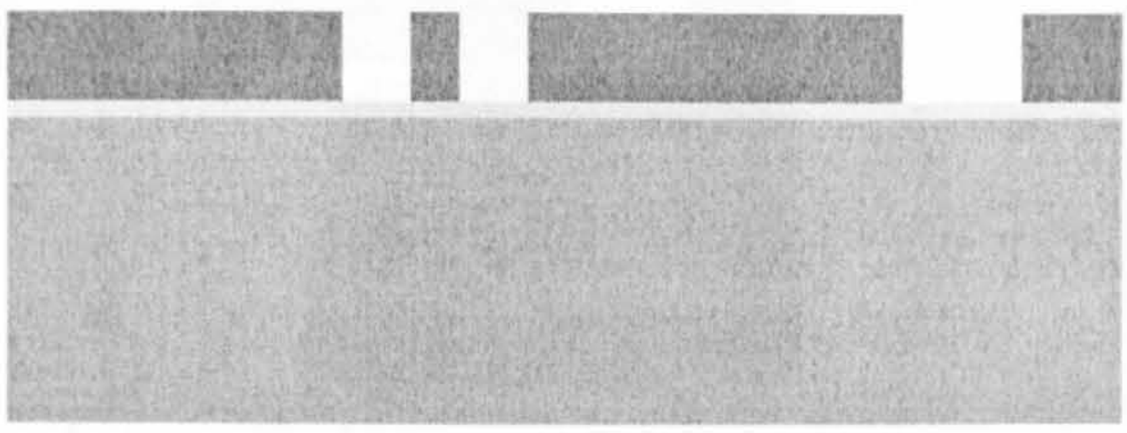

Fig. 3-3 (b). Patterning top silicon. Mask level: SOI

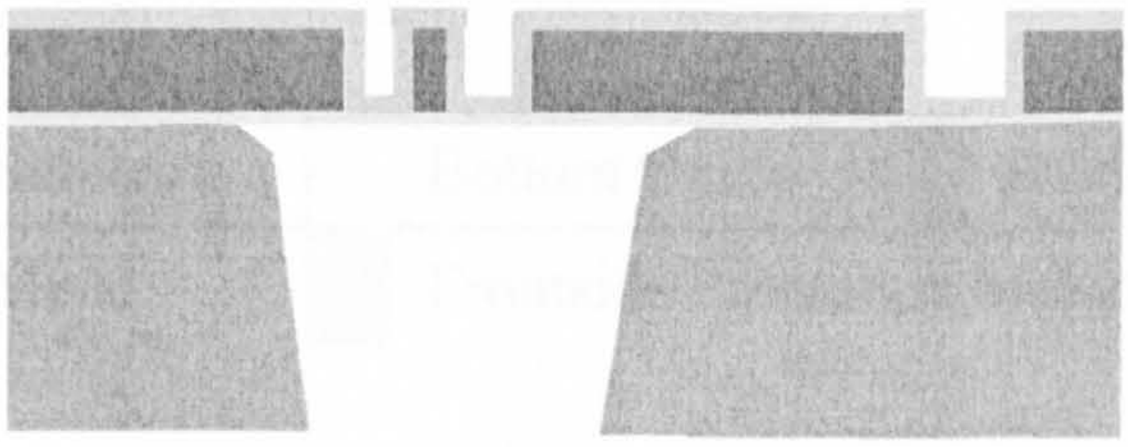

Fig. 3-3 (c). Patterning bottom substrate. Mask level: TRENCH

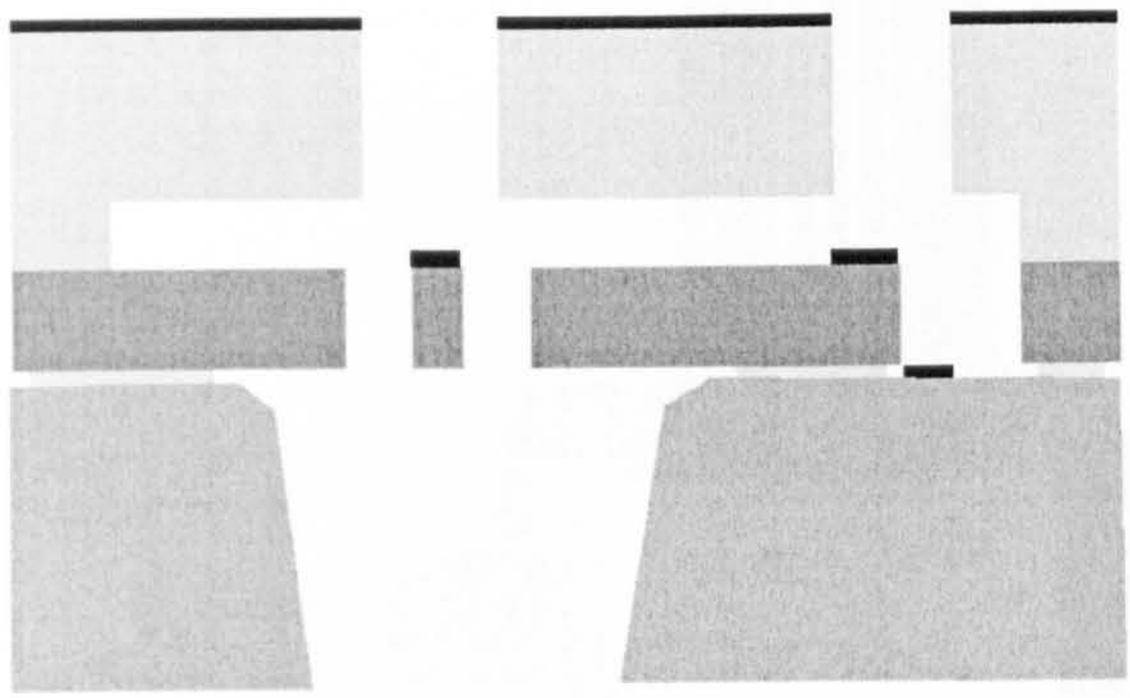

Fig. 3-3 (d). Patterning metal using shadow mask. Mask level: Blanket METAL

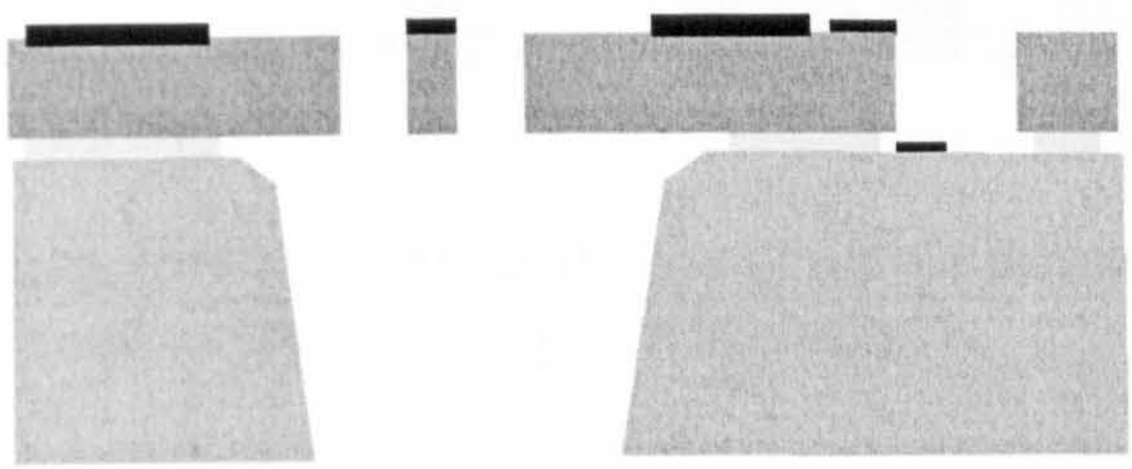

Fig. 3-3 (e). Final step: shadow mask removed

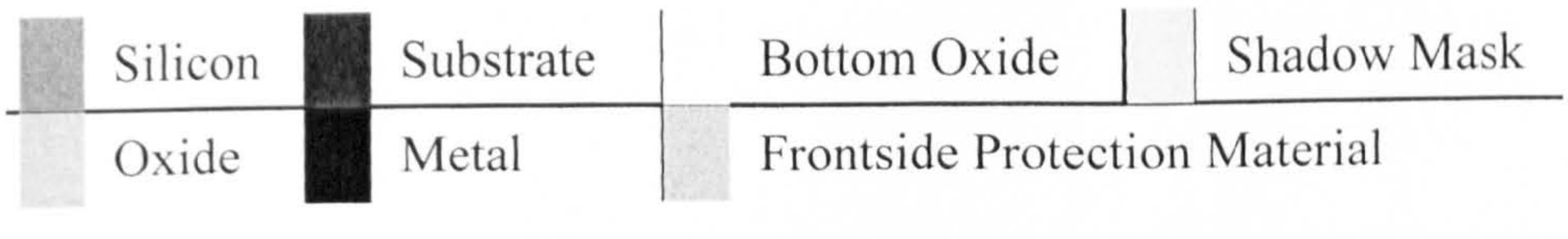

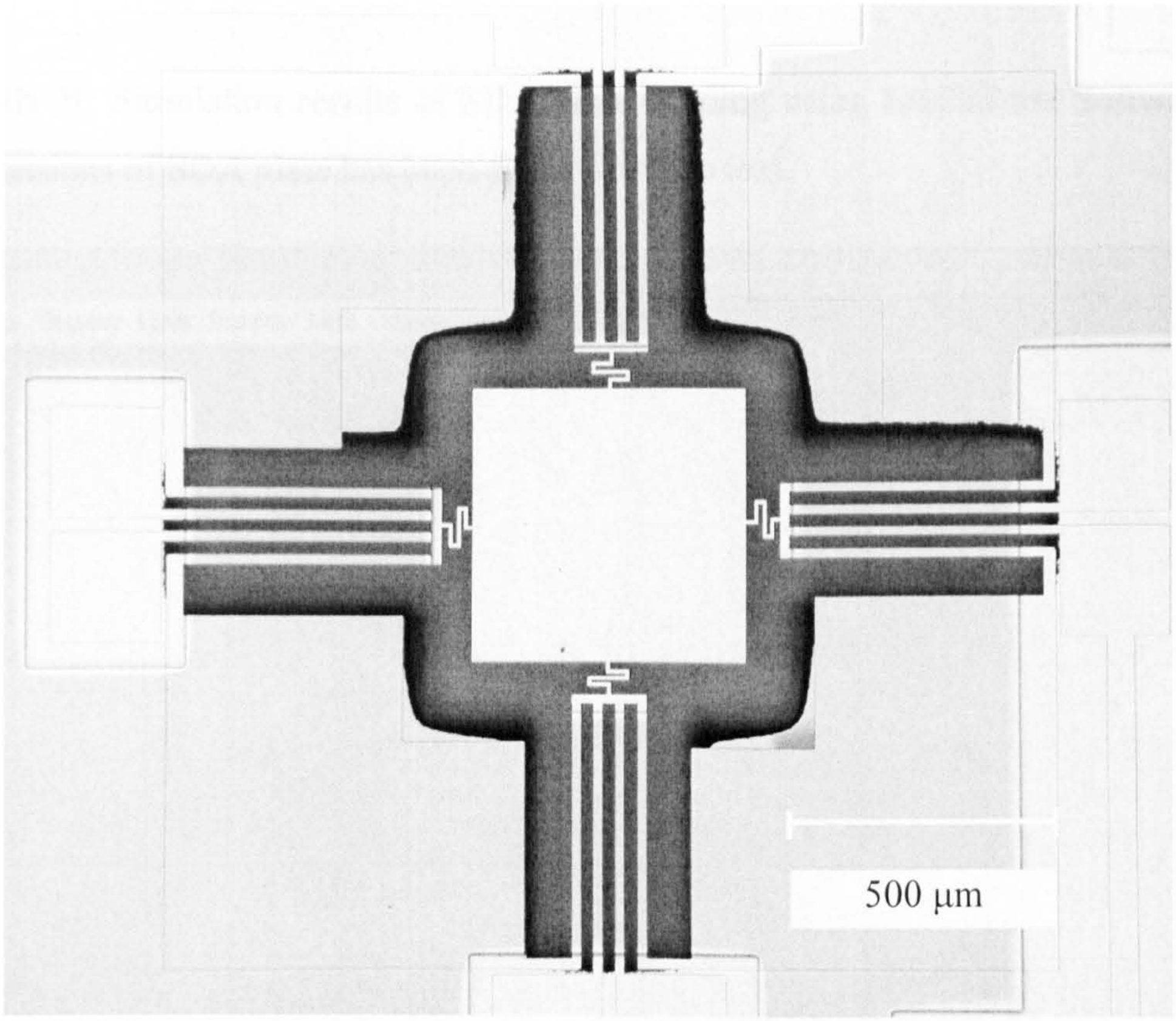

Fig. 3-4. Example Strathclyde device (Tiltable micromirror actuated by vertical thermal actuator) fabricated by SOIMUMPs.

Reference:

1. MEMSCAP Inc, http://www.memsrus.com/CIMSsvcs.html.

Appendix B: Simulation results of SDA plate bending using IntelliSuite Software, the dimensions of SDA plate has been shown in main text.

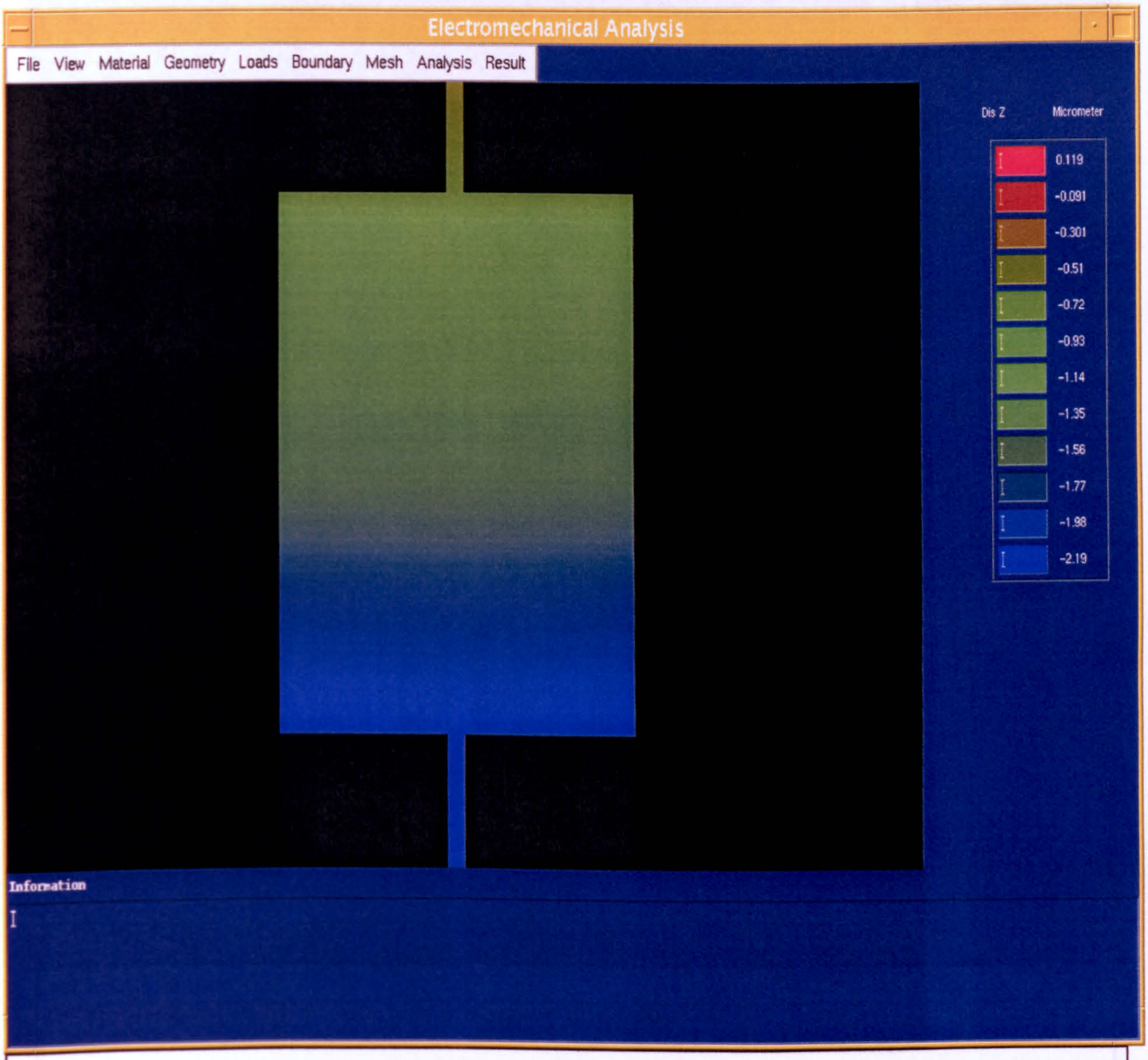

(a). V = 60 V

The results from IntelliSuite. The colours represent the different Z-axis displacements due to different applied voltages.

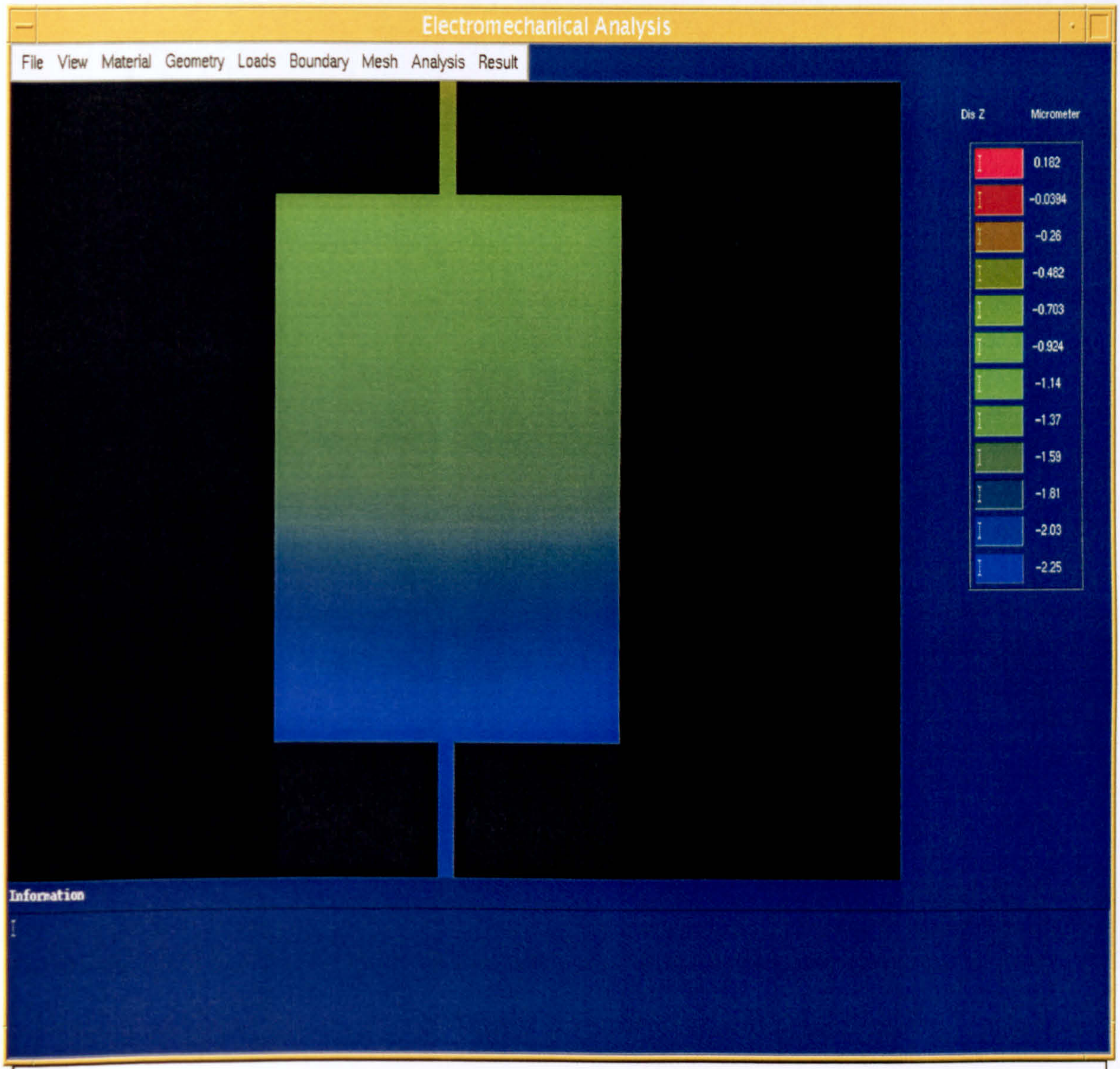

(b). V = 100 V

The results from IntelliSuite. The colours represent the different Z-axis displacements due to different applied voltages.

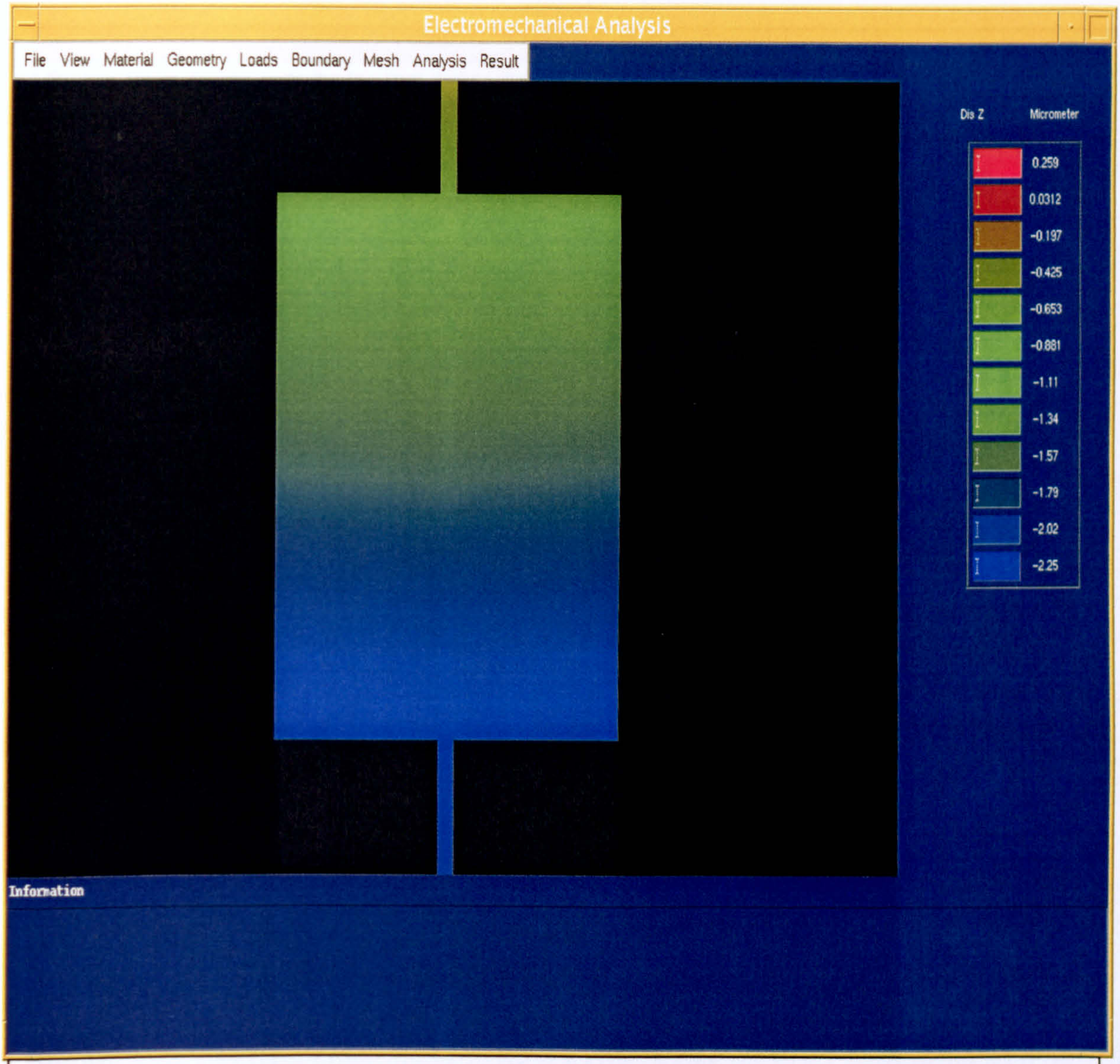

(c) V = 150 V

The results from IntelliSuite. The colours represent the different Z-axis displacements due to different applied voltages.

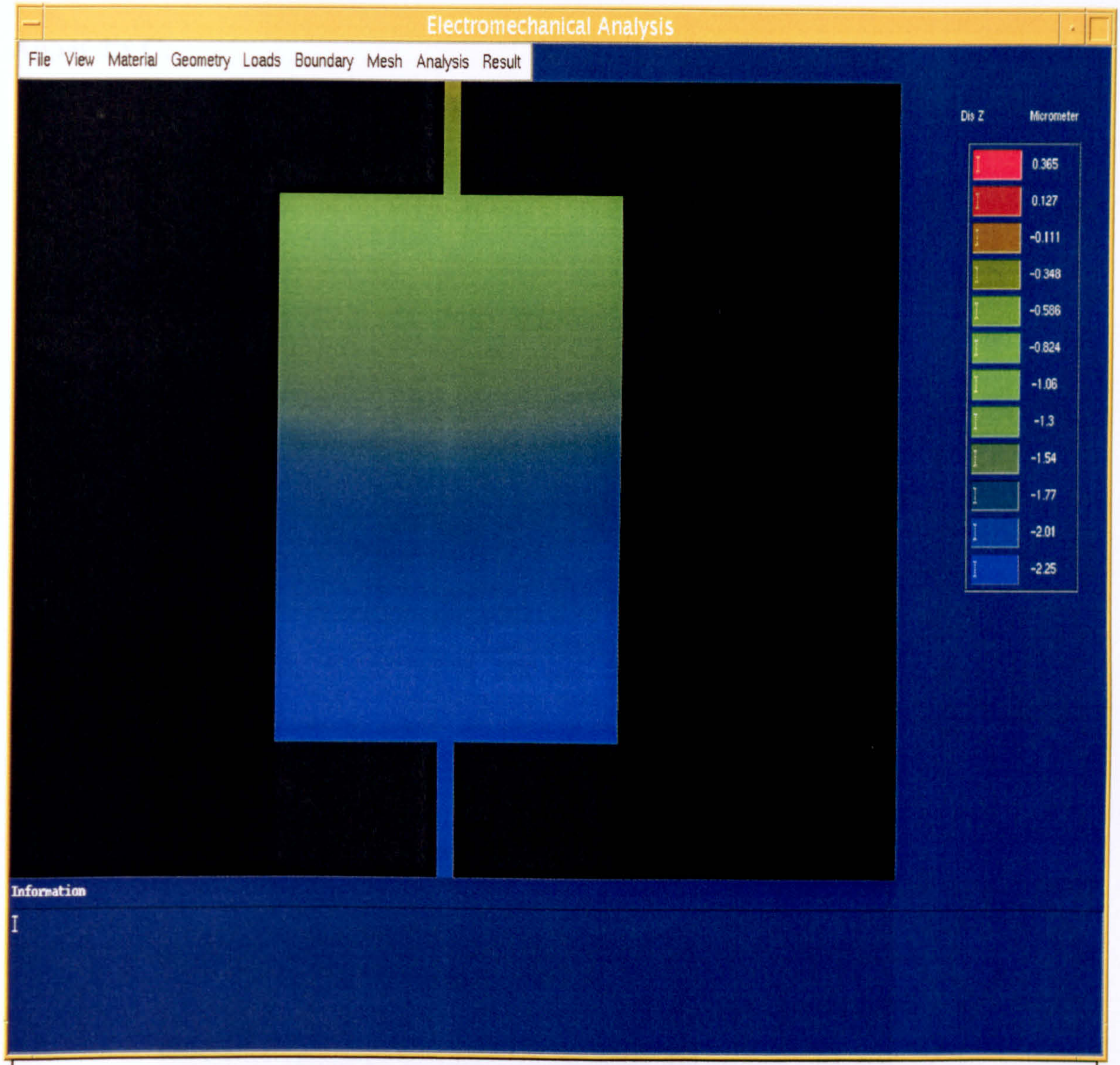

(d) V = 200 V

The results from IntelliSuite. The colours represent the different Z-axis displacements due to different applied voltages.

Appendix C:

SEM pictures of devices operated using SDAs

1. Micromirror erected by SDA array.

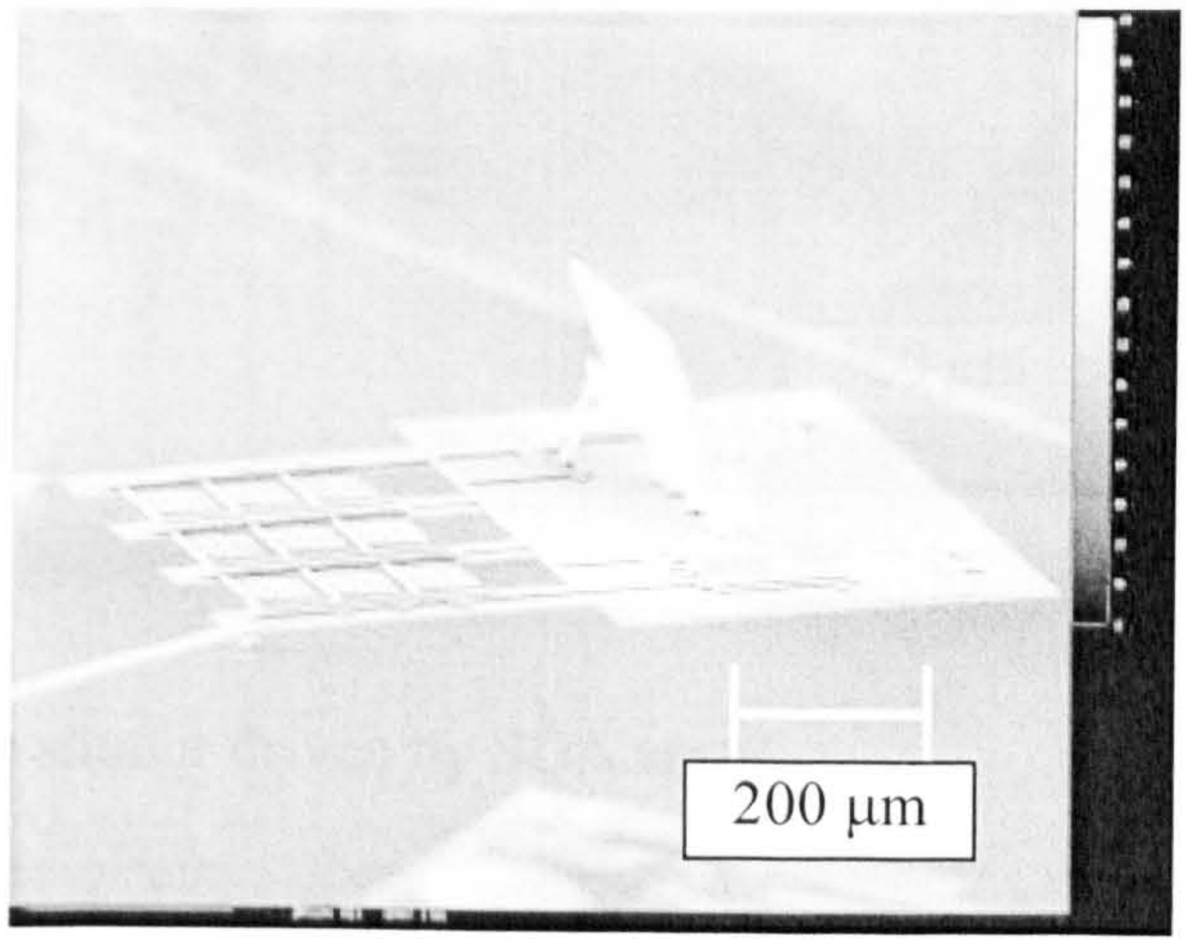

2. Micromirror lifted up by four SDA arrays.

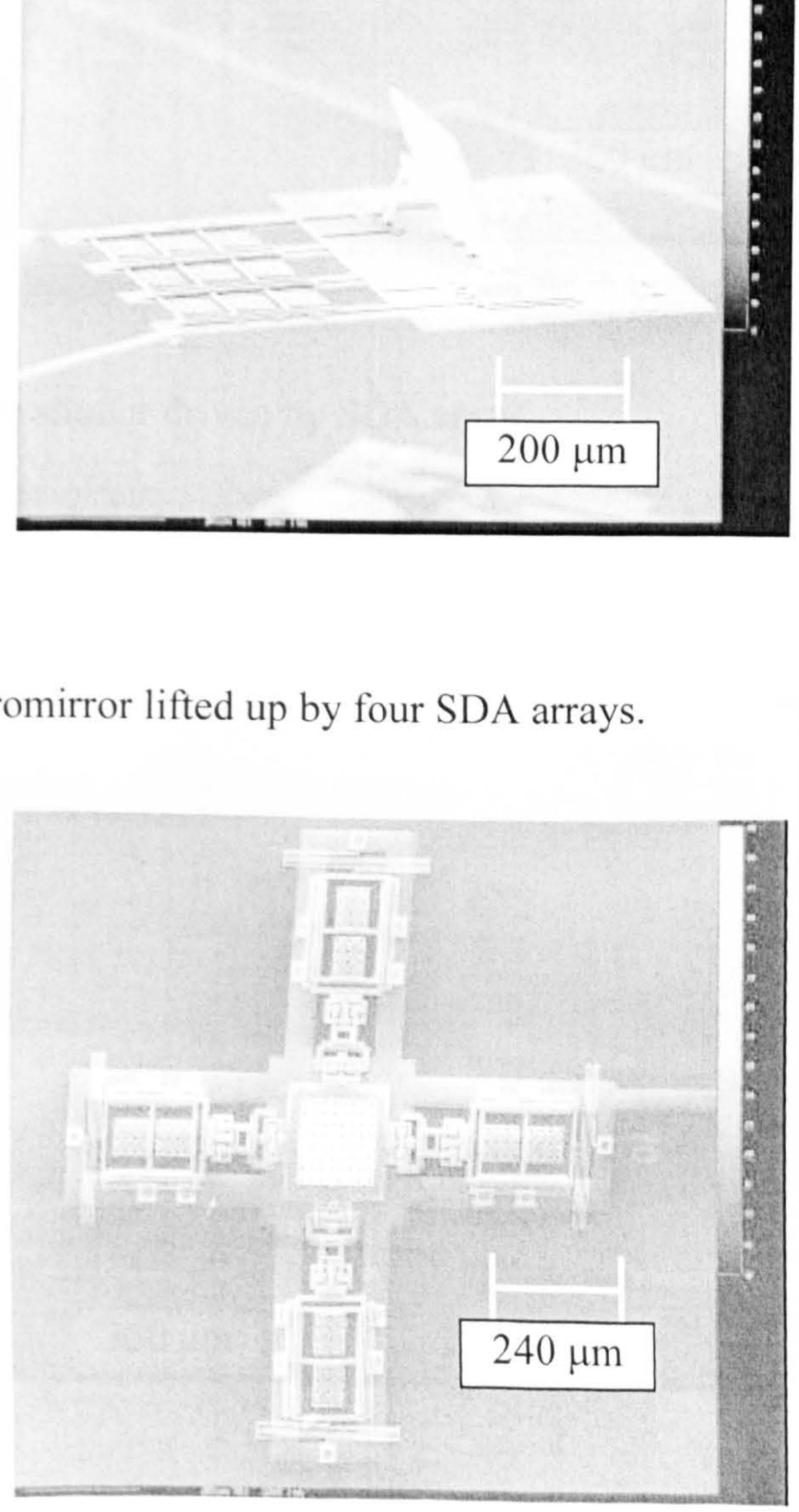

3. Microshutter driven by SDA array.

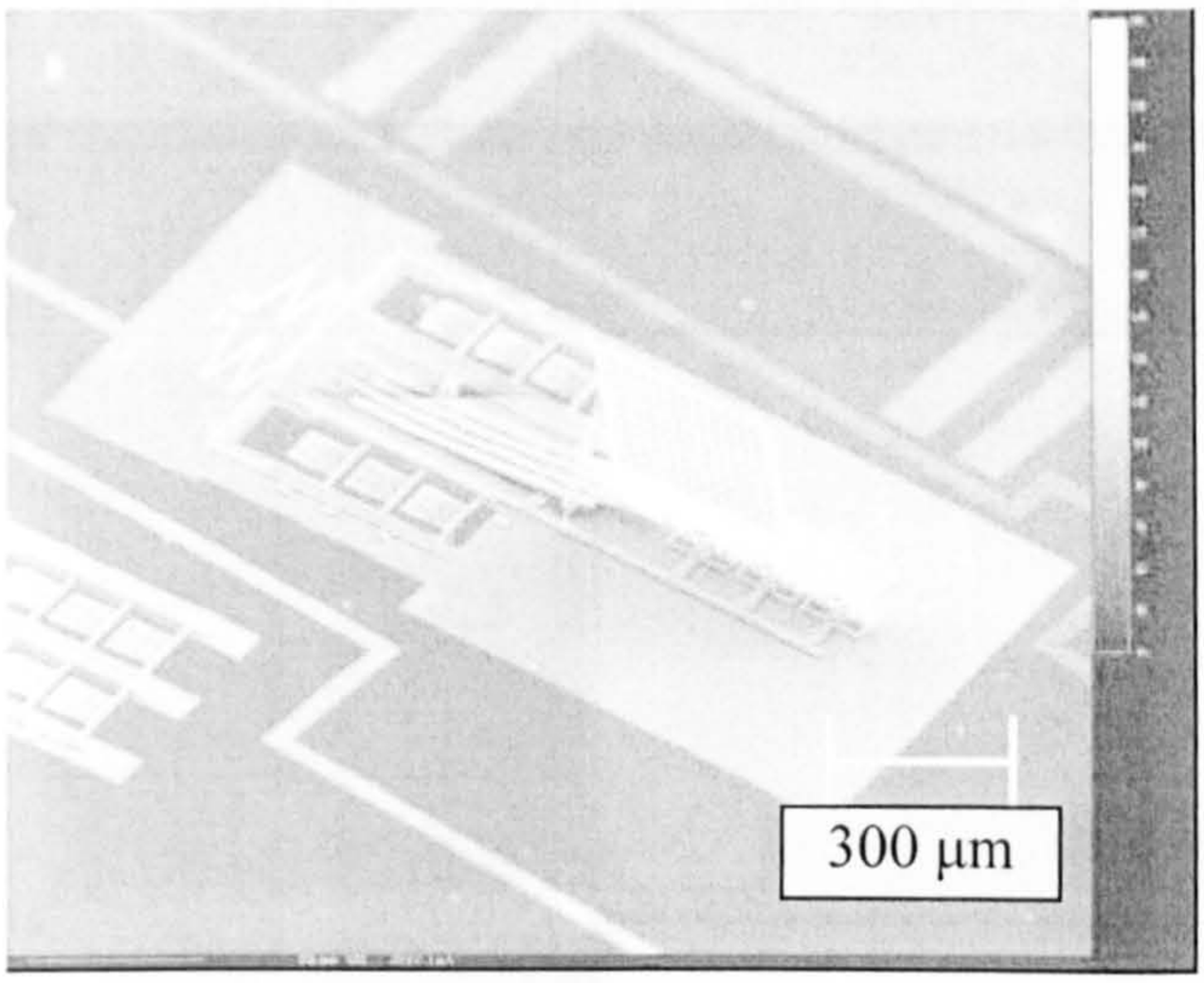

4. Micro shutter driven by SDA array.

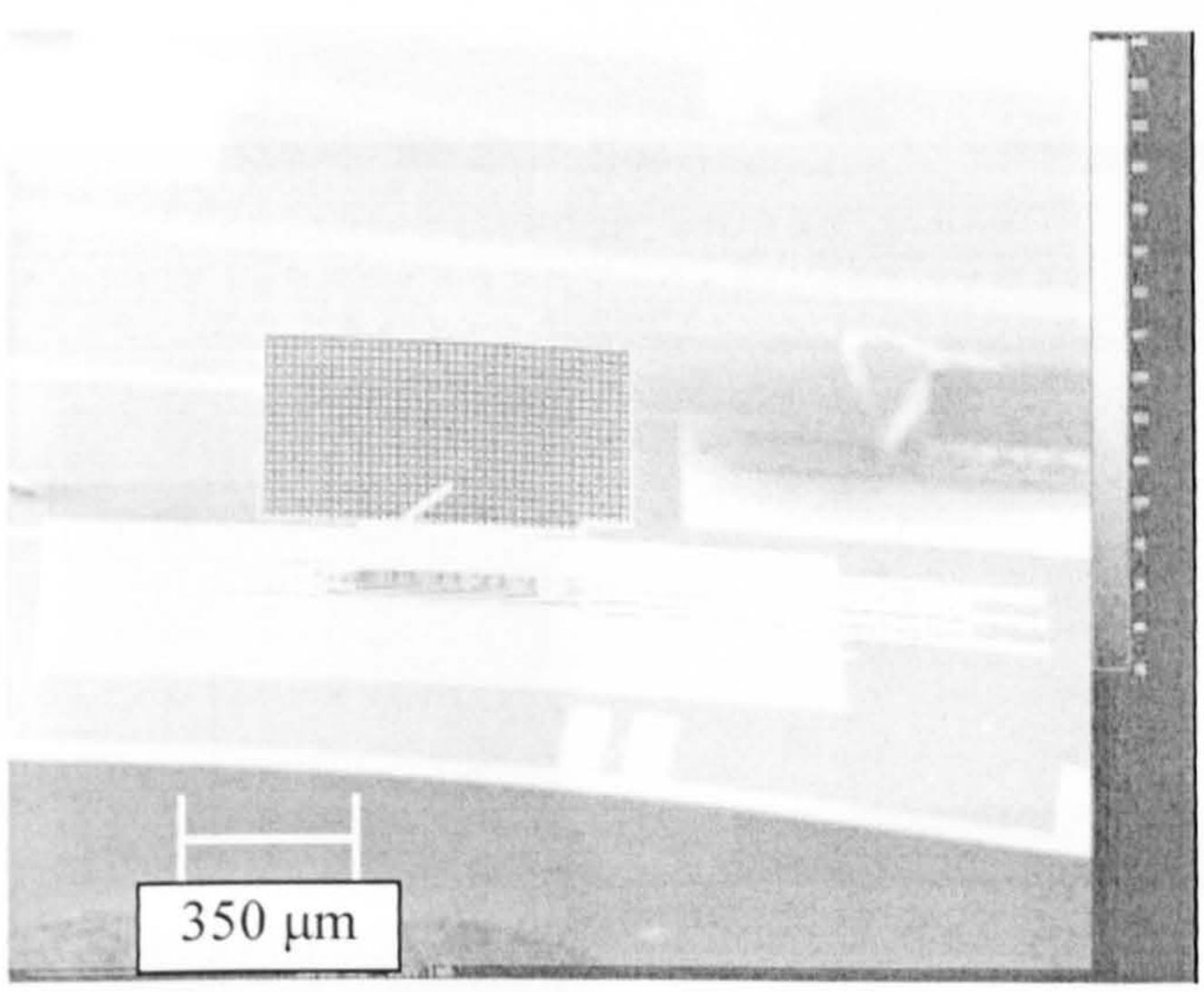

Appendix D:

Layouts for novel and traditional thermal actuators

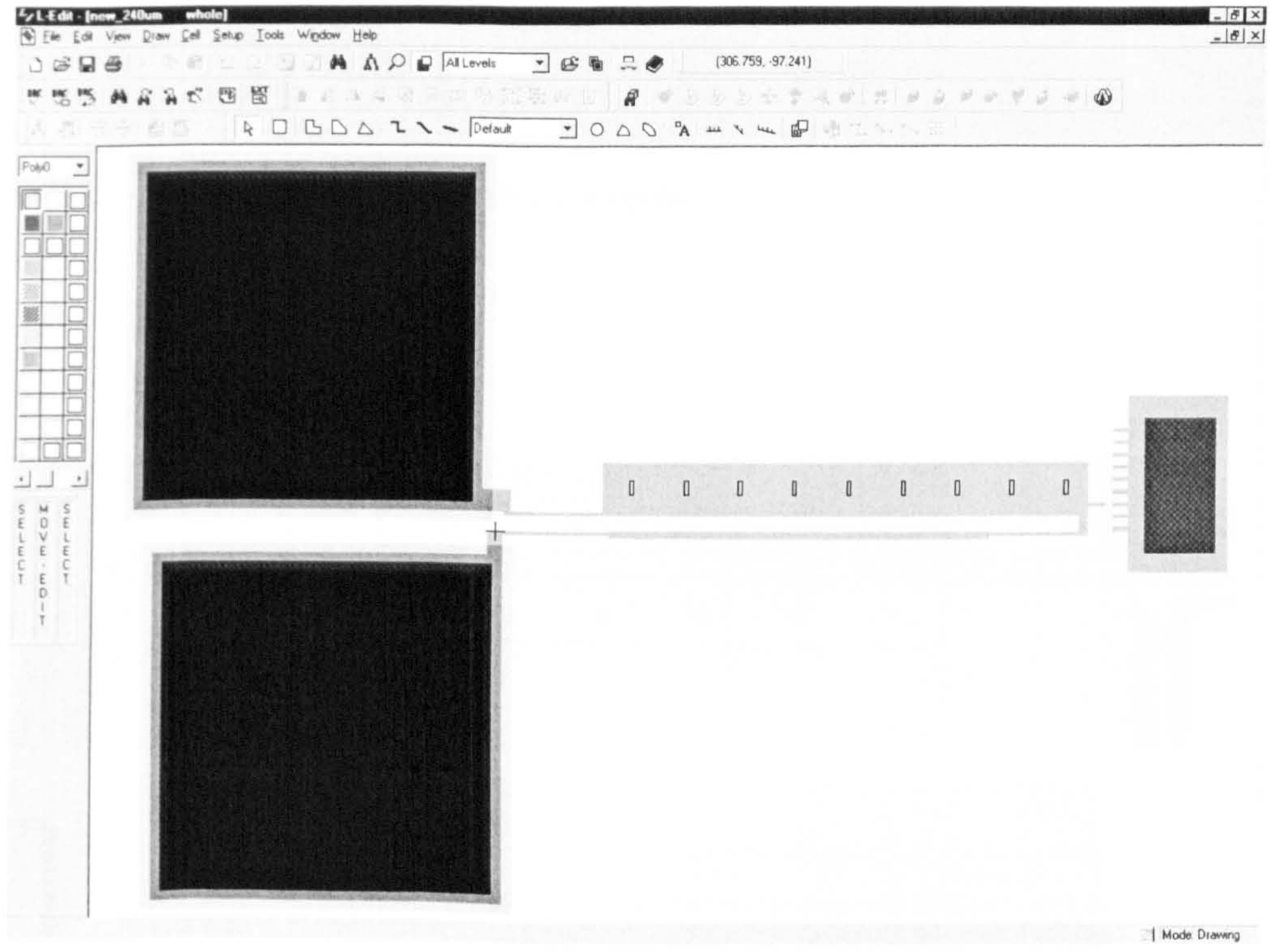

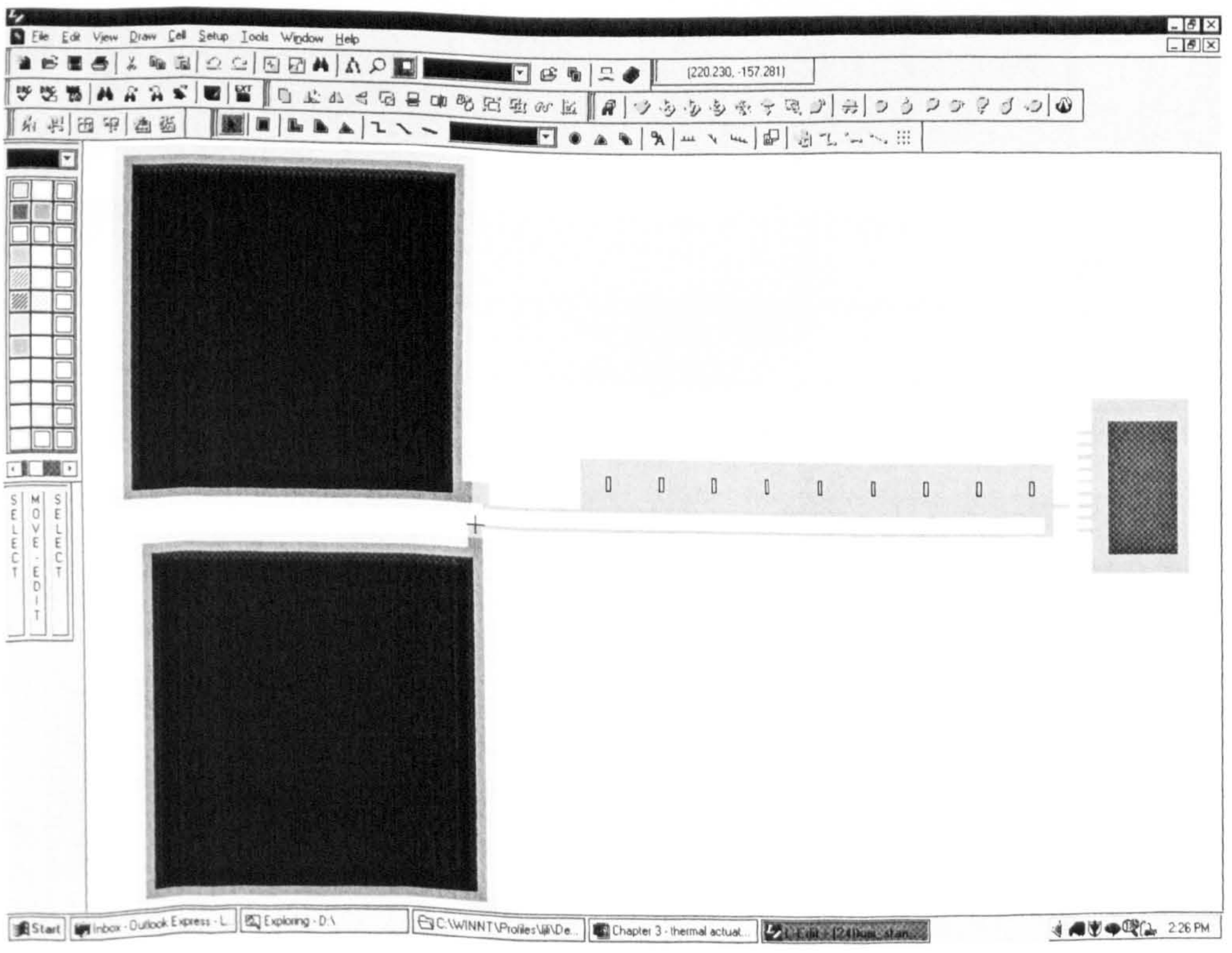

Appendix E:

Images from testing novel and traditional thermal actuators

1. DC 1.12 V is applied to both structures.

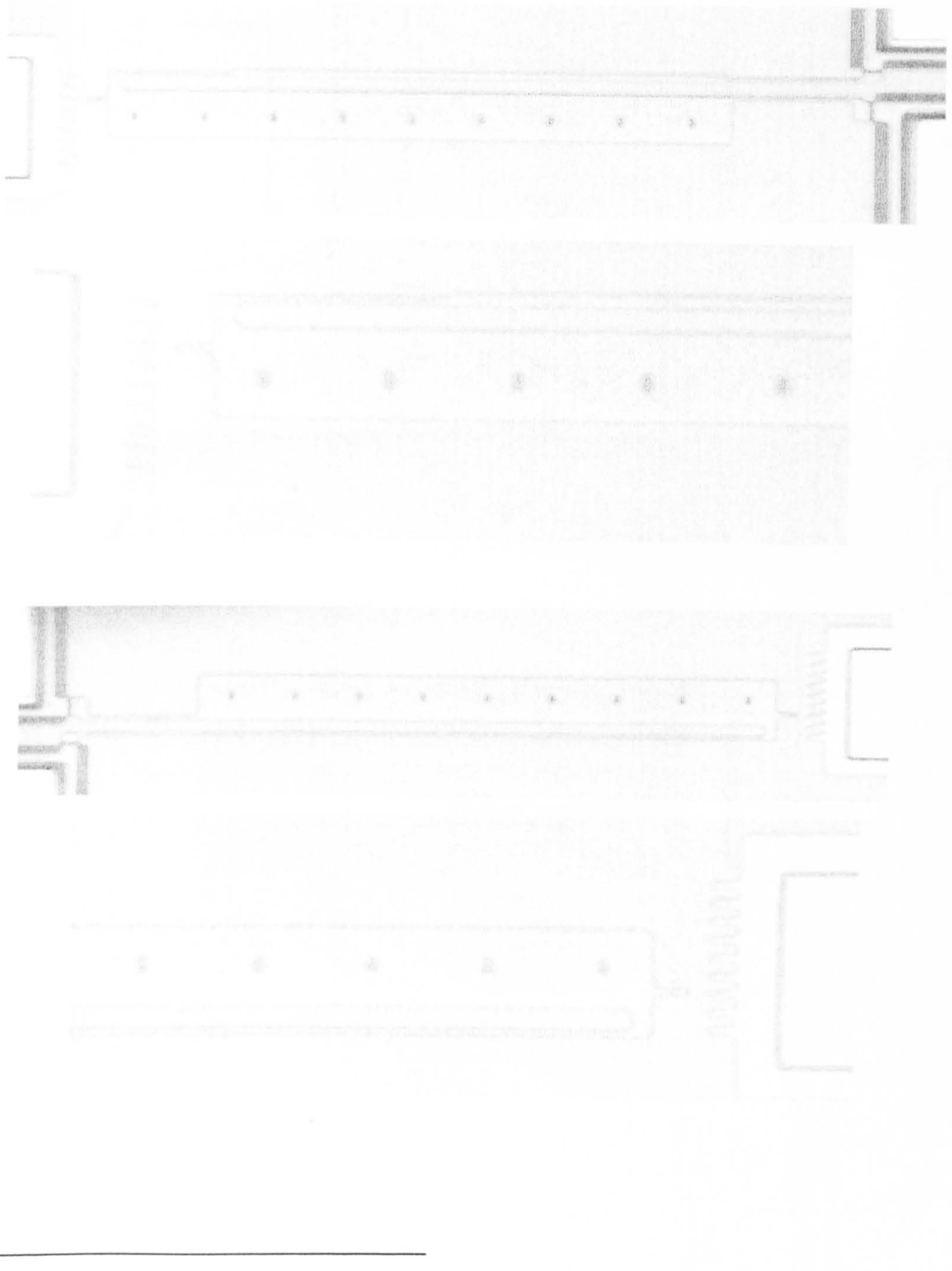

2. DC 4.4 V is applied to both structures.

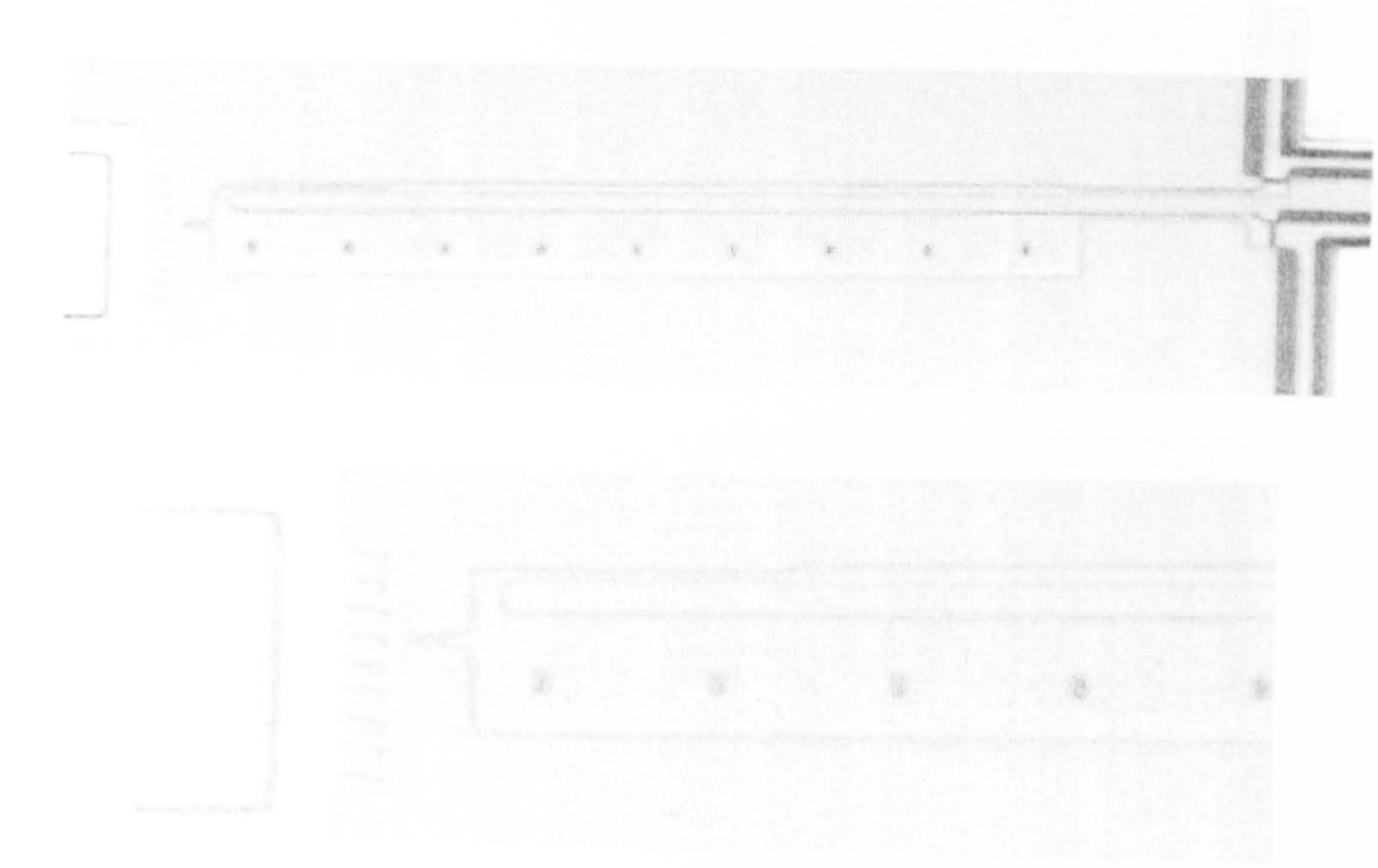

3. DC 7.4 V is applied to both structures.

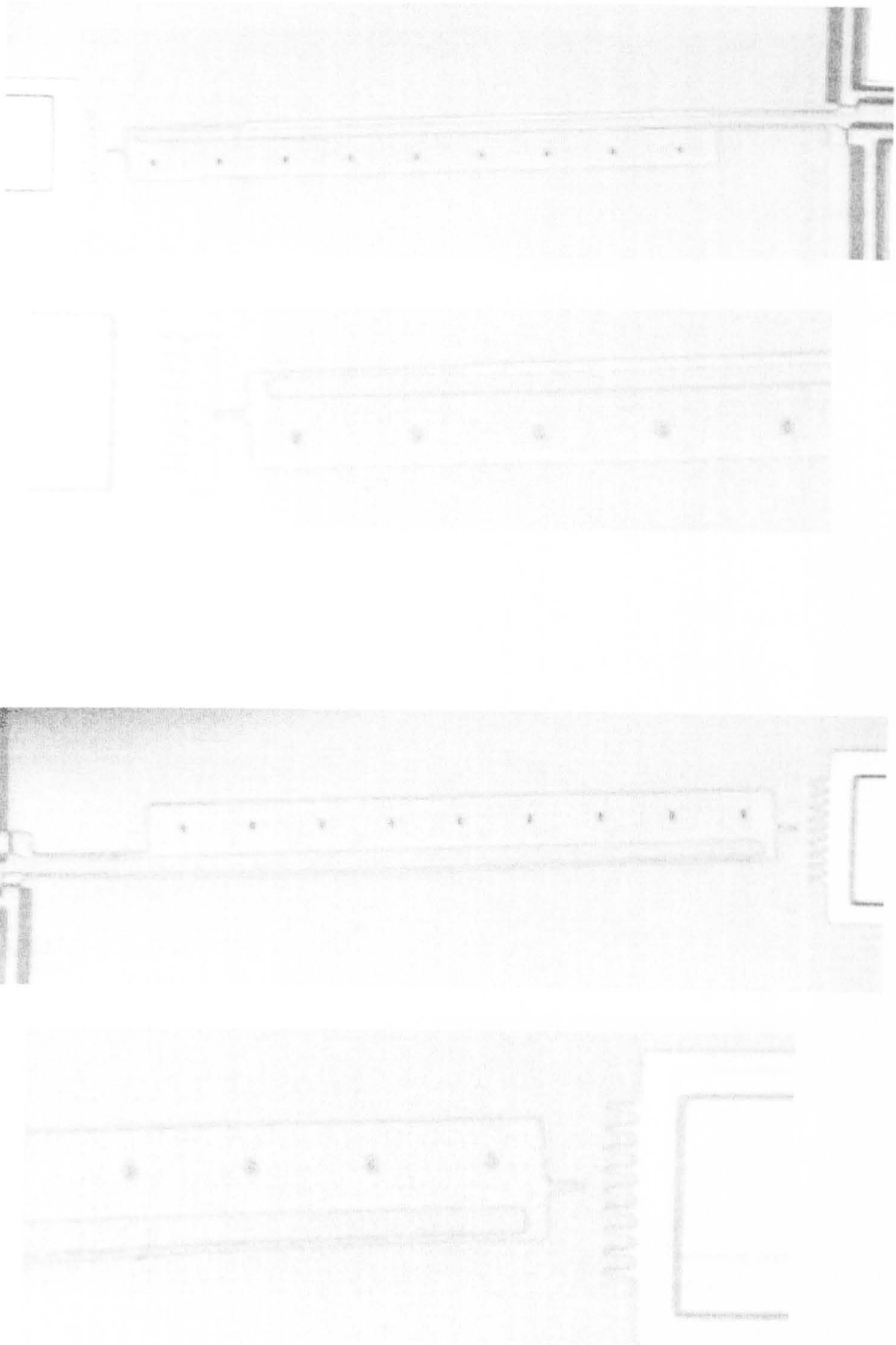

4. DC 4.4 V is applied to both structures.

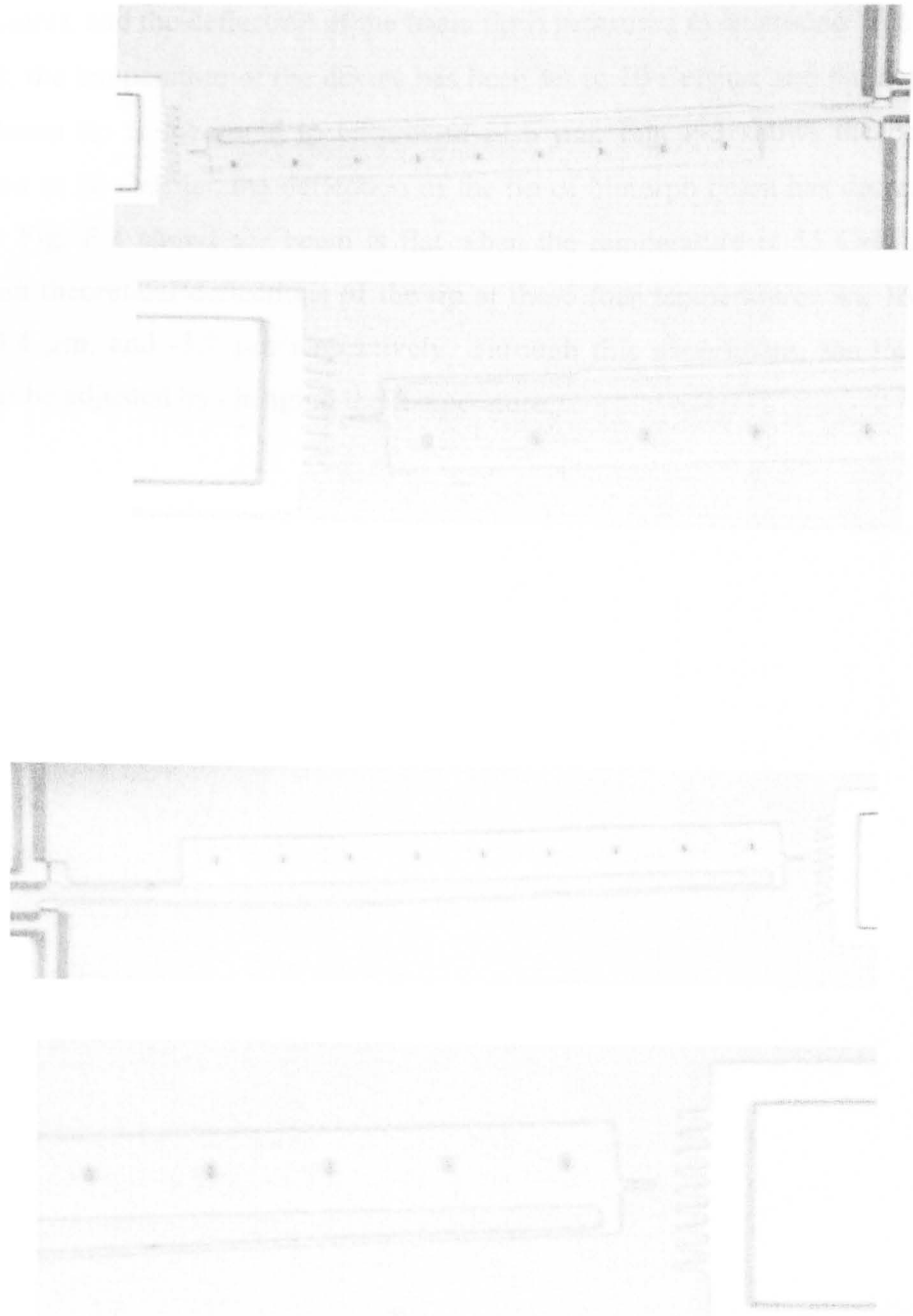

Appendix F:

Measurements of Stress-induced beam under different temperatures.

In Figure F-1, the temperature of the device has been set to 20 Celsius (room temperature), and the deflection of the beam tip is measured to be around 16.6 μm. In Fig. F-2, the temperature of the device has been set to 10 Celsius, and the deflection of the beam tip is measured to be around 21.6 μm. Fig. F-3 shows the beam tip deflection at 30 Celsius; the deflection of the tip of bimorph beam has decreased to 8.4 μm. Fig. F-4 shows the beam is flat when the temperature is 55 Celsius. The expansion theoretical deflections of the tip at these four temperatures are 16.6 μm, 23.3, 10.4 μm, and -5.7 μm respectively. Through this experiment, the tip of the beam can be adjusted by changing the temperature.

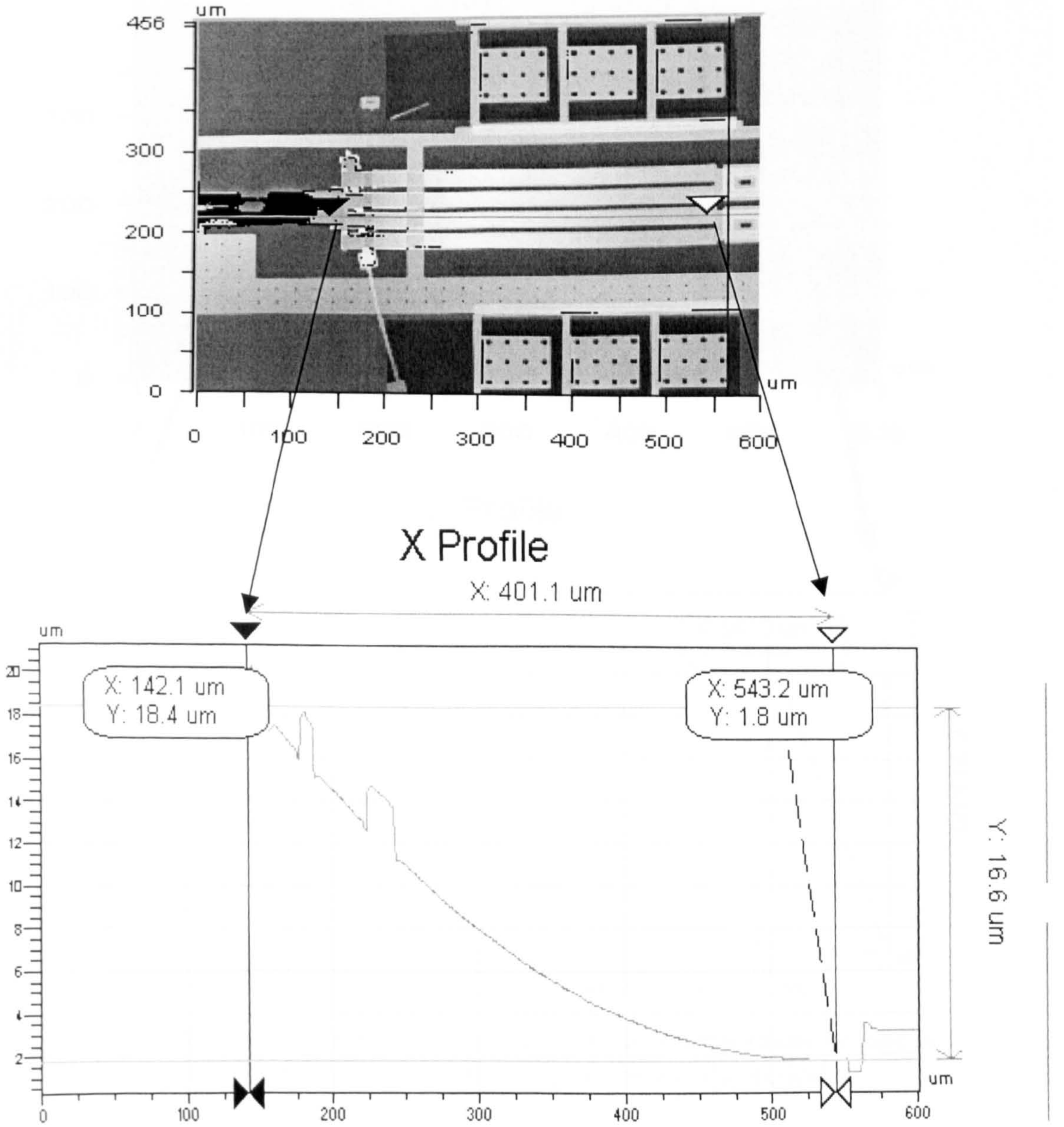

Fig. F-1: The temperature is set to be 20 °C (room temperature), and temperature change is 0 K. Measured deflection is 16.6 μm and theoretical deflection is 17 μm from figure 11.

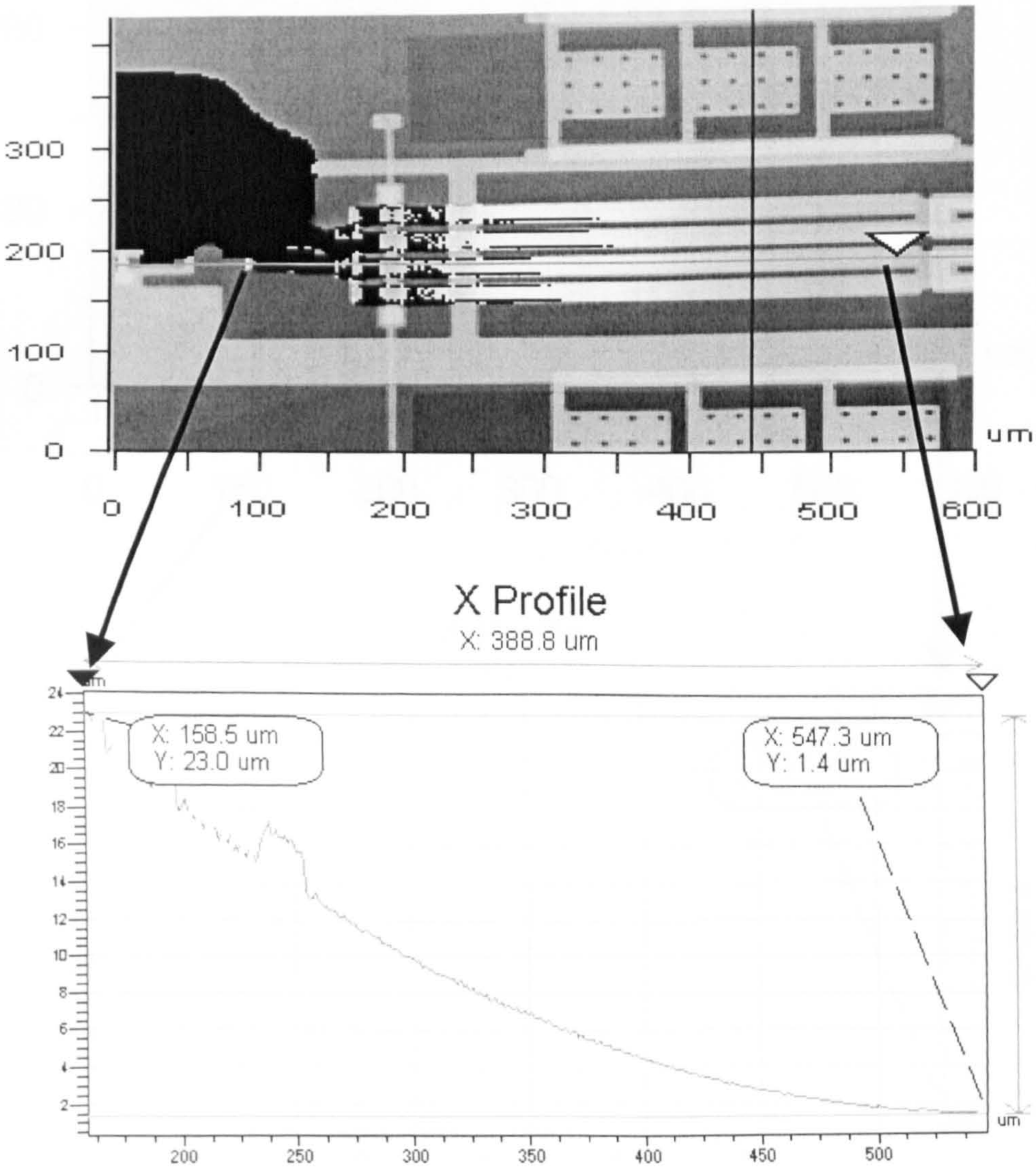

Fig. F-2: The temperature is set to be 10 °C, and temperature change is -10 K. Measured deflection is 21.6 μm and theoretical deflection is 23.3 μm from figure 11.

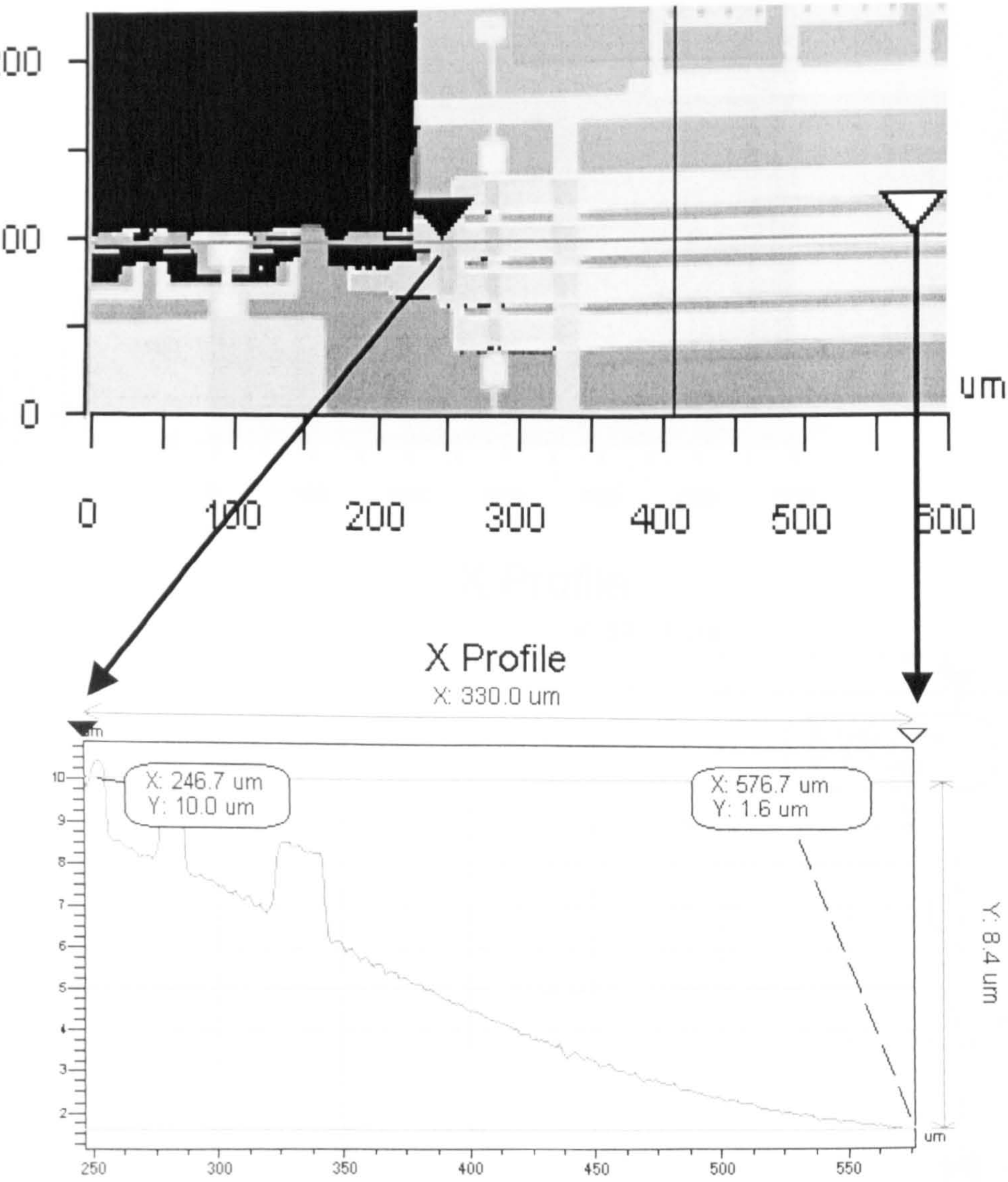

Fig. F-3: The temperature is set to be 30 °C, and temperature change is 10 K. Measured deflection is 8.4 μm and theoretical deflection is 10.4 μm from figure 11.

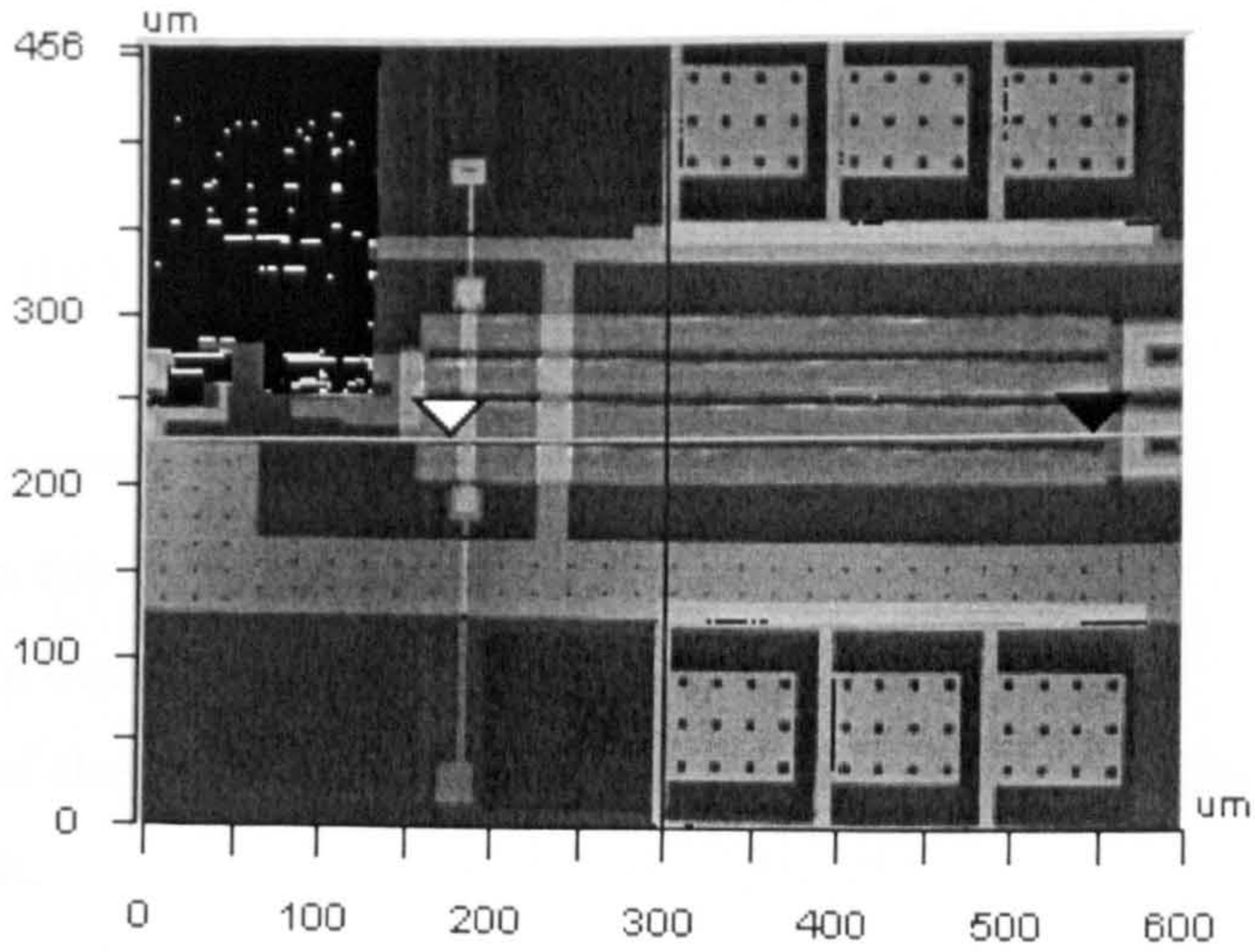

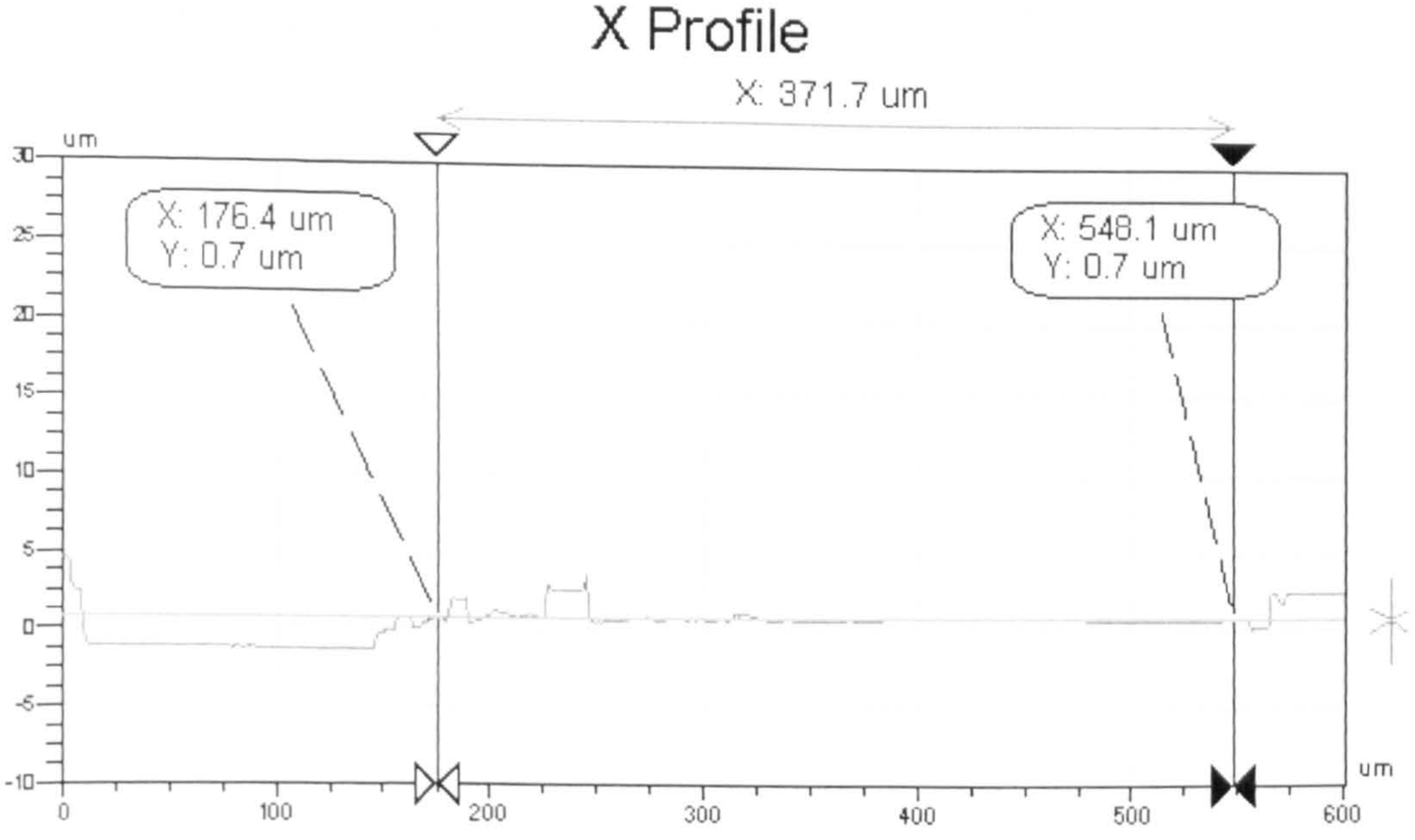

Fig. F-4: The temperature is set to be 55 °C, and temperature change is 35 K. Measured deflection is 0 μm and theoretical deflection is –5.7 μm from figure 11.

Appendix G:

Matlab script for optimising the structure of the novel asymmetric thermal actuators.

```
%June 2002. (Lijie)

%**********************************************
%This program for calculating the relationship between
%W and Trm in certain length. where W is the width of the
%central part of the hot beam. Trm is the minimum value of Tr (Tmax/Tav).
%L is the length.
%w1 is the width of other part of hot beam, which is fixed to be 2 um.
%Pa1=L1/ L;   Pa2= L2/ L; (0~1).
%
%**********************************************
w2=1e-6;
for xx=1:10
  w2=w2+1e-6;
Pa1=-0.01;
for m=1:101
Pa1=Pa1+0.01;
Pa2=-0.01;
for n=1:101
Pa2=Pa2+0.01;
T0=20;
U=15000;
k=50;
r=22e-6;
```

```
I=7e-3;

w1=2e-6;  % variable width of wider
beam
%w2=3.5e-6;
w3=w1;
w4=22e-6;  % wide beam width
w5=w1;
t=2e-6;

A1=t*w1;
A2=t*w2;
A3=t*w3;
A4=t*w4;
A5=t*w5;

L=240e-6;
    L1=Pa1*L;    % variable length of
thin beam
L2=Pa2*L;   % variable length of
wide beam
L3=L-Pa1*L-Pa2*L;
L4=200/240*L;

R1=r*L1/A1;
R2=r*L2/A2;
R3=r*L3/A3;
R4=r*L4/A4;
R5=r*(L1+L2+L3-L4)/A5;

P1=2*(w1+t);
P2=2*(w2+t);
P3=2*(w3+t);
P4=2*(w4+t);
P5=2*(w5+t);

V=I*(R1+R2+R3+R4+R5);

V1=V*R1/(R1+R2+R3+R4+R5);
V2=V*R2/(R1+R2+R3+R4+R5);
V3=V*R3/(R1+R2+R3+R4+R5);
V4=V*R4/(R1+R2+R3+R4+R5);
V5=V*R5/(R1+R2+R3+R4+R5);

m1=(U*P1/(A1*k))^(1/2);
m2=(U*P2/(A2*k))^(1/2);
m3=(U*P3/(A3*k))^(1/2);
m4=(U*P4/(A4*k))^(1/2);
m5=(U*P5/(A5*k))^(1/2);

if Pa1==0 & Pa2~=0 & Pa1+Pa2<1

c=exp(m2*(L1+L2));
d=exp(m3*(L1+L2));
e=exp(m3*(L1+L2+L3));
f=exp(m4*(L1+L2+L3));
g=exp(m4*(L1+L2+L3+L4));
h=exp(m5*(L1+L2+L3+L4));
k=exp(m5*(L1+L2+L3)*2);

T0=20;
T02=T0+(V2^2)/(U*P2*R2*L2);
T03=T0+(V3^2)/(U*P3*R3*L3);
T04=T0+(V4^2)/(U*P4*R4*L4);
T05=T0+(V5^2)/(U*P5*R5*(L1+L2+L3-L4));

%syms a b c d e f g h k m1 m2 m3 m4 m5 T0
T01 T02 T03 T04 T05
A=[1 1 0 0 0 0 0 0;c 1/c -d -1/d 0 0 0 0;c -1/c -
m3*w3/m2/w2*d m3*w3/m2/w2/d 0 0 0 0;0 0 e
1/e -f -1/f 0 0;0 0 e -1/e -m4*w4/m3/w3*f
m4*w4/m3/w3/f 0 0;0 0 0 0 g 1/g -h -1/h;0 0 0 0 g
-1/g -m5*w5/m4/w4*h m5*w5/m4/w4/h;0 0 0 0 0
0 k 1/k];
```

```
B=[T0-T02;T03-T02;0;T04-
T03;0;T05-T04;0;T0-T05];
C=A^(-1);
D=C*B;

C3=[1 0 0 0 0 0 0 0]*D;
C4=[0 1 0 0 0 0 0 0]*D;
C5=[0 0 1 0 0 0 0 0]*D;
C6=[0 0 0 1 0 0 0 0]*D;
C7=[0 0 0 0 1 0 0 0]*D;
C8=[0 0 0 0 0 1 0 0]*D;
C9=[0 0 0 0 0 0 1 0]*D;
C10=[0 0 0 0 0 0 0 1]*D;

x2=L1:2e-6:(L1+L2);
T2=T02+C3*exp(m2*x2)+C4*exp(-
m2*x2);

x3=(L1+L2):2e-6:(L1+L2+L3);
T3=T03+C5*exp(m3*x3)+C6*exp(-
m3*x3);

x4=(L1+L2+L3):2e-
6:(L1+L2+L3+L4);
T4=T04+C7*exp(m4*x4)+C8*exp(-
m4*x4);

x5=(L1+L2+L3+L4):2e-
6:(L1+L2+L3)*2;
T5=T05+C9*exp(m5*x5)+C10*exp(-
m5*x5);

Tavh=(2e-6*sum(T2)+2e-
6*sum(T3))/(L1+L2+L3)-T0;
Tavc=(2e-6*sum(T4)+2e-
6*sum(T5))/(L1+L2+L3)-T0; %cold
beam and flexture beam average
tempereture:
Tav=Tavh-Tavc;

T=[T2 T3 T4 T5]';
Tmax=max(T);
Tr(m,n)=Tmax/Tav;
if Tav<0
  Tr(m,n)=inf;
end

elseif Pa2==0 & Pa1~=0 & Pa1+Pa2<1

  a=exp(m1*L1);
b=exp(m3*L1);
e=exp(m3*(L1+L2+L3));
f=exp(m4*(L1+L2+L3));
g=exp(m4*(L1+L2+L3+L4));
h=exp(m5*(L1+L2+L3+L4));
k=exp(m5*(L1+L2+L3)*2);

T0=20;
T01=T0+(V1^2)/(U*P1*R1*L1);
T03=T0+(V3^2)/(U*P3*R3*L3);
T04=T0+(V4^2)/(U*P4*R4*L4);
T05=T0+(V5^2)/(U*P5*R5*(L1+L2+L3-L4));

%syms a b c d e f g h k m1 m2 m3 m4 m5 T0
T01 T02 T03 T04 T05
Aa=[1 1 0 0 0 0 0 0;a 1/a -b -1/b 0 0 0 0;a -1/a -
m3*w3/m1/w1*b m3*w3/m1/w1/b 0 0 0 0;0 0 e
1/e -f -1/f 0 0;0 0 e -1/e -m4*w4/m3/w3*f
m4*w4/m3/w3/f 0 0;0 0 0 0 g 1/g -h -1/h;0 0 0 0 g
-1/g -m5*w5/m4/w4*h m5*w5/m4/w4/h;0 0 0 0 0
0 k 1/k];
Bb=[T0-T01;T03-T01;0;T04-T03;0;T05-
T04;0;T0-T05];
Cc=Aa^(-1);
Dd=Cc*Bb;

C11=[1 0 0 0 0 0 0 0]*Dd;
C22=[0 1 0 0 0 0 0 0]*Dd;
```

```
C55=[0 0 1 0 0 0 0 0]*Dd;
C66=[0 0 0 1 0 0 0 0]*Dd;
C77=[0 0 0 0 1 0 0 0]*Dd;
C88=[0 0 0 0 0 1 0 0]*Dd;
C99=[0 0 0 0 0 0 1 0]*Dd;
C100=[0 0 0 0 0 0 0 1]*Dd;

x1=0:2e-6:L1;
T1=T01+C11*exp(m1*x1)+C22*exp(-
m1*x1);

x3=(L1+L2):2e-6:(L1+L2+L3);
T3=T03+C55*exp(m3*x3)+C66*exp(-
m3*x3);

x4=(L1+L2+L3):2e-
6:(L1+L2+L3+L4);
T4=T04+C77*exp(m4*x4)+C88*exp(-
m4*x4);

x5=(L1+L2+L3+L4):2e-
6:(L1+L2+L3)*2;
T5=T05+C99*exp(m5*x5)+C100*exp(-
m5*x5);

Tavh=(2e-6*sum(T1)+2e-
6*sum(T3))/(L1+L2+L3)-T0;
Tavc=(2e-6*sum(T4)+2e-
6*sum(T5))/(L1+L2+L3)-T0; %cold
beam and flexture beam average
tempereture;
Tav=Tavh-Tavc;

T=[T1 T3 T4 T5]';
Tmax=max(T);
Tr(m,n)=Tmax/Tav;

if Tav<0
  Tr(m,n)=inf;
end

elscif Pa1+Pa2==1 & Pa1~=0 & Pa2~=0

  a=exp(m1*L1);
b=exp(m2*L1);
c=exp(m2*(L1+L2));
d=exp(m4*(L1+L2));
g=exp(m4*(L1+L2+L3+L4));
h=exp(m5*(L1+L2+L3+L4));
k=exp(m5*(L1+L2+L3)*2);

T0=20;
T01=T0+(V1^2)/(U*P1*R1*L1);
T02=T0+(V2^2)/(U*P2*R2*L2);
T04=T0+(V4^2)/(U*P4*R4*L4);
T05=T0+(V5^2)/(U*P5*R5*(L1+L2+L3-L4));

%syms a b c d e f g h k m1 m2 m3 m4 m5 T0
T01 T02 T03 T04 T05
A=[1 1 0 0 0 0 0 0;a 1/a -b -1/b 0 0 0 0;a -1/a -
m2*w2/m1/w1*b m2*w2/m1/w1/b 0 0 0 0;0 0 c
1/c -d -1/d 0 0;0 0 c -1/c -m4*w4/m2/w2*d
m4*w4/m2/w2/d 0 0;0 0 0 0 g 1/g -h -1/h;0 0 0 0 g
-1/g -m5*w5/m4/w4*h m5*w5/m4/w4/h;0 0 0 0 0
0 k 1/k];
B=[T0-T01;T02-T01;0;T04-T02;0;T05-
T04;0;T0-T05];
C=A^(-1);
D=C*B;

C1=[1 0 0 0 0 0 0 0]*D;
C2=[0 1 0 0 0 0 0 0]*D;
C3=[0 0 1 0 0 0 0 0]*D;
C4=[0 0 0 1 0 0 0 0]*D;
C7=[0 0 0 0 1 0 0 0]*D;
C8=[0 0 0 0 0 1 0 0]*D;
```

```
C9=[0 0 0 0 0 0 1 0]*D;
C10=[0 0 0 0 0 0 0 1]*D;

x1=0:2e-6:L1;
T1=T01+C1*exp(m1*x1)+C2*exp(-
m1*x1);

x2=L1:2e-6:(L1+L2);
T2=T02+C3*exp(m2*x2)+C4*exp(-
m2*x2);

x4=(L1+L2+L3):2e-
6:(L1+L2+L3+L4);
T4=T04+C7*exp(m4*x4)+C8*exp(-
m4*x4);

x5=(L1+L2+L3+L4):2e-
6:(L1+L2+L3)*2;
T5=T05+C9*exp(m5*x5)+C10*exp(-
m5*x5);

Tavh=(2e-6*sum(T1)+2e-
6*sum(T2))/(L1+L2+L3)-T0;
Tavc=(2e-6*sum(T4)+2e-
6*sum(T5))/(L1+L2+L3)-T0; %cold
beam and flexture beam average
tempereture;
Tav=Tavh-Tavc;
T=[T1 T2 T3 T4 T5]';
Tmax=max(T);
Tr(m,n)=Tmax/Tav;

if Tav<0
  Tr(m,n)=inf;
end


elseif Pa1==1 & Pa2==0
   a=exp(m1*L1);
b=exp(m4*L1);
g=exp(m4*(L1+L2+L3+L4));
h=exp(m5*(L1+L2+L3+L4));
k=exp(m5*(L1+L2+L3)*2);

T0=20;
T01=T0+(V1^2)/(U*P1*R1*L1);
T04=T0+(V4^2)/(U*P4*R4*L4);
T05=T0+(V5^2)/(U*P5*R5*(L1+L2+L3-L4));

%syms a b c d e f g h k m1 m2 m3 m4 m5 T0
T01 T02 T03 T04 T05
A=[1 1 0 0 0 0;a 1/a -b -1/b 0 0;a -1/a -
m4*w4/m1/w1*b m4*w4/m1/w1/b 0 0;0 0 g 1/g -
h -1/h;0 0 g -1/g -m5*w5/m4/w4*h
m5*w5/m4/w4/h;0 0 0 0 k 1/k];
B=[T0-T01;T04-T01;0;T05-T04;0;T0-T05];
C=A^(-1);
D=C*B;

C1=[1 0 0 0 0 0]*D;
C2=[0 1 0 0 0 0]*D;
C7=[0 0 1 0 0 0]*D;
C8=[0 0 0 1 0 0]*D;
C9=[0 0 0 0 1 0]*D;
C10=[0 0 0 0 0 1]*D;

x1=0:2e-6:L1;
T1=T01+C1*exp(m1*x1)+C2*exp(-m1*x1);

x4=(L1+L2+L3):2e-6:(L1+L2+L3+L4);
T4=T04+C7*exp(m4*x4)+C8*exp(-m4*x4);

x5=(L1+L2+L3+L4):2e-6:(L1+L2+L3)*2;
T5=T05+C9*exp(m5*x5)+C10*exp(-m5*x5);
```

```
Tavh=(2e-6*sum(T1))/(L1+L2+L3)-
T0;
Tavc=(2e-6*sum(T4)+2e-
6*sum(T5))/(L1+L2+L3)-T0; %cold
beam and flexture beam average
tempereture;
Tav=Tavh-Tavc;

% the maximum temperature of the
hot beam;

T=[T1 T4 T5]';
Tmax=max(T);
Tr(m,n)=Tmax/Tav;

if Tav<0
  Tr(m,n)=inf;
end

  elseif Pa2==1 & Pa1==0


c=exp(m2*(L1+L2));
d=exp(m4*(L1+L2));
g=exp(m4*(L1+L2+L3+L4));
h=exp(m5*(L1+L2+L3+L4));
k=exp(m5*(L1+L2+L3)*2);

T0=20;
T02=T0+(V2^2)/(U*P2*R2*L2);
T04=T0+(V4^2)/(U*P4*R4*L4);
T05=T0+(V5^2)/(U*P5*R5*(L1+L2+L
3-L4));

%syms a b c d e f g h k m1 m2 m3 m4
m5 T0 T01 T02 T03 T04 T05
A=[1 1 0 0 0 0;c 1/c -d -1/d 0 0;c -1/c -
m4*w4/m2/w2*d m4*w4/m2/w2/d 0
0;0 0 g 1/g -h -1/h;0 0 g -1/g -m5*w5/m4/w4*h
m5*w5/m4/w4/h;0 0 0 0 k 1/k];
B=[T0-T01;T02-T01;0;T03-T02;0;T04-
T03;0;T05-T04;0;T0-T05];
C=A^(-1);
D=C*B;

C3=[1 0 0 0 0 0]*D;
C4=[0 1 0 0 0 0]*D;
C7=[0 0 1 0 0 0]*D;
C8=[0 0 0 1 0 0]*D;
C9=[0 0 0 0 1 0]*D;
C10=[0 0 0 0 0 1]*D;


x2=L1:2e-6:(L1+L2);
T2=T02+C3*exp(m2*x2)+C4*exp(-m2*x2);

x4=(L1+L2+L3):2e-6:(L1+L2+L3+L4);
T4=T04+C7*exp(m4*x4)+C8*exp(-m4*x4);

x5=(L1+L2+L3+L4):2e-6:(L1+L2+L3)*2;
T5=T05+C9*exp(m5*x5)+C10*exp(-m5*x5);

Tavh=(2e-6*sum(T2))/(L1+L2+L3)-T0;
Tavc=(2e-6*sum(T4)+2e-
6*sum(T5))/(L1+L2+L3)-T0; %cold beam and
flexture beam average tempereture;
Tav=Tavh-Tavc;

% the maximum temperature of the hot beam:

T=[T2 T4 T5]';
Tmax=max(T);
Tr(m,n)=Tmax/Tav;

if Tav<0
  Tr(m,n)=inf;
end
```

```
elseif Pa1==0 & Pa2==0

e=exp(m3*(L1+L2+L3));
f=exp(m4*(L1+L2+L3));
g=exp(m4*(L1+L2+L3+L4));
h=exp(m5*(L1+L2+L3+L4));
k=exp(m5*(L1+L2+L3)*2);

T0=20;
T03=T0+(V3^2)/(U*P3*R3*L3);
T04=T0+(V4^2)/(U*P4*R4*L4);
T05=T0+(V5^2)/(U*P5*R5*(L1+L2+L
3-L4));

%syms a b c d e f g h k m1 m2 m3 m4
m5 T0 T01 T02 T03 T04 T05
A=[1 1 0 0 0 0;e 1/e -f -1/f 0 0;e -1/e -
m4*w4/m3/w3*f m4*w4/m3/w3/f 0 0;0
0 g 1/g -h -1/h;0 0 g -1/g -
m5*w5/m4/w4*h m5*w5/m4/w4/h;0 0
0 0 k 1/k];
B=[T0-T03;T04-T03;0;T05-T04;0;T0-
T05];
C=A^(-1);
D=C*B;

C5=[1 0 0 0 0 0]*D;
C6=[0 1 0 0 0 0]*D;
C7=[0 0 1 0 0 0]*D;
C8=[0 0 0 1 0 0]*D;
C9=[0 0 0 0 1 0]*D;
C10=[0 0 0 0 0 1]*D;

x3=(L1+L2):2e-6:(L1+L2+L3);
T3=T03+C5*exp(m3*x3)+C6*exp(-
m3*x3);
x4=(L1+L2+L3):2e-6:(L1+L2+L3+L4);
T4=T04+C7*exp(m4*x4)+C8*exp(-m4*x4);

x5=(L1+L2+L3+L4):2e-6:(L1+L2+L3)*2;
T5=T05+C9*exp(m5*x5)+C10*exp(-m5*x5);

Tavh=(2e-6*sum(T3))/(L1+L2+L3)-T0;
Tavc=(2e-6*sum(T4)+2e-
6*sum(T5))/(L1+L2+L3)-T0; %cold beam and
flexture beam averagе tempereture;
Tav=Tavh-Tavc;

% the maximum temperature of the hot beam;

T=[T3 T4 T5]';
Tmax=max(T);
Tr(m,n)=Tmax/Tav;

if Tav<0
  Tr(m,n)=inf;
end

elseif Pa1+Pa2<1 & Pa1~=0 & Pa2~=0

  a=exp(m1*L1);
b=exp(m2*L1);
c=exp(m2*(L1+L2));
d=exp(m3*(L1+L2));
e=exp(m3*(L1+L2+L3));
f=exp(m4*(L1+L2+L3));
g=exp(m4*(L1+L2+L3+L4));
h=exp(m5*(L1+L2+L3+L4));
k=exp(m5*(L1+L2+L3)*2);

   T0=20;
T01=T0+(V1^2)/(U*P1*R1*L1);
```

```
T02=T0+(V2^2)/(U*P2*R2*L2);
T03=T0+(V3^2)/(U*P3*R3*L3);
T04=T0+(V4^2)/(U*P4*R4*L4);
T05=T0+(V5^2)/(U*P5*R5*(L1+L2+L
3-L4));

%syms a b c d e f g h k m1 m2 m3 m4
m5 T0 T01 T02 T03 T04 T05
A=[1 1 0 0 0 0 0 0 0 0 0;a 1/a -b -1/b 0 0 0
0 0 0;a -1/a -m2*w2/m1/w1*b
m2*w2/m1/w1/b 0 0 0 0 0 0;0 0 c 1/c -d
-1/d 0 0 0 0;0 0 c -1/c -m3*w3/m2/w2*d
m3*w3/m2/w2/d 0 0 0 0;0 0 0 0 e 1/e -f
-1/f 0 0;0 0 0 0 e -1/e -m4*w4/m3/w3*f
m4*w4/m3/w3/f 0 0;0 0 0 0 0 0 g 1/g -h
-1/h;0 0 0 0 0 0 g -1/g -
m5*w5/m4/w4*h m5*w5/m4/w4/h;0 0
0 0 0 0 0 0 k 1/k];
B=[T0-T01;T02-T01;0;T03-
T02;0;T04-T03;0;T05-T04;0;T0-T05];
C=A^(-1);
D=C*B;

C1=[1 0 0 0 0 0 0 0 0 0 0]*D;
C2=[0 1 0 0 0 0 0 0 0 0 0]*D;
C3=[0 0 1 0 0 0 0 0 0 0 0]*D;
C4=[0 0 0 1 0 0 0 0 0 0 0]*D;
C5=[0 0 0 0 1 0 0 0 0 0 0]*D;
C6=[0 0 0 0 0 1 0 0 0 0 0]*D;
C7=[0 0 0 0 0 0 1 0 0 0 0]*D;
C8=[0 0 0 0 0 0 0 1 0 0 0]*D;
C9=[0 0 0 0 0 0 0 0 1 0 0]*D;
C10=[0 0 0 0 0 0 0 0 0 0 1]*D;

x1=0:2e-6:L1;
T1=T01+C1*exp(m1*x1)+C2*exp(-
m1*x1);

x2=L1:2e-6:(L1+L2);
T2=T02+C3*exp(m2*x2)+C4*exp(-m2*x2);

x3=(L1+L2):2e-6:(L1+L2+L3);
T3=T03+C5*exp(m3*x3)+C6*exp(-m3*x3);

x4=(L1+L2+L3):2e-6:(L1+L2+L3+L4);
T4=T04+C7*exp(m4*x4)+C8*exp(-m4*x4);

x5=(L1+L2+L3+L4):2e-6:(L1+L2+L3)*2;
T5=T05+C9*exp(m5*x5)+C10*exp(-m5*x5);

%plot(x1,T1,'b',x2,T2,'b',x3,T3,'b',x4,T4,'b',x5,
T5,'b')

% the average temperature is
Tavi=1/Li*int(T(x)i,x1,x2); only calculate the
average beam along the hot beam;

Tavh=(2e-6*sum(T1)+2e-6*sum(T2)+2e-
6*sum(T3))/(L1+L2+L3)-T0;
Tavc=(2e-6*sum(T4)+2e-
6*sum(T5))/(L1+L2+L3)-T0; %cold beam and
flexture beam average tempereture;
Tav=Tavh-Tavc;

% the maximum temperature of the hot beam;

T=[T1 T2 T3 T4 T5]';
Tmax=max(T);
Tr(m,n)=Tmax/Tav;

if Tav<0
  Tr(m,n)=inf;
end

else
  Tr(m,n)=inf;
end
```

```
end
end

Trm(xx)=min(min(Tr));
%|Q1,Q2|=find(Tr==Trm);
%Q11=Q1*0.01-0.01;
%Q12=Q2*0.01-0.01;

%Q11*L;
%Q12*L;
if w2==w1 | L2==0  %fixed the value
for w=2 um.

[pa1,pa2]=find(Tr==inf);
Nu=size(find(Tr==inf))*[1;0];
Tr(pa1,pa2)=Trm;
Trm(xx)=sum(sum(Tr))/(m*n);
end

end

qw=1e-6;
for No=1:10
  qw=qw+1e-6;
 wq(No)=qw;
end
plot(wq,Trm)
```